



AFRL-RB-WP-TR-2009-3139

THERMO-VIBRO-ACOUSTIC LOADS AND FATIGUE OF HYPERSONIC FLIGHT VEHICLE STRUCTURE

**Robert D. Blevins, Dimitri Bofilios, Ian Holehouse, Vicky W. Hwa, Matthew D. Tratt,
Anthony L. Laganelli, Peter Pozefsky, and Mauro Pierucci**

Goodrich Aerostructures Group

**JUNE 2009
Final Report**

Approved for public release; distribution unlimited.

See additional restrictions described on inside pages

STINFO COPY

**AIR FORCE RESEARCH LABORATORY
AIR VEHICLES DIRECTORATE
WRIGHT-PATTERSON AIR FORCE BASE, OH 45433-7542
AIR FORCE MATERIEL COMMAND
UNITED STATES AIR FORCE**

NOTICE AND SIGNATURE PAGE

Using Government drawings, specifications, or other data included in this document for any purpose other than Government procurement does not in any way obligate the U.S. Government. The fact that the Government formulated or supplied the drawings, specifications, or other data does not license the holder or any other person or corporation; or convey any rights or permission to manufacture, use, or sell any patented invention that may relate to them.

This report was cleared for public release by the USAF 88th Air Base Wing (88 ABW) Public Affairs Office (PAO) and is available to the general public, including foreign nationals. Copies may be obtained from the Defense Technical Information Center (DTIC) (<http://www.dtic.mil>).

AFRL-RB-WP-TR-2009-3139 HAS BEEN REVIEWED AND IS APPROVED FOR PUBLICATION IN ACCORDANCE WITH ASSIGNED DISTRIBUTION STATEMENT.

*//Signature//

S. MICHAEL SPOTTSWOOD
Project Engineer
Analytical Mechanics Branch
Structures Division

//Signature//

ANDREW G. SPARKS, Chief
Analytical Mechanics Branch
Structures Division

//Signature//

DAVID M. PRATT
Technical Advisor
Structures Division
Air Vehicles Directorate

This report is published in the interest of scientific and technical information exchange, and its publication does not constitute the Government's approval or disapproval of its ideas or findings.

*Disseminated copies will show “//Signature//” stamped or typed above the signature blocks.

REPORT DOCUMENTATION PAGE					<i>Form Approved</i> OMB No. 0704-0188			
The public reporting burden for this collection of information is estimated to average 1 hour per response, including the time for reviewing instructions, searching existing data sources, gathering and maintaining the data needed, and completing and reviewing the collection of information. Send comments regarding this burden estimate or any other aspect of this collection of information, including suggestions for reducing this burden, to Department of Defense, Washington Headquarters Services, Directorate for Information Operations and Reports (0704-0188), 1215 Jefferson Davis Highway, Suite 1204, Arlington, VA 22202-4302. Respondents should be aware that notwithstanding any other provision of law, no person shall be subject to any penalty for failing to comply with a collection of information if it does not display a currently valid OMB control number. PLEASE DO NOT RETURN YOUR FORM TO THE ABOVE ADDRESS.								
1. REPORT DATE (DD-MM-YY) June 2009		2. REPORT TYPE Final		3. DATES COVERED (From - To) 17 November1987 – 17 November 1989				
4. TITLE AND SUBTITLE THERMO-VIBRO-ACOUSTIC LOADS AND FATIGUE OF HYPERSONIC FLIGHT VEHICLE STRUCTURE				5a. CONTRACT NUMBER F33615-87-C-3227				
				5b. GRANT NUMBER				
				5c. PROGRAM ELEMENT NUMBER 62201F				
6. AUTHOR(S) Robert D. Blevins, Dimitri Bofilios, Ian Holehouse, Vicky W. Hwa, Matthew D. Tratt, Anthony L. Laganelli, Peter Pozefsky, and Mauro Pierucci				5d. PROJECT NUMBER 2401				
				5e. TASK NUMBER 04				
				5f. WORK UNIT NUMBER 24010439				
7. PERFORMING ORGANIZATION NAME(S) AND ADDRESS(ES) Goodrich Aerostructures Group 850 Lagoon Drive Chula Vista, CA 91910-2098				8. PERFORMING ORGANIZATION REPORT NUMBER				
9. SPONSORING/MONITORING AGENCY NAME(S) AND ADDRESS(ES) Air Force Research Laboratory Air Vehicles Directorate Wright-Patterson Air Force Base, OH 45433-7542 Air Force Materiel Command United States Air Force				10. SPONSORING/MONITORING AGENCY ACRONYM(S) AFRL/RBSM				
				11. SPONSORING/MONITORING AGENCY REPORT NUMBER(S) AFRL-RB-WP-TR-2009-3139				
12. DISTRIBUTION/AVAILABILITY STATEMENT Approved for public release; distribution unlimited.								
13. SUPPLEMENTARY NOTES PAO Case Number: 88ABW 2009-2326; Clearance Date: 03 Jun 2009. Report contains color. This is the best quality available of this report.								
14. ABSTRACT Research was completed in 1989. A three-phase study of the “Thermo-Vibro-Acoustic Loads and Fatigue of Hypersonic Flight Vehicle Structure” is being performed by Rohr Industries, Inc., McDonnell Douglas Corporation and Science Applications International Corporation. The Phase I Study (AFWAL-TR-89-3014) evaluated various hypersonic vehicle designs and identified potential fatigue related issues resulting from high temperature vibroacoustic loads. This report contains the results of Phase II. A typical trajectory calling for ascent to orbit in 15 minutes and a generic Blended Wing Body vehicle design have been identified. Detailed designs for forebody, ramp, stabilizer, and nozzle skin panels are developed. Aerothermal and acoustic loads are determined. Analysis is made to determine temperatures, mean stress, and dynamic stress in panels. The results show that aeroacoustic loading will be critical for the design of ramp, stabilizer and nozzle vehicle skin panels.								
15. SUBJECT TERMS transatmospheric vehicle; sonic fatigue; high temperature fatigue; acoustic susceptibility; hypersonic; combined environment; hot structure								
16. SECURITY CLASSIFICATION OF: <table border="1" style="width: 100%; border-collapse: collapse;"> <tr> <td style="padding: 2px;">a. REPORT Unclassified</td> <td style="padding: 2px;">b. ABSTRACT Unclassified</td> <td style="padding: 2px;">c. THIS PAGE Unclassified</td> </tr> </table>			a. REPORT Unclassified	b. ABSTRACT Unclassified	c. THIS PAGE Unclassified	17. LIMITATION OF ABSTRACT: SAR		18. NUMBER OF PAGES 482
a. REPORT Unclassified	b. ABSTRACT Unclassified	c. THIS PAGE Unclassified						
			19a. NAME OF RESPONSIBLE PERSON (Monitor) S. Michael Spottswood		19b. TELEPHONE NUMBER (Include Area Code) N/A			

CONTENTS

<u>Section</u>	<u>Page</u>
FOREWORD	XX
EXECUTIVE SUMMARY	1
1 INTRODUCTION	1-1
1.1 Transatmospheric Hypersonic Vehicle Mission and Trajectory	1-1
1.2 Skin Environment and Materials	1-10
1.3 Description of Transatmospheric Vehicle	1-18
1.3.1 Design Considerations	1-18
1.3.2 Blended Wing Body (BWB) Vehicle and Skin Panels	1-21
1.4 Evaluation of Thermo-Vibro-Acoustic Loads and Fatigue	1-30
1.5 References	1-34
2 AEROACOUSTIC LOADS	2-1
2.1 Introduction	2-1
2.2 Aeroacoustic Loads in Attached Flow	2-3
2.3 Aeroacoustic Loads for Shock-Boundary Layer Interaction Flows	2-7
2.3.1 Influence of Geometry on Shock-Boundary Layer Interaction	2-8
2.3.2 Correlation of Shock-Boundary Layer Interactions	2-11

CONTENTS

<u>Section</u>		<u>Page</u>
2.4	Boundary Layer Transition	2-26
2.5	Application to Blended Wing Body Transatmospheric Vehicle	2-32
2.5.1	External Flow Field	2-32
2.5.2	Loads in Attached Turbulent Boundary Layer Flow	2-33
2.5.3	Aeroacoustic Loads for Shock- Boundary Layer Interaction Regions	2-40
2.5.4	Pressure and Heat Transfer Predictions for Shock-Boundary Layer Interactions ...	2-47
2.6	Conclusions and Recommendations	2-55
2.7	Nomenclature	2-59
2.8	References	2-60
3	ENGINE ACOUSTIC LOADS	3-1
3.1	Introduction	3-1
3.2	Techniques for Prediction of Engine Induced Acoustic Loads	3-1
3.3	Sound Levels Due to Engines of Transatmospheric Aircraft	3-4
3.3.1	Sound Levels Due to Rocket Engines	3-4
3.3.2	Scramjet Engine Sound Levels	3-18
3.3.3	Combined Sound Levels	3-24
3.4	Results and Conclusions	3-29
3.5	References	3-30

CONTENTS

<u>Section</u>	<u>Page</u>
4 ANALYSIS OF FOREBODY PANEL	4-1
4.1 Introduction	4-1
4.2 Thermal Analysis	4-3
4.3 Static Stress Analysis	4-15
4.3.1 Properties and Finite Element Model	4-15
4.3.2 Panel Loads and Constraints	4-24
4.3.3 Results	4-28
4.4 Dynamic Analysis	4-33
4.4.1 Introduction	4-33
4.4.2 Modal Analysis	4-33
4.4.3 Sonic Fatigue Analysis	4-38
4.5 Results	4-45
4.6 References	4-49
5 ANALYSIS OF RAMP PANEL	5-1
5.1 Introduction	5-1
5.2 Thermal Analysis	5-3
5.3 Static Stress Analysis	5-14
5.3.1 Properties and Finite Element Model	5-14
5.3.2 Panel Loads and Constraints	5-17
5.3.3 Results	5-17
5.4 Dynamic Analysis	5-22
5.4.1 Introduction	5-22

CONTENTS

<u>Section</u>	<u>Page</u>
5.4.2	Modal Analysis 5-22
5.4.3	Sonic Fatigue Analysis 5-27
5.5	Results 5-31
5.6	References 5-32
6	ANALYSIS OF STABILIZER PANEL 6-1
6.1	Introduction 6-1
6.2	Loading on Horizontal Stabilizer Panel 6-3
7	ANALYSIS OF ACTIVELY COOLED PANEL 7-1
7.1	Introduction 7-1
7.2	Panel Geometry 7-3
7.3	Vehicle Loads 7-4
7.4	Preliminary Analysis 7-8
7.5	Finite Element Modeling 7-11
7.6	Finite Element Analysis 7-14
7.7	Results and Conclusions 7-23
7.8	References 7-24
8	EXPERIMENTAL PLAN 8-1
8.1	Introduction 8-1
8.2	Test Articles 8-3
8.3	Test Facilities 8-15
8.3.1	Electrodynamic Shakers 8-15

CONTENTS

<u>Section</u>		<u>Page</u>
	8.3.2	Progressive Wave Tube 8-15
	8.3.3	Modal Analysis Test System 8-21
	8.3.4	Calibration, Data Acquisition, and Data Reduction Systems 8-23
	8.3.5	High-Temperature Instrumentation 8-25
	8.4	Shaker Tests 8-26
	8.5	Progressive Wave Tube Panel Tests 8-35
	8.6	Program Schedule 8-44
	8.7	References 8-44
9		DYNAMIC ANALYSIS OF CARBON-CARBON TEST PANELS 9-1
	9.1	Modal Analysis 9-1
	9.1.1	Concept 1 9-3
	9.1.2	Concept 2 9-3
	9.1.3	Concept 3 9-3
	9.2	Sonic Fatigue Analysis 9-13
	9.2.1	Concept 1 9-14
	9.2.2	Concept 2 9-14
	9.2.3	Concept 3 9-19
	9.3	Conclusions 9-19
	9.4	References 9-19
10		CONCLUSIONS 10-1

CONTENTS

<u>Section</u>	<u>Page</u>
APPENDIX A: PNS SOLUTIONS OF HEAT TRANSFER AND SUBSEQUENT ACOUSTIC LOAD DEFINITION ON THE BLENDED WING BODY	A-1
APPENDIX B: ENGINE ACOUSTIC ANALYSIS SUPPORTING DATA	B-1
APPENDIX C: FINITE ELEMENT ACTIVELY COOLED PANEL RESULTS	C-1
APPENDIX D: DAMAGE ACCUMULATION FOR HIGH CYCLE FATIGUE	D-1
APPENDIX E: VEHICLE CARRY-THROUGH LOADS	E-1

LIST OF FIGURES

<u>Figure</u>	<u>Page</u>
1-1 Comparison of Space Shuttle and Transatmospheric Vehicle Trajectories	1-4
1-2 Transatmospheric Hypersonic Vehicle Flight Envelopes	1-9
1-3 Transatmospheric Hypersonic Vehicle Maximum Skin Surface Temperatures	1-12
1-4 Transatmospheric Vehicle Skin Temperatures: (a) Upper Surface; (b) Lower Surface	1-13
1-5 Comparison of Strength of Various Structural Materials as a Function of Temperature	1-14
1-6 Transatmospheric Vehicle Shock-Boundary Layer Interaction Characteristics	1-16
1-7 Acoustic Levels in Disturbed Flow	1-17
1-8 Transatmospheric Vehicle Concepts	1-19
1-9 Cryogenic Fuselage Tank Concepts	1-20
1-10 Blended Wing Body (a) Bottom and (b) Top Perspectives	1-22
1-11 Blended Wing Body Section	1-23
1-12 Blended Wing Body Fore and Aft Views	1-23
1-13 Lower Forebody Panel Located 20 Feet Aft of Nose on Under Body	1-26
1-14 Aftbody Panel Located 90 Feet Aft of Nose on Upper Body	1-28

LIST OF FIGURES

<u>Figure</u>	<u>Page</u>
1-15 Ramp Panel Located 60 Feet Aft of Nose on Underside of Vehicle	1-29
1-16 Actively Cooled Nozzle Panel Located 95 Feet Aft of Nose on Underside of Vehicle	1-31
1-17 Horizontal Stabilizer Skin Panel Located 90 Feet Aft of Nose	1-32
1-18 Flow Chart for Evaluation of Thermo-Vibro-Acoustic Loads and Fatigue of Hypersonic Flight Vehicle Structure	1-33
2-1 Space Transportation System with Flow Interaction Regimes	2-2
2-2 Comparison of Normalized Spectral Measurements and Theory	2-5
2-3 RMS Pressure Variation with Mach Number - Attached Turbulent Boundary Layer Flow (Smooth Wall)	2-6
2-4 Characteristics of Shock-Boundary Layer Interactions on 2D Compression Ramp	2-9
2-5 RMS Fluctuating Pressure Distribution (2D Interaction) ...	2-10
2-6 Mean and Fluctuating Pressure Characteristics for Sharp Fin Shock Generators	2-12
2-7 Peak rms Fluctuating Pressure Augmentation over Approach Flow Levels for 2D and 3D Shock Interactions	2-13
2-8 Basic Fin Generated Shock-Boundary Layer Interaction with Peak Wall Heat Transfer (Shear) Location	2-16
2-9 Correlation of Peak rms Pressure for Shock-Boundary Layer Interactions	2-18
2-10 Power Spectra Characteristics of Approach Flow (a) and Interaction Region (b) Compared with Prediction	2-21
2-11 Typical Power Spectrum Along the Longitudinal Survey Line for Various 3D Shock Generators: $\alpha = 20^\circ$	2-22
2-12 Metallic Frusta Re-Entry Vehicle Transition Data Base - Re_θ versus M_e	2-27

LIST OF FIGURES

<u>Figure</u>	<u>Page</u>
2-13	Re_{θ}/M_e Variation with Altitude 2-29
2-14	Laminar Boundary Layer Solutions for BWB with Transition Onset Parameter 2-30
2-15	Laminar Heat Transfer Solutions for BWB 2-31
2-16	Blended Wing Body Investigation Regions 2-34
2-17	Acoustic Loads and Surface Conditions on Windward Meridian of BWB Configuration at Mach 10 2-35
2-18	Acoustic Loads and Surface Conditions on Leeward Meridian of BWB Configuration at Mach 10 2-36
2-19	RMS Pressure Distribution on Leeward and Windward Meridians of BWB Configuration at Mach 10 2-37
2-20	Power Spectra on Windward Meridian of BWB at Mach 10 2-38
2-21	Power Spectra on Leeward Meridian of BWB at Mach 10 2-39
2-22	Views of BWB (a-d) and Potential Shock-Boundary Layer Interactions (e-h) 2-41
2-23	Correlation of Maximum Heating Rate of 2D Type Shock Induced, Turbulent Separated Flows 2-49
2-24	Correlation of Plateau Heat Transfer with Plateau Pressure 2-50
2-25	Surface Heat Transfer Correlations for 3D Type Shock-Boundary Layer Interaction 2-51
3-1	Normalized Power Spectrum for Standard Rocket Engines 3-5
3-2	Axial Location of Apparent Sound Source 3-7
3-3	Directivity Pattern of Engine Sound 3-8
3-4	Sketch of Blended Wing Body Model Used in Sound Level Analysis of Upper Surface 3-9

LIST OF FIGURES

<u>Figure</u>	<u>Page</u>
3-5	Sketch of Blended Wing Body Model Used in Sound Level Analysis of Lower Surface 3-10
3-6	Sound Power Level for Upper and Lower Rocket Engines 3-13
3-7	Sound Pressure Level (Ref. 20 μ PA) on Upper Surface due to Rocket Engines 3-14
3-8	Sound Pressure Level (Ref. 20 μ PA) on Lower Surface due to Rocket Engines 3-15
3-9	Sound Power Level for Scramjet and Rocket Engines 3-21
3-10	Sound Pressure Level on Lower Surface due to Scramjet Engine 3-23
3-11	Sound Pressure Level on Lower Surface due to Combined Effect of Scramjet and Rocket Engines 3-26
3-12	Overall Sound Pressure Levels (Ref. 20 μ PA) at Selected Locations on Upper Surface 3-27
3-13	Overall Sound Pressure Levels (Ref. 20 μ PA) at Selected Locations on Lower Surface 3-28
4-1	Lower Forebody Panel Located 20 Feet Aft of Nose on Underside of Vehicle 4-2
4-2	Forebody Panel Turbulent Heat Flux Profiles During Ascent 4-6
4-3	Thermal Boundary Conditions for Carbon-Carbon Panels 4-8
4-4	P/THERMAL Model of Forebody Panel 4-10
4-5	Forebody Panel Temperature Distribution for 1000 psf at 15 Minutes 4-11
4-6	Forebody Panel Temperature Distribution for 2600 psf at 15 Minutes 4-12
4-7	Forebody Panel Temperature Distribution for 1000 psf During Ascent 4-13
4-8	Forebody Panel Temperature Distribution for 2600 psf During Ascent 4-14

LIST OF FIGURES

<u>Figure</u>	<u>Page</u>
4-9 Forebody Panel Heat Flux Profiles for 1000 psf During Ascent	4-16
4-10 Forebody Panel Temperature Distribution for 1000 psf at 15 Minutes, Laminar Heating from Mach 10	4-17
4-11 Forebody Panel Temperature Distribution for 1000 psi During Ascent, Laminar Heating from Mach 10	4-18
4-12 Maximum Panel Temperature versus Peak Heat Flux	4-19
4-13 Forebody Panel NASTRAN Model	4-21
4-14 Panel Laminate Construction	4-23
4-15 Forebody Panel Loads and Constraints	4-25
4-16 Forebody Panel Deformed Shape	4-29
4-17 Forebody Panel Stress Contours	4-31
4-18 First Buckling Mode of Forebody Panel (for Load Condition No. 2)	4-32
4-19 Forebody Panel Geometry and Boundary Conditions	4-35
4-20 Forebody Panel In-Phase and Out-of-Phase Modes for Flight Condition 2	4-36
4-21 Forebody Panel Modal Stress Fields for In-Phase and Out-of-Phase Modes Shown in Figure 4-20	4-37
4-22 Effect of Mechanical Loads on Frequency for Forebody Panel	4-39
4-23(a) Sound Pressure Level on Lower Surface due to Combined Effect of Scramjet and Rocket Engines	4-40
4-23(b) Sketch of Blended Wing Body Model Used in Sound Level Analysis of Lower Surface	4-40
4-24 One Octave Band Overall Sound Pressure Levels	4-41
4-25 Boundary Layer Induced Noise as a Function of Vehicle Location	4-42
4-26 Fatigue Data for Uncoated HTC Bar Specimens	4-44

LIST OF FIGURES

<u>Figure</u>	<u>Page</u>
4-27 Sonic Stress Levels at Forebody Panel	4-46
4-28 Forebody Panel Carbon-Carbon Sonic Stress Field with Effect of Joint Acceptance Included	4-47
5-1 Ramp Panel Located 60 Feet Aft of Nose on Underside of Vehicle	5-2
5-2 Ramp Panel Turbulent Heat Flux Profiles During Ascent	5-4
5-3 P/THERMAL Model of Ramp Panel	5-6
5-4 Ramp Panel Temperature Distribution for 1000 psf at 15 Minutes	5-7
5-5 Ramp Panel Temperature Distribution for 2600 psf at 15 Minutes	5-8
5-6 Ramp Panel Temperature Distribution for 1000 psf During Ascent	5-9
5-7 Ramp Panel Temperature Distribution for 2600 psi During Ascent	5-10
5-8 Ramp Panel Heat Flux Profiles for 1000 psf During Ascent	5-11
5-9 Ramp Panel Temperature Distribution for 1000 psf at 15 Minutes, Laminar Heating from Mach 10	5-12
5-10 Ramp Panel Temperature Distribution for 1000 psi During Ascent, Laminar Heating from Mach 10	5-13
5-11 Ramp Panel NASTRAN Model	5-15
5-12 Ramp Panel Loads and Constraints	5-18
5-13 Ramp Panel Deformed Shape	5-20
5-14 Ramp Panel Stress Contours	5-21
5-15 Ramp Panel Geometry and Boundary Conditions	5-24
5-16 Ramp Panel In-Phase and Out-of-Phase Modes for Flight Condition 2	5-25

LIST OF FIGURES

<u>Figure</u>	<u>Page</u>
5-17 Ramp Panel Modal Stress Fields for In-Phase and Out-of-Phase Modes Shown in Figure 5-16	5-26
5-18 Sonic Stress Levels at Ramp Panel	5-29
5-19 Ramp Panel Carbon-Carbon Sonic Stress Field with Effect of Joint Acceptance Included	5-30
6-1 Horizontal Stabilizer Skin Panel Located 90 Feet Aft of Nose	6-2
7-1 Typical Panel Cross-Section	7-2
7-2 Panel Geometries Used in Thermoacoustic Response Analysis	7-5
7-3 Typical Vehicle Loads	7-6
7-4 Nozzle Heat Flux Envelope	7-7
7-5 Model Used in Thermal/Hydraulic Analysis of Actively Cooled Panel	7-9
7-6 Thermal Gradient at Center of Panel	7-10
7-7 Fatigue Analysis Summary for Panel 1 Outer Face Sheet	7-12
7-8 Fatigue Analysis Summary for Panel 2 Outer Face Sheet	7-13
7-9 NASTRAN Symmetric Panel Model	7-15
7-10 NASTRAN Model Static Checkout	7-16
7-11 NASTRAN Model Dynamic Checkout	7-17
7-12 Heat Flux for Panels 1 and 2	7-18
7-13 Temperature Distribution Along Panel as a Function of Heat Flux (4 inches from Inlet Manifold)	7-19
7-14 Temperature Distribution Along Panel as a Function of Heat Flux (4 inches from Exit Manifold)	7-20
7-15 Combined Fatigue Ratios for Panel 1	7-22

LIST OF FIGURES

<u>Figure</u>	<u>Page</u>
8-1 Carbon-Carbon Test Panels	8-8
8-2 Actively Cooled Panel	8-9
8-3 Locations of Carbon-Carbon and Actively Cooled Test Panels	8-10
8-4 TMC Hat-Stiffened Panel (plus Duplicate Panel in 6-4 Titanium)	8-11
8-5 Monolithic Titanium Hat-Stiffened Panel	8-12
8-6 Monolithic Titanium Truss Core Panel	8-13
8-7 Locations of Stiffened TMC Test Panels	8-14
8-8 Ling Shaker with High-Temperature Test Furnace	8-16
8-9 Schematic of Sonic Fatigue Test Facility	8-17
8-10 PWT Facility Layout	8-18
8-11 PWT Facility Layout - Side View	8-18
8-12 Infrared Quartz Heat Lamp Array	8-22
8-13 T.S.I. LDV Schematic	8-27
8-14 Schematic of High-Temperature, High-Cycle Fatigue Apparatus	8-31
8-15 Shaker Specimens - Test Setup and Instrumentation	8-33
8-16 Strain Gauge Locations for Carbon-Carbon Panels	8-38
8-17 Strain Gauge Locations for Actively Cooled Panel (13 Gauges)	8-39
8-18 Strain Gauge Locations for Titanium Hat-Stiffened Panels	8-40
8-19 Strain Gauge Locations for Monolithic Titanium Truss Core Panel (10 Gauges)	8-41
8-20 Program Schedule	8-45

LIST OF FIGURES

<u>Figure</u>	<u>Page</u>
9-1 Finite Element Model for Carbon-Carbon Test Panel Design Concept 1	9-4
9-2 Modal Shapes for Carbon-Carbon Test Panel Design Concept 1	9-5
9-3 Modal Stress Fields for Carbon-Carbon Test Panel Design Concept 1	9-6
9-4 Finite Element Model for Carbon-Carbon Test Panel Design Concept 2	9-7
9-5 Modal Shape for Carbon-Carbon Test Panel Design Concept 2	9-8
9-6 Modal Stress Field for Carbon-Carbon Test Panel Design Concept 2	9-9
9-7 Finite Element Model for Carbon-Carbon Test Panel Design Concept 3	9-10
9-8 Modal Shapes for Carbon-Carbon Test Panel Design Concept 3	9-11
9-9 Modal Stress Fields for Carbon-Carbon Test Panel Design Concept 3	9-12
9-10 Sonic Stress Levels for Carbon-Carbon Test Panel Design Concept 1	9-15
9-11 RMS Sonic Stress Levels Obtained with Broad Band Loading for Carbon-Carbon Test Panel Design Concept 1	9-16
9-12 Sonic Stress Levels for Carbon-Carbon Test Panel Design Concept 2	9-17
9-13 RMS Sonic Stress Levels Obtained with Broad Band Loading for Carbon-Carbon Test Panel Design Concept 2	9-18
9-14 Sonic Stress Levels for Carbon-Carbon Test Panel Design Concept 3	9-20
9-15 RMS Sonic Stress Levels Obtained with Broad Band Loading for Carbon-Carbon Test Panel Design Concept 3	9-21
9-16 Comparison of Sonic Stress Levels for Carbon-Carbon Test Panel Design Concepts 1, 2, and 3; Joint Acceptance Correction Incorporated	9-22

LIST OF TABLES

<u>Table</u>	<u>Page</u>
1-1 1000 q_{∞} Ascent Trajectory	1-6
1-2 2600 q_{∞} Ascent Trajectory	1-7
1-3 200 q_{∞} Descent Trajectory	1-8
2-1 Properties on the BWB at $x/R_N = 201.3$	2-44
2-2 Bow Shock-HS Interaction	2-54
3-1 Comparison of Von Gierke and NASA Models	3-3
3-2 Octave Band Sound Pressure Level due to Rocket Thrusters (Ref. 20 μ PA) at Eight Locations on the Model Upper Surface	3-16
3-3 Octave Band Sound Pressure Level due to Rocket Thrusters (Ref. 20 μ PA) at Eight Locations on the Model Lower Surface	3-17
3-4 Bandwidth and Center Frequencies for Octave Band	3-19
3-5 Scramjet Engine Power Level Spectrum and Location of Source	3-20
3-6 Octave Band Sound Pressure Level (dB) on Vehicle Lower Surface due to Scramjet Engine Alone	3-22
3-7 Octave Band Sound Pressure Level (dB) on Vehicle Lower Surface due to Combined Sound Levels of Scramjet and Rocket Engines	3-25

LIST OF TABLES

<u>Table</u>	<u>Page</u>
4-1 1000-psf Ascent Trajectory	4-4
4-2 2600-psf Ascent Trajectory	4-5
4-3 Thermal Properties of Carbon-Carbon	4-7
4-4 Laminate Layup Configurations for Forebody Panel	4-22
4-5 Forebody Panel Loads	4-27
5-1 Laminate Layout Configurations for Ramp Panel	5-16
5-2 Ramp Panel Loads	5-19
8-1 Random Fatigue Shaker Test Specimens	8-5
8-2 High-Temperature Sonic Fatigue Test Panels	8-6
8-3 Sonic Fatigue Facility Design Specifications	8-20
8-4 Comparative LDV Specifications	8-28
8-5 Factors in the Choice of an LDV	8-29
8-6 Shaker Specimen Test Temperatures	8-34
9-1 Test Panel Design Concepts	9-2
9-2 Summary of Sonic Fatigue Analysis Results for Carbon-Carbon Test Panel Design Concepts 1, 2, and 3	9-23

FOREWORD

Work performed under Contract Number F33615-87-C-3227 began on November 17, 1987. Mr. Kenneth R. Wentz, Technical Manager, Acoustics and Sonic Fatigue Group, is the Project Engineer for Air Force Wright Aeronautical Laboratories, Air Force Systems Command, Wright-Patterson Air Force Base, Ohio.

This report covering Phase II activities was submitted in November 1989.

EXECUTIVE SUMMARY

BACKGROUND

The purpose of this report is to identify thermo-vibro-acoustic issues in the design of skin panels of transatmospheric hypersonic vehicles. This has been accomplished by identifying a single-stage-to-orbit mission and a Blended Wing Body vehicle configuration that is typical of transatmospheric vehicles currently being considered. Vehicle skin panel materials and skin panel designs are developed. Loads due to flow, called aeroacoustic loads, and engine-induced sound loads are determined. The thermal, static, and dynamic responses of the panels are found using finite element methods.

This is the Phase II report of a three-phase study. The Phase I report has been issued as AFWAL-TR-89-3014, "Thermo-Vibro-Acoustic Loads and Fatigue of Hypersonic Flight Vehicle Structure, Interim Report for Period November 1987 - May, 1988," Wright-Patterson Air Force Base, Ohio, February 1989. Material from the Phase I report has been incorporated in the present report, and there is considerable new analysis. Phase III of the program will contain the results of testing material coupons and panels which are representative of skin panels from transatmospheric hypersonic vehicles.

The work reported herein was performed by a team comprising Rohr Industries, Inc., San Diego, California; McDonnell Douglas Corporation, St. Louis, Missouri; and Science Applications International Corporation, Ft. Washington, Pennsylvania. Rohr Industries provided testing, thermal and sonic fatigue analysis, fabrication of carbon-carbon specimens, and overall coordination. McDonnell Douglas Corporation provided the vehicle concept, design and mission data, metallic test specimens, and analysis of actively cooled panels. Science Applications International Corporation provided flow field analysis and aerothermal loads on the skin. Authors of this report and their areas of contribution are as follows: Robert D. Blevins, Rohr -- summary, introduction, conclusions, and coordination; Dimitri Bofilios, Rohr -- finite element sonic fatigue analysis; Ian Holehouse, Rohr -- test plan; Vicky W. Hwa, Rohr -- finite element thermal analysis; Anthony L. Laganelli, Science Applications International Corporation -- flow field analysis and aerothermal loads; Mauro Pierucci, San Diego State University (Consultant) -- sound radiated by engines; Peter Pozefsky, McDonnell Douglas Corporation -- vehicle and mission description and actively cooled panel analysis; Matthew D. Tratt, Rohr -- finite element stress and buckling analysis.

MISSION AND DESIGN

In order to develop representative designs and loads for analysis, a single-stage-to-orbit mission has been postulated using a vehicle which primarily utilizes airbreathing propulsion. This is consistent with transatmospheric vehicles currently being considered in the United States. A 15-minute generic ascent trajectory to low earth orbit at Mach 25 is postulated at constant acceleration along lines of constant aerodynamic pressure $Q = 1000 \text{ lb/ft}^2$ and $Q = 2600 \text{ lb/ft}^2$. The 1-hour descent occurs at $Q = 200 \text{ lb/ft}^2$. Since aerothermal and aeroacoustic loads increase with aerodynamic pressure, the ascent produces more severe loading than the descent. The transatmospheric vehicle loading is also more severe than that on the space shuttle, which has a maximum aerodynamic pressure $Q = 600 \text{ lb/ft}^2$. The high aerodynamic pressures on the transatmospheric vehicle are required by the airbreathing scramjet engines to support combustion of the liquid hydrogen fuel.

The need to contain large quantities of liquid hydrogen fuel within an efficient hypersonic shape has given rise to a Blended Wing Body (BWB) vehicle, 100 feet in overall length, with the scramjet engine on the lower midsurface and twin vertical stabilizers. The skin panels forming the forebody of the vehicle and ramp to the engine inlet are fabricated from carbon-carbon. These panels have relatively thin skins and integral blade stiffeners. The horizontal and vertical stabilizers are fabricated from metal matrix titanium composite with bonded channel stiffeners at close intervals to provide sufficient stiffness to prevent the panels from buckling under overall vehicle inplane loads carried by the panels. The aftbody panels, like the stabilizer panels, are titanium metal matrix composite because the heat loading on these panels is sufficiently low so as not to require use of carbon-carbon or active cooling. The panels in the nozzle aft of the scramjet engines are exposed to impingement of burning hydrogen, and they would see temperatures of approximately 3500°F, well above the 3000°F maximum temperature of carbon-carbon or the 1500°F maximum temperature of metal matrix composite, unless provided with cooling. These actively cooled titanium metal matrix composite panels have a milled surface plate that provides a large number of small passages for the circulation of liquid hydrogen, which then is pumped to the engines.

AEROTHERMAL LOADS

The loading on the skin panels was developed in three stages. First, the external flow field and boundary layer were analyzed using a parabolized Navier-Stokes code with a two-dimensional representation of the vehicle. This gives the boundary layer thickness and local free stream velocity over the vehicle for several Mach numbers along the ascent trajectory. Second, existing semiempirical techniques were applied to determine the oscillating skin surface pressure and aerothermal heating associated with the turbulent boundary layer. Third, shock waves and separated flow were considered. The results show that aerothermal heating due to attached turbulent boundary layers increases with Mach number and dynamic pressure. The heating rates are high by conventional

standards: $20 \text{ Btu/ft}^2\text{-sec}$ along the lower surface ramp at Mach 20 and $Q = 1000 \text{ lb/ft}^2$ and $40 \text{ Btu/ft}^2\text{-sec}$ at Mach 20 and $Q = 2600 \text{ lb/ft}^2$.

The oscillating surface pressures produced by the attached boundary layer are broad band in nature, rolling off beyond 10,000 Hz. The maximum overall Sound Pressure Levels on the skin produced by the turbulent boundary layer are moderate, reaching a maximum of approximately 145 dB. In contrast, the sound radiated directly by the engines to adjacent fuselage and tail surfaces will exceed 175 dB adjacent to the engine. Hence, engine noise rather than boundary layer oscillation will govern the design of near-engine structures. The engine acoustic loads will be broad band owing to the absence of any rotating machinery or blades in the scramjet and rocket jet engines to create discrete frequencies.

Hypersonic flow produces shock waves from the bow and stabilizers and at any change in cross section. At speeds in excess of Mach 10, the bow shock can bend aft sufficiently far to intercept the horizontal and vertical stabilizers. Shock waves from the vertical and horizontal stabilizers will interact with each other and with the adjacent fuselage. A pattern of shocks will be formed about the scramjet engine inlet and exhaust. New methods have been developed by Science Applications International Corporation to estimate the magnitude of pressure oscillation and heating within the shock. The results indicate that Sound Pressure Levels of 165 to 175 dB and heating rates as high as 50 to $150 \text{ Btu/ft}^2\text{-sec}$ will be produced where the shock wave intercepts the vehicle. These are local loads, on the order of 1 inch in width, which will generally exceed other loads along their line of shock-skin interaction.

ANALYSIS AND RESULTS

Three panels were chosen for detailed finite analysis: the forebody, ramp, and actively cooled panels. In addition, load analysis was made of the stabilizer panel.

Analysis of the carbon-carbon forebody skin panel was made using the finite element method. The forebody panel is located on the lower surface of the vehicle, 20 feet aft of the nose and 40 feet forward of the scramjet inlet. The panel has a skin thickness of 0.115 inch and has 2-inch-high blade stiffeners at 6-inch intervals. A layer of alumina insulation rests between the panel and the cryogenic tank structure beneath it. The forebody panel bears inplane loads as high as 1200 lb/in. These loads are due to distortion of the vehicle under thermal and aerodynamic loads. While these loads do not buckle the panel, they overstress the panel slightly in the first ply adjacent to the attachment line. The maximum skin temperature rises from 70°F at takeoff to 2100°F at top of ascent for a $Q = 1000 \text{ lb/ft}^2$ ascent and 3200°F for a $Q = 2600 \text{ lb/ft}^2$ ascent. The latter temperature exceeds the capability of carbon-carbon. These temperatures could be 1100°F lower if the boundary layer were laminar rather than turbulent as assumed in this analyses. The through-the-skin-thickness temperature gradient is negligible owing to the high thermal conductivity of carbon-carbon, but the difference between the maximum and minimum temperature is approximately 1200°F because of thermal lag between the thick sides of panels where fasteners are attached and the skin surface, which is heated directly.

Dynamic analysis shows that the first panel mode occurs at 524 Hz and corresponds to in-phase motion of adjacent panels. Out-of-phase motion of adjacent panel bays occurs at 591 Hz. Experience with aircraft skin panels shows that these in-phase and out-of-phase modes are the dominant modes under sonic loading. Based on the very conservative assumption that the distribution of oscillating pressure matches the mode shape, the combined engine and boundary loading results in 4000 psi rms oscillating stress. A less conservative assumption on pressure distribution gives 2300 psi rms. Both are below the 6000 psi rms allowable for carbon-carbon under random loading.

Analysis of the carbon-carbon ramp panel was also made using the finite element method. The ramp panel is located on the underside of the vehicle, 60 feet aft of the nose, forward of the engine inlet. The ramp forms a compression surface that conditions air before it enters the

engine inlet. This carbon-carbon panel is a heat shield for the underlying cryogenic structures. It bears no inplane loads but does bear normal pressure load. The panel has a skin thickness of 0.065 inch and is stiffened with blade stiffeners on 10-inch centers. The ramp panel heat load is similar to that of the forebody panel. The ramp panel maximum temperature at the top of ascent is 2500°F for the $Q = 1000 \text{ lb/ft}^2$ ascent and 3000°F for the $Q = 2600 \text{ lb/ft}^2$ ascent. Dynamic analysis shows that the first panel bending mode is at 258 Hz with alternate bays going in and out of phase. The panel sees relatively high acoustic loads due to noise radiated from the engine inlet. The sound is estimated at 165 dB. This is predicted to produce 16,000 psi rms acoustic stress, which is well in excess of the 6000 psi rms allowable. Thus, the ramp panel is not adequate to withstand the dynamic loading as presently designed. Moreover, this analysis does not include the effect of shock waves that will exist in the inlet at supersonic Mach numbers. As noted earlier, shock waves can generate pressure loads as high as 175 dB and local heat loads well in excess of the turbulent boundary layer heating. These loads would also contribute to the negative margins of safety on the ramp panel. Redesign with increased thickness or decreased stiffener spacing to accommodate the dynamic loads is required to achieve positive margins in the ramp panel.

The horizontal stabilizer panels are fabricated from titanium metal matrix composite. The panels consist of a face sheet 0.045 inch thick with channel section stiffeners diffusion bonded to the inner surface to form a corrugation stiffened panel. Aerothermal analysis indicates that the aeroheating rates due to the turbulent boundary layer are 2 to 5 Btu/ft²-sec, which is a factor of 5 below those of the forebody and ramp panels, indicating that the mean thermal environment is within the capability of metallic panels. The greatest loads placed on the horizontal and vertical stabilizer panels are associated with engine and shock interaction. Engine noise loads range from 160 to over 170 dB for those surfaces which are in line of sight from the engine exhaust. Shock interaction loads can be very high. For Mach 10 and higher, the bow shock can impinge on the horizontal surface and there will be a shock-shock interaction in the corner between the horizontal and vertical

surfaces. These shocks will lead to local pressure fluctuations of 175 dB and maximum local heating as high as $100 \text{ Btu/ft}^2\text{-sec}$, a factor of 20 higher than that produced by the boundary layer. Comparison with the thermal analysis of the forebody panel suggests that this heating will produce local temperatures well in excess of the 1500°F limit of the metallic structure. Thus, the shock interaction loading on the vertical and horizontal stabilizer surfaces will require local thermal protection or active cooling at areas of shock impingement.

Actively cooled panels are located in the nozzle region, aft of the scramjet exhaust. The inner and outer face sheets are thin titanium metal matrix composites. The outer face sheet is bonded to a heat exchanger consisting of a monolithic sheet of titanium having a series of grooves running along its length. The face sheets and heat exchanger are bonded to a titanium honeycomb core to form a sandwich panel which contains integral cooling passages for the cryogenic liquid hydrogen coolant. The design panels are 48 inches square. Panel heating results from expansion of the engine combustion gases. Heat fluxes associated with the exhaust flow drop off dramatically down the length of the nozzle surface from a peak $250 \text{ Btu/ft}^2\text{-sec}$ at the combustor exit to $50 \text{ Btu/ft}^2\text{-sec}$ at the aft edge, $180 \text{ Btu/ft}^2\text{-sec}$ being a typical mean value. These heat fluxes would lead to temperatures in excess of 3000°F if active cooling were not provided. As noted earlier, sound levels in the 170 to 180 dB range are predicted owing to scramjet exhaust.

NASTRAN finite element dynamic analysis of the actively cooled panel shows that the fundamental bending mode occurs at 82 Hz. This relatively low frequency and the associated low stiffness result from the 48-inch span of the panel. While the panel can bear the mean aerodynamic and carry-through loads imposed on it, the engine-induced acoustic loads at takeoff exceed the fatigue capability of the panel. Additional analysis suggests that by incorporating intermediate supports at 12-inch intervals, the stresses will be reduced below the fatigue allowable. Because the actively cooled panel is itself a pressure vessel and contains highly combustible hydrogen, it is extraordinarily sensitive to damage and will require higher margins of safety than other panels.

In summary, dynamic aeroacoustic loads on the skin panels have been found to provide design critical dynamic loads for (1) panels at or adjacent to the inlet and engine exhaust and (2) panels subject to shock impingement and separated flow. The latter include inlet, aft body, and stabilizer surfaces. In order of importance, the dynamic aeroacoustic loads are (1) engine-generated loads, (2) shock interaction loads, and (3) attached turbulent boundary layer loads. The engine-induced acoustic loads and shock impingement loads generate overall skin pressures of 170 dB to 180 dB or higher, whereas the turbulent boundary layer generates approximately 145 dB. Shock impingement will also create local heating that is a factor of 3 to 5 higher than that produced by the turbulent boundary layer alone.

SECTION 1 INTRODUCTION

1.1 TRANSATMOSPHERIC HYPERSONIC VEHICLE MISSION AND TRAJECTORY

It is possible that an aircraft could take off from an airport, rise through the earth's atmosphere at hypersonic speeds, cruise the inner boundaries of space in low earth orbit, and then return to land on a conventional runway without refueling. Today such a mission is possible only through staged rockets or by releasing expendable fuel tanks as is done by the space shuttle. A completely reusable space aircraft -- or vehicle as it is generally called because it is neither an aircraft nor a spacecraft but both -- is being developed in the United States, Europe, and the Soviet Union. In the United States, this vehicle is called the NASP (National Aerospace Plane) or the X-30. In England, it is called the Hotol. In France and Germany, similar vehicles are called Hermes and Sanger II. These vehicles will incorporate technologies that will form the basis for future aircraft and spacecraft.

Transatmospheric vehicles capable of single stage to orbit have airbreathing propulsion systems that are an integrated part of the airframe. The need to obtain oxygen to support combustion in the engines in the thin air at extreme altitudes requires operation at very high dynamic pressures, leading to severe aerothermal heating and acoustic environments on skin panels. Local flow separation and shock impingement will aggravate both the acoustic and thermal environments. The vehicle skin will also be exposed to high sonic levels radiated by the engines.

The high temperatures and fluctuating pressures experienced by the skin panels of hypersonic vehicles are a primary design consideration because of their impact on the weight and durability of vehicle structures. Hypersonic vehicle skin panels are thermal and acoustic barriers between severe aeroacoustic and aerothermal loading on the skin exterior surface and environmentally sensitive internal equipment such as internal cryogenic fuel tanks. Certain thermal barrier skin panels bear little or no inplane or pressure loads and are sized entirely by the unsteady aeroacoustic loads, including shock impingement loads, and engine noise. Moreover, the extreme thermal environment requires use of special skin materials such as carbon-carbon composites, Rapid Solidification Technology (RST) titanium, and titanium aluminide alloys whose properties are not well known because these materials are only now becoming available in production quantities.

The vehicle performance and environment are dictated by its mission trajectory. Current transatmospheric hypersonic vehicle concepts call for a manned single-stage-to-orbit vehicle capable of extended hypersonic cruise utilizing primarily airbreathing propulsion (Reference [1-1]). Because the engines require atmospheric air to support combustion, the vehicle must attain the high Mach numbers required for orbit while relatively low in the denser portion of the atmosphere. Overall fluctuating aeroacoustic loads, i.e., fluctuating pressures imposed by the turbulent boundary layer, are proportional to the dynamic pressure and their low frequency components increase with boundary layer thickness. (See Section 2.) Aeroacoustic thermal loading increases with the cube of velocity. Transatmospheric vehicles will be exposed to large areas of fully developed turbulent flow at higher dynamic pressures for long periods of time than any other operational missile, aircraft, or spacecraft.

Location of the engine on the vehicle is important. Missiles and the space shuttle have engines conventionally placed to the rear of the body and avoid most engine acoustic damage. Transatmospheric vehicles will have the engines placed well forward on the body, exposing large areas of the vehicle to the engine acoustic field for the entire powered

flight. For takeoff and the brief subsonic portions of the flight, sound radiating from the inlet and exhaust will impinge on the entire vehicle lower surface. Overall sound levels as high as 180 dB are expected. In addition, the vehicle afterbody will serve as the engine nozzle, directing the combustion exhaust flow. The high heat flux of burning gas and the static pressure of the impinging flow require intricate actively cooled nozzle panels.

The transatmospheric vehicle mission trajectory can be divided into three phases: ascent, cruise, and descent. The ascent phase will typically last approximately 15 minutes and will be characterized by high dynamic pressure as the vehicle accelerates to orbital velocity. Thermoacoustic environments in the aft end will be severe because engines will be running continuously. Large areas of the forward vehicle will be subjected to the severe environment associated with turbulent boundary layer flow and shock impingement. The cruise phase will last several hours but will not have such severe environments. At orbital cruise altitude, flow will be laminar and engines will be inactive.

Descent will take approximately one hour and will be characterized by relatively lower thermoacoustic environments compared with the ascent phase. Engines will be off as the vehicle descends through the atmosphere at much lower dynamic pressure. The upper surface (leeside) of the vehicle will be exposed to low laminar heating. The lower surface (windward) will develop only moderate thermoacoustic environment due to the low dynamic pressure.

The transatmospheric vehicle trajectory and that of the space shuttle are shown for comparison in Figure 1-1. The transatmospheric vehicle achieves hypersonic velocities (greater than five times the speed of sound, 1100 ft/sec) at much lower altitudes than the space shuttle. The maximum dynamic pressure (one-half the atmospheric air density times the square of the vehicle velocity) of the space shuttle is approximately 600 lb/ft^2 , and this occurs as the space shuttle ascends through 50,000 feet. The maximum aerodynamic pressure on the transatmospheric vehicle also occurs on ascent, but it is between 1000 and 2600 lb/ft^2 .

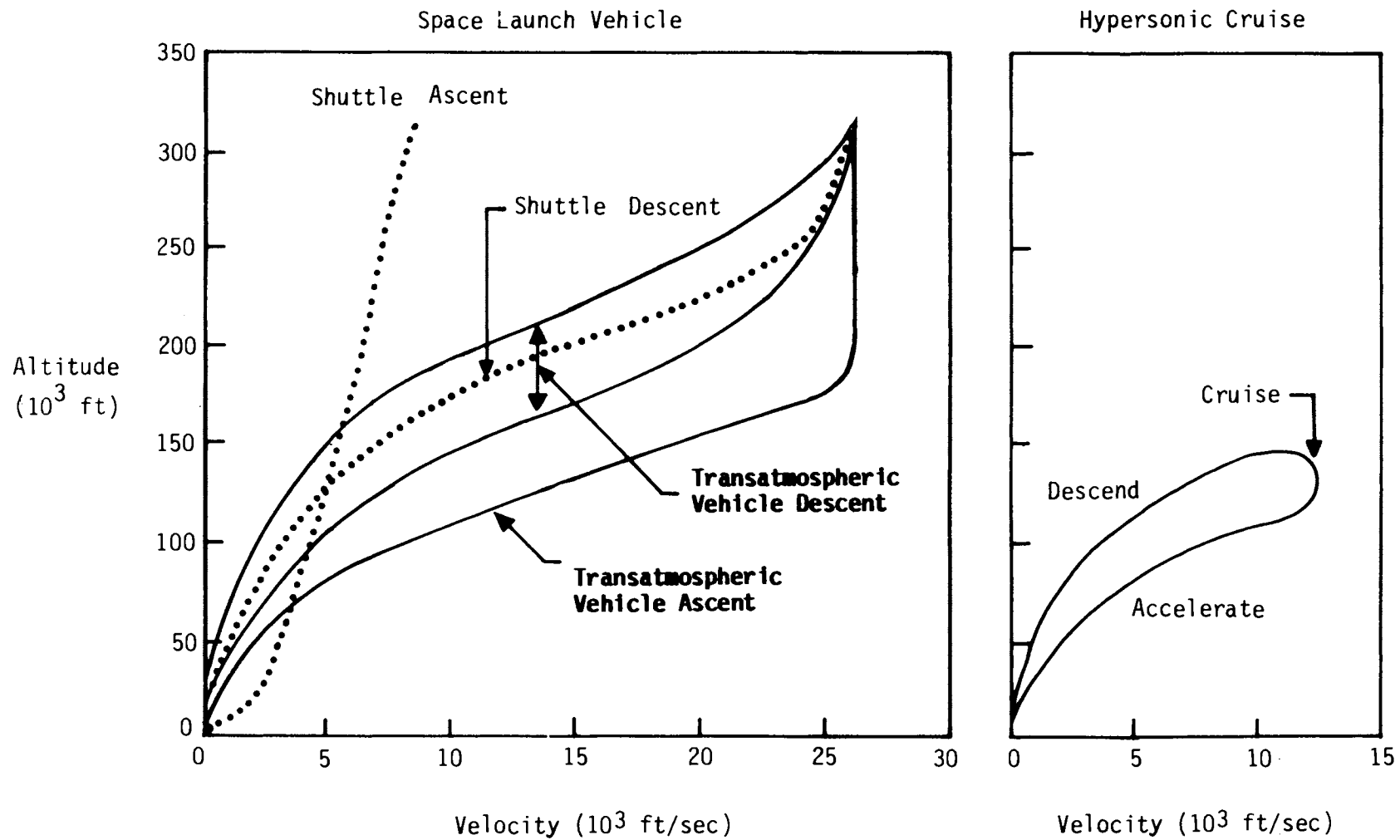


Figure 1-1. Comparison of Space Shuttle and Transatmospheric Vehicle Trajectories.

Aerodynamic load is proportional to dynamic pressure and it will be 1.5 to 4 times higher on the space shuttle than on the transatmospheric vehicle. Aerodynamic heating is proportional to aerodynamic pressure raised to the 1.5 power, and it will be a factor of 2 to 8 times higher on the transatmospheric vehicle. The space shuttle and the transatmospheric vehicle have similar descent trajectories with dynamic loading of 200 lb/ft^2 , and thus descent is a less severe loading condition than ascent for the transatmospheric vehicle.

For this study, ascent, descent, and cruise trajectories have been chosen which are characteristic of recent studies of transatmospheric hypersonic vehicles (Reference [1-2]). The ascent and descent trajectories, including the timescale, are given in Tables 1-1 through 1-3 and all three trajectories are plotted as Mach number versus altitude in Figure 1-2. Two ascent trajectories are considered: $1000 q_\infty$ and $2600 q_\infty$, where q_∞ is the aerodynamic pressure of the free stream in pounds per square foot. For ascent, the acceleration of the vehicle is assumed to be a constant $0.93g$, which provides efficient use of constant thrust engines. The time to orbit is 15 minutes. The vehicle covers approximately 2300 miles for the $1000 q_\infty$ case and 1700 miles for the $2600 q_\infty$ case. The principal difference between the two ascent cases is that in the $2600 q_\infty$ ascent, the vehicle is at low altitudes and in denser air for a given Mach number than in the $1000 q_\infty$ ascent. As a result, vehicle skin heating is higher for the $2600 q_\infty$ ascent than for the $1000 q_\infty$ ascent. In both cases, the vehicle will experience skin temperatures in excess of 1800°F .

The details of the trajectories will be optimized integrally with the engine performance curves and the thermal capability of the vehicle. Excessive skin temperature forces deviations from the ascent trajectories of Tables 1-1 and 1-2. To slow the rate of temperature rise, the vehicle must gain altitude rapidly into less dense air and reduce the rate of heating as shown by the kinked trajectory lines in Figure 1-2. The descent is made at $200 q_\infty$ over approximately 45 minutes.

Table 1-1. 1000 q_{∞} Ascent Trajectory (a)

Altitude (10^3 ft)	Density (lb/ft ³)	Sound Speed (ft/sec)	Mach Number	Velocity (ft/sec)	q (pSf)	Accl. (g)	Distance (10^6 ft)	Time (sec)
0	7.6×10^{-2}	1116	0	0	0	0.93	0	0
59.0	7.25×10^{-3}	968	3	2914	1000	0.93	0.141	97
71.0	4.48×10^{-3}	971	4	3899	1000	0.93	0.252	130
80.5	2.75×10^{-3}	978	5	4906	1000	0.93	0.399	163
88.4	1.86×10^{-3}	983	6	5919	1000	0.93	0.582	197
95.1	1.35×10^{-3}	987	7	6936	1000	0.93	0.799	231
110.9	6.65×10^{-4}	1003	10	10075	1000	0.93	1.69	335
129.9	2.63×10^{-4}	1038	15	15617	1000	0.93	4.06	520
144.1	1.37×10^{-4}	1064	20	21310	1000	0.93	7.55	710
155.7	9.04×10^{-5}	1081	25	27108	1000	0.93	12.22	903
							(2314 miles)	(15.0 minutes)

(a) Based on constant q_{∞} and acceleration and published flight profiles.

$\Delta T = \Delta V/A$. Time to ascent = 15 minutes.

838PROP
3-T1-1.BB
11-11-89

Table 1-2. 2600 q_{∞} Ascent Trajectory (a)

Altitude (10^3 ft)	Density (lb/ft ³)	Sound Speed (ft/sec)	Mach Number	Velocity (ft/sec)	q (psf)	Acc1. (g)	Distance (10^6 ft)	Time (sec)
0	0.07647	1116	0	0	0	0.93	0	0
39	0.01984	968	3	2904	2600	0.93	0.141	97
51	0.01117	968	4	3872	2600	0.93	0.251	129
60	0.007259	968	5	4840	2600	0.93	0.391	161
68	0.00497	969	6	5814	2600	0.93	0.564	193
75	0.00351	974	7	6818	2600	0.93	0.776	226
90	0.00171	984	10	9840	2600	0.93	1.616	327
107	0.000773	997	15	14955	2600	0.93	3.733	498
120	0.0004151	1021	20	20420	2600	0.93	6.955	680
132	0.000243	1044	25	26100	2600	0.93	9.140	870

(1731 miles) (14.5 minutes)

(a) Based on constant q_{∞} and acceleration and published flight profiles.

$\Delta T = \Delta V/A$. Time to ascent = 14.5 minutes.

838PROP
3-T1-2.BB
11-11-89

Table 1-3. 200 q_{∞} Descent Trajectory (a)

Altitude (10^3 ft)	Density (lb/ft ³)	Sound Speed (ft/sec)	Mach Number	Velocity (ft/sec)	q (psf)	Deaccl. (g)	Distance (10^6 ft)	Time (sec)
195	2.05×10^{-5}	1054	25	26350	200	0.23	0	0
187	2.25×10^{-5}	1063	20	21260	200	0.23	16.5	695
172	4.77×10^{-4}	1081	15	16215	200	0.23	29.4	1384
150	1.11×10^{-4}	1073	10	10730	200	0.23	39.5	2134
131	2.63×10^{-4}	1039	7	7273	200	0.23	43.8	2606
123	3.64×10^{-4}	1026	6	6156	200	0.23	44.7	2759
116	5.02×10^{-4}	1013	5	5065	200	0.23	45.6	2908
104	8.89×10^{-4}	993	4	3972	200	0.23	46.3	3057
92	1.56×10^{-3}	985	3	2955	200	0.23	46.8	3195

(a) Based on constant q_{∞} and acceleration and published flight profiles.

$\Delta T = \Delta V/A$. Time to descent = 45 minutes.

838PROP
3-T1-3.BB
11-11-89

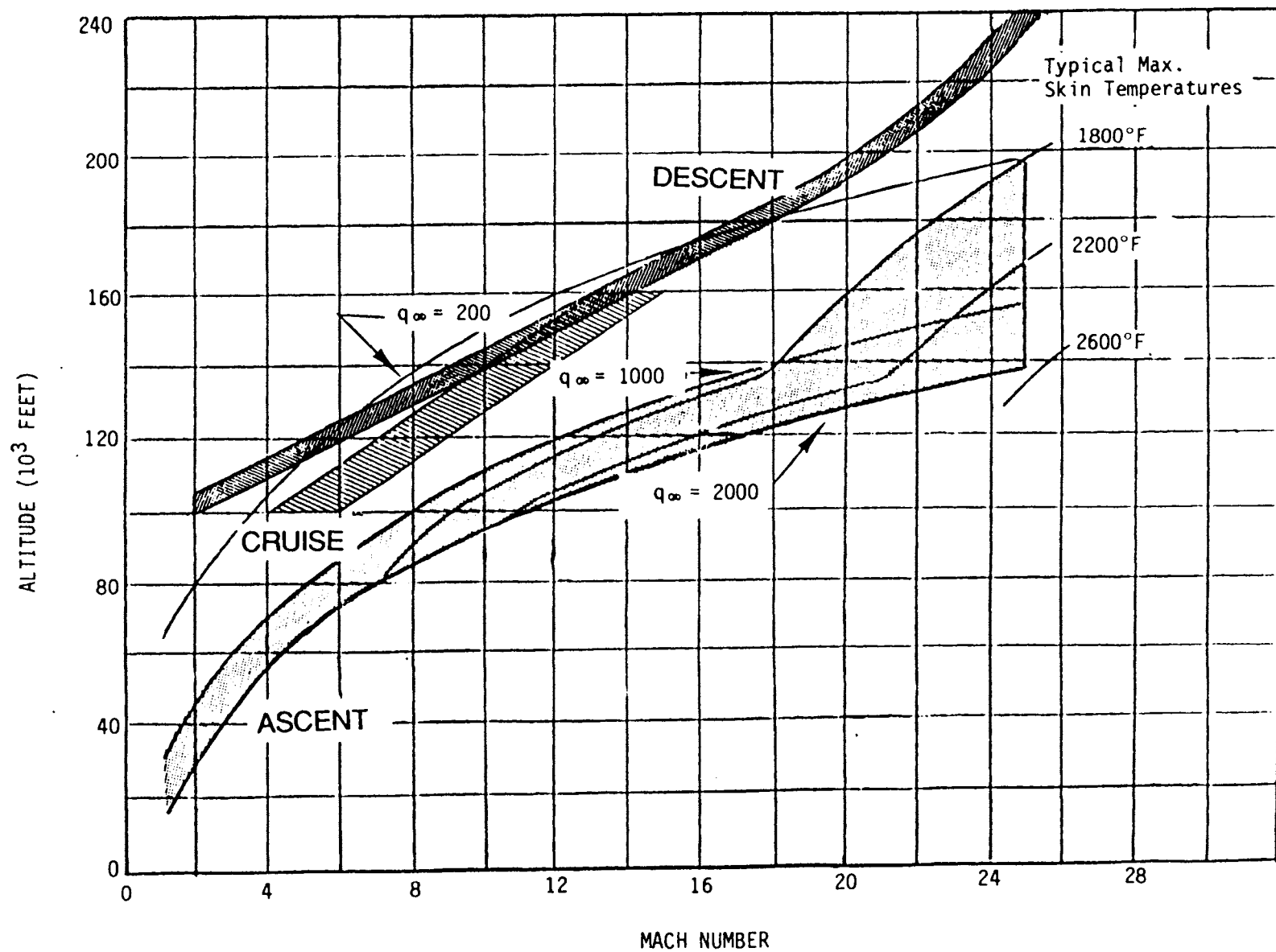


Figure 1-2. Transatmospheric Hypersonic Vehicle Flight Envelopes.

This transatmospheric vehicle aerothermal acoustic study is focused on the ascent phase, where acoustic and thermal environments are most severe. The combined effects of high temperatures and fluctuating pressures on the skin panels of a single-stage-to-orbit hypersonic vehicle are considered.

1.2 SKIN ENVIRONMENT AND MATERIALS

Thermal, acoustic, and steady loads are imposed by the airflow directly on vehicle skin panels by five aerothermal mechanisms:

- a. Steady aerodynamic pressure induced by attached and separated flow about the vehicle contours.
- b. Unsteady aeroacoustic pressures generated by eddies in the turbulent boundary layer that covers most of the vehicle surface. Portions of the nose and forebody of the vehicle may remain laminar, which would lead to lower heating and the elimination of unsteady pressure in these areas.
- c. Aerothermal heating of the skin by viscous friction in the boundary layer. The shearing of fluid against the vehicle skin generates heat which transfers to the vehicle skin.
- d. Shock impingement loads generated by the bow shock and abrupt changes in contour. Experimental data show that a hypersonic shock wave impinging upon a turbulent boundary layer creates local areas of intensive pressure oscillation and heating associated with shock turbulence interaction.
- e. Separated flow loads due to detachment of flow contours from abrupt changes in contour. Experimental data show that unsteady separated flow loads are comparable in magnitude to the local dynamic head.

Large portions of the vehicle skin must also bear in-plane "carry-through" loads that result from semimonocoque construction. These arise from mean aerodynamic loading and thermal distortion of the vehicle as a whole. The net aerodynamic pressure on the vehicle supports the vehicle weight. The distribution of pressure results in moments and shears through the vehicle cross-section. These are borne both by the internal network of beams and frames that interface the vehicle internal and fuel tanks and by the vehicle skin as in-plane loads. Thermal gradients on the vehicle as a whole also result in in-plane loads on skin panels. During ascent at positive angles of attack, the lower surface is heated by impinging air while the upper surface is shielded. The heated lower surface expands, tending to deform the vehicle into a banana shape with the result that skin panels bear compressive loads and are buckling critical, while upper skin panels bear high mean loads that reduce the residual capability available for fatigue (Appendix D).

The vehicle skin temperatures, with the possible exception of the actively cooled nozzle temperatures, rise continually from takeoff to orbit. Figures 1-3 and 1-4 show typical maximum skin surface temperatures. Skin panel materials are chosen which are compatible with these temperatures. No existing reusable structural material can withstand temperatures in excess of 3000°F, and in those areas, such as the nozzle, where higher temperatures are expected, active cooling of the panel with circulating propellants is utilized to reduce the temperatures to metallic limits.

Refractory metals and refractory composites (primarily carbon-carbon) are utilized in the 1800° to 3000°F temperature range, which includes the lower forebody and ramp panels. Nickel-based superalloys are usable up to approximately 1800°F where their strength falls off and creep deformations become substantial, as shown in Figure 1-5. Advanced silicon fiber-titanium matrix composites and RST titanium are projected to be capable of 1500°F and are the alloys of choice for the horizontal and vertical stabilizers, the upper midbody and aftbody, and the actively cooled panel. Conventional titanium, aluminum, and ferrous alloys are

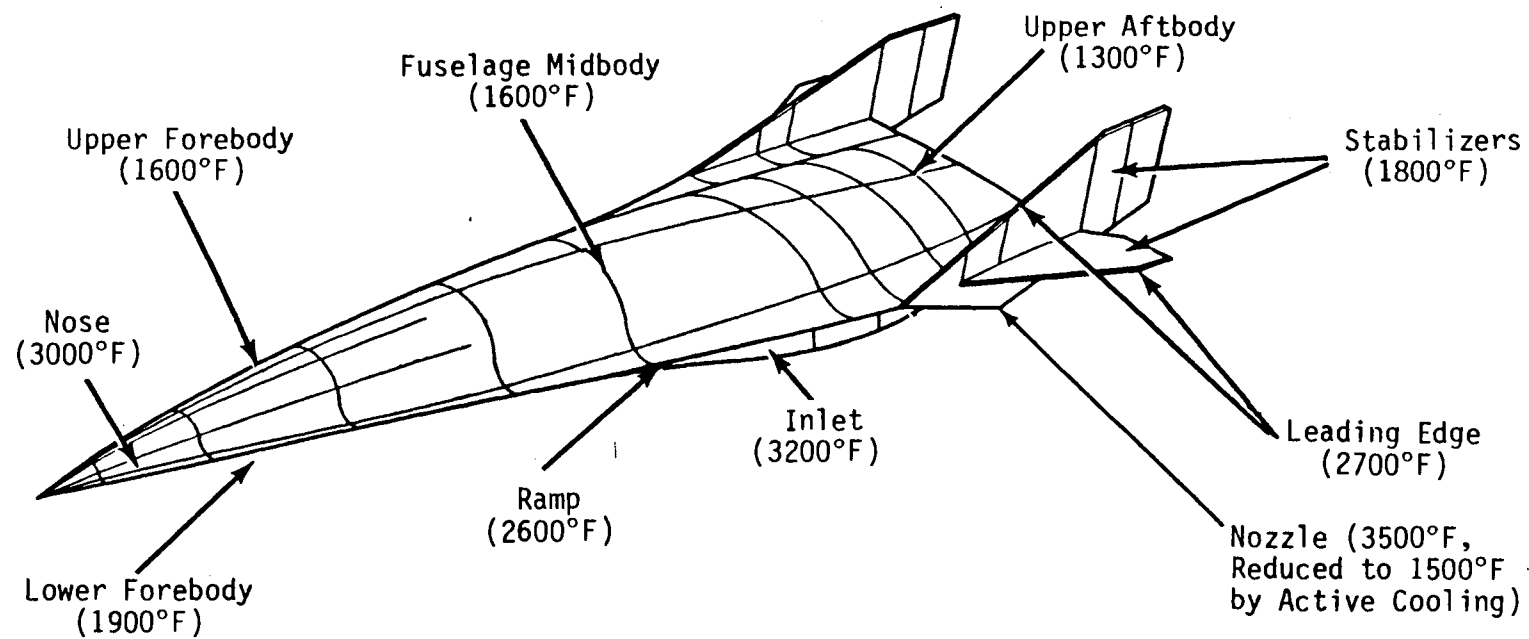
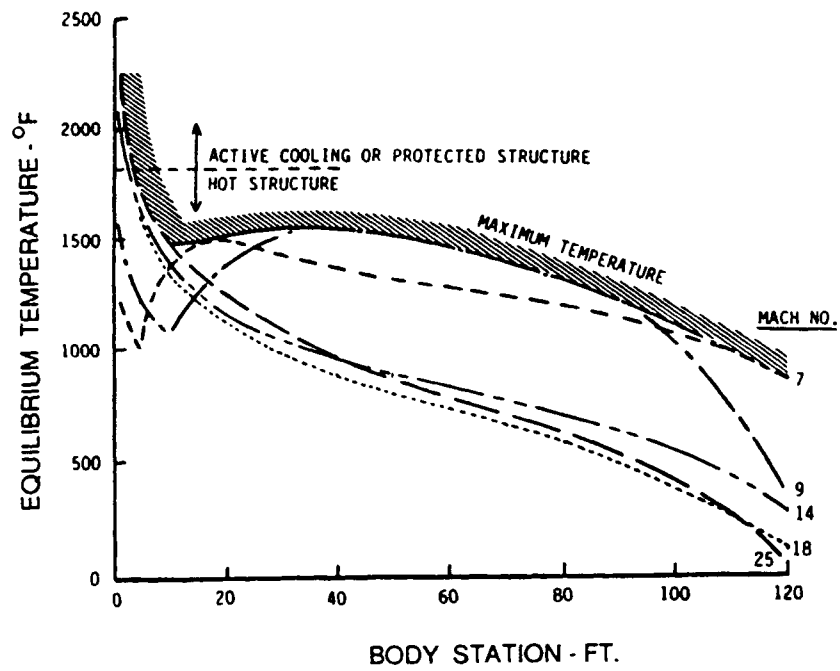
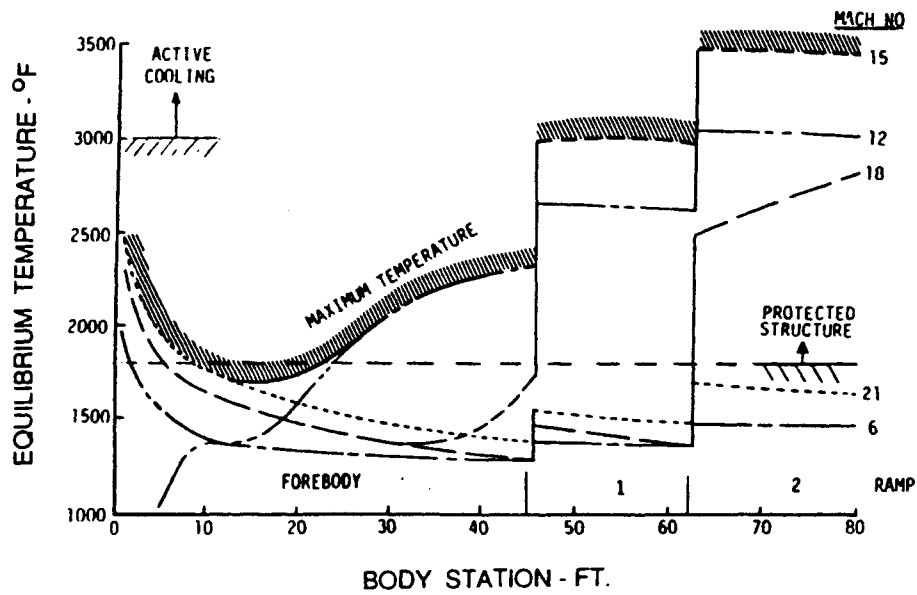


Figure 1-3. Transatmospheric Hypersonic Vehicle Maximum Skin Surface Temperatures.



(a) Upper Surface



(b) Lower Surface

Figure 1-4. Transatmospheric Vehicle Skin Temperatures: (a) Upper Surface; (b) Lower Surface

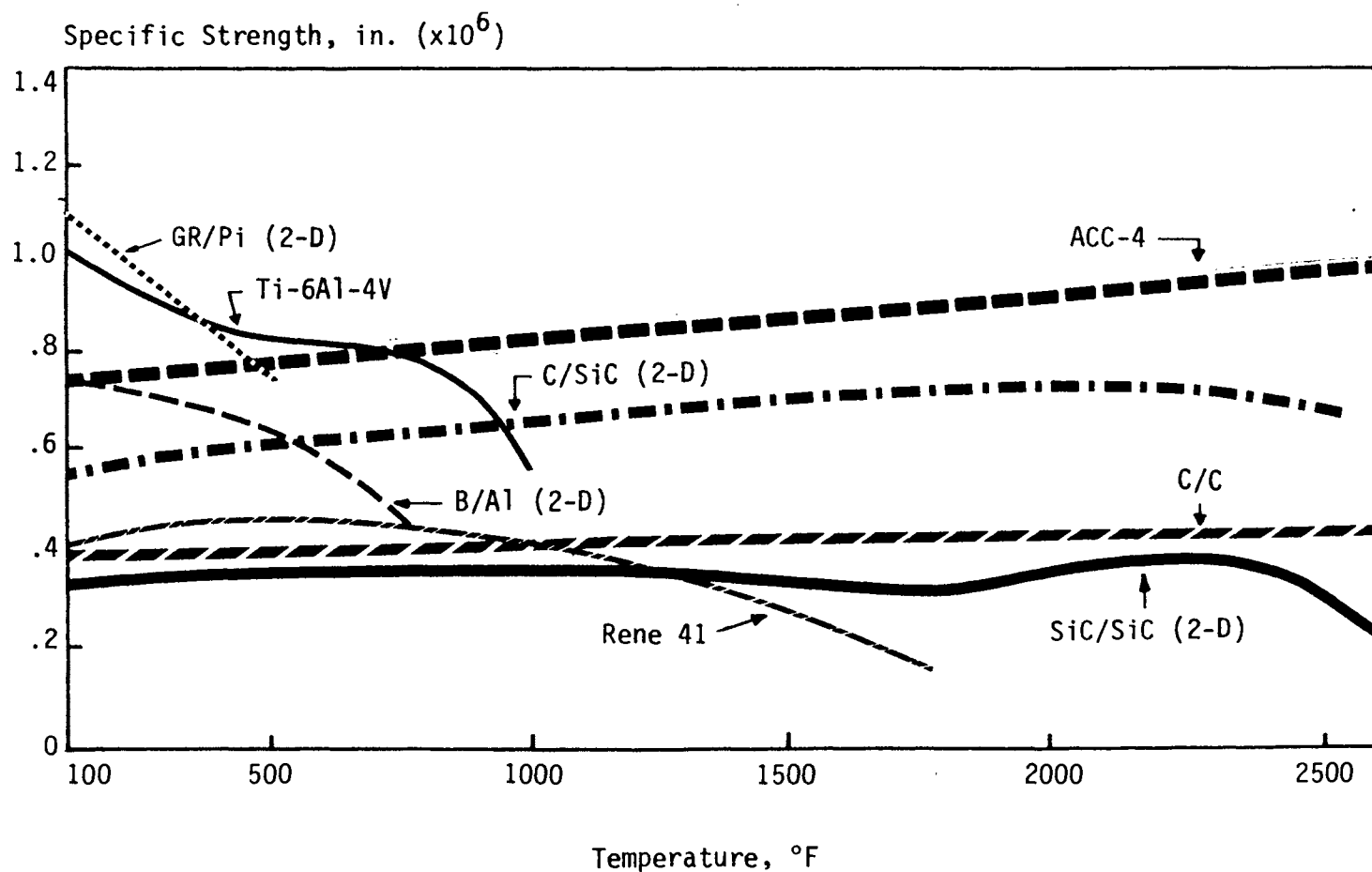


Figure 1-5. Comparison of Strength of Various Structural Materials as a Function of Temperature.

used in the -30°F to 1000°F range. Materials for the internal cryogenic tank structures include aluminum alloys and thermoplastic composites. Aluminum alloys have been traditionally used for cryogenic applications, but thermoplastic and thermoset composites offer similar strengths and stiffness at lower weight.

Acceleration of hypersonic flow leads to expansion fans and deceleration leads to shock waves. Shock waves originate at the nose, at leading edges of the stabilizers, and at other protrusions into the free stream as shown in Figure 1-6. Shock waves interact strongly with turbulent boundary layers to locally increase the magnitude of the fluctuating pressure and heat transfer. Various sources (References [1-3] through [1-6] indicate a 10 to 45 dB increase in oscillating pressure. The analysis of Section 2 predicts a 30 to 50 dB increase in oscillating pressure due to interaction of the bow shock with the horizontal stabilizer. Figure 1-7 shows that shock interaction can greatly increase oscillating spectra. There are four primary areas at which shocks are generated that lead to shock-boundary layer interaction:

- a. Bow shock interaction with the horizontal stabilizer. The bow shock will fold in at increasing Mach number, eventually impinging on the horizontal stabilizer at greater than Mach 10.
- b. Horizontal and vertical stabilizer shock interaction with the boundary layer in a classical corner flow.
- c. Horizontal and vertical stabilizer shock interaction with boundary layers at their origin with the aftbody.
- d. Protrusions from the streamlines, such as cowls, antennae, fairings, leading edges, and other details, will also create local areas of shock-boundary layer interaction.

Acoustic and pressure loads are discussed in detail in Section 2.

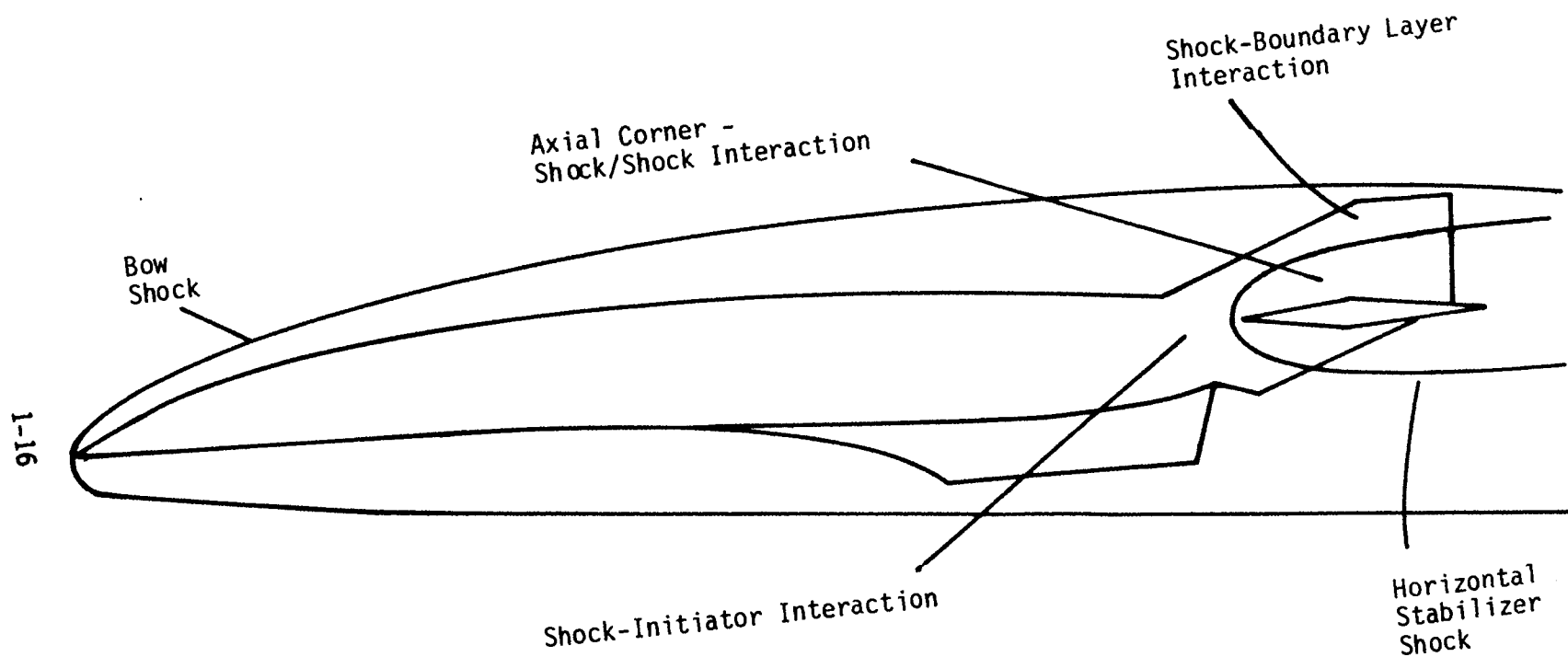


Figure 1-6. Transatmospheric Vehicle Shock-Boundary Layer Interaction Characteristics.

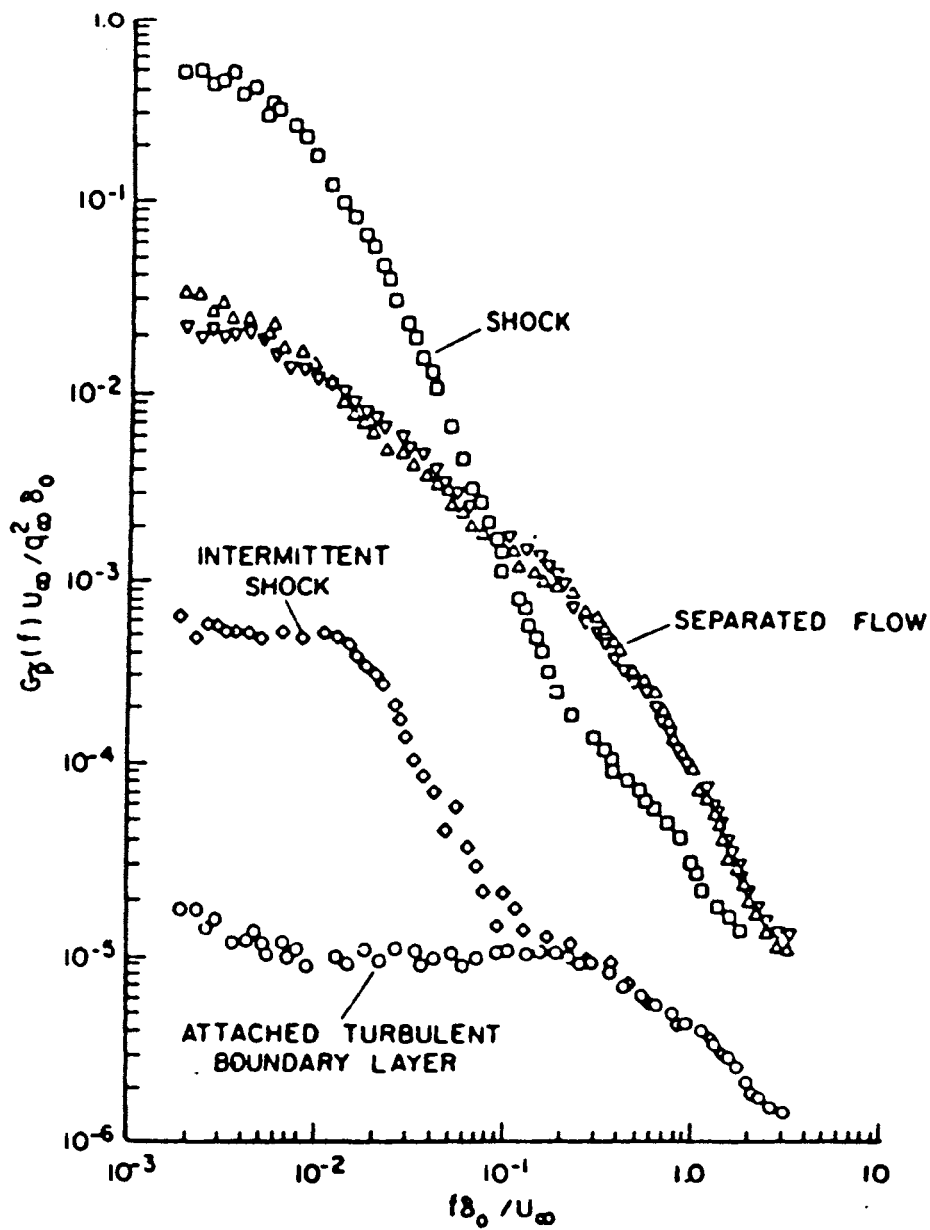


Figure 1-7. Acoustic Levels in Disturbed Flow (Reference [3-1]).

1.3 DESCRIPTION OF TRANSATMOSPHERIC VEHICLE

1.3.1 Design Considerations

For a given trajectory, potential transatmospheric vehicle design concepts are optimized. Optimized vehicles are markedly alike in external appearance owing to their similar flight trajectories. All designs currently being considered have:

- a. Large, twin horizontal and vertical control surfaces.
- b. Engine location at lower midbody.
- c. Integrated aftbody/nozzle.
- d. Similar body length/width/height ratios.
- e. Broad, nearly flat surface areas.

Location of the engine on the vehicle is important. Hypersonic vehicles will be subsonic for only brief periods of time. At supersonic/hypersonic velocity, the structure forward of the engines will be moving faster than the forward propagation of acoustic pressure and will "outrun" engine noise. Missiles have engines conventionally placed to the rear of the body and will avoid most of the engine acoustic damage. Transatmospheric vehicles will have engines placed well forward on the body, exposing large areas of the vehicle to the engine acoustic field for the entire powered flight. In addition, the vehicle afterbody will serve as the engine nozzle, directing the combustion exhaust flow. The high heat flux and static pressure associated with exhaust impingement will increase acoustic susceptibility.

Four potential vehicle designs are shown in Figure 1-8. Propellant tank concepts are important because the local structural concepts for the external skins are often driven by tank selection. The tank contains cryogenic fuels, stored at approximately -400°F . Tanks can be integral or non-integral. A tank is defined as integral when the vehicle structural skin also serves as the tank walls as shown in Figure 1-9. A tank is defined as non-integral when the tank exists separately from the vehicle structure. Tank geometries include cylindrical, conformal, and

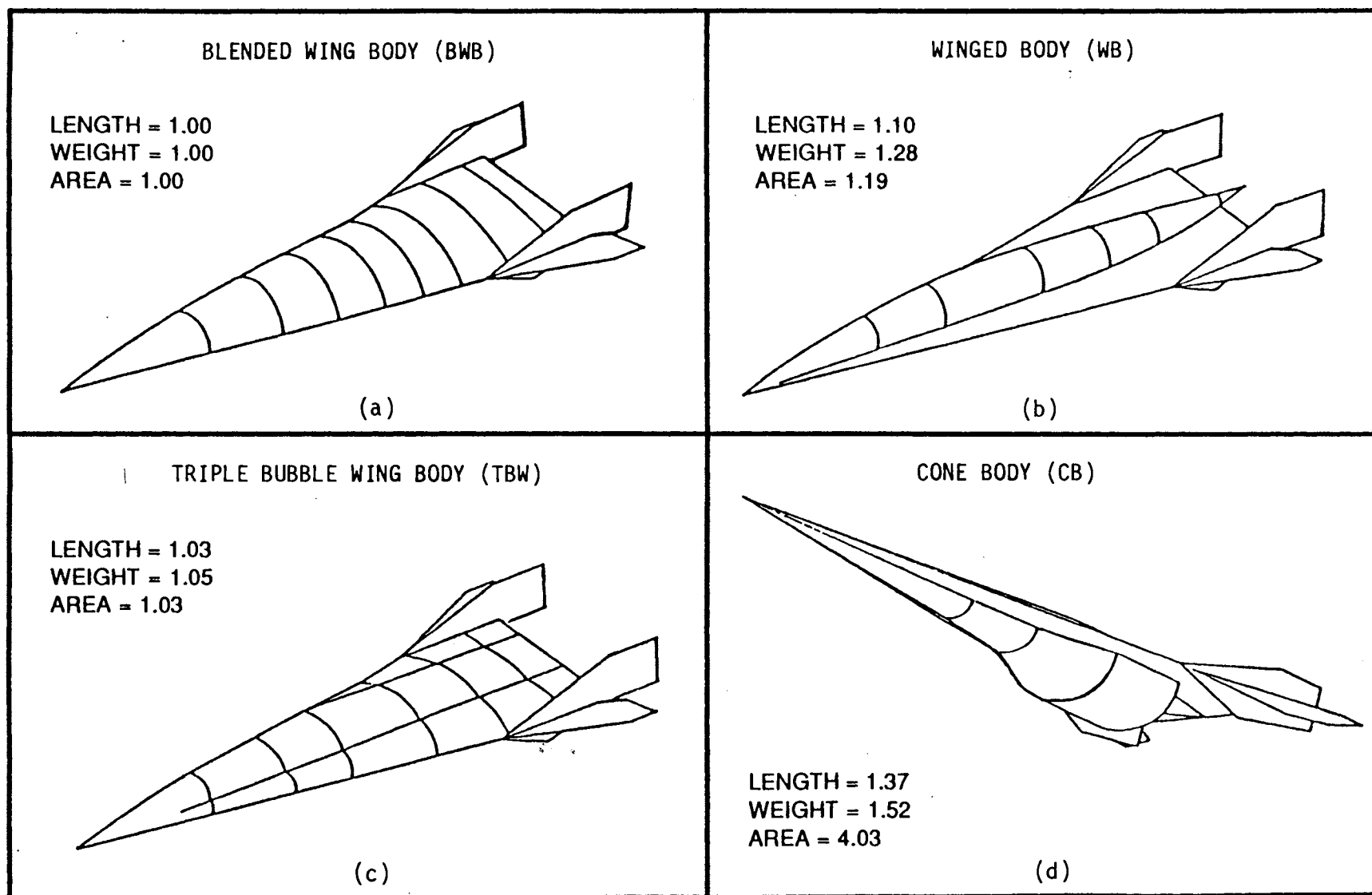


Figure 1-8. Transatmospheric Vehicle Concepts.

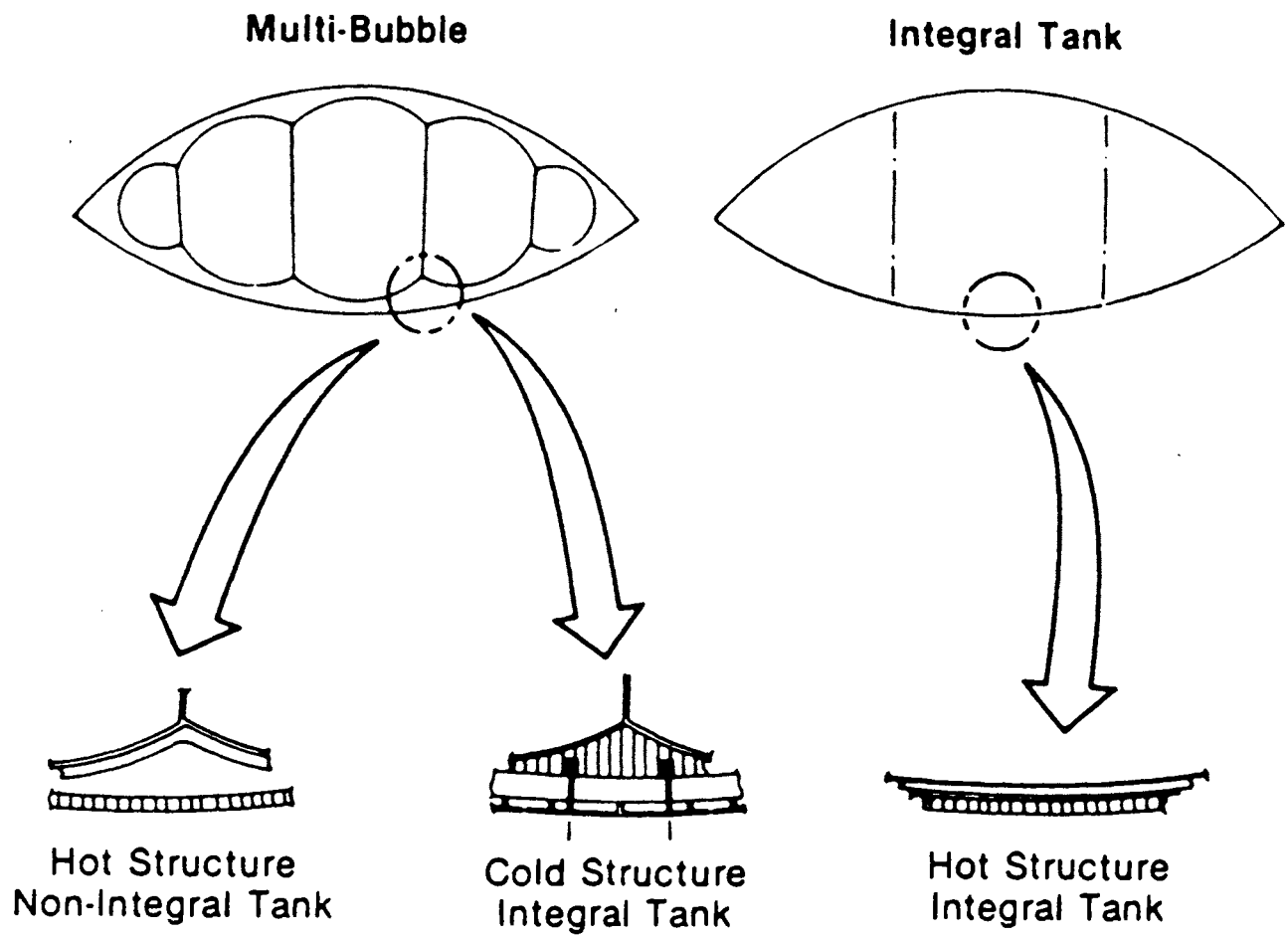


Figure 1-9. Cryogenic Fuselage Tank Concepts (Reference [1-7]).

multi-bubble. A cylindrical tank is the typical integral tank concept employed for most launch vehicles and is very efficient for carrying pressure loads. However, this type of tank is not volumetrically efficient for vehicles such as the Blended Wing Body (BWB) that have noncylindrical contours. The conformal integral tank closely follows vehicle internal contours, yielding very high volumetric efficiencies, but it is not very effective in carrying tank pressure loads.

The multi-bubble non-integral tank combines some of the better features of both the cylindrical and conformal tanks. The multi-bubble tank is more volumetrically efficient than the cylindrical tank for non-circular cross-sections, but it is not as efficient as the conformal tank. The multi-bubble tank can handle the pressure load better than the conformal tank but not as efficiently as the cylindrical tank. Optimal designs for the multi-bubble tank incorporate thermally compliant structural trusses inside the tank rather than shear webs to provide the link from top to bottom.

The BWB class of vehicle requires integral tankage or a conformal/multi-bubble, non-integral tankage concept. Cylindrical tankage concepts do not provide the required volumetric efficiencies for achieving the mission statement. The Triple Bubble Wing Body concept is designed around multi-bubble tankage. Tanks for this concept can be integral or non-integral. The Winged Body and the Cone Body vehicle classes are most amenable to the cylindrical tankage concepts, either integral or non-integral.

1.3.2 Blended Wing Body (BWB) Vehicle and Skin Panels

A BWB hypersonic transatmospheric vehicle design was selected for generic analysis of the response of skin panels to aero-thermo-acoustic loads. The vehicle design is shown in Figures 1-10 through 1-12. The vehicle uses a semi-integral multi-bubble tank as shown in Figure 1-8(c). The tank is internally braced with beams and shear webs that support overall vehicle loads as well as tank internal pressure. With the exception of certain high-temperature heat shield panels in the ramp and

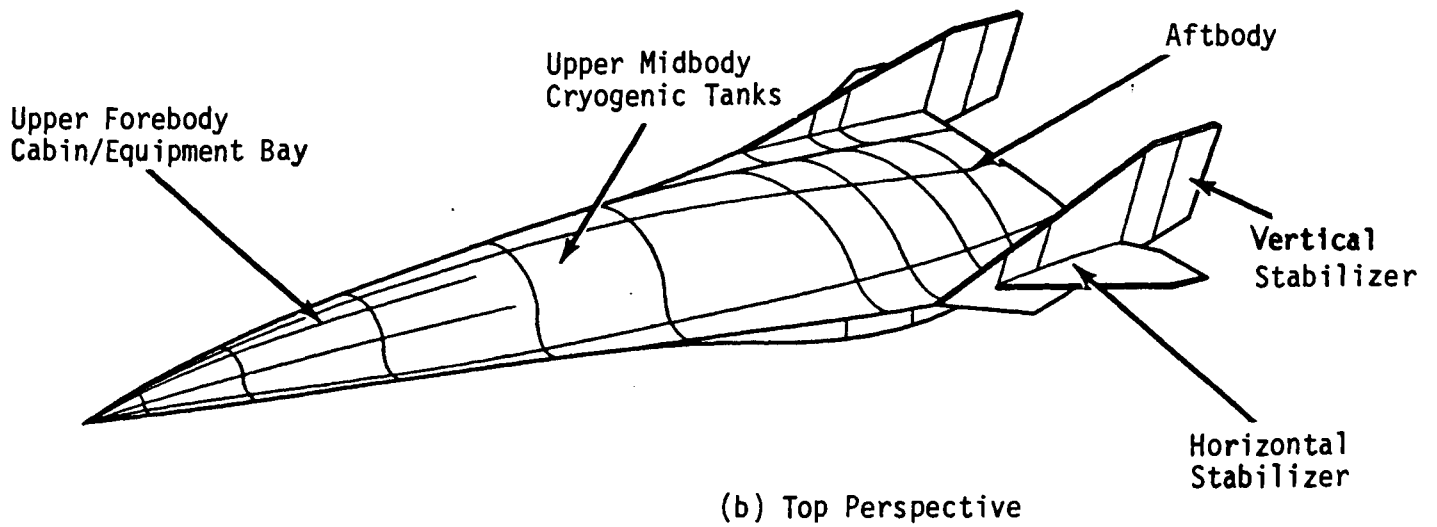
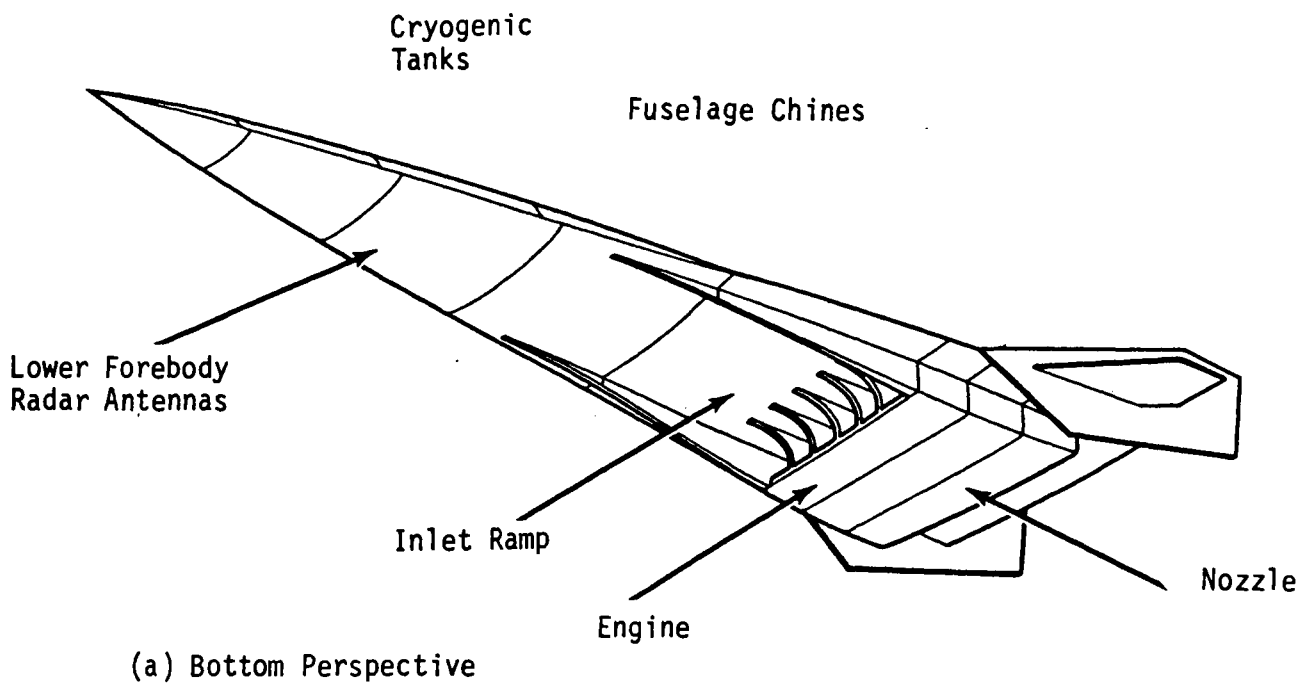


Figure 1-10. Blended Wing Body (a) Bottom and (b) Top Perspectives.

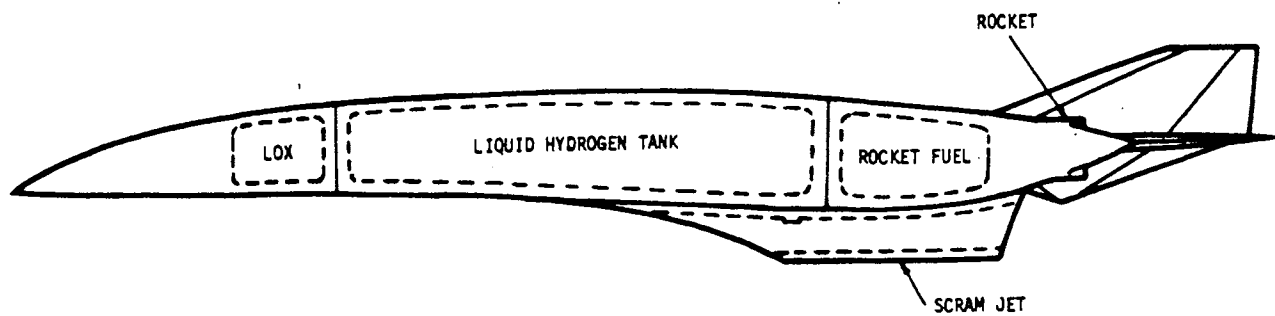


Figure 1-11. Blended Wing Body Section.

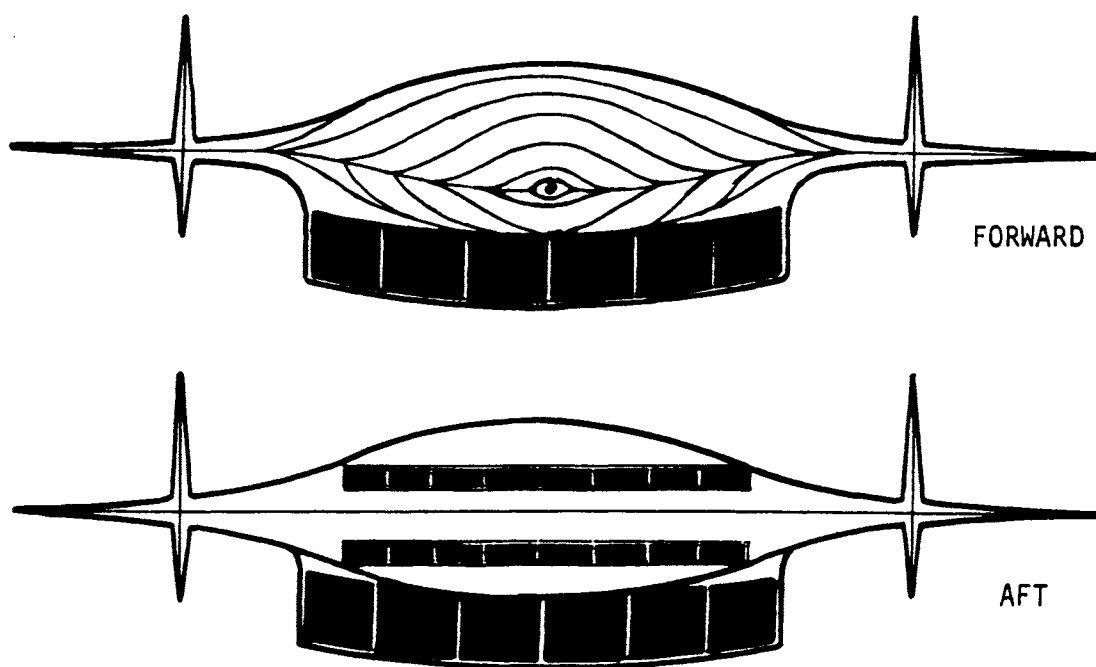


Figure 1-12. Blended Wing Body Fore and Aft Views.

leading edge areas, the vehicle skin is a primary load-bearing structure. As can be seen in Figures 1-10 through 1-12, many of the skin panels are flat or nearly flat. Unlike the cylindrical skins of missiles, these flat panels possess low-frequency bending modes which are susceptible to excitation by low-frequency components of engine sound, turbulent boundary layer fluctuating pressures, and shock-interaction loads.

The greatest part of the interior volume of the vehicle contains liquid hydrogen fuel for the scramjet engine, which is located in the lower aft surface. Air into the scramjet engine is compressed and conditioned by a planar ramp that extends between the lower forebody and the engine inlet. A liquid oxygen tank forward of the liquid hydrogen tank provides supplemental oxygen. A series of rocket thrusters extend horizontally across the upper and lower aftbody. Each rocket thruster is approximately 2 inches by 2 inches. They provide supplemental thrust at low Mach numbers below 2 where the scramjet becomes effective and for maneuvering in orbit. The lower aftbody forms a nozzle surface which is exposed to the scramjet engine exhaust.

The vehicle has an overall length of approximately 100 feet and can be divided into eight different areas to distinguish directional and environmental concepts: (1) upper forebody (8 to 30 feet aft of nose), (2) upper midbody (30 to 60 feet aft of nose), (3) upper aftbody (60 to 100 feet aft of nose), (4) lower forebody (4 to 35 feet aft of nose), (5) engine inlet ramps (35 to 60 feet aft of nose), (6) engine and nozzle (70 to 100 feet), (7) wing, i.e., horizontal surfaces, and (8) tail, vertical surfaces.

The forebody is defined as the portion of the vehicle aft of the nose and ending at the beginning of the midbody. Upper and lower forebody structural concepts are identical, consisting of integrally stiffened carbon-carbon skins attached to underlying carbon-carbon ring frames and longerons. Carbon-carbon was chosen for this application because of thermal and weight considerations. The structural temperatures in this area of the fuselage are above 1800°F (the upper use temperature for advanced titanium matrix composites), but below 3000°F

(the upper use temperature for carbon-carbon). In addition, trade studies have shown that structural carbon-carbon is more weight efficient than actively cooled structure for areas where carbon-carbon use temperature is not exceeded.

The detailed dimensions of the lower forebody panels are shown in Figure 1-13. The carbon-carbon is assumed to be quasi-isotropic and possesses ACC-4 properties, at a minimum. The stiffener heights and widths are 2.0 inches and 0.115 inch, respectively. The skin thickness is 0.15 inch (minimum gage is approximately 0.065 inch). The stiffener spacing is 6 inches. The stiffeners consist of uniaxial blades that tie into thickened side rails to minimize rotation. The blade type stiffener is chosen over "T," "L," and hat stiffeners because it contains no re-entrant corners. Fabrication and coating of re-entrant corners or biaxially stiffened carbon-carbon panels are not within current carbon-carbon capability, although development efforts are under way. There is a thick layer of alumina insulation between the panel and the cryogenic tank structure. The panel side rails are picked up by attachments that allow relative thermal displacement between the tank and the panel.

The upper fuselage midbody is defined as the portion of the vehicle aft of the forebody and ending at the beginning of the aft fuselage. This includes the structure from 30 feet to 60 feet. The midbody structural concept consists of single-faced corrugated skin panels of formed advanced titanium matrix composite which are attached to underlying titanium matrix ring frames and longerons. The skin panels are 4 feet by 4 feet with 32 stiffeners per panel. Advanced titanium matrix composites were chosen for this application based on mechanical properties at use temperatures. Titanium matrix composites possess the high stiffness required to resist local panel buckling (failure mode for much of the midbody) at temperatures that preclude use of other typical materials.

The upper fuselage aftbody is defined as the portion of the vehicle aft of the midbody. This includes the structure from 60 to 100 feet aft. The aftbody structural concept consists of single-faced corrugated

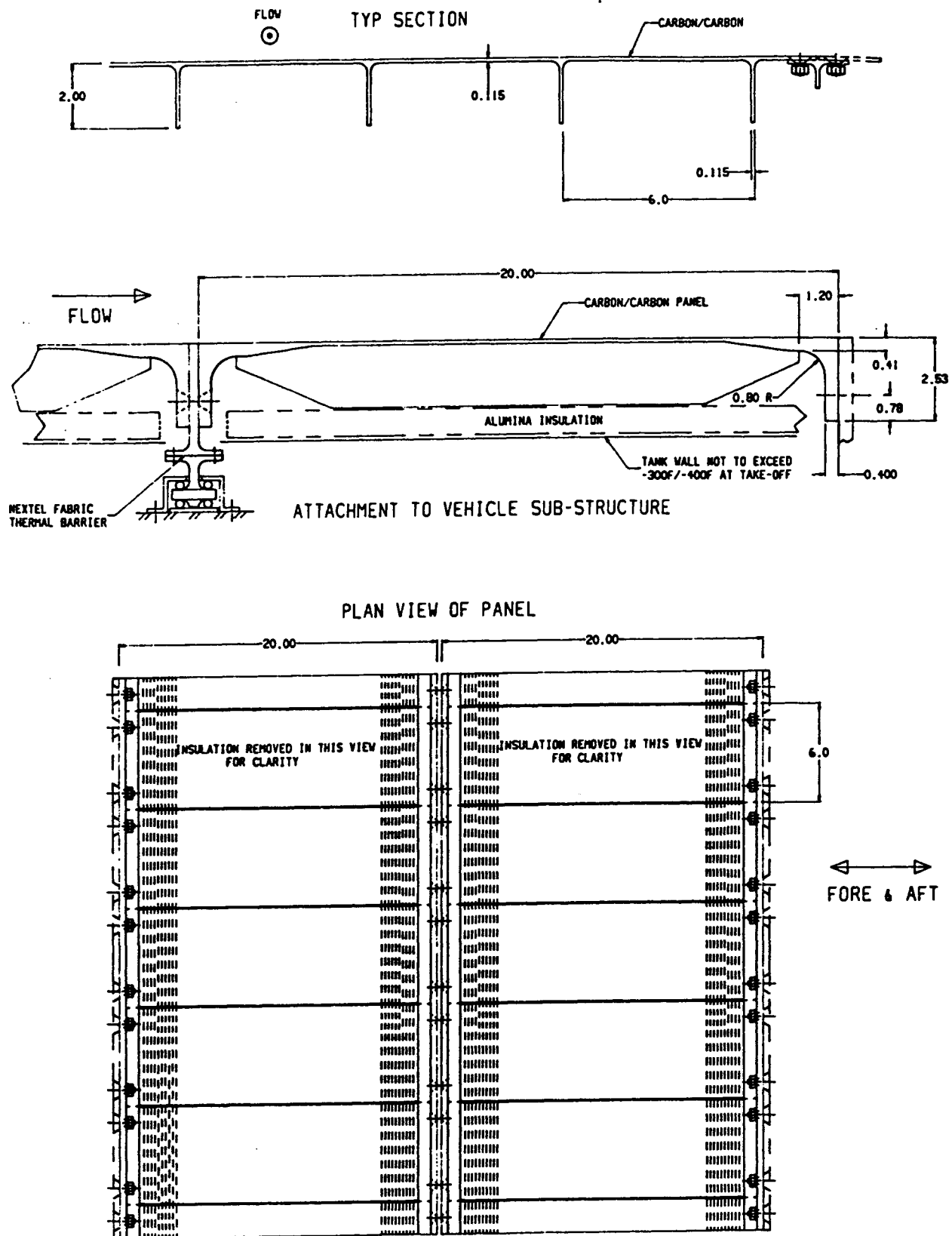


Figure 1-13. Lower Forebody Panel Located 20 Feet Aft of Nose on Under Body.

skin panels (advanced titanium matrix composite) attached to underlying titanium matrix composite ring frames and longerons. The skin panels are 4 feet by 4 feet with 30 stiffeners per panel. Advanced titanium matrix composites were chosen for this application because of their mechanical properties at use temperatures. Like the midbody, the aftbody requires high stiffness to resist local panel buckling.

The detailed dimensions of the aftbody skin panel are shown in Figure 1-14. The titanium matrix composite face sheet is 0.030 inch thick. The panel has integral corrugated stiffeners with corrugations that are on 1.6-inch centers and 1.75 inches in height. All webs and flanges are 0.015 inch thick (minimum gage for this material). The panel insulation and support are similar to those of the forebody panel.

The engine inlet ramp is defined as the portion of the vehicle aft of the forebody and ending at the engine inlet. This includes the structure from 35 to 60 feet. The ramp structural concept consists of single-faced corrugated skin protected by stiffened carbon-carbon panels. The skin panels are supported by carbon-carbon joints which allow thermal expansion relative to the underlying skin structure. The skin panels are 48 inches by 48 inches with frames on 20-inch centers. This structural concept (metallic structure protected by passively cooled heat shields) was selected based on studies showing weight benefits for this type of structure versus actively cooled structure.

The detailed dimensions of the carbon-carbon ramp skin panel are shown in Figure 1-15. The single blade stiffeners are 1.25 inches high and 0.065 inch thick, spaced 10 inches apart to form equilateral triangles. These panels do not bear structural in-plane loads. They are heat shields and their thickness is sized by aeroacoustic loads.

The nozzle is defined as the portion of the vehicle aft of the engine and continuing to the aft fuselage closeout. The nozzle structural concept consists of honeycomb actively cooled skin panels. Active cooling is achieved using coolants passed through integral channels in the face sheets. The face sheets are advanced titanium

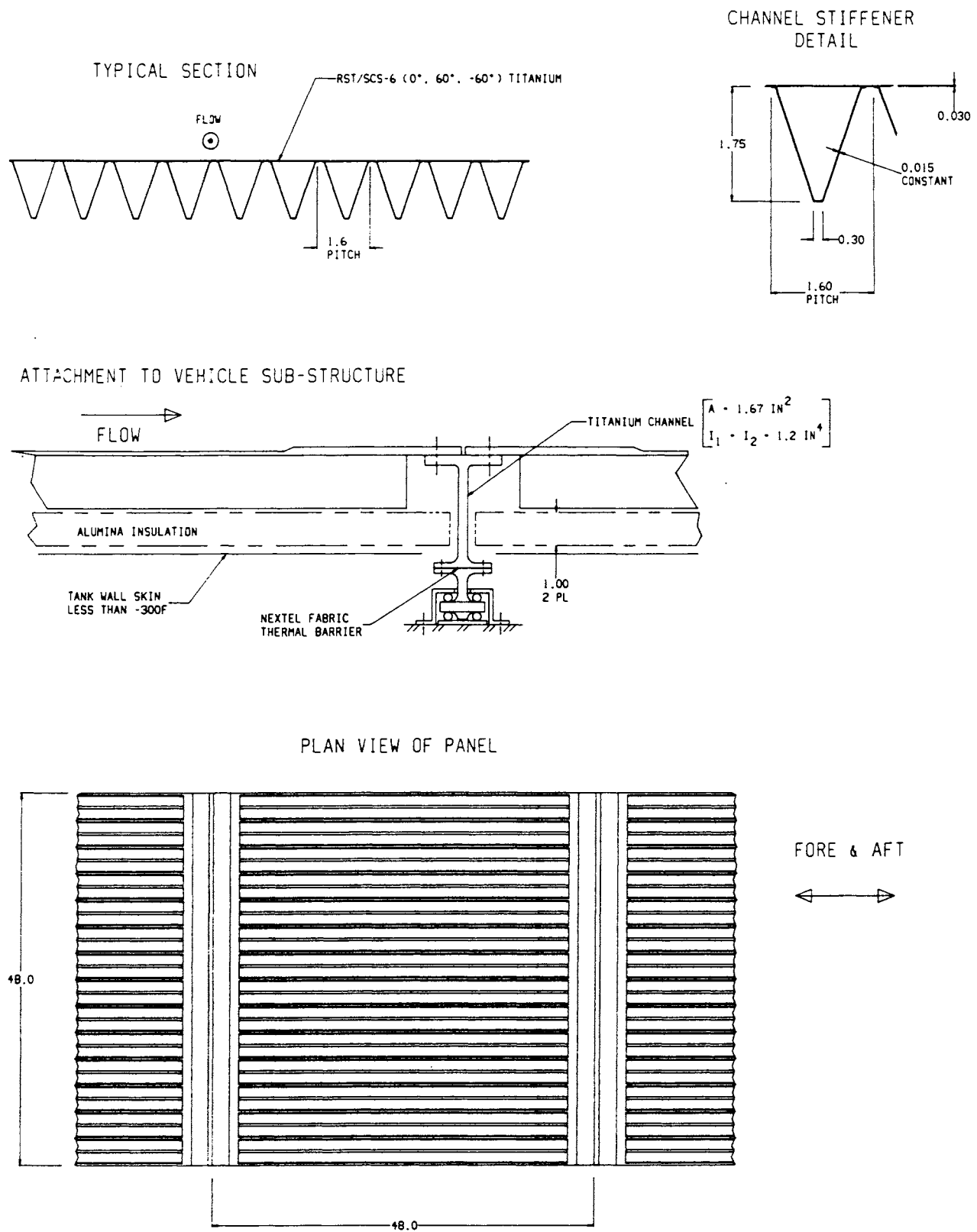


Figure 1-14. Aftbody Panel Located 90 Feet Aft of Nose on Upper Body.

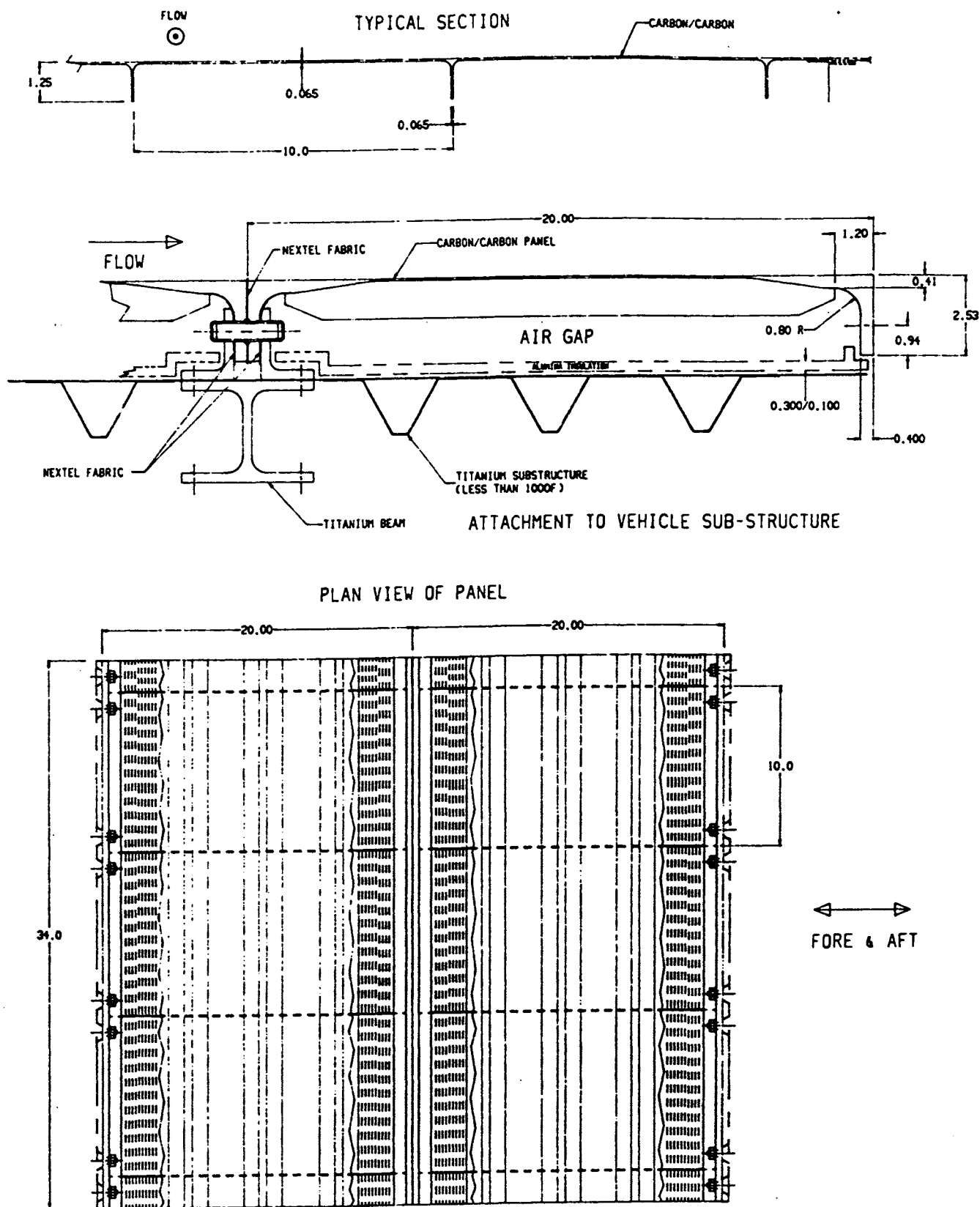


Figure 1-15. Ramp Panel Located 60 Feet Aft of Nose on Underside of Vehicle.

matrix composites and the core is titanium. The skin panels are supported by advanced titanium matrix composite frames which are attached to the underlying skin structure. This structural concept (metallic actively cooled honeycomb structure) was selected based on the extreme temperatures and heat fluxes that would make passively cooled structures untenable.

The detailed dimensions of the nozzle honeycomb panels are shown in Figure 1-16. The face sheets are 0.015 inch thick and the overall panel height is 1.10 inch.

The horizontal and vertical stabilizers are fabricated from corrugation stiffened panels separated by I-section spars. The horizontal stabilizer upper surface structural concept consists of single-faced corrugated skin panels (advanced titanium matrix composite) attached to underlying titanium matrix composite sine-wave spars and ribs. The skin panels are approximately 74 inches by 36 inches with 43 stiffeners per panel. Advanced titanium matrix composites were chosen for this application because of their mechanical properties at use temperatures. Like the midbody and the aftbody, the horizontal stabilizer upper surface requires high stiffness to resist local panel buckling.

The detailed dimensions of the horizontal stabilizer upper skins are shown in Figure 1-17. The titanium matrix composite face sheet is 0.030 inch thick. Corrugations are on 1.7-inch centers and are 2.5 inches in height. All webs and flanges are 0.015 inch thick (minimum gage for this material). The design concepts and details of the horizontal stabilizer lower surface and vertical stabilizer surfaces are similar to those of the horizontal stabilizer upper skin.

1.4 EVALUATION OF THERMO-VIBRO-ACOUSTIC LOADS AND FATIGUE

The evaluation of the skin panels of the transatmospheric hypersonic vehicle follows the steps shown in Figure 1-18. The vehicle mission and trajectory (Section 1.1) dictate structure and design concepts and

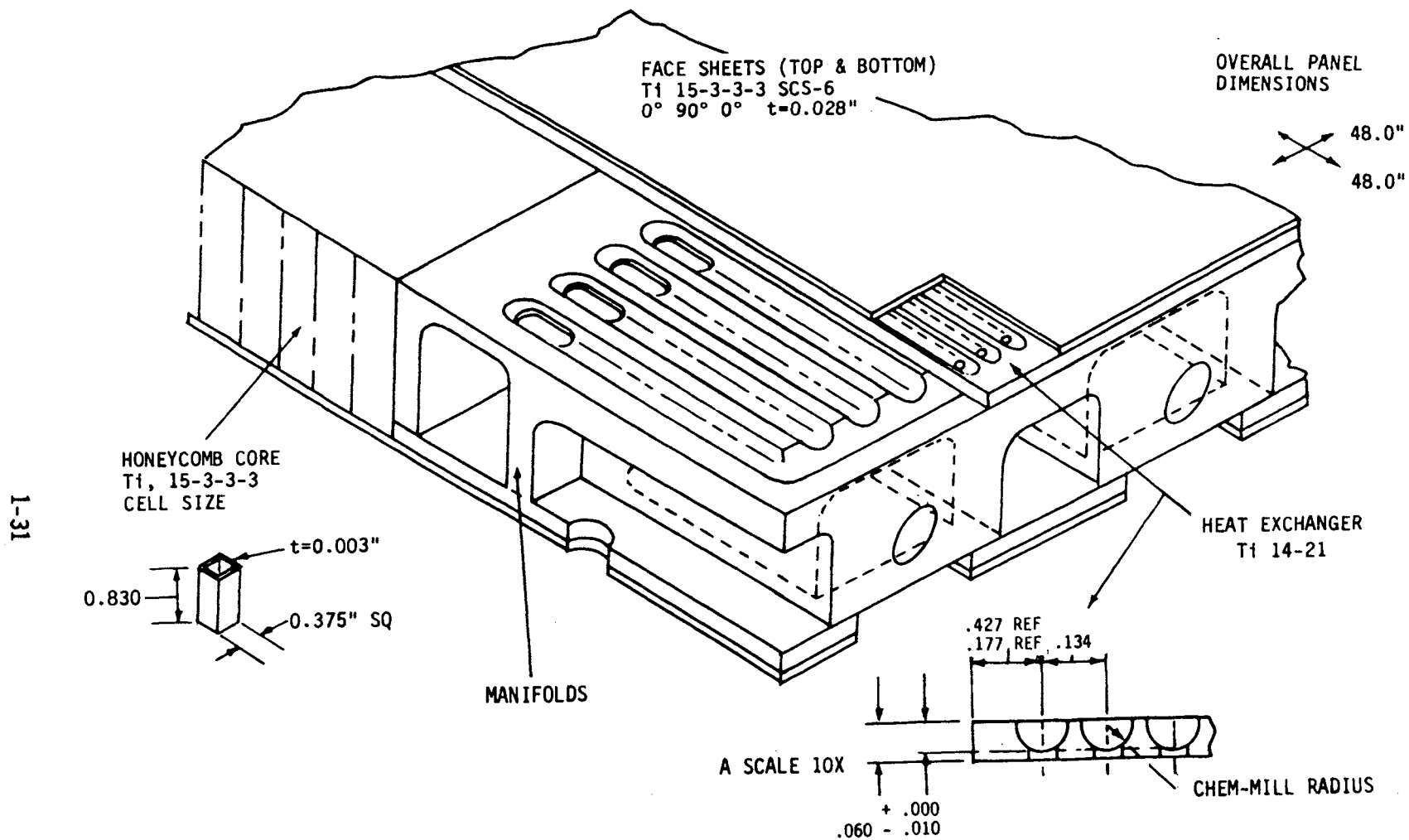


Figure 1-16. Actively Cooled Nozzle Panel Located 95 Feet Aft on Nose on Underside of Vehicle.

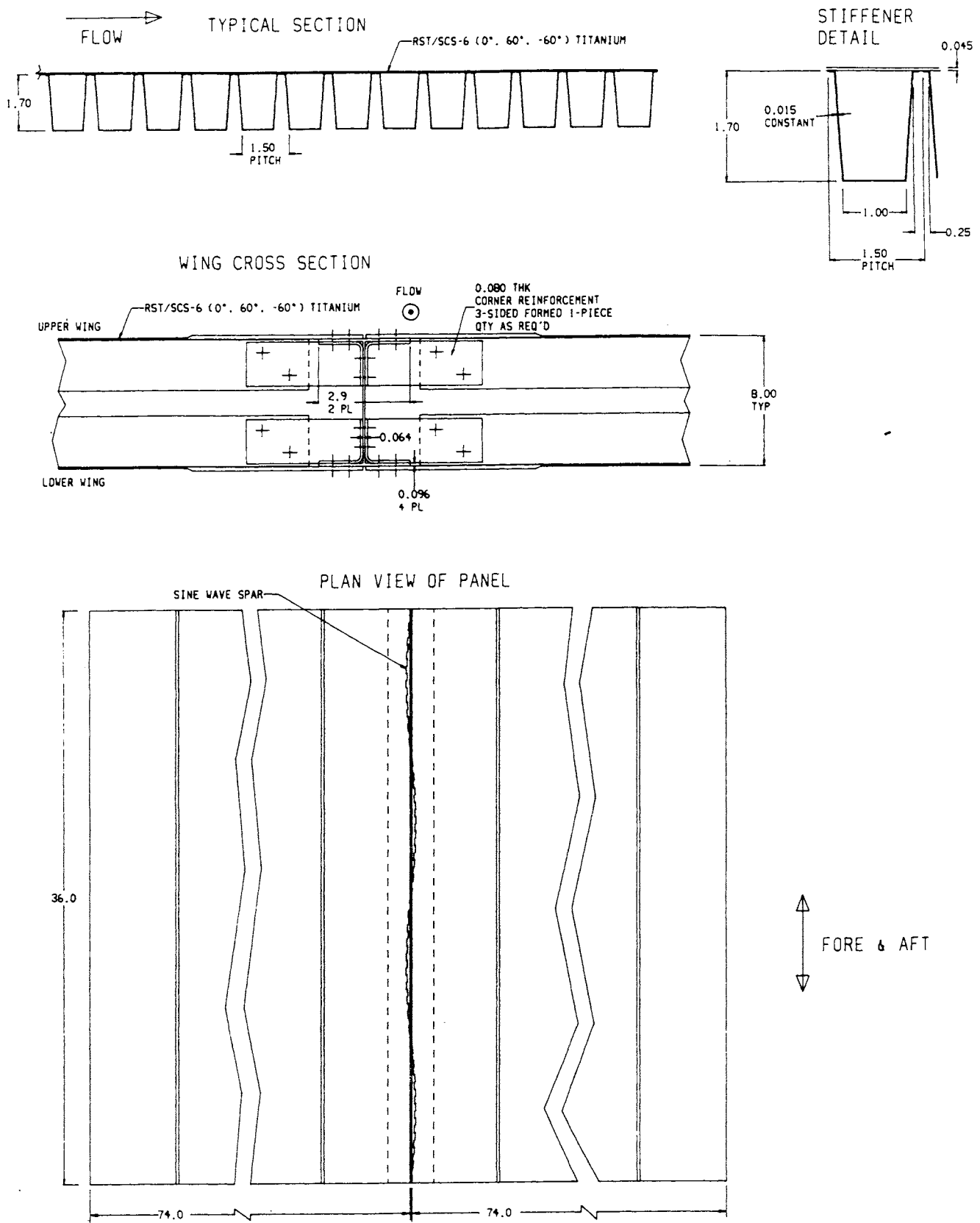


Figure 1-17. Horizontal Stabilizer Skin Panel Located 90 Feet Aft of Nose.

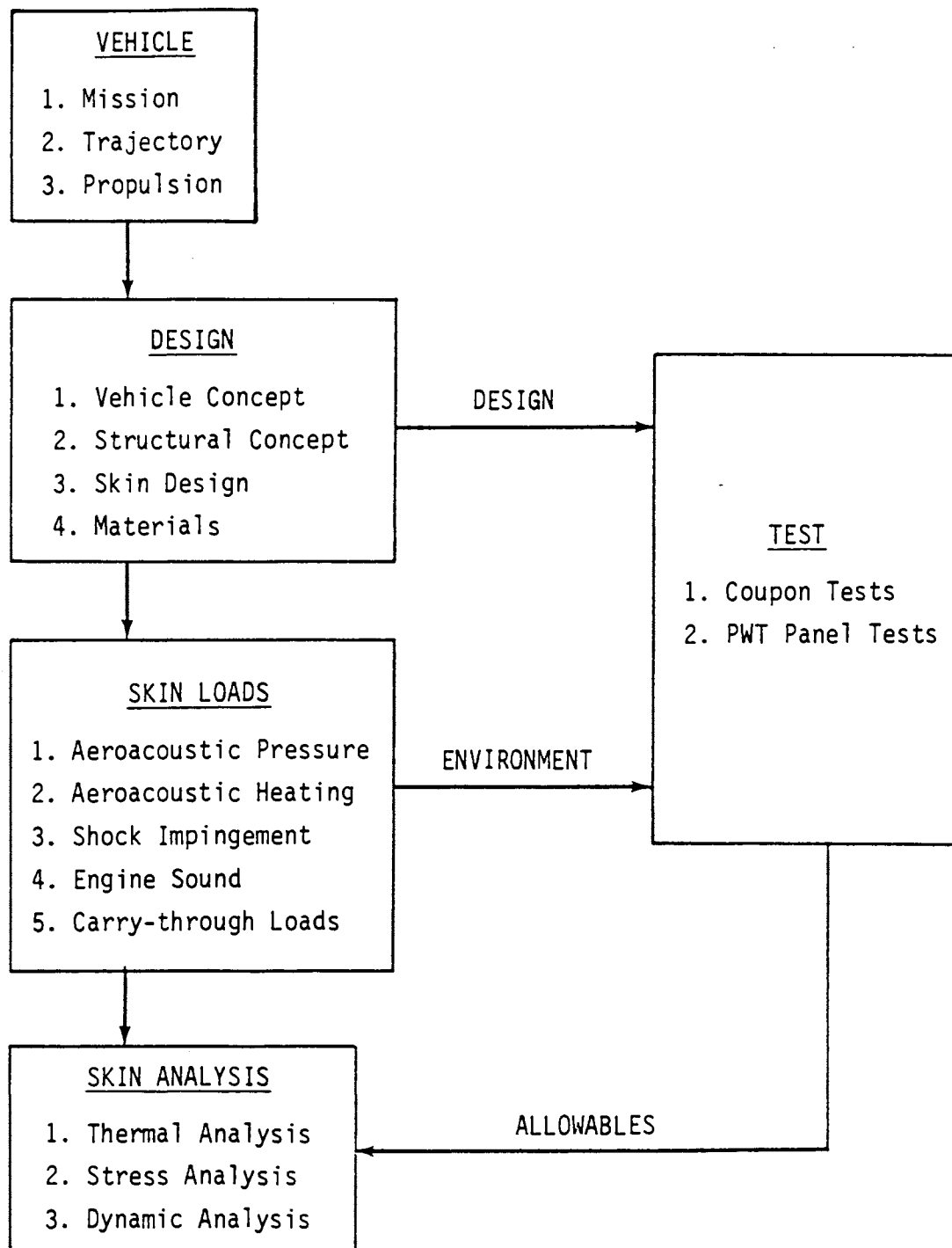


Figure 1-18. Flow Chart for Evaluation of Thermo-Vibro-Acoustic Loads and Fatigue of Hypersonic Flight Vehicle Structure.

material choices (Section 1.2). Skin loads are the sum of steady and fluctuating aeroacoustic pressures, engine sound, and carry-through loads. The analysis of these loads is presented in Sections 2 and 3 of this report.

Four skin panels have been chosen for detailed analysis:

- (1) Forebody panel (Figure 1-13), 20 feet from nose on under body.
- (2) Ramp panel (Figure 1-15), 60 feet from nose on under body.
- (3) Horizontal stabilizer (Figure 1-17), 90 feet from nose.
- (4) Actively cooled panel (Figure 1-16), 95 feet from nose.

The analyses of these panels are presented in Section 4, 5, 6, and 7, respectively. They include thermal analysis to obtain temperature fields and thermal stress, stress analysis to determine the adequacy of the structure to bear mean loads without buckling or fracture, and dynamic analysis to determine the propensity for high cycle fatigue under the unsteady aeroacoustic loads and engine sound. Section 8 describes the experimental plan for testing coupons and panels. Appendix A presents PNS solutions of heat transfer and subsequent acoustic load definition on the Blended Wing Body. Appendix B contains engine acoustic analysis supporting data. Appendix C provides finite element actively cooled panel results. Appendix D addresses damage accumulation for high cycle fatigue, and Appendix E describes vehicle carry-through loads.

1.5 REFERENCES

- 1-1 Report of the Defense Science Board Task Force on the National Aerospace Plane (NASP), AD-A201-124, Department of Defense, Washington, D.C., September 1988.
- 1-2 Billig, F.S., et al., Proposed Supplement to Propulsion System Management Plan, Johns Hopkins University, APL Report JHU/APL-NASP-86-1.

- 1-3 Coe, C.F., Chyu, W.J., and Dods, J.B., Pressure Fluctuations Underlying Attached and Separated Supersonic Turbulent Boundary Layers and Shock Waves, AIAA-75-996, October 1973.
- 1-4 Zorumski, William. E., Fluctuating Pressure Loads Under High Speed Boundary Layers, NASA Technical Memorandum 100517, October 1987.
- 1-5 Ungar, Eric E., Wilby, John F., and Bliss, Donald B., A Guide for the Estimation of Aeroacoustic Loads on Flight Vehicle Surfaces, AFFDL-TR-76-91, February 1977.
- 1-6 Tran, T.T., Tan, D.K.M., and Bogdonoff, S.M., Surface Pressure Fluctuations in a Three-Dimensional Shock Wave/Turbulent Boundary Layer Interaction at Various Shock Strengths, AIAA-85-1562, July 1985.
- 1-7 Ellis, D.A., Overview - Design of an Efficient Lightweight Airframe Structure for the National Aerospace Plane, AIAA Paper 89-1406-CP, American Institute of Aeronautics and Astronautics, Washington, D.C., 1989.

838PROP/3-1.BB
12-11-89

SECTION 2

AEROACOUSTIC LOADS

2.1 INTRODUCTION

The algorithms developed to date for predicting aeroacoustic loads on hypersonic structures have been based on ground test data and limited flight data for axisymmetric bodies (Reference [2-1]) as well as 3D maneuvering bodies (References [2-2, 2-3]), both of which are an order of magnitude smaller than the transatmospheric vehicle. Moreover, most of these algorithms are generally for attached turbulent boundary layers. Regions experiencing flow separation as developed on compression surfaces (ramps) or by shock-boundary layer interactions present a much more complex structure for modeling. Figure 2-1 shows a typical Space Transportation System representative of hypersonic configurations featuring 3D non-circular cross-sections with ramps, control surfaces, and shock-boundary layer interactions.

References [2-3] and [2-4] review the state-of-the-art of aeroacoustic load prediction techniques for supersonic/hypersonic conditions with attached and separated turbulent flow, respectively. The attached flow prediction techniques were enhanced by Laganelli and Scaggs (Reference [2-5]), who extended the analysis to high Reynolds number flows and added surface roughness effects, while Reference [2-6] considers coupled surface roughness and blowing. Relative to flow interaction phenomena for steady and unsteady flows, Settles and Dolling (Reference [2-7]) reviewed swept shock wave-boundary layer interactions, including classification of flow regimes. As a result of the complex 3D nonlinear interaction, experiments have led the way in investigating the interacting phenomena because of restrictive assumptions

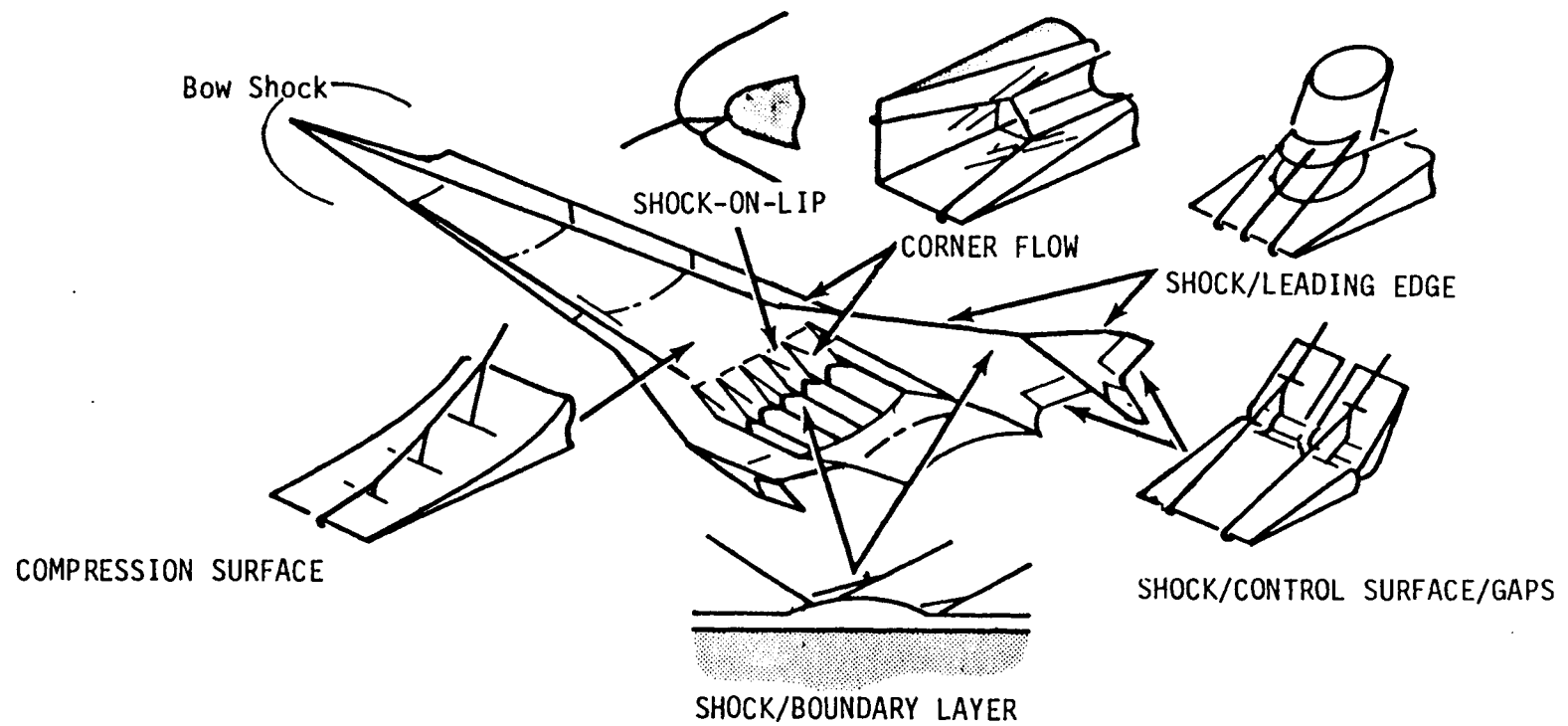


Figure 2-1. Space Transportation System with Flow Interaction Regimes.

and limitations in analysis. Reference [2-7] also reviews the experimental work performed at Princeton University, including References [2-8] through [2-13], which provided the basis for developing acoustic algorithms for shock-boundary layer interactions presented in Reference [2-4].

The following sections develop aeroacoustic methods for attached and shock-interaction loads and boundary layer transition. In Section 2.5 these methods are applied to the transatmospheric vehicle.

2.2 AEROACOUSTIC LOADS IN ATTACHED FLOW

This section briefly reviews acoustic load prediction techniques for attached turbulent boundary layer flows. Details concerning the development of these techniques can be found in the cited literature.

The rms pressure fluctuations in attached turbulent boundary layer flows have been found to scale with the boundary layer dynamic pressure, Mach number, and wall temperature ratio. Generally, power spectral density (PSD) and rms pressure (\bar{p}) prediction methods were developed independently from experimental evidence. The methodology presented in References [2-3] and [2-4] relates these two functions using definitions of power spectra with the Houbolt algorithm (Reference [2-14]). The results for smooth wall and rough wall conditions are given below.

(a) Smooth Walls

rms fluctuating pressure:

$$\bar{p}/q = 0.006 F_c^{\lambda(1+b)} \quad (2-1)$$

power spectrum:

$$\frac{\phi(\omega)v}{q^2 \ell} = \frac{(\bar{p}/q)^2 k' \frac{2}{\pi}}{1 + \left(k' \frac{\ell}{v} \omega\right)^2} \quad (2-2)$$

where

$$F_c = \frac{C_{f,i}}{C_f} = h^*/h_e = \frac{1}{2} + \frac{h_w}{h_{aw}} \left(\frac{1}{2} + r \frac{\gamma - 1}{2} M_e^2 \right) + 0.22r \frac{\gamma - 1}{2} M_e^2 \quad (2-3)$$

$$\lambda = [2m - (1 + n)] / (3 + n) \quad (2-4)$$

$$b = 2(m + 1) / [(1 + n) - 2m] \quad (2-5)$$

$$k' = F_c^{-2\lambda} \quad (2-6)$$

The characteristic length (ℓ) is generally chosen as the boundary layer displacement thickness (δ^*) and the characteristic velocity (v) as the boundary layer edge value (U_e). The parameter k' appeared to have physical interpretation representing compressibility and heat transfer of the fluid medium (see Figure 2-2). This is a consequence of the magnitude of the PSD as $\omega \rightarrow 0$ as well as the roll-off of the PSD as $\omega \rightarrow 10^4$.

The parameters n and m represent velocity and viscous power law exponents, while b represents an interpretation between the power intensity and power spectra. For incompressible flow, $F_c \rightarrow$ unity such that $(\bar{p}/q)_i \rightarrow 0.006$, a value that, while accepted by the scientific community, is believed to be in error (Reference [2-11]) as a result of instrumentation gage size limitations. The errors could yield incompressible values of $(\bar{p}/q)_i \rightarrow 0.010$. Pending further definition concerning transducer size errors, the value of 0.006 has been used herein.

With realistic values of the velocity power law exponent ($7 \leq n \leq 12$) together with the viscous power law exponent ($0.6 < m < 1.0$), values of b fall in the range $0.3 < b < 0.6$, which is consistent with values experimentally determined by Laganelli (Reference [2-3]) in the range $0.3 < b < 0.5$. It should be noted that for values of $m = 0.7$, $n = 9$, and $b = 0.4$, Equation 2-1 becomes $\bar{p}/q \rightarrow 0.006/F_c$, which for adiabatic conditions reduces to the Lowson algorithm (Reference [2-15]). Figure 2-3 compares predicted normalized rms pressure and data with compressibility and heat transfer as parameters.

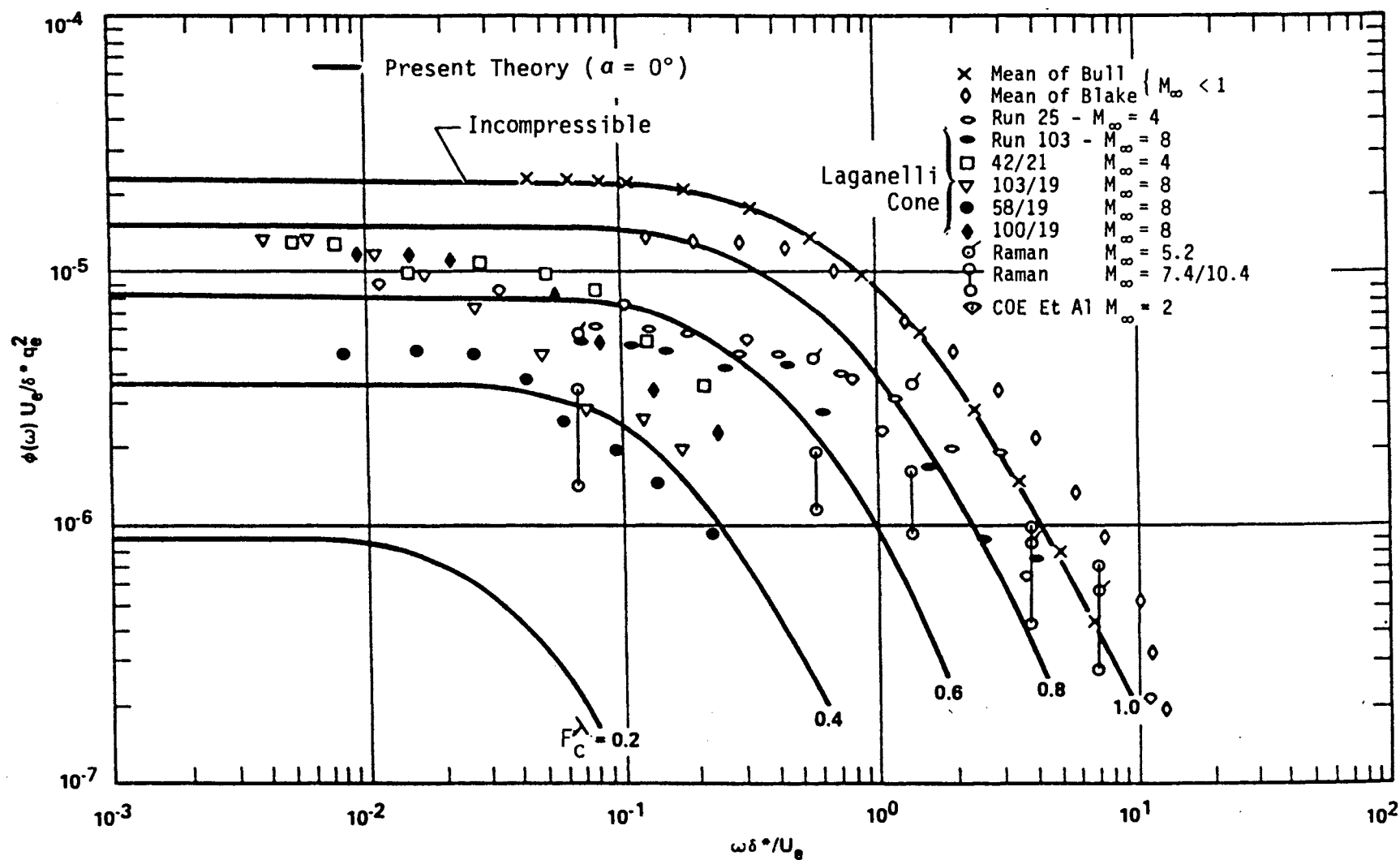


Figure 2-2. Comparison of Normalized Spectral Measurements (Reference [2-2]) and Theory.

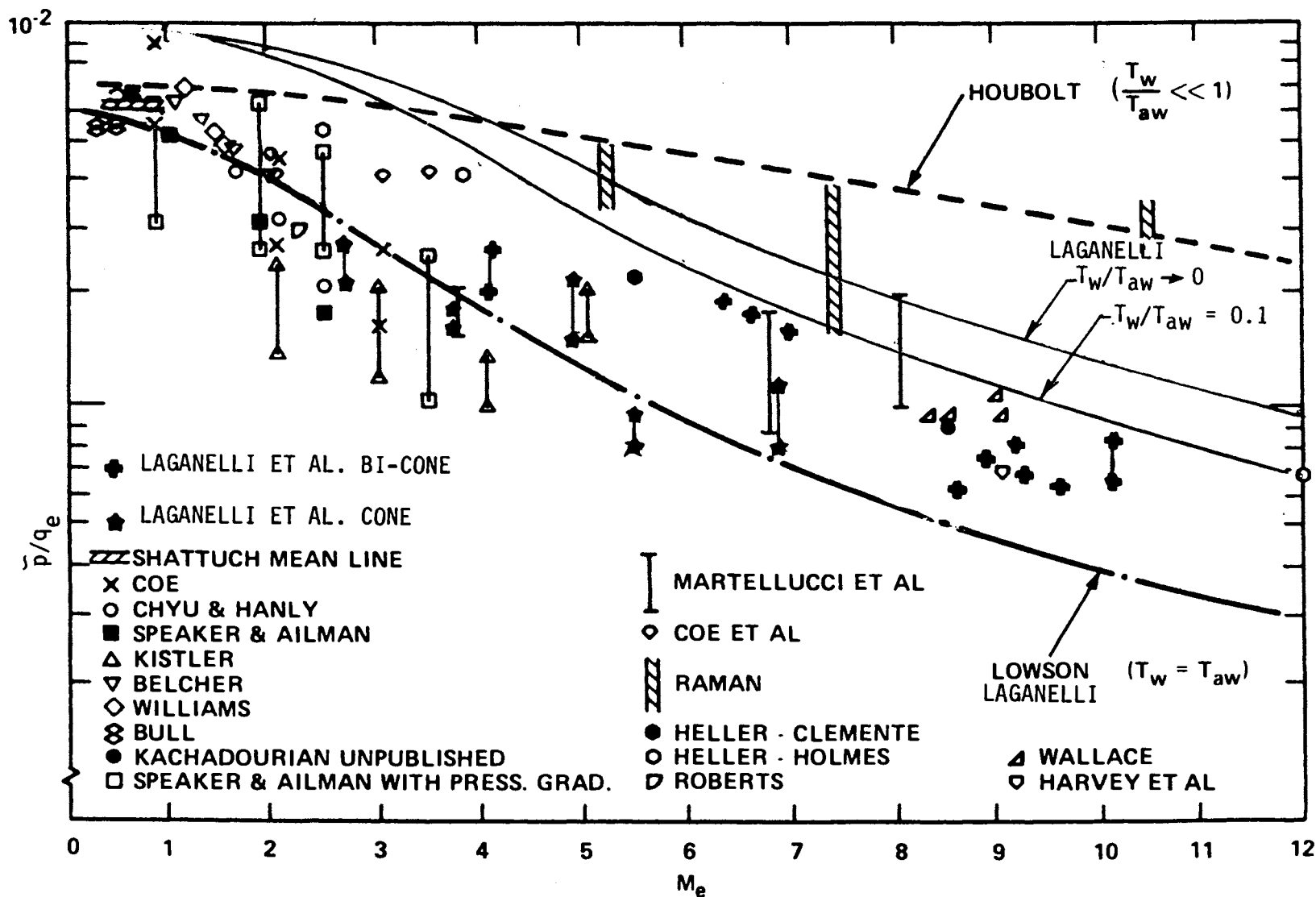


Figure 2-3. RMS Pressure Variation with Mach Number - Attached Turbulent Boundary Layer Flow (Smooth Wall) (from References [2-2, 2-3]).

Equations 2-1 and 2-2 provide the PSD, which can be written as

$$\frac{\phi(\omega)v}{q^2\ell} = \frac{2.293 \times 10^{-5} F_C^{-0.5733}}{1 + F_C^{2.867} \left(\frac{\ell}{v} \omega\right)^2} \quad (2-7)$$

As $\omega \rightarrow 0$,

$$\frac{\phi(\omega \rightarrow 0)v}{q^2\ell} \rightarrow 2.293 \times 10^{-5} F_C^{-0.5733} \quad (2-8)$$

and for adiabatic flow,

$$\left. \frac{\phi(\omega \rightarrow 0)v}{q^2\ell} \right|_{aw} \rightarrow \frac{2.293 \times 10^{-5}}{(1 + 0.13 M_e^2)^{0.5733}} \quad (2-9)$$

(b) Rough Walls

rms power spectrum:

$$\bar{p}/q = 0.006 F_{C_o}^{\lambda(1+b)} (C_f/C_{f_o}) \quad (2-10)$$

where the sole effect of roughness on rms fluctuating pressure is expressed through the skin-friction relation C_f/C_{f_o} . The subscript o refers to smooth wall conditions. Power spectrum is predicted using Equation (2-2) with the augmented value of rms power intensity from Equation (2-10).

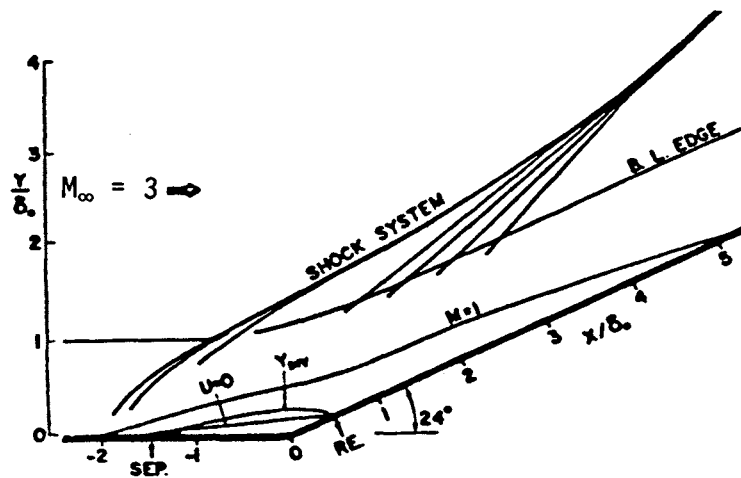
2.3 AEROACOUSTIC LOADS FOR SHOCK-BOUNDARY LAYER INTERACTION FLOWS

This section is concerned with developing acoustic load algorithms in regions influenced by shock-boundary layer interactions. The methodology has been motivated by experimental data as well as fluid dynamic principles.

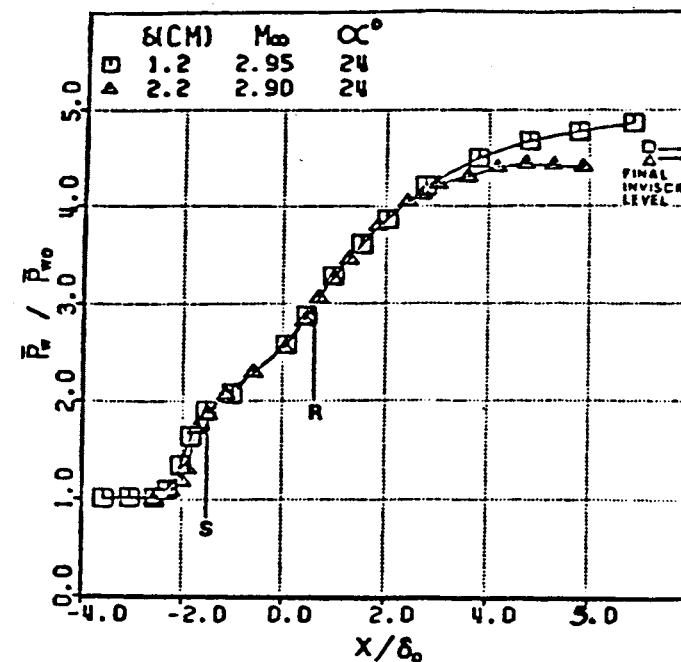
2.3.1 Influence of Geometry on Shock-Boundary Layer Interaction

Compression Corner. The 2D compression corner is an excellent geometry for investigating shock-boundary layer behavior, since this type of configuration has received significant attention in the literature. However, fluctuating pressure and associated spectra have been limited to Mach numbers less than or equal to 3. Figure 2-4 shows the shock-boundary layer characteristics of flow over a 24° compression ramp (Reference [2-16]). Figure 2-4(a) shows the wave interpretation of the interaction, while Figures 2-4(b) and 2-4(c) represent mean and fluctuating pressure distributions. Relative to the mean pressure distribution, the pressure starts to rise upstream of the corner, creating a flow separation region (subsonic) that reattaches on the ramp. The extent of this region and the strength of the shock are dependent upon the angle of deflection of the ramp (α). The shock wave motion has been shown to have the potential to convert mean flow energy into fluctuating energy. The unsteadiness of the interaction, shown in Figures 2-4(c) and 2-4(d), is characterized by three peak positions relative to the points of flow separation and reattachment. The peak value located at approximately $2\delta_0$ upstream of the corner is characteristic of shock oscillations observed in other experiments experiencing the 2D flow separation. The time trace [Figure 2-4(d)] of the pressure signal shows an increase in the pulse frequency with distance in the upstream influence region (distance from corner to position where pressure starts to rise).

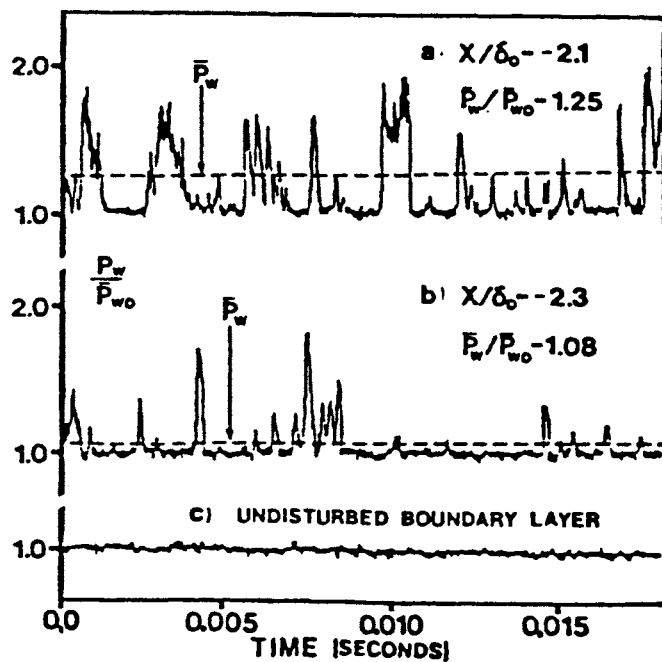
The work of Reference [2-16] was extended by Dolling and Or (Reference [2-13]) to include the effects of shock strength (ramp angle), while Tran (Reference [2-8]) investigated the geometric effects of generating the shock with swept corner interactions. Figure 2-5 shows the fluctuating pressures, normalized by static wall pressure, for the various ramp angles tested in Reference [2-13]. A decrease in rms fluctuating peak pressure as well as plateau levels is experienced with decreasing shock strength. It is interesting that the lowest ramp angle, which displays attached flow characteristics, has a significant rise in the rms fluctuating peak level. Varying the shock generating geometry (Reference [2-8]) while maintaining the same shock strength caused no variation for a fixed inviscid shock strength, suggesting that the unsteadiness within the interaction is a result of the same mechanism.



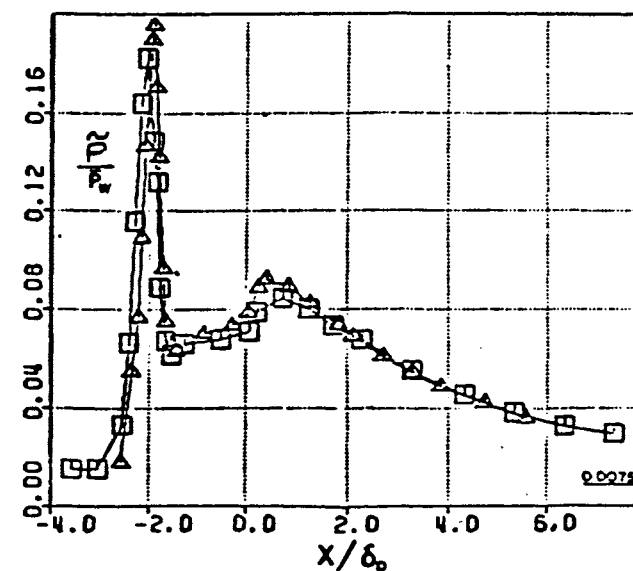
(a) Flow Field Model of Interaction



(b) Mean Wall Pressure Distribution



(d) Pressure-Time History Near Separation



(c) RMS Pressure Distribution

Figure 2-4. Characteristics of Shock-Boundary Layer Interactions on 2D Compression Ramp (References [2-2, 2-16]).

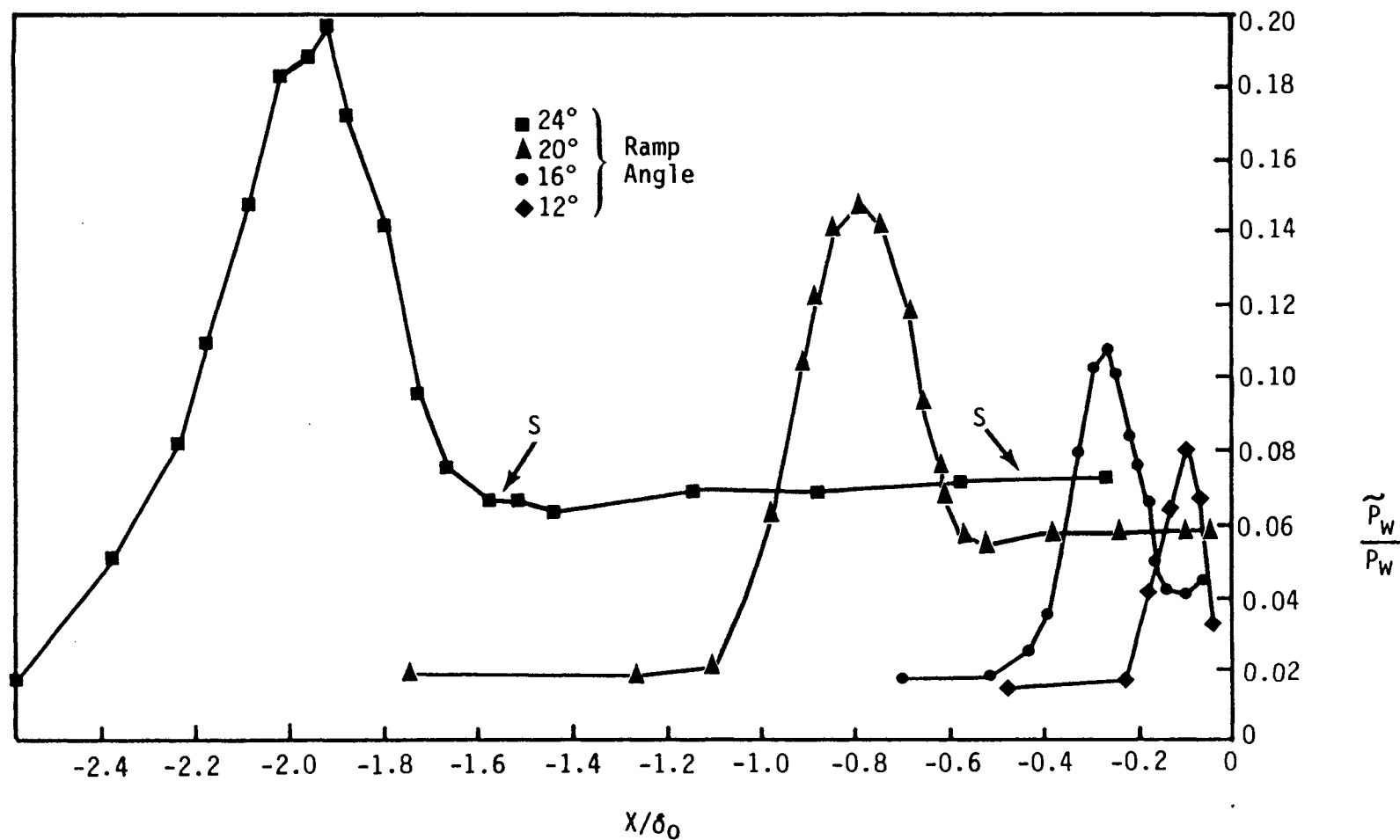


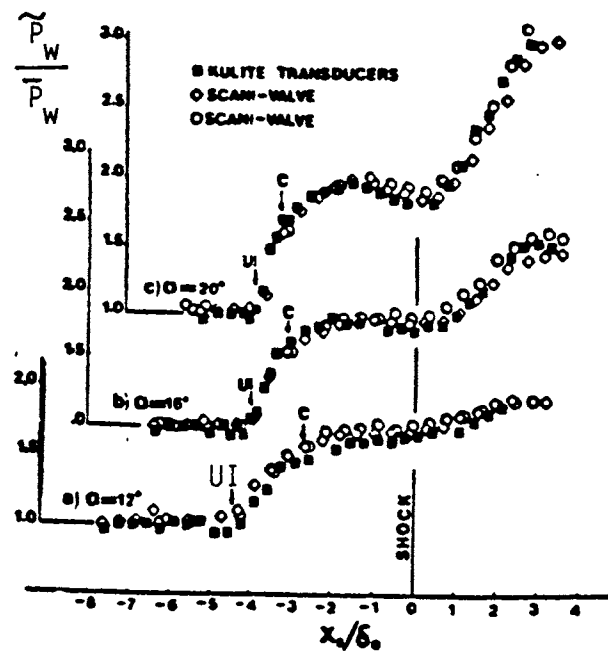
Figure 2-5. RMS Fluctuating Pressure Distribution (2D Interaction) (Reference [2-13]).

Fin Generated Shock-Boundary Layer Interactions. Figure 2-6 shows the results of the various sharp fin-generated interactions for both mean and fluctuating pressure. In Figure 2-6(a), the mean distribution shows locations for the upstream influence (UI) and coalescence (C) line, where the latter is the location of flow separation. It is also noted that the response is similar to that of the corner interaction. The UI line corresponds to the position of initial pressure rise, while the coalescence line does not appear to relate to any flow feature of the mean distribution. Both mean pressure (20° fin data shown) and rms pressure show a dependence on shock strength as experienced in the 2D ramp experiments. However, the rms peak for the 3D swept interaction appears to be approximately one-half the value experienced in the 2D ramp rise for similar approach flow and similar shock strength. Also, the rms fluctuating pressure peaks suggest an intermittent action at the start of the interaction even though the mean pressure has not shown a significant increase.

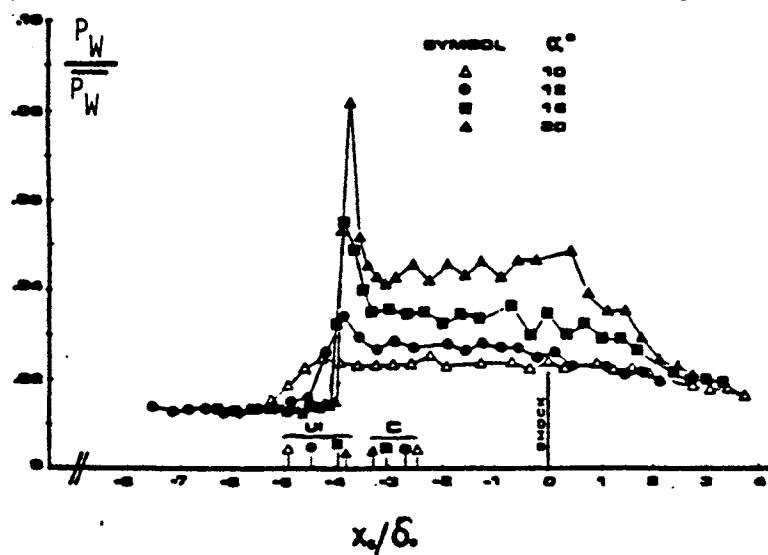
A comparison of 2D ramp and swept type interactions was made by Tran (References [2-8, 2-10, 2-17]) based on the similar behavior at the start of the interaction. It was shown that the 2D (compression corner) and swept shock-boundary layer interactions, while providing similar characteristics, were inherently different in response to the same approach flow. Figure 2-7 compares the peak rms pressure normalized with approach flow fluctuating pressure for the 2D ramp and swept interactions. The rms peak increases with shock strength and magnitude, and for a given inviscid pressure rise, the swept interaction is approximately half of the corresponding 2D ramp interaction. Clearly, both 2D and 3D interactions can significantly augment the attached flow rms pressure levels.

2.3.2 Correlation of Shock-Boundary Layer Interactions

RMS Pressure. An examination of the normalized rms fluctuating pressure distributions for 2D ramp (corner flow) and 3D swept interactions shows a peak and a plateau region prior to reduction to the approach flow levels. Data suggest that the peak rms fluctuating pressure level occurs prior to separation and rapidly reduces to the plateau level. This level appears to be related to the magnitude of the initial pressure gradient and the spatial



a) Mean Pressure Distribution for Fin Interaction at Different Shock Strength



b) Distribution of rms of Wall Pressure Fluctuation for Fin Interaction

Figure 2-6. Mean and Fluctuating Pressure Characteristics for Sharp Fin Shock Generators (Reference [2-8]).

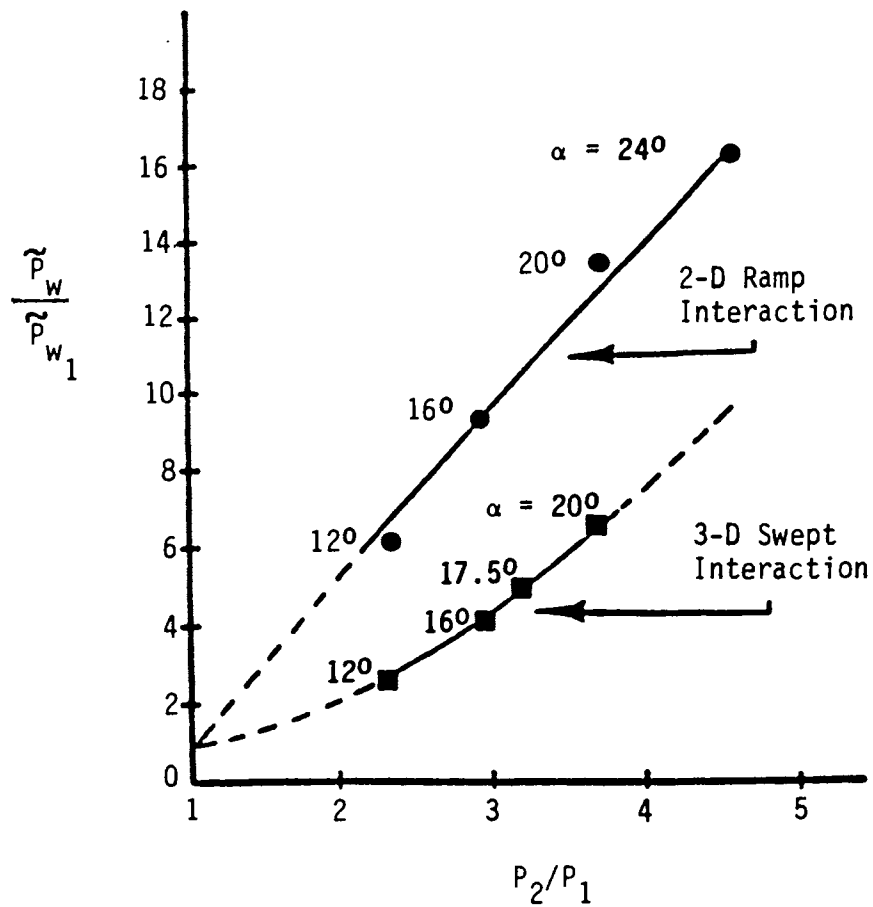


Figure 2-7. Peak rms Fluctuating Pressure Augmentation over Approach Flow Levels for 2D and 3D Shock Interactions (Reference [2-8]).

extent of the gradient. However, in the plateau region, the effect of the pressure gradient or its spatial extent does not appear to be strong, suggesting a correlation relating the approach flow and shock strength, namely

$$\left(\frac{\tilde{P}_{W2}}{P_{W2}} \right)_{\text{plateau}} \approx \left(\frac{\tilde{P}_{W1}}{P_{W1}} \right) \left(\frac{P_{W2}}{P_{W1}} \right)_{\text{max}} \quad (2-11)$$

With consideration of Equation 2-1 and dynamic pressure [$q_1 = (\gamma/2) P_1 M_1^2$], the rms pressure for the approach flow can be written as

$$\frac{\tilde{P}_{W1}}{P_{W1}} \approx 0.006 \frac{\gamma}{2} M_1^2 F_c^{\lambda(1+b)} \quad (2-12)$$

Let $\tilde{p}/q \rightarrow 0.006/F_c$ (i.e., $n = 7$, $m = 0.8$, and $b = 0.4$) at adiabatic wall conditions. The approach flow can then be expressed as

$$\frac{\tilde{P}_{W1}}{P_{W1}} \approx \frac{0.006 (\gamma/2) M_1^2}{1 + 0.13 M_1^2} \quad (2-13)$$

where for $M_1 \approx 3$, $\tilde{P}_{W1}/P_{W1} \approx 0.0174$, which compares with the data of Figures 2-4 and 2-5. The maximum inviscid pressure rise (shock strength) is obtained from the oblique shock relation (2D)

$$\left(\frac{P_{W2}}{P_{W1}} \right)_{\text{max}} = \frac{2\gamma M_1^2 \sin^2 \theta_s - (\gamma - 1)}{\gamma + 1} \quad (2-14)$$

where the shock angle θ_s is approximated (Reference [2-3]) by

$$\theta_s \approx \alpha + \sin^{-1} (1/M_1) \quad (2-15)$$

for α , the shock generator angle.

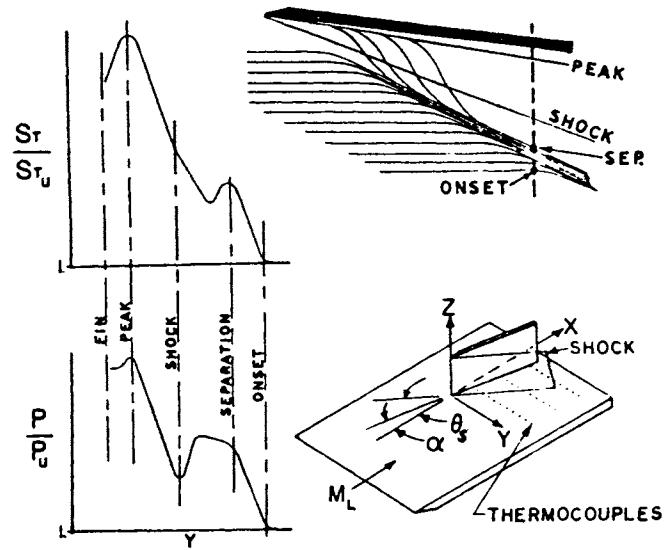
For the 2D corner flow of References [2-13] and [2-18] at a ramp angle α equal to 24° , the maximum inviscid pressure rise becomes $(P_{W2}/P_{W1})_{\max} \approx 4.6$ such that the normalized fluctuating pressure (Equation 2-11) has a value of 0.078, which shows good comparison with the data of Figure 2-5. On a 16° ramp, the normalized fluctuating pressure in the plateau region has a value of 0.0552, which also shows good comparison with the data of Figure 2-5.

For fluctuating pressure levels generated by swept shock-boundary layer interactions (3D fin), the technique overpredicts the experimental results. Accordingly, the flow field structure was re-examined relative to mean flow and wall (heat transfer/shear) characteristics to determine the variation in the inviscid pressure rise. Figure 2-8 shows the basic characteristics of a 3D swept shock interaction of a fin/plate as described by Neumann and Hayes (Reference [2-19]). The pressure distribution is shown divided into two regions by the fin generated oblique shock wave. An outer region extends from onset of the interaction to the shock wave, representing a region of separated flow displaying 2D characteristics. The inner region is characterized by a sharp peak in pressure that lies close to the fin.

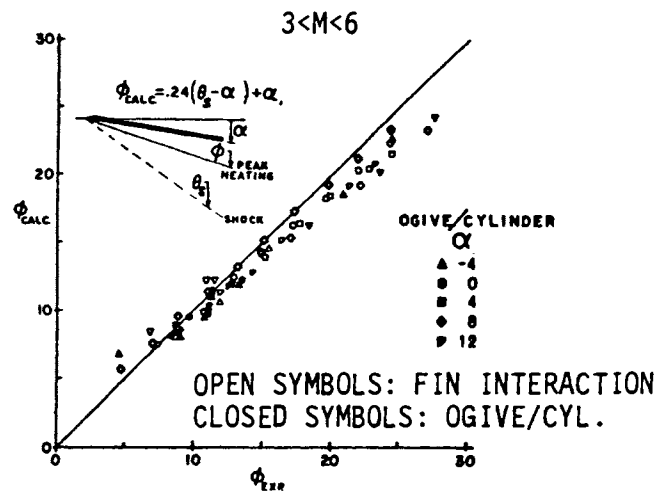
Peak pressure and heating occur along a divergent streamline close to the shock generator. Maximum streamline divergence occurs at the shock location as determined by oblique shock relations. The line of boundary layer separation is observed to be the inner edge of the oil accumulation line, and onset is the point at which the undisturbed streamlines first begin to curve.

The peak mean pressure and heating occur approximately along a streamline from the shock generator leading edge. The angle ϕ between this ray and the freestream direction has been correlated as $\phi = 0.24 (\theta_s - \alpha) + \alpha$. If one generalizes this to consider an arbitrary constant, β , there results

$$\phi = \alpha + \beta \sin^{-1} (1/M) \quad (2-16)$$



a) Basic Interaction Characteristics



b) Peak Heating Location

Figure 2-8. Basic Fin Generated Shock-Boundary Layer Interaction with Peak Wall Heat Transfer (Shear) Location (Reference [2-19]).

where

$$\left. \begin{array}{l} \beta = \text{unity at 2D flow } (\phi = \theta_s) \\ 1/2 < \beta < 1 \text{ at rms peak fluctuating pressure} \\ \text{for swept shock-boundary layer interactions (3D)} \end{array} \right\} \quad (2-17)$$

Inasmuch as the maximum rms fluctuating pressure can be expected to occur at the approximate location of peak pressure and heating (shear), the normalized rms fluctuations can be exposed in terms of the shock strength with the new definition of shock angle with β determined from experimental measurements. With reference to Figure 2-7, the normalized peak rms fluctuating pressure for a 2D/3D shock-boundary layer interaction is correlated as (Figure 2-9)

$$\frac{(\bar{P}_w)_{\text{peak}}}{P_{w_1}} \approx -1.181 + 1.713 (P_{w_2}/P_{w_1}) + 0.468 (P_{w_2}/P_{w_1})^2 \quad (2-18)$$

for $P_{w_2}/P_{w_1} \geq 1$. The inviscid pressure rise is obtained using Equation 2-14.

An inspection of the oblique shock strength relation (Equation 2-14) together with the definition of the 3D swept shock angle location for peak rms fluctuating pressure (Equation 2-16) could provide a pressure ratio $P_{w_2}/P_{w_1} < 1$. This is a result of the parameter $\beta < \text{unity}$. Since $P_{w_2}/P_{w_1} \geq 1$, solution of Equation 2-14 with the shock angle ϕ and limiting value of $P_{w_2}/P_{w_1} = \text{unity}$ gives

$$\phi = \sin^{-1} (1/M)$$

This implies that the shock angle describing the rms pressure for 3D interactions approaches the asymptotic value of the shock strength more rapidly than the 2D interaction as shown in Figure 2-7. Hence, Equation 2-18 has the condition $P_{w_2}/P_{w_1} \geq 1$.

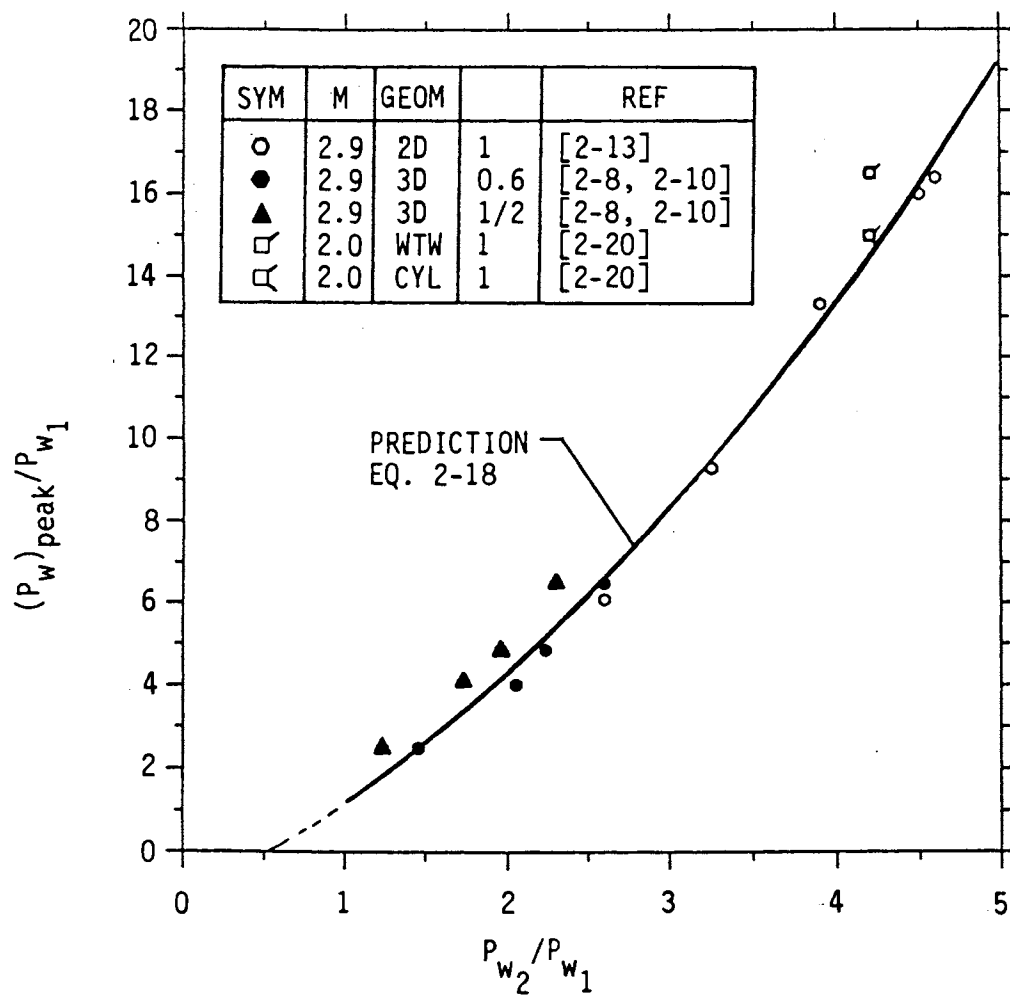


Figure 2-9. Correlation of Peak rms Pressure for Shock-Boundary Layer Interactions

Relative to the plateau region of a swept shock-boundary layer interaction (3D), Equation 2-11 is used together with $\beta = 0.6$ in Equation 2-16. For the fin angle $\alpha = 20^\circ$, the normalized rms plateau pressure has a value of 0.0452, which is representative of the levels shown in Figure 2-6(b). Similar results that show good comparison with measured data are easily obtained for other fin angles.

Plateau Region Mean Pressure Coefficient. Since it is difficult to define the location within the boundary layer, other techniques were used to estimate the mean pressure rise associated with the plateau region of separated boundary layer flow. In particular, the correlations of Kaplan (Reference [2-21]) and Nestler (Reference [2-22]) are recommended for forward facing steps. The Kaplan correlation is expressed as

$$\frac{(P_P / P_{W_1}) - 1}{(\gamma/2) M_1^2} = \frac{4.7}{(M_1^5 Re_x)^{0.148}} \quad (2-19)$$

Moreover, if one considers the pressure rise for an oblique compression shock together with Equation (2-19) and compressible flow tables for shock separation angles over a range of Reynolds and Mach numbers, a value of $\theta \approx 10^\circ$ is a representative average flow turning angle. For this condition, the mean pressure rise in the plateau region can be approximated by (Reference [2-22])

$$\frac{P_{\text{plateau}}}{P_{W_1}} \approx [1 + (\gamma/2) \bar{C}_p M_1^2]^{0.8} \quad (2-20)$$

where \bar{C}_p is the pressure coefficient based on a 10° ramp angle with approach flow Mach number M_1 (and one notes the elimination of the Reynolds number dependence).

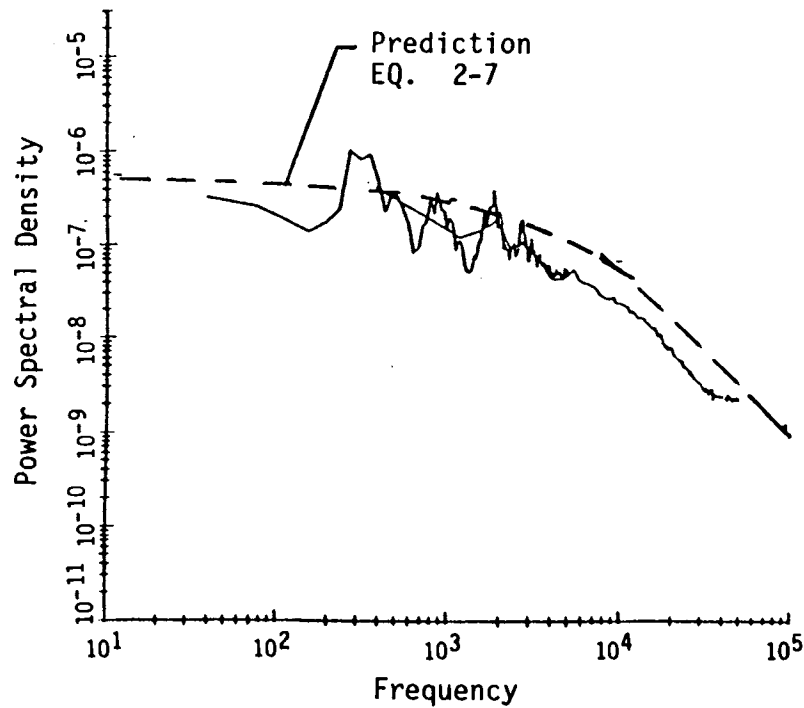
Swept shock-boundary layer interactions (3D) were extensively investigated by Neumann and Hayes (Reference [2-19]), Holden (Reference [2-23]), and Scuderi (Reference [2-24]) and reviewed in Reference [2-25]. It was shown that the correlation given by Equations 2-19 and 2-20 are

representative of the mean pressure data in the plateau level region for both 2D and 3D shock-boundary layer interactions.

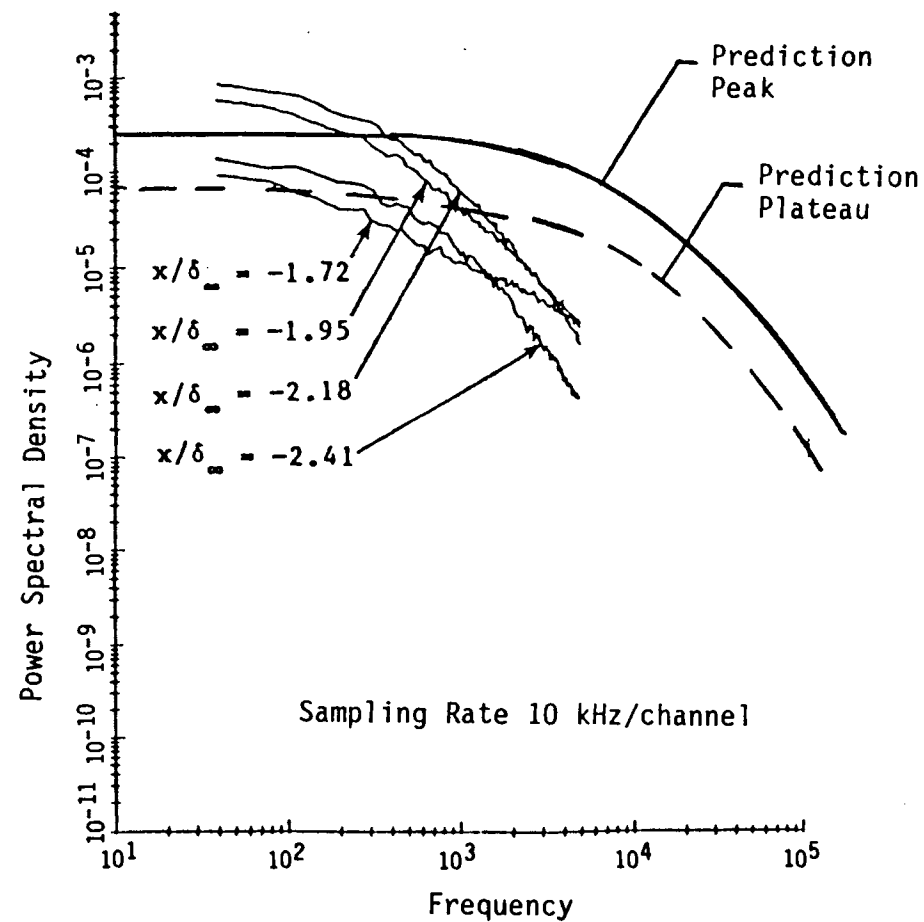
Power Spectral Density. Power spectra characterizing shock-boundary layer interactions have been investigated in early studies by Coe et al. (Reference [2-20]) and Robertson (Reference [2-26]) as well as in recent work reported in References [2-13, 2-18, 2-27]). An increase in the power spectra of the pressure fluctuations due to interaction phenomena is experienced above the attached flow level. While the spectra tend to converge toward a common level and slope at high frequencies, a significant variation exists between the separated flow spectra and that of the attached flow distribution. It was noted that the very-low-frequency components of the fluctuating pressures are increased in intensity, while the intermediate- and high-frequency components retain the characteristics of the approach (attached) boundary layer. Approach flow boundary layer parameters are generally selected for normalizing the power spectra as a matter of convenience, since local scale lengths and velocities in the interaction region are not well defined. Moreover, with consideration of engineering design requirements, it would be useful to develop prediction algorithms employing boundary layer approach flow characteristics that are deterministic.

Figure 2-10 shows the compression corner results for a 24° ramp. For this case the PSD's were not normalized. The approach flow displays a characteristic that is typical of power spectra that include low-frequency peaks associated with facility generated noise. A comparison is made with the prediction technique of Laganelli (Reference [2-3]). Figure 2-10(b) shows the spectra at several locations relative to the corner of the ramp. These do not indicate a frequency peak and tend to display broad band characteristics.

Power spectra of swept shock-boundary layer interactions were measured by Tran et al. (Reference [2-27]) at various shock strengths and are shown in Figure 2-11 for a 20° shock generator. The measurements were made from the undisturbed flow (#1) through the interaction regime, notably at the position of peak rms pressure (#2), plateau (#3), and second pressure rise (#4) levels. The data are not normalized owing to the inability to definitize length and velocity scales.



(a) Pressure Spectra in the Incoming Boundary Layer



(b) Pressure Spectra in the Intermittent Region of the Interaction

Figure 2-10. Power Spectra Characteristics of Approach Flow (a) and Interaction Region (b) Compared with Prediction (Data from Reference [2-18]).

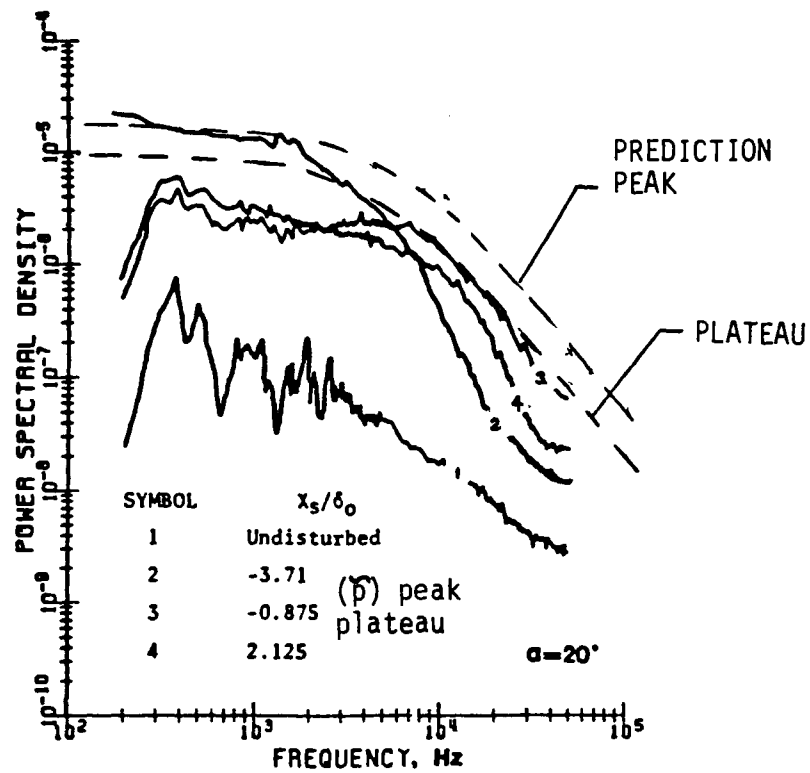


Figure 2-11. Typical Power Spectrum Along the Longitudinal Survey Line for Various 3D Shock Generators: $\alpha = 20^\circ$

As previously noted, because of the ambiguity in definitizing length and velocity scales, it would be desirable to characterize the normalized power spectra using approach boundary layer flow parameters leading to the shock-boundary layer interaction zone. Accordingly, the power spectrum for attached flow was used as given by Equation 2-2, where k' has been defined as $k' = 2F_c^{-2\lambda}$ to match the roll-off at high frequency ($f > 2000$ Hz) for attached boundary layer flow. Moreover, the boundary layer characteristic parameters of velocity and length will assume the approach flow values designated by the subscript 1. The augmentation in the power spectra due to the low-frequency components will be the sole effect of the normalized rms fluctuating pressure at peak and plateau levels.

Consider the amplitude of the power spectra at low frequencies such that

$$\phi(f \rightarrow 0) \rightarrow \frac{4 q^2 l}{v} F_c^{1.433} (\bar{p}/q)^2 \quad (2-21)$$

and restructure of the normalized rms pressure in terms of approach flow and peak and/or plateau levels as follows:

$$(\bar{p}/q)_{\text{plateau}} = \frac{\bar{p}_{w2}}{p_{w2}} \cdot \frac{p_{w2}}{q_2} = \frac{\bar{p}_{w1}}{p_{w1}} \left(\frac{p_{w2}}{p_{w1}} \right)_{\text{max}} \frac{p_{w2}}{q_2} \quad (2-22)$$

which in terms of approach flow parameters can be written as

$$(\bar{p}/q)_{\text{plateau}} = (\bar{p}_{w1}/q_1) (p_{w2}/p_{w1})_{\text{max}} (M_1/M_2)^2 \quad (2-23)$$

where the Mach number in the plateau region (M_2) is determined from oblique shock relations, namely

$$M_2^2 \sin^2 (\theta_s - \alpha) = \frac{(\gamma - 1) M_1^2 \sin^2 \theta + 2}{2\gamma M_1^2 \sin^2 \theta_s - (\gamma - 1)} \quad (2-24)$$

The augmented amplitude of the power spectra in the plateau pressure region resulting from the rms fluctuating pressure at low frequency is then described as

$$\phi(f \rightarrow 0)_{\text{plateau}} + \phi(f \rightarrow 0)_{\text{approach flow}} \left[\frac{M_1^2 (\gamma + 1) (P_{W2}/P_{W1})^2_{\text{max}} \sin^2 (\theta_s - \alpha)}{(\gamma - 1) M_1^2 \sin^2 \theta_s + 2} \right]^2 \quad (2-25)$$

where use of Equation 2-14 was made with Equation 2-24. In the above, the approach flow amplitude of the power spectra is given in Equation 2-8 such that

$$\phi(f \rightarrow 0)_{\text{approach}} = \frac{4 q_1^2 \delta_1^*}{u_1} (0.006)^2 F_c^{-0.5733} \quad (2-26)$$

noting the relations $\omega = 2\pi f$ and $\theta(f) = 2\pi \phi(\omega)$. Solution to Equation 2-25 is made with Equations 2-14, 2-15, 2-26, and 2-3.

For peak power spectra conditions, the augmentation at low frequencies requires modification of Equation 2-18 to include the dynamic pressure. Hence,

$$(\bar{p}/q)_{\text{peak}} = \frac{(\bar{p})_{\text{peak}}}{\bar{p}_{W1}} \cdot \frac{\bar{p}_{W1}}{q_1} \cdot \frac{q_1}{q_p} = \frac{(\bar{p})_{\text{peak}}}{\bar{p}_{W1}} \frac{\bar{p}_{W1}}{q_1} \frac{P_{W1}}{P_p} \left(\frac{M_1}{M_2} \right)^2 \quad (2-27)$$

where the dynamic pressure is evaluated at plateau levels. (The point of separation actually should be the location of maximum pressure gradient; however, this location is difficult to determine a priori.) The amplitude of the augmented peak power spectra becomes

$$\phi(f \rightarrow 0)_{\text{plateau}} + \phi(f \rightarrow 0)_{\text{approach flow}} \left[\frac{(\bar{p})_{\text{peak}}}{\bar{p}_{W1}} \left(\frac{M_1}{M_2} \right)^2 \frac{P_{W1}}{P_p} \right]^2 \quad (2-28)$$

where $(\bar{p})_{\text{peak}}/\bar{p}_{W_1}$ is determined by Equation 2-18, M_1/M_2 by Equation 2-24, and P_{W_1}/P_p by Equation 2-20. Note that Equations 2-24 and 2-14 can be written as

$$\left(\frac{M_1}{M_2}\right)^2 = \frac{M_1^2 (\gamma + 1) (P_{W_2}/P_{W_1})_{\text{max}} \sin^2 (\theta_s - \alpha)}{(\gamma - 1) M_1^2 \sin^2 \theta_s + 2} \quad (2-29)$$

Describing the spectral distribution of the shock-boundary layer interactions as shown in Figures 2-10 and 2-11 will require modification of the prediction technique described by Equation 2-7. This is a consequence of the roll-off with increasing frequency, which displays a steep slope of the energy with interactions when compared with the approach flow characteristics in the low-frequency range (<500 Hz). Recall that the roll-off was characterized by the compressibility and heat transfer of the medium in the Strouhal number, i.e., $k' = 2F_c^{-2\lambda}$. Because of the limited data, the characterization of the power spectra over the entire frequency range is beyond the scope of the present investigation. However, engineering solutions can be made for the interaction behavior over the spectrum by using Equations 2-25 and 2-28 together with Equation 2-7.

Figure 10(b) shows peak and plateau level predictions with the compression corner data of Reference [2-18]. While the amplitude ($f \rightarrow 0$) is reasonably predicted, the spectral distribution is overpredicted. Although not shown, it is expected that the data would tend toward the approach flow at the higher frequencies. Finally, Figure 2-11 compares the prediction technique with the swept shock-boundary layer interaction of Reference [2-27]. It appears that the roll-off characteristics for the 3D type interactions are most typical of attached flow behavior, thereby allowing a reasonable engineering estimate of the power spectra.

Boundary layer transition has a twofold effect on vehicle design. First, heat loads are an order of magnitude greater with turbulent boundary layers than with laminar boundary layers. Exposure in a turbulent flow environment can drive the thermal protection design. Second, the aeroacoustic loads are primarily associated with turbulent boundary layer flow; hence, the state of the flow on the body as well as the period in which the fluctuating components

work on the surface will drive the structural/fatigue design requirements. Accordingly, predicting boundary layer transition for space transportation systems is considered a critical design issue.

2.4 BOUNDARY LAYER TRANSITION

This section briefly reviews the state of the art in predicting boundary layer transitions on re-entry vehicles. Recognizing the difference in length scales of re-entry vehicles compared with those of future space transportation systems, interpretation of prediction techniques for the latter is provided.

A recent examination (Reference [2-28]) of boundary layer transition was made to extend the data base of ballistic and maneuvering re-entry vehicles for the purpose of application to hypersonic transatmospheric vehicle type configurations. The objective of the investigation was to determine local boundary layer parameters (Re_θ and M_e) at transition onset using parabolized Navier-Stokes (PNS) codes and to compare these values with those generated by integral boundary layer codes used in the boundary layer transition investigations of References [2-29] and [2-30]. While the major emphasis of the investigation of Reference [2-28] was to update the Re_θ versus X_{TR}/R_n transition onset and propagation correlation reflecting PNS calculations for boundary layer edge properties, the correlation of the form $Re_\theta/M_e = \text{constant}$ was also examined. Relative to the former type, Re_θ based on integral codes was consistently higher than values obtained using PNS solutions. The re-entry vehicle data base was used to assess the variation of Re_θ with M_e and is shown in Figure 2-12.

Superimposed in Figure 2-12 are lines of constant Re_θ/M_e . The data are shown to fall in the range $50 \leq Re_\theta/M_e \leq 150$ for both PNS and integral code calculations. The PNS solutions have lower values than the integral type as a result of the definition of boundary layer thickness as generated from the individual codes. Integral techniques employ shock layer mass entrainment (entropy swallowing) balancing coupled with similarity profiles to locate a matching point in the inviscid shock layer solution. On the other hand, PNS calculations solve the PNS equations from body to shock (full viscous-inviscid

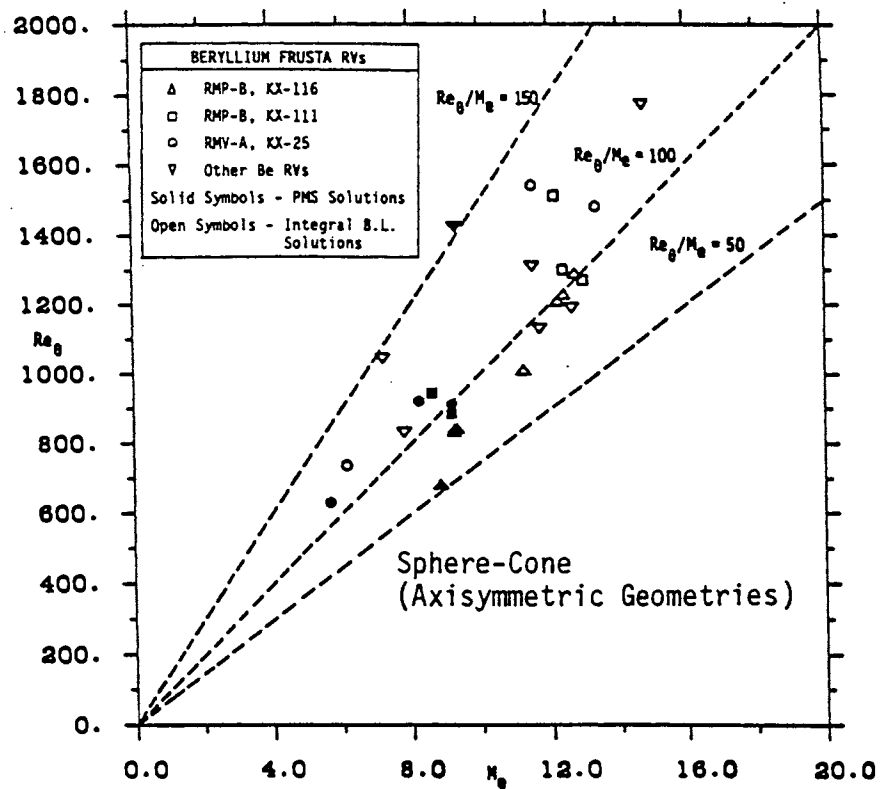


Figure 2-12. Metallic Frusta Re-Entry Vehicle Transition Data Base - Re_θ versus M_e (Reference [2-28]).

interactions) and do not require boundary layer integral properties as parameters.

The PNS generated data fall near the $Re_\theta/M_e = 100$ line, while the integral code data are slightly above. It appears that a Re_θ/M_e value on the order of 90 to 100 would be a reasonable transition onset criterion. For reference, the variation of transition onset altitude with Re_θ/M_e is shown in Figure 2-13 for RMP-B (KX-116). A transition onset altitude of 125 KFT is predicted using $Re_\theta/M_e = 90$ and an altitude of 120 KFT is predicted using $Re_\theta/M_e = 100$. A significantly lower altitude (102 KFT) results when using $Re_\theta/M_e = 150$.

In order to further illustrate the impact of boundary layer transition, Figures 2-14 and 2-15 were structured to show laminar boundary layer characteristics. Both 2D planar and axisymmetric solutions were obtained on the windward meridian of the Blended Wing Body (BWB) at Mach 10 for the nominal 1000-psf dynamic pressure trajectory. Figure 2-14 shows the transition onset criterion parameter Re_θ/M_e along the surface. The solutions, which were generated using the Science Applications International Corporation (SAIC) SCRAMP PNS code (Reference [2-31]), should not be used beyond the cowl inlet ($x/R_N \approx 190$). It is apparent that the 2D planar solution provides greater values for the transition onset criterion (Re_θ/M_e) than for the axisymmetric case. The latter case is representative of re-entry vehicles which are sphere-cone configured and were the basis of the studies noted above. The McDonnell Douglas Corporation (MDC) position on transition (Reference [2-32]) has allowed the onset criterion to be in the range of $375 < Re_\theta/M_e < 560$. An inspection of Figure 2-14 shows this to be possible if a 2D planar solution was used to generate re-laminarization of the boundary layer along the surface during ascent of the BWB vehicle.

Since the BWB vehicle does not represent a true axisymmetric configuration, its 3D characteristics would tend more toward an axisymmetric body than a 2D planar type. Although the body is locally planar (along the main meridian from which PNS solutions were generated), the flow has 3D influences and would experience pressure relief. The 2D planar solution is an

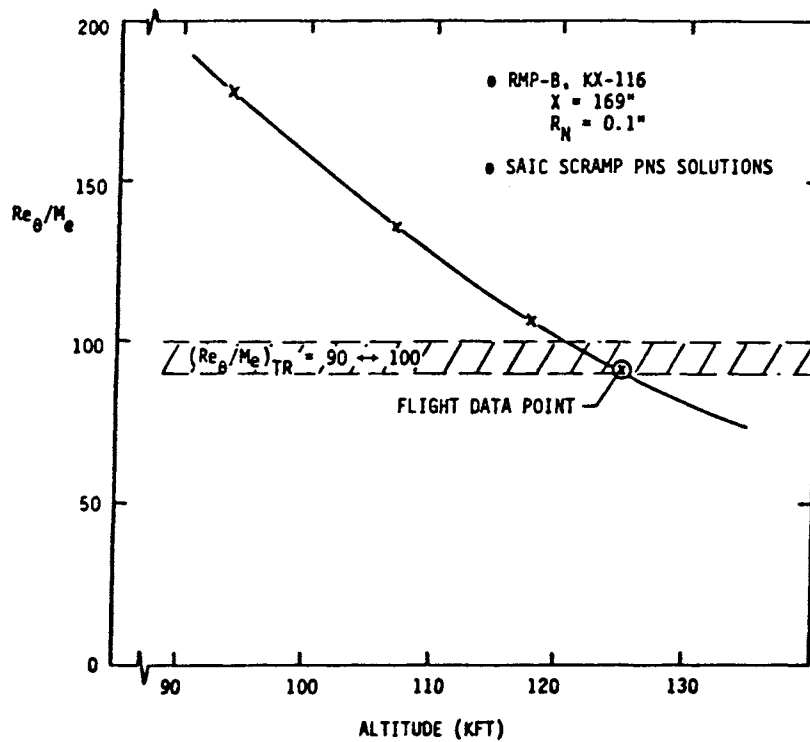


Figure 2-13. Re_{θ}/M_e Variation with Altitude (Reference [2-28]).

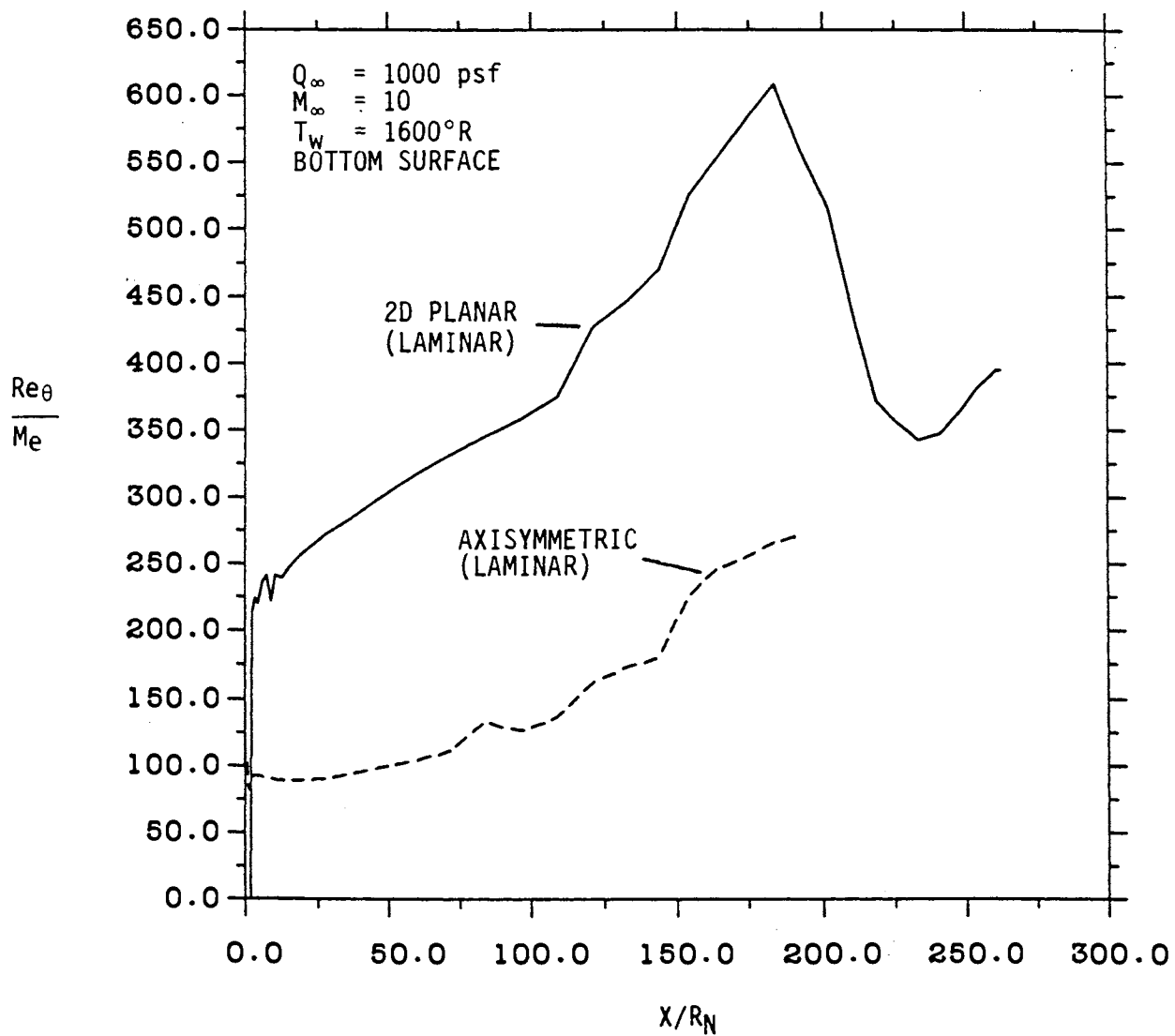


Figure 2-14. Laminar Boundary Layer Solutions for BWB with Transition Onset Parameter.

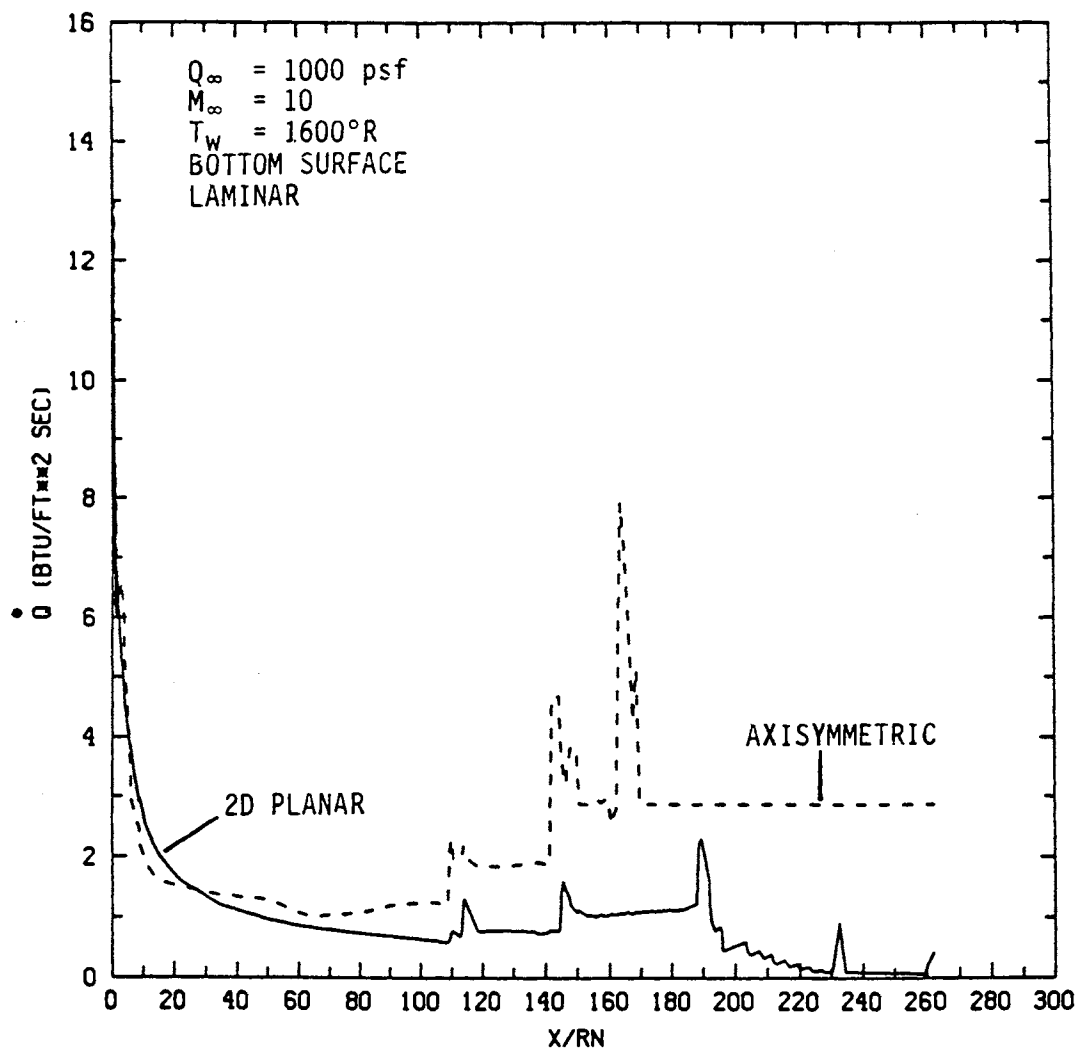


Figure 2-15. Laminar Heat Transfer Solutions for BWB.

unrealistic upper bound for judging the transition criterion. Moreover, test data obtained at the Naval Surface Weapons Center, Tunnel 2, have shown that 2D entropy swallowing is much slower than for 3D bodies, which subsequently affects local properties, hence the transition onset criterion parameter Re_θ/M_e . While the actual 3D case would be representative between the axisymmetric and 2D planar cases, it would lie closer to the axisymmetric results and would be more consistent with the transition criterion presented for the re-entry vehicle investigations.

Figure 2-15 shows the laminar heat transfer results for the 2D planar and axisymmetric bodies. Again, both cases represent the windward meridian. A comparison of these results with turbulent heat transfer generated at a similar 1000-psf dynamic pressure trajectory would yield turbulent heating levels an order of magnitude greater than the laminar levels. The higher heating rates will increase the wall temperature accordingly, which further illustrates the importance of transition onset (or re-laminarization) for heating and acoustic load predictions.

2.5 APPLICATION TO BLENDED WING BODY TRANSATMOSPHERIC VEHICLE

This section considers a generic transatmospheric vehicle design and applies the aeroacoustic algorithms in regions on the body experiencing attached and shock-boundary layer interactions. First, the external flow field is generated using parabolized Navier-Stokes (PNS) codes. Then attached flow aeroacoustic loads are predicted. Particular attention is given to the control area (wing/tail/stabilizer) where significant flow interactions are occurring. Techniques are also presented for predicting heat transfer loads for these complex regions.

2.5.1 External Flow Field

The prediction techniques developed in the previous section have been applied to the BWB transatmospheric vehicle, which represents a generic class of transatmospheric airbreathing systems. While the aeroacoustic environment is strongly related to mission profiles (trajectory), spatial and temporal resolution of the power spectra also depends upon location along the structure

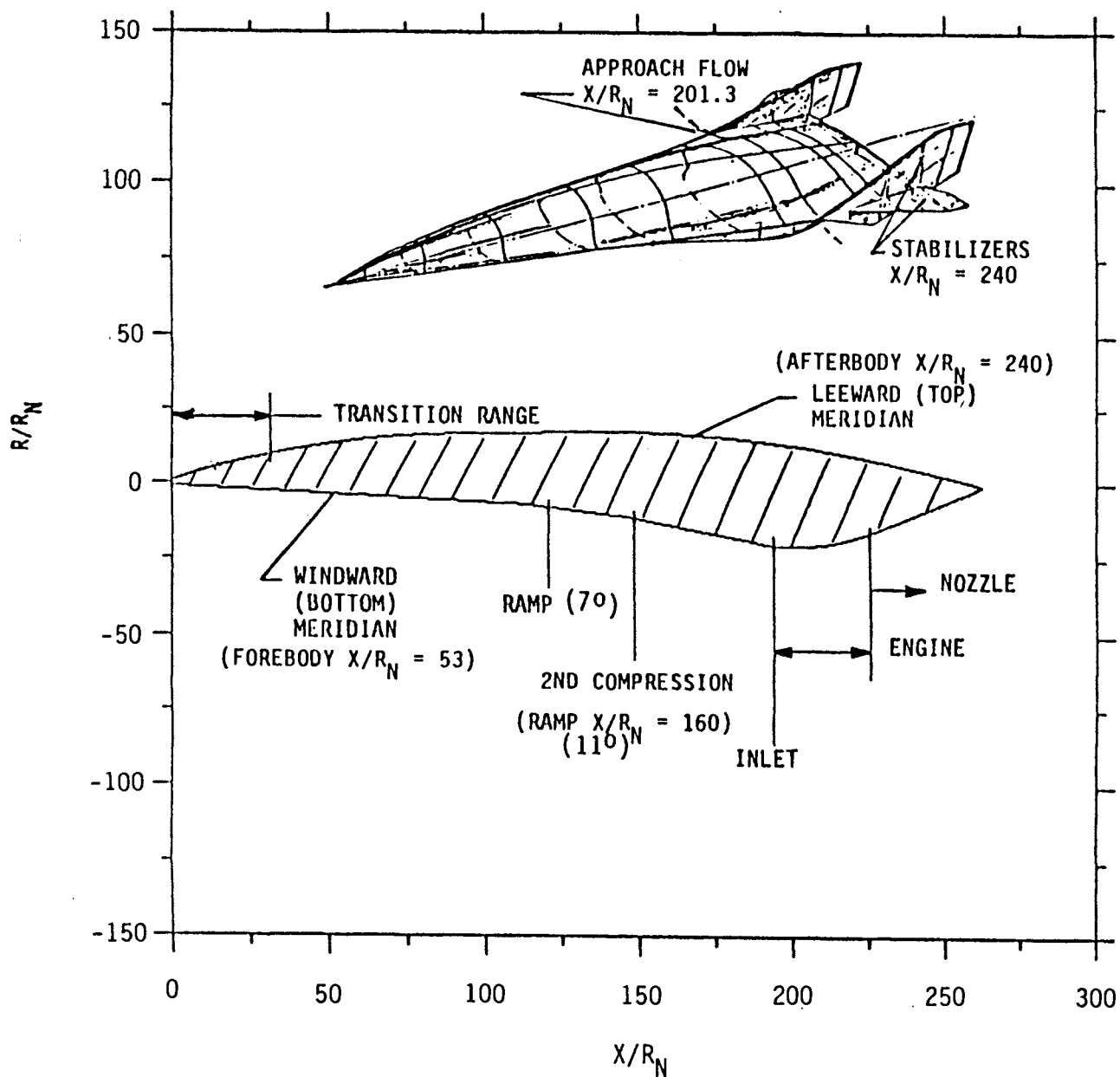
(boundary layer growth parameters). Several vehicle stations were selected to investigate both attached and nonattached boundary layer acoustic loads. The PNS solutions were used to provide the approach flow conditions for the shock-boundary layer interactions.

Figure 2-16 shows the generic transatmospheric vehicle configuration together with the regions of interest (x/R_N) and flight conditions to be investigated. Trajectory (Mach number and altitude), transition (x_{TR}), and wall temperature are identified for nominal freestream dynamic pressure (q_∞) conditions of 1000 and 2600 psf. The trajectory conditions are based on the generic transatmospheric vehicle flight envelope (Reference [2-33]) subject to equilibrium wall conditions. The trajectory, obtained from Billig et al. (Reference [2-34]), is based on an adiabatic compression for high contraction ratio at a freestream dynamic pressure of 1000 psf. The 2600-psf dynamic pressure conditions were generated by assuming a fixed Mach number and using standard atmospheric tables to determine the equivalent altitude to meet the Mach number/dynamic pressure levels.

2.5.2 Loads in Attached Turbulent Boundary Layer Flow

Solutions were generated for acoustic loads (rms fluctuating, sound pressure level, and power spectra) as well as pressure and heat transfer along the top and bottom meridians of the BWB for attached turbulent boundary layer flow conditions. For attached flow behavior, the BWB configuration was considered without the stabilizers. It should be noted that the top aftbody region ($x/R_N \approx 240$) could experience shock-boundary layer interaction effects as a result of the shock generated by the VS. The impact of these interactions is addressed in Section 2.5.3.

Figures 2-17 through 2-21 show typical acoustic loads and surface conditions (pressure and heat flux) on the BWB configuration at Mach 10. The results of trajectory conditions shown in Figure 2-16 are presented in Appendix A of this report. The Mach 10 results were used as an example. Figures 2-17 and 2-18 show rms pressure, sound pressure level, surface pressure, and heat transfer on the BWB windward and leeward meridians, respectively. A comparison is made between nominal ($q_\infty = 1000$ psf) and maximum

**CONDITIONS *** $R_N = 4.5$ INCHES $Q_\infty = 1000$ PSF

M_∞	ALT (KFT)	X_{TR} (FT)	T_w (°R)	SURFACE
4	71	6	540	B/T
6	88.4	6	1600	B/T
			2000	B/T
10	110.9	12	1600	B/T
15	129.9	15	1600	B/T
20	144.1	0	1600	B/T
25	155.7	0	1600	B/T

 $Q_\infty = 2600$ PSF

6	68.0	0	1600	B
10	89.75	0	1600	B/T
15	107.6	0	1600	B
20	120.5	0	1600	B
25	131.5	0	1600	B

B - Bottom (Windward)

T - Top (Leeward)

* Transition Zones have been designed for the $Q_\infty = 1000$ psf trajectory while all turbulent conditions designated for $Q_\infty = 2600$ psf trajectory - see Section 2.3 for transition phenomena discussion.

Figure 2-16. Blended Wing Body Investigation Regions.

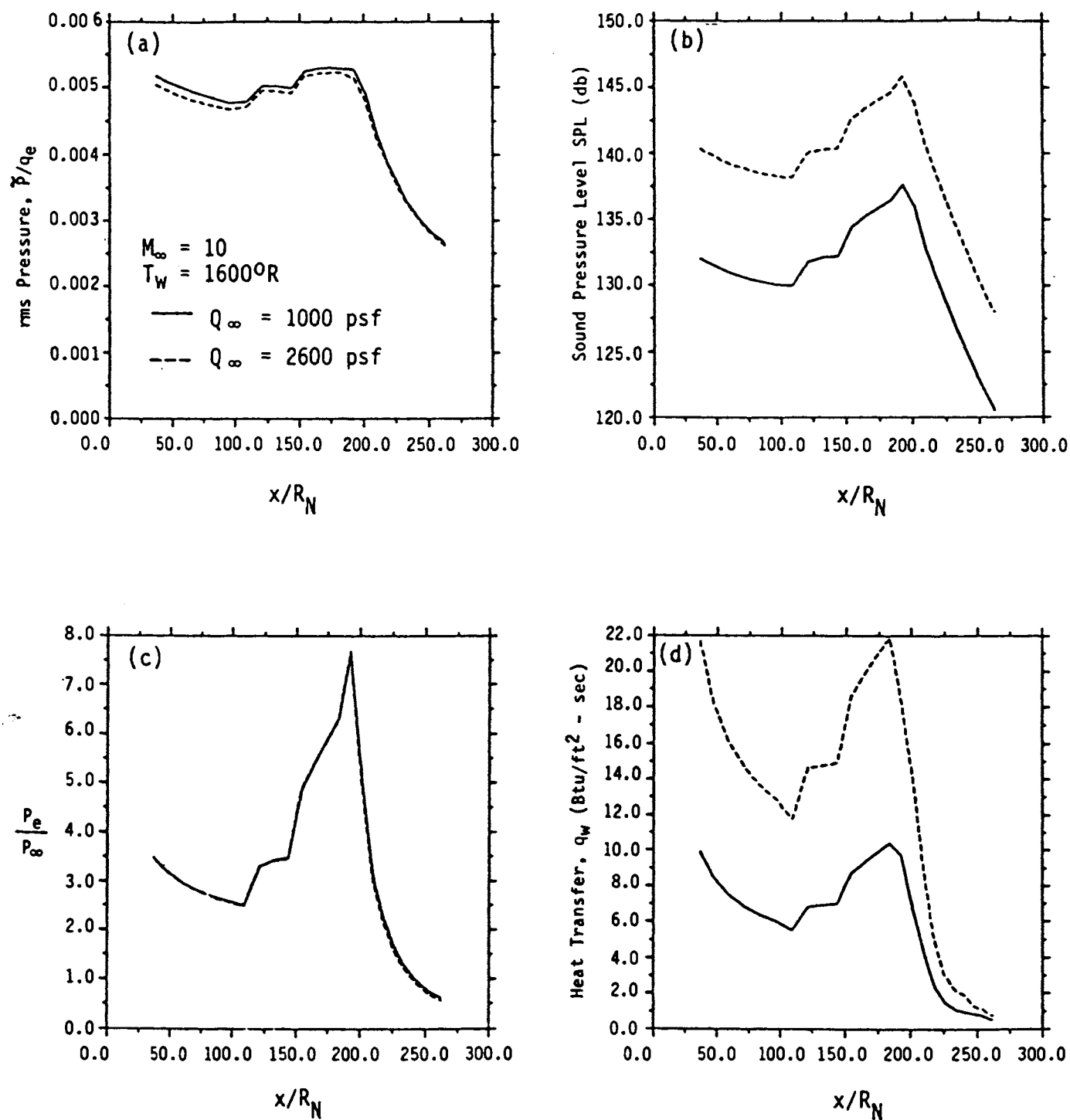


Figure 2-17. Acoustic Loads and Surface Conditions on Windward Meridian of BWB Configuration at Mach 10.

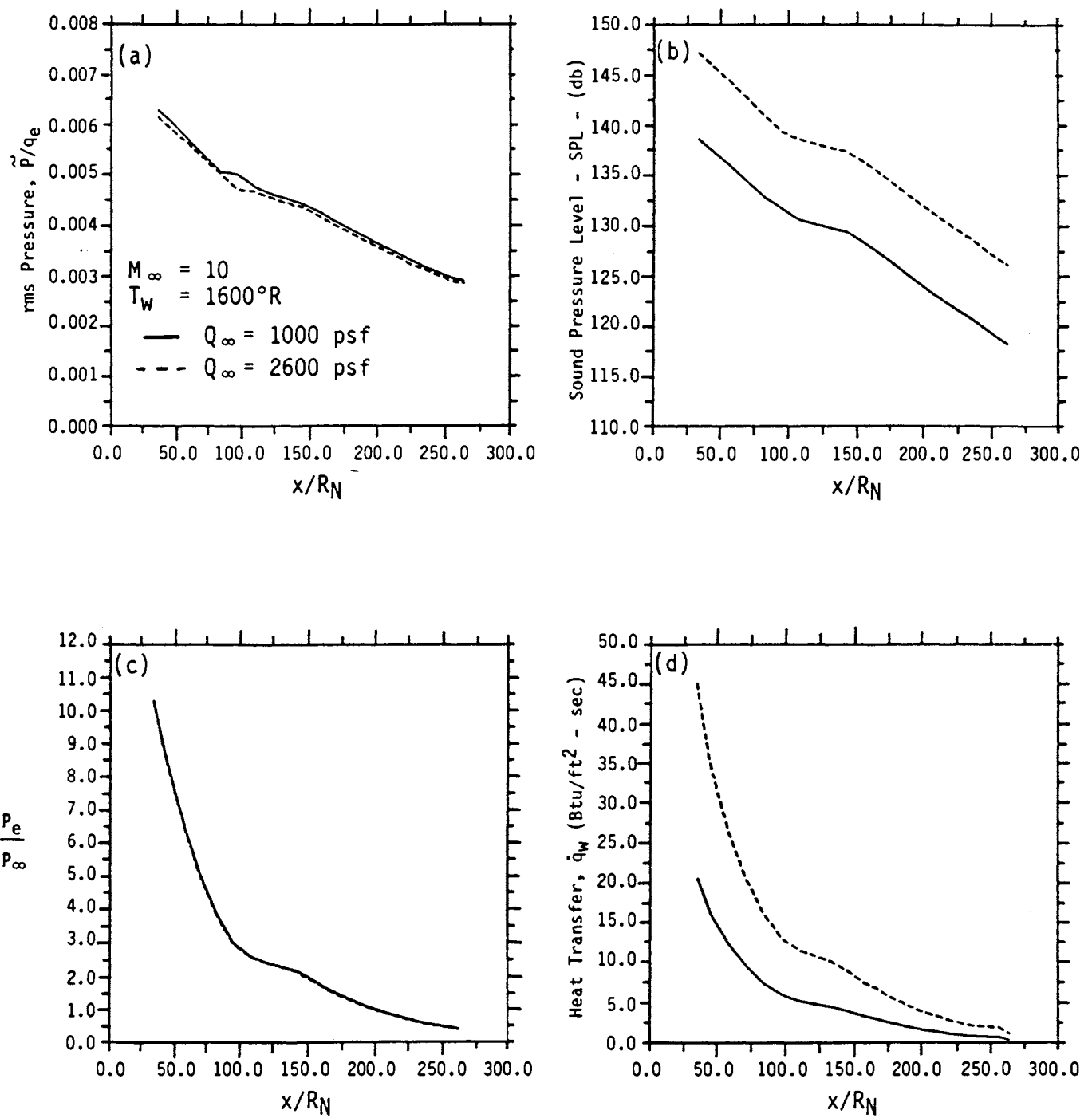


Figure 2-18. Acoustic Loads and Surface Conditions on Leeward Meridian of BWB Configuration at Mach 10.

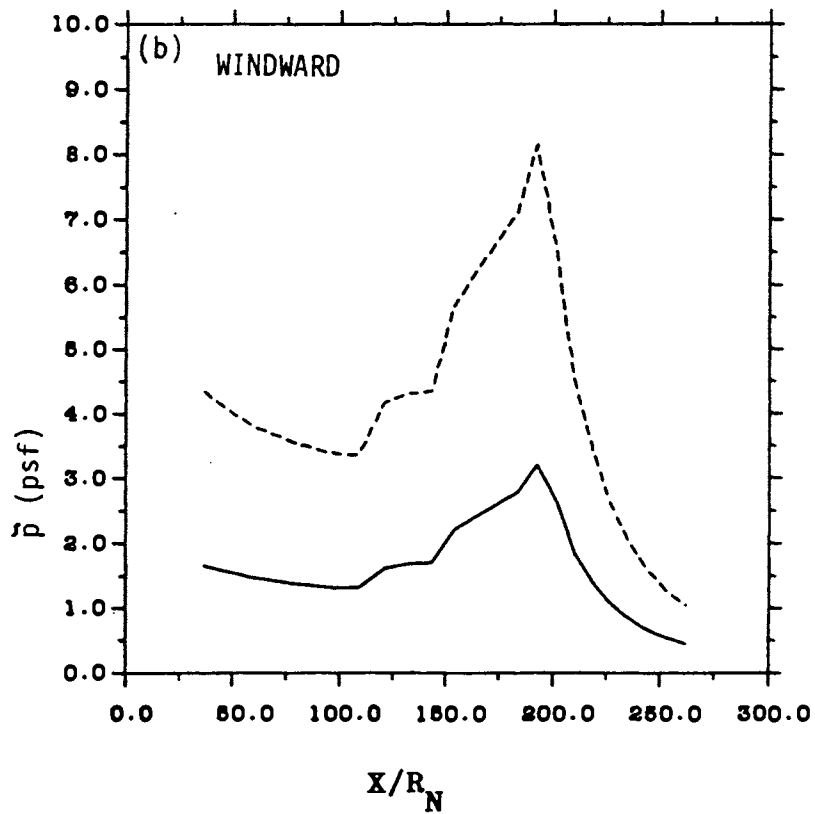
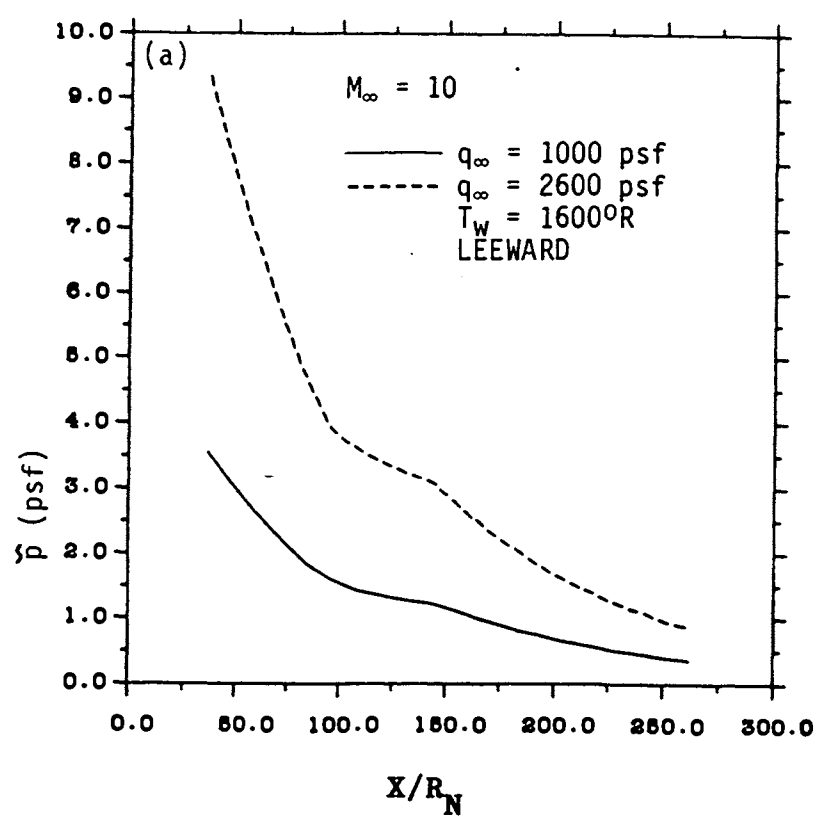


Figure 2-19. RMS Pressure Distribution on Leeward and Windward Meridians of BWB Configuration at Mach 10.

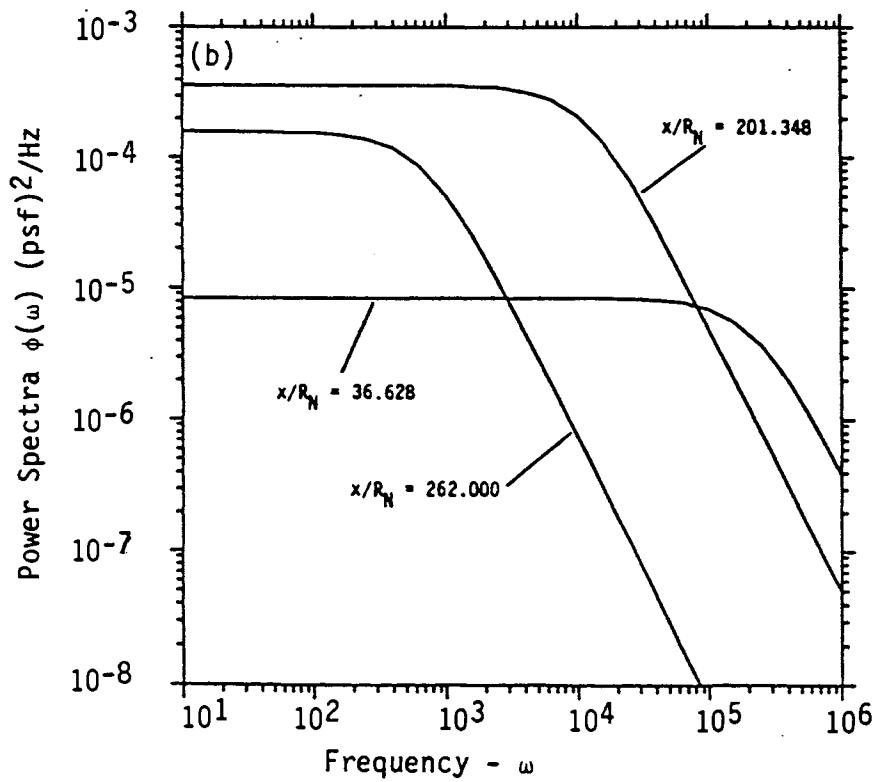
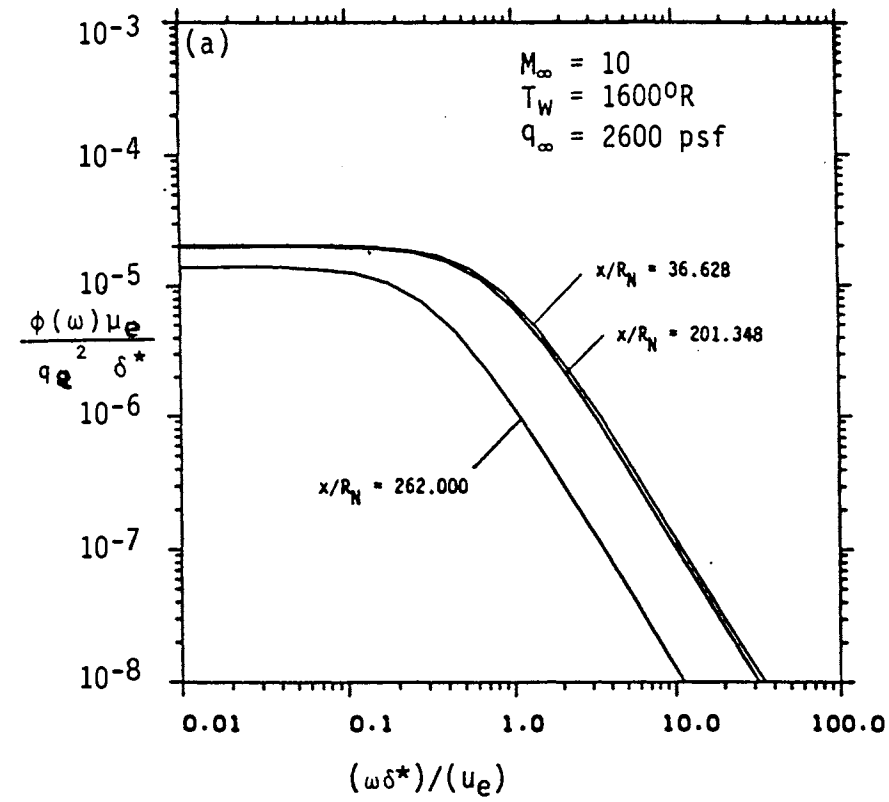


Figure 2-20. Power Spectra on Windward Meridian of BWB at Mach 10.

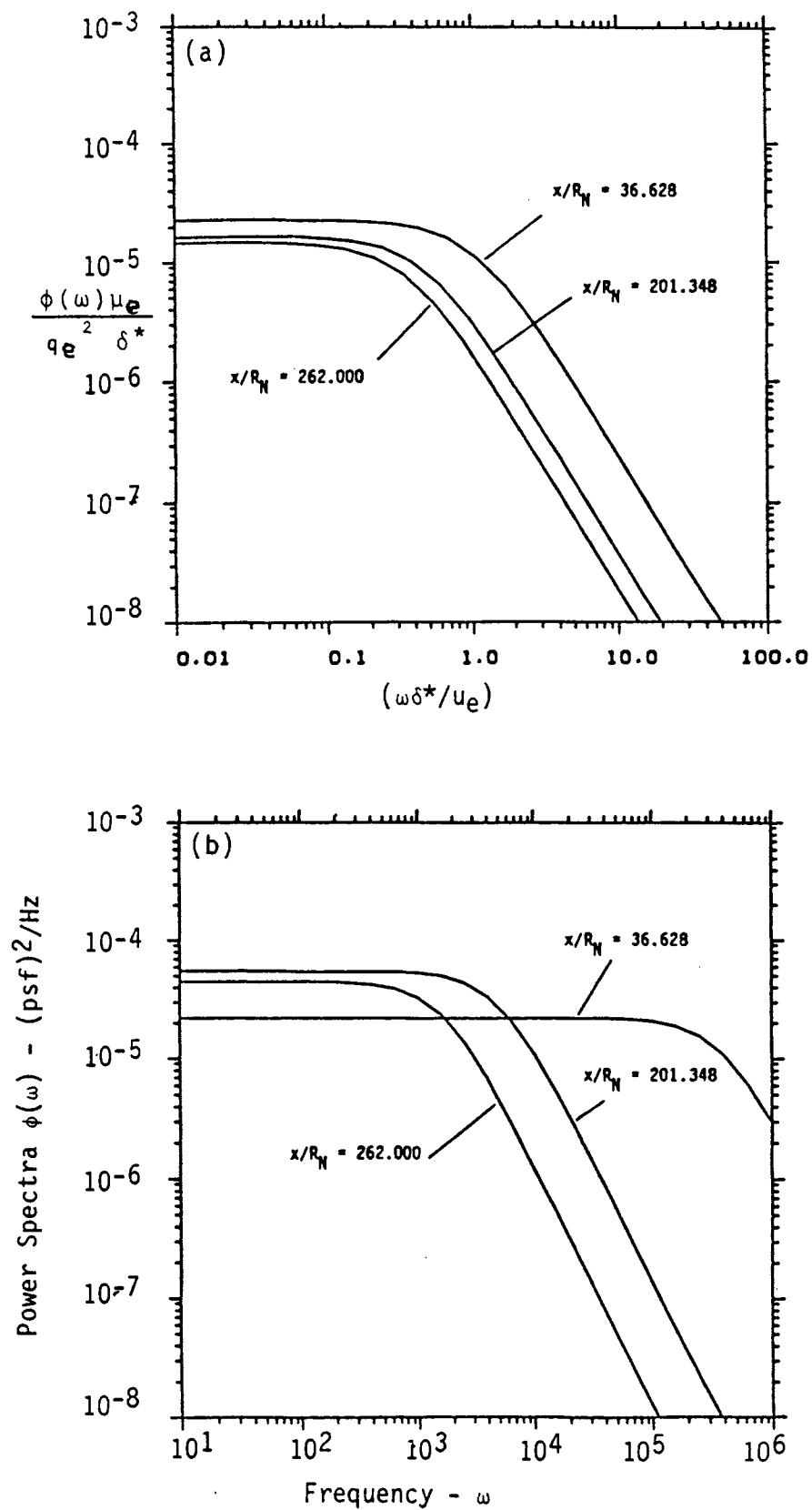


Figure 2-21. Power Spectra on Leeward Meridian of BWB at Mach 10.

($q_\infty = 2600$ psf) dynamic pressure conditions. As expected, normalized parameters (\bar{p}/q_e and p_e/p_∞) show no variation since for fixed Mach number, the dynamic pressure is related to the pressure.

The same characteristics are demonstrated for the power spectra relative to normalization of the PSD (Figures 2-20 and 2-21). The shortest distance (x/R_N) shown in these figures represents a location after transition where fully developed turbulent flow commences. As shown, the normalized PSDs do not vary significantly along the configuration or from top to bottom surfaces. The purpose of normalizing acoustic and flow field parameters is to provide users with the opportunity of predicting loads using boundary layer parameters from viscous codes of arbitrary nature.

In general, the rms fluctuating pressure decreased with distance along the top surface while increasing in regions where static pressure increased (ramps). Also, the rms pressure decreased with compressibility (Mach number) in regions in the absence of pressure gradients. Lowering wall temperature (Mach 6 at $q_\infty = 1000$ psf) increased the rms pressure. The normalized power spectra tended to show small variations with compressibility and heat transfer. On the other hand, when presented in dimensional format, the PSD showed a dependence on compressibility and wall temperature. Moreover, the roll-off in PSD with frequency did not appear to be sensitive to Mach number. However, the amplitude ($\omega \rightarrow 0$) where the PSD is generally flat tended to increase with decreasing Mach number and wall temperature.

2.5.3 Aeroacoustic Loads for Shock-Boundary Layer Interaction Regions

The regions on the BWB that were investigated for shock-boundary layer interactions consist of the top aftbody ($x/R_N \approx 240$) and the horizontal stabilizer (HS)/vertical stabilizer (VS). The HS is also subject to potential bow shock interaction with the shock-boundary layer of the HS/VS. The types of interactions that could be generated are illustrated in Figure 2-22 and include:

- (1) Fin generated: VS shock with aftbody boundary layer ($x/R_N > 200$).

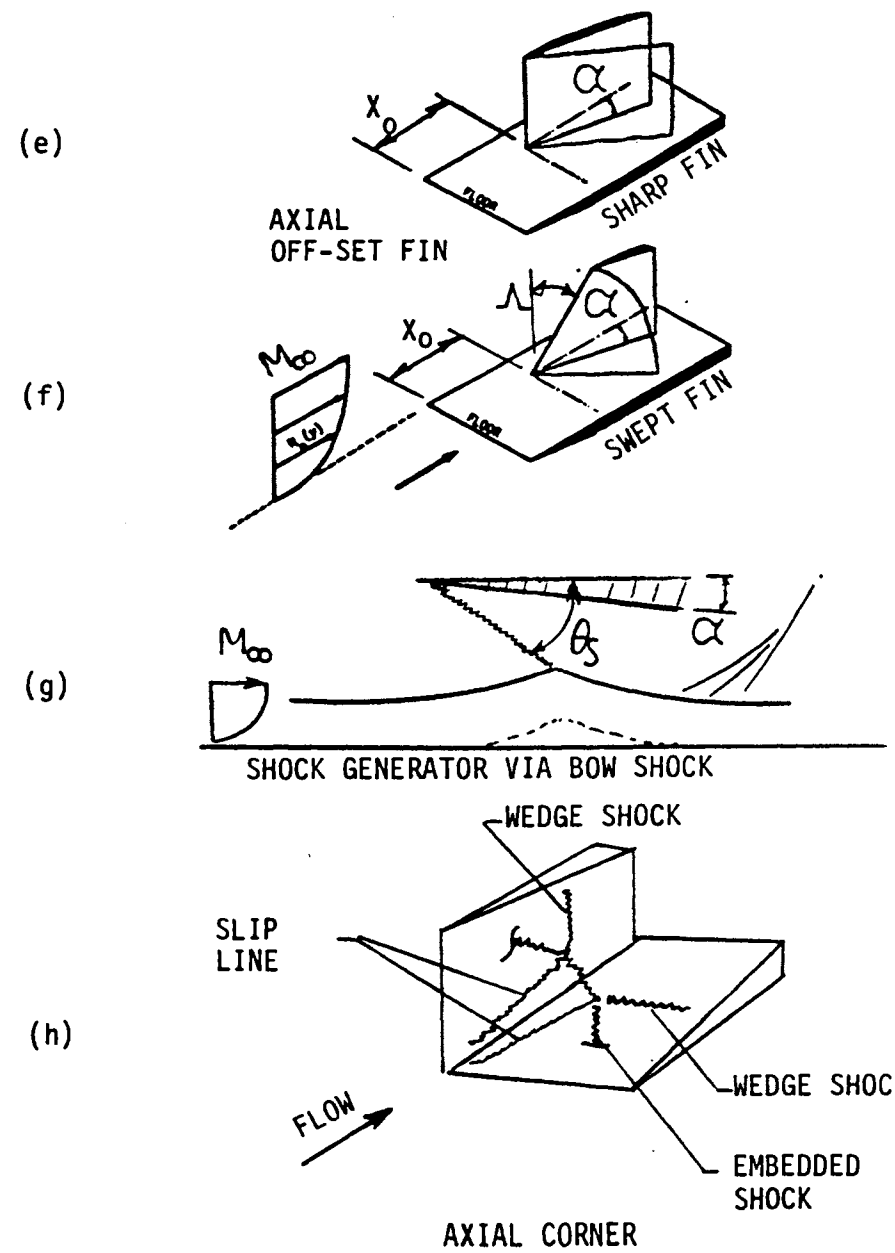
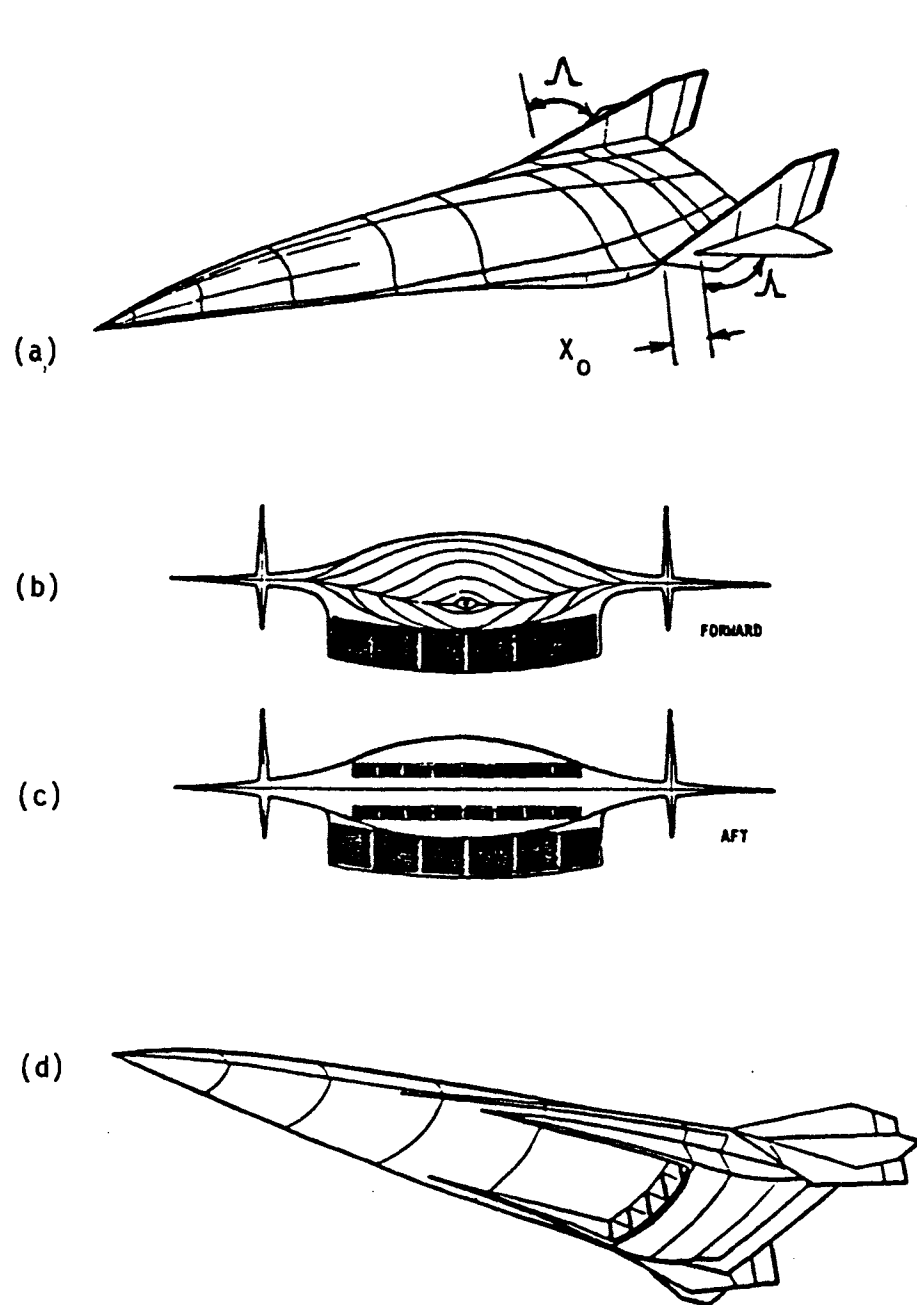


Figure 2-22. Views of BWB (a-d) and Potential Shock-Boundary Layer Interactions (e-h).

- (2) Axial offset fin: HS shock with VS boundary layer; treat problem for $X_0 \gg \delta$ to use swept fin and sharp fin data base.
- (3) Axial corner: both HS/VS shock-boundary layer interactions where $X_0 \sim O(\delta)$. While the cowl inlet represents a classic axial corner flow, the impact of the distance X_0 for the stabilizers of the BWB was examined.
- (4) Fin generated: bow shock interaction with HS boundary layer (2D flow).
- (5) Compression corner: second compression ramp on windward side of body. Although the body has been designed to eliminate flow separation with gradual surface contouring, the variation between the first ramp (7°) and second ramp (11°) could cause an augmentation in rms pressure due to the compression waves. Recall the attached flow experiment of Reference [2-13] (see Figure 2-5) for a ramp angle of 12° . For this case the flow was attached; however, an increase in rms pressure was experienced because of the compression of flow over the ramp.

The characteristics of swept shock-boundary layer interactions propagating from spanwise inboard corners have been investigated by Settles and Dolling (Reference [2-7]) and by Inger (Reference [2-35]). Figure 2-22 represents a subset of these interactions. Fin generated shock-boundary layer interactions, as previously described, represent a class of 2D and 3D flows for which $X_0 \gg \delta_0$. Pressure (rms and mean), profile, and heat transfer data have been obtained for this type of interaction. The rms pressure has generally been restricted in Mach number ($M \leq 3$), while mean pressure and heat flux data are available over an extensive Mach number range.

The axial offset fins represent a potential new class of interaction (Reference [2-36]) relative to the offset distance (X_0) compared with the boundary layer thickness developed over the distance X_0 [i.e., $X_0 \sim O(\delta)$]. For this condition, the shock-boundary layer interaction could behave as an axial corner flow in one limit ($X_0 \rightarrow 0$) to the sharp/swept fin interaction

limit $X_0 \gg \delta$. No rms pressure data exist for this condition. Moreover, to the present authors' best knowledge, the sensitivity of X_0 to mean flow characteristics (pressure/heat transfer) does not exist. The HS and VS could potentially be subject to an axial offset shock-boundary layer interaction for which no information is known.

Finally, the axial corner ($X_0 = 0$) shock-boundary layer interaction, while investigated for mean flow (pressure/heat transfer) behavior (Reference 2-37)) has no available rms pressure data base. In the axial offset and axial corner shock-boundary layer interaction studies, the approach flow has been inviscid as opposed to a boundary layer flow. The impact of a variable Mach number [$M = M(y)$] on the shock strength and subsequent interaction further complicates the prediction of power intensity and power spectra. Accordingly, the fin generated shock-boundary layer interaction ($X_0 \gg \delta$) data base was used together with heuristic techniques based on mean flow information and similarity parameters to obtain engineering level estimates of the dynamic loading for $X_0 \rightarrow 0$. Table 2-1 has been structured from PNS solutions to provide all pertinent approach flow boundary layer parameters at $\approx x/R_N$ 200. This represents an axial location at the leading edge of the VS.

VS Shock-Aftbody Boundary Layer ($x/R_N > 200$). As an example, consider $M_\infty = 10$ using boundary layer properties along the main meridian of the top surface. The VS is assumed to have a 10-inch thickness (Reference [2-32]) at the center of the axial length (approximately 15 feet), which yields a shock generator angle to the approach flow of 1.6° . The swept shock angle, obtained from Equation 2-16, has a value of 9.88° . The inviscid pressure rise is obtained from Equation 2-14, providing a value less than unity. Since the inviscid pressure through an oblique shock \geq unity, a value of unity is used. For this condition, both peak and plateau rms pressure levels will assume approach flow values according to Equations 2-11 and 2-18. It appears that the low angle wedge (1.6°) of the shock generator (VS) together with the 3D effect of relieving pressure has no impact on the interaction and subsequent rms pressure augmentation of the approach flow.

Table 2-1. Properties on the BWB at $x/R_N = 201.3$.

TOP SURFACE
 $X/R_N = 201.3$
 $R_B/R_N = 12.679$

 $Q_{INF} = 1000 \text{ LB/FT}^2$ $T_{WALL} = 1600 \text{ R (540 R @ MACH 4)}$

FREESTREAM CONDITIONS			EDGE CONDITIONS							WALL CONDITIONS			
MACH NO	ALT (KFT)	TOTAL ENTHALPY (BTU/LBM)	REYNOLDS NO $\times 1.0E4$ (1/FT)	MACH NO	VELOCITY (FT/SEC)	PRESS (PSF)	DYNAMIC PRESS (PSF)	DELTA (FT)	DEL+ (FT)	PRESS (PSF)	RMS PRESS (PSF)	QDOT (BTU/FT ² -SEC)	SHOCK RADIUS (FT)
25	155.7	14667.1	1.24	5.05	24703.6	19.11	341.1	6.95	3.17	9.93	1.288	10.4294	20.49
20	144.1	9055.1	1.76	4.60	19138.1	21.34	316.0	7.32	3.19	11.56	1.309	7.5457	21.77
15	129.9	4850.0	1.79	4.45	13994.3	12.60	174.2	3.63	1.27	8.77	0.700	4.0110	19.89
10	110.9	1999.5	4.53	4.19	9033.9	15.04	164.2	2.96	0.95	11.18	0.674	1.9582	21.60
6	88.40	667.4	16.62	3.69	5355.3	25.66	244.3	2.17	0.64	21.14	0.650	0.6907	26.33
4	71.00	269.2	66.25	3.37	3690.5	55.86	443.9	2.54	0.71	46.47	1.471	1.1015	33.61

 $Q_{INF} = 2000 \text{ LB/FT}^2$ $T_{WALL} = 1600 \text{ R}$

FREESTREAM CONDITIONS			EDGE CONDITIONS							WALL CONDITIONS			
MACH NO	ALT (KFT)	TOTAL ENTHALPY (BTU/LBM)	REYNOLDS NO $\times 1.0E4$ (1/FT)	MACH NO	VELOCITY (FT/SEC)	PRESS (PSF)	DYNAMIC PRESS (PSF)	DELTA (FT)	DEL+ (FT)	PRESS (PSF)	RMS PRESS (PSF)	QDOT (BTU/FT ² -SEC)	RSHOCK (FT)
10	89.75	1898.3	11.96	4.18	8845.3	38.35	468.8	2.78	0.83	29.06	1.675	4.1299	21.44

BOTTOM SURFACE
 $X/R_N = 201.3$
 $R_B/R_N = 20.619$

 $Q_{INF} = 1000 \text{ LB/FT}^2$ $T_{WALL} = 1600 \text{ R (540 R @ MACH 4)}$

FREESTREAM CONDITIONS			EDGE CONDITIONS							WALL CONDITIONS			
MACH NO	ALT (KFT)	TOTAL ENTHALPY (BTU/LBM)	REYNOLDS NO $\times 1.0E4$ (1/FT)	MACH NO	VELOCITY (FT/SEC)	PRESS (PSF)	DYNAMIC PRESS (PSF)	DELTA (FT)	DEL+ (FT)	PRESS (PSF)	RMS PRESS (PSF)	QDOT (BTU/FT ² -SEC)	RSHOCK (FT)
25	155.7	14667.1	2.41	4.18	23823.0	60.86	744.3	3.09	1.54	27.78	3.573	22.2903	10.04
20	144.1	9055.1	2.27	3.27	17571.1	64.75	485.6	2.89	1.22	30.26	2.941	17.1033	11.64
15	129.9	4850.0	4.49	3.44	13133.8	60.87	504.2	1.58	0.71	30.78	2.841	12.2964	23.91
10	110.9	1999.5	11.32	3.26	8441.5	72.14	536.1	1.34	0.55	45.84	2.632	6.4153	10.52
6	88.40	667.4	33.89	2.87	4942.4	99.16	573.0	1.12	0.38	75.22	2.153	2.2273	14.86
4	71.00	269.2	107.24	2.64	3381.7	170.58	834.6	1.44	0.51	125.5	3.874	0.1319	21.46

 $Q_{INF} = 2000 \text{ LB/FT}^2$ $T_{WALL} = 1600 \text{ R}$

FREESTREAM CONDITIONS			EDGE CONDITIONS							WALL CONDITIONS			
MACH NO	ALT (KFT)	TOTAL ENTHALPY (BTU/LBM)	REYNOLDS NO $\times 1.0E4$ (1/FT)	MACH NO	VELOCITY (FT/SEC)	PRESS (PSF)	DYNAMIC PRESS (PSF)	DELTA (FT)	DEL+ (FT)	PRESS (PSF)	RMS PRESS (PSF)	QDOT (BTU/FT ² -SEC)	RSHOCK (FT)
25	131.5	13510.4	6.42	4.14	22878.5	153.00	1840.6	3.13	1.55	70.31	8.890	40.4607	17.89
20	120.5	8313.6	11.41	4.15	18009.8	165.76	2009.3	3.27	2.25	75.07	9.350	32.2899	19.07
15	107.6	4447.4	11.87	3.40	12589.8	152.39	1236.7	1.47	0.63	86.71	6.339	23.5684	24.21
10	89.75	1898.3	30.22	3.26	8273.9	183.80	1369.1	1.28	0.51	117.1	6.574	14.0932	10.59
6	68.00	636.5	95.33	2.92	4902.1	261.78	1560.0	1.14	0.40	194.1	5.540	3.68845	14.88

VS Shock-HS Boundary Layer. Both the VS and HS are swept at angles of approximately 20° to the axis for the BWB. Since the HS is offset from the leading edge of the VS ($X_0 \approx 3$ feet), shocks developed from the VS will not intersect with the boundary layer flow of the HS. Again, since the shock generator angle is small ($\alpha = 1.6^\circ$), the pressure rise through the oblique shock is not sufficient to cause separation and subsequent augmentation in the approach flow values. On the other hand, the low Mach number cases produce shock angles greater than the HS swept angle (20°), which does not interact with the HS flow. It should be noted that this condition is a consequence of the offset distance.

HS Shock-VS Boundary Layer. The approach flow leading to the VS-HS interaction is boundary layer flow that will rapidly expand toward freestream values as the flow turns into the intersection of the two surfaces. A new boundary layer will commence on the VS that can interact with the HS shock. The problem was treated for the axial offset case when $X_0 \gg \delta$ (here δ being the new boundary layer generated along the VS).

As in the previous case, the small shock generator angle ($\alpha = 1.6^\circ$) together with the 3D shock correlation (Equation 2-16) yields oblique shock pressure rise $< \text{unity}$ (hence, one uses a value of unity) such that the peak and plateau rms pressures are the same as the approach flow values.

In order to have rms pressures above the approach flow levels, the shock generator angle must have a value that yields a pressure rise $\geq \text{unity}$. If one considers Equation 2-14 for P_{w2}/P_{w1} equal to unity, there results

$$M \sin \theta \rightarrow \text{unity} \quad \text{at } P_{w2}/P_{w1} = 1$$

and for a fin generated interaction, use of Equation 2-16 gives

$$\alpha = (1 - \beta) \sin^{-1} (1/M) \quad \text{at } P_{w2}/P_{w1} = 1 \quad (2-30)$$

For the range of local Mach numbers ($2.6 < M_e < 5.1$), Table 2-1 shows that $9^\circ > \alpha > 4.5^\circ$, which is greater than the shock generator angle (1.6°) of the

HS-VS on the BWB. Hence, Equation 2-30 represents a potential design criterion for setting the stabilizer thickness (shock generator angle) to eliminate augmentation of approach flow acoustic loads.

Bow Shock-HS. Solutions provided by 3D PNS codes show that the bow shock is capable of interacting with the HS. These interactions can include the shock-shock as well as shock-boundary layer type. Since no information is known for the former, the 2D shock-boundary layer interaction will be used for engineering estimates.

The body angle (shock generator) for this case is $\alpha = 9.4^\circ$, which for a Mach 10 trajectory yields a shock angle of $\theta_s = 15.1^\circ$. The inviscid pressure rise (Equation 2-14) has a value $P_{W2}/P_{W1} \approx 7.75$. The peak rms pressure is obtained using Equation 2-18 such that $(\bar{p}_{W_{HS \text{ peak}}})/(\bar{p}_{W1}) \approx 40.2$. From Equation 2-11, in the plateau region of the interaction, the rms pressure $(\bar{p}_{W_{HS \text{ plat}}})/P_{W2} \approx 7.75 (\bar{p}_{W1}/P_{W1})$. Hence, a significant rise in rms pressure on the HS resulting from the bow shock interaction is possible.

Compression Corner (Ramp) Interaction. The compression ramp (windward) of the BWB has been contoured to eliminate potential flow separation leading into the cowl. However, experience has shown that approach flow rms pressure levels can be augmented by a factor of eight (see Figure 2-5 at $\alpha = 12^\circ$) for attached flow over a ramp. If one considers the second compression ramp of the BWB, the ramp angle changes from approximately 7° to 11° , providing an effective ramp angle of 4° . For an approach flow Mach number of 4, a shock angle of 18.5° results in an inviscid pressure rise of $P_{W2}/P_{W1} = 1.7$. The corresponding peak rms pressure (Equation 2-18) is approximately three times the approach flow level. To ensure that rms pressure augmentation is possible along ramps with pressure gradients due to compression waves would require more definitive information as obtained in experiments featuring low ramp angles ($\alpha < 8^\circ$) or the possibility of accurate flow field calculations using NS solutions.

Axial Corner Flow HS/VS ($X_0 \rightarrow 0$). Since the HS is offset from the VS, a true axial corner would not occur. However, if the offset distance were on the order of the local boundary layer thickness in the offset region, the flow could be characterized as axial corner flow for $X_0 \rightarrow 0$. While it is recognized that the pressure rise in an axial corner is greater than that in the 2D compression corner, the rms fluctuating pressure loads on the VS are on the same order as the approach flow because of weak interaction of the low angle shock generator, and the power spectra could differ since a new boundary layer is starting from the leading edge of the VS. The characteristic velocity (approach flow boundary layer edge value) will not change significantly owing to the small turn angle of the ramp (1.6°) as well as the Mach number and wall enthalpy ratio. Since the characteristic length (displacement thickness) can be an order of magnitude less than that of the approach flow, further investigation of this problem is required.

2.5.4 Pressure and Heat Transfer Predictions for Shock-Boundary Layer Interactions

Although considerable improvements have been made in computational fluid dynamics, prediction of surface heating resulting from shock-boundary layer interactions remains a difficult problem because of boundary layer separation, limitations on turbulence closure models, and localized regions of gradients associated with high pressure. These shock-boundary layer interactions, which occur on control surfaces, wing-body junctions, engine inlets, and generic aerodynamic components, can have a significant impact on the design process.

Two-dimensional interactions, which occur on ramps or control surface hinge lines, have received more attention than 3D interactions, which are characteristic of deflected fins, boundary layer diverters, and wing/tail-fuselage areas. Moreover, 3D interactions have been shown to present conflicting trends in peak heating which is a result of the complex flow structure. The 2D experiments have been emphasized where conceptual modeling of the interaction is easier than its 3D counterpart. An excellent review of the subject has been presented by Neumann and Hayes (Reference [2-38]).

Figure 2-23 shows a correlation of the results from the experiments of Holden (Reference [2-39]) for a maximum heating rate on ramp (wedge) and 2D fin generated shock induced separation. Wedge and external shock induced separated regions having the same shock strength exhibited similar heat transfer distributions. Moreover, the maximum heating (normalized by the upstream undisturbed value) was shown to correlate with the maximum inviscid oblique shock pressure rise. An attempt was made to correlate plateau region heating levels for wedge and external shock induced interactions. The results are shown in Figure 2-24 in terms of plateau pressure. The data scatter is within $\pm 15\%$ of the suggested correlation. This includes data obtained from skewed shock generated ($\psi > 0^\circ$) interactions of Reference [2-23].

Three-dimensional shock-boundary layer interactions were investigated as described in References [2-19], [2-23], and [2-24]. Figure 2-25 shows the results of Reference [2-23] for 3D (swept shock) interaction. Maximum heating is displayed as a function of the inviscid pressure rise (maximum pressure) for both swept (3D) and skewed induced shock interactions. Data have been added from Reference [2-40] at Mach 3. The data tend to follow the inviscid oblique shock strength correlation of 2D interactions as shown in Figure 2-23. The results suggest that peak heating resulting from 2D and 3D interactions can be described by the oblique shock pressure rise in the form

$$\dot{q}_{\text{peak}}/\dot{q}_0 = (p_{\text{max}}/p_0)^{0.85} \quad (2-31)$$

where the subscript 0 refers to the undisturbed approach flow levels.

Relative to the plateau region level of heating (Figure 2-24), a modification of the above is recommended, namely

$$\dot{q}_{\text{plateau}}/\dot{q}_0 = (p_{\text{plateau}}/p_0)^{5/8} \quad (2-32)$$

where the plateau pressure is given by Equation 2-19 or 2-20. Further discussions concerning heating are given in References [2-19] and [2-38].

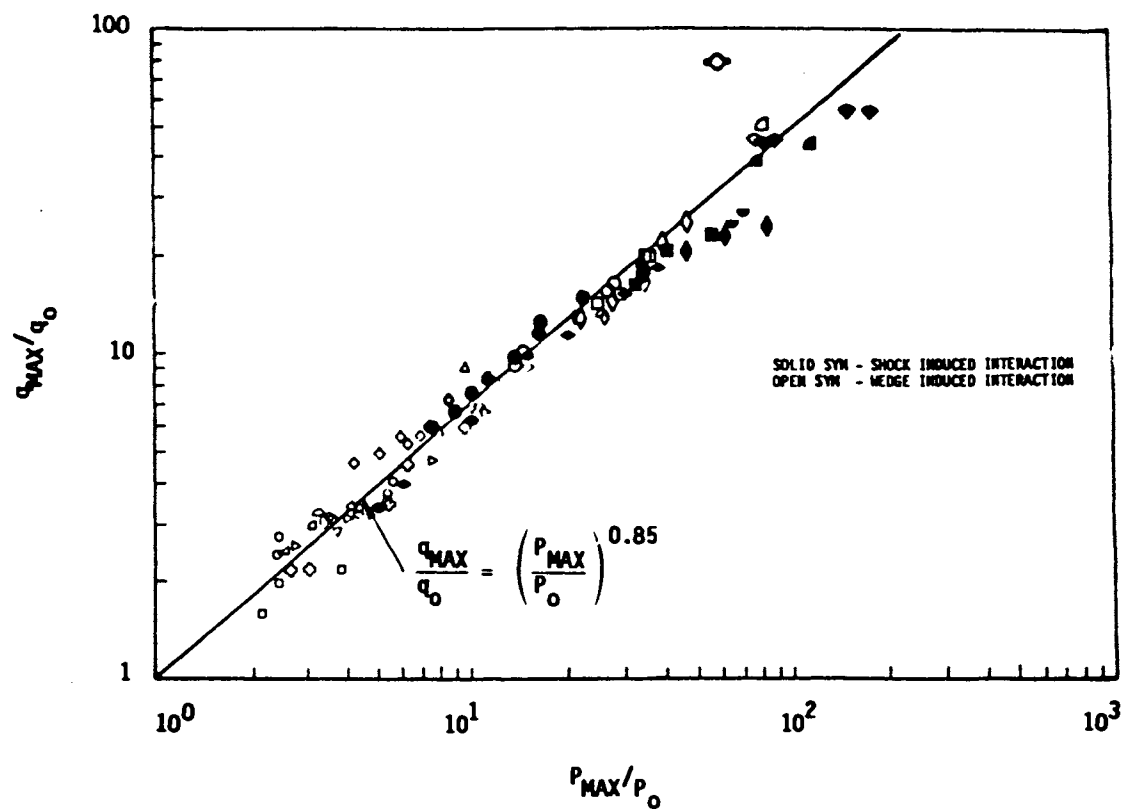


Figure 2-23. Correlation of Maximum Heating Rate of 2D Type Shock Induced, Turbulent Separated Flows (Reference [2-39]).

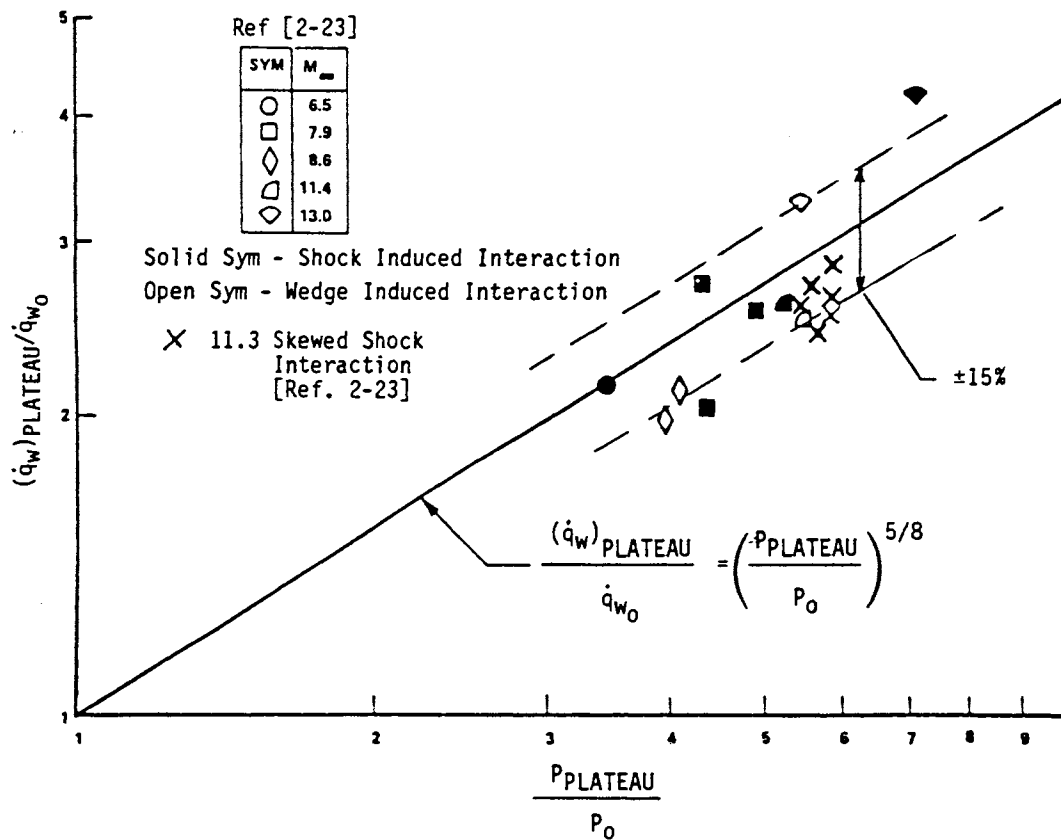


Figure 2-24. Correlation of Plateau Heat Transfer with Plateau Pressure (Reference [2-23]).

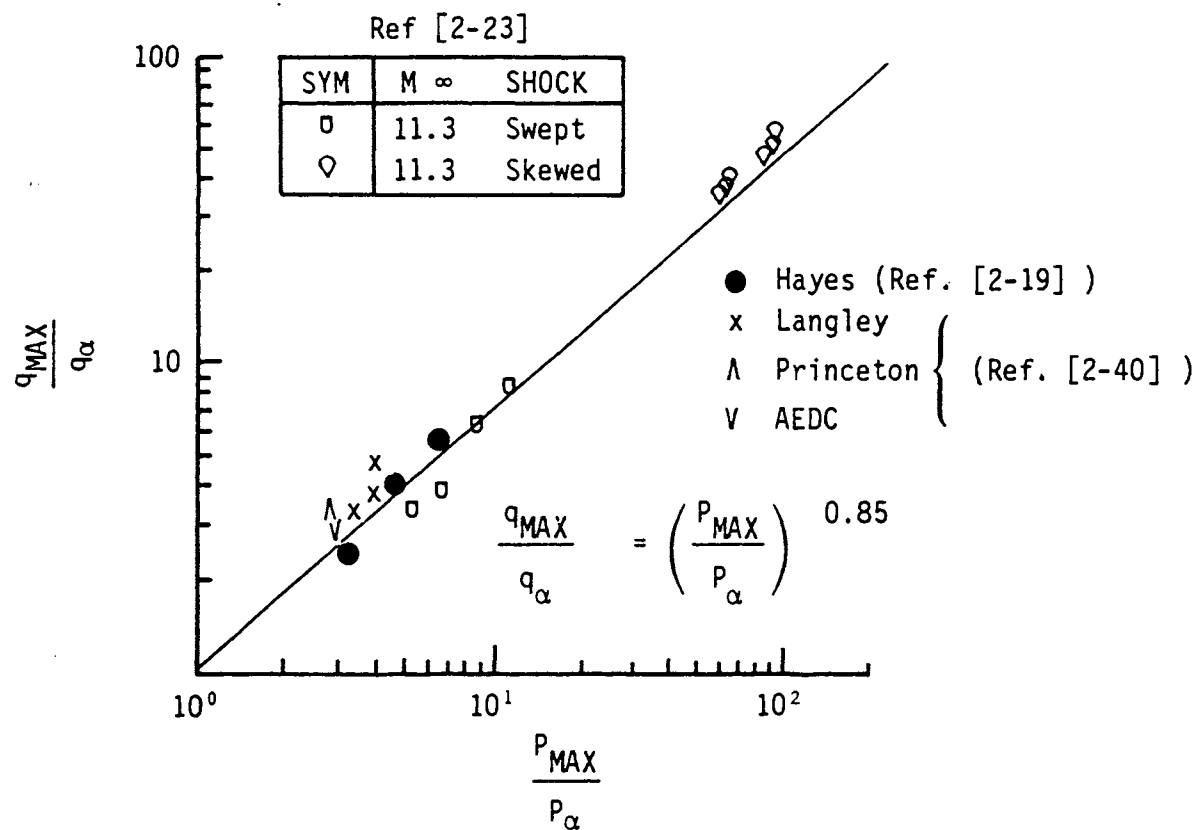


Figure 2-25. Surface Heat Transfer Correlations for 3D Type Shock-Boundary Layer Interaction.

Cross Power Spectral Density. Data acquisition and interpretation of cross-spectra associated with shock-boundary layer interactions are very limited. Typically, 2D type ramp experiments showed that the peak value of the longitudinal space-time correlation $R_{pp}(\xi_1, 0, \omega)$ at the start of the interaction ($\sqrt{1/3}$), was considerably lower than the approach flow level ($\sqrt{4/5}$), which then increased in the region of maximum rms pressure ($\sqrt{1/2}$) and subsequently decreased to the initial level further downstream. In general, the rate of decrease of the space-time correlation in the intermittent region was lower than the approach flow levels for both 2D and 3D type interactions. It appears that the intermittency is dominated by the shock motion as opposed to the convective transport of turbulent eddies.

Because of the limitation of cross-spectra data, particularly for shock generating angles less than 10° , no attempt was made to develop algorithms for the attached flow cross-spectral coefficients

$$A(\xi_1, \omega) = e^{-a\xi_1/\delta^*} e^{-b\xi_1\omega/u_c}$$

$$A(\xi_2, \omega) = e^{-c\xi_2/\delta^*} e^{-d\xi_2\omega/u_c}$$

The constants a, b, c, and d in the exponents have the following values: $a = -0.025$, $b = -0.16$, $c = -0.016$, $d = -0.95$. Since the coherence for shock-boundary layer interactions has been shown to decay more rapidly than the approach (attached) flow levels, an increase in the spatial extent for the constants a and c can be expected.

To address the issues of prediction capability for cross-spectra, a review of existing data together with the algorithms for PSD developed in the present investigation should be made in concert with NS solutions of the wave interactions. Until a more in-depth examination of the cross-spectra is performed, engineering estimates can be made by allowing a reduction of 3 to 6 dB in overall sound pressure level to account for the effects of shock-boundary layer interactions on cross-spectral density. These estimates are based on experimental observations of the spectra in separated flow regions generated by large deflection angles ($> 16^\circ$). Moreover, they are consistent

with the results in the above discussion, which have shown the cross-spectral coefficients to decay more rapidly than the undisturbed (approach) flow levels.

Results of Shock-Boundary Layer Interactions on BWB. Because of the low angle shock generator, HS-VS boundary layer interactions produced weak interactions that did not augment the approach flow characteristics. These results are consistent with the mean flow experiments that showed a pressure rise > 1.5 is required to induce separation in a 3D swept shock-boundary layer interaction.

Weak shock interactions were also produced on the aftbody of the BWB as a result of shocks generated by the VS. The acoustic loads and surface pressure/heat transfer conditions, as described herein (see results in Appendix A), can be used to characterize the aftbody region of the configuration.

The potential interaction produced by the bow shock and HS could have a significant impact on the BWB. However, this interaction has a result that is different from those previously investigated in the literature. For this condition, the bow shock would interact with the HS shock as well as the boundary layer. In both cases, the plane of the bow shock interaction would be approximately 90° to the HS generated shock and boundary layer. The impact of the bow shock and HS shock and the subsequent result on the boundary layer have not been investigated.

In order to treat this problem, the bow shock was assumed to interact with the HS boundary layer as a 2D fin generated shock (conservative). Table 2-2 shows the results of this interaction. If one considers the body radius of the BWB at the VS/HS intersection ($R_b = 12.875$ feet) together with the width of the HS (8 feet) and an axial distance of 100 feet, which is the approximate location of the HS most extended point, an angle of 12° is generated from the nosetip. This implies that bow shock angles $> 12^\circ$ would not interact with the HS. Table 2-2 shows that for $M_\infty < 15$, the bow shock would not interact with the HS. However, an accurate definition of the body shock is required; hence, the investigation considered the range of $10 \leq M_\infty$

Table 2-2. Bow Shock-HS Interaction.

$q_\infty = 1000$ PSF $\alpha_{\text{BODY}} = 9.4^\circ$

M_∞	θ_s	ALT (KFT)	BL	(P_{W2}/P_{W1}) (max)	P_{W1} (psi)	$(P_W)_{\text{plat}}$ (psi)	\tilde{P}_{W1} (psi)	\tilde{P}_{peak} (psi)	\tilde{P}_{plat} (psi)	δ (ft)	δ^* (ft)	$\phi(f \rightarrow 0)_{\text{APP}}$ psi ² /Hz x 10 ⁻⁸	$\phi(f \rightarrow 0)_{\text{PEAK}}$ psi ² /Hz x $\phi(0)_{\text{APP}}$	$\phi(f \rightarrow 0)_{\text{PLAT}}$ psi ² /Hz x $\phi(0)_{\text{APP}}$	\dot{q}_{w0} Btu/ ft ² -sec	$\dot{q}_{w\text{peak}}$ Btu/ ft ² -sec
4	23.9	71	T	2.9	.62											
6	19.	88.4	T	4.29	.276											
10	15.1	110.9	T	7.25	.099	.448	.0063	.25	.22	.093	.052	1.22	1200	910	5.1	26.2
15	13.2	129.9	L/T	13.5	.044	.355	.0036	.39	.39	.103	.063	0.688	4000	3920	7.2	57.8
20	12.3	144.1	L*	21.0	.0248	.294	.0023	.55	.57	.11	.07	0.441	12800	13700	8.1	92.5
25	11.7	155.7	L	29.8	.016											
$q_\infty = 2600$ PSF																
10	15.1	89.75	T	7.75	.26	1.176	.016	.658	.58	.076	.043	7.1	1200	910	9.44	48.6
15	13.2	107.6	T	13.5	.115	0.93	.0094	1.0	1.02	.083	.052	4.14	4000	3920	11.9	95.5
20	12.3	120.5	T	21.0	.0667	.791	.0061	1.46	1.51	.089	.057	2.72	12800	13700	13.2	151.

*Boundary Layer shown Laminar - Predictions based on Turbulent Conditions.

≤ 20 . Moreover, laminar boundary layers would probably occur on the surface for altitudes > 130 KFT.

2.6 CONCLUSIONS AND RECOMMENDATIONS

A methodology was developed that considers the prediction of fluctuating rms pressure and power spectra for attached and separated turbulent boundary layer flow. The attached flow results for both smooth and rough surfaces were based on an extensive data base and turbulent boundary layer shear flow principles. The separated flow characteristics as generated by 2D compression corner or fin generated shock impingement as well as 3D swept shock-boundary layer interactions were found to scale with the inviscid oblique shock pressure rise. A modified shock angle was defined in the inviscid oblique shock pressure relationship to characterize the 2D/3D shock-boundary layer interactions to provide peak and plateau level rms pressure and power spectra.

The technique was applied to the Blended Wing Body (BWB) transatmospheric vehicles with PNS solutions being used to obtain boundary layer parameters for the acoustic loads. Regions on the BWB involving shock-boundary layer interactions (control surfaces) required engineering correlations of the interactions based on the approach (undisturbed) boundary layer flow. Turbulent boundary layer conditions were assumed for the ascent trajectory range $4 \leq M_\infty \leq 25$ at nominal ($q_\infty = 1000$ psf) and high ($q_\infty = 2600$ psf) dynamic pressure conditions. While laminar boundary layer flow should prevail for $M_\infty > 12$ ~ 15 , turbulent flow was used to generate acoustic loads.

The results of this investigation are as follows:

- (1) In attached flow without shock interaction, the acoustic loads and heat transfer tended to follow the pressure distribution as generated by surface geometry and trajectory. The levels were commensurate with those experienced on re-entry vehicles subject to hypersonic flow conditions.

- (2) In attached flow without shock interaction, the overall sound pressure levels on the BWB (without control surfaces) ranged from 120 to 150 dB, with the high levels being experienced in the nosetip region and along the ramp toward the cowl inlet region.
- (3) There is significant uncertainty in predicting boundary layer transition altitude and subsequent movement along the configuration. Since heat and aeroacoustic loads are an order of magnitude greater for a turbulent boundary layer than the corresponding loads with a laminar boundary layer, the location of transition can have a major impact on design of skin panels.
- (4) Interaction of the shock-boundary layer on control surfaces was shown to be a strong function of shock strength ($M \sin \theta_s$). A prediction technique, with shock generating angles $\alpha > 12^\circ$, was developed based on physical laws, flow similitude, and $M \leq 3$ experimental data.
- (5) The strongest potential interaction involved the bow shock and horizontal control surface boundary layer. For this condition, peak rms fluctuating pressure was shown to increase by factors of 30 (30 dB) to 240 (48 dB) over the approach flow level for $10 < M_\infty < 20$. Interaction of the bow shock-horizontal control surface boundary layer for $M_\infty < 10$ did not appear likely because of the wide shock angle. The power spectrum was shown to increase by factors of 10^3 to 10^4 for the same range.
- (6) Potential interaction could exist between the horizontal and vertical control surfaces as generated by axial corner flow when the two surfaces approach a common origin. For this condition, the acoustic loads were estimated from mean flow data and heuristic techniques that showed the loads to be enhanced by the square of the inviscid pressure rise. However, with small angled shock generators ($\alpha < 4^\circ$) on the BWB, the impact was shown to be on the order of 3 times the approach flow levels (10 dB).

Several issues concerning the prediction of acoustic loads on large structures ($\sqrt{100}$ feet) featuring control surfaces and power generation (air-breathing system) were identified during this investigation. The following technology areas are recommended for further development in order to assess the impact of acoustic loads and structural integrity of these large configurations.

Data Base. While the data base for attached hypersonic turbulent boundary layer flow is not extensive, shock-boundary layer interaction type flow is very limited ($M < 3$). It is recommended that a program be structured to obtain acoustic data for $M > 3$ that includes X-PSD as well as rms pressure and power spectra. These experiments should include approach flows that are boundary layer as well as inviscid with axial corner and axial offset shock generating geometries. Angles $< 9^\circ$ should be considered. The experiments should also encompass:

- Shock orientation with the boundary layer; simulation of the potential bow shock-HS boundary layer interaction.
- Shock-laminar boundary layer interactions that are characteristic at the higher Mach number altitudes.
- Shock on shock-boundary layer interactions; bow shock on control surface shock-boundary layer.

Transition. This phenomenon is a continuing problem to the design engineer. The extensive work in References [2-28] through [2-30] was conducted on a re-entry vehicle data base featuring body length on the order of 10 feet. Using this information for ascent trajectories on bodies an order of magnitude longer may not involve the same transition onset and propagation criteria. It is recommended that the data base for boost vehicles be reviewed and the correlations described in References [2-28] through [2-30] be used to establish the application of the re-entry vehicle data base to transatmospheric vehicles.

Other Technology Issues. Other technology issues concerning acoustic loads that can impact transatmospheric vehicles include:

- Angle of attack effects where boundary layer scales differ from leeward to windward planes and change approach flow as well as control surface flow regions.
- Off-design conditions where separation can occur on ramp and control surface regions.
- Boundary layer roughness where augmentation in shear by a factor of 3 can cause the same levels in acoustic loads.
- Coupling of far field noise generation (rocket engine) to near field boundary and shock-boundary layer interactions.

2.7 NOMENCLATURE

b	Compressibility exponent - Equation 2-5
C_p	Pressure coefficient - $(P - P_1)/q_1$
C_f	Skin-friction coefficient
f, ω	Frequency
F_c	Compressible/incompressible transformation functions - Equation 2-3.
h	Enthalpy
k'	Parameter defined in Equation 2-6, $F_c^{-2\lambda}$
ℓ	Characteristic length
m	Viscous power law exponent, $\mu/\mu_e = (T/T_e)^m$
M	Mach number
n	Velocity power law exponent, $u/u_e = (y/\delta)^{1/n}$
\bar{p}, p_{rms}, P'	rms fluctuating pressure
P_w, \bar{P}_w	Local boundary layer static pressure
q	Dynamic pressure $[(\gamma/2) \rho M^2]$
r	Recovery factor (0.896 for turbulent flow)
Re	Reynolds number
u, v	Velocity in stream directions, normal direction
V	Characteristic velocity
x, y	Coordinate distance in stream and spanwise directions, respectively

Greek Symbols

α	Shock generator angle
β	Correction to swept shock - Equation 2-16
γ	Ratio of specific heats (1.4 for air)
δ, δ^*	Boundary layer and displacement thicknesses
θ_s	Oblique shock angle
λ	Parameter, viscous/velocity power law exponents $[2m - (1 + n)]/3 + n$ - Equation 2-4
ϕ	Shock angle based on swept shock-boundary layer interaction - Equation 2-16
$\phi(\omega), \phi(f)$	Power spectral density

Subscripts

0	Reference condition (smooth or upstream of interaction)
1	Approach flow upstream of interaction
2	Shock-boundary layer interaction region (peak, plateau)
aw	Adiabatic wall
c	Compressible conditions
e	Evaluated at edge of boundary layer
i	Incompressible conditions
x	Based on wetted length, axial length
w	Wall
∞	Freestream conditions

Superscript

*	Based on reference temperature conditions
---	---

2.8 REFERENCES

- 2-1 Chaump, L.E., Martellucci, A., and Monfort, A., Aeroacoustic Loads Associated with High Beta Vehicles, AFFDL-TR-72-138, May 1973.
- 2-2 Laganelli, A.L., Martellucci, A., and Shaw, L.L., "Wall Pressure Fluctuations in Attached Boundary Layer Flow." AIAA J., Vol. 21, No. 4, April 1983 (also AFFDL-TR-77-59).
- 2-3 Laganelli, A.L., Prediction of the Pressure Fluctuations on Maneuvering Re-entry Weapons, AFWAL-TR-83-3133, February 1984.
- 2-4 Laganelli, A.L., and Wolfe, H., Prediction of Fluctuating Pressure in Attached and Separated Boundary Layer Flow, AIAA Paper 89-1064, AIAA Aeroacoustics Conference, San Antonio, Texas, April 1989.
- 2-5 Laganelli, A.L., and Scaggs, N.E., Wall Shear Characteristics on Smooth and Rough Surfaces Based on Acoustic Measurements, AFWAL TR-85-3114, January 1986.

- 2-6 Laganelli, A.L., and Sontowski, J., Drag and Aeroacoustic Noise Characteristics Generated by Surfaces Featuring Coupled Roughness and Blowing, ASME Energy Sources Tech. Conf., New Orleans, February 1984, FED-VOL II.
- 2-7 Settles, G.S., and Dolling, D.S., "Swept Shock Wave/Boundary Layer Interactions." Tactical Missile Aerodynamics, Progress in Astronautics-Aeronautics (AIAA), Vol. 104.
- 2-8 Tran, T.T., An Experimental Investigation of Unsteadiness in Swept Shock Wave/Turbulent Boundary Layer Interactions, Ph.D. Thesis, Princeton University, ME Department, March 1987.
- 2-9 Dolling, D.S., and Smith, D.R., Unsteady Shock-Induced Turbulent Separation in Mach 5 Cylinder Interactions, AIAA Paper 88-0305, 26th Aero. Sci, Reno, January 1988.
- 2-10 Tran, T.T., and Bogdonoff, S.M., A Study of Unsteadiness of Shock Wave/Turbulent Boundary Layer Interactions from Fluctuating Wall Pressure Measurements, AIAA Paper 87-0552, 25th Aero, Sci, Reno, January 1987.
- 2-11 Dolling, D.S., and Dussauge, J.P., "Fluctuating Wall Pressure Measurements," Chapter 8, A Survey of Measurements and Measuring Techniques in Rapidly Distorted Compressible Turbulent Boundary Layers, Agardograph published Spring 1988.
- 2-12 Andreopoulos, J., and Muck, K.C., "Some New Aspects of the Shock Wave Boundary Layer Interaction in Compression Ramp Flows." Journal of Fluid Mechanics, Vol. 180, pp. 405-428, 1987.
- 2-13 Dolling, D.S., and Or, C.T., "Unsteadiness of the Shock Wave Structure in Attached and Separated Compression Ramp Flowfields." Experiments in Fluids, Vol. 3, pp. 24-32, 1985.

- 2-14 Houbolt, J.D., On the Estimation of Pressure Fluctuations in Boundary Layers and Wakes, GE TIS 66SD296, April 1966.
- 2-15 Lowson, M.V., Prediction of Boundary Layer Pressure Fluctuations, AFFDL-TR-67-167, April 1968.
- 2-16 Dolling, D.S., and Murphy, M.T., "Unsteadiness of the Separation Shock Wave Structure in a Supersonic Compression Ramp Flowfield." AIAA Journal, Vol. 21, pp. 1628-1634, December 1983.
- 2-17 Tan, D.K., Tran, T.T., and Bogdonoff, S.M., "Wall Pressure Fluctuations in a 3-D Shock-Wave/Turbulent Boundary Layer Interaction." AIAA Journal, Vol. 25, No. 1, January 1987.
- 2-18 Muck, K.C., Dussauge, J.P., and Bogdonoff, S.M., Structure of the Wall Pressure Fluctuations in a Shock-Induced Separated Turbulent Flow, AIAA Paper 85-0179, 23rd Aero Sci., Reno, January 1985.
- 2-19 Neumann, R.D., and Hayes, J.R., Prediction Techniques for the Characteristics of the 3D Shock Wave Turbulent Boundary Layer Interactions, AIAA Paper 77-46, January 1977.
- 2-20 Coe, C.F., Chyu, W.J., and Dods, J.B., Pressure Fluctuations Underlying Attached and Separated Supersonic Turbulent Boundary Layers and Shock Waves, Presented at Aeroacoustic Conference, Seattle, Washington, October 1973, Paper No. 73-996.
- 2-21 Kaplan, M., High Speed Boundary Layer Separation in a Compression Corner, GE MSVD TFM-HTT-8151-001, May 1962.
- 2-22 Nestler, D.E., Heat Transfer to Steps and Cavities in Hypersonic Turbulent Flow, AIAA Paper 68-673, Fl. Plasma Dyn., Los Angeles, June 1968.

- 2-23 Holden, M.S., Experimental Studies of Quasi-Two-Dimensional and Three-Dimensional Viscous Interaction Regions Induced by Skewed-Shock and Swept-Shock Boundary-Layer Interaction, AIAA Paper No. 84-1677, June 1984.
- 2-24 Scuderi, L.F., Expressions for Predicting 3D Shock Wave - Turbulent Boundary Layer Interaction Pressure and Heating Rates, AIAA Paper 78-162, January 1978.
- 2-25 Nestler, D.E., and Hall, D.W., Flow Field Separation Approximations for Hypersonic Aerodynamics, AFWAL-TR-88-3025, May 1988.
- 2-26 Robertson, J.E., Prediction of In-Flight Fluctuating Pressure Environments Including Protuberance Induced Flow, Wyle Laboratories, Huntsville, AL, Research Staff Report WR71-10, March 1971.
- 2-27 Tran, T.T., Tan, D.K., and Bogdonoff, S.M., Surface Pressure Fluctuations in Three-Dimensional Shock Wave Turbulent Boundary Layer Interactions at Various Shock Strengths, AIAA Paper 85-1562, July 1985.
- 2-28 Weinberg, S.A., Laganelli, A.L., and Martellucci, A., Boundary Layer Transition Study (Task 3) - Progress Report, SAIC/VFC-880-083, May 1987.
- 2-29 Martellucci, A., et al., Boundary Layer Transition Flight Test Observations, AIAA Paper 77-125, January 1977.
- 2-30 Berkowitz, A.M., and Kyriss, C.L., Boundary Layer Transition Study, Volume I, Task 1 Final Report - Correlation of Flight Test Transition Onset and Movement Data, AFFDL-TR-78-4, July 1978.
- 2-31 Krawczyk, W.J., and Harris, T.B., Analysis of Aerospace Vehicle Scramjet Propulsive Flow Fields: 2-D Forebody/Inlet Code Development - Phase I, NASP CR-1003, June 1987.
- 2-32 Pozefsky, P., Private Communication, McDonnell Douglas (St. Louis), December 1988.

- 2-33 Pozefsky, P., Blevins, R.D., and Laganelli, A.L., Thermo-Vibro-Acoustic Loads and Fatigue of Hypersonic Flight Vehicle Structure - Phase I Report, Rohr Report RHR 88-113, June 1988.
- 2-34 Billig, F.S., et al., Proposed Supplement to Propulsion System Management Plan, Johns Hopkins University, APL Report JHU/APL-NASP-86-1, July 1986.
- 2-35 Inger, G.R., "Spanwise Propagation of Upstream Influence in Conical Swept Shock/Boundary-Layer Interactions." AIAA Journal, Vol. 25, No. 2, February 1987.
- 2-36 Inger, G.R., Private Communication, Science Applications International Corporation Consultant - Iowa State University, December 1988.
- 2-37 West, J.E., and Korkegi, R.H., "Supersonic Interaction on the Corner of Intersecting Wedges at High Reynolds Numbers." AIAA Journal, Vol. 10, No. 5, May 1972.
- 2-38 Neumann, R.D., and Hayes, J.R., "Introduction to Aerodynamic Heating Analysis of Supersonic Missiles. Tactical Missile Aerodynamics, Progress in Astro/Aeronautics, Vol. 104.
- 2-39 Holden, M.S., Shock Wave - Turbulent Boundary Layer Interaction in Hypersonic Flow, AIAA Paper 77-45, 15th Aero. Sci. Meeting, Los Angeles, 1977.
- 2-40 Patterson, J.L., Investigation of Test Facility Effects on the Three-Dimensional Boundary Layer Interaction, AFFDL-TR-77-113, November 1977.

838PROP
3-2.BB
12-11-89

SECTION 3

ENGINE ACOUSTIC LOADS

3.1 INTRODUCTION

The engine induced sound levels in transatmospheric hypersonic vehicles have two sources: (1) the rocket engines used to propel the vehicle to Mach 2-3 where the scramjet engines become efficient and (2) the scramjet engines. The noisiest section of the flight occurs during takeoff when both the rocket engines and the scramjet engine are operating. The sound levels on the lower half of the vehicle are different from those on the upper half. The reflections from the airport ground as well as the presence of the scramjet engine make the lower half susceptible to much higher sound levels compared with the upper half. Following an extensive literature search, three different mathematical models for predicting sound levels were considered and compared as described in Section 3.2. The model selected for the present analysis is the model proposed by NASA and is outlined in Section 3.3.1. For the purpose of this analysis, the vehicle was divided into upper and lower surfaces, with a total of sixteen locations being selected for sound level evaluation. At each of these locations, the sound pressure level spectrum and the overall sound pressure level were evaluated for the different cases of interest.

3.2 TECHNIQUES FOR PREDICTION OF ENGINE INDUCED ACOUSTIC LOADS

Various mathematical models exist for the prediction of the overall sound power level of a rocket engine. All of the models are semiempirical and rely on some type of curve fitting.

A modification of Lighthill V^8 jet noise law has been used by Eldred (Reference [3-1]). For exit Mach numbers greater than 3, the V^8 law becomes a V^3 law, so the overall sound power level can be written as

$$dB_E = 10 \log_{10} \frac{5 \times 10^{-5} (M)^5 \rho A V^3 F}{10^{-12}} \quad (3-1)$$

where M = the exit Mach number not to exceed 3

ρ = ambient density, slugs/ft³

A = throat area, ft²

V = exhaust velocity, ft/sec

F = temperature factor varying from 1 at 600°R to 0.1 at 4000°R.

A more empirical relationship has been reported by Von Gierke (Reference [3-2]):

$$dB_{VG} = 70 + 13.5 \log_{10} W_m \quad (3-2)$$

where W_m = power exhaust in watts, (1/2) VT

V = exhaust velocity, m/s

T = rocket engine thrust, N

The accuracy of this model has been tested up to a value of W_m equal to about 4×10^8 watts.

The model used in the present study is that given by the NASA study reported in Reference [3-3]:

$$dB_{NASA} = 100 + 10 \log_{10} W_m \quad (3-3)$$

with the values of W_m defined the same as in Equation 3-2. In the range of exhaust powers varying from 10^7 to 10^{10} , the difference between the Von Gierke (VG) and the NASA models is shown in Table 3-1.

Table 3-1. Comparison of Von Gierke and NASA Models.

W_m (watts)	dB_{VG}	dB_{NASA}
10^7	165	170
10^8	178	180
10^9	192	190
10^{10}	205	200

838PROP
3-T3-1.BB
11-11-89

The two limiting conditions of interest to this study are a total thrust of 450,000 N (100,000 lb) and 1.8×10^6 N (400,000 lb) with a corresponding fluid exit velocity of 3050 m/s (10,000 fps) and 6100 m/s (20,000 m/s). Utilizing these values in Equations 3-1, 3-2, and 3-3 provides a comparison of the three models for the lower and upper bounds:

<u>Thrust (N)</u>	<u>dB_E</u>	<u>dB_{VG}</u>	<u>dB_{NASA}</u>
450,000	188	189	188
1,800,000	204	202	197

The three models are thus seen to be practically the same at the lower thrust level with a difference of 7 dB evident at the higher thrust level.

The directivity patterns utilized in this study and the dimensionless sound pressure levels have all been obtained empirically and depend upon the same set of measurements. Hence, all the results presented in this study will change by a constant amount if the overall sound power levels are changed.

3.3 SOUND LEVELS DUE TO ENGINES OF TRANSATMOSPHERIC AIRCRAFT

3.3.1 Sound Levels Due to Rocket Engines

After an intensive literature search that included a computer printout of relevant papers and abstracts, it was determined that the prediction technique in NASA report SP-8072 (Reference [3-3]) is the approach that includes most of the acoustic phenomena of interest.

The analysis assumes that the overall acoustic power is equal to 1% of the overall fluid power. The overall sound power level is then converted to an acoustic sound pressure level per octave band. The conversion is obtained from Figure 3-1, which shows the collapse of the acoustic data for many different types of rocket engines. $W(f)$ is the acoustic power spectrum, W_{OA} is the overall acoustic power, U_e is the

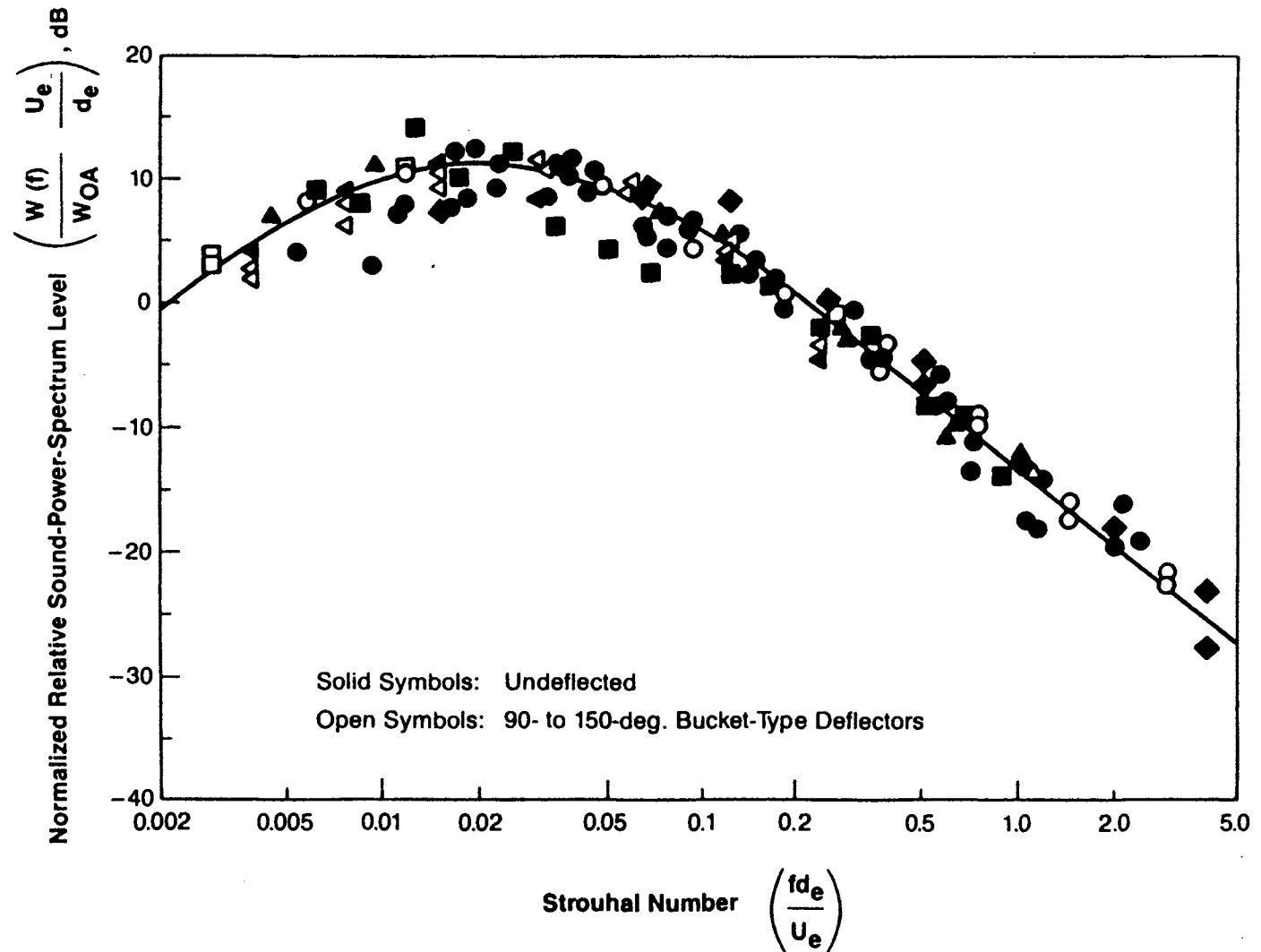


Figure 3-1. Normalized Power Spectrum for Standard Rocket Engines (from Ref. [3-3]).

rocket exit velocity, d_e is the effective exit-nozzle diameter, and f is the frequency. Each dimensionless frequency corresponding to the center frequency of each octave band gives a corresponding normalized spectrum level. The normalized spectrum level is then converted to a sound power level (Ref. 10^{-12} watts).

The rocket engine sound produces a spectrum with each frequency band having an effective sound source location. The axial location of the apparent source as a function of frequency for different typical nozzles is given in Figure 3-2. The apparent source axial position is the distance from the rocket nozzle exit to the source location of the particular dimensionless frequency as defined by the Strouhal number; the distance is nondimensionalized with respect to the nozzle effective diameter d_e . Note that a very wide band exists for the apparent sound source location. Spherical spreading for the waves emanating from the effective sound source location is then assumed, and the sound pressure level for each bandwidth is evaluated at different typical locations of the vehicle. In the evaluation of the sound pressure level, the directivity pattern for the different frequency bands is given by Figure 3-3. In this figure, the directivity index in dB is plotted as a function of angular position for different dimensionless frequencies. Note that a value of θ equal to zero corresponds to the downstream direction, while a value of 180° corresponds to locations toward the fore section of the vehicle.

Figures 3-4 and 3-5 are sketches of the Blended Wing Body (BWB) model used in the present analysis. The rocket engines are assumed to be at locations I and II on the upper and lower surfaces of the body. The sketches and the performance characteristics of the rocket engines were provided by MDC. In general, instead of one individual thruster, the engine is composed of a series of 10 to 100 small modules, with each module being a small thruster. The dimensions of the individual rocket engine can vary from a 3 by 3 inch size down to a 1 by 1 inch size. For the purpose of this study, a typical size of 2 inches was selected. The rocket engine was also assumed to be composed of 80 individual modules. The overall thrust required for vehicle operation can vary from 100,000

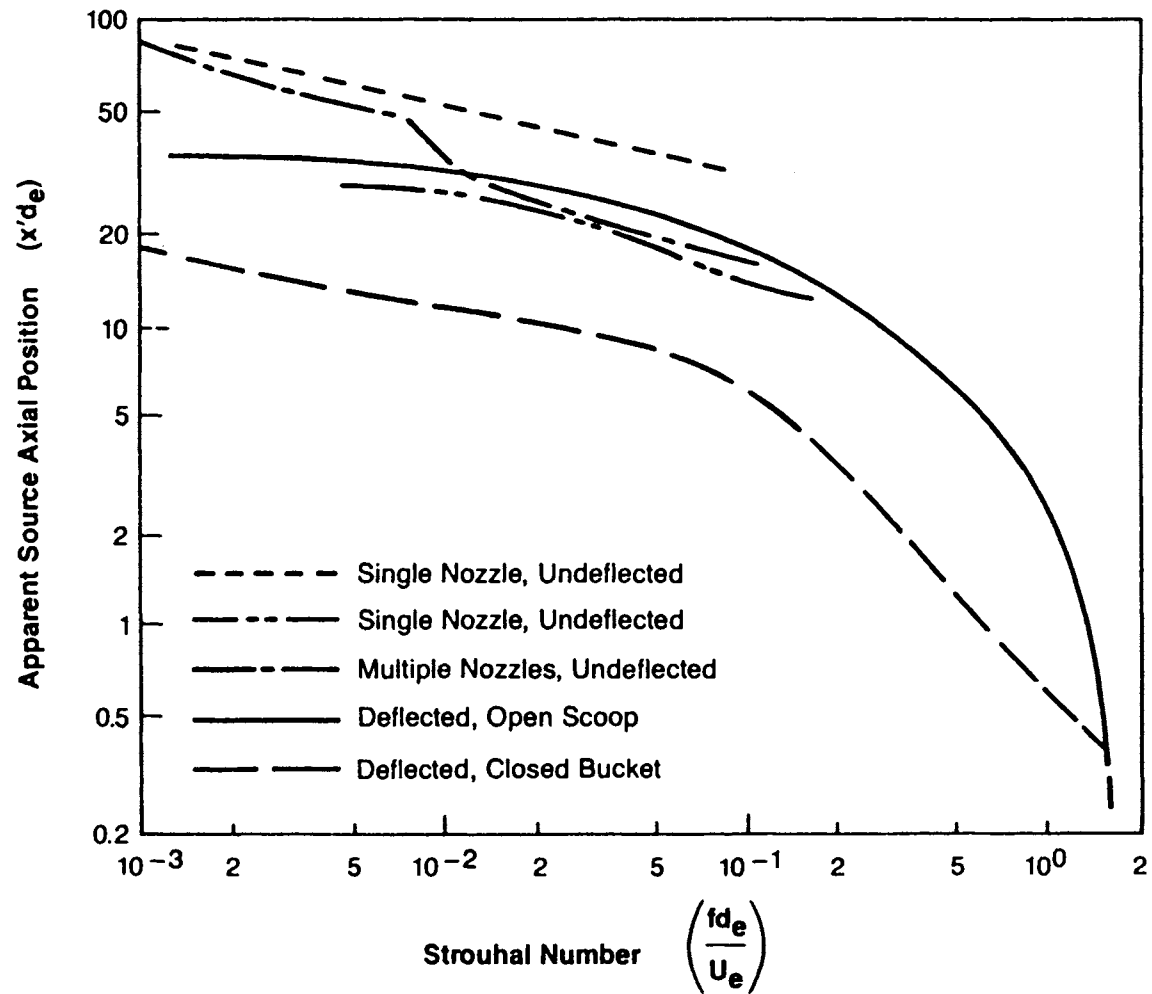


Figure 3-2. Axial Location of Apparent Sound Source (from Ref. [3-3]).

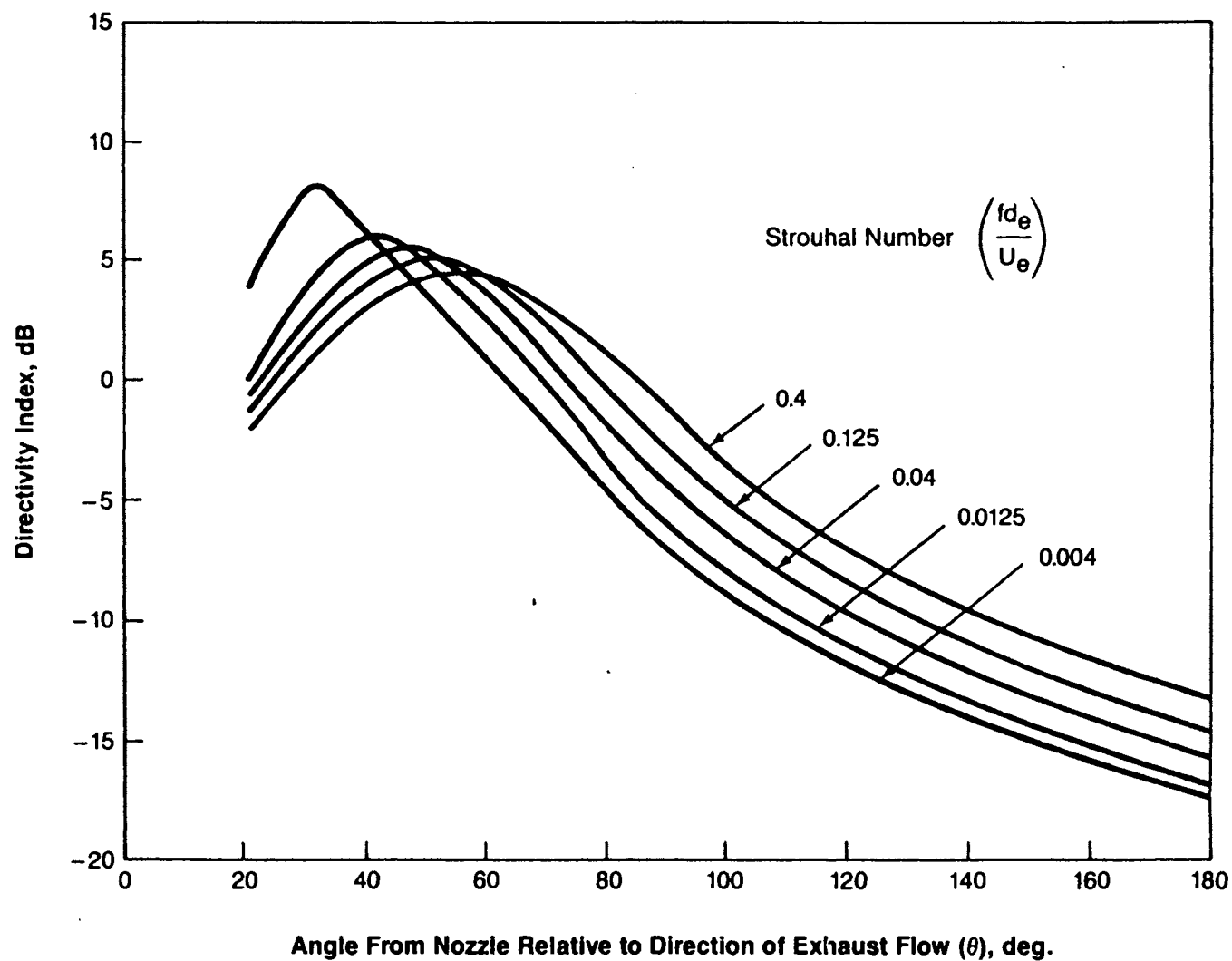


Figure 3-3. Directivity Pattern of Engine Sound (from Ref. [3-3]).

3-9

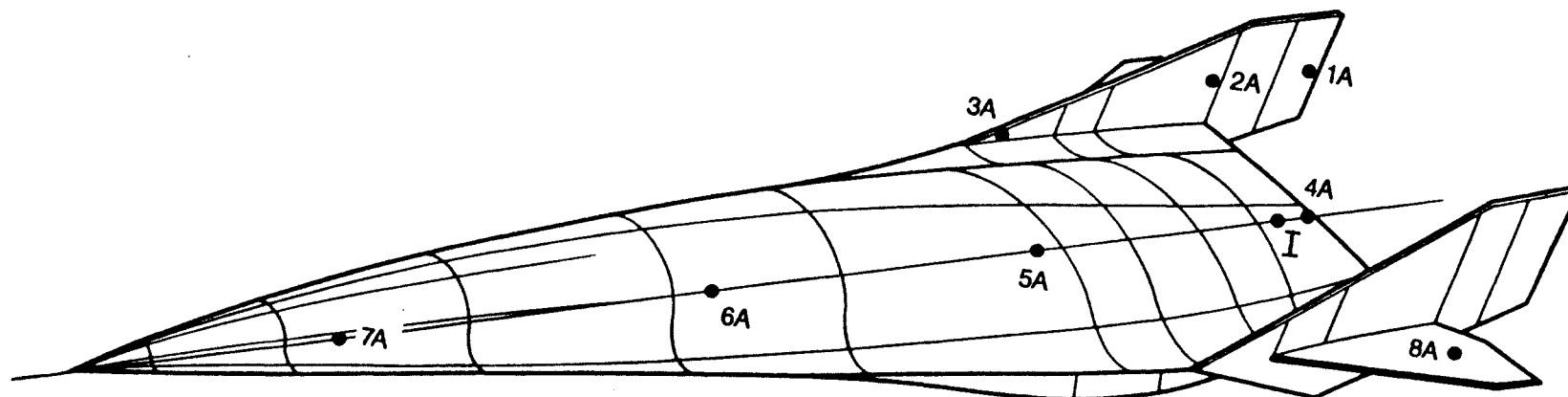


Figure 3-4. Sketch of Blended Wing Body Model Used in Sound Level Analysis of Upper Surface.

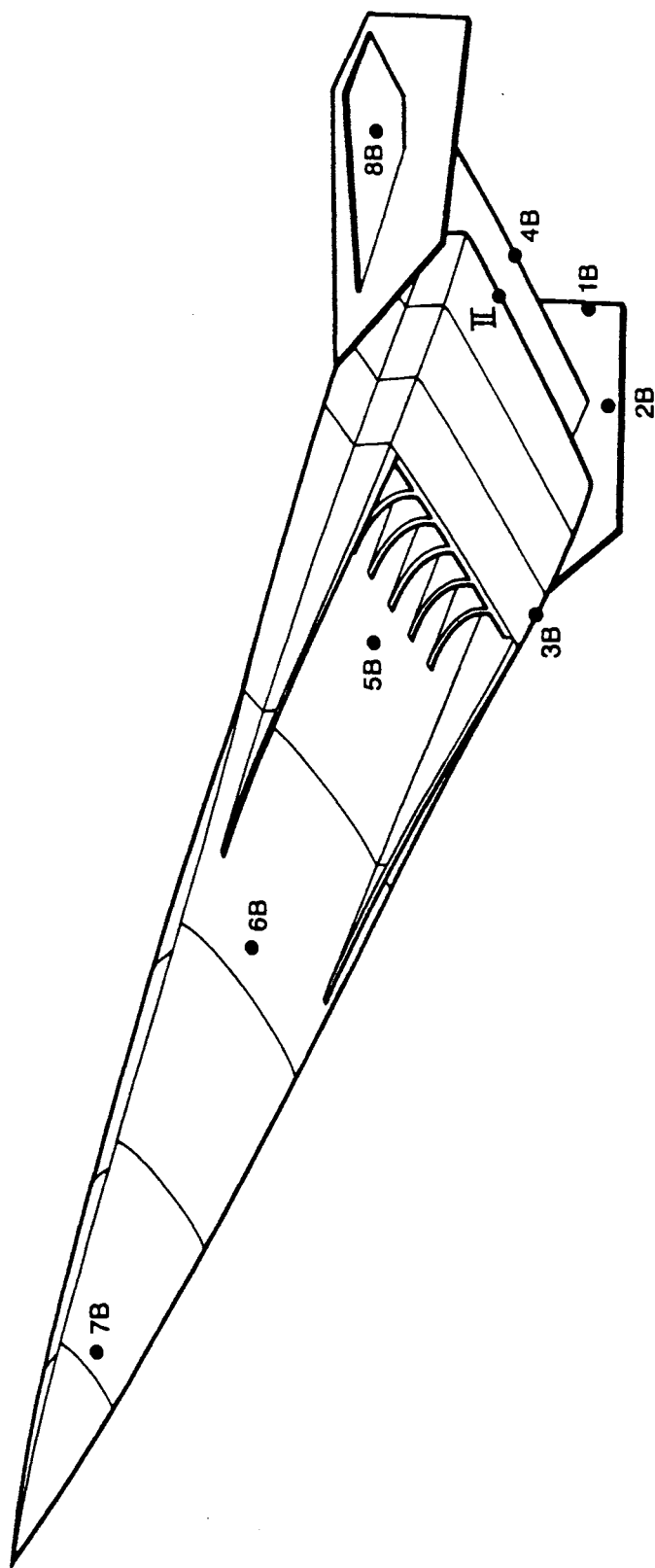


Figure 3-5. Sketch of Blended Wing Body Model Used in Sound Level Analysis of Lower Surface.

to 400,000 pounds. The exit velocity of the gases (per MDC) can vary from 10,000 to 20,000 feet per second. The two rocket engines were assumed to be of equal power. Locations 5, 6, and 7 represent typical aft-body, mid-body, and fore-body locations of the model. Locations 1, 2, and 3 represent typical locations of the vertical tail, while location 8 is the typical horizontal tail location.

The sound levels in locations 1 through 7 were obtained by the analysis outlined above. The sound level at location 8 was obtained by assuming diffraction around the vertical tail with the analysis of Reference [3-4].

The present analysis was performed using available data and theory. The noise data and theories assume far field results. Applications to the near field would require a new approach where the interaction between the pseudo-sound pressure fluctuations (i.e., the aerodynamic pressure fluctuations) and the local flow fields due to the boundary layer, the scramjet, and the rocket exhaust would be considered.

All of the results presented in this section assumed negligible forward motion of the vehicle; this is the takeoff mode where both the scramjet and the rocket thrusters are operating and also where acoustic reflections from the runway will increase the acoustic pressure on the plane's surfaces. As the speed of the hypersonic vehicle increases beyond the subsonic range, the presence of the shock waves will prevent the noise from traveling beyond a given region. At higher speeds, the angles of the shock waves will be shallower, with the rocket and the scramjet noise being felt in a corresponding smaller region.

For the present analysis, it was assumed that a thrust of 9×10^5 N (200,000 lb) exists on the upper surface and an equivalent thrust of 9×10^5 N exists on the lower surface. The exit velocity of the gases was assumed to be equal to 6100 m/s (20,000 fps). These conditions give rise to an overall acoustic power of 194 dB (Ref. 10^{-12} watts). Section 3.6.1 gives the equations used in the present analysis and also a sample calculation utilized to obtain the present results. If it is assumed

that a spectrum is given by Figure 3-1, then the sound power levels for the octave bands are as given in Figure 3-6. The sound power level values for each octave band are plotted as a function of the center frequency of each bandwidth. For clarity, the values are connected by a series of lines.

Figure 3-7 shows the results of the analysis for the eight different locations selected on the upper surface of the model.

For the lower surface, it was assumed that complete reflections occur along the ground and that each octave band radiates with its own characteristics. Figure 3-8 shows the results of these series of calculations. It should be noted that at locations 2, 3, 5, 6, and 7, the dB level on the lower surface is 4 to 6 dB higher than on the upper surface. The reason that it is not always 6 dB is that the distance traveled by the reflected wave from its apparent source in the wake to the location on the model is a function of frequency. The sound level at location 1B is about 2 to 5 dB higher than that at location 1A. The sound level at location 4B is 0 to 5 dB higher than that at location 4A depending upon the octave band chosen. The largest difference between the upper and lower curves is seen to occur at location 8, where on the upper surface the sound arrives at point 8A by means of diffraction around the vertical tail, while at location 8B the most effective means of travel for the sound is the reflected sound from the ground.

Tables 3-2 and 3-3 present the sound pressure level in the different octave bands for the eight locations selected. These results are also plotted in Figures 3-7 and 3-8.

If the sound pressure level at a particular frequency with a bandwidth of 1 Hz is desired, the following formula is used:

$$SPL_f = SPL_b - 10 \log_{10} \Delta f_b$$

where SPL_b is the sound pressure level in the octave band center frequency and Δf_b is the bandwidth of that particular band and is given

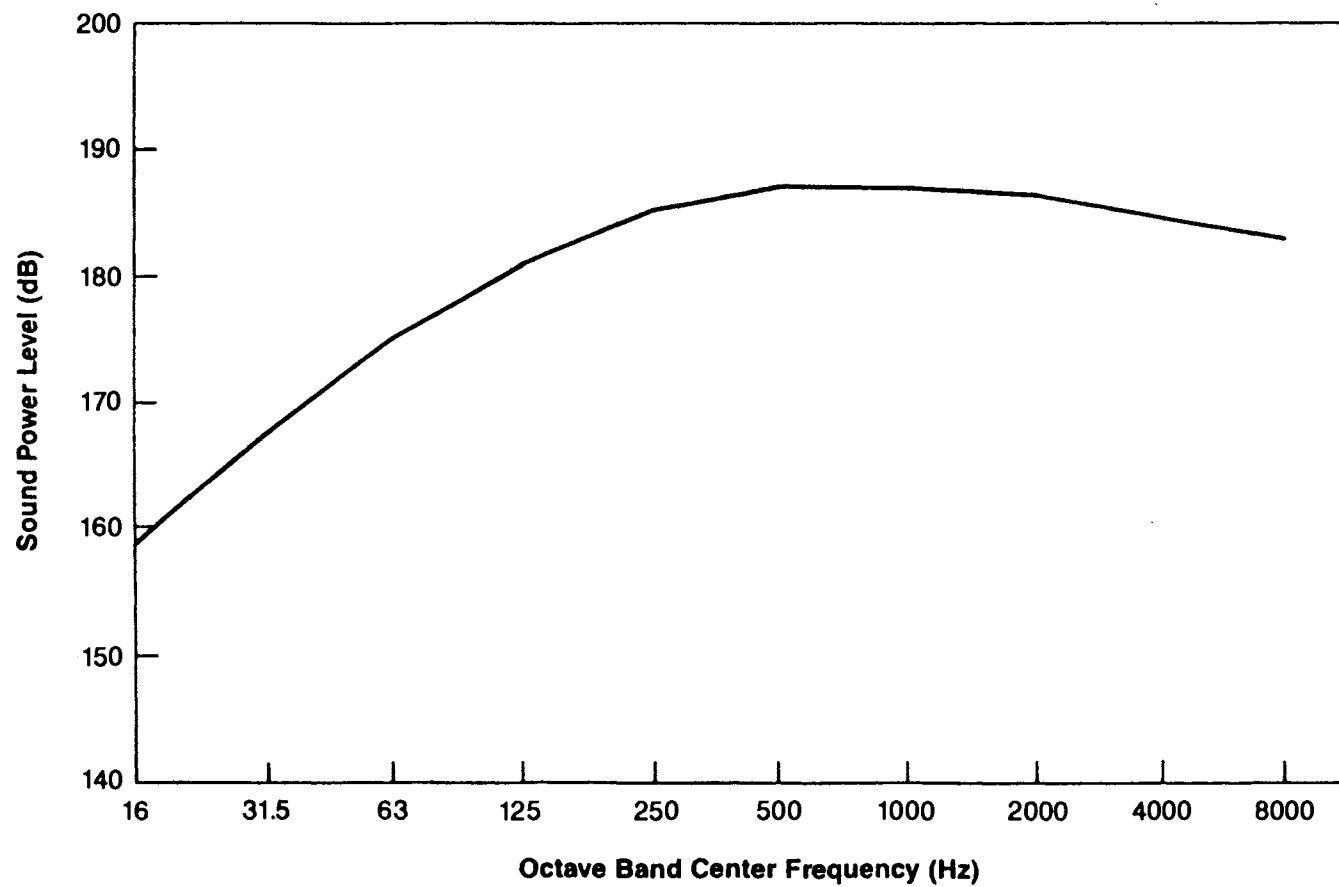


Figure 3-6. Sound Power Level for Upper and Lower Rocket Engines.

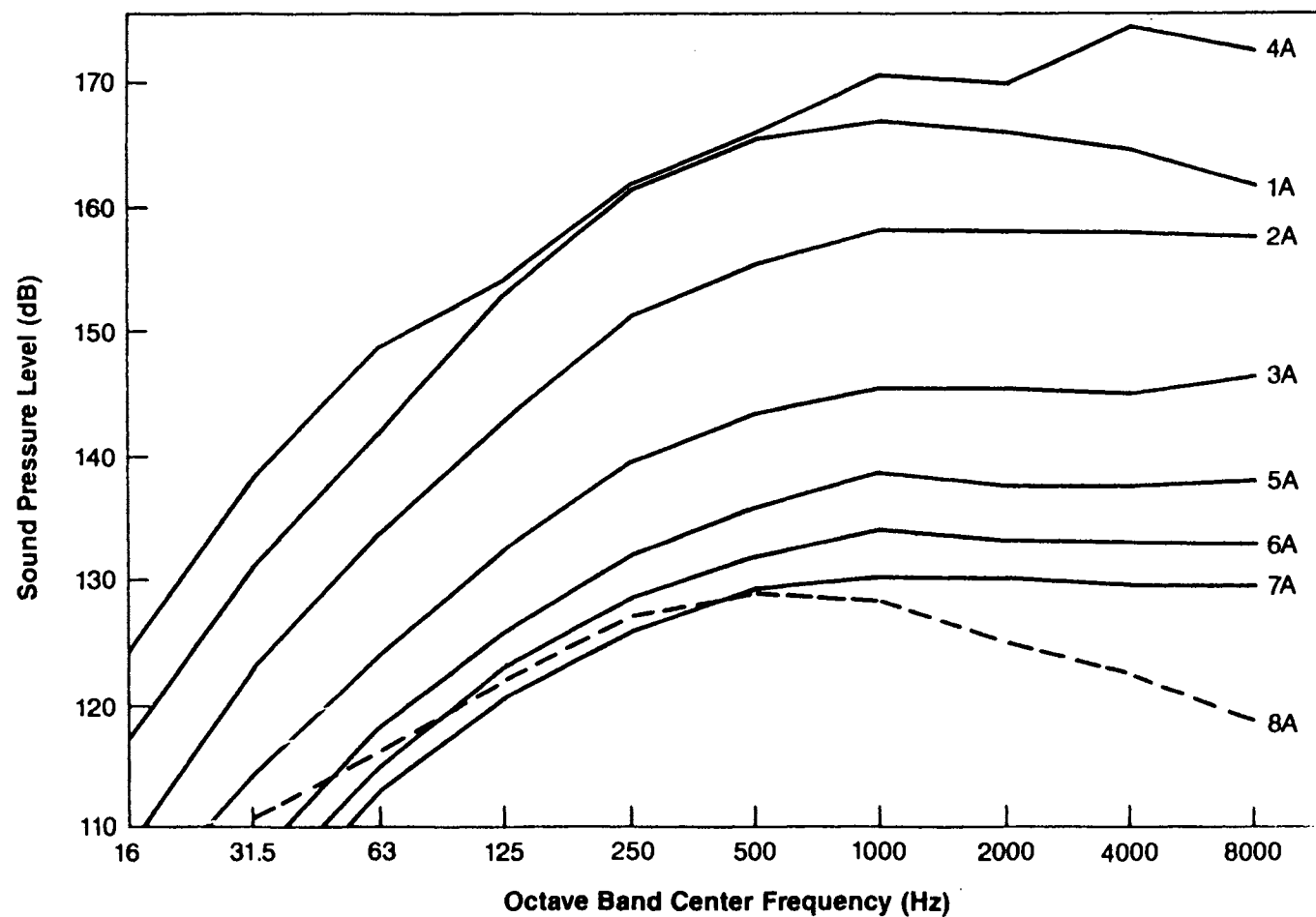


Figure 3-7. Sound Pressure Level (Ref. 20 μ PA) on Upper Surface due to Rocket Engines.

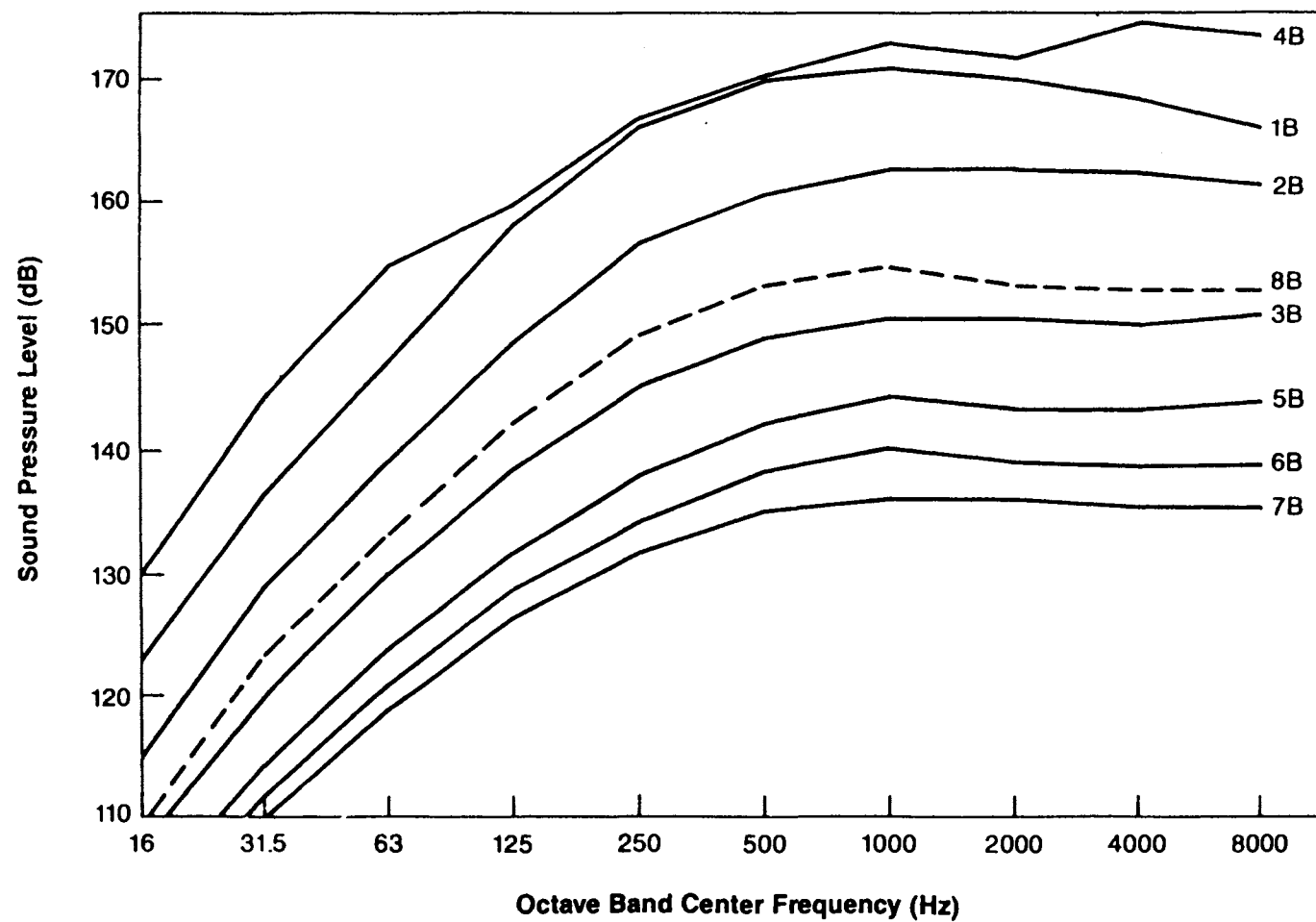


Figure 3-8. Sound Pressure Level (Ref. 20 μ PA) on Lower Surface due to Rocket Engines.

Table 3-2. Octave Band Sound Pressure Level due to Rocket Thrusters (Ref. 20 μ PA) at Eight Locations on the Model Upper Surface (in dB).

Center Frequency (Hz)	(a) Location							
	1A	2A	3A	4A	5A	6A	7A	8A
16	116.8	108.6	101.3	124.0	96.0	94.3	92.9	98.6
32	131.4	123.3	114.2	138.2	108.5	106.1	104.3	110.6
63	142.0	134.0	124.0	148.7	118.0	115.3	113.3	116.0
125	152.9	143.0	132.3	154.1	125.9	122.8	120.5	122.0
250	161.5	151.3	139.7	161.7	132.1	128.4	125.9	127.3
500	165.6	155.5	143.4	166.2	136.1	132.1	129.4	128.5
1000	167.2	158.0	145.5	170.4	138.2	133.9	130.0	128.0
2000	166.0	158.0	145.4	169.9	137.6	133.1	130.2	125.0
4000	164.5	158.2	145.2	174.8	137.6	132.8	129.8	122.2
8000	161.5	157.5	146.2	172.6	138.1	132.8	129.6	118.5
OVERALL	172.6	164.8	152.5	178.8	144.9	140.4	137.2	134.2

(a) See Figure 3-4.

838PROP
3-T3-2.BB
11-11-89

Table 3-3. Octave Band Sound Pressure Level due to Rocket Thrusters (Ref. 20 μ PA) at Eight Locations on the Model Lower Surface (in dB).

Center Frequency (Hz)	(a) Location							
	1B	2B	3B	4B	5B	6B	7B	8B
16	122.8	114.6	107.3	130.0	102.0	104.3	98.9	108.6
32	136.8	129.0	120.2	144.2	114.5	112.1	110.3	123.3
63	147.0	139.5	130.0	154.7	124.0	121.3	119.3	133.4
125	158.2	148.4	138.3	159.7	131.9	128.8	126.5	142.1
250	166.2	156.5	145.3	166.4	138.1	134.4	131.9	149.5
500	169.9	160.4	149.0	170.3	142.1	138.1	135.4	153.1
1000	171.3	162.6	150.9	173.3	144.2	139.9	136.0	154.7
2000	170.1	162.5	150.7	171.8	143.6	139.1	136.2	153.4
4000	168.6	162.4	150.4	176.1	143.6	138.8	135.8	154.1
8000	165.9	161.6	151.1	173.9	144.1	138.8	135.6	153.1
OVERALL	176.9	169.2	157.8	180.7	150.9	146.4	143.2	161.1

(a) See Figure 3-5.

838PROP
3-T3-3.BB
11-11-89

in Table 3-4. For example, if the sound pressure level at a frequency of 150 Hz is needed, the frequency of 150 Hz is contained in the band with a center frequency of 125 Hz and a width of 88 Hz. Figure 3-7 shows that the sound pressure level at location 3A at the center frequency of 125 Hz is 132.5 dB. Thus,

$$SPL_{150} = 132.5 - 10 \log_{10} 88 = 113.1 \text{ dB}$$

Section B.2.2 of Appendix B shows that in order to go from the octave band to the one-third octave band level, a subtraction of 4.85 dB from the octave band level is required.

3.3.2 Scramjet Engine Sound Levels

The data received from McDonnell Douglas Corporation in relation to the power level spectrum of the scramjet engine is given in Table 3-5.

The worst condition from a sound pressure level point of view is on the lower surface of the vehicle. It occurs during takeoff when the reflections from the ground must be considered in the analysis.

Figure 3-9 shows a comparison of the sound pressure levels for the scramjet engine and for the rocket engines. Note that while the overall sound power level is about equal (194 dB) for both sources, the spectrum is completely different. The scramjet engine has most of its acoustic energy in the low-frequency region, while the rocket engines have their peak acoustic energy in the mid-high-frequency region. The main difference is due to the dimensions of the scramjet engine as compared with those of the rocket engines. The scramjet engine has very large dimensions, so its main frequency is low, whereas the rocket engines have very small nozzles, resulting in a very high-frequency signature.

Table 3-6 and Figure 3-10 give the sound pressure level spectrum for the different locations selected on the vehicle lower surface. The same technique that was used for the rocket engine sound level analysis was used in this analysis.

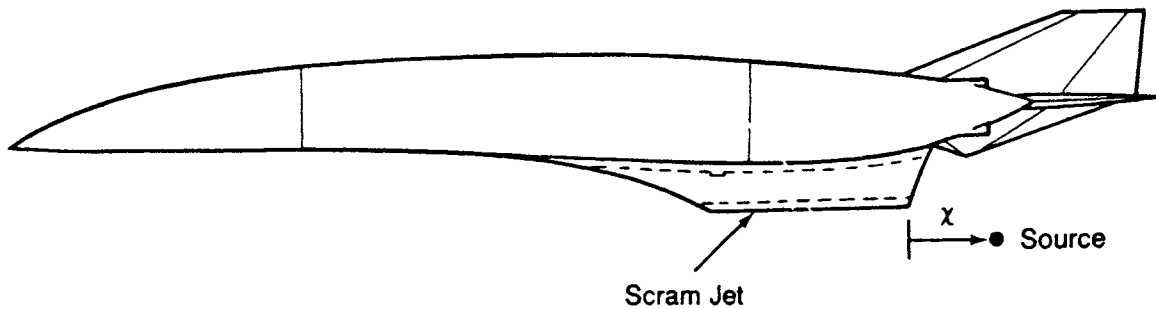
Table 3-4. Bandwidth and Center Frequencies for Octave Band (in Hz).

Octave Band Center Frequency	Bandwidth	Lower-Upper Frequency
16	11	11-22
31.5	22	22-44
63	44	44-88
125	88	88-177
250	177	177-355
500	355	355-710
1000	710	710-1420
2000	1420	1420-2840
4000	2840	2840-5680
8000	5680	5680-11360

838PROP
3-T3-4.BB
11-11-89

Table 3-5. Scramjet Engine Power Level Spectrum and Location of Source.

f (Hz)	PWL (dB)	x, Location of Source (m)
16	192.3	22.7
31.5	188.3	16.2
63	183.3	9.3
125	177.8	4.6
250	172.3	1.8
500	167.3	0.7
1000	161.8	0.4
2000	156.3	0.2
4000	150.8	0.1
8000	145.3	0



838PROP
3-T3-5.BB
11-11-89

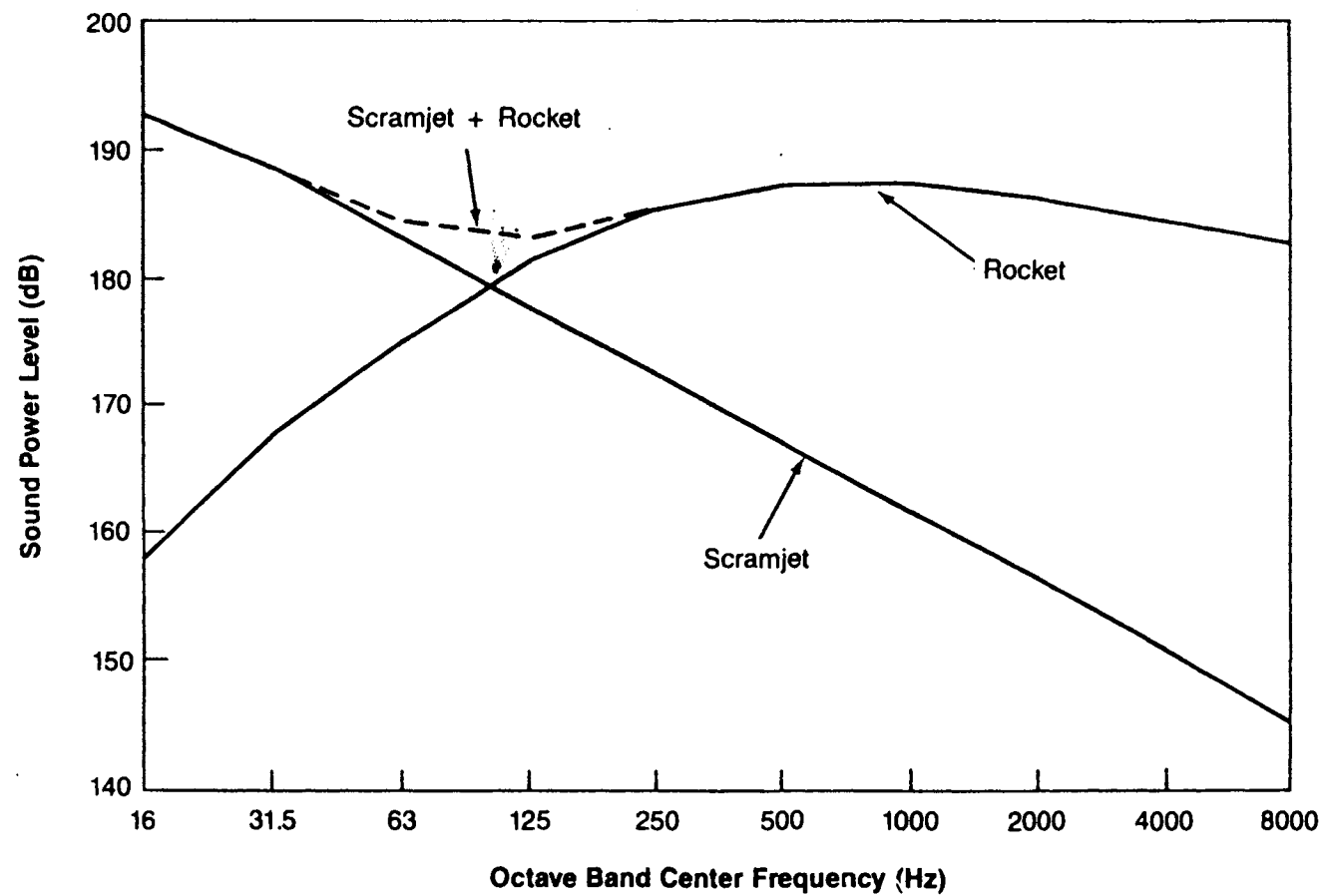


Figure 3-9. Sound Power Level for Scramjet and Rocket Engines.

Table 3-6. Octave Band Sound Pressure Level (dB) on Vehicle Lower Surface due to Scramjet Engine Alone.

f (Hz)	L o c a t i o n						
	1B	2B	3B	4B	5B	6B	7B
16	158.2	149.6	141.7	165.1	136.0	133.7	131.9
31.5	158.0	149.5	140.0	164.8	134.2	131.1	129.0
63	158.5	150.1	138.7	165.8	131.9	128.4	125.9
125	157.5	148.6	136.7	166.1	129.1	124.9	122.0
250	151.3	145.0	134.4	165.8	125.9	120.9	117.7
500	146.0	140.3	130.7	153.7	122.7	117.3	114.0
1000	140.7	135.1	125.9	146.6	118.4	112.9	109.1
2000	135.1	130.5	121.6	139.9	113.5	108.0	104.6
4000	130.0	126.0	116.7	133.6	109.1	103.6	100.2
8000	124.9	121.0	112.3	127.4	104.7	99.1	95.7
Overall	164.4	156.0	146.2	172.6	139.8	136.8	134.8

838PROP
3-T3-6.BB
11-11-89

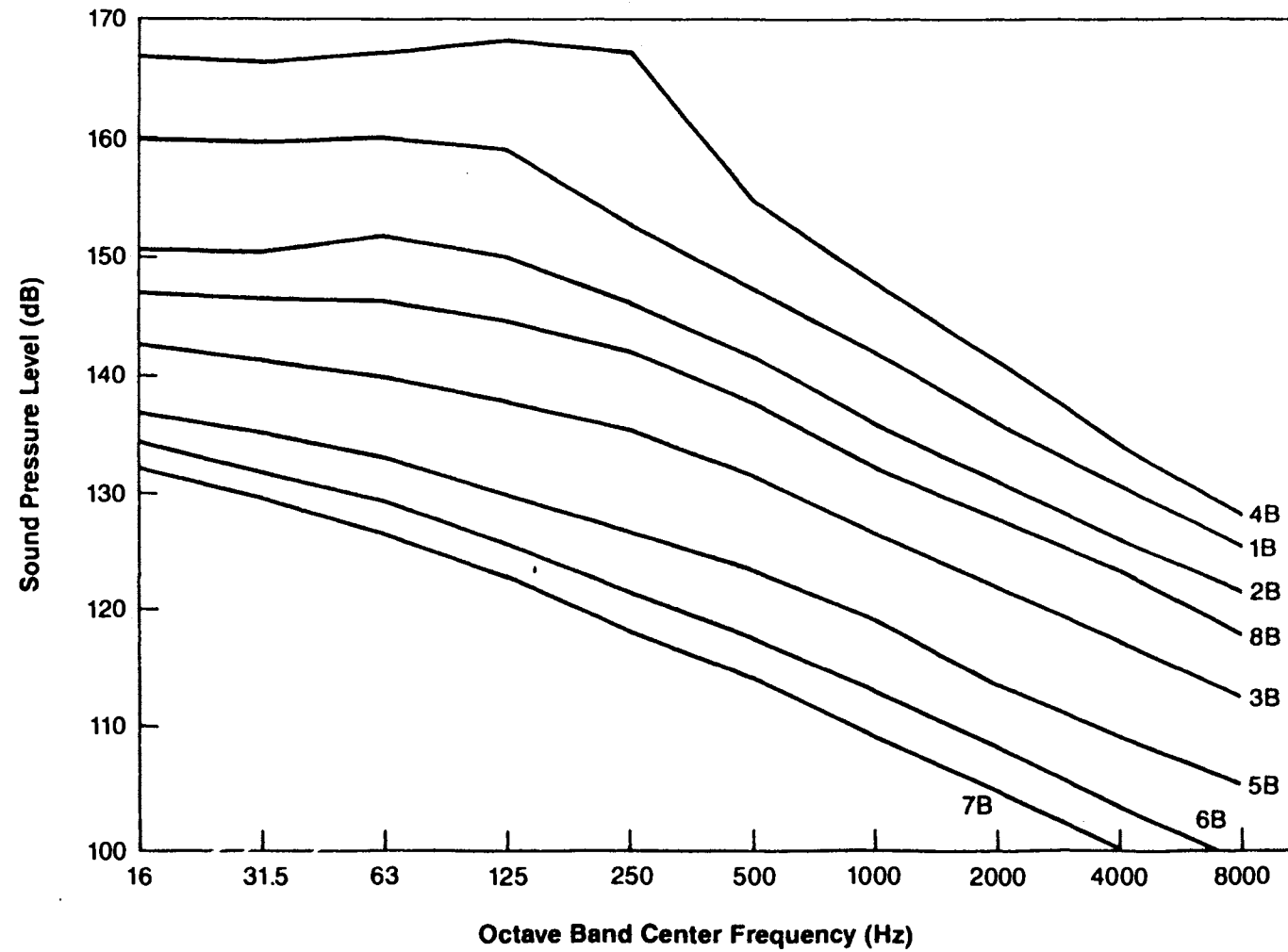


Figure 3-10. Sound Pressure Level on Lower Surface due to Scramjet Engine.

Table 3-7 and Figure 3-11 give the combined effect of the rocket engines and the scramjet engine on the sound pressure level. Figure 3-11 shows that the effect of the scramjet engine is to increase the sound pressure level at the lower frequency so that the spectrum is relatively flat.

3.3.3 Combined Sound Levels

Figures 3-12 and 3-13 show contours of overall sound pressure levels at the eight locations of interest on the vehicle upper and lower surfaces. These sound pressure levels are appropriate at takeoff when the vehicle is on the runway and both scramjet and rocket engines are operating. The overall sound pressure level was obtained by summing all of the acoustic pressure over the octave bands in question. In this analysis, the effects of the rocket thrusters and the scramjet exhaust were evaluated analytically, while the values of the inlet noise given in Figure 3-13 were estimated by assuming that the scramjet geometry allows the combustion and the internal noise to travel toward the inlet as well as toward the exhaust side. The effect of the scramjet inlet noise is presented only in Figure 3-13. The remainder of this section refers solely to the noise field due to rocket thrusters and the scramjet exhaust.

Figures 3-4 and 3-5 show the locations on the upper and lower surfaces where the sound level was evaluated. Figures 3-7 and 3-8 give the sound pressure level on the upper and lower surfaces due to the rocket engines as a function of the octave band center frequency. The sound pressure level peak at all locations is at the high frequency; this is consistent with the small dimensions of the rockets. As expected, the sound level is higher on the lower surface of the vehicle because of the reflection of sound from the ground. The large difference between the sound levels at location 8 on the lower and upper surfaces is due to the fact that the vertical tails hide point 8A from the sound source, while on the lower surface the sound which is reflected from the ground is much larger than the diffracted value. Section 3.3.1 details the analysis and the complete results for sound levels due to the rocket engines.

Table 3-7. Octave Band Sound Pressure Level (dB) on Vehicle Lower Surface due to Combined Sound Levels of Scramjet and Rocket Engines.

f (Hz)	L o c a t i o n							
	1B	2B	3B	4B	5B	6B	7B	8B
16	158.2	149.6	141.7	165.1	136.0	133.7	131.9	145.9
31.5	158.0	149.5	140.0	164.8	134.2	131.1	129.0	145.6
63	158.8	150.2	139.6	165.8	132.0	129.1	126.7	145.7
125	160.9	151.5	140.8	167.0	133.7	130.3	127.8	146.0
250	166.3	156.8	145.7	169.1	138.3	134.6	132.1	150.1
500	169.9	160.4	149.1	170.3	142.1	138.1	135.4	153.1
1000	171.3	162.6	150.9	173.3	144.2	139.9	136.0	154.7
2000	170.1	162.5	150.7	171.8	143.6	139.1	136.2	153.4
4000	168.6	162.4	150.4	176.1	143.6	138.8	135.8	154.1
8000	165.9	161.6	151.1	173.9	144.1	138.8	135.6	153.1
Overall	177.2	169.4	158.1	181.3	151.2	146.8	143.8	161.6

838PROP
3-T3-7.BB
11-11-89

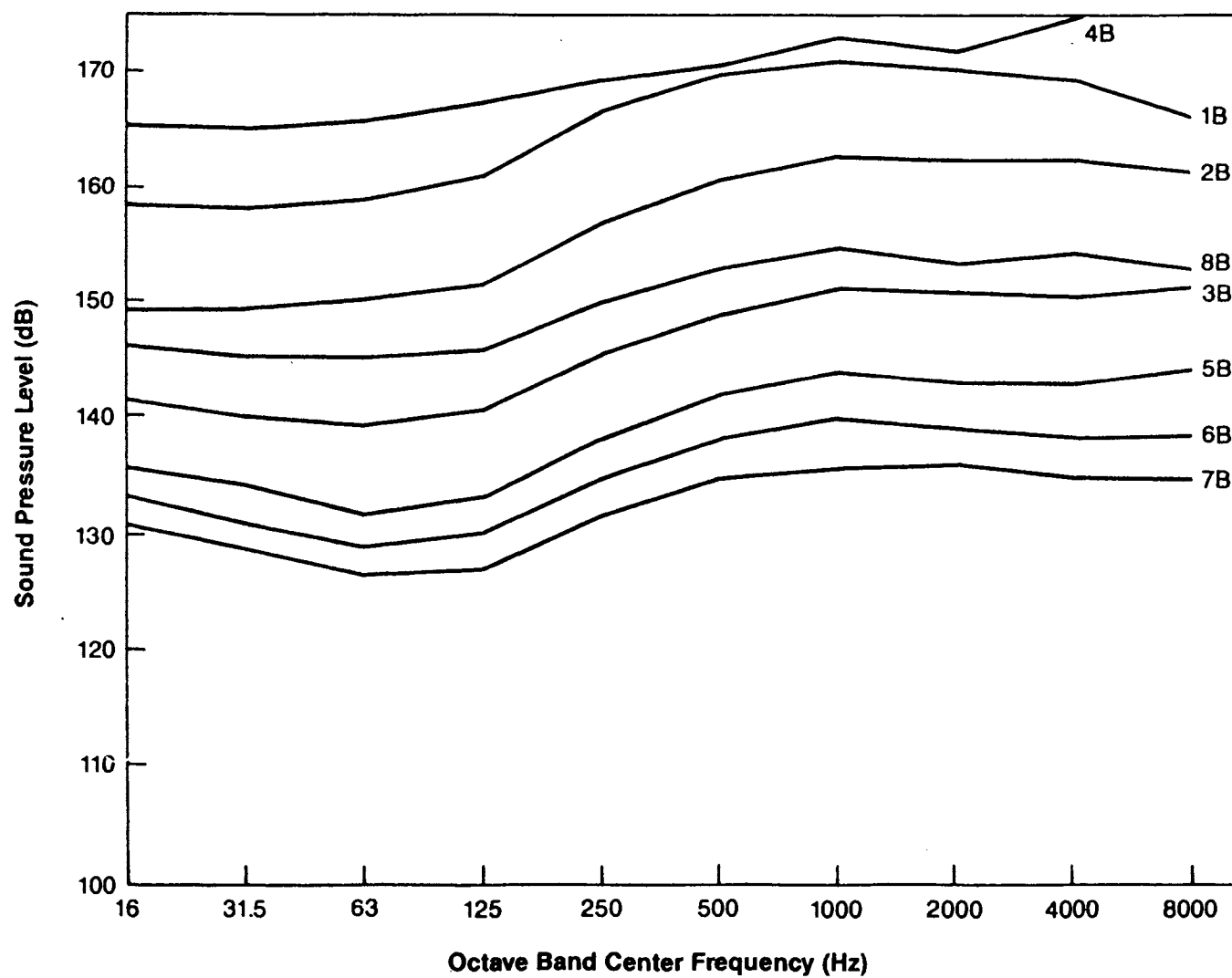


Figure 3-11. Sound Pressure Level on Lower Surface due to Combined Effect of Scramjet and Rocket Engines.

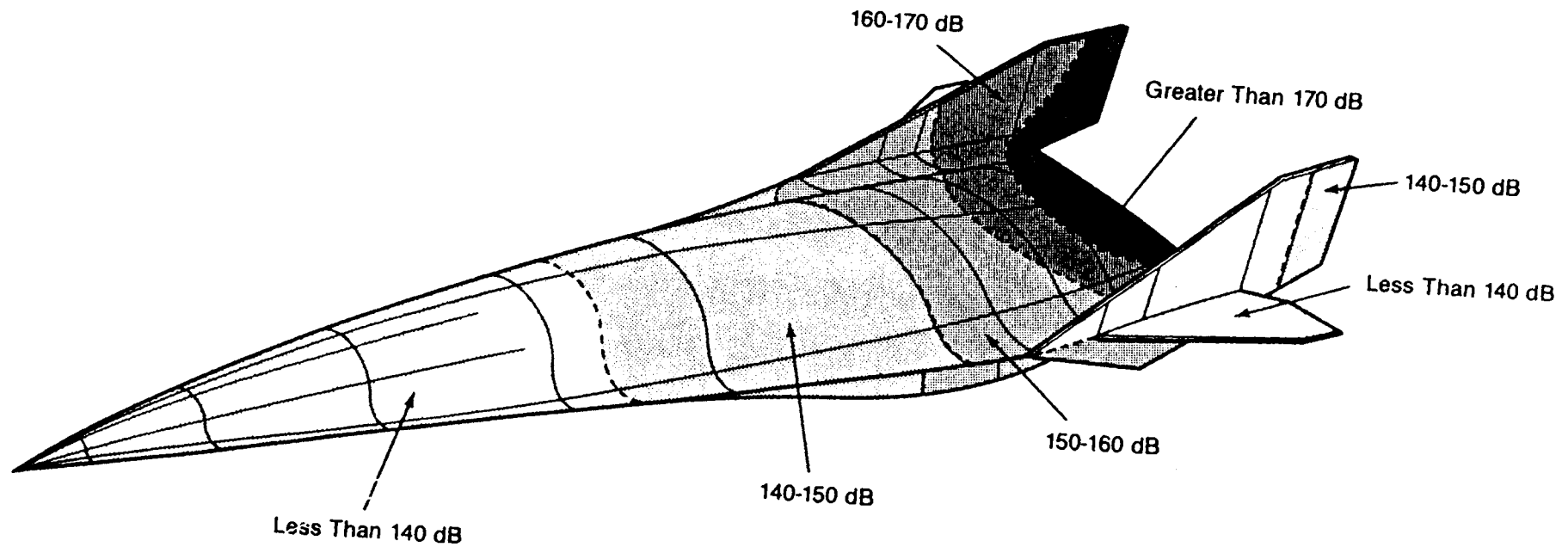


Figure 3-12. Overall Sound Pressure Levels (Ref. 20 μ PA) at Selected Locations on Upper Surface.

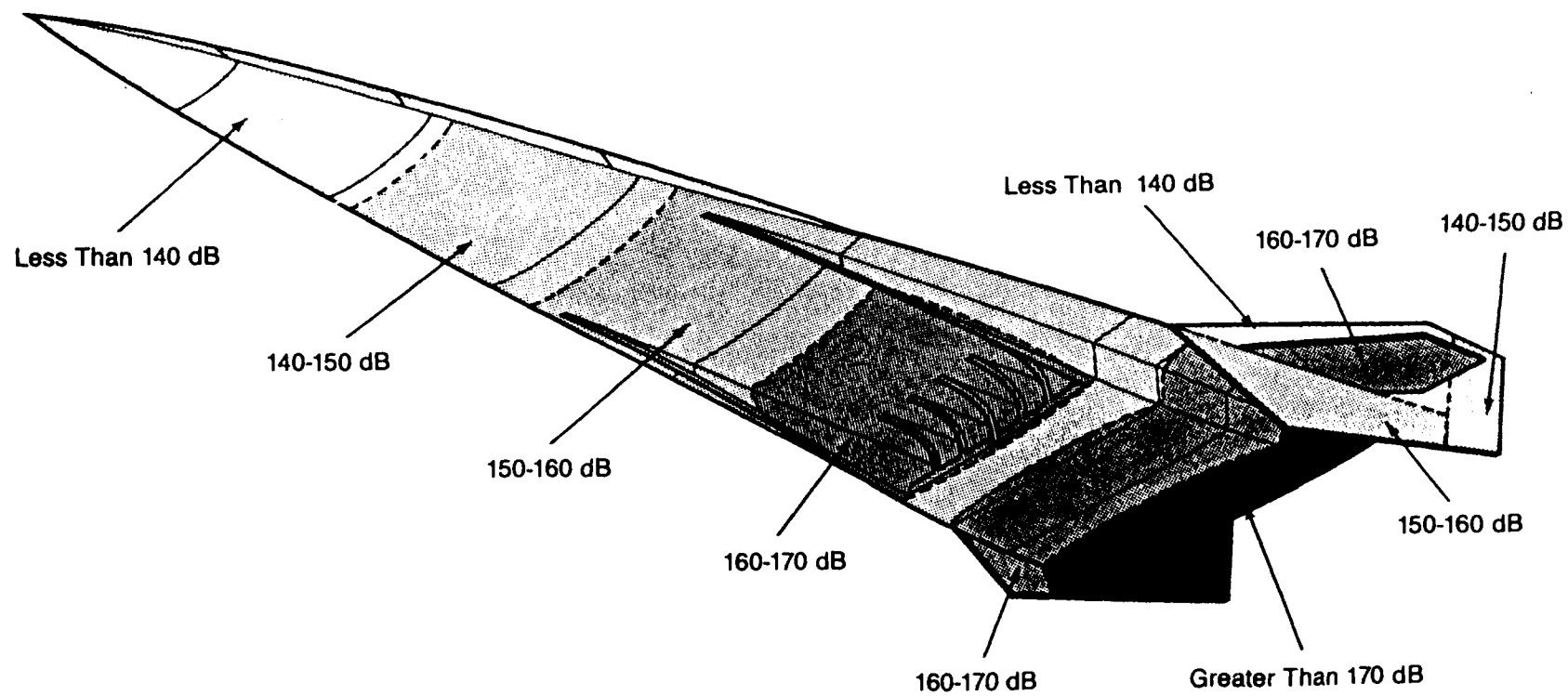


Figure 3-13. Overall Sound Pressure Levels (Ref. 20 μ PA) at Selected Locations on Lower Surface.

The analysis of sound levels due to the scramjet engine is presented in Section 3.3.2. Figure 3-10 shows the sound pressure level at the eight locations on the lower surface. The main difference between the scramjet sound level and the rocket engine sound level is the low-frequency content of the scramjet pressure spectrum, which is due to the large size of the scramjet exhaust system. Combining the sound level of the rocket engines with that of the scramjet engine gives the sound pressure level during takeoff conditions when both systems are operating. Figure 3-11 shows the sound pressure level due to the combined effect of scramjet and rocket engines at the eight locations. It is interesting to note the relative flatness of the spectrum; only about 10 dB separate the magnitudes of the sound pressure level in the frequency range of 16 to 8000 Hz.

3.4 RESULTS AND CONCLUSIONS

High acoustic loads are imposed on the Blended Wing Body transatmospheric vehicle by both scramjet and rocket engines. These loads have been predicted using methods developed by NASA. The conclusions from this study are as follows:

- (1) The relationships developed by Eldred, NASA, and Von Gierke (References [3-1, 3-2, 3-3]) for sound radiated by rocket engines agree to within 7 dB at a thrust of 1.8×10^6 N (40,000 lb) and to within 1 dB at a thrust of 450×10^3 N (100,000 lb).
- (2) The highest sound levels generated by the transatmospheric vehicle occur on the ground when both rocket and scramjet engines are operating.
- (3) The maximum sound engine levels on the vehicle lie between 170 and 180 dB overall. The sound levels are highest adjacent to the rocket engine exhausts and the inlet and exhaust of the scramjet engines. The lower surface of the vehicle receives

higher sound levels than the upper surface owing to reflection from the runway.

- (4) The present analysis does not include aerodynamic pressure fluctuations associated with turbulence and boundary layer development (Section 2); only direct sound from engines is considered. Aerodynamic turbulence will further raise the pressure on the surface. As the speed of the hypersonic vehicle increases beyond the subsonic range, the presence of shock waves will restrict the forward travel of sound, with the rocket and scramjet noise being felt in a corresponding smaller region.

3.5 REFERENCES

- 3-1 Potter, R.C., and M.J. Crocker, Acoustic Prediction Methods for Rocket Engines, Including the Effect of Clustered Engines and Deflected Exhaust Flow, NASA CR-566, October 1966.
- 3-2 Von Gierke, H.E., "Aircraft Noise Sources," Chapter 33 in Handbook of Noise Control, C.M. Harris (Ed.), McGraw Hill, 1957.
- 3-3 Acoustic Loads Generated by the Propulsion System, NASA SP-8072, June 1971.
- 3-4 Pierce, Allan D., Acoustics - An Introduction to Its Physical Principles and Applications, McGraw Hill, 1981.

838PROP
3-3.BB
11-11-89

SECTION 4

ANALYSIS OF FOREBODY PANEL

4.1 INTRODUCTION

The forebody panels located in the forward underbody region of a generic Blended Wing Body (BWB) were analyzed for response to the thermoacoustic and engine induced sound environments.

The forebody is defined as the portion of the vehicle aft of the nose and ending at the beginning of the midbody (Figure 1-3). Upper and lower forebody structural concepts are identical, consisting of integrally stiffened carbon-carbon skins attached to underlying carbon-carbon ring frames and longerons. Carbon-carbon was chosen for this application because of thermal and weight considerations. The structural temperatures in this area of the fuselage are above 1800°F (the upper use temperature for advanced titanium matrix composites), but below 3000°F (the upper use temperature for carbon-carbon). In addition, trade studies have shown that structural carbon-carbon is more weight efficient than actively cooled structure for areas where carbon-carbon use temperature is not exceeded.

The detailed dimensions of the lower forebody panel are shown in Figure 4-1. This panel is located 20 feet from the nose on the lower surface. The stiffener height and width are 2.0 inches and 0.115 inch, respectively. The skin thickness is 0.115 inch (minimum gage is approximately 0.065 inch). The stiffener spacing is 6 inches. The stiffeners consist of uniaxial blades that tie into thickened skin to minimize

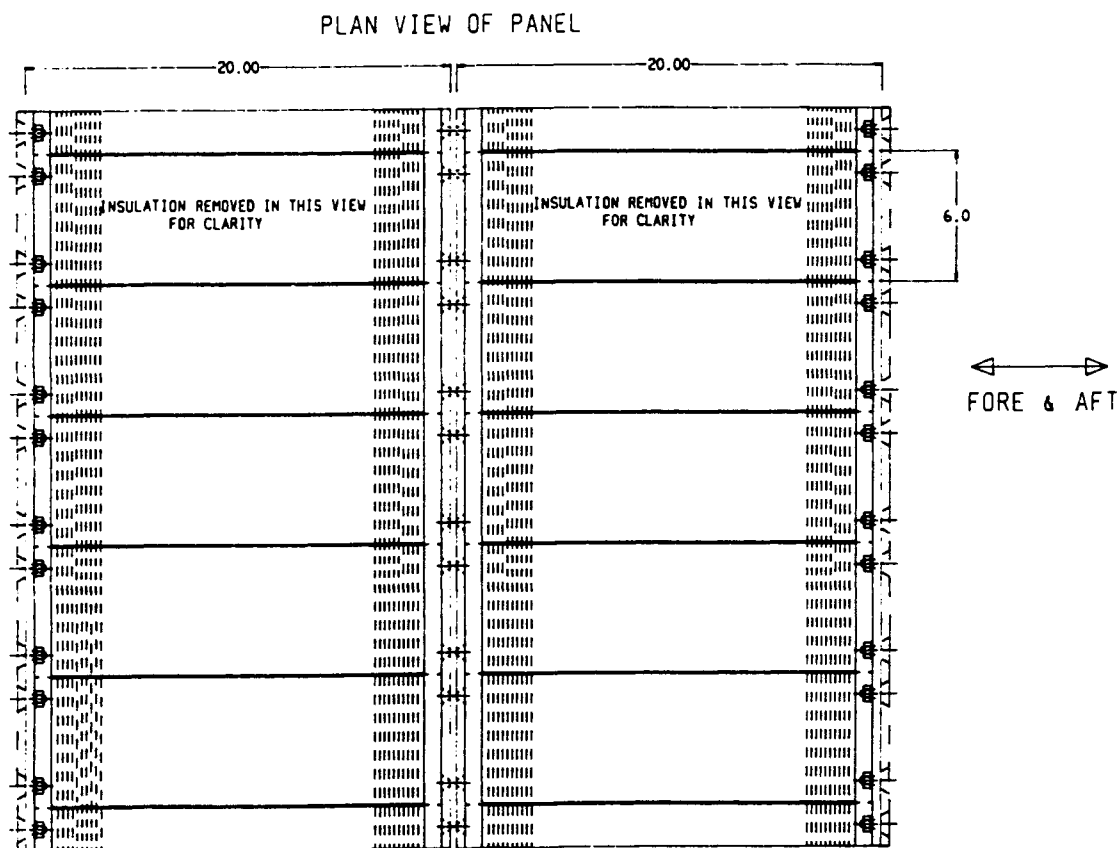
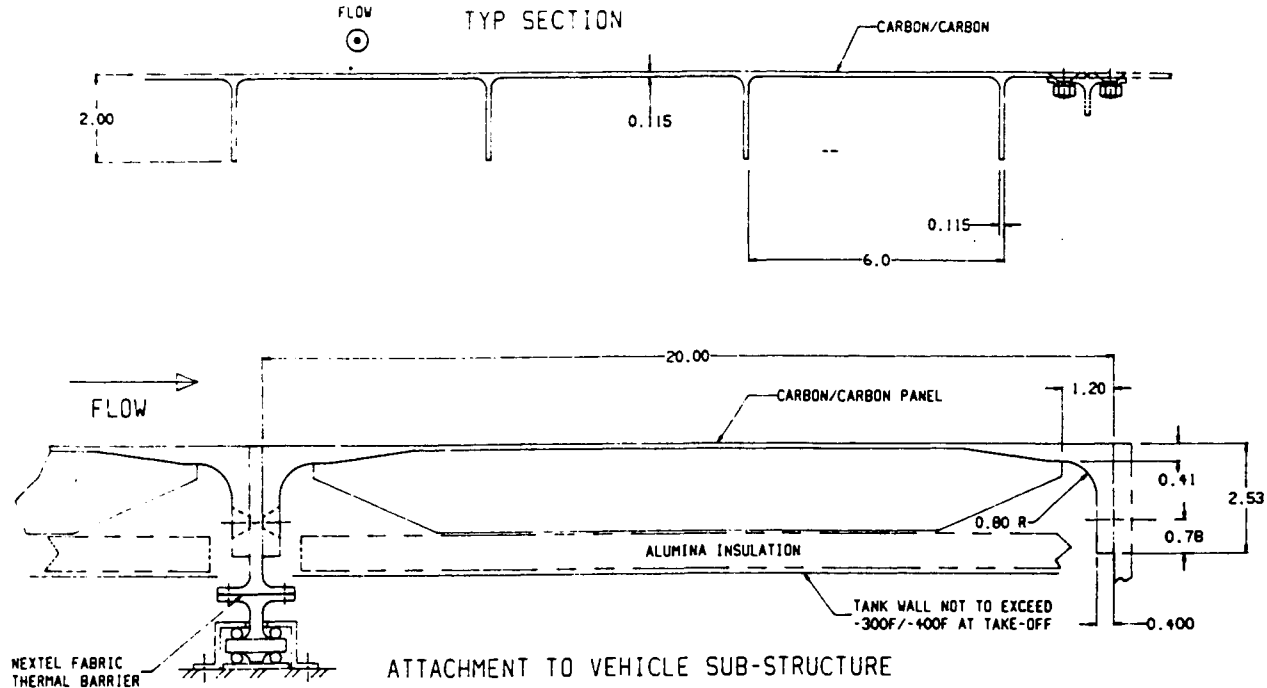


Figure 4-1. Lower Forebody Panel Located 20 Feet Aft of Nose on Underside of Vehicle.

rotation. The blade type stiffener is chosen over "T," "L," and hat stiffeners because it contains no re-entrant corners. Fabrication and coating of re-entrant corners or biaxially stiffened carbon-carbon panels are not within current carbon-carbon capability, although development efforts are under way. There is a 1-inch-thick layer of alumina insulation between the panel and the cryogenic tank structure. The panel side rails are picked up by attachments that allow relative thermal displacement between the tank and the panel.

The forebody panel analysis was made with the finite element method using a common geometry. The steps in the analysis are as follows:

- (1) Thermal analysis using P/THERMAL (Reference [4-1]).
- (2) Static stress and stability analysis using MSC/NASTRAN (Reference [4-2]).
- (3) Dynamic analysis using MSC/NASTRAN (Reference [4-2]).

The thermal aeroacoustic loading is developed in Section 2. The engine acoustic loads are developed in Section 3.

4.2 THERMAL ANALYSIS

For a hypersonic flight vehicle, detailed thermal analyses were performed to determine the temperature profiles of a forebody panel. The heat flux profiles were derived from the generic trajectories listed in Tables 4-1 and 4-2 and the SAIC turbulent heating rates compiled in Appendix A. Panel temperatures during ascent for 1000- and 2600-psf free stream dynamic pressures were calculated based on the heating profiles depicted in Figure 4-2. The initial temperature was assumed to be 70°F.

The forebody panel is made of carbon-carbon with the thermal properties summarized in Table 4-3. The thermal boundary conditions for the panel are illustrated in Figure 4-3. The outer skin is subject to aerodynamic heating and radiates to the atmosphere. Heat will conduct

Table 4-1. 1000-psf Ascent Trajectory (a)

Altitude (10 ³ ft)	Density (lb/ft ³)	Sound Speed (ft/sec)	Mach Number	Velocity (ft/sec)	q (psf)	Accl. (g)	Distance (10 ⁶ ft)	Time (sec)
0	7.6×10^{-2}	1116	0	0	0	0.93	0	0
59.0	7.25×10^{-3}	968	3	2,914	1000	0.93	0.141	97
71.0	4.48×10^{-3}	971	4	3,899	1000	0.93	0.252	130
80.5	2.75×10^{-3}	978	5	4,906	1000	0.93	0.399	163
88.4	1.86×10^{-3}	983	6	5,919	1000	0.93	0.582	197
95.1	1.35×10^{-3}	987	7	6,936	1000	0.93	0.799	231
110.9	6.65×10^{-4}	1003	10	10,075	1000	0.93	1.69	335
129.9	2.63×10^{-4}	1038	15	15,617	1000	0.93	4.06	520
144.1	1.37×10^{-4}	1064	20	21,310	1000	0.93	7.55	710
155.7	9.04×10^{-5}	1081	25	27,108	1000	0.93	12.22	903
							(2,314 miles)	(15.0 minutes)

(a) Based on constant q_{∞} and acceleration and published flight profiles.

$\Delta T = \Delta V/A$. Time to ascent = 15 minutes.

838PROP/3-T4-1.BB
11-11-89

Table 4-2. 2600-psf Ascent Trajectory (a)

Altitude (10 ³ ft)	Density (lb/ft ³)	Sound Speed (ft/sec)	Mach Number	Velocity (ft/sec)	q (p _s [∞])	Accl. (g)	Distance (10 ⁶ ft)	Time (sec)
0	0.07647	1116	0	0	0	0.93	0	0
39.0	0.01984	968	3	2,904	2600	0.93	0.141	97
51.0	0.01117	968	4	3,872	2600	0.93	0.251	129
60.0	0.007259	968	5	4,840	2600	0.93	0.391	161
68.0	0.00497	969	6	5,814	2600	0.93	0.564	193
75.0	0.00351	974	7	6,818	2600	0.93	0.776	226
90.0	0.00171	984	10	9,840	2600	0.93	1.616	327
107.0	0.000773	997	15	14,955	2600	0.93	3.733	498
120.0	0.0004151	1021	20	20,420	2600	0.93	6.955	680
132.0	0.000243	1044	25	26,100	2600	0.93	9.140	870
							(1,731 miles)	(14.5 minutes)

(a) Based on constant q_{∞} and acceleration and published flight profiles.

$\Delta T = \Delta V/A$. Time to ascent = 14.5 minutes.

838PROP/3-T4-2.BB
11-11-89

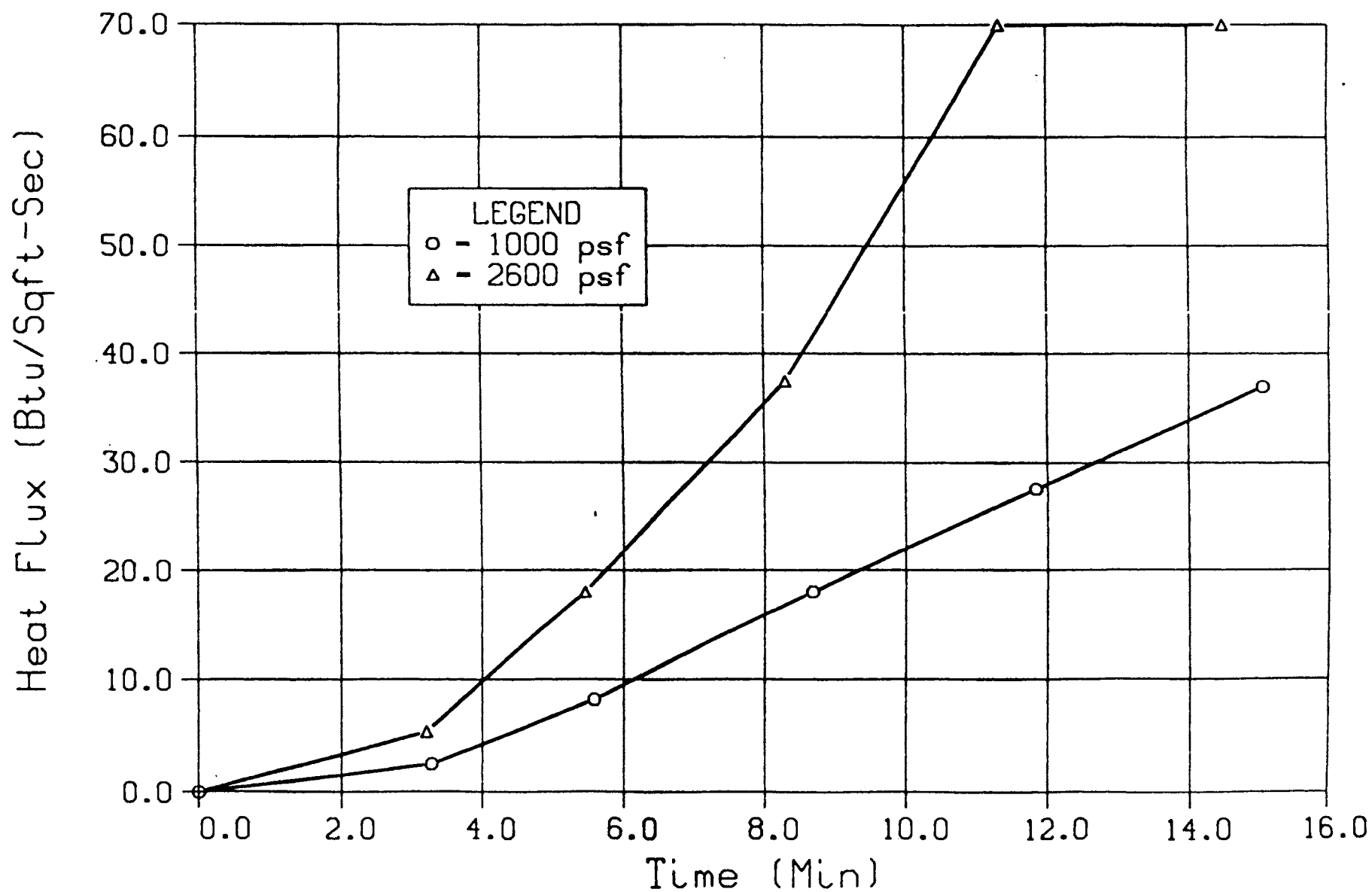


Figure 4-2. Forebody Panel Turbulent Heat Flux Profiles During Ascent.

Table 4-3. Thermal Properties of Carbon-Carbon (a)

T (°F)	Warp Thermal Conductivity ($\frac{\text{Btu}}{\text{in.-sec.-}^\circ\text{F}}$)
0	4.05×10^{-4}
200	4.83×10^{-4}
500	5.46×10^{-4}
750	5.60×10^{-4}
1000	5.60×10^{-4}
1250	5.54×10^{-4}
1500	5.40×10^{-4}
1750	5.35×10^{-4}
2000	5.21×10^{-4}
2250	5.08×10^{-4}
2500	4.96×10^{-4}
2750	4.83×10^{-4}
3000	4.69×10^{-4}

T (°F)	Specific Heat ($\frac{\text{Btu}}{\text{lb-}^\circ\text{F}}$)
0	0.17
500	0.242
1000	0.295
1500	0.33
2000	0.36
2500	0.39
3000	0.42

(a) Density = 0.065 lb/in.³; emissivity = 0.8.

838PROP
3-T4-3.8B
11-11-89

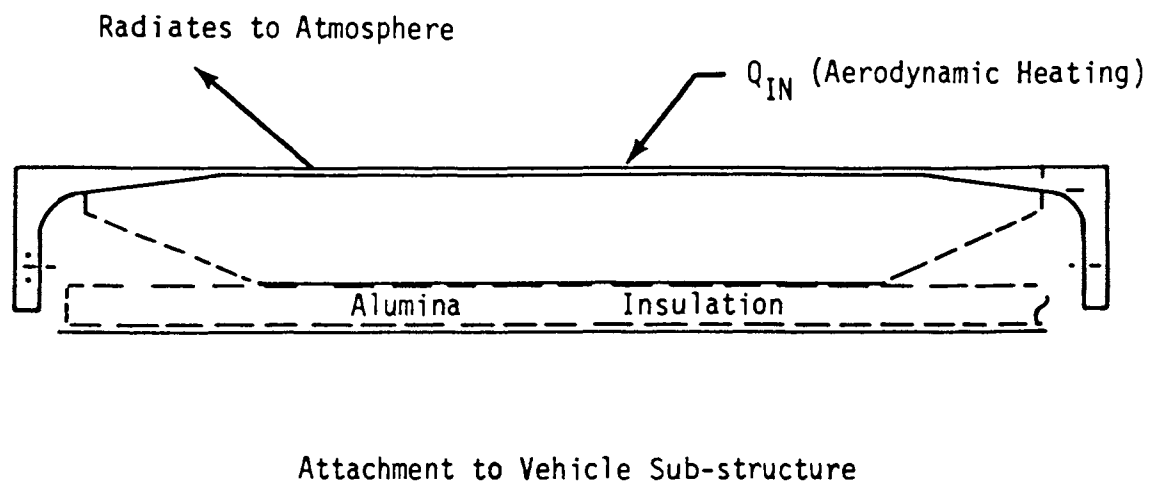


Figure 4-3. Thermal Boundary Conditions for Carbon-Carbon Panels.

through the skin and the stiffener and along the edge of the fastener area on the panel. Alumina insulation will be applied between the panel and the vehicle substructure.

Transient thermal analysis was conducted using P/THERMAL. P/THERMAL is a finite element thermal analysis code developed by PDA Engineering. It uses PATRAN for pre- and post-processing. The data transfer between thermal and structural models can be easily accomplished through PATRAN neutral files.

Before constructing the model for a full-size panel, the temperature gradient through the skin thickness was first checked out with a finite element P/THERMAL model of the cross-thickness cut of the panel. The temperature gradient was found to be negligible, and 2D QUAD elements were therefore used for the full-size panel thermal analysis. The P/THERMAL finite element model of the forebody panel is shown in Figure 4-4.

The panel temperature distributions at the end of ascent are given in Figures 4-5 and 4-6. With the current technology, the upper use temperature for carbon-carbon is 3000°F. The coating starts to deteriorate when it gets hotter than this temperature limit. For the 1000-psf case, the calculated peak temperature was 2670°F for the forebody. However, for the 2600-psf condition, the maximum temperature would exceed 3000°F based on the conservative assumption of turbulent heating throughout the entire ascent phase.

The panel maximum temperatures occurring on the skin and the minimum temperatures taking place over the tip of the fastener area are summarized in Figures 4-7 and 4-8. The temperature difference on a forebody panel could be as large as 1200°F or 1400°F, depending on the aerodynamic pressure of 1000 or 2600 psf.

The effect of laminar versus turbulent heating on the panel temperature prediction was also investigated. From SAIC's laminar heat transfer results for an axisymmetric body, assuming that re-laminarization is

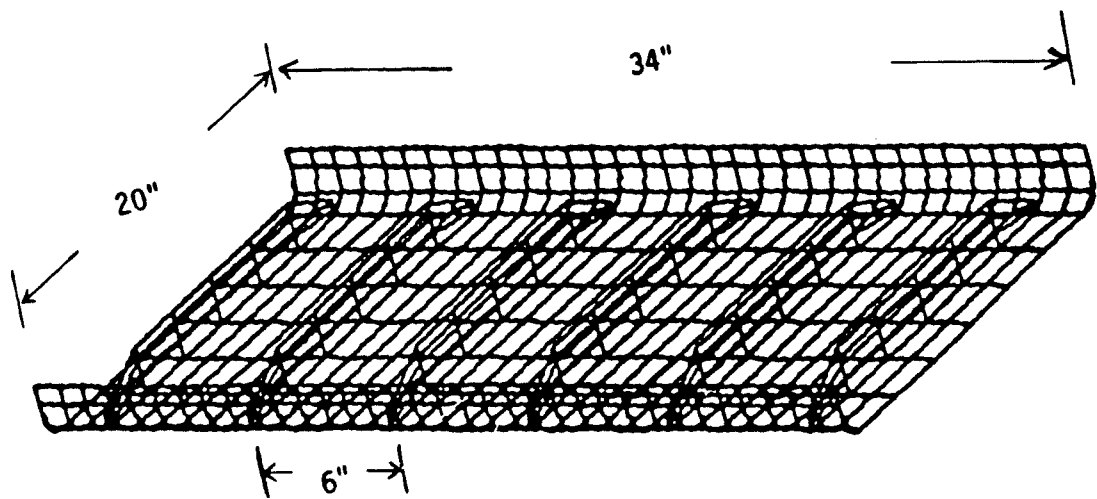


Figure 4-4. P/THERMAL Model of Forebody Panel.

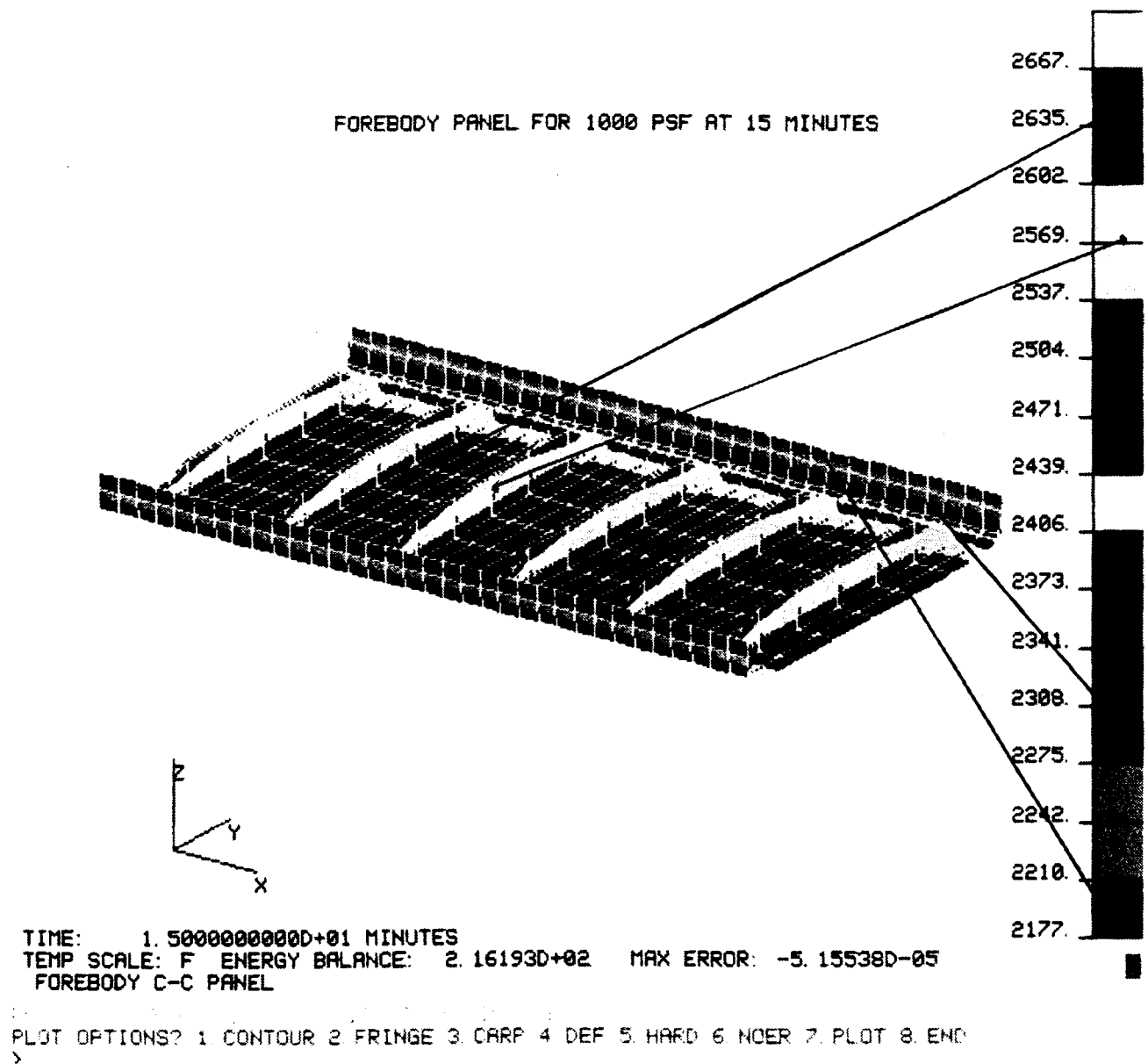


Figure 4-5. Forebody Panel Temperature Distribution for 1000 psf at 15 Minutes.

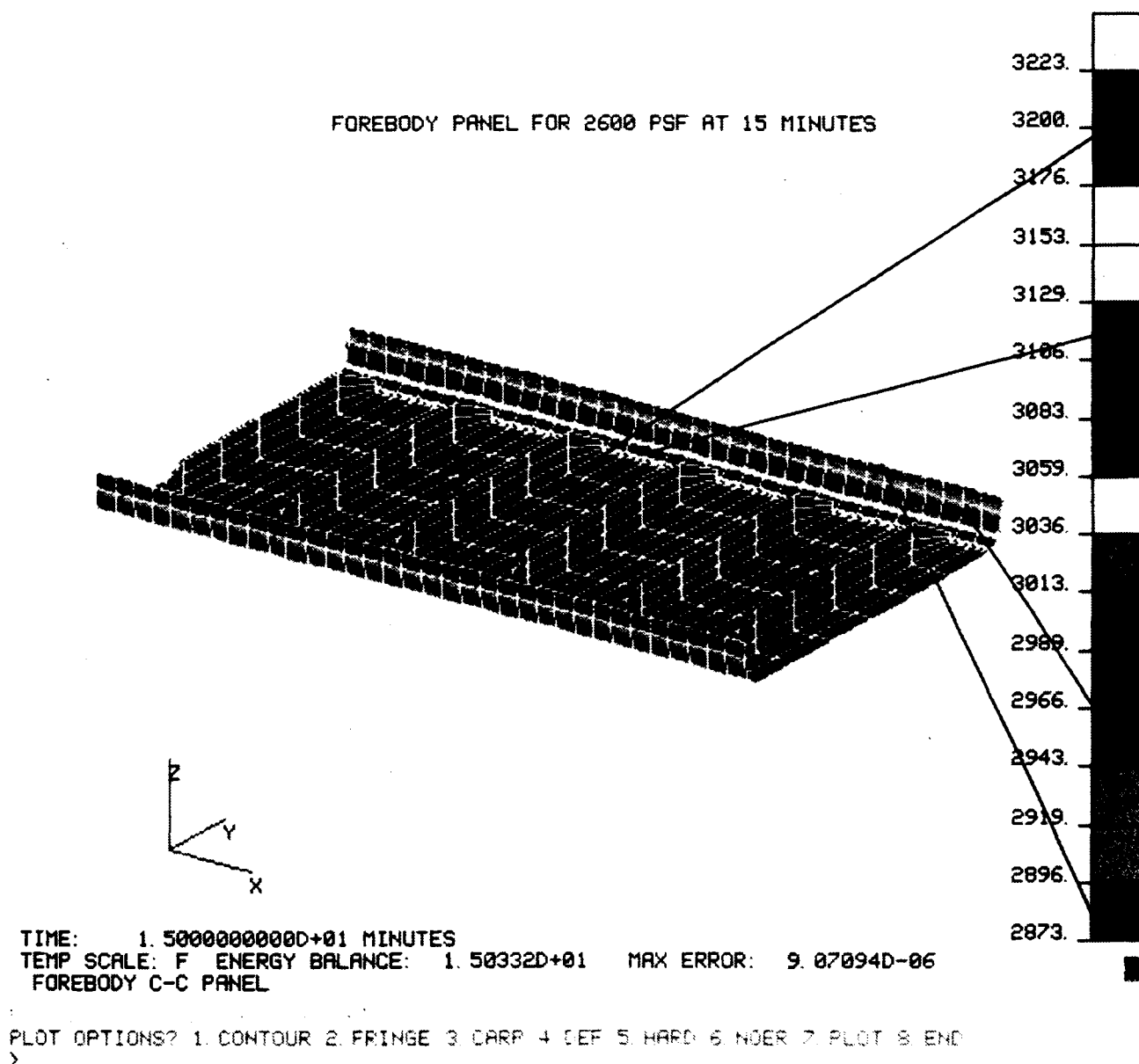


Figure 4-6. Forebody Panel Temperature Distribution for 2600 psf at 15 Minutes.

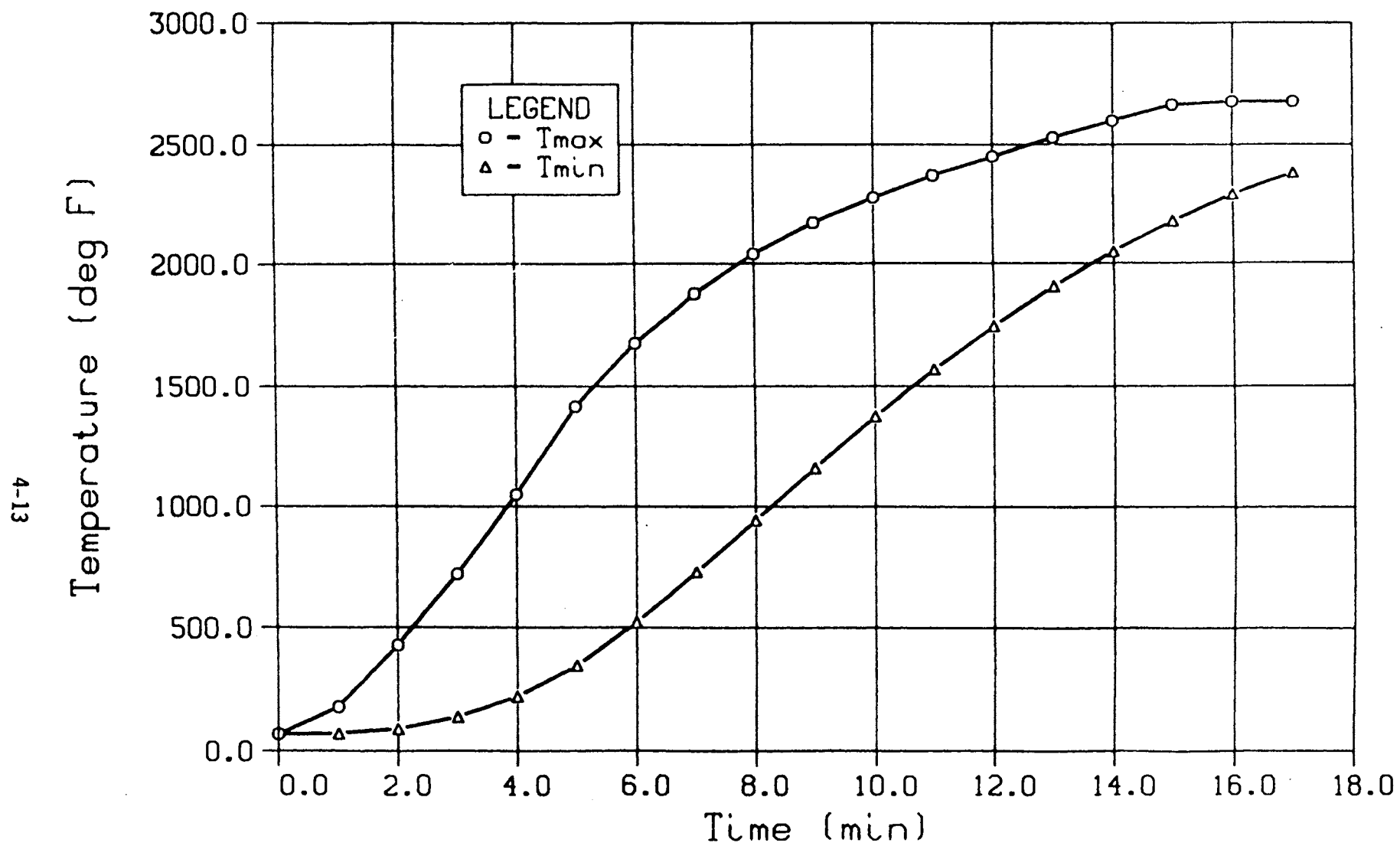


Figure 4-7. Forebody Panel Temperature Distribution for 1000 psf During Ascent.

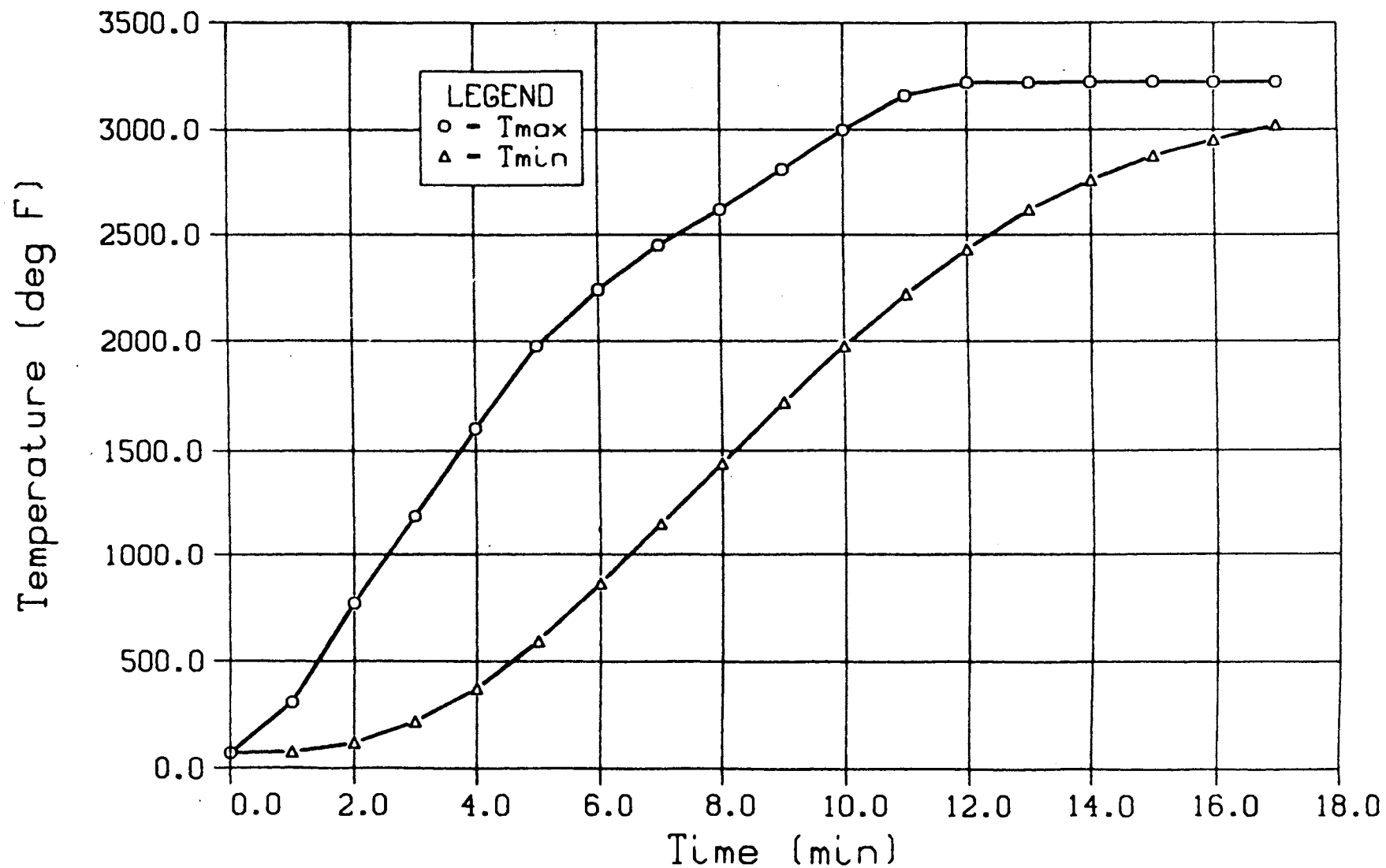


Figure 4-8. Forebody Panel Temperature Distribution for 2600 psf During Ascent.

established at Mach 10, the heat flux profiles during ascent for 1000-psf aerodynamic pressure are presented in Figure 4-9. The panel temperature distribution at 15 minutes after takeoff is depicted in Figure 4-10. The forebody panel estimated peak temperature was 1500°F, which is about 1200°F lower than the results based on turbulent heating throughout the ascent phase. The maximum and minimum temperatures on the panel during ascent are summarized in Figure 4-11. The re-laminarization results in the dip in panel skin temperatures.

The sensitivity of maximum panel temperature to peak heating rate is indicated in Figure 4-12. The impact of major difference between turbulent and laminar heating rates on the panel skin temperature is significant. The approach of assuming turbulent heating is conservative and represents the upper limit of the estimated panel temperature.

4.3 STATIC STRESS ANALYSIS

4.3.1 Properties and Finite Element Model

An analysis was undertaken to evaluate the adequacy of the forebody panel design with respect to static loads. Static loads are both thermal and mechanical in nature.

Thermal loads arise from two sources. First, they are imposed by the constraints acting on the panels which prevent free thermal expansion. These constraints are provided by adjacent panels as well as by the panel attachment to the vehicle substructure. Second, thermal loads are caused by differential heating and cooling within the panels and within the vehicle as a whole. The resulting temperature gradients induce thermal stresses in the panel structure. Mechanical static (or quasi-static) loads result from vehicle maneuvers. Such loads are in the form of aerodynamic pressure and inertia forces. This section describes the analytical techniques and the results obtained from the static analysis.

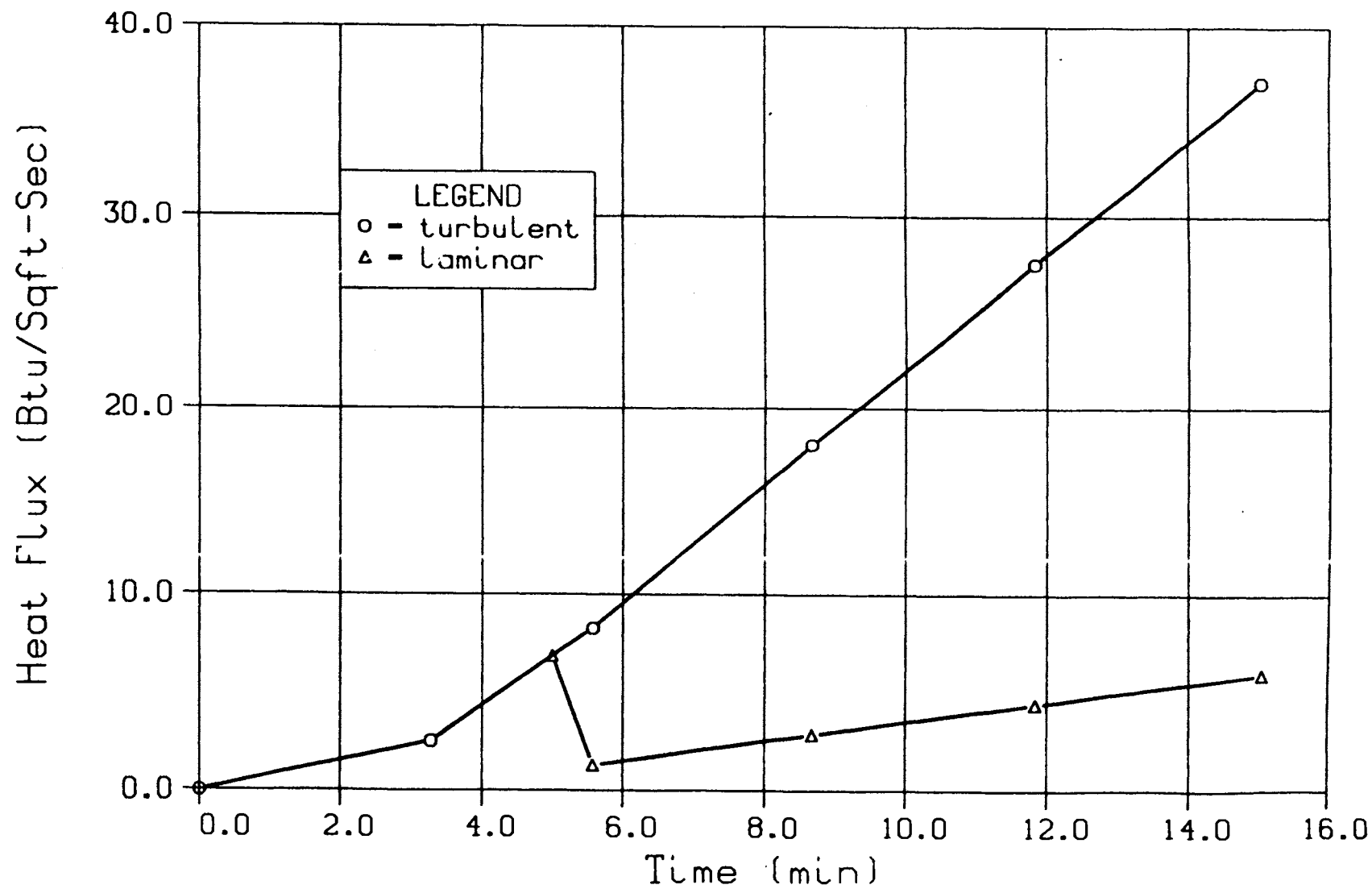


Figure 4-9. Forebody Panel Heat Flux Profiles for 1000 psf During Ascent.

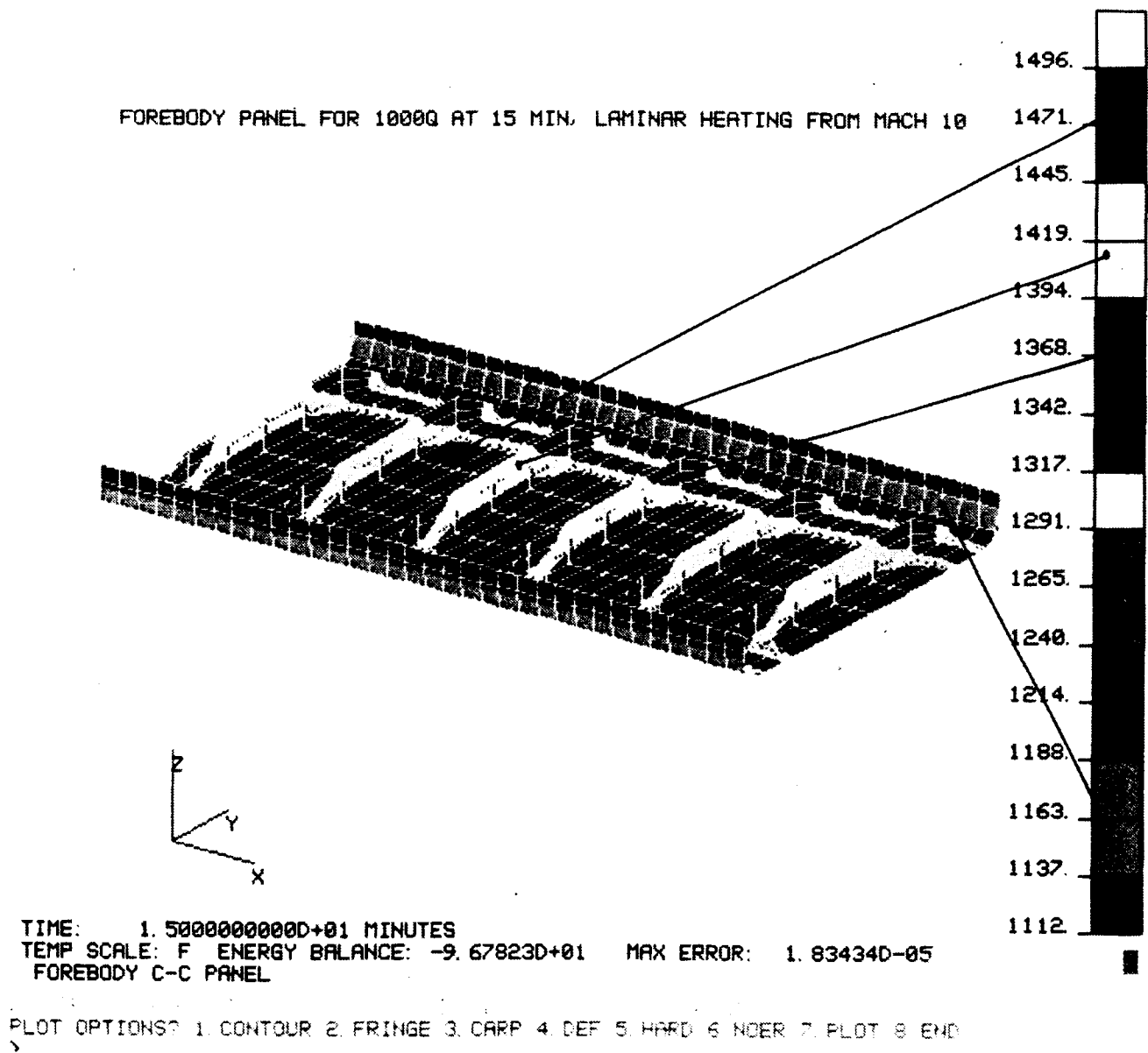


Figure 4-10. Forebody Panel Temperature Distribution for 1000 psf at 15 Minutes, Laminar Heating from Mach 10.

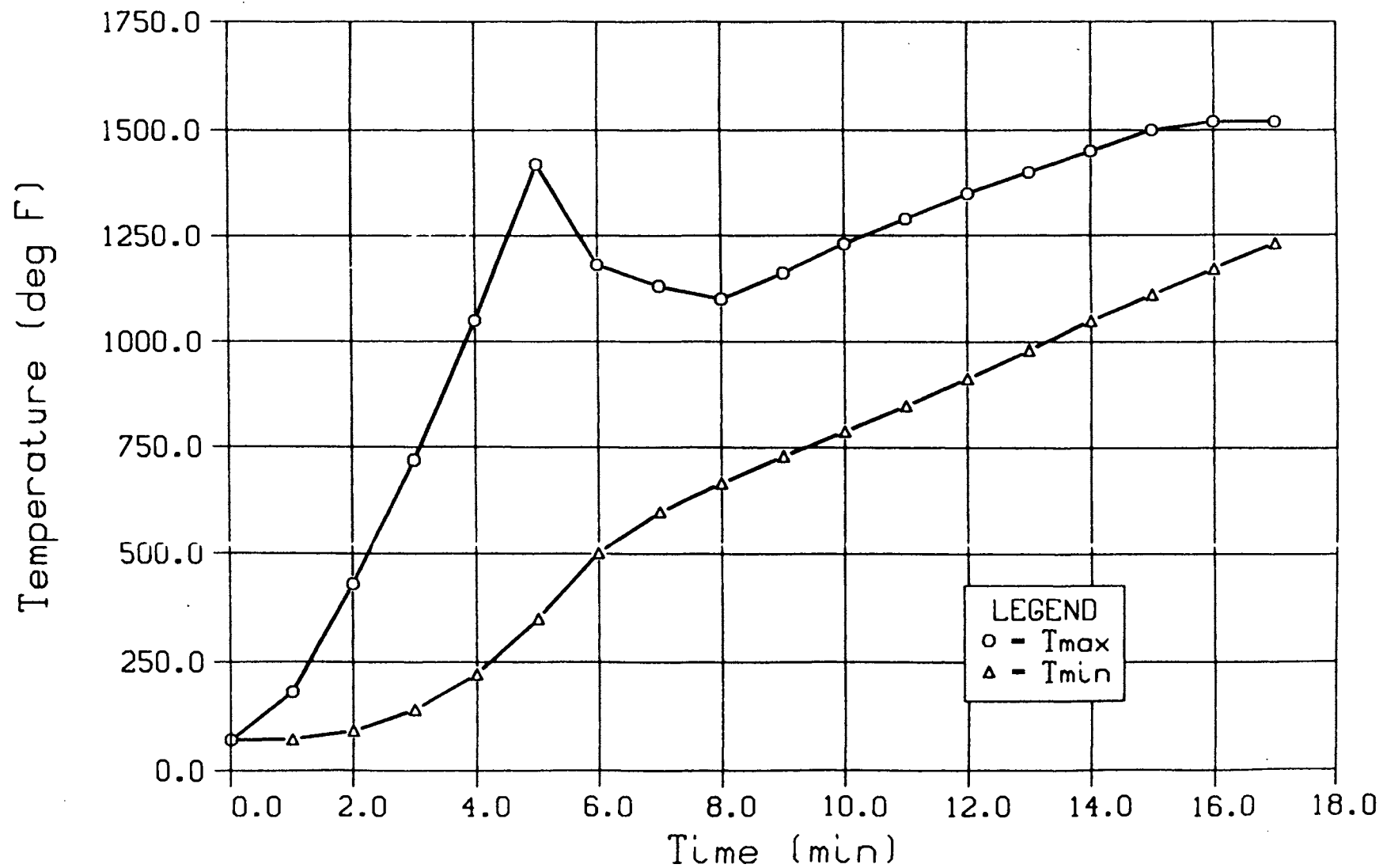


Figure 4-11. Forebody Panel Temperature Distribution for 1000 psf During Ascent, Laminar Heating from Mach 10.

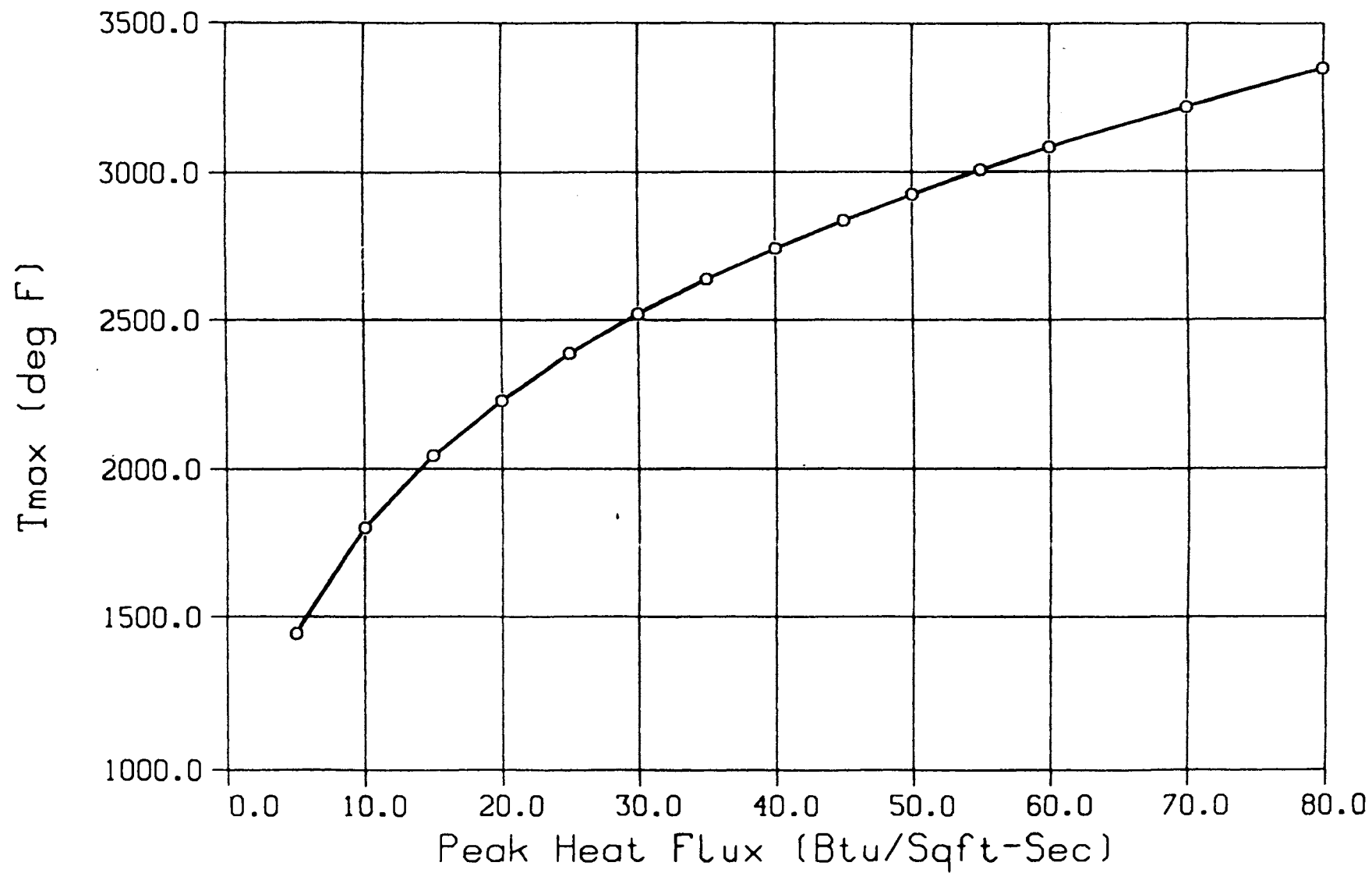


Figure 4-12. Maximum Panel Temperature versus Peak Heat Flux.

The panel structures were analyzed by means of the NASTRAN general-purpose finite element computer code. The finite element models were constructed using the PATRAN interactive graphics code. The use of PATRAN not only simplified model construction but also greatly enhanced data post-processing.

A plot of the forebody panel finite element model is shown in Figure 4-13. The model was representative of a typical forebody panel with dimensions of 34 inches by 20 inches. The panel had six 2.00-inch blade stiffeners at a pitch of 6.0 inches.

The model was subdivided into four regions, each with a different laminate layup configuration. These four regions, indicated in Figure 4-13, consisted of the blade stiffeners, the skin, the flanges, and the skin-flange transition. Laminate configurations for each region were selected to be consistent with laminate thicknesses prescribed on the engineering drawings. All the laminates were composed primarily of internal $0^{\circ}/90^{\circ}$ plies of carbon-carbon fabric, sandwiched between two outer plies of fabric oriented at 45° . The 45° fabric plies were included to increase buckling allowables. Laminate configurations for the forebody panel are given in Table 4-4. General laminate construction is illustrated in Figure 4-14.

The model was constructed exclusively using NASTRAN CQUAD4 quadrilateral flat shell elements. The elements were endowed with orthotropic membrane, bending, and transverse shear material properties which were assigned by means of PSHELL and MAT2 NASTRAN bulk data input. Laminate stiffnesses were calculated using basic lamination theory and Rohr-generated (unpublished) test data for carbon-carbon fabric laminates.

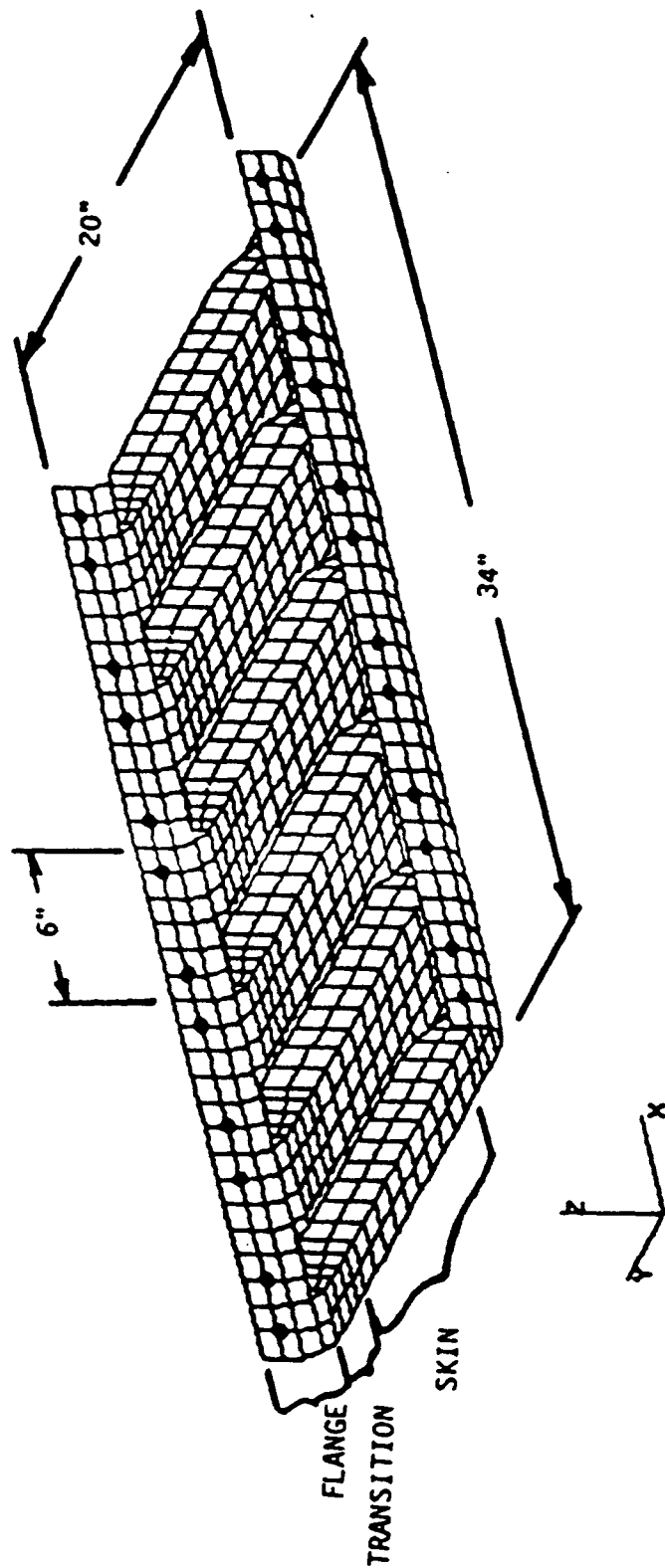


Figure 4-13. Forebody Panel NASTRAN Model.

Table 4-4. Laminate Layup Configurations for Forebody Panel.

Region	Layup
Flange	$(45^\circ, 0_{26}^\circ, 45^\circ)$
Skin/Flange Transition	$(45^\circ, 0_{16}^\circ, 45^\circ)$
Skin	$(45^\circ, 0_6^\circ, 45^\circ)$
Stiffeners	$(45^\circ, 0_6^\circ, 45^\circ)$

838PROP
3-T4-4.BB
12-11-89

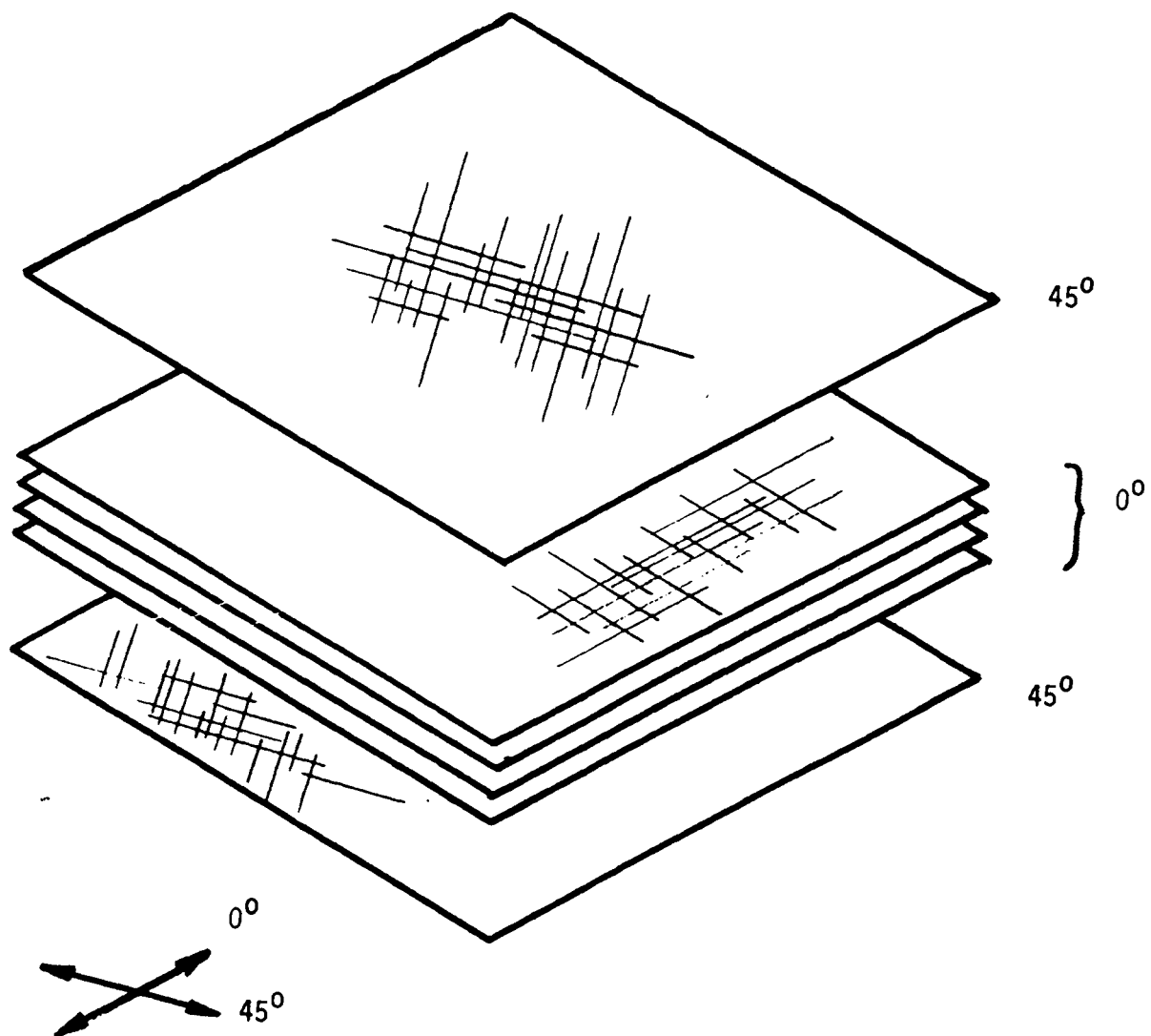


Figure 4-14. Panel Laminate Construction.

4.3.2 Panel Loads and Constraints

The panel loads and constraints which were applied in the analysis are illustrated in Figure 4-15. The two forebody panel flanges are attached to the vehicle substructure by 12 pairs of fasteners. The locations of the fasteners are indicated in Figure 4-15. One flange is attached to a relatively rigid element of the vehicle substructure. It therefore follows that fasteners at these locations restrict the vertical translations (i.e., in the z-direction) and rotations of the panel.

The other flange is connected to an adjacent panel. It is also attached to the substructure by an arrangement which eliminates vertical translations but leaves other degrees of freedom unhindered. If it is assumed, however, that the adjacent panel carries an identical load, then a condition of symmetry would exist at the adjacent flanges. (This is not an unreasonable assumption given the proximity of the panels.) In this case, rotational degrees of freedom are eliminated along these flanges.

For the above reasons, vertical displacements and rotational degrees of freedom were contained at the fastener locations on both flanges. It was also assumed that a symmetry condition exists along the 20-inch edges of the panel. Consequently, rotations about those edges were eliminated so as to enforce a zero-slope condition. The constraint conditions are summarized in Figure 4-15. The numbers in the figure are the NASTRAN codes corresponding to the constrained degrees of freedom. The degrees of freedom are defined on the coordinate axes in the figure.

Normal loads (N_y) and shear loads (N_{yx}) on the forebody panel flanges were distributed equally among all the fasteners. The loads were applied to the corresponding finite element nodes by means of NASTRAN FORCE bulk data input.

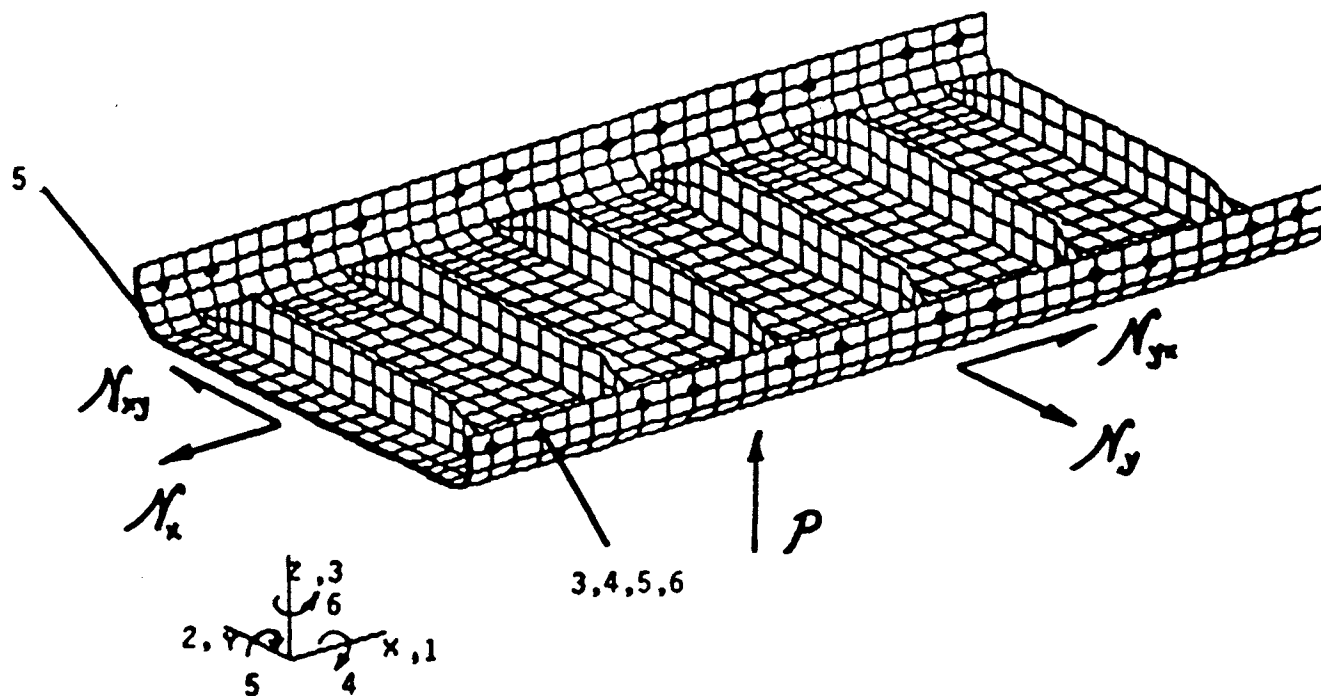


Figure 4-15. Forebody Panel Loads and Constraints.

Normal loads (N_x) were distributed at nodes along the 20-inch edges in such a way as to produce uniform axial strain. Shear loads (N_{xy}) were applied at these nodes so as to yield a uniform load distribution. Nodal forces were therefore determined taking into account variations in material stiffness and thickness along the edge and element dimensions. Again, these forces were applied to the model by means of FORCE bulk data input.

Aerodynamic pressure loads were imposed on the skin and skin-flange transition using NASTRAN PLOAD4 input. Forebody panel loads throughout the vehicle trajectory were provided by MDC and are shown in Table 4-5. In this table, the stress resultants (N_x , N_y , and N_{xy}) are reported as the combination of a thermal and a mechanical component. The thermal component is due to overall thermal deformations of the vehicle. The mechanical component represents vehicle maneuver loads. The net static loads were taken to be the sum of the two components.

It should be noted that the bending moment resultants reported in Table 4-5 (M_x , M_y , and M_{xy}) were not applied directly to the finite element model. These moments are reactions to the pressure load and hence were taken into account by imposing the corresponding pressure conditions (taken from the right-hand column of the table).

It was concluded from inspection of Table 4-5 that the critical static load case would be that of Condition No. 9. At this point in the trajectory, the forebody panel is subjected to maximum or near-maximum tensile and shear loads ($N_x = 1914$ lb/in., $N_y = 766$ lb/in., $N_{xy} = -202$ lb/in.) and peak temperatures. The most severe compressive load occurs at Condition No. 2 for which $N_x = 1221$ lb/in., $N_y = -207$ lb/in., and $N_{xy} = 85$ lb/in. These loads were used in the buckling analysis of the forebody panel.

Table 4-5. Forebody Panel Loads.

Condition No.	N _x lb/in	N _y lb/in	N _{xy} lb/in	M _x in-lb/in	M _y in-lb/in	M _{xy} in-lb/in	OML Temp Deg. F	Delta T Deg. F	Pressure psi
1 MCH	-16	69	-7	0	0	0	70	0	0.00
THM	1	-3	1	0	0	0			
2 MCH	1158	-241	94	33	37	1	200	0	-0.83
THM	63	34	-9	0	0	0			
3 MCH	135	-88	34	37	-44	1	504	0	-0.74
THM	191	112	-23	0	0	0			
4 MCH	-376	48	27	11	-14	0	504	0	-0.18
THM	191	112	-23	0	0	0			
5 MCH	291	-176	61	46	-54	1	1350	0	-0.95
THM	540	241	-90	-7	-15	0			
6 MCH	-167	-77	15	20	-24	0	1350	0	-0.38
THM	540	241	-90	-7	-15	0			
7 MCH	162	-130	41	38	-45	1	1292	0	-0.77
THM	1153	666	-198	17	-24	0			
8 MCH	-217	-57	15	19	-22	0	1292	0	-0.34
THM	1153	666	-198	17	-24	0			
9 MCH	130	-55	23	16	-19	0	1826	0	-0.32
THM	1784	821	-225	-22	-31	0			
10 MCH	-7	-38	9	6	-7	0	1826	0	-0.13
THM	1784	821	-225	-22	-31	0			
11 MCH	68	-29	12	8	-10	0	1422	0	0.00
THM	1493	623	-164	-18	-22	0			
12 MCH	-4	-20	5	0	0	0	1422	0	0.00
THM	1493	623	-164	-18	-22	0			
13 MCH	65	-52	17	15	-18	0	864	0	0.00
THM	905	414	-116	-11	-16	0			
14 MCH	-87	-23	6	7	-9	0	864	0	0.00
THM	905	414	-116	-11	-16	0			

838PROP/3-T4-5.BB
11-11-89

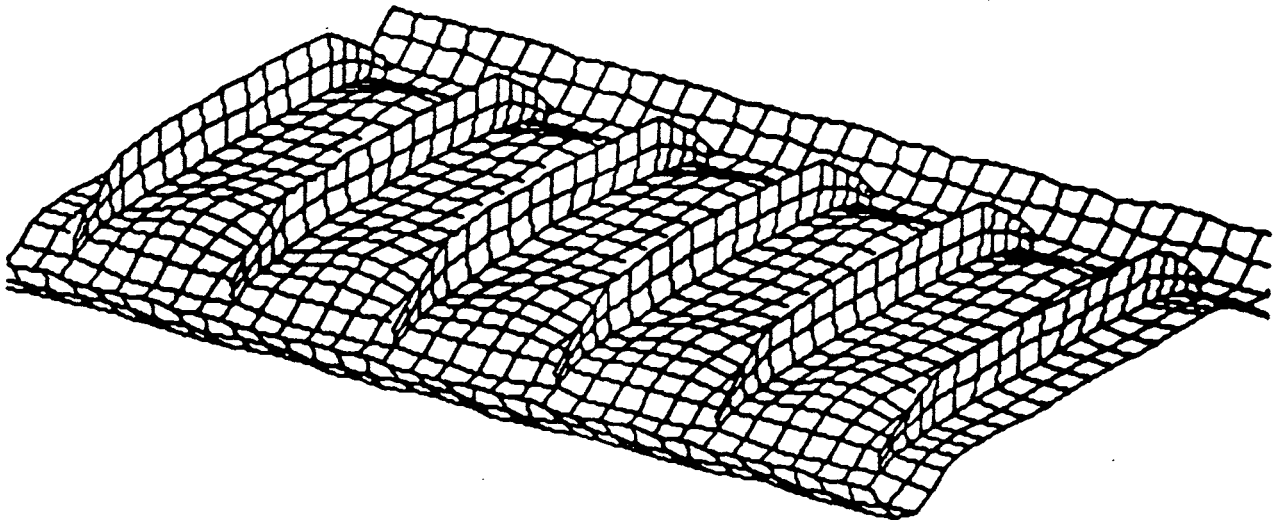
Stresses due to thermal gradients in the panel were incorporated into the analysis by assigning a nodal temperature distribution to the model. The temperatures from the thermal analysis model (Figure 4-4) were mapped onto the stress analysis model. This process was accomplished by means of the P/THERMAL computer code. P/THERMAL interpolated temperatures between nodes in the thermal analysis model and assigned corresponding values to the nodes in the stress analysis model. The result was the generation of NASTRAN TEMP bulk data input.

4.3.3 Results

Stress analysis was performed by invoking the NASTRAN static solution sequence, SOL 24. Extensive use was made of PATRAN data post-processing to assist in data assimilation and interpretation.

A plot of the model deformed shape is shown in Figure 4-16. In this plot, deformations are exaggerated for reasons of clarity. The plot highlights the relatively large displacement of the flanges under the applied tensile load. This indicates potential problems with regard to interlaminar tensile failure in the vicinity of the flange radius. However, laminate interlaminar stress analysis was beyond the scope of the present study and should be addressed in future work.

Strength analysis was limited to that of 2D lamination theory. PATRAN was used to plot Von Mises stresses within the four regions of the structure (the blade stiffeners, the skin, the flanges, and the skin-flange transition). These values were of little significance in the absolute sense but were useful in identifying critical CQUAD4 elements. Stresses for critical elements in each of the four laminates were retrieved from the NASTRAN output and used in strength calculations. Lamination theory was used in conjunction with a maximum stress failure criterion to determine margins of safety for these elements relative to the applied stress state.



CARBON/CARBON FOREBODY PANEL
LOAD CASE 9
COMBINED THERMAL/MECHANICAL LOADS SUBCASE 12

Figure 4-16. Forebody Panel Deformed Shape.

Figure 4-17 shows the Von Mises stress contours for load Condition No. 9. As suggested by the contours, it was found that the most critical regions were in the flanges adjacent to the fasteners. In these regions, the structure is subject to high in-plane loads and bending moments.

As indicated in Figure 4-17, the lowest margin of safety was found to be near the outermost fasteners. Here, the margin of safety for first ply failure was calculated to be -0.17. This corresponded to fiber failure in an outermost 0°/90° ply of carbon-carbon fabric. However, two points can be made with some optimism. First, this negative margin of safety was for a first ply failure. The margin of safety associated with the laminate ultimate strength (i.e., for complete failure of the laminate) was actually 3.29. Second, it is anticipated that the negative margin of safety could be resolved by modifying the laminate layup configuration.

Buckling analysis was performed for load Condition No. 2 using the NASTRAN eigenvalue solution sequence SOL 5. The lowest eigenvalue, corresponding to the first buckling mode, was found to be 21.7. The mode shape is illustrated in Figure 4-18. Since the margin of safety with respect to buckling is 20.7, buckling will not occur under this load condition.

The following conclusions were made from the static analysis:

- (1) The current design proposed for the forebody panel would suffer first ply fiber failures under worst case load conditions. However, the panel ultimate strength was found to be adequate.
- (2) Buckling analysis revealed that even for the worst case compressive loads, there are high margins of safety with respect to the buckling of the forebody panel.
- (3) More detailed analysis of the forebody panel is required to evaluate interlaminar stress effects in the panel flanges.

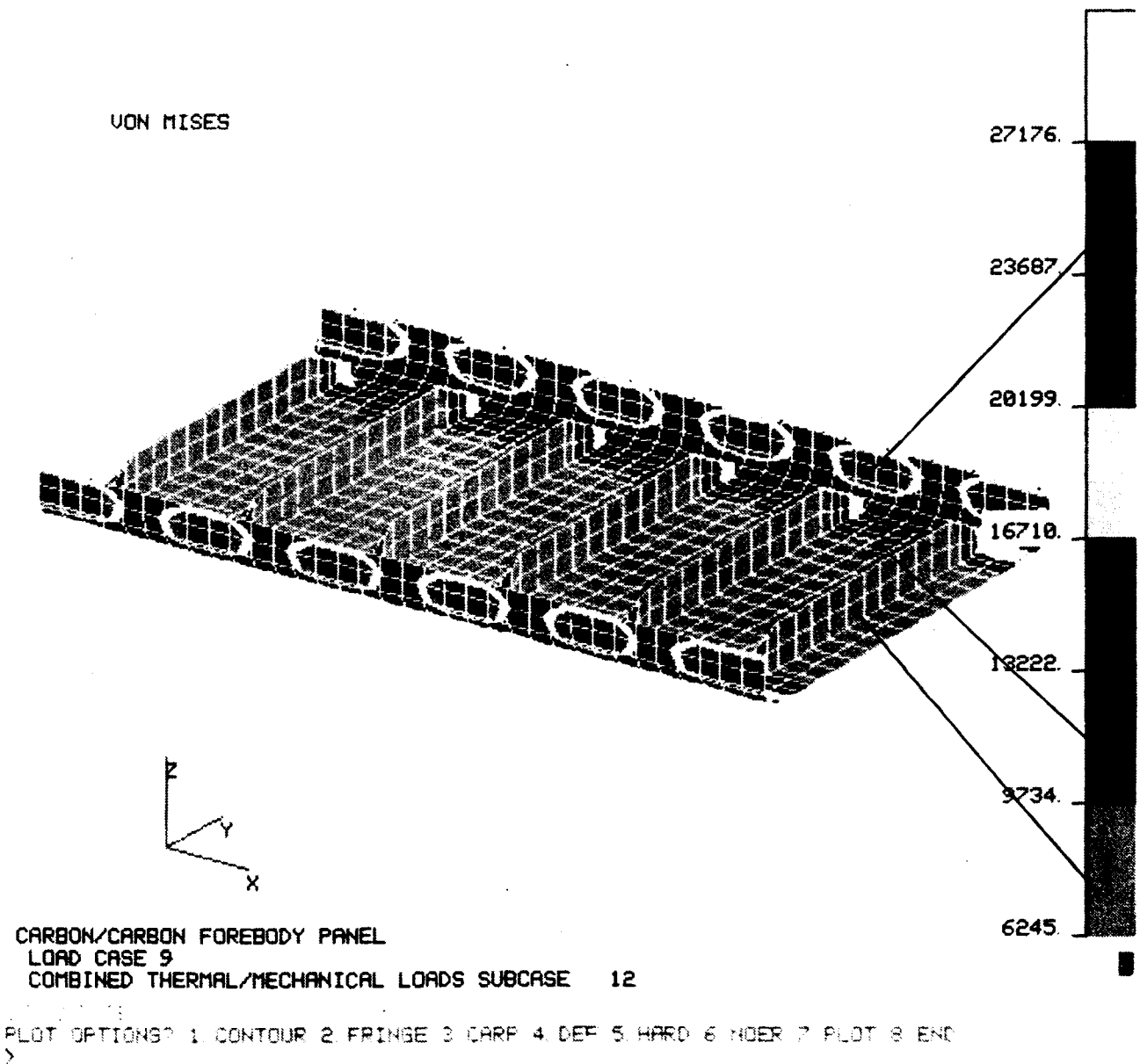
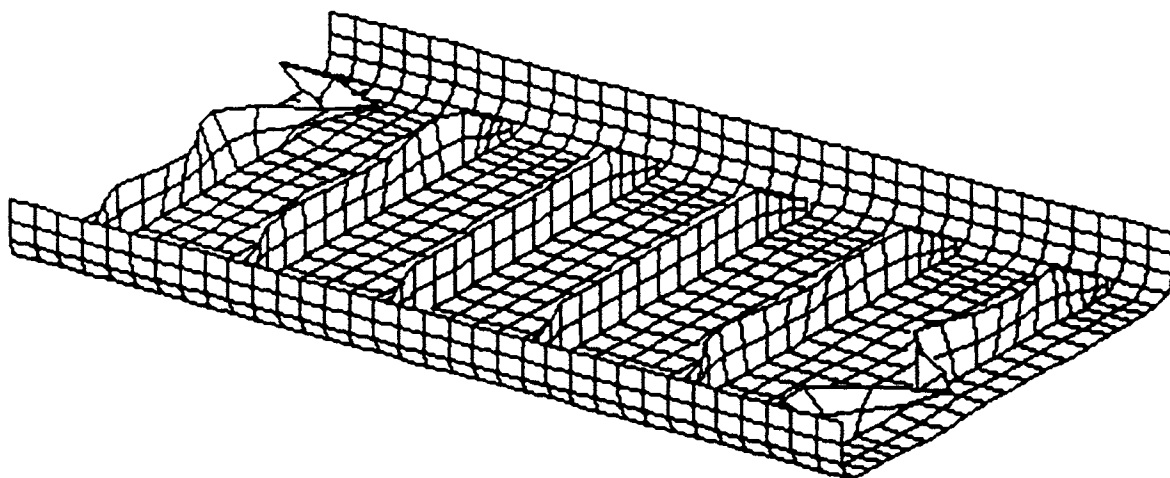


Figure 4-17. Forebody Panel Stress Contours.



CARBON/CARBON FOREBODY PANEL
LOAD CASE 2
MODE NUMBER = 1 EIGENVALUE = 0.2173694E+02

Figure 4-18. First Buckling Mode of Forebody Panel
(for Load Condition No. 2)

- (4) The results of the analysis were dependent on the boundary conditions that were assumed. The assumptions made were considered to be reasonable, but further investigation might pursue the influence of boundary conditions on panel stresses and margins of safety.

4.4 DYNAMIC ANALYSIS

4.4.1 Introduction

Modal and acoustic fatigue analyses of a typical forebody panel were performed in order to determine its modal characteristics and acoustic fatigue susceptibility. Both aeroacoustic and engine induced dynamic loading (Sections 2 and 3) were considered as well as the effect of mean loads. The dynamic analysis was made using MSC/NASTRAN in two stages: (1) modal analysis and (2) response analysis.

4.4.2 Modal Analysis

A complex static preload condition exists in the external vehicle skin panels. The primary effect of preload is to increase the mean stress about which the acoustically induced stress will oscillate. This will result in lower fatigue life for a given rms acoustic stress and will alter the natural frequencies of the skin panels. A compressive load will lower panel natural frequencies, while a tensile preload will increase frequencies. This affects overall panel response levels, as well as the number of load cycles the panel will accumulate.

The normal modes analysis is carried out using NASTRAN. The natural frequencies and modal shapes are determined while including the appropriate stiffness corrections due to edge loads and pressures. Natural frequencies and modal shapes for the free stress state are also obtained in order to investigate the effect of preload. In incorporating the effect of preload on the structural behavior of the panels, the following operations are implemented in the finite element analysis: (1) load increment applications, (2) internal force equilibrium iterations,

and (3) element stiffness matrix updates. The element stiffness matrix updates reflect the sequential change in stiffness due to the applied loads. The solution algorithm is implemented by SOL 66 - NASTRAN (nonlinear static analysis). Once the updated stiffness matrices have been obtained, modal analysis is carried out using SOL 63 - NASTRAN (superelement normal modes) by fetching the required information from the data base.

The material model for carbon-carbon is idealized as orthotropic with transverse shear flexibility while excluding the effects of membrane-bending coupling and shear coupling. In addition, the stress-strain relationship is assumed to be linear and the effect of temperature on the stiffness properties is incorporated. The effect of temperature on the stiffness properties of carbon-carbon has been investigated experimentally, and results were reported in Reference [4-3]. However, the acquired data indicated appreciable scatter, precluding postulation of any reliable assumptions. It is speculated that the size of the glass particulates imbedded in the matrix for oxidation protection directly affects the flexural behavior at elevated temperatures. When the particulate size is relatively small and their spatial distribution is uniform, the effect of temperature remains modest. To avoid any erroneous disposition, it was decided that the stiffness characteristics remain unchanged at elevated temperatures, a conservative assumption.

The finite element model for the forebody panel along with the proper boundary conditions and a static preload case corresponding to flight condition 2 (selected as the most severe one) (Reference [4-4]) is shown in Figure 4-19. The first mode occurs at 146 Hz and corresponds to a quasi "rigid body" mode that exhibits the stiffness of the attachment mechanisms. The second mode occurs at 524 Hz and corresponds to an in-phase mode. The out-of-phase mode occurs at 592 Hz. Experience has shown that in-phase and out-of-phase panel modes are the dominant participating modes and they contribute the most to the response under fluctuating load conditions such as sonic loading. These modal shapes are depicted graphically in Figure 4-20. The corresponding modal stress fields are shown in Figure 4-21, where the highest modal stresses are

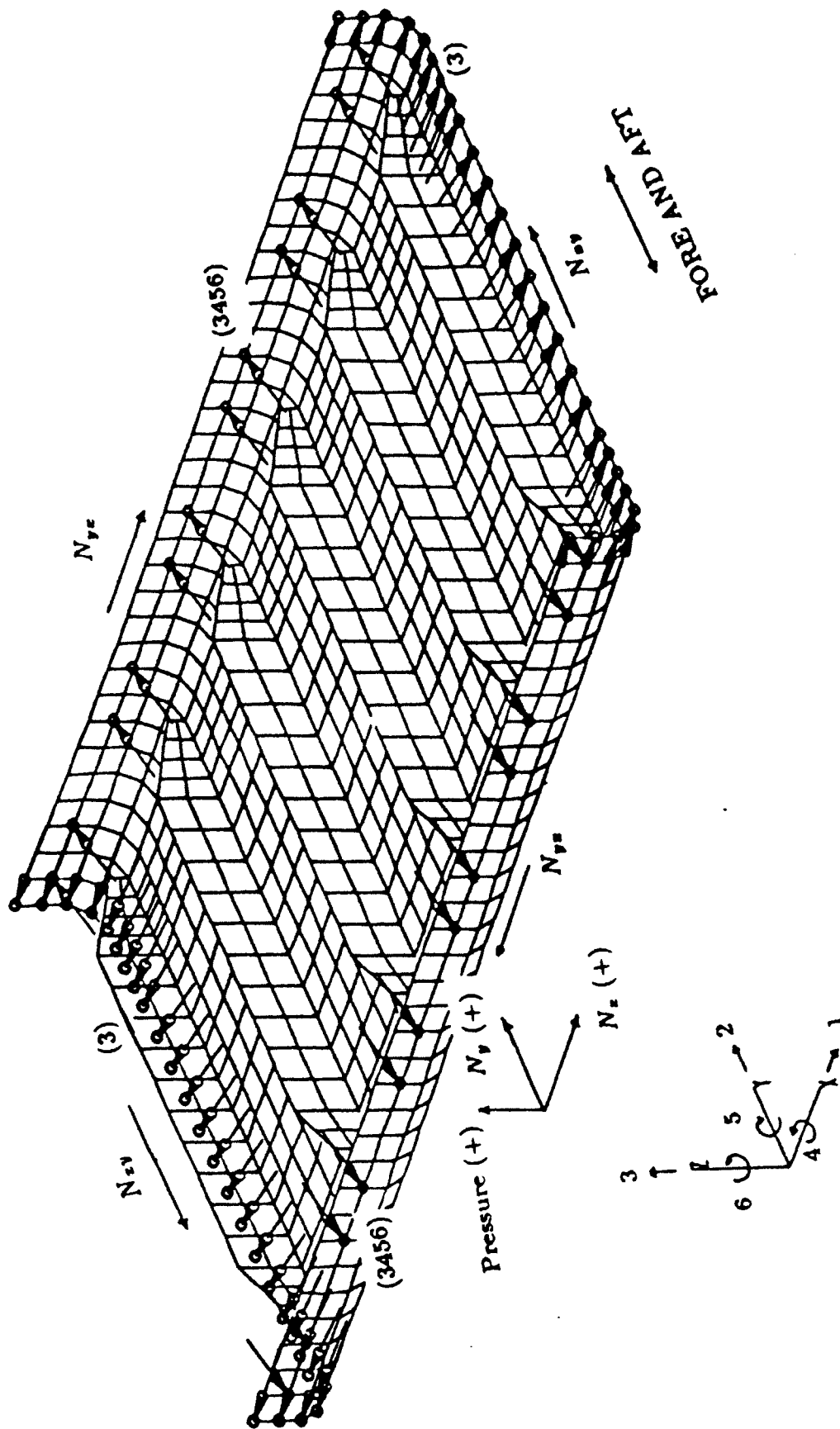
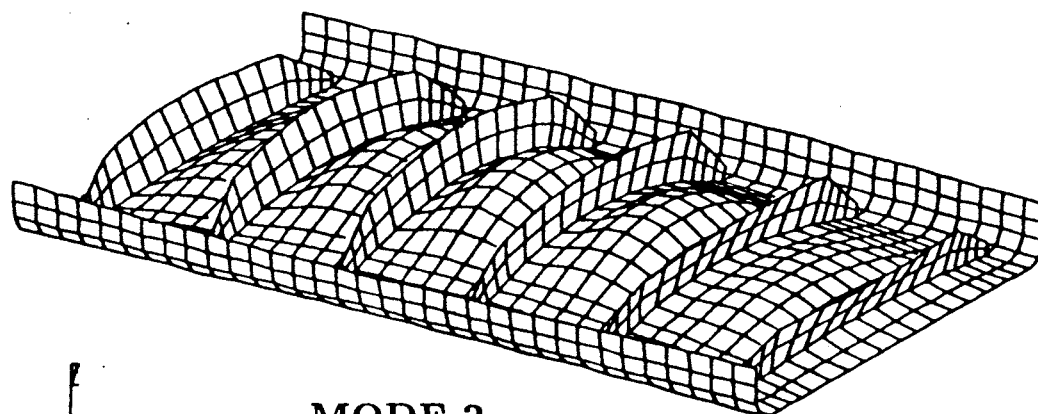
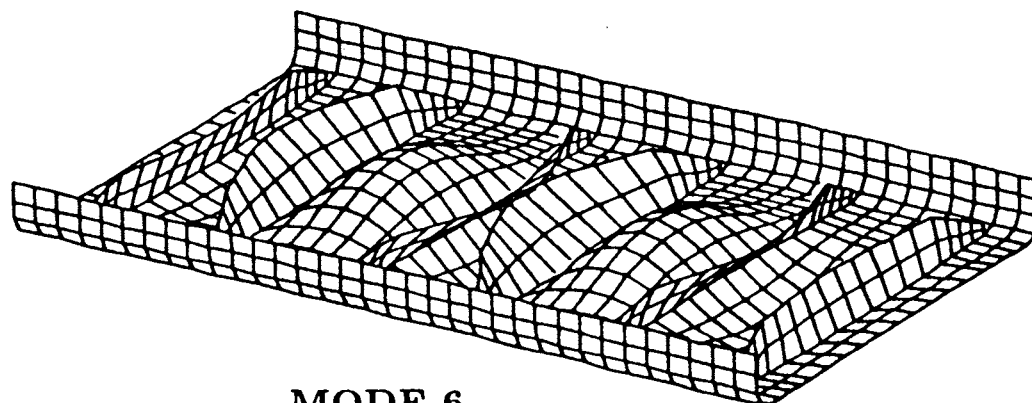


Figure 4-19. Forebody Panel Geometry and Boundary Conditions.



MODE 2



MODE 6

MODE	FREQ
----	----
2	0.5237E+03
3	0.5380E+03
4	0.5597E+03
5	0.5803E+03
6	0.5921E+03
7	0.7700E+03
8	0.7775E+03
9	0.8432E+03

Figure 4-20. Forebody Panel In-Phase and Out-of-Phase Modes for Flight Condition 2.

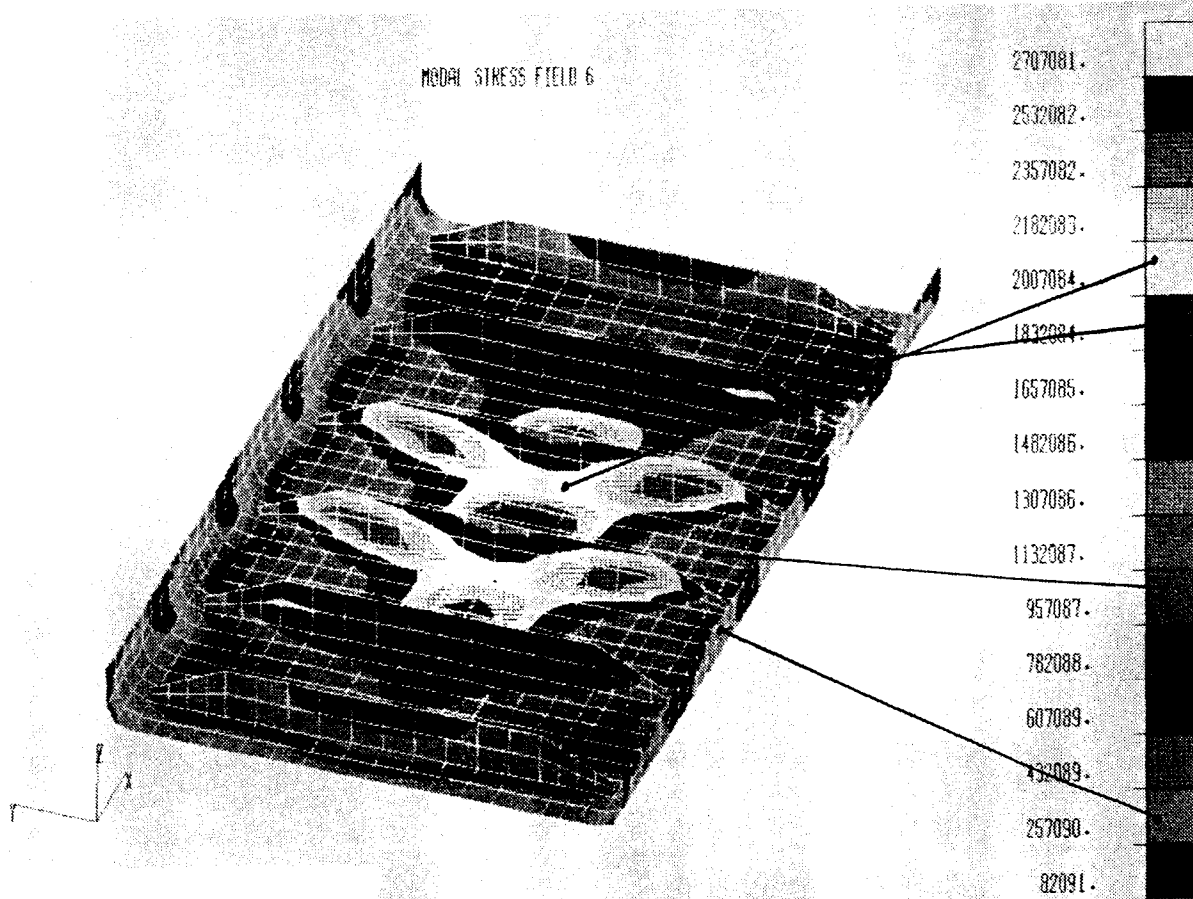
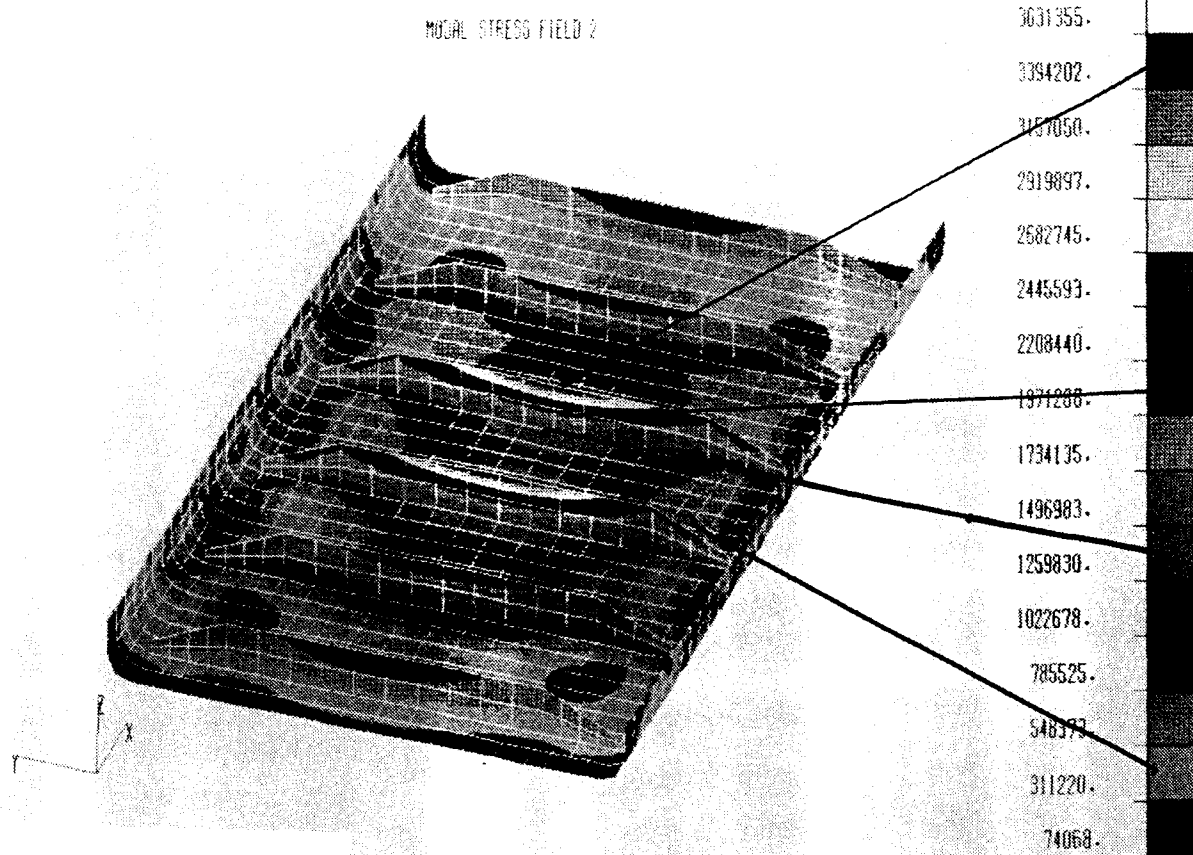


Figure 4-21. Forebody Panel Modal Stress Fields for In-Phase and Out-of-Phase Modes Shown in Figure 4-20.

observed on the top side of the two middle stiffeners for the in-phase mode and at the center of the midbay for the out-of-phase mode. At the free stress state, the order of in-phase and out-of-phase modes is reversed with the out-of-phase mode occurring at 449.2 Hz and the in-phase mode at 496.0 Hz. The effect of preload on frequency is shown in Figure 4-22.

4.4.3 Sonic Fatigue Analysis

Sonic Loads. The sound levels in transatmospheric vehicles originate from boundary layer induced noise or from the rocket and scramjet engines. The noisiest section of the flight occurs during takeoff when both the rocket engines and the scramjet engine are operating. For the lower surface, it was assumed that complete reflections occur along the ground and that each octave band radiates with its own characteristics. Combining the sound level of the rocket engines with that of the scramjet engine gives the sound pressure level during takeoff conditions. The results and a roadmap of the vehicle are shown in Figures 4-23(a) and 4-23(b), respectively. If it is assumed that the scramjet geometry allows the combustion and the internal noise to travel toward the inlet as well as toward the exhaust side, the estimated inlet noise for the various locations on the lower side of the vehicle is then as shown in Figure 4-24. The boundary layer induced noise for different Mach numbers as a function of vehicle location is shown in Figure 4-25. It is evident that the most severe case is the one where both exhaust and inlet noise are combined, and thus the one octave sound pressure levels for the forebody regions are 150-160 dB.

The analytical approach used in determining the response and ultimately the fatigue behavior of panels exposed to the sound fields discussed earlier is an extension of Miles' work. The method uses the modal analysis results, i.e., normalized modal displacements and modal stresses, to obtain the load-deflection relationship. The effect of finite acoustic wavelengths on the panel response is incorporated through simultaneous consideration of spatial characteristics for both the structural modes and the sound field. Initially, the surface pressure

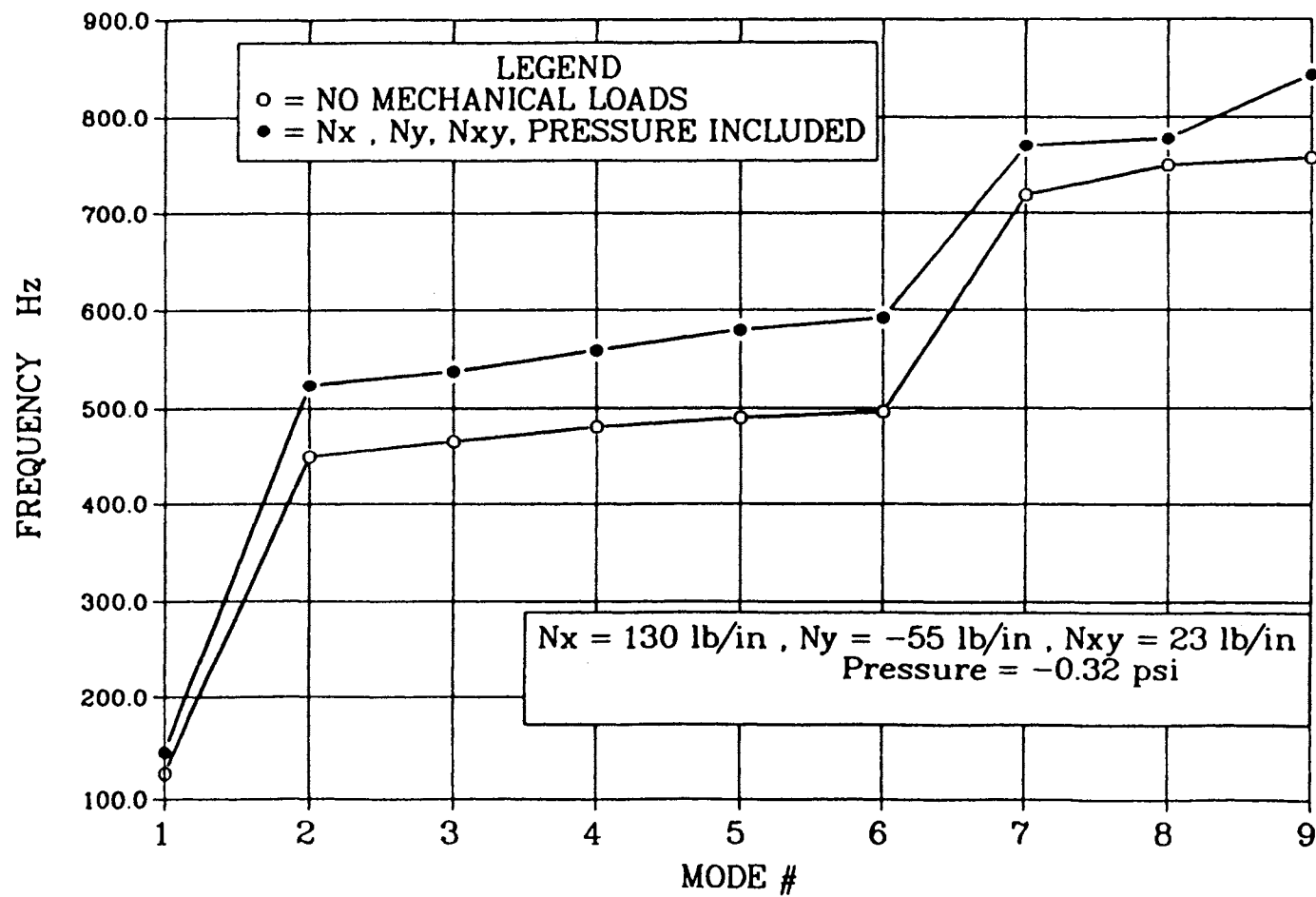


Figure 4-22. Effect of Mechanical Loads on Frequency for Forebody Panel.

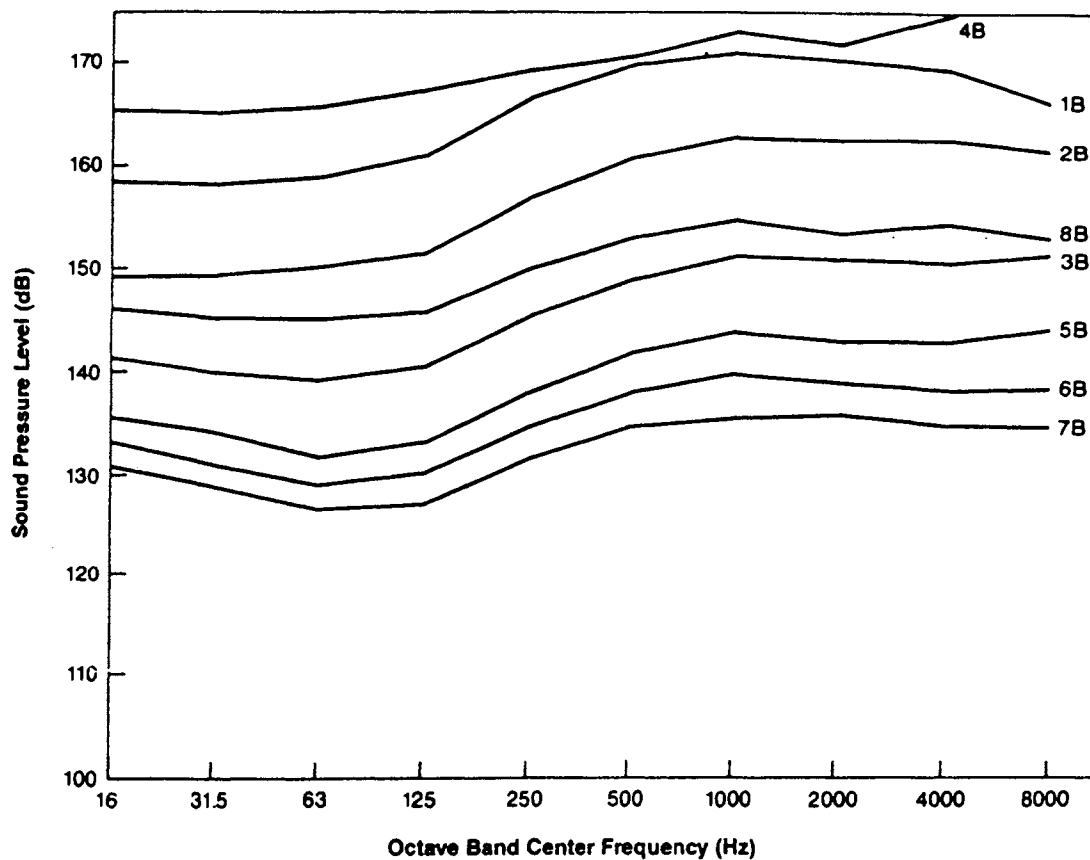


Figure 4-23(a). Sound Pressure Level on Lower Surface due to Combined Effect of Scramjet and Rocket Engines.

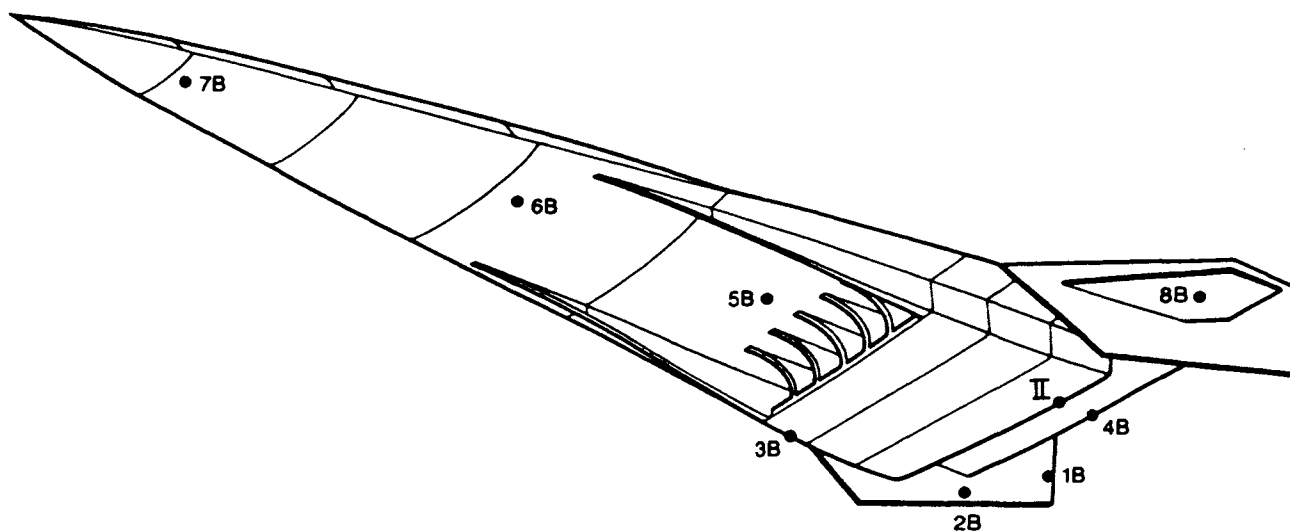


Figure 4-23(b). Sketch of Blended Wing Body Model Used in Sound Level Analysis of Lower Surface.

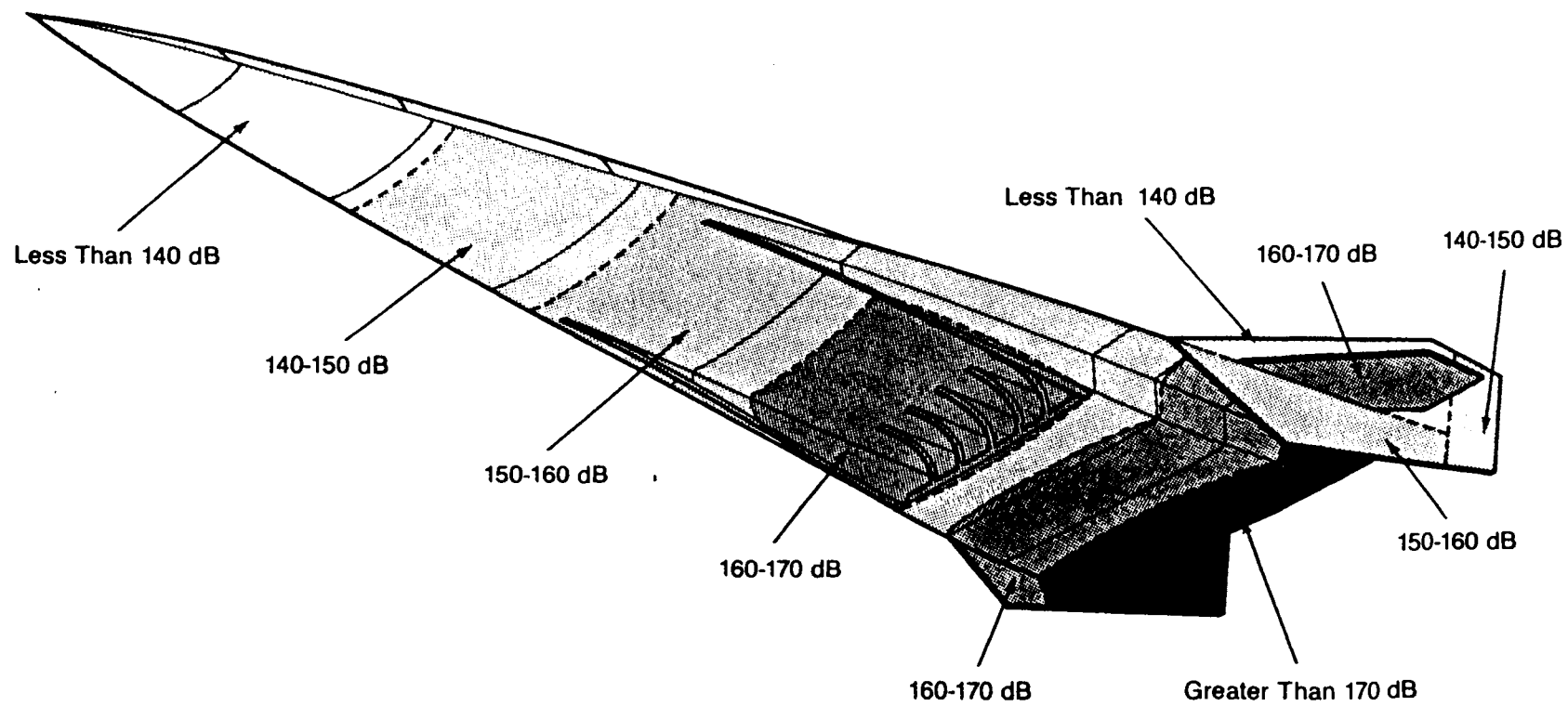


Figure 4-24. One Octave Band Overall Sound Pressure Levels.

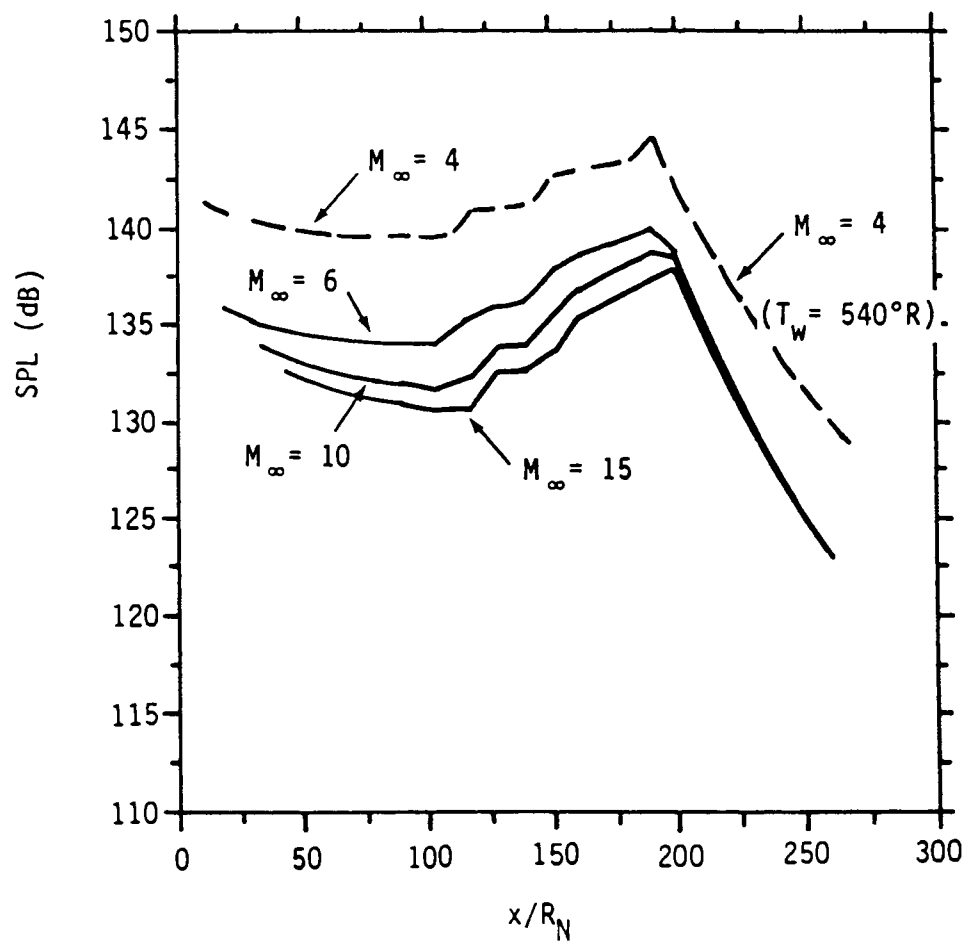


Figure 4-25. Boundary Layer Induced Noise as a Function of Vehicle Location.

distribution is approximated by the mass-weighted structural mode shape. For the fundamental mode of the panel, the estimate is similar to the assumption of uniform pressure. The advantage of this assumption is that it tends to produce a conservative estimate for each mode and the measure of spatial correlation (joint acceptance) between modal and acoustic fields is rendered unity. The accuracy of this approximation depends on the degree to which the mass-weighted mode shape reflects the actual pressure field shape. However, improvements to that joint acceptance estimate are developed which do not require detailed modeling of the acoustic field or numerical integration. This improvement is based on the relation between the structural and acoustic wavelengths. Thus, after a mode-by-mode evaluation of sonic stresses is performed initially, the joint acceptance correction detects and adjusts underpredicted and/or overpredicted sonic stress estimates. Finally, the overall stresses are obtained by summing the squares of contributions of the individual modes. A more detailed presentation of the analytical procedure is given in Reference [4-5]. Once the acoustically induced stresses have been determined, a direct comparison with available random fatigue data provides estimates for the number of mechanical cycles that can be sustained.

Carbon-Carbon Fatigue Data. Random fatigue data for uncoated (HTC) carbon-carbon bar specimens are shown in Figure 4-26. Data are included for specimens with various types of inhibitors as well as uninhibited ones. All specimens were made from 3K tow T-300 carbon fabric heat treated to 2150°C (3900°F). Fiber volumes for the inhibited, filled specimens ranged from 42% to 48%. The fillers were added to the phenolic prepregging resin in particulate form. All panels were densified using four cycles of 50-50 pitch-funaldelyde impregnation to a target porosity of less than 5%. To prevent reaction of the fillers with the fibers, the graphitization temperature was limited to 1650°C (3000°F). For infinite life (10^8 cycles), the lower fatigue limit is approximately 6000 psi (rms) and the upper limit is 12,000 psi (rms).

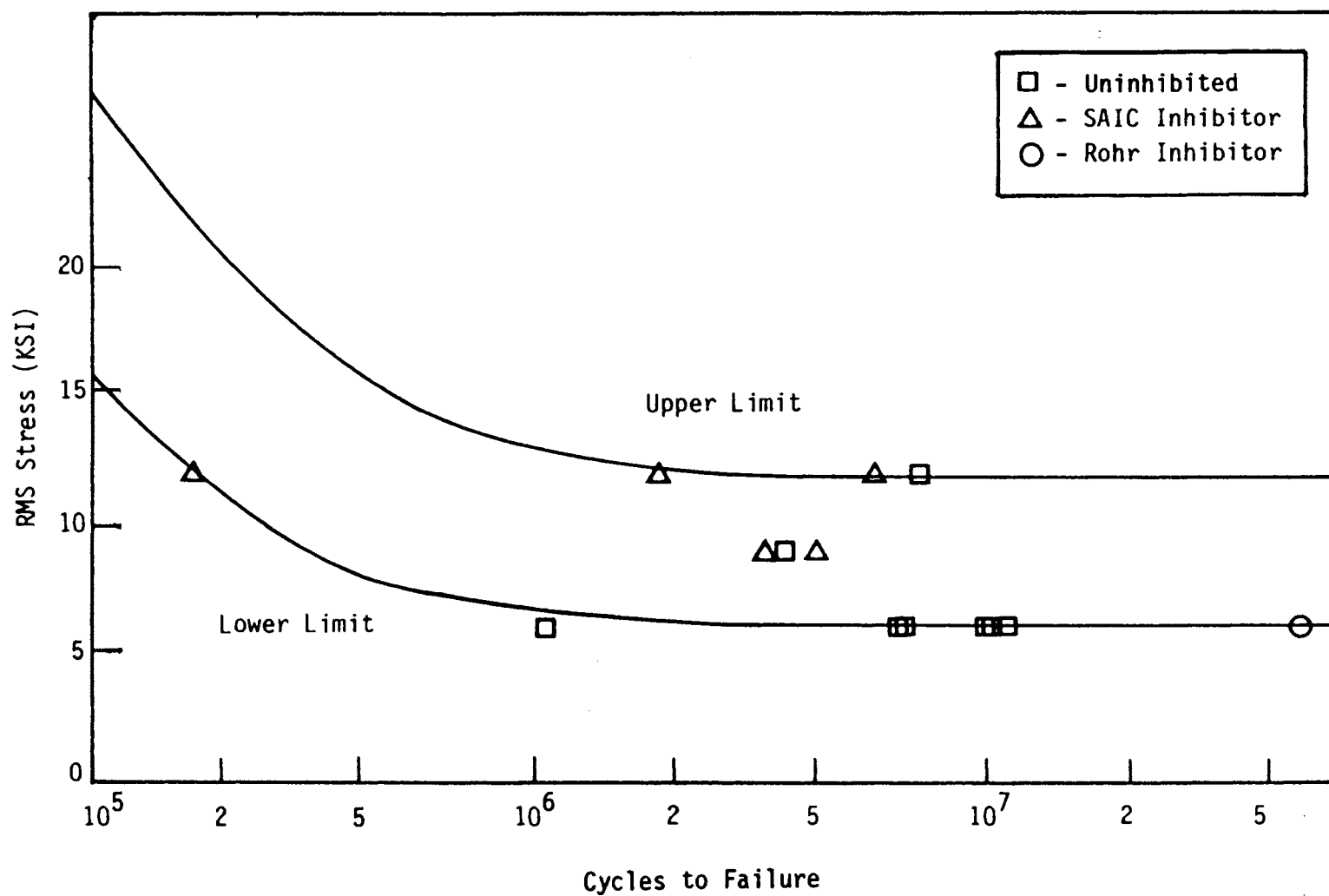


Figure 4-26. Fatigue Data for Uncoated HTC Bar Specimens.

Following the analytical procedures outlined previously, sonic stress levels for the forebody panel were calculated and are shown in Figure 4-27. Sonic loading corresponds to exhaust and combined exhaust/inlet contributions. The maximum sonic stress is approximately 4000 psi and occurs at 770 Hz for a combined one-third octave sound pressure level of 155 dB when the panel is preloaded. When the sonic loading is exhaust noise only, the sonic stress reaches a value of 700 psi at 770 Hz. When the improved joint acceptance estimates are incorporated, the overall rms stress distribution is represented by Figure 4-28, with a maximum value of 2319 psi. The highest stresses are observed on the upper side of the stiffeners and the center of the middle bay. These stress levels are well below the fatigue allowable, and therefore the forebody panel will be able to sustain the loading environment for its design life.

4.5 RESULTS

Thermal, static stress, and dynamic analyses have been made of the carbon-carbon forebody panel.

The thermal analysis shows:

- (1) The maximum skin temperature at end of ascent is 2667°F for the 1000 q_{∞} ascent and 3223°F for the 2600 q_{∞} ascent. These results are based on turbulent heating. If a laminar boundary layer exists, the maximum temperature could be 1100°F lower.
- (2) The maximum temperature difference between the fastener locations on the panel edges is 1400°F for 2600 q_{∞} and 1200°F for 1000 q_{∞} . The temperature difference through the skin thickness is negligible.

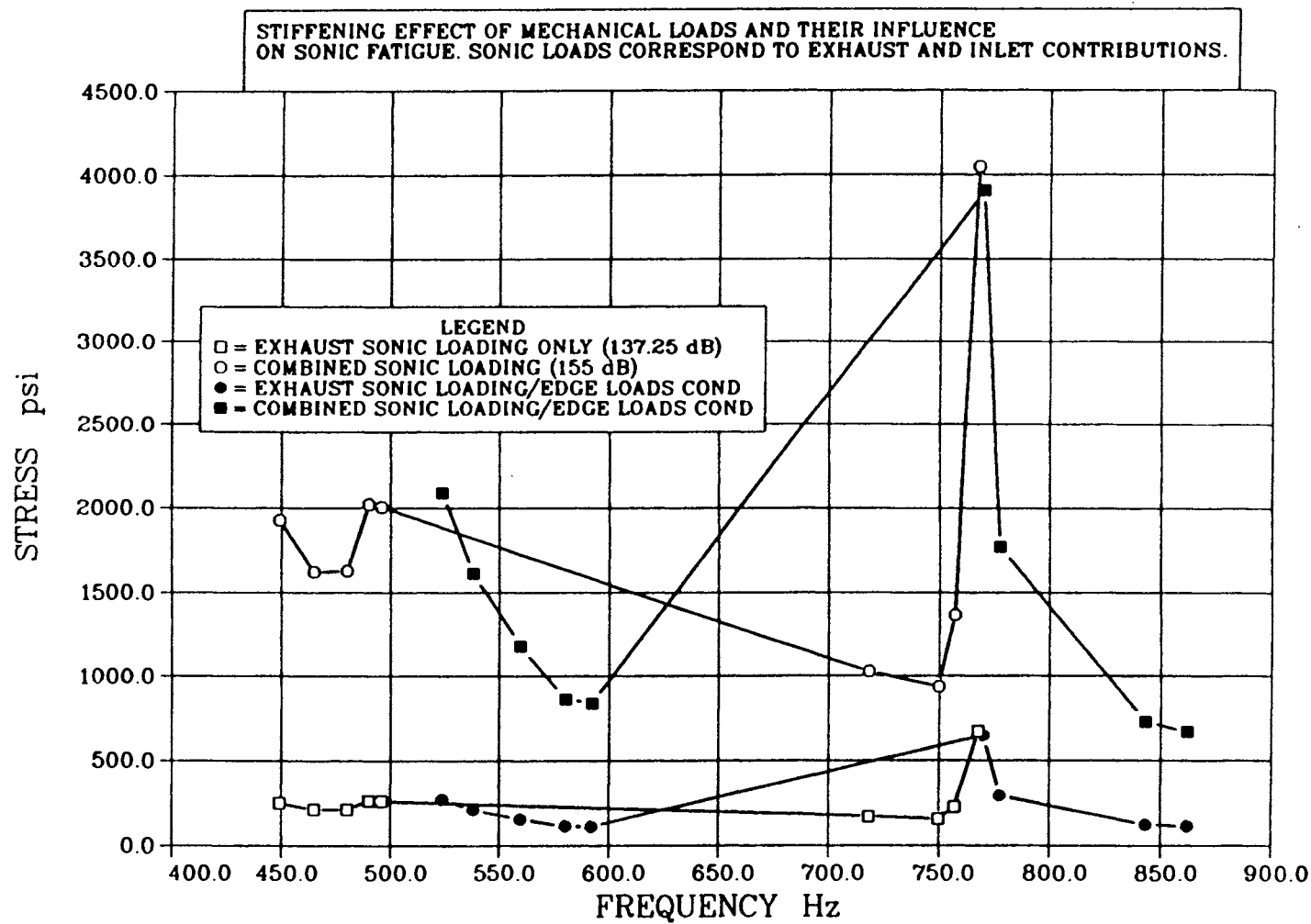
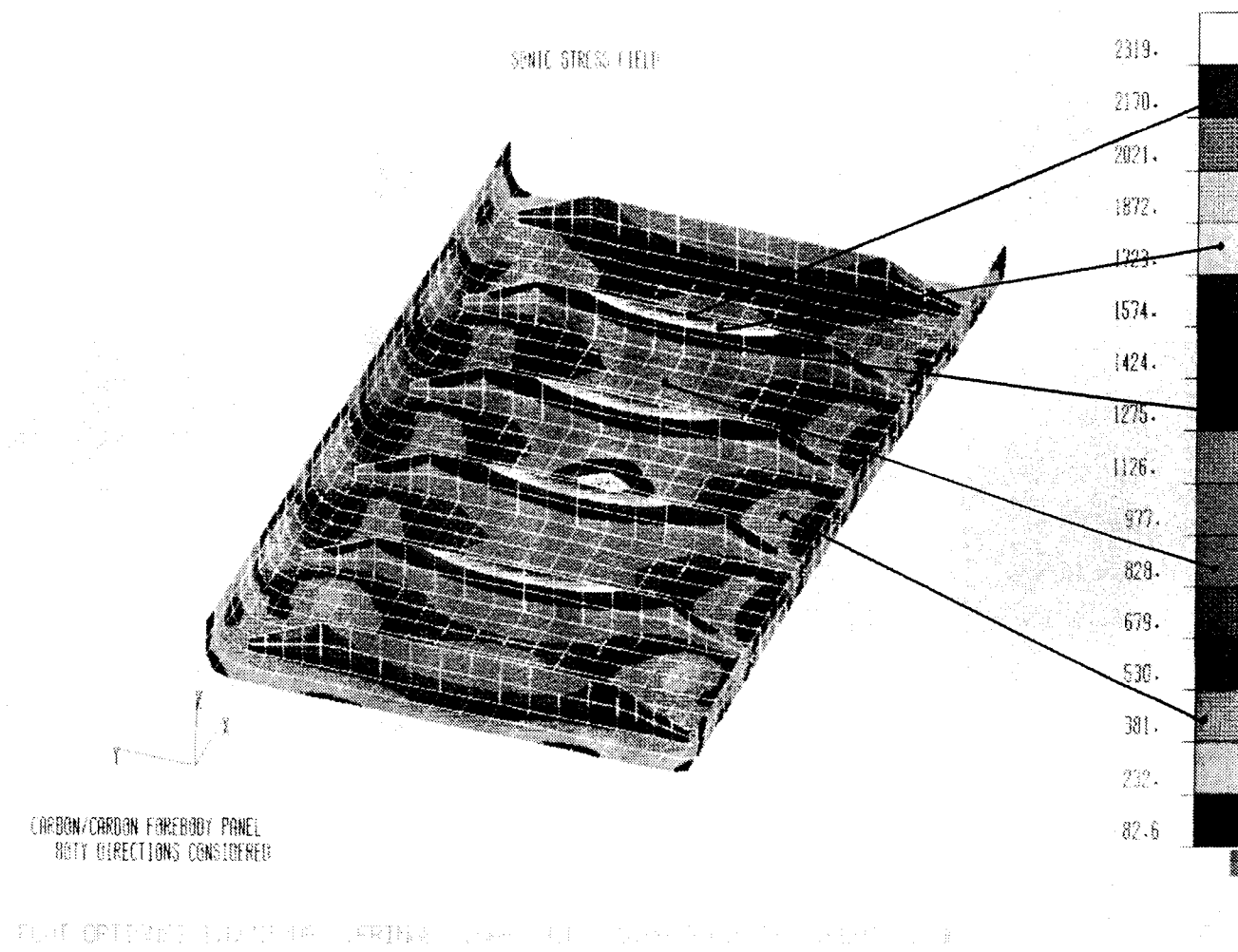


Figure 4-27. Sonic Stress Levels at Forebody Panel.



Static stress analysis considering thermal loads, vehicle carry-through loads, and aerodynamic press indicates:

- (1) The current design proposed for the forebody panel would suffer first ply fiber failures under worst case load conditions. However, the panel ultimate strength was found to be adequate.
- (2) More detailed analysis of the forebody panel is required to evaluate interlaminar stress effects in the panel flanges.
- (3) Buckling was not found to be a concern for the forebody panel.

Dynamic analysis of the forebody panel under aeroacoustic and engine excitation shows:

- (1) The maximum sonic stress is approximately 4000 psi and occurs at 770 Hz for a combined one-third octave sound pressure level of 155 dB when the panel is preloaded. When the sonic loading is exhaust noise only, the sonic stress reaches a value of 700 psi at 770 Hz. When the improved joint acceptance estimates are incorporated, the overall rms stress distribution has a maximum value of 2319 psi.
- (2) The highest stresses are observed on the upper side of the stiffeners and the center of the middle bay. These stress levels are below the fatigue allowable, and therefore the forebody panel will be able to sustain the loading environment for its design life.

4.6 REFERENCES

- 4-1 P/THERMAL User Manual, PAD Engineering, July 1988.
- 4-2 MSC/NASTRAN Version 66, The MacNeal-Schwendler Corporation, 1988.
- 4-3 Gray, P.E., et al., The Effect of Temperature on the Flexural Modulus of Carbon-Carbon, 13th Conference for Ceramic and Carbon-Carbon Composites, Cocoa Beach, Florida, January 20-22, 1987.
- 4-4 Design Conditions, unpublished data, McDonnell Douglas Corporation, January 26, 1988.
- 4-5 Blevins, R.D., "Approximate Methods for Sonic Fatigue Analysis of Plates and Shells," Journal of Sound and Vibration, Vol. 129, pages 51-71, 1989.

838PROP
3-4.BB
12-11-89

SECTION 5

ANALYSIS OF RAMP PANEL

5.1 INTRODUCTION

The ramp compresses and conditions the air entering the vehicle engines. A typical ramp panel located 60 feet aft of the nose was analyzed for response to the thermoacoustic and engine induced sound environment.

The engine inlet ramp is defined as the portion of the vehicle aft of the forebody and ending at the engine inlet (Section 1, Figure 1-3). This includes the structure from 35 feet to 60 feet. The ramp structural concept consists of single-faced corrugated skin protected by stiffened carbon-carbon panels. The skin panels are supported by carbon-carbon joints which allow thermal expansion relative to the underlying skin structure. The skin panels are 48 inches by 48 inches with frames on 20-inch centers. This structural concept (metallic structure protected by passively cooled heat shields) was selected based on studies showing weight benefits for this type of structure versus actively cooled structure.

The detailed dimensions of the carbon-carbon ramp skin panel are shown in Figure 5-1. The single blade stiffeners are 1.25 inches high and 0.065 inch thick, spaced 10 inches apart. There is a 0.3-inch-thick layer of alumina insulation between the carbon-carbon skin and the

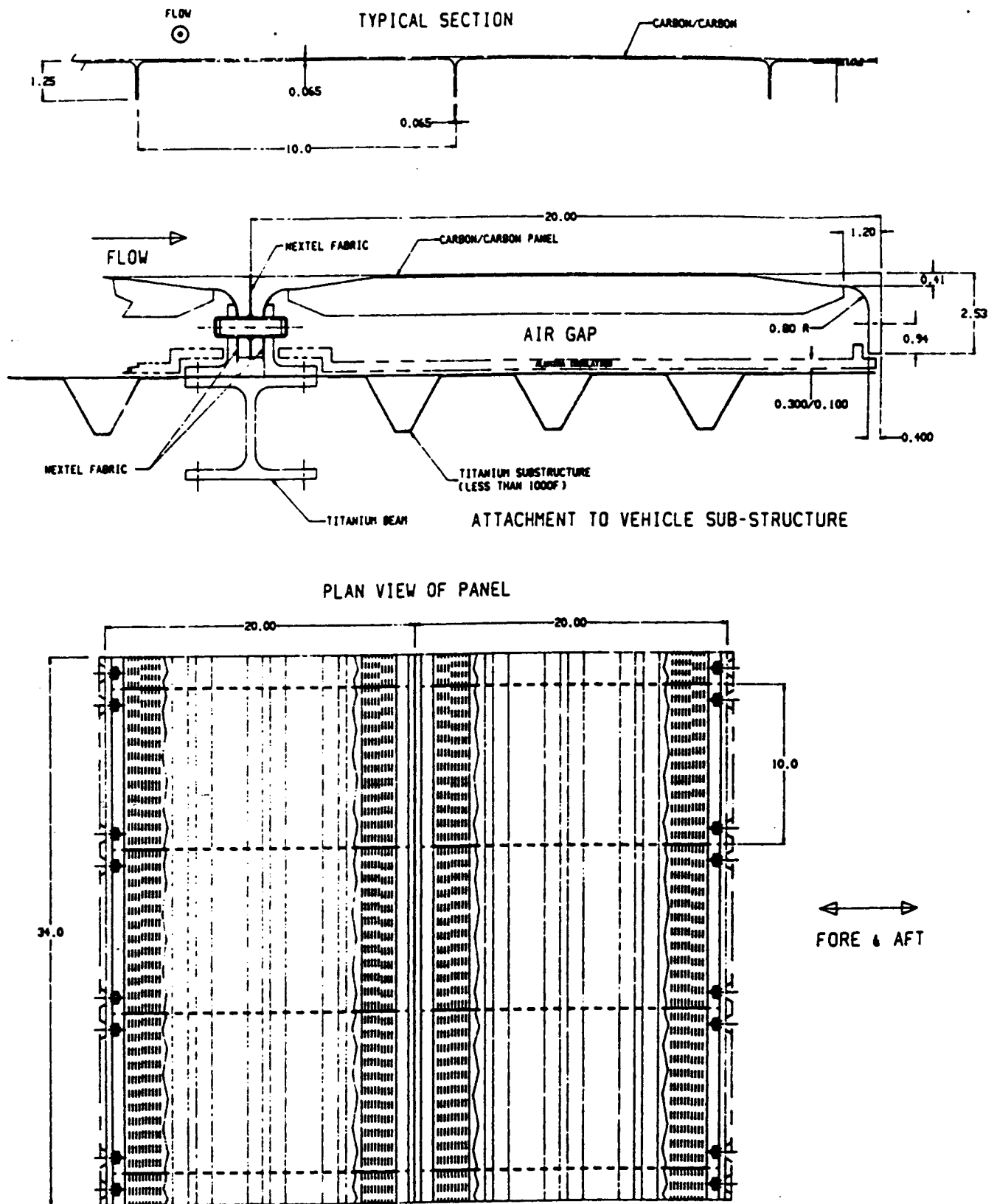


Figure 5-1. Ramp Panel Located 60 Feet Aft of Nose of Underside of Vehicle.

titanium substructure. The carbon-carbon skin panels do not bear structural in-plane loads. They are heat shields and their thickness is sized by aeroacoustic loads.

The ramp panel analysis was made with the finite element method using a common geometry. The steps in the analysis are as follows:

- (1) Thermal analysis using P/THERMAL (Reference [5-1]).
- (2) Static stress and stability analysis using MSC/NASTRAN (Reference [5-2]).
- (3) Dynamic analysis using MSC/NASTRAN (Reference [5-2]).

The thermal, aeroacoustic loading is developed in Section 2. The engine acoustic loads are developed in Section 3.

5.2 THERMAL ANALYSIS

For a hypersonic flight vehicle, detailed thermal analyses were performed to determine the temperature profiles of a ramp panel. The ramp extends from 35 to 60 feet. The ramp panel analyzed is located 55 feet downstream from the vehicle nose. Based on the generic trajectories listed in Tables 4-1 and 4-2 and the SAIC turbulent heating rates profiled in Figure 5-2, temperatures were evaluated during ascent for 1000- and 2600-psf free stream dynamic pressures. The initial temperature was assumed to be 70°F.

The ramp panel is made of carbon-carbon with the thermal properties summarized in Table 4-3. The thermal boundary conditions for the panels are illustrated in Figure 4-3. The outer skin is subject to aerodynamic heating and radiates to the atmosphere. Alumina insulation will be applied between the panel and the vehicle substructure.

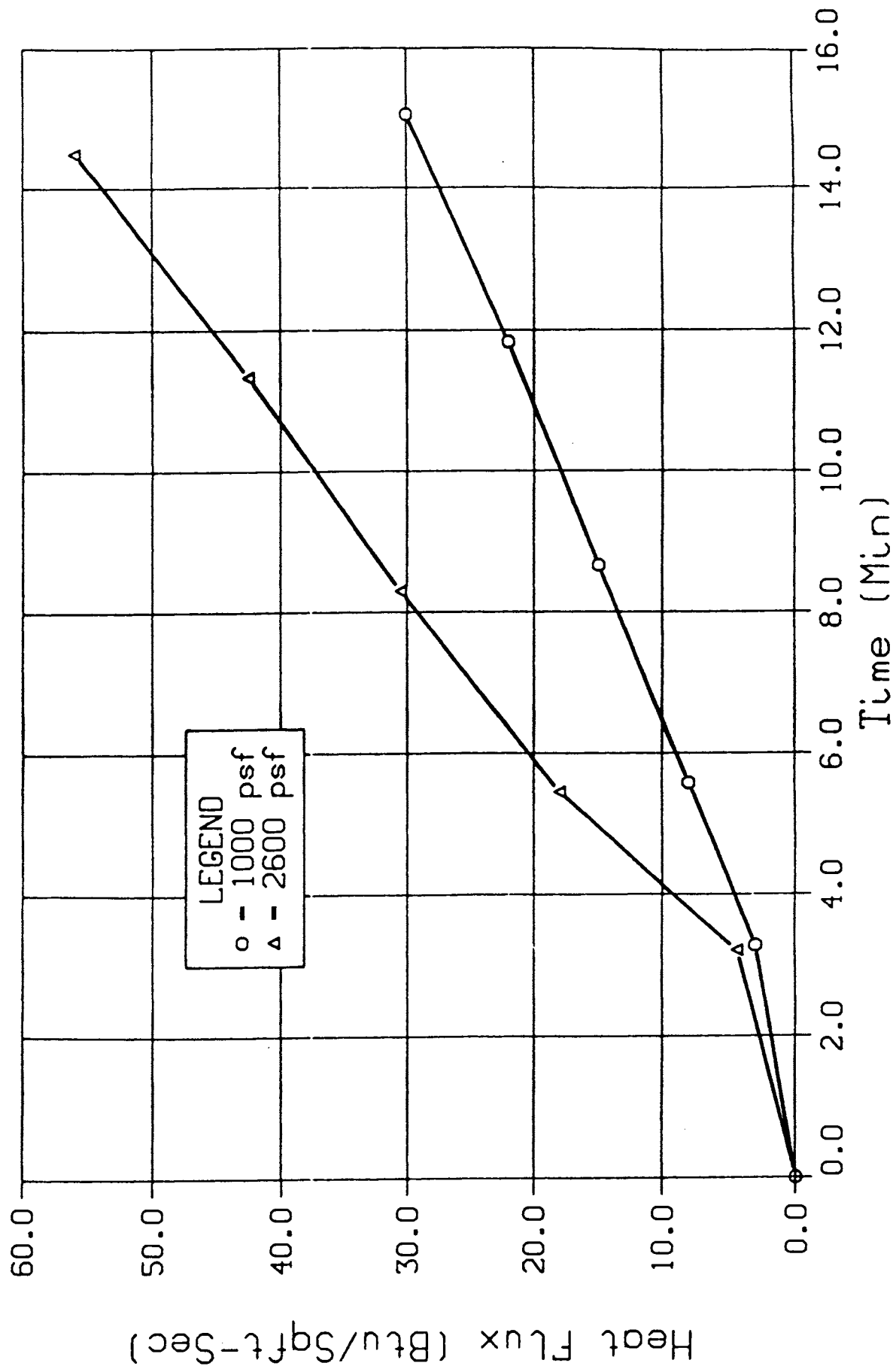


Figure 5-2. Ramp Panel Turbulent Heat Flux Profiles During Ascent.

Transient thermal analysis was conducted using the P/THERMAL code. The P/THERMAL finite element model of the ramp panel is shown in Figure 5-3.

The panel temperature distributions at the end of ascent are given in Figures 5-4 and 5-5. With the current technology, the upper use temperature for carbon-carbon is 3000°F. The coating starts to deteriorate when it gets hotter than this temperature limit. For the 1000-psf case, the calculated peak temperature was 2510°F for the ramp. However, for the 2600-psf condition, the maximum temperature would exceed 3000°F based on the conservative assumption of turbulent heating throughout the entire ascent phase.

The panel maximum temperatures occurring on the skin and the minimum temperatures taking place over the tip of the fastener area are summarized in Figures 5-6 and 5-7. The largest temperature difference on a ramp panel is about 800°F. The temperature gradient through the skin thickness was found to be negligible.

The effect of laminar versus turbulent heating on the panel temperature prediction was also investigated. From SAIC's laminar heat transfer results for an axisymmetric body, assuming that re-laminarization is established at Mach 10, the heat flux profiles during ascent for 1000-psf aerodynamic pressure are presented in Figure 5-8. The panel temperature distribution at 15 minutes after takeoff is depicted in Figure 5-9. The ramp panel peak temperature was calculated to be 1860°F versus 2510°F obtained from the assumption of turbulent heating. The maximum and minimum temperatures on the panels during ascent are summarized in Figure 5-10. The re-laminarization results in the dip in panel skin temperatures.

The sensitivity of maximum panel temperature to peak heating rate is indicated in Figure 4-12. The impact of major difference between turbulent and laminar heating rates on the panel skin temperature is significant. The approach of assuming turbulent heating is conservative and represents the upper limit of the estimated panel temperature.

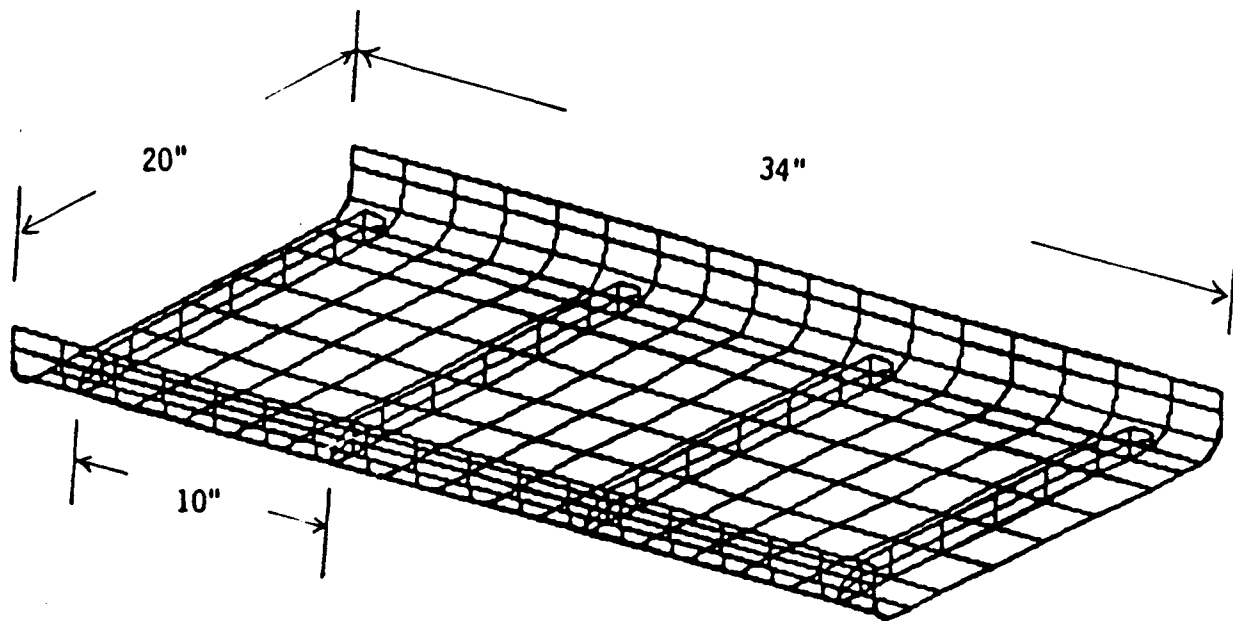


Figure 5-3. P/THERMAL Model of Ramp Panel.

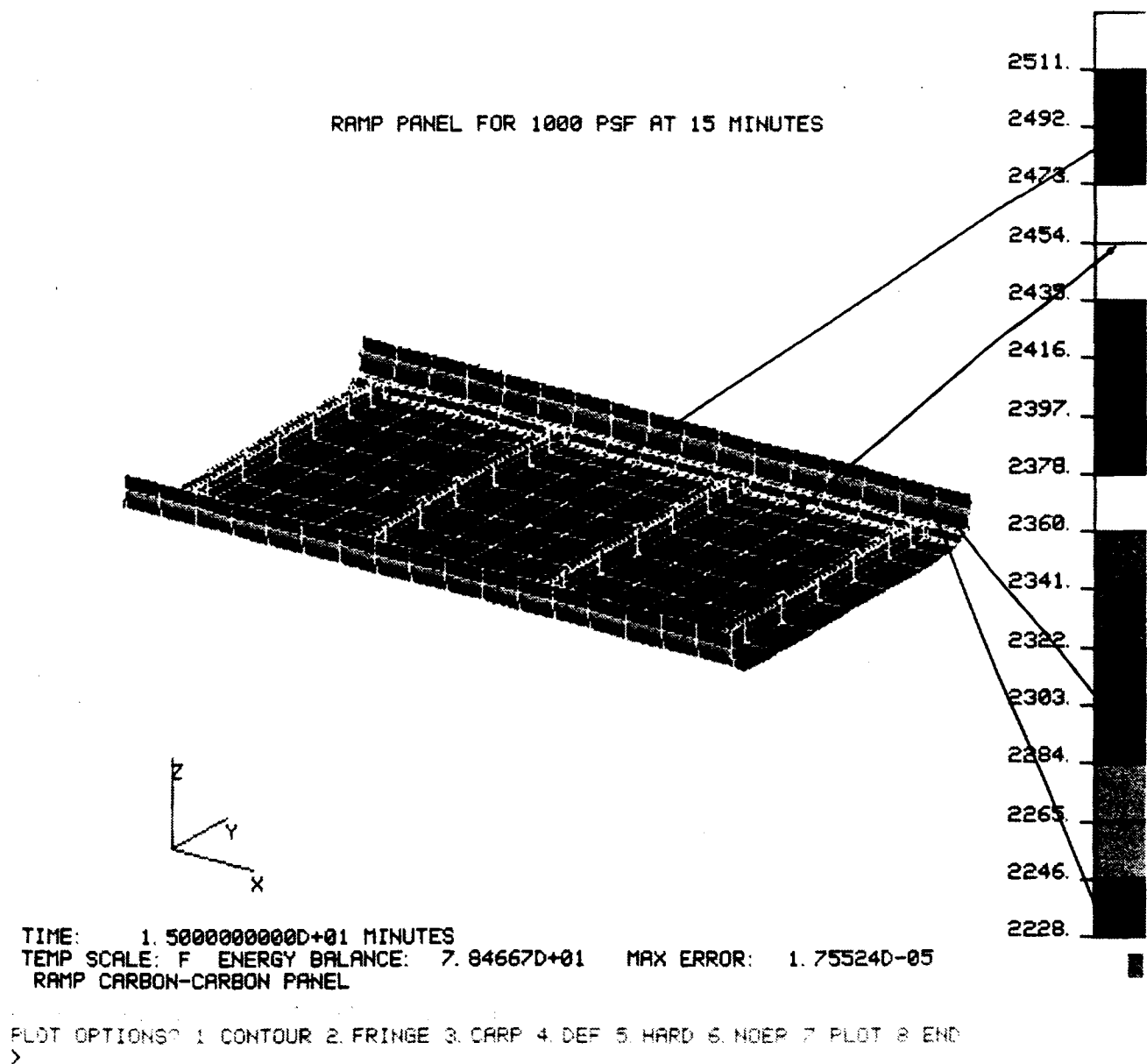


Figure 5-4. Ramp Panel Temperature Distribution for 1000 psf at 15 Minutes.

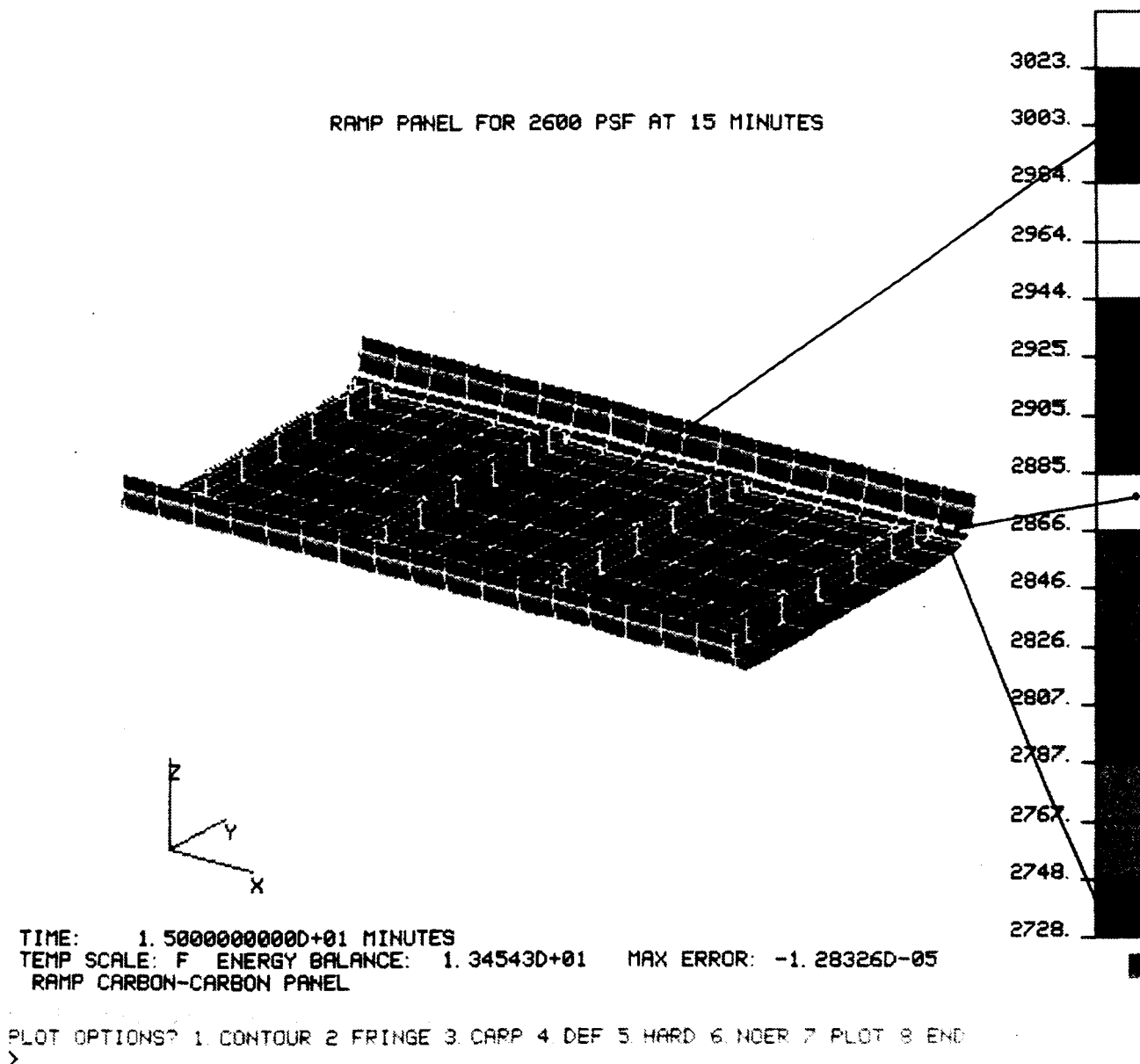


Figure 5-5. Ramp Panel Temperature Distribution for 2600 psf at 15 Minutes.

6-5

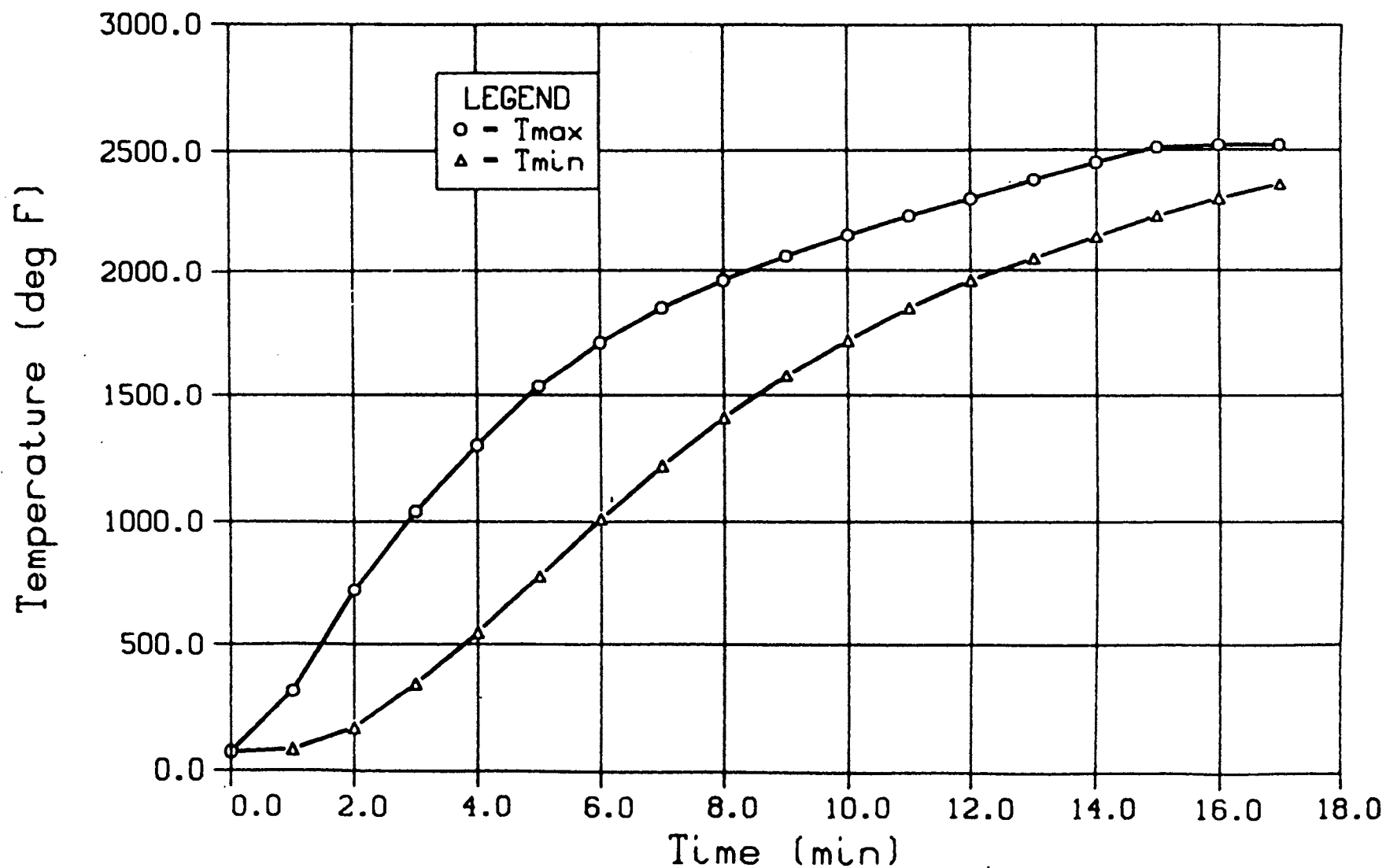


Figure 5-6. Ramp Panel Temperature Distribution for 1000 psf During Ascent.

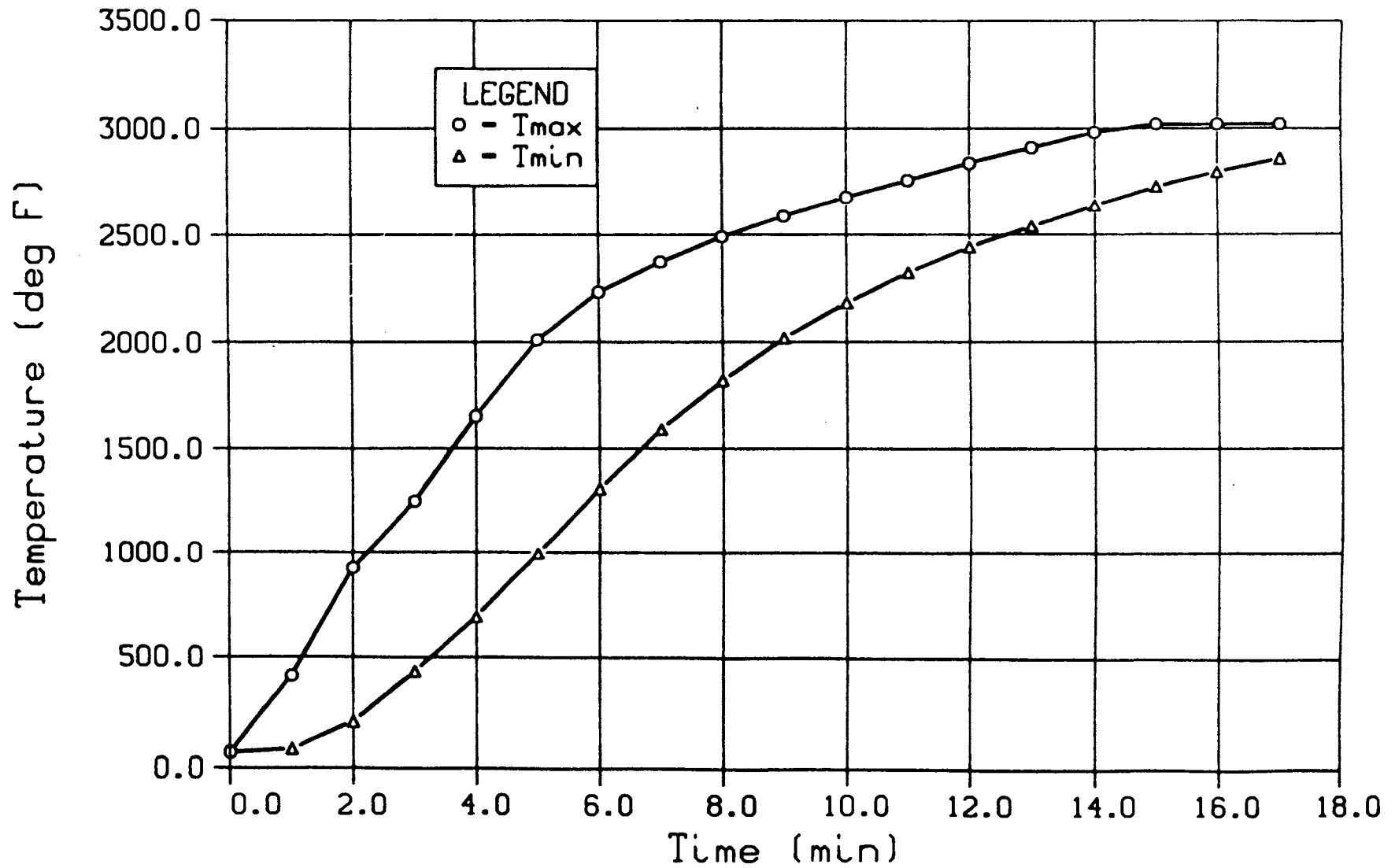


Figure 5-7. Ramp Panel Temperature Distribution for 2600 psf During Ascent.

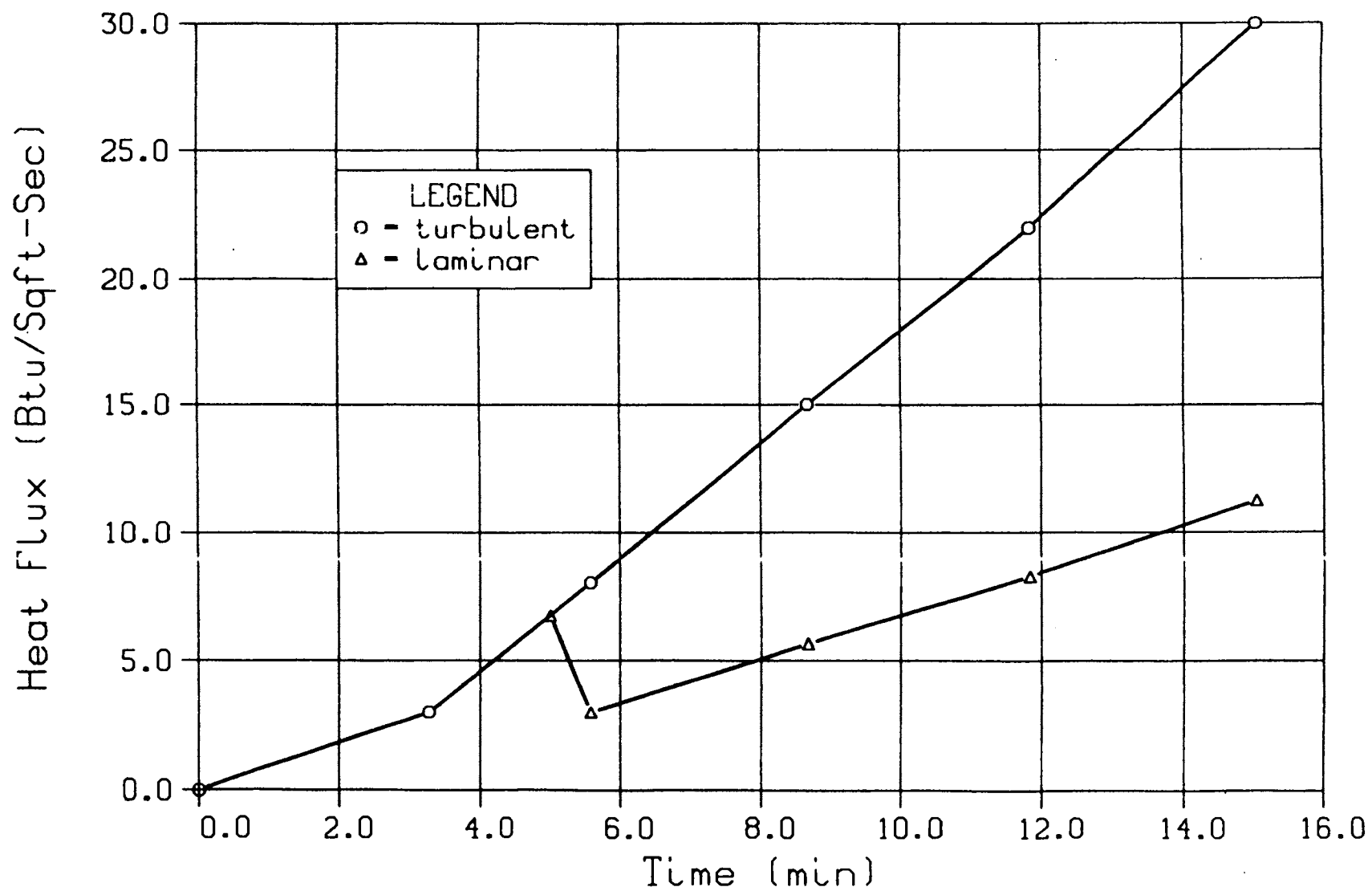


Figure 5-8. Ramp Panel Heat Flux Profiles for 1000 psf During Ascent.

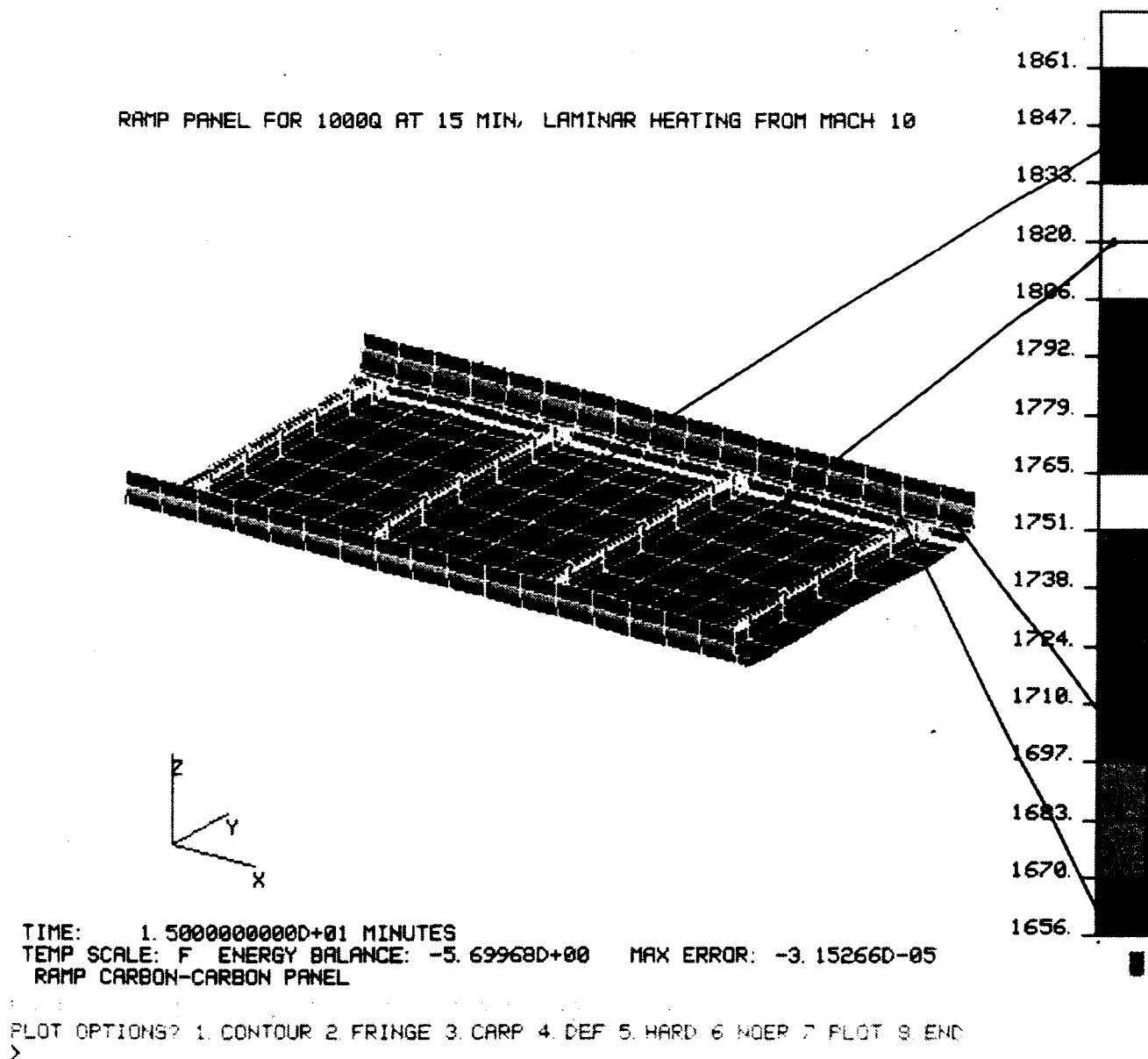


Figure 5-9. Ramp Panel Temperature Distribution for 1000 psf at 15 Minutes, Laminar Heating from Mach 10.

5-13

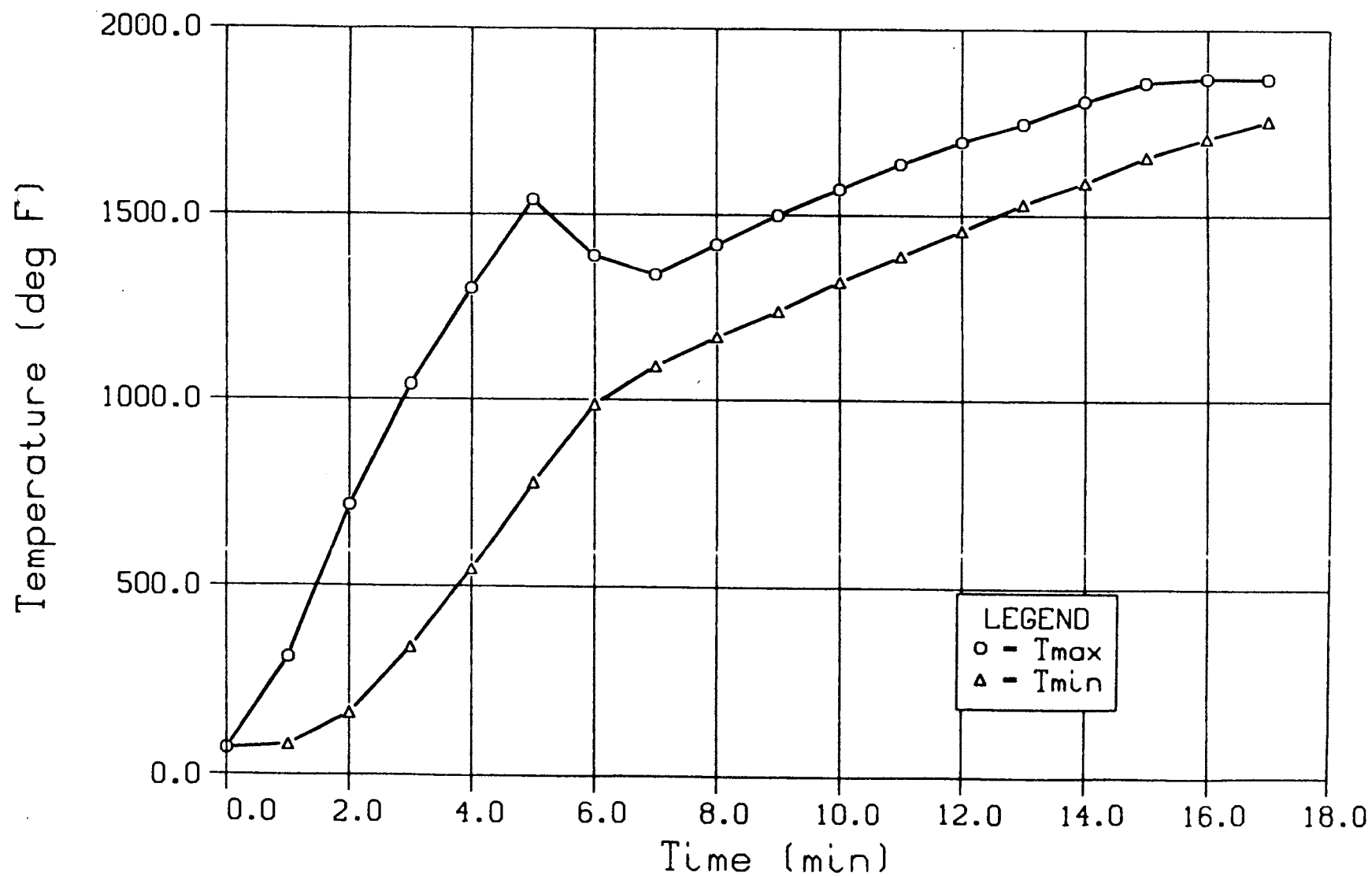


Figure 5-10. Ramp Panel Temperature Distribution for 1000 psf During Ascent, Laminar Heating from Mach 10.

5.3 STATIC STRESS ANALYSIS

5.3.1 Properties and Finite Element Model

An analysis was undertaken to evaluate the adequacy of the ramp panel design with respect to static loads. The analysis was performed by means of the NASTRAN finite element computer code.

A plot of the ramp panel finite element model is shown in Figure 5-11. The model was representative of a typical ramp panel with dimensions of 34 inches by 20 inches. The panel had four 1.25-inch stiffeners spaced 10.0 inches apart.

The model was subdivided into four regions, each with a different laminate layup configuration. These four regions, indicated in Figure 5-11, consisted of the blade stiffeners, the skin, the flanges, and the skin-flange transition. Laminate configurations for each region were selected to be consistent with laminate thicknesses prescribed on the engineering drawings. All the laminates were composed primarily of internal $0^\circ/90^\circ$ plies of carbon-carbon fabric, sandwiched between two outer plies of fabric oriented at 45° . The 45° fabric plies were included to increase buckling allowables. Laminate configurations for the ramp panel are given in Table 5-1. General laminate construction is illustrated in Figure 4-14.

The models were constructed exclusively using NASTRAN CQUAD4 quadrilateral flat shell elements. The elements were endowed with orthotropic membrane, bending, and transverse shear material properties which were assigned by means of PSHELL and MAT2 NASTRAN bulk data input. Laminate stiffnesses were calculated using basic lamination theory and Rohr-generated (unpublished) test data for carbon-carbon fabric laminates.

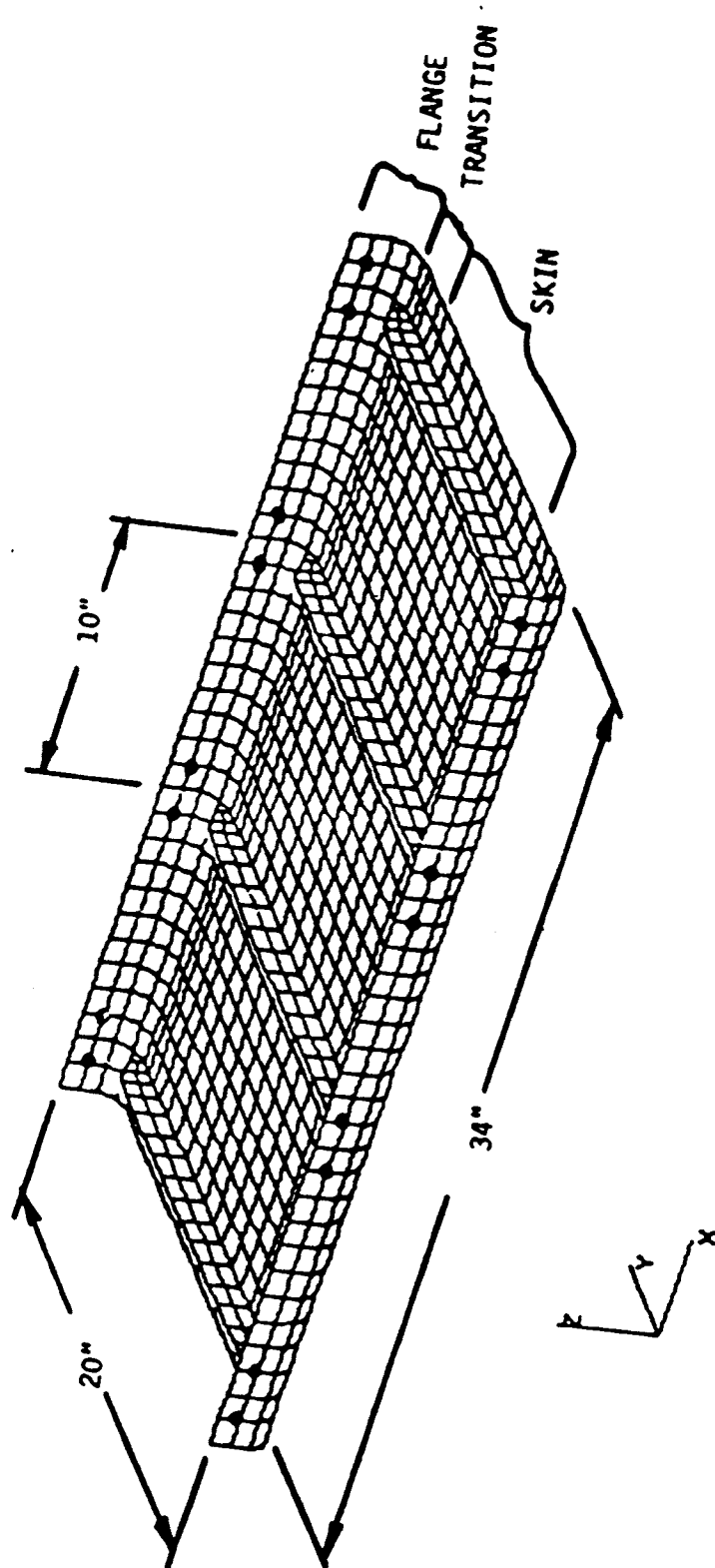


Figure 5-11. Ramp Panel NASTRAN Model.

Table 5-1. Laminate Layup Configurations for Ramp Panel.

Region	Layup
Flange	$(45^\circ, 0_{26}^\circ, 45^\circ)$
Skin/Flange Transition	$(45^\circ, 0_{14}^\circ, 45^\circ)$
Skin	$(45^\circ, 0_3^\circ, 45^\circ)$
Stiffeners	$(45^\circ, 0_2^\circ, 45^\circ)$

838PROP
3-T5-1.BB
12-11-89

5.3.2 Panel Loads and Constraints

The panel loads and constraints which were applied in the analysis are illustrated in Figure 5-12.

The ramp panel flanges are attached to the vehicle substructure by eight pairs of fasteners. The fastener locations are indicated in Figure 5-12. As in the forebody panel, vertical displacements and rotational degrees of freedom were constrained at those locations. These were the only constraints applied, with the exception of the node in the center of the panel. This node was fixed with respect to in-plane movement in order to eliminate free-body motion.

The ramp panel is subjected only to pressure and thermal loading. Pressures throughout the vehicle trajectory were provided by MDC as shown in Table 5-2. The peak pressure load occurs at Condition No. 5, for which the pressure is 1.25 psi. It was not possible, however, to determine accurate temperature conditions for this point in the trajectory. For this reason, Condition No. 3 was selected for the static analysis. In this case, the pressure is very nearly equal to the peak pressure ($P = 1.23$ psi) and the OML temperature is low enough to assume that there are no significant thermal effects.

5.3.3 Results

Strength analysis was performed on the ramp panel in a similar fashion to the forebody panel analysis. Figure 5-13 shows the deformed shape of the panel with the pressure-induced deflection clearly visible.

Von Mises stress contours are shown in Figure 5-14. The lowest margins of safety were found at the top of the blade stiffeners, where bending stresses were the greatest. The lowest margin of safety was 3.12. It can therefore be concluded that the ramp panel design is acceptable with respect to the applied load conditions.

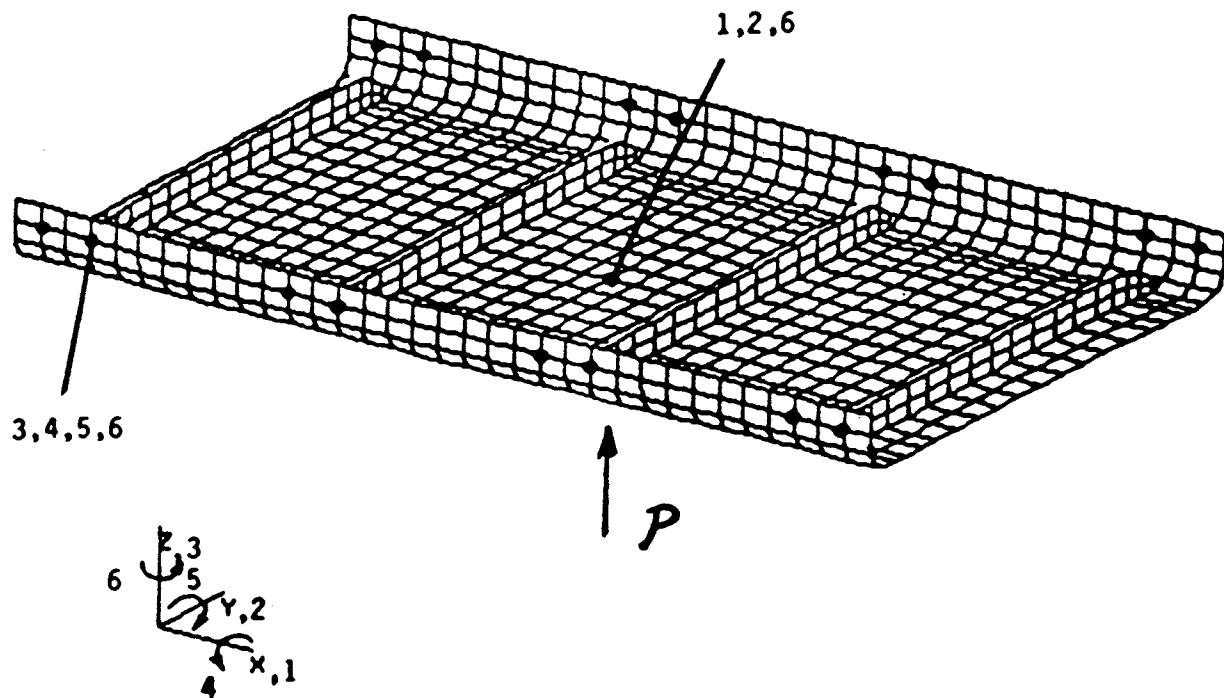
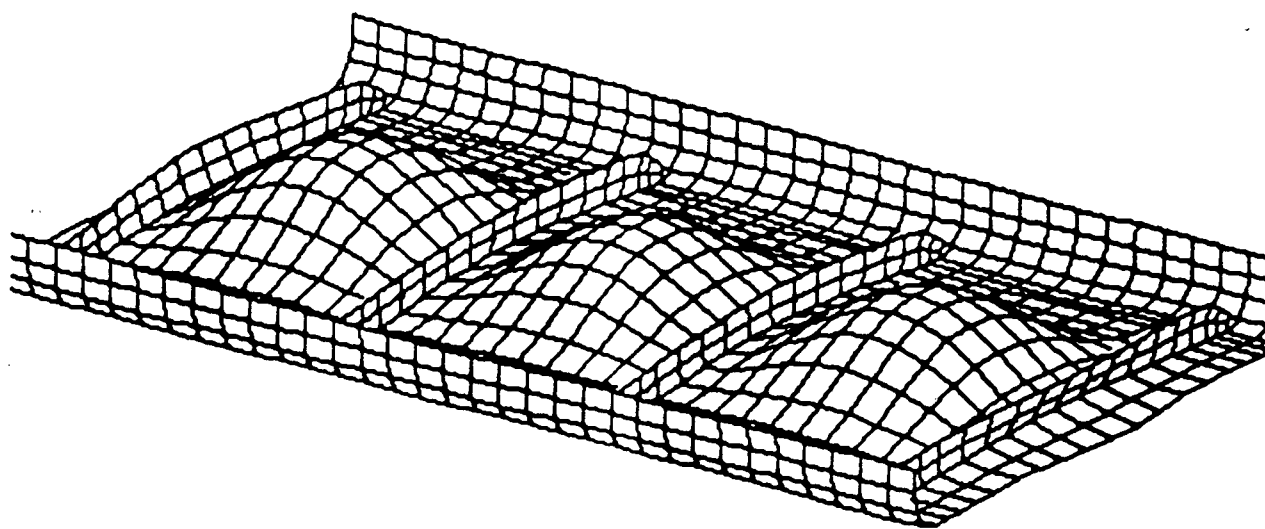


Figure 5-12. Ramp Panel Loads and Constraints.

Table 5-2. Ramp Panel Loads.

Load Condition	OML Temperature (°F)	Pressure (psi)
1	5	0
2	10	-0.56
3	50	-1.23
4	50	-0.25
5	320	-1.25
6	320	-0.47
7	1240	-0.88
8	1240	-0.37
9	1800	-0.35
10	1800	-0.12
11	690	0
12	690	0
13	950	0
14	950	0



CARBON/CARBON RAMP PANEL
LOAD CASE 9
COMBINED THERMAL/PRESSURE LOADS SUBCASE 12

Figure 5-13. Ramp Panel Deformed Shape.

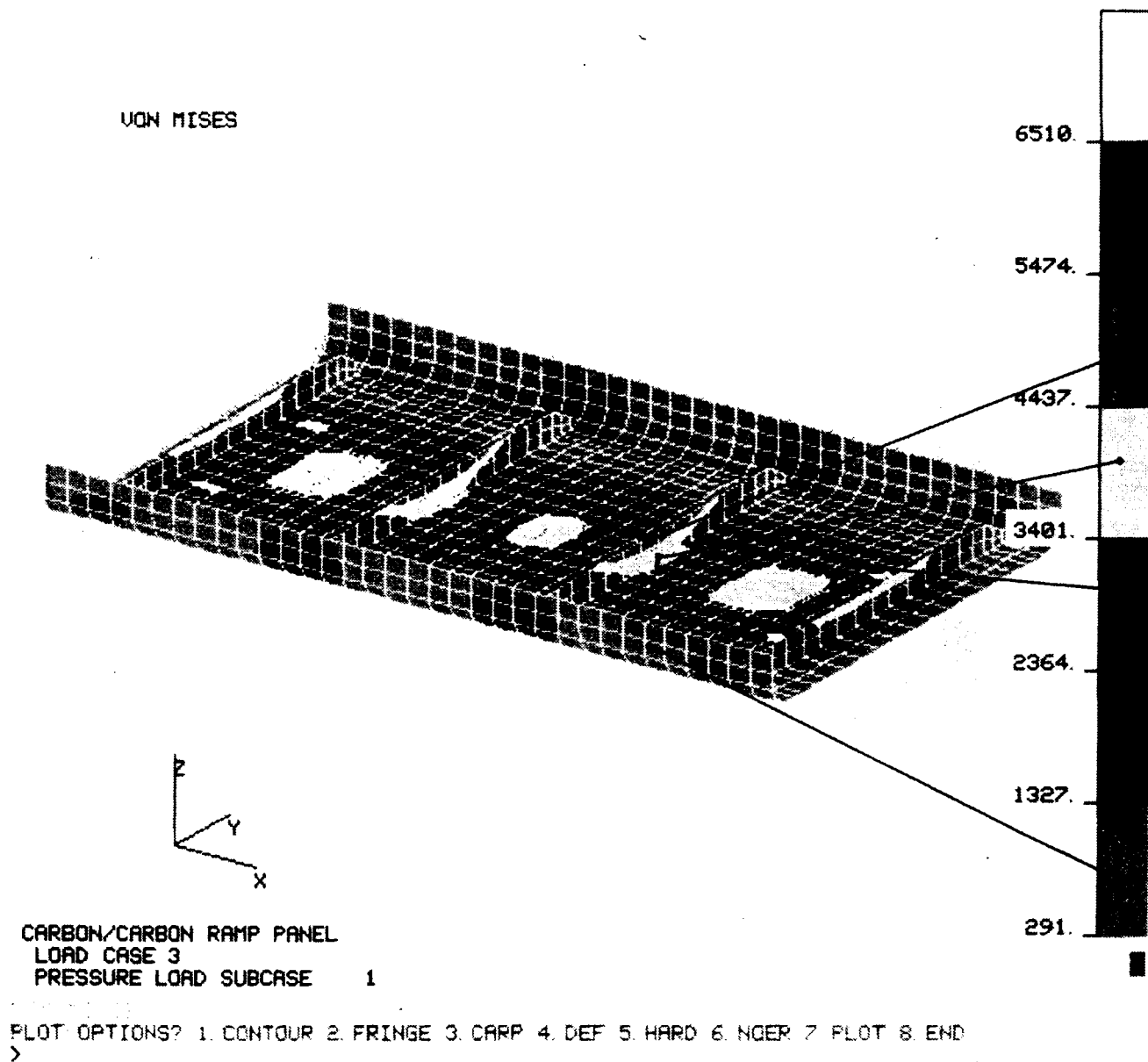


Figure 5-14. Ramp Panel Stress Contours.

The following conclusions were made from the static analysis:

- (1) The ramp panel design was found to be acceptable.
- (2) Buckling is not a concern for the ramp panel because it is not subjected to in-plane loads.

5.4 DYNAMIC ANALYSIS

5.4.1 Introduction

Modal and acoustic fatigue analyses of a typical ramp panel were performed in order to determine its modal characteristics and acoustic fatigue susceptibility. Both aeroacoustic and engine induced dynamic loading (Sections 2 and 3) were considered as well as the effect of mean loads. The dynamic analysis was made using MSC/NASTRAN in two stages: (1) modal analysis and (2) response analysis.

5.4.2 Modal Analysis

A complex static preload condition exists in the external vehicle skin panels. The primary effect of preload is to increase the mean stress about which the acoustically induced stress will oscillate. This will result in lower fatigue life for a given rms acoustic stress. A secondary effect of preload is to alter the natural frequencies of the skin panels. A compressive load will lower panel natural frequencies, while a tensile preload will increase frequencies. This affects overall panel response levels, as well as the number of load cycles the panel will accumulate. The normal modes analysis is carried out using NASTRAN. The natural frequencies and modal shapes are determined while including the appropriate stiffness corrections due to edge loads and pressures. Natural frequencies and modal shapes for the free stress state are also obtained in order to investigate the effect of preload. In incorporating the effect of preload on the structural behavior of the panels, the following operations are implemented in the finite element analysis: (1) load increment applications, (2) internal force equilibrium iterations,

and (3) element stiffness matrix updates. The element stiffness matrix updates reflect the sequential change in stiffness due to the applied loads. The solution algorithm is implemented by SOL 66 - NASTRAN (nonlinear static analysis). Once the updated stiffness matrices have been obtained, modal analysis is carried out using SOL 63 - NASTRAN (superelement normal modes) by fetching the required information from the data base.

The material model for carbon-carbon is idealized as orthotropic with transverse shear flexibility while excluding the effects of membrane-bending coupling and shear coupling. In addition, the stress-strain relationship is assumed to be linear and the effect of temperature on the stiffness properties is incorporated. The effect of temperature on the stiffness properties of carbon-carbon has been investigated experimentally, and results were reported in References [5-3]. However, the acquired data indicated appreciable scatter, precluding postulation of any reliable assumptions. It is speculated that the size of the glass particulates imbedded in the matrix for oxidation protection directly affects the flexural behavior at elevated temperatures. When the particulate size is relatively small and their spatial distribution is uniform, the effect of temperature remains modest. To avoid any erroneous disposition, it was decided that the stiffness characteristics remain unchanged at elevated temperatures, a conservative assumption.

The finite element model for the ramp panel is shown in Figure 5-15. The static preload case corresponds to a uniformly applied pressure of 1.25 psi. The effect of pressure on the natural frequencies was negligible. The first mode occurs at 94.1 Hz and exhibits the stiffness of the attachment mechanism. The second mode occurs at 258.5 Hz and corresponds to an out-of-phase mode. The in-phase mode occurs at 267.2 Hz. These modal shapes are graphically depicted in Figure 5-16. The corresponding modal stress fields are shown in Figure 5-17. The highest modal stresses are observed at the center of the outer bays for the out-of-phase mode and at the center of the midbay and the top of the two middle stiffeners for the in-phase mode.

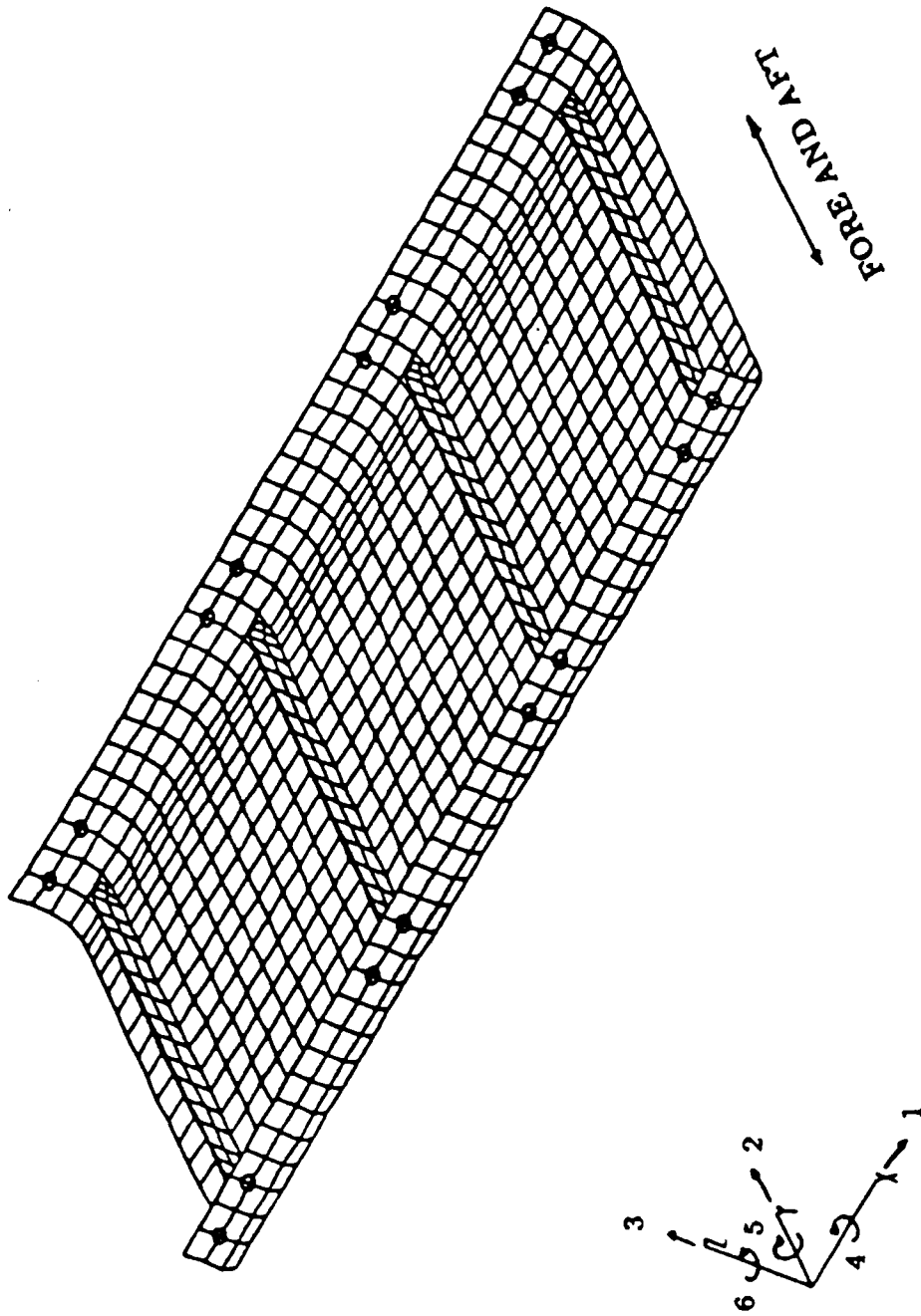
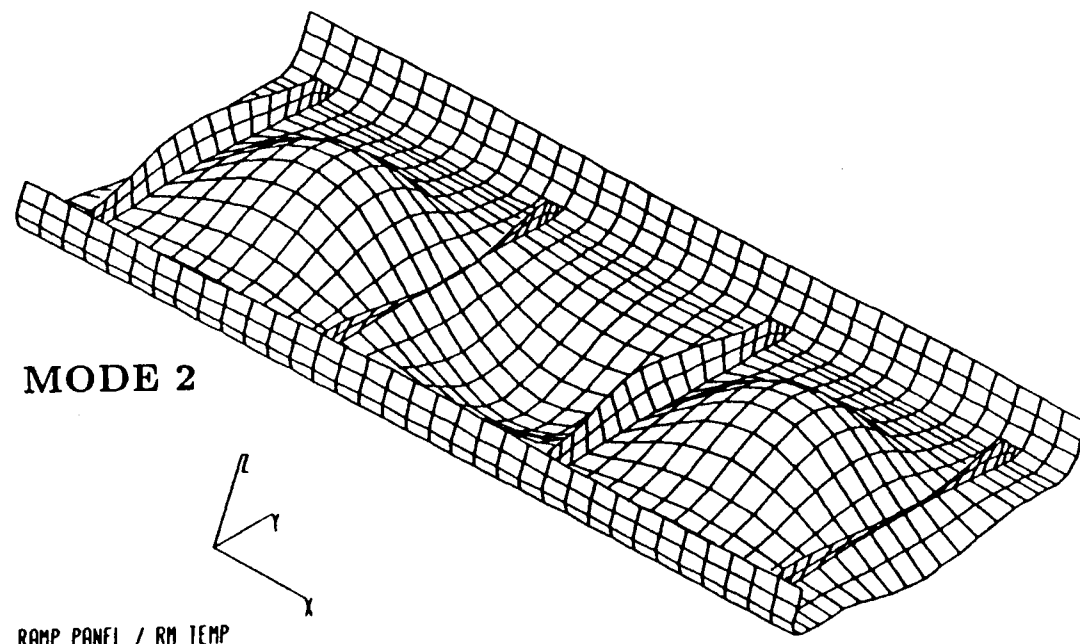
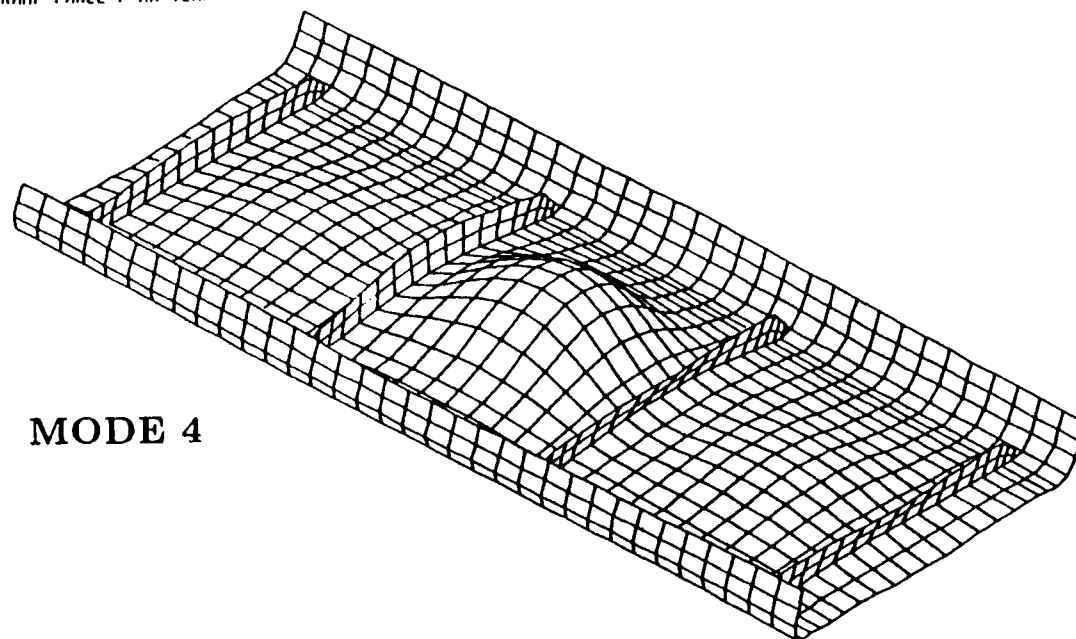


Figure 5-15. Ramp Panel Geometry and Boundary Conditions.



MODE 2

RAMP PANEL / RM TEMP



MODE 4

MODE NO.	CYCLES
1	9.410761E+01
→ 2	2.585276E+02
3	2.607168E+02
→ 4	2.672496E+02
5	4.228980E+02
6	4.231156E+02
7	4.648826E+02
8	4.866226E+02
9	4.970390E+02
10	5.094961E+02
11	5.108704E+02
12	5.867449E+02
13	6.672592E+02
14	7.040771E+02
15	7.103026E+02
16	7.697690E+02
17	8.489349E+02
18	8.551215E+02
19	8.774711E+02
20	8.828617E+02

Figure 5-16. Ramp Panel In-Phase and Out-of-Phase Modes for Flight Condition 2.

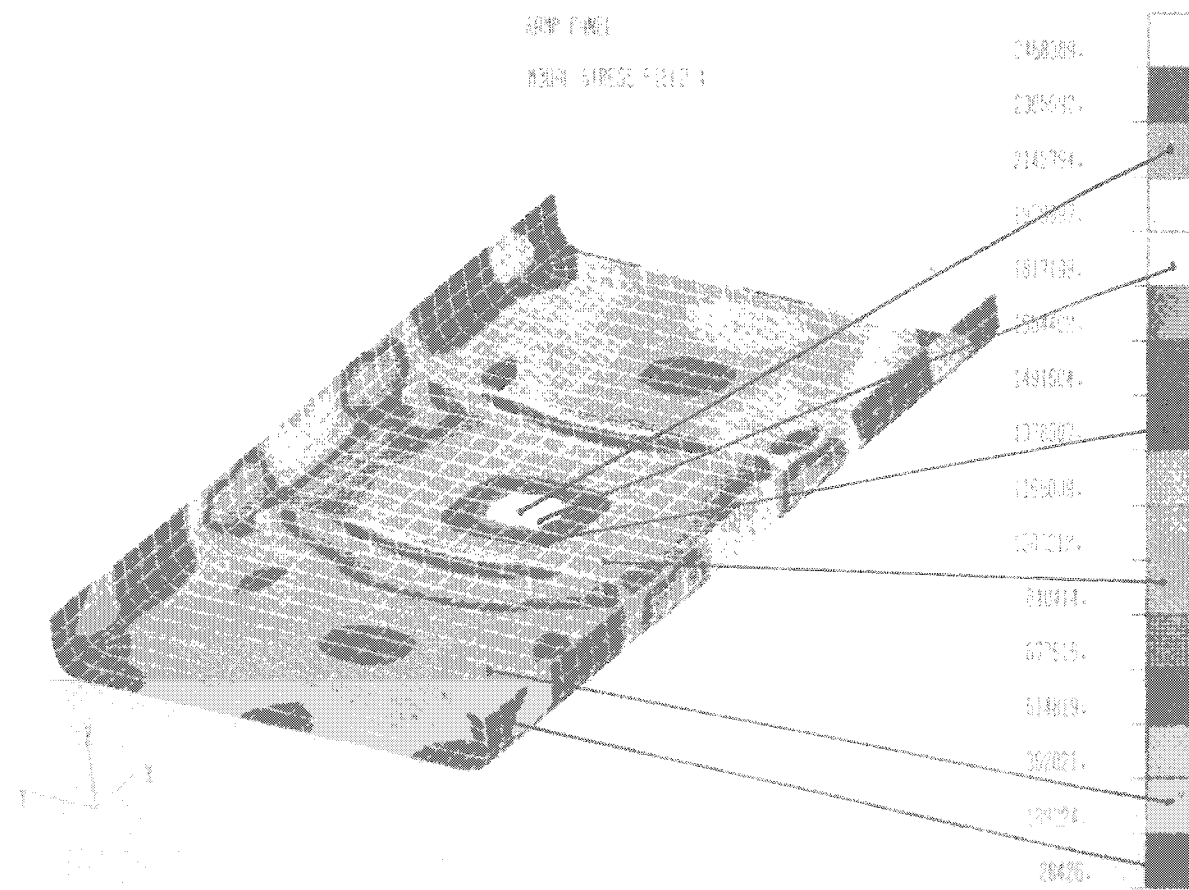
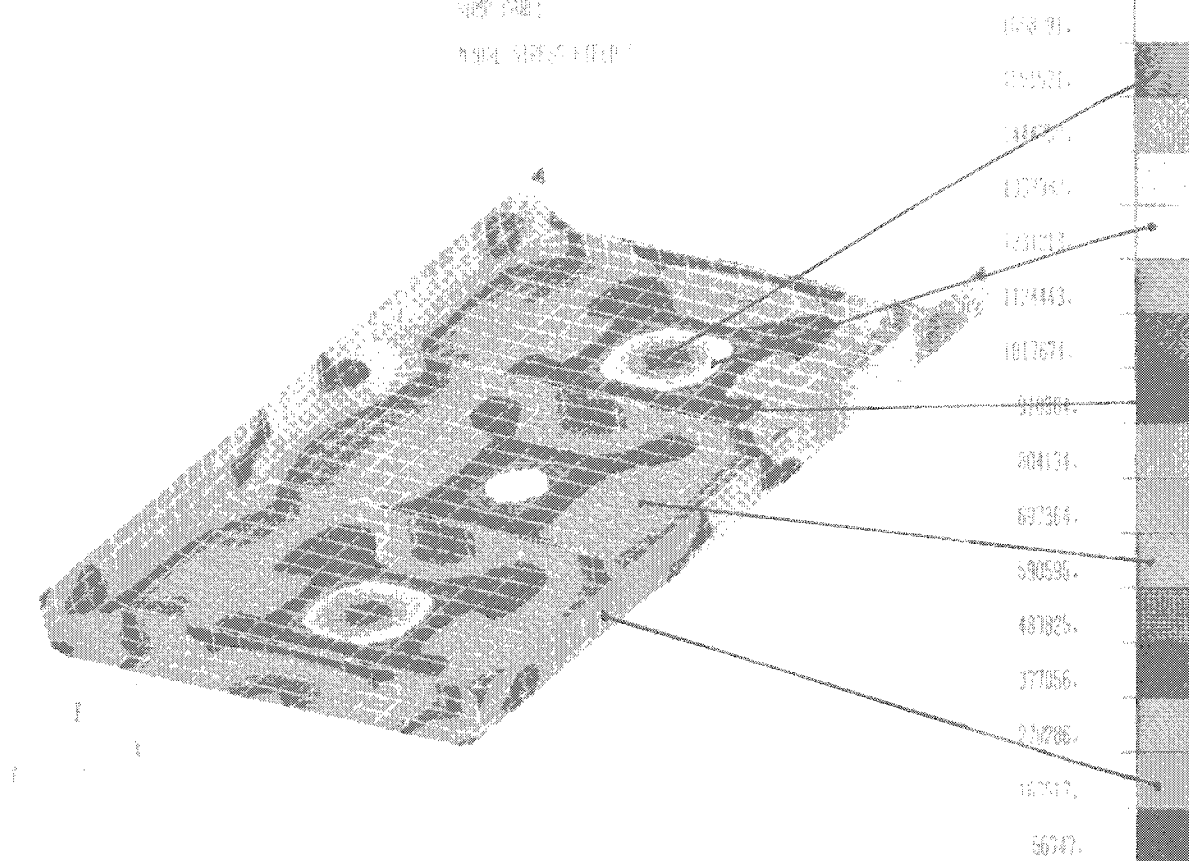


Figure 5-17. Ramp Panel Modal Stress Fields for In-Phase and Out-of-Phase Modes shown in Figure 5-16.

5.4.3 Sonic Fatigue Analysis

The sound levels in transatmospheric vehicles originate from boundary layer induced noise or from the rocket and scramjet engines. The noisiest section of the flight occurs during takeoff when both the rocket engines and the scramjet engine are operating. Combining the sound level of the rocket engines with that of the scramjet engine gives the sound pressure level during takeoff conditions. The results are shown in Figure 4-23. If it is assumed that the scramjet geometry allows the combustion and the internal noise to travel toward the inlet as well as toward the exhaust side, the estimated inlet noise for the various locations on the lower side of the vehicle is then as shown in Figure 4-24. The boundary layer induced noise for different Mach numbers as a function of vehicle location is shown in Figure 4-25. It is evident that the most severe case is that where the inlet noise and thus the one octave sound pressure levels for the ramp region are 160-170 dB.

The analytical approach used in determining the response and ultimately the fatigue behavior of panels exposed to the sound fields discussed earlier is an extension of Miles' work. The method uses the modal analysis results, i.e., normalized modal displacements and modal stresses, to obtain the load-deflection relationship. The effect of finite acoustic wavelengths on the panel response is incorporated through simultaneous consideration of spatial characteristics for both the structural modes and the sound field. Initially, the surface pressure distribution is approximated by the mass-weighted structural mode shape. For the fundamental mode of the panel, the estimate is similar to the assumption of uniform pressure. The advantage of this assumption is that it tends to produce a conservative estimate for each mode and the measure of spatial correlation (joint acceptance) between modal and acoustic fields is rendered unity. The accuracy of this approximation depends on the degree to which the mass-weighted mode shape reflects the actual pressure field shape. However, improvements to that joint acceptance estimate are developed which do not require detailed modeling of the acoustic field or numerical integration. This improvement is based on the relation between the structural and acoustic wavelengths. Thus,

after a mode-by-mode evaluation of sonic stresses is performed initially, the joint acceptance correction detects and adjusts underpredicted and/or overpredicted sonic stress estimates. Finally, the overall stresses are obtained by summing the squares of contributions of the individual modes. A more detailed presentation of the analytical procedure is given in Reference [5-4]. Once the acoustically induced stresses have been determined, a direct comparison with available random fatigue data provides estimates for the number of mechanical cycles that can be sustained.

Random fatigue data for uncoated (HTC) carbon-carbon bar specimens are shown in Figure 4-26. Data are included for specimens with various types of inhibitors as well as uninhibited ones. All specimens were made from 3K tow T-300 carbon fabric heat treated to 2150°C (3900°F). Fiber volumes for the inhibited, filled specimens ranged from 42% to 48%. The fillers were added to the phenolic prepregging resin in particulate form. All panels were densified using four cycles of 50-50 pitch-funaldelyde impregnation to a target porosity of less than 5%. To prevent reaction of the fillers with the fibers, the graphitization temperature was limited to 1650°C (3000°F). For infinite life (10^8 cycles), the lower fatigue limit is approximately 6000 psi and the upper limit is 12,000 psi.

Sonic stress levels for the ramp panel were estimated similarly to the forebody stress levels and are depicted in Figure 5-18. The maximum stress level due to combined exhaust and inlet noise for a one-third octave level of 165 dB is approximately 21,000 psi at 855 Hz. For exhaust noise only and a one-third level of 138.25 dB, the maximum sonic stress is about 800 psi. When the joint acceptance improvement is employed, then the rms stress levels are as shown in Figure 5-19, with a maximum value of 16,081 psi. The highest stresses are observed on the upper side of the middle stiffeners and the center of the middle bay. The analytically obtained stresses exceed the fatigue allowable, and therefore the anticipated fatigue life would not satisfy design requirements.

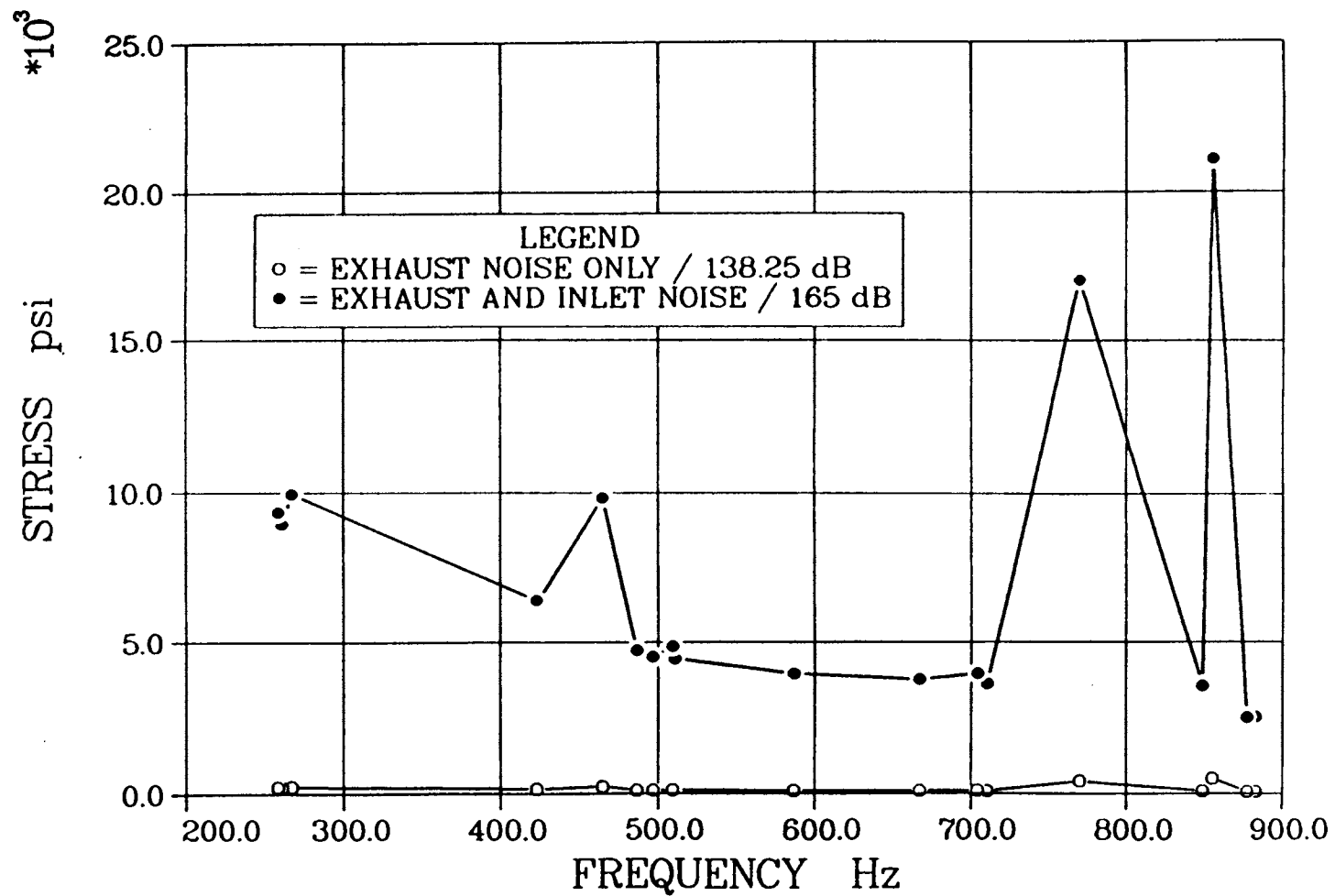


Figure 5-18. Sonic Stress Levels at Ramp Panel.

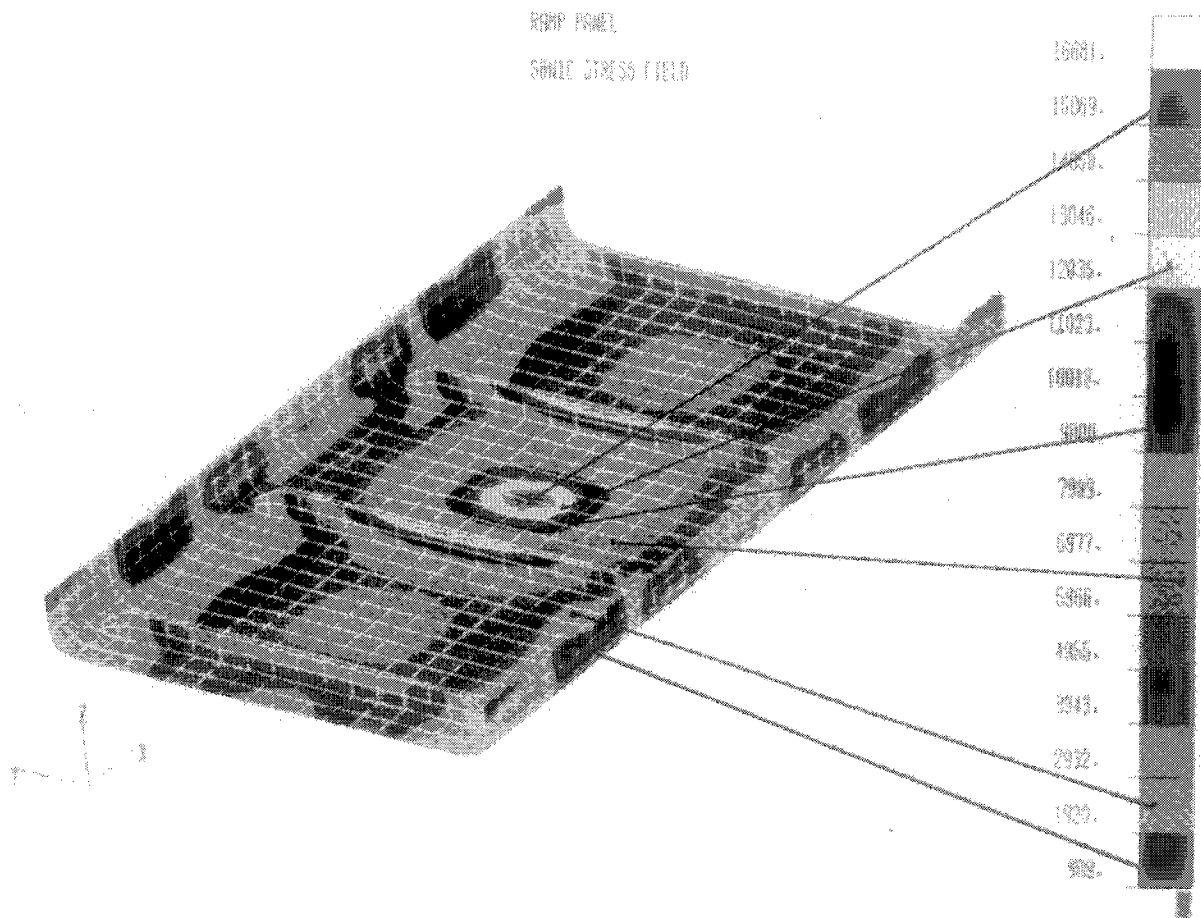


Figure 5-19. Ramp Panel Carbon-Carbon Sonic Stress Field with Effect of Joint Acceptance Included.

5.5 RESULTS

Thermal, static stress, and dynamic analyses have been made of the carbon-carbon ramp panel.

The thermal analysis shows:

- (1) The maximum skin temperature at end of ascent is 2510°F for the 1000 q_{∞} ascent and 3023°F for the 2600 q_{∞} ascent. These results are based on turbulent heating. If a laminar boundary layer exists, the maximum temperature could be 700°F lower.
- (2) The maximum temperature difference between fastener locations on the panel edges is 800°F. The temperature difference through the skin thickness is negligible.

The following conclusions were made from the static stress analysis:

- (1) The ramp panel design was found to be acceptable.
- (2) The results of the analysis were dependent on the boundary conditions that were assumed. The assumptions made were considered to be reasonable, but further investigation might pursue the influence of boundary conditions on panel stresses and margins of safety.
- (3) Buckling was not found to be a concern for the ramp panel.

The dynamic analysis shows:

- (1) The maximum stress level due to inlet noise for a one-third octave level of 165 dB is approximately 21,000 psi at 855 Hz. When the joint acceptance improvement is employed, the maximum rms stress is 16,081 psi.

- (2) The highest stresses are observed on the upper side of the middle stiffeners and the center of the middle bay. The analytically obtained stresses exceed the fatigue allowable, and therefore the anticipated fatigue life would not satisfy design requirements.

5.6 REFERENCES

- 5-1 P/THERMAL User Manual, PAD Engineering, July 1988.
- 5-2 MSC/NASTRAN Version 66, The MacNeal-Schwendler Corporation, 1988.
- 5-3 Gray, P.E., et al., The Effect of Temperature on the Flexural Modulus of Carbon-Carbon, 13th Conference on Ceramic and Carbon-Carbon Composites, Cocoa Beach, Florida, January 20-22, 1987.
- 5-4 Blevins, R.D., "Approximate Methods for Sonic Fatigue Analysis of Plates and Shells," Journal of Sound and Vibration, Vol. 129, pages 51-71 (1989).

838PROP
3-5.BB
12-11-89

SECTION 6

ANALYSIS OF STABILIZER PANEL

6.1 INTRODUCTION

The vehicle horizontal and vertical stabilizers are fabricated from corrugation-stiffened panels separated by I-section spars. The horizontal stabilizer upper surface structural concept consists of single-faced corrugated skin panels fabricated from advanced titanium metal matrix composite attached to underlying titanium matrix composite sine wave spars and ribs. The skin panels are approximately 74 inches by 36 inches with 43 stiffeners per panel. Advanced titanium matrix composites were chosen for this application because of their mechanical properties at use temperatures. Like the midbody and aftbody, the horizontal stabilizer upper surface requires high stiffness to resist local panel buckling.

The detailed dimensions of the horizontal stabilizer upper skins are shown in Figure 6-1. Based on preliminary design, the titanium matrix composite face sheet is 0.030 inch thick. Corrugations are on 1.7-inch centers and are 2.5 inches in height. All welds and flanges are 0.015 inch thick, minimum gage for this material. The design concepts and details of the horizontal stabilizer lower surface and vertical stabilizer surfaces are similar to those of the horizontal stabilizer upper skin.

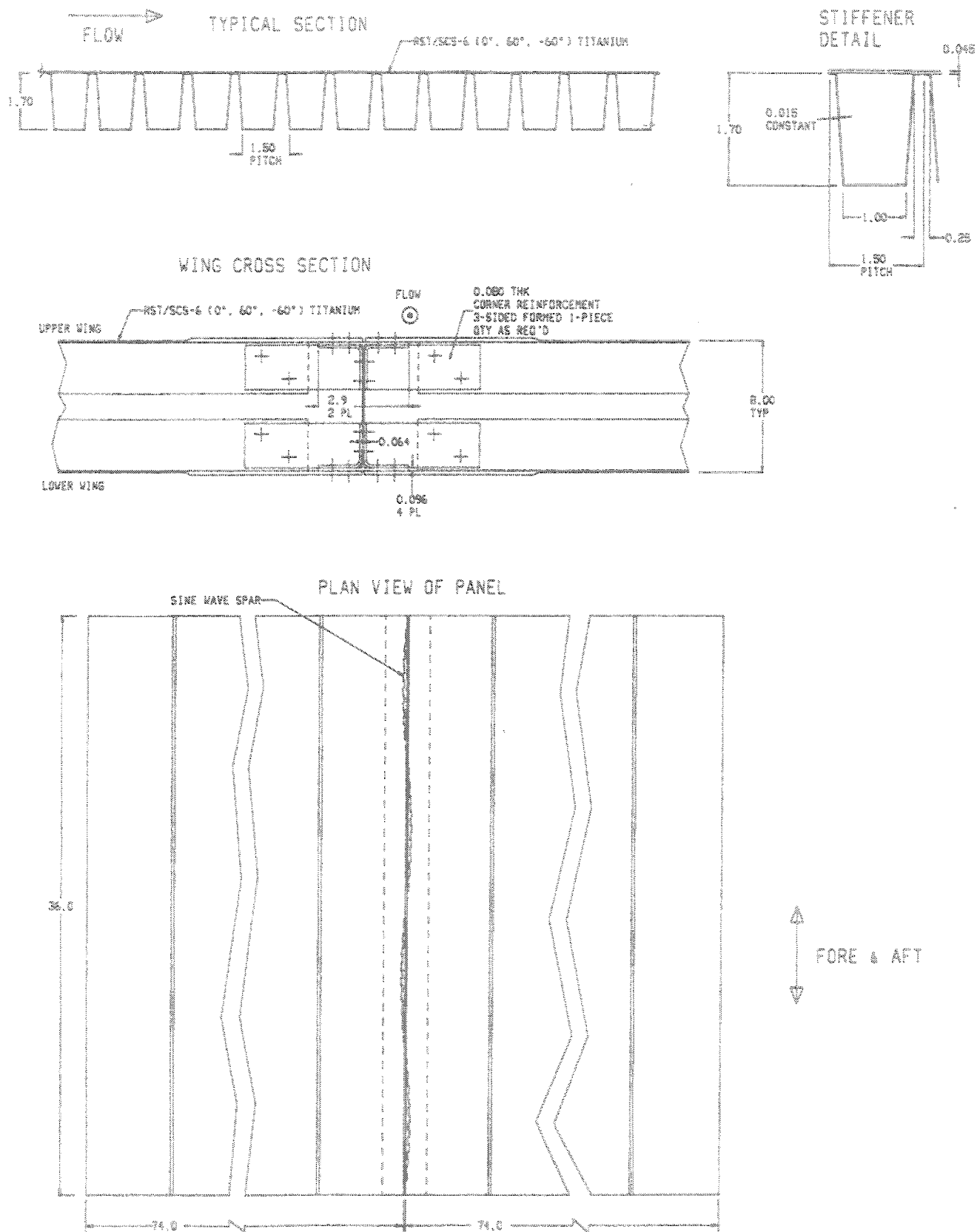


Figure 6-1. Horizontal Stabilizer Skin Panel Located 90 Feet Aft of Nose.

6.2 LOADING ON HORIZONTAL STABILIZER PANEL

The loading on the horizontal stabilizer panel originates from four sources:

- (1) Carry-through loads associated with thermal and mechanical loads on the horizontal stabilizer as a whole. These loads are given in Table 2-4.
- (2) Aerothermal loads associated with the turbulent boundary layer. These are given in Figures 2-17 through 2-21 corresponding to $x/R_N = 240$.
- (3) Shock interaction loads due to interaction of the bow shock with the horizontal stabilizer at high Mach numbers and interaction with the shock from the vertical stabilizer. These loads are given in Table 2-2.
- (4) Engine acoustic loads. These acoustic pressures are given in Tables 3-6 and 3-7 and Figures 3-12 and 3-13.

In reviewing these loads, it can be seen that the overall aeroacoustic load at Mach 10 is 128 dB at $Q = 1000 \text{ lb/ft}^2$ and 135 dB at $Q = 2600 \text{ lb/ft}^2$. Table 2-4 shows that the inplane carry-through loads are significantly higher than for the forebody panel and much higher than for the ramp panel; hence, panel buckling is a concern. Figures 2-17 and 2-18 show that heating rates for attached boundary layer flow at 2 to 5 Btu/ft²/sec are a factor of 5 lower than for the forebody and ramp panels, which implies that temperatures will be greatly reduced, indicating that the use of metallic structure is justified.

The greatest loads imposed on the horizontal and vertical stabilizers are associated with engine acoustic loads and shock interaction loads. Figures 3-12 and 3-13 show that engine noise can induce maximum acoustic pressures from 160 to over 170 dB for those surfaces which are in the line of sight from the engine exhaust.

As noted in Sections 2.5.3 and 2.5.4, it is possible for the bow shock to intersect the horizontal stabilizer at speeds in excess of Mach 10. By reviewing these loads from Table 2-2, it can be seen that peak oscillating shock pressure is approximately 1.5 psi, which corresponds to 175 dB, well in excess of the turbulent boundary layer pressures. The maximum shock heating is over 100 Btu/ft²/sec, roughly a factor of 20 higher than the turbulent boundary layer heating and higher than the heating rates on the forebody and ramp panels, which result in temperatures in excess of 2500°F. The width of the shock interaction region is expected to be comparable to the boundary layer thickness, approximately 0.1 foot. Thus, shock-boundary layer interaction on the horizontal or vertical stabilizer surfaces could lead to local hot spots with heating rates that have the capability of melting their metallic skins unless active cooling is provided.

838PROP
3-6.BB
12-11-89

SECTION 7

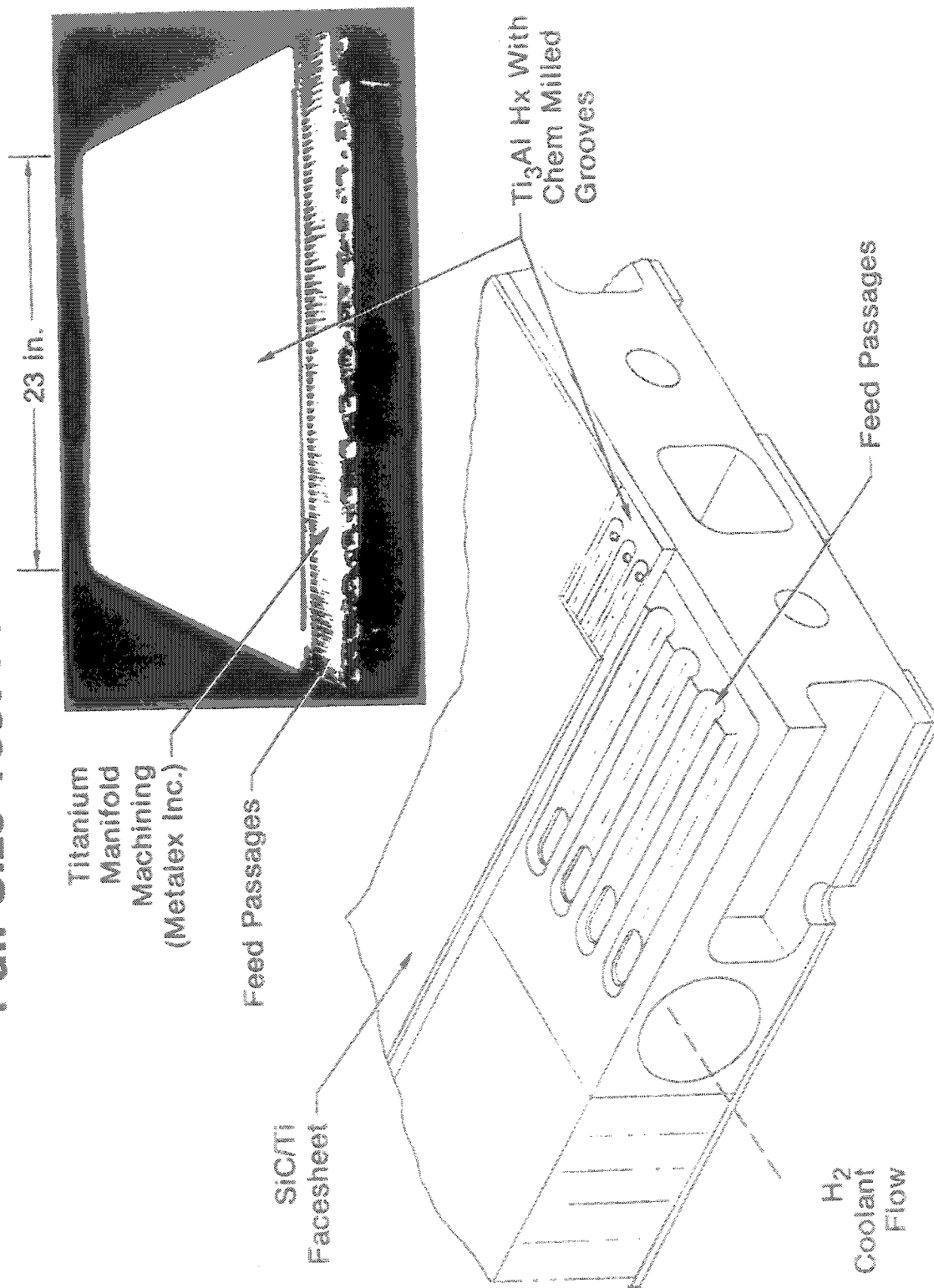
ANALYSIS OF ACTIVELY COOLED PANEL

7.1 INTRODUCTION

The actively cooled panels located in the nozzle region of a generic transatmospheric vehicle were analyzed for response to the thermoacoustic environment. A typical actively cooled structural panel consists of a complex arrangement of titanium matrix composite materials which carry hydrogen coolant to dissipate the high heat flux associated with engine combustion. These panels are described in Section 1 and the following paragraphs.

A typical panel cross-section is shown in Figure 7-1. The inner and outer face sheets are thin, titanium matrix composite (TMC) laminates. The outer face sheet is bonded to a heat exchanger (HX) consisting of a monolithic sheet of titanium having a series of grooves running along its length. The face sheets and heat exchanger are bonded to a titanium honeycomb core to form the basic sandwich structure. Heavy, machined monolithic titanium manifolds are bonded to each end of the sandwich. The manifolds have machined holes which accommodate fasteners for mechanical joining of the panels to both the substructure and adjacent panels. Cryogenic hydrogen is introduced through the center of the input manifold into machined feeder passages which meter the coolant into the heat exchanger. The hydrogen flows down the length of the panel in the parallel grooves of the heat exchanger, removing excess heat from the outer face sheet. The hydrogen exits the panel in the reverse manner through a manifold located at the opposite end.

Full Size Test Panel Hardware



7-2

Figure 7-1. Typical Panel Cross-Section.

The vehicle nozzle structure consists of many individual panels fastened together to form the exterior moldline surface. Individual panel geometries are optimized to the local thermomechanical environment by varying ply thickness, orientation, and face sheet separation distance. The present study focused on two typical panels having distinctly different geometries due to their local environments.

The analysis considered both the static thermomechanical and dynamic acoustic responses. A two-stage process was employed to evaluate the fatigue life of the panels. First, the panels were evaluated over the entire vehicle mission trajectory using approximate, classical techniques. The resulting responses were used in a simple fatigue model to identify critical load conditions.

The second stage involved detailed structural modeling using finite elements. The critical loads identified in stage one were used to drive the models and refine response predictions. These responses were fed into the fatigue model to evaluate panel life.

7.2 PANEL GEOMETRY

The panels are sized to minimize unit area weights. Panel dimensions are optimized based on combined static thermomechanical loads obtained from a full transatmospheric vehicle structural model. The loads are used as input to a honeycomb panel optimization program which determines structurally acceptable geometry having the lowest weight. The program analyzes a specific range of face sheet materials, thicknesses, ply orientations, honeycomb properties, and sandwich depths to obtain the minimum weight honeycomb structure that will carry the static loads. Panel analyses include face sheet strength, panel buckling, core dimpling, and delamination.

The panels are attached end-to-end with threaded fasteners through the manifold machinings. Thus, the "hot" edge of a panel is in contact with the "cold" edge of the next panel in line, down the length of the actively cooled surface. The manifold also provides a slotted hole for

attachment to the substructural framework. The slots allow the panels to slide relative to the substructure and minimize loads resulting from differential thermal growth.

Two typical panels were selected for evaluation. The first panel is located 15 feet aft of the engine combustor where high in-flight thermomechanical loads occur. The second panel, only 7 feet aft of the combustor, is in the area of peak acoustic loading. Specific panel geometries are shown in Figure 7-2.

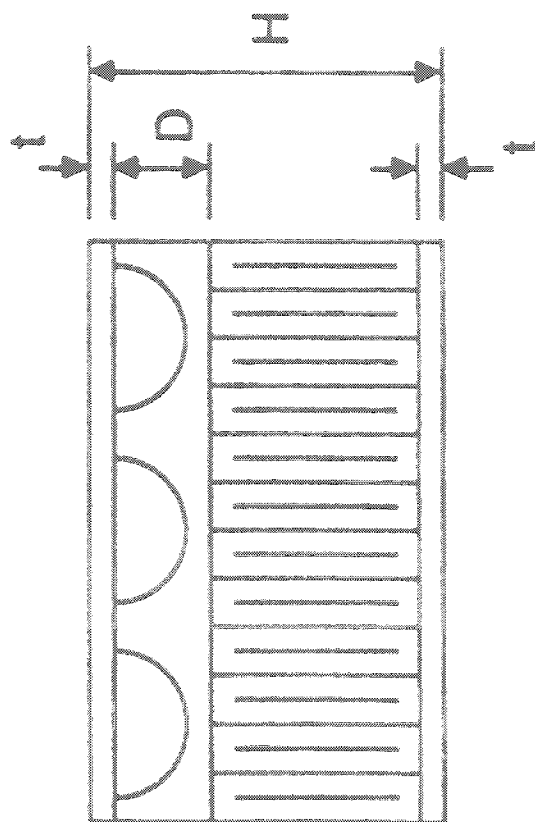
7.3 VEHICLE LOADS

Vehicle loads were predicted for 14 conditions representing critical points in the flight trajectory, including taxi, ascent, cruise, and descent. For both panels the local thermomechanical forces, acoustic pressure, and through-thickness temperature gradient for each condition were determined. A summary of the screening loads is shown in Appendix C, Figures C-1 through C-6.

The thermomechanical loads were supplied by MDC and are based on a linear NASTRAN finite element model of a specific vehicle configuration. The model includes effects of flight maneuvers, aerodynamic surface pressures, and thermal growth due to unequal vehicle heating.

A typical set of loads is shown in Figure 7-3. The panels are designed so that vehicle loads are transferred as membrane loads through the TMC face sheets. Bending moments in the panel are induced only by the aerodynamic pressures on the external panel skins. The relative magnitude of the membrane forces will be much greater than the bending moments since local aerodynamic forces are small. Thus, the panels are designed as membrane elements which transfer forces biaxially.

Panel heating results from expansion of the engine combustion gases along the lower surface of the vehicle. The heat fluxes associated with the exhaust flow drop off dramatically (Figure 7-4) down the length of the nozzle surface from a peak $250 \text{ Btu/ft}^2\text{-sec}$ at the combustor exit to



	PANEL 1 (15' AFT)	PANEL 2 (7' AFT)
OVERALL	48" x 48"	48" x 48"
t (in)	.016	.016
H(in)	.830	1.080
D(in)	.080	.080
Wt(lb)	42.4	51.7

Figure 7-2. Panel Geometries Used in Thermoacoustic Response Analysis.

MACH 10 PULL-UP, 15 FT. AFT

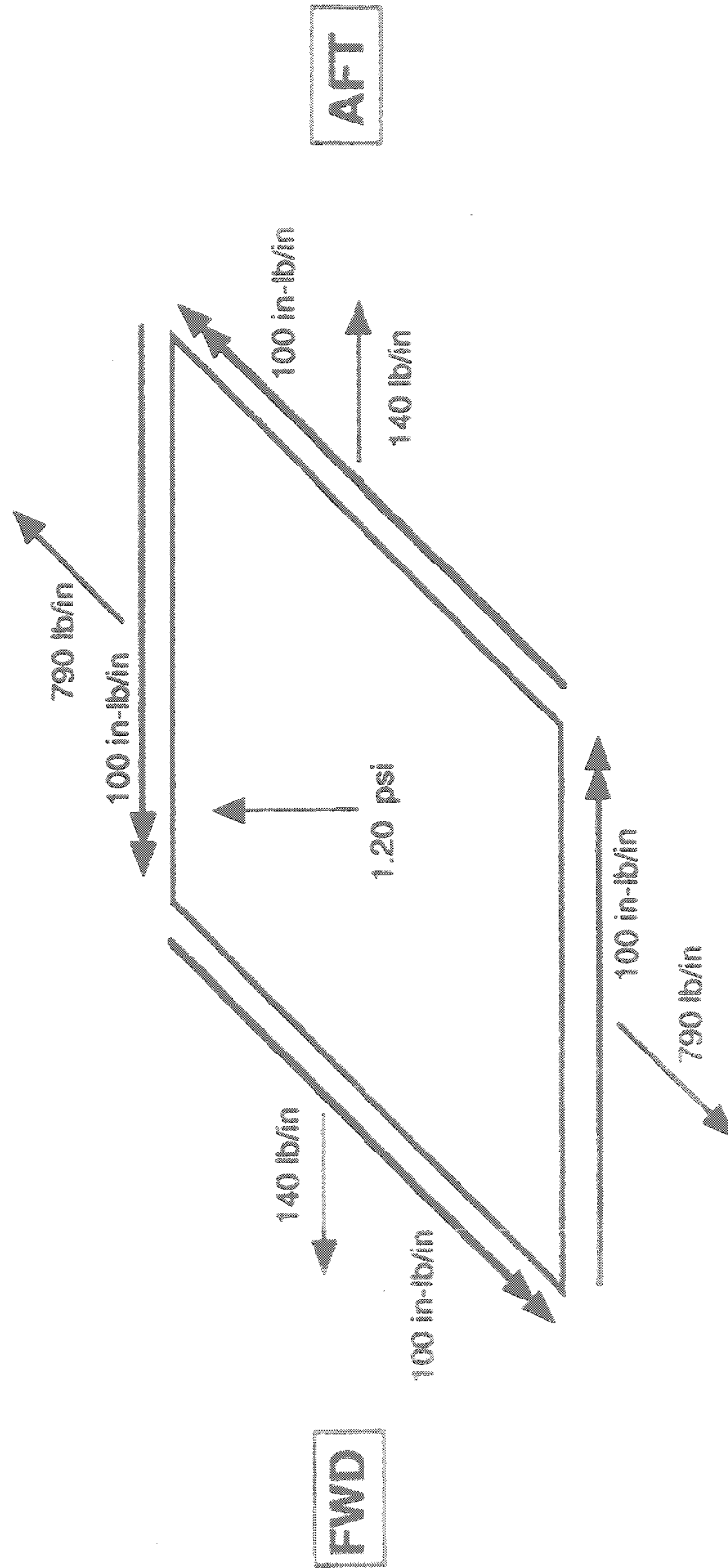


Figure 7-3. Typical Vehicle Loads.

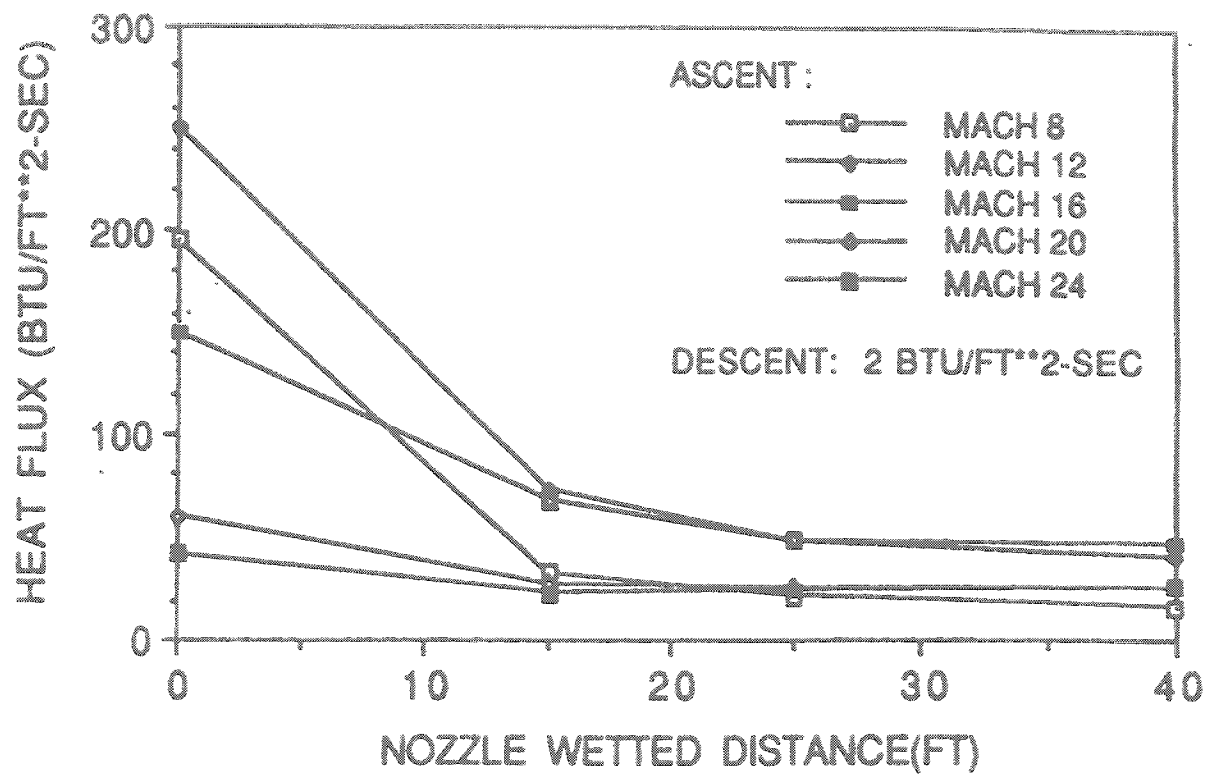


Figure 7-4. Nozzle Heat Flux Envelope.

less than 50 Btu/ft²-sec at the aft edge of the lower vehicle surface. These fluxes were used to determine the thermal gradient through the panel thickness.

The through-thickness thermal gradient was evaluated using a 2D finite difference model. The model (Figure 7-5) was used to evaluate three areas of the panel: near the inlet manifold, the center of the panel, and near the exit manifold. Temperature distributions were computed for heat fluxes of 30 to 180 Btu/ft²-sec representing the range of fluxes that the panels will experience (Figure 7-4).

The acoustic pressures were determined from flow analysis over the vehicle. Noise generated by both the scramjets and supplemental rockets was considered and is described in detail in Section 3 of this report.

7.4 PRELIMINARY ANALYSIS

The first stage of the analysis involved preliminary fatigue screening of the two actively cooled panels using approximate, classical techniques. All 14 conditions were evaluated. The resulting static and dynamic stress responses were input to a simple fatigue model to determine critical load conditions.

For screening it was assumed that all load is taken up in the face sheets. The thermomechanical loads and approximate face sheet stresses are shown in Appendix C, Figures C-2, C-5, C-7, and C-8. To simplify the analysis, the thermal gradient at the panel center associated with a flux of 180 Btu/ft²-sec was used for all load conditions (Figure 7-6). Thermal stresses are shown in Appendix C, Figures C-1, C-4, C-7, and C-8.

Acoustic stress was approximated by using the Miles equation. Panel frequencies were approximated using classical plate theory. The acoustic pressure loads computed for Panel 1 were also used for screening of Panel 2. The resulting loads and rms acoustic stresses are shown in Appendix C, Figures C-3 and C-6.

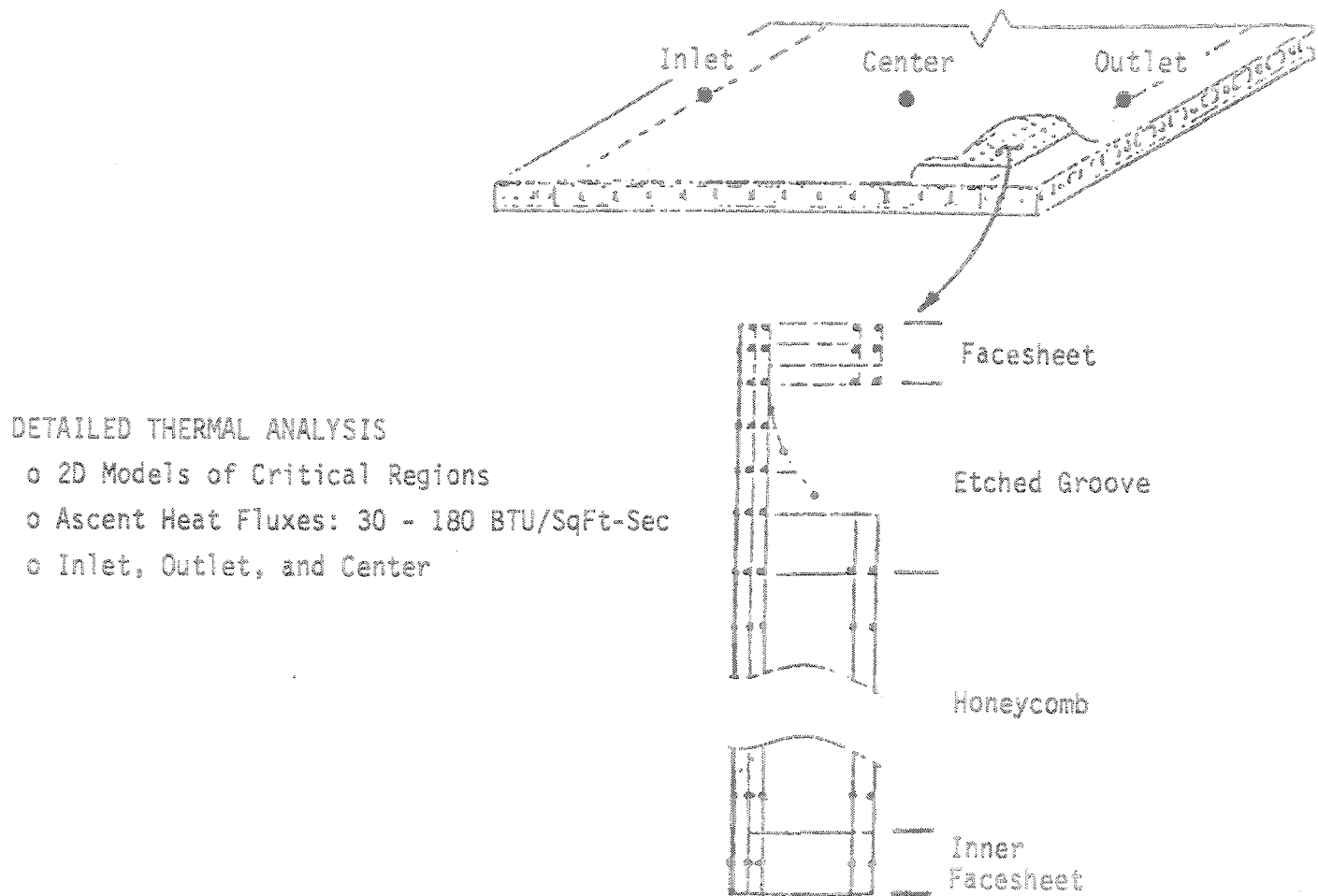


Figure 7-5. Model Used in Thermal/Hydraulic Analysis of Actively Cooled Panel.

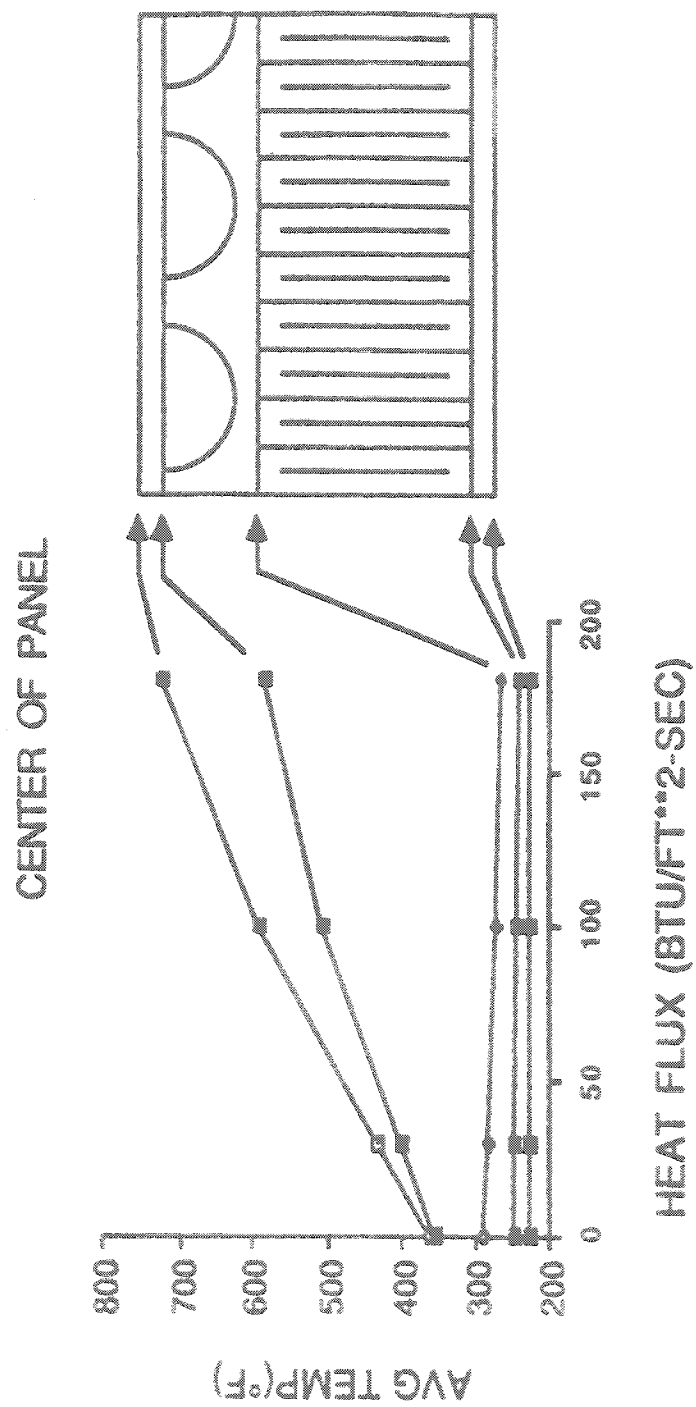


Figure 7-6. Thermal Gradient at Center of Panel.

The fatigue model is described in Appendix A of Reference [7-1]. Critical load conditions were identified as those having the largest combined static and dynamic stress ratios described by the relationship

$$\frac{\sigma_s}{F_{tu}} + \frac{\sigma_a}{CN^b}$$

where σ_s = static stress (psi)

F_{tu} = ultimate tensile strength (psi)

σ_a = acoustic rms stress (psi)

CN^b = fatigue allowable stress (psi)

Figures 7-7 and 7-8 show the fatigue analysis summary for the outer face sheet of Panels 1 and 2. The complete face sheet summary is shown in Appendix C, Figures C-9 and C-10. Highlighted areas in Figures 7-7 and 7-8 indicate critical load conditions. These cases of interest are candidates for detailed analysis using finite elements.

The acoustic load for Case #1 is representative for vehicle takeoff, when both the scramjet and supplemental rockets are operating. These dual noise sources are amplified by the ground reflective plane and combine to produce the severest acoustic environment (see Section 3). The loading from Case #1 results in the most critical structural response for both panels. The fatigue ratios associated with this condition are greater than three times those which are predicted to induce fatigue failure. Acoustic response accounts for 70 percent to 80 percent of the total fatigue damage.

7.5 FINITE ELEMENT MODELING

A detailed finite element model was utilized to refine the response predictions and evaluate panel fatigue life for the critical load conditions. A 1/4 symmetric NASTRAN finite element model was generated

OUTER F/S STRESS PANEL 1 (15' AFT)

CASE	$\frac{\sigma_A}{CN^b}$	$\frac{\sigma_{STATIC}}{F_{IU}}$	TOTAL
1	3.41	.28	3.69
2	.51	.11	.62
3	.12	.22	.34
4	.12	.25	.37
5	.19	.23	.42
6	.19	.26	.45
7	.33	.06	.40
8	.33	.09	.42
9	.23	.05	.28
10	.23	.05	.28
11	<.05	.12	>.12
12	<.05	.13	>.13
13	<.05	.28	>.28
14	<.05	.29	>.29

Figure 7-7. Fatigue Analysis Summary for Panel 1 Outer Face Sheet.

OUTER F/S STRESS PANEL 2 (7' AFT)

CASE	$\frac{\sigma_A}{CN^b}$	$\frac{\sigma_{STATIC}}{F_{tu}}$	TOTAL
1	2.70	.54	3.24
2	.40	.26	.67
3	.10	.33	.42
4	.10	.06	.16
5	.15	.33	.48
6	.15	.14	.29
7	.26	.27	.53
8	.26	.44	.70
9	.18	.40	.58
10	.18	.44	.63
11	<.05	.13	>.13
12	<.05	.15	>.15
13	<.05	.23	>.23
14	<.05	.30	>.30

Figure 7-8. Fatigue Analysis Summary for Panel 2 Outer Face Sheet.

(Figure 7-9). The panel face sheets, heat exchanger, honeycomb, manifolds, and edge closeouts were represented as different layers of solid elements. The model was simply supported along the edge member centerline, representing the bolting arrangement to other panels. Backup structure was not modeled.

The model incorporated anisotropic, temperature dependent material properties. Element material properties were modified to account for reduced stiffness of the heat exchanger and honeycomb.

The model was validated under normal static pressure to within 3% of plate theory (Figure 7-10). The model was also verified dynamically with plate theory (Figure 7-11).

7.6 FINITE ELEMENT ANALYSIS

Finite element analysis was performed only on Panel 1 owing to budgetary constraints. Analyses used to evaluate the panel fatigue life included NASTRAN linear static, nonlinear static, modal, and acoustic response analysis solutions. Modal analysis was performed using the updated stiffness matrix from nonlinear static analysis.

The thermal gradient was refined to account for changing heat flux along the vehicle trajectory. Figure 7-12 shows the heat flux for Panels 1 and 2. Figures 7-6, 7-13, and 7-14 show the temperature distribution along the entire panel as a function of heat flux.

The matrix of critical static loads was applied to the finite element model. The elastic static stress due to thermomechanical loads is shown in Appendix C, Figure C-11. The residual elastic static stress due to manufacturing cooldown from a 1200°F consolidation temperature of 70°F is also shown in Figure C-11. The linear static stresses due to a constant thermal gradient along the panel were also computed. The gradient induced stresses are as much as 20 times greater than that produced by thermomechanical loads.

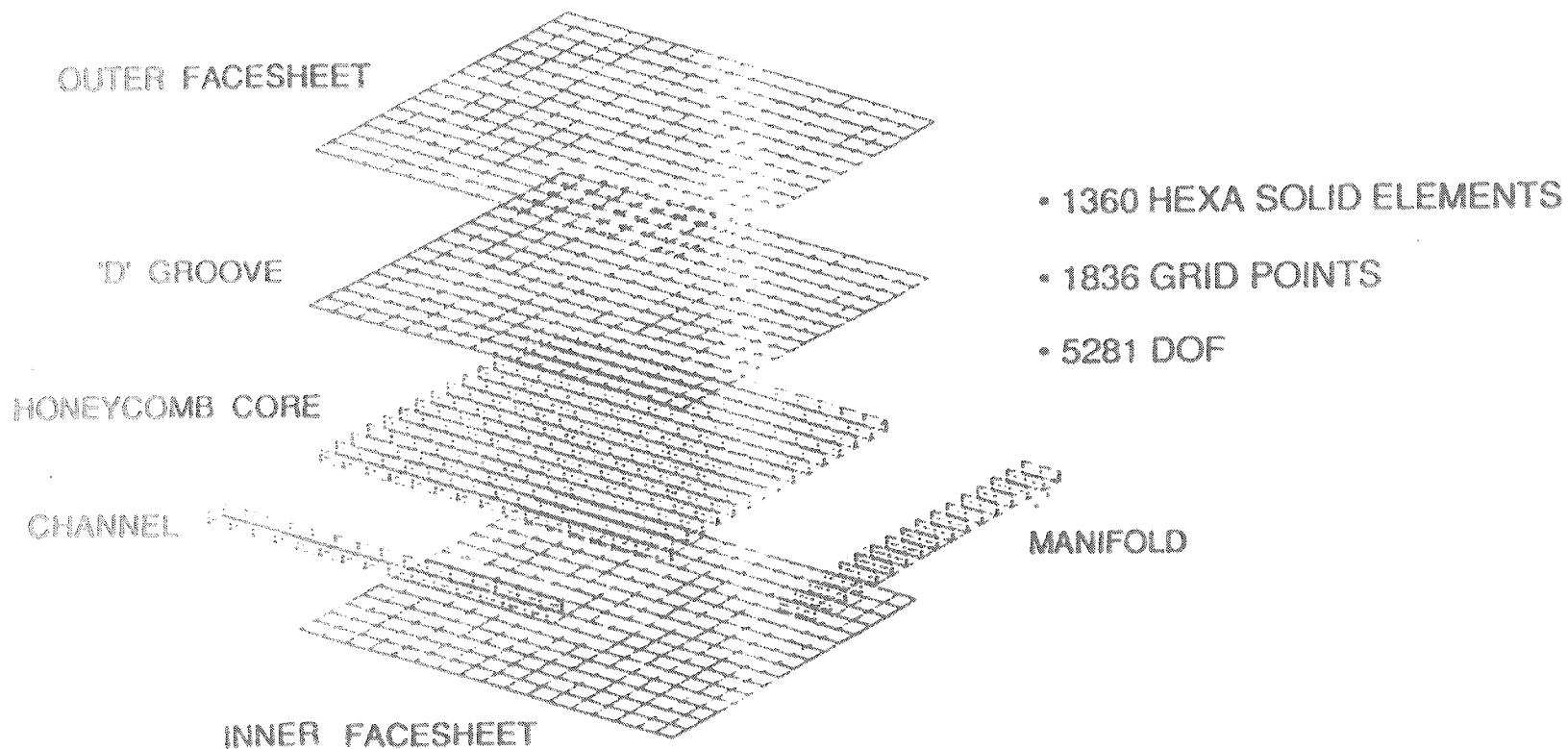


Figure 7-9. NASTRAN Symmetric Panel Model.

1 PSI LOAD

PANEL 1 (15' AFT)

	<u>PLATE THEORY</u>	<u>NASTRAN</u>
CENTER DEFL	.183 in	.177 in
INNER F/S STRESS	9538 psi	10162 psi

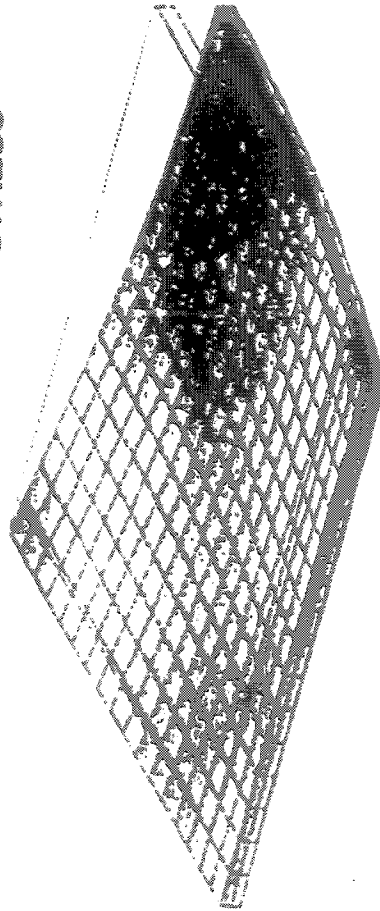


Figure 7-10. NASTRAN Model Static Checkout.

PANEL 1 (15' AFT)

PLATE THEORY NASTRAN

1st BENDING
MODE

82 Hz

76 - 186 Hz

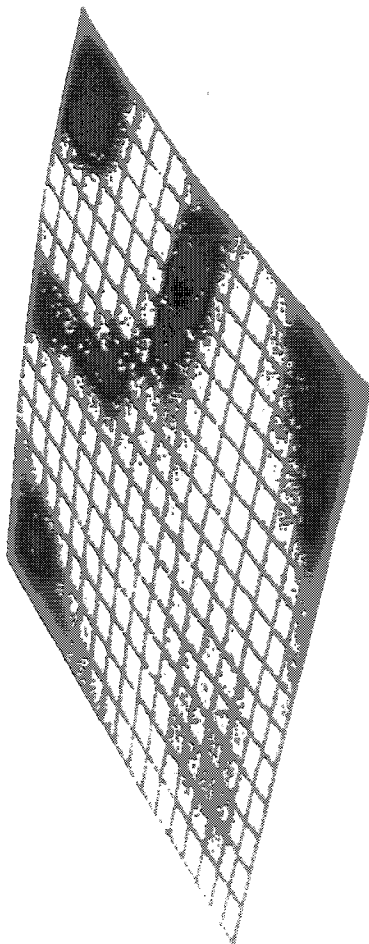


Figure 7-11. NASTRAN Model Dynamic Checkout.

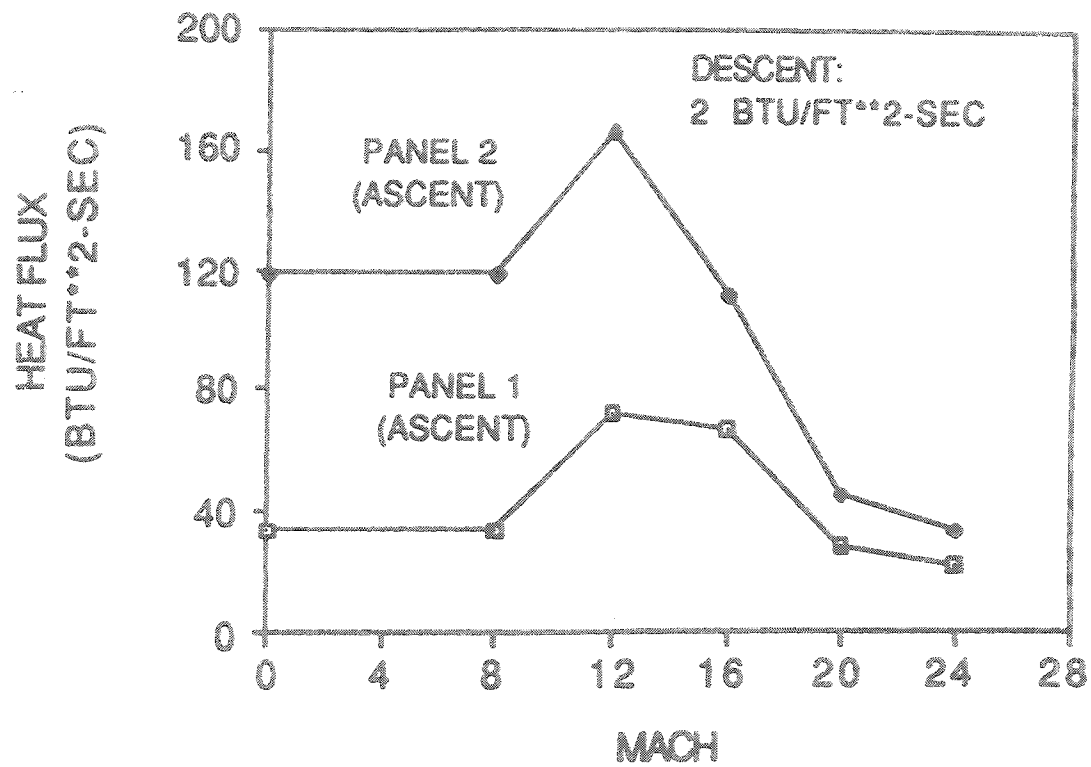


Figure 7-12. Heat Flux for Panels 1 and 2.

4" FROM INLET MANIFOLD

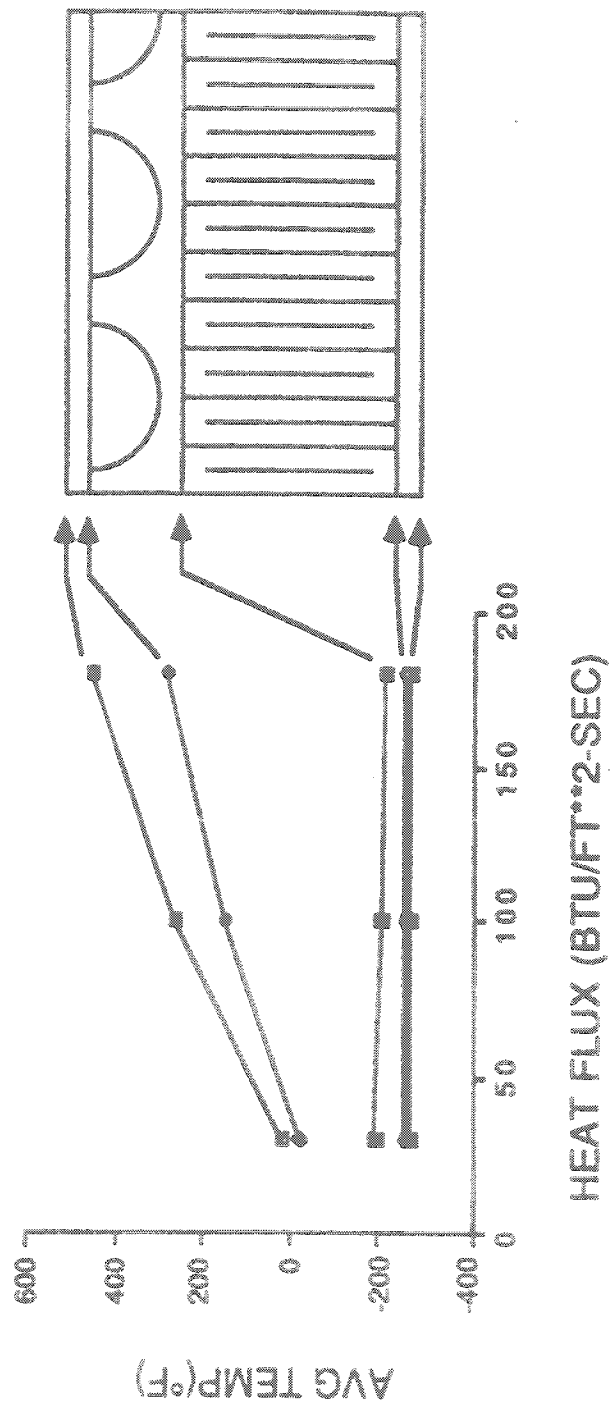


Figure 7-13. Temperature Distribution Along Panel as a function of Heat Flux (4 Inches from Inlet Manifold).

4" FROM EXIT MANIFOLD

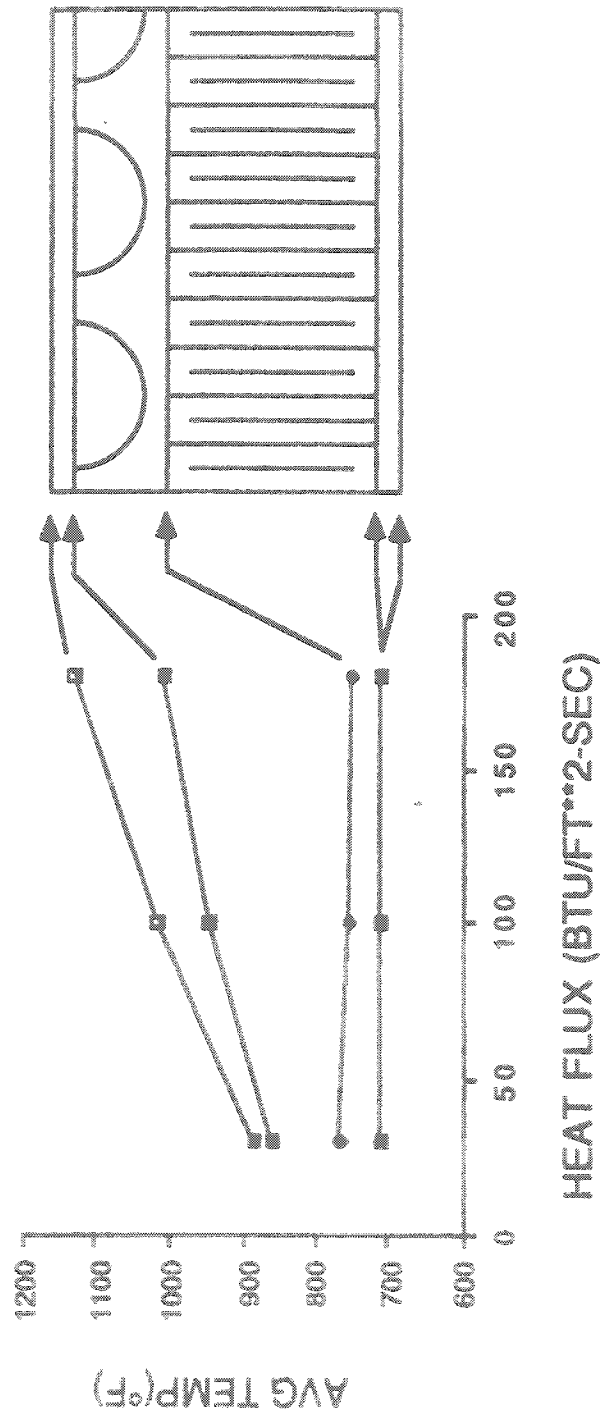


Figure 7-14. Temperature Distribution Along Panel as a Function of Heat Flux (4 Inches from Exit Manifold).

The acoustic response stress results including the thermomechanical preload are shown in Appendix C, Figure C-12. Acoustic response of the thermally loaded panel was not completed owing to difficulties with NASTRAN nonlinear static solution convergence. The NASTRAN nonlinear static solution is highly CPU intensive and very inefficient. Detailed plots of the finite element results are shown in Appendix C, Figures C-14 through C-35.

The fatigue analysis load summary is based on the preliminary screening and is shown in Appendix C, Figure C-13. The peak face sheet stress occurs at the panel center for all load conditions. The ratio of acoustic stress to high cycle allowable is greater than the ratio of static stress to ultimate allowable for many conditions. For this reason, Case #1, which has the highest acoustic load, is the most critical fatigue condition. The acoustic response analysis did not include thermal effects.

The stress induced by thermal gradients is compressive and significantly higher than the thermomechanical stress. Combined with high acoustic loading, such as Case #1, thermal effects are a major factor in fatigue life evaluation. Thermal effects must be included for a complete fatigue analysis, requiring a more efficient nonlinear analysis method than NASTRAN.

A summary of the finite element analyses for Panel 1 is shown in Figure 7-15. The analyses verify those trends shown by preliminary screening analyses. The summary shows that:

- (1) The critical condition is Case #1.
- (2) The inner face sheet is more prone to fatigue than the outer face sheet.
- (3) The critical locations on the panel are the centers of the panel face sheets.

CASE	INNER FACESHEET						OUTER FACESHEET					
	1	2	3	4	5	6	1	2	3	4	5	6
1	<u>5.71</u>	0.761	0.521	0.741	0.475	0.643	<u>2.77</u>	0.682	0.451	0.290	0.264	0.406
2	0.837	0.141	0.122	0.205	0.271	0.291	0.461	0.139	0.114	0.089	0.098	0.100
6	0.257	0.086	0.063	0.054	0.061	0.080	0.103	0.044	0.026	0.020	0.016	0.039

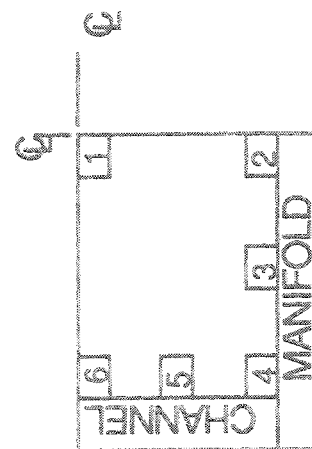


Figure 7-15. Combined Fatigue Ratios for Panel 1.

- (4) Failure is predicted only for Case #1, the failure points being at the center of the inner and outer face sheets.

7.7 RESULTS AND CONCLUSIONS

The static and dynamic finite element analyses show that:

- (1) The area of the panel with the highest acoustic stresses throughout the trajectory is at the center of the inner face sheet. This was expected since the loading is normal to the panel and the bonded heat exchanger shares some of the outer face sheet load. The manifolds are not stiff enough to provide good edge fixity, so the panel responds as if simply supported.
- (2) The highest static stresses are evenly distributed through the panel face sheets since the loads are primarily membrane loads. The outer surface of the outer face sheet is most highly stressed through Mach 6, where mechanical loads are higher than thermal growth loads. At higher Mach numbers, the thermal loads dominate, causing the highest loads to be imposed on the inner face sheets.
- (3) The highest fatigue loadings result from ground taxi condition and will cause fatigue failure. Nearly all the damage will be caused by the acoustic response. The acoustic environment is high, having energy concentrated at the primary resonant frequencies of the panels. The high levels are a function of ground reflections and the use of rocket thrust augmentation.
- (4) During ascent, the contribution of acoustics dominates the thermomechanical loads through the transonic regime. However, the levels at transonic conditions are much lower than at takeoff, resulting in stresses much below the fatigue threshold.

- (5) The relative contribution of the thermomechanical stresses increases with Mach number. The loads resulting from overall vehicle thermal growth and from the through-thickness panel gradients dominate the mechanical loads. Acoustic response becomes less important with increasing Mach number. Even though the structures become highly preloaded, the overall response is still below the panel fatigue threshold.
- (6) Descent conditions are relatively benign. The major loading results from differential growth as the vehicle heats up. The acoustic environment (and resulting panel response) is an order of magnitude lower than for ascent.

7.8 REFERENCES

- 7-1 Thermo-Vibro-Acoustic Loads and Fatigue of Hypersonic Flight Vehicle Structure, Interim Report for Period November 1987 - May 1988,
AFWAL-TR-89-3014, Air Force Wright Aeronautical Laboratories,
Wright-Patterson Air Force Base, Ohio, February 1989.

838PROP
3-7.88
12-11-89

SECTION 8 EXPERIMENTAL PLAN

8.1 INTRODUCTION

This section presents the Experimental Plan, in accordance with the proposal statement-of-work (Reference [8-1], paragraph 4.2.3.4), that will be followed in Phase III of the present program. The plan defines all tests to be performed, including their purposes, specimen details, materials, numbers of specimens, test fixtures, loads and loading sequences, load exposure times, and data to be generated. The test facilities to be used are fully described along with the specimen heating methods to be employed. The primary test facilities are Rohr's electrodynamic shakers and progressive wave tube (PWT) (currently under construction), both of which will be capable of testing at temperatures up to 1800°F. Instrumentation details include transducer types and locations, along with details of their operating temperature ranges. High-temperature strain gauges, Laser Doppler Velocimeters, accelerometers, and microphones will be utilized. Details of data acquisition equipment, calibration procedures, recording equipment, and data reduction facilities are provided.

The test scheduling and sequencing are also presented. In general, shaker tests will be performed on coupons and subelements prior to testing panels having the same materials and/or construction details. This is done for two reasons: (1) to ensure that any unexpected material or fabrication defects are discovered prior to committing the more

expensive panels to the PWT tests and (2) because shaker generated fatigue data will be used in selecting panel test loads.

Following Air Force approval of this Experimental Plan, the test specimen and fixturing fabrication will be initiated. All test specimens will be subject to standard quality assurance and inspection procedures. This applies to both the materials as received and to fabrication processes subsequently employed. The specimens will then be instrumented and tested in accordance with the approved plan.

These tests will include vibration shaker tests on material coupons and subelement (joints) at selected temperatures ranging from ambient to 1800°F. Dynamic load input on the shaker will consist of sinusoidal sweeps to identify mode shapes and frequencies, followed by Gaussian random loading endurance testing. The primary objectives of these tests are to obtain random response and fatigue life data and to identify material fatigue mechanisms.

The test panels will then be tested in the PWT. Following panel installation, the modal response characteristics will be determined by applying local excitation and utilizing modal-analysis test equipment. Modal response measurements will determine natural frequencies, mode shapes, modal stiffnesses, masses, and damping and will be conducted at the test temperatures designated for a particular panel. The panels will then be subjected to acoustic excitation, first with a sine-sweep, then by broad band random noise, applied incrementally in order to obtain a broad base of response data and to observe any nonlinear response effects, followed by random endurance testing at a selected broad band noise level. For panels to be tested at high temperatures, the sine-sweep and incremental broad band random acoustic excitation procedures will be conducted first at room temperature and then at elevated temperatures.

The resulting test data will be formulated for presentation and reporting purposes (e.g., fatigue curves, response levels versus loads and panel dimensional parameters, etc.) and for comparison with the

analytical results from Phase II. The results will then be formulated into fatigue prediction methods and design criteria.

The experimental work focuses primarily on two material types: titanium based metal matrix composites (TMC) and carbon-carbon. TMC structures are applicable in the 1000°F to 1500°F temperature range and are used in actively cooled panels, shielded inlet ramps, and wing-fuselage areas. Carbon-carbon is used in higher-temperature environments, up to 3000°F, in areas such as forward fuselage, inlet ramps, and nozzle structures. The Experimental Plan also includes testing an actively cooled panel. Some conventional material specimens are included in order to provide connections to a broader existing empirical data base. By simultaneously exposing realistic structures to high temperatures and random acoustic loading, structural response characteristics can be identified and quantified in relation to the load environment. Such tests also may identify areas of particular susceptibility to failure and provide the data necessary to optimize the structural designs. By testing the panels to failure, important correlations can be made between basic material fatigue data from the shaker tests and the fatigue lives that are achieved when these materials are utilized in representative vehicle structures.

8.2 TEST ARTICLES

During the formulation of the technical approach and cost proposal for this program, it was necessary to make preliminary material and design concept selections for the experimental program. These selections were based on those materials having the highest likelihood of being generic to critically loaded hypersonic vehicle structures. In the proposal (Reference [8-1]), material coupon and joint subelement specimens for random fatigue shaker testing were given in Table 4.3-2. Test panel configurations for the high-temperature sonic fatigue program were given in Table 4.3-3.

In general, these preliminary selections of test specimens have been substantiated by the ongoing development of actual hypersonic vehicle

structures and the results from Phases I and II of this program. The most significant exceptions are the rapid solidification rate titanium (RST) specimens. This material is still undergoing development and neither Rohr nor MDC is currently able to procure any RST for this program. Tables 8-1 and 8-2 are updated lists of the shaker test specimens and PWT test panels, respectively.

Tables 8-1 and 8-2 have columns indicating the current availability status of each specimen type. In the case of the shaker test specimens, there are material availability problems with some of the advanced titanium specimens:

- TMC skin-stiffener joints - MDC has recently advised Rohr that it will provide these specimens.
- RST material coupons and skin-stiffener joints - Material is not currently available and is unlikely to be available for this program. However, procurement efforts will continue.
- Titanium aluminide - Material availability is uncertain. It is currently likely that material for coupons will be available. It is unlikely that a stiffener will be available for joint specimens. Procurement efforts are continuing.

In the case of the PWT test panels, significant changes had to be made to the TMC stiffened-skin specimens. Only one TMC hat-stiffened panel is available instead of the two originally proposed. The corrugation-stiffened panel is not available in titanium aluminide and is represented by a 6-4 titanium substitute. In order to provide a direct comparison between the hat-stiffened and corrugation-stiffened design concepts, a hat-stiffened panel fabricated from 6-4 titanium has been added. A 6-4 titanium truss-core honeycomb sandwich panel has also been added to the test specimens. The total number of test panels has been increased from seven to eight.

Table 8-1. Random Fatigue Shaker Test Specimens.

Material	Specimen Type (Overall Size = 8" x 2")	Quantity	Availability Status
Carbon-Carbon	Material Coupon A	14	OK Rohr to provide
	Skin-Integral Stiffener Joint A	8	OK Rohr to provide
	Skin-Stiffener Joint - Inconel Fasteners A	8	OK Rohr to provide
Titanium Metal Matrix Composite (15-3 TMC)	Material Coupon B	10	OK MDC to provide
	Skin - Diffusion Bonded Stiffener Joint C	6	OK MDC to provide
Rapid Solidification Rate (RST) Titanium	Material Coupon C	10	Availability unlikely
	Skin - Diffusion Bonded Stiffener Joint C	6	Availability unlikely
Titanium Aluminide	Material Coupon A	10	Availability likely
	Skin - Diffusion Bonded Stiffener Joint A	6	Availability unlikely
6-2-4-2 Titanium	Material Coupon A	10	OK Rohr to provide
	Skin - Diffusion Bonded Stiffener Joint A	6	OK Rohr to provide
6-4 Titanium	Material Coupon A	10	OK Rohr to provide
	Skin - Diffusion Bonded Stiffener Joint A	6	OK Rohr to provide

Skin Material Thickness = 0.06-inch Carbon-Carbon
= 0.05-inch Titanium
= 0.032-inch TMC

Additional Specimens
6, Truss - Core Honeycomb Specimens,
8 inches by 2 inches, 6-4 Titanium

NOTE: Stiffeners at Skin Center, Running in 2-inch Direction.

A = Supplied by Rohr
B = Supplied by MDC
C = Supplied by MDC (IRAD) at No Cost

838PROP/3-T8-1.BB
12-15-89

Table 8-2. High-Temperature Sonic Fatigue Test Panels.

Panel Type	Materials and Configuration Description	Overall Panel Size	Availability Status
Carbon-Carbon Stiffened-Skin Panels A	<u>Carbon-Carbon Skins and Integral Stiffeners</u>		
	Configuration 1: Skin Laminate Thickness = 0.065" Stiffener Spacing = 6"	20" x 24"	OK Rohr to provide
	Configuration 2: Skin Laminate Thickness = 0.065" Stiffener Spacing = 9"	20" x 24"	OK Rohr to provide Change to 10"
	Configuration 3: Skin Laminate Thickness = 0.125" Stiffener Spacing = 6"	20" x 24"	OK Rohr to provide
Actively Cooled Panel B	<u>Face Sheets:</u> Titanium Metal Matrix Composite	24" x 24"	OK MDC to provide
	<u>Core:</u> 15-3 Titanium		
Titanium Metal Matrix Composite Stiffened-Skin Panels	<u>Hat Stiffened Panels: Skins and Stiffener Material</u> <u>Titanium Aluminide Based Metal Matrix Composite</u>		
	Configuration 1: Skin Laminate Thickness = 0.05" C Stiffener Thickness = 0.022"	17" x 22"	One panel OK. MDC to provide. Size: 15" x 9.5" Matl: 15-3Ti TMC Thickness: 0.032"
	Configuration 2: Skin Laminate Thickness = TBD C Stiffener Thickness = TBD	17" x 22"	
	<u>Corrugation-Stiffened Panels: Titanium Aluminide Metal</u> <u>Matrix Composite Skins and Superplastically Formed</u> <u>Titanium Aluminide Corrugations</u>		
	Configuration 1: Skin Laminate Thickness = 0.05" D Corrugation Thickness = 0.022"	17" x 22"	Corrugated panel only available in 6-4 Ti Size: 24" x 24" Thickness: 0.032"

A = Supplied by Rohr Using Existing Tooling
 B = Supplied by MDC
 C = Supplied by MDC
 D = Supplied by MDC (IRAD) at No Cost

Additional Panels

- Hat Stiffened Panel 6-4 Ti for Comparison with 6-4 Ti Corrugated Panel
- Truss Core Honeycomb Panel

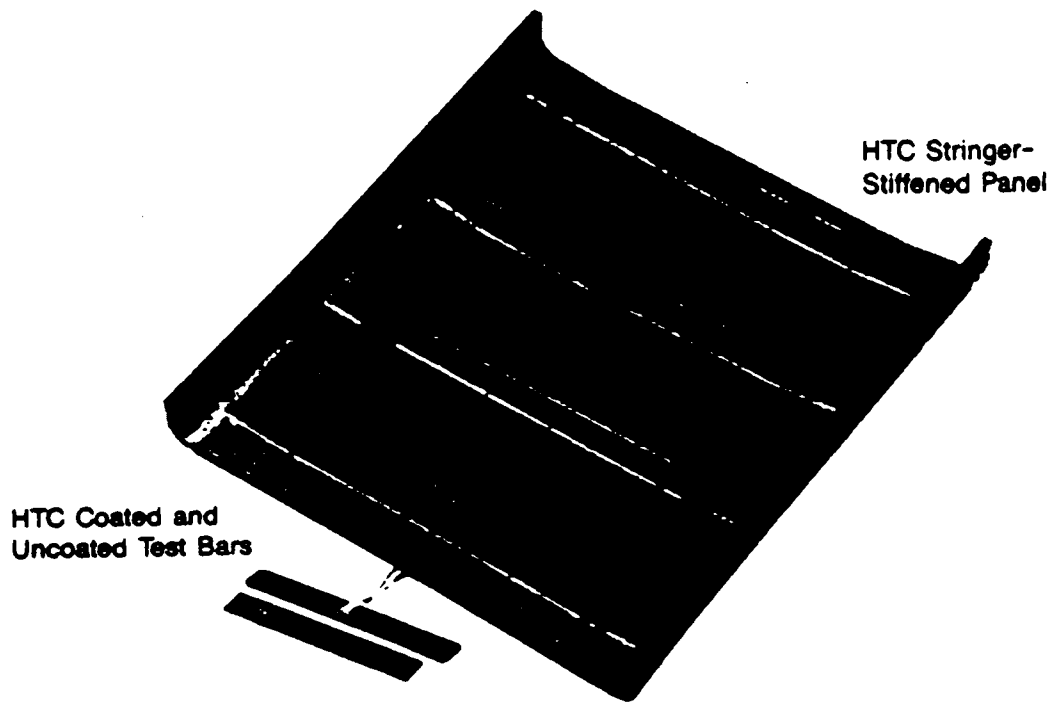
838PROP/3-T8-2.BB
 12-15-89

Figures 8-1 through 8-7 show the test panels and their potential application locations on a vehicle. Also shown in the figures are the vehicle structures represented, temperature application ranges, and proposed test temperatures.

MDC and Rohr will jointly fabricate the titanium and metal matrix joint specimens and panels. Liquid interface diffusion (LID) bonding is extensively used for joining titanium structures on hypervelocity vehicles. Consequently, the shaker test program includes skin-stiffener subelements having LID bonded joints. LID is a Rohr developed process and has been widely used for bonding titanium honeycomb sandwich panels. The actively cooled panel will be supplied by MDC at no fabrication cost. The design of this panel was sponsored by the NASP JPO.

Rohr will fabricate all of the carbon-carbon specimens. These specimens will incorporate Rohr's proprietary oxidation protection system, which consists of an in-depth particulate filler added to the prepregging resin, a thin seal coat applied over the densified part, and a Si/SiC coating over the entire substrate to a depth of 10 to 12 mils. The particulate inhibitor consists of metallic powders which oxidize, swelling and forming a borate glass which in turn seals the microcracks that exist in the Si/SiC coating. The CVD coating will be applied by Chromalloy Research and Technology of Orangeburg, New York. This approach to oxidation protection minimizes the chance of component failure in the event of a large-scale coating breach caused, for example, by foreign object impact. Rohr has already fabricated stiffened panels for thermoacoustic testing and prototype two-dimensional nozzle parts successfully from prepreps containing these particulate inhibitors.

Panel edge details and fixturing are currently being developed by Rohr in conjunction with MDC. Details will be made available to the Air Force when complete.



CARBON-CARBON TEST PANELS: 3

Vehicle Structure Represented: Forebody, Engine Inlet Ramp Shield for TMC

Temperature Application Range: 1500°F to 3000°F

Test Temperature: Response at R.T., 400°F, 600°F, 1000°F, 1200°F,
1500°F, 1800°F, 2000°F (if possible)

Endurance at 1800°F

Figure 8-1. Carbon-Carbon Test Panels.

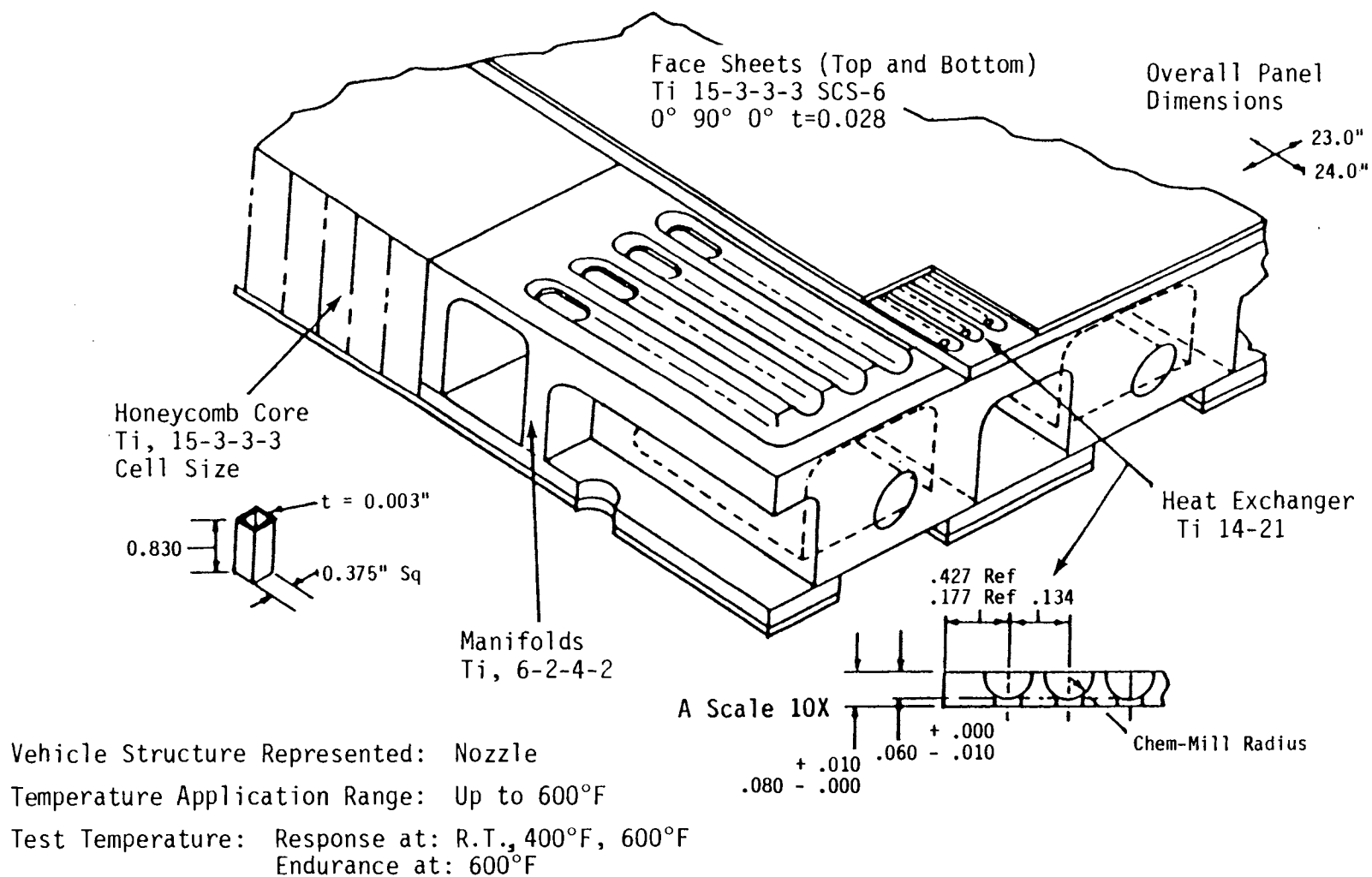


Figure 8-2. Actively Cooled Panel.

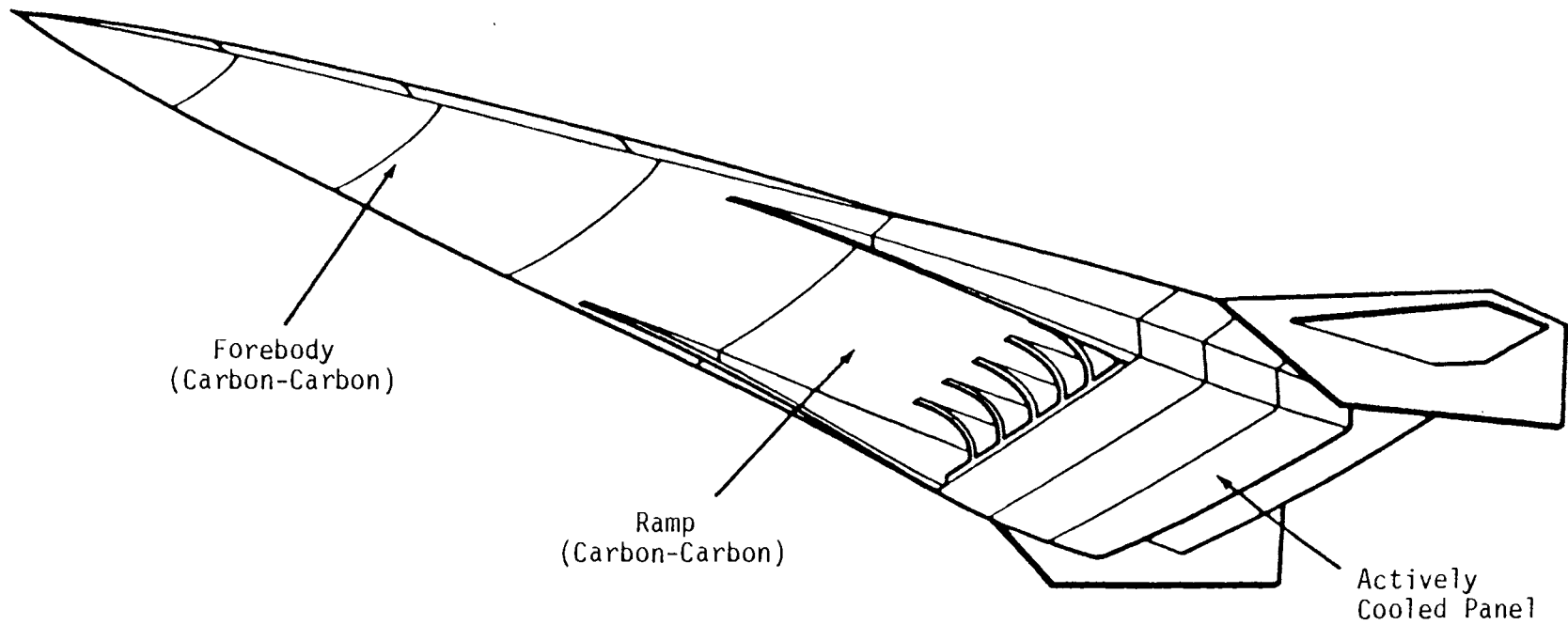
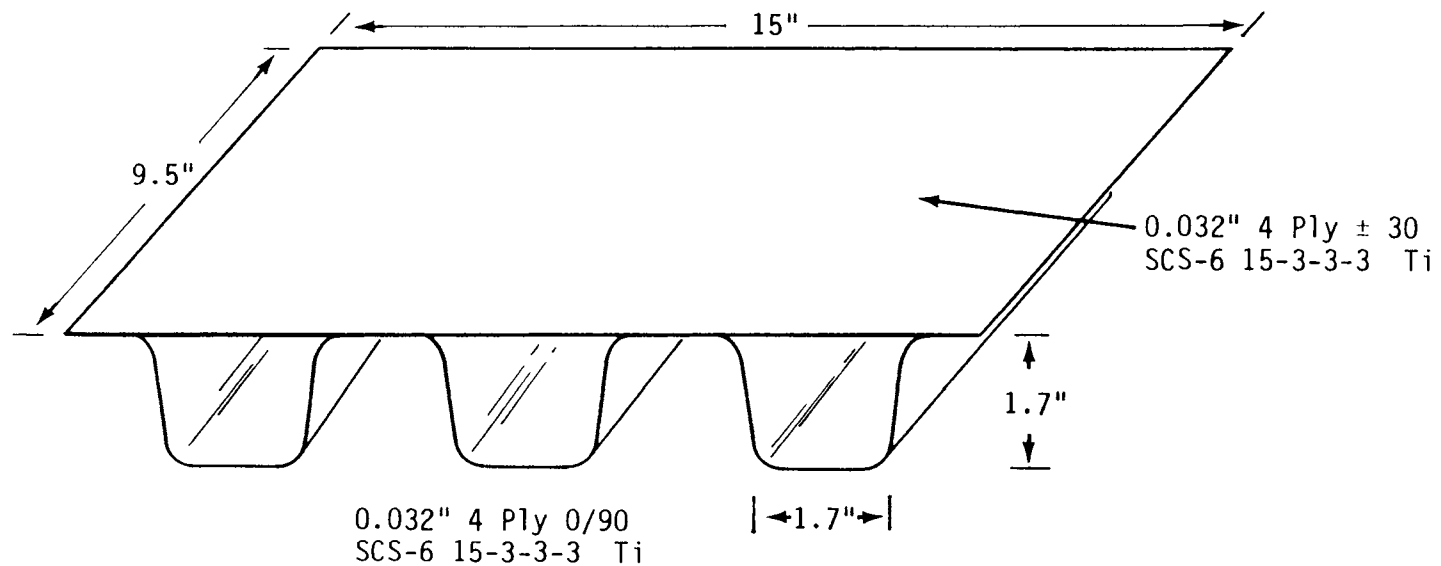
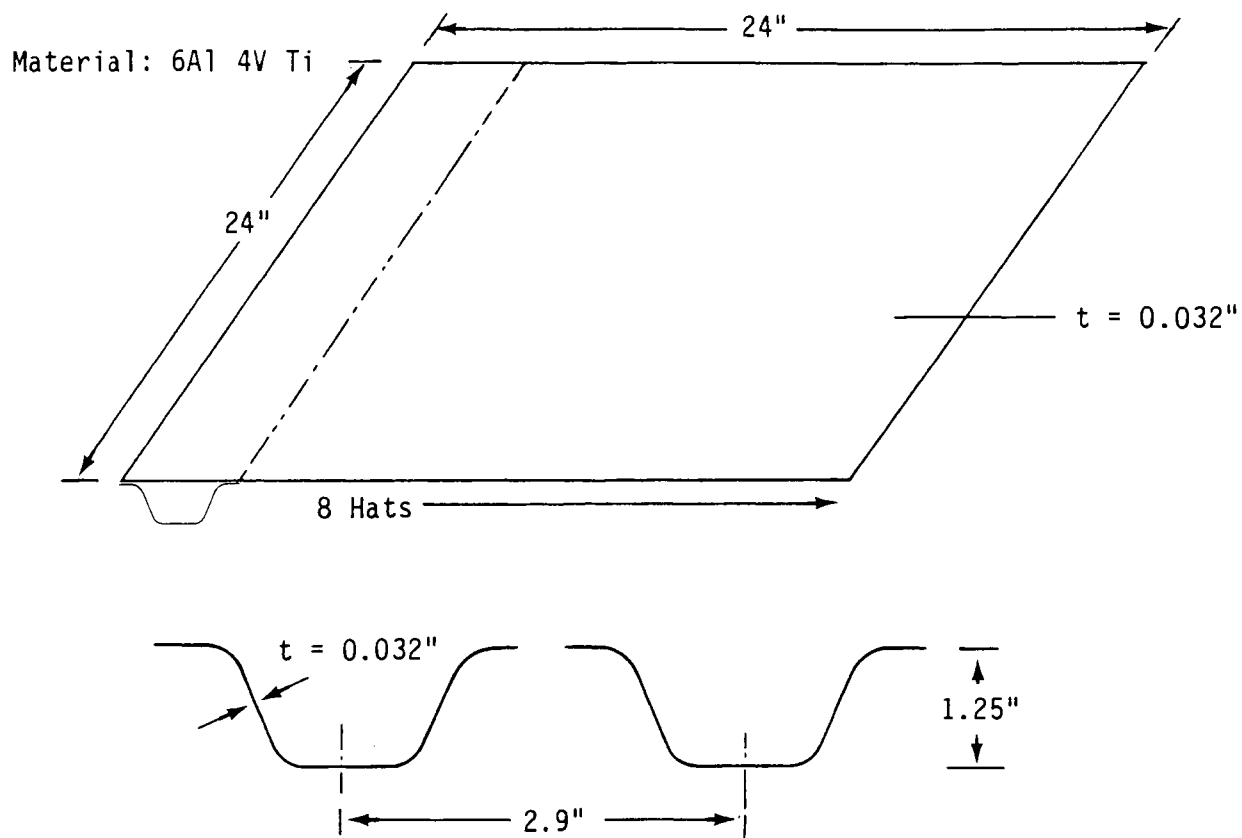


Figure 8-3. Locations of Carbon-Carbon and Actively Cooled Test Panels.



Vehicle Structure Represented: Upper Body-Fuselage, Wing
 Temperature Application Range: 1200°F to 1500°F
 Test Temperature Response at : RT, 400°F, 600°F, 1000°F, 1200°F, 1500°F
 Endurance at: 1200°F or 1500°F Depending Upon Shaker Test Results

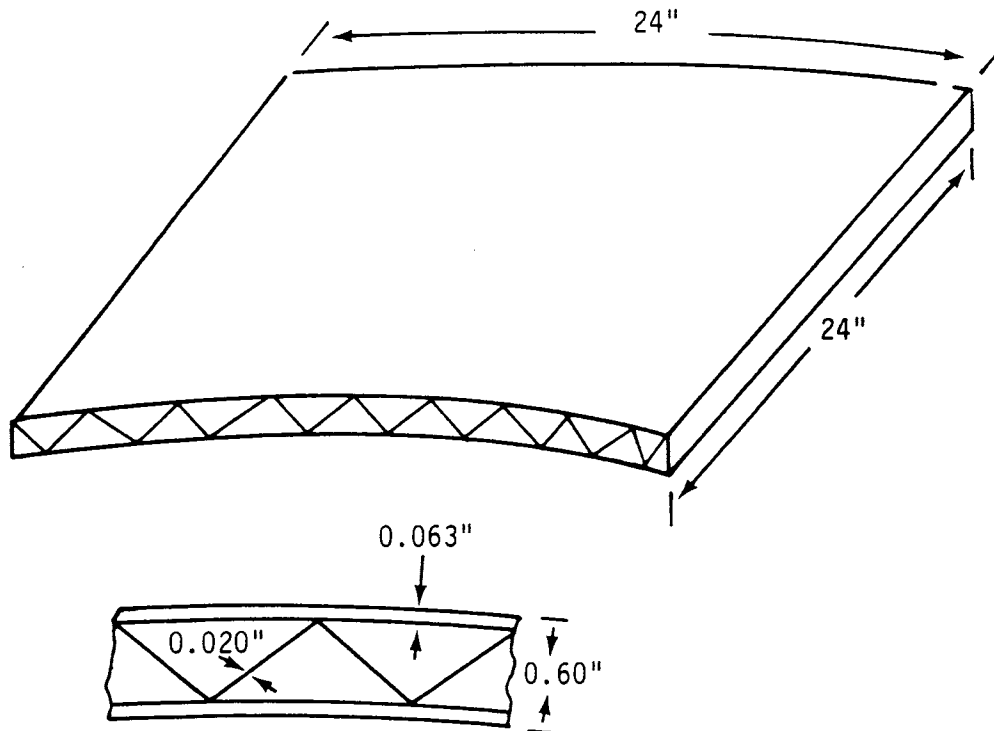
**Figure 8-4. TMC Hat-Stiffened Panel
 (plus Duplicate Panel in 6-4 Titanium).**



Vehicle Structure Represented: 6-4Ti Substitute for TMC Upper Body Panels
 Test Temperature: Response At: R.T., 400°F, 600°F, 800°F
 Endurance At: 600°F or 800°F Depending Upon Shaker Test Results

Figure 8-5. Monolithic Titanium Hat-Stiffened Panel.

Material: 6Al-4V



Vehicle Structure Represented: Fluid Tank, 6-4Ti Substitute for TMC
Upper Body Panels

Test Temperature: Response at: R.T., 400°F, 600°F, 800°F
Endurance at: 600°F or 800°F Depending upon
Shaker Test Results

Figure 8-6. Monolithic Titanium Truss Core Panel.

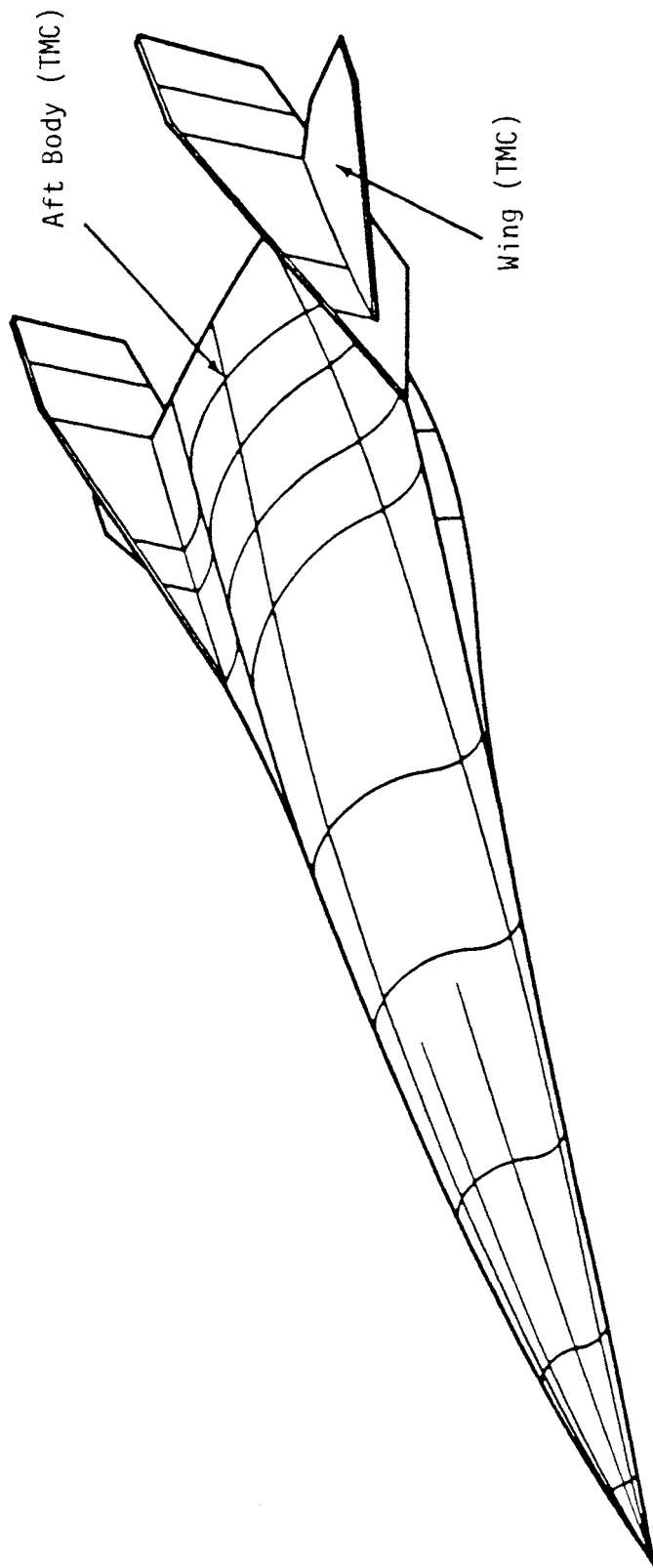


Figure 8-7. Locations of Stiffened TMC Test Panels.

8.3 TEST FACILITIES

8.3.1 Electrodynamic Shakers

The Rohr laboratory is equipped with three electrodynamic shaker systems for conducting dynamic testing:

- An Unholtz Dickie Model 1509 with a capacity of 7000 pounds sine wave and 5000 pounds random excitation.
- A Ling Electronics Model B290 with a capacity of 1500 pounds sine wave and 1000 pounds random excitation. This shaker has been modified to allow coupon testing to 2000°F as shown in Figure 8-8.
- An Unholtz Dickie Model TA 139-70 with a capacity of 130 pounds sine wave and 70 pounds random excitation.

Numerous digital console, computer console, and analog data acquisition systems with the paper and magnetic tape output are available for data acquisition and "on-line" readout. Data are reduced to engineering units and output is produced on standard format for reports and presentations utilizing in-plant digital computer facilities.

It is anticipated that the 1500-pound Ling shaker will be primarily used in this program.

8.3.2 Progressive Wave Tube

Panel tests will be conducted in Rohr's PWT facility, currently under construction and now scheduled for completion in February 1990. Figures 8-9 through 8-11 show the facility layout. This facility is designed to produce, in a test section, as close an approximation as possible to a plane progressive acoustic wave over a broad frequency range. Particular attention was applied to the design to minimize

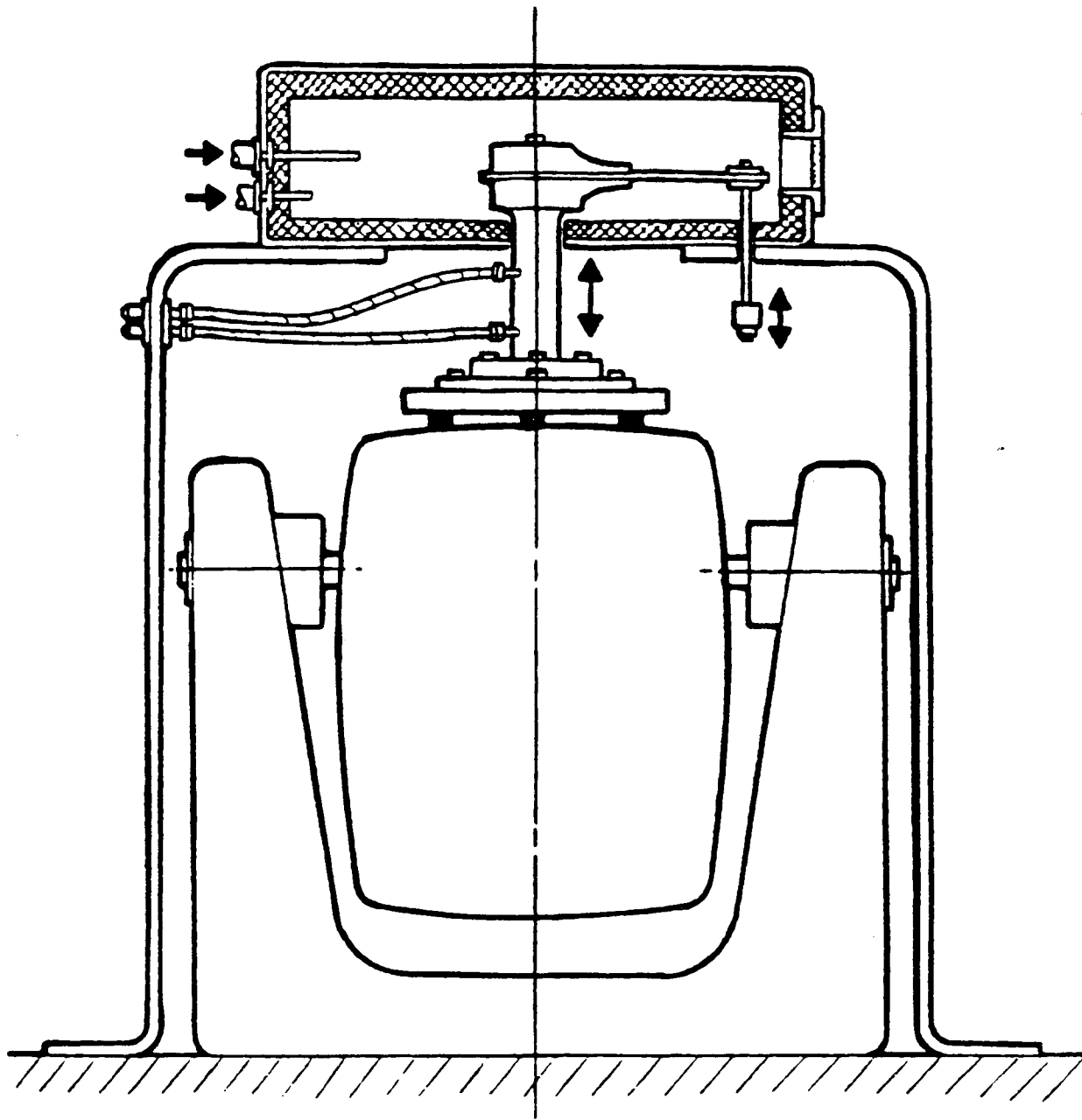


Figure 8-8. Ling Shaker with High-Temperature Test Furnace.

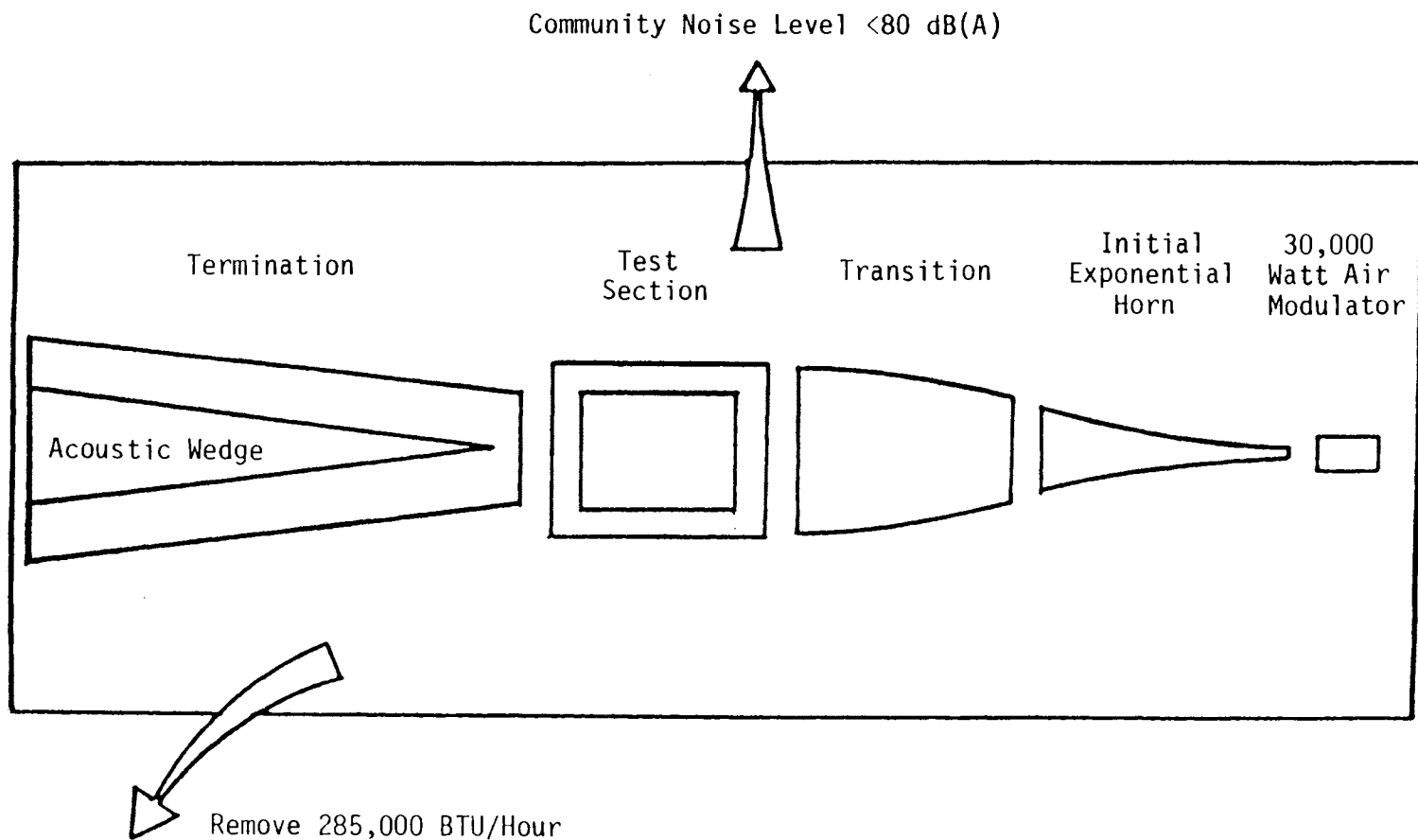


Figure 8-9. Schematic of Sonic Fatigue Test Facility.

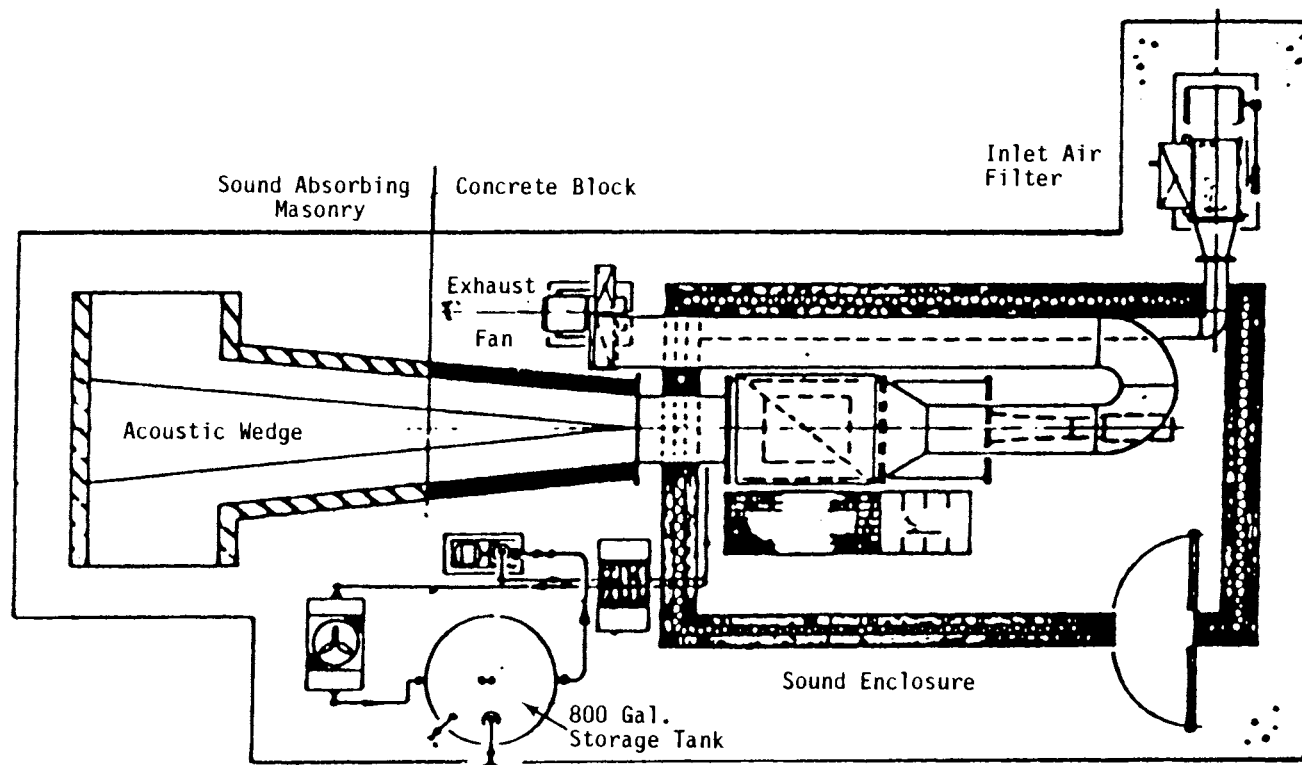


Figure 8-10. PWT Facility Layout.

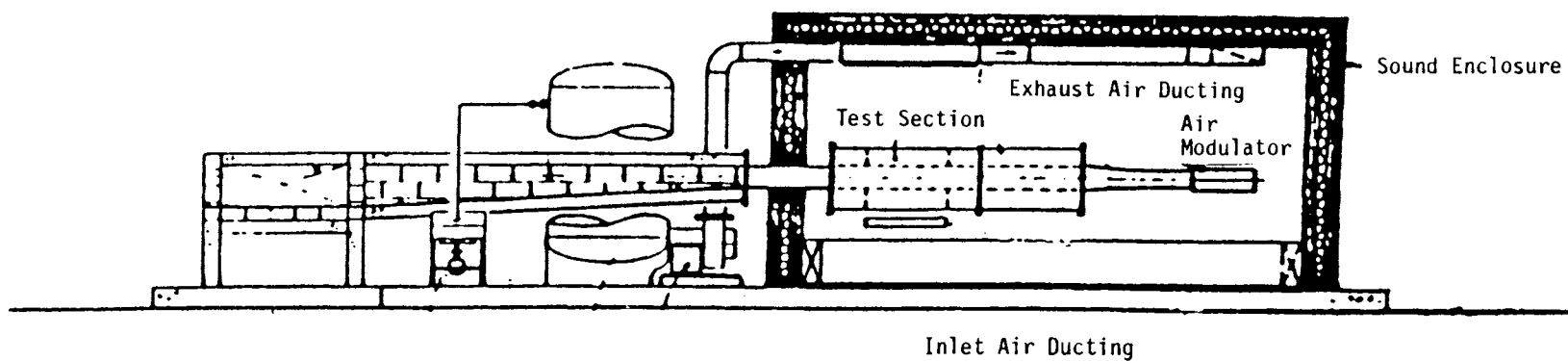


Figure 8-11. PWT Facility Layout - Side View.

standing waves, tube cross-modes, and tube damping of the test articles. The design specifications for the facility are:

- Test sound pressure level, 168 dB overall (broad band random).
- Controllable spectrum frequency range, 50-630 Hz.
- Test article accommodated, 33 by 23 inches.
- Provisions incorporated for test article heating, for combined environment tests.
- Driver source power, 30,000 acoustic watts air modulator.

Table 8-3 gives the facility specifications.

The PWT is unusual in that the test section opening is in the horizontal plane. This feature eases the problem of suspending the test articles on an antivibration system and provides a frame forming the required edge fixation. In combined thermo-acoustic tests, this "picture frame" approach to vibration isolation from the facility structure also lends itself to ease of thermal isolation.

The test section will be constructed of steel and refractory concrete, with combined thermal testing in mind. A concrete pit will be provided below the test section, which will house the heating equipment used to irradiate the test articles from the opposite wall of the tube.

The test panel will be heated by radiation through a quartz window from a quartz lamp array. Air source for the air modulated acoustic drivers (15,000 watts of acoustical power) will come from the existing Airflow Facility. When high-temperature testing is required, diesel engine driven generators on trailers will be leased. This facility will contain water and air cooling systems for the quartz lamps and a ventilation system for the acoustic enclosure. Estimates of the attainable test article temperatures, with the test article mounted in

Table 8-3. Sonic Fatigue Facility Design Specifications.

- Test Sound Pressure Level: 168 dB, Broad Band Random Noise
- Maximum Test Panel Size: 33 by 23 inches
- Type of Acoustic Field: Progressive Wave, Grazing Incidence
- Panel Test Temperatures: Up to 2000°F
- Allowable Sound Pressure Level at Nearest Property Line: 80 dB (A)
- Location: Chula Vista Plant
- Acoustical Source: Electropneumatic Air Modulator
- Thermal Source: Quartz Infrared Lamps
- Airflow Required: 3000 scfm at 40 psig (maximum)
- Electrical power: 240 V, 3-Phase, 400 amps per Leg
- Test Section, Transition, and Initial Horn to be Removable
- Forced Air Ventilation and Cooling of Enclosure

838PROP
3-T8-3.BB
11-11-89

one wall of the sonic fatigue test facility and irradiated from the opposite wall, indicate that a reasonable target is 1800°F to 2000°F. These figures are based on this radiation equilibrium temperature being attained in a reasonable warm-up time (20 minutes) with a radiant flux density of approximately 17 Btu/ft²-sec. The proposed test articles can be irradiated with sufficient overlap, within an area of 5 square feet. The lamp array will incorporate separately controllable heating zones. This will minimize the potential for unwanted thermally induced buckling of the test articles during test warm-up and cooling cycles.

A layout of the quartz infrared heat lamp array is shown in Figure 8-12. The lamp array will be built using commercially available modules containing the quartz lamps behind a quartz-glass window. This window will form a section of one wall of the acoustic facility test section. The window will reduce the sound pressure levels to which the lamps are subjected by the amount of the acoustical transmission loss of the material, thereby prolonging lamp life. Additionally, the window will minimize acoustical discontinuity in the walls of the progressive wave test section. The electrical power to the modules forming the array will be distributed between the individually controllable phases of a three-phase supply. The geometry of the modules and their phase distribution to the electrical supplies will allow different thermal fluxes to be applied to the center, the edges, and the corners of the test articles.

8.3.3 Modal Analysis Test System

Rohr has a complete model test system. The system consists of a Hewlett Packard Series 300 microcomputer with a 40-Mbyte disc drive, a B&K Model 2032 Two Channel Test Fourier Analyzer, Structural Measurement Systems Model 3.0 software, and a range of exciters and transducers including tap hammers, impedance heads, and small shakers.

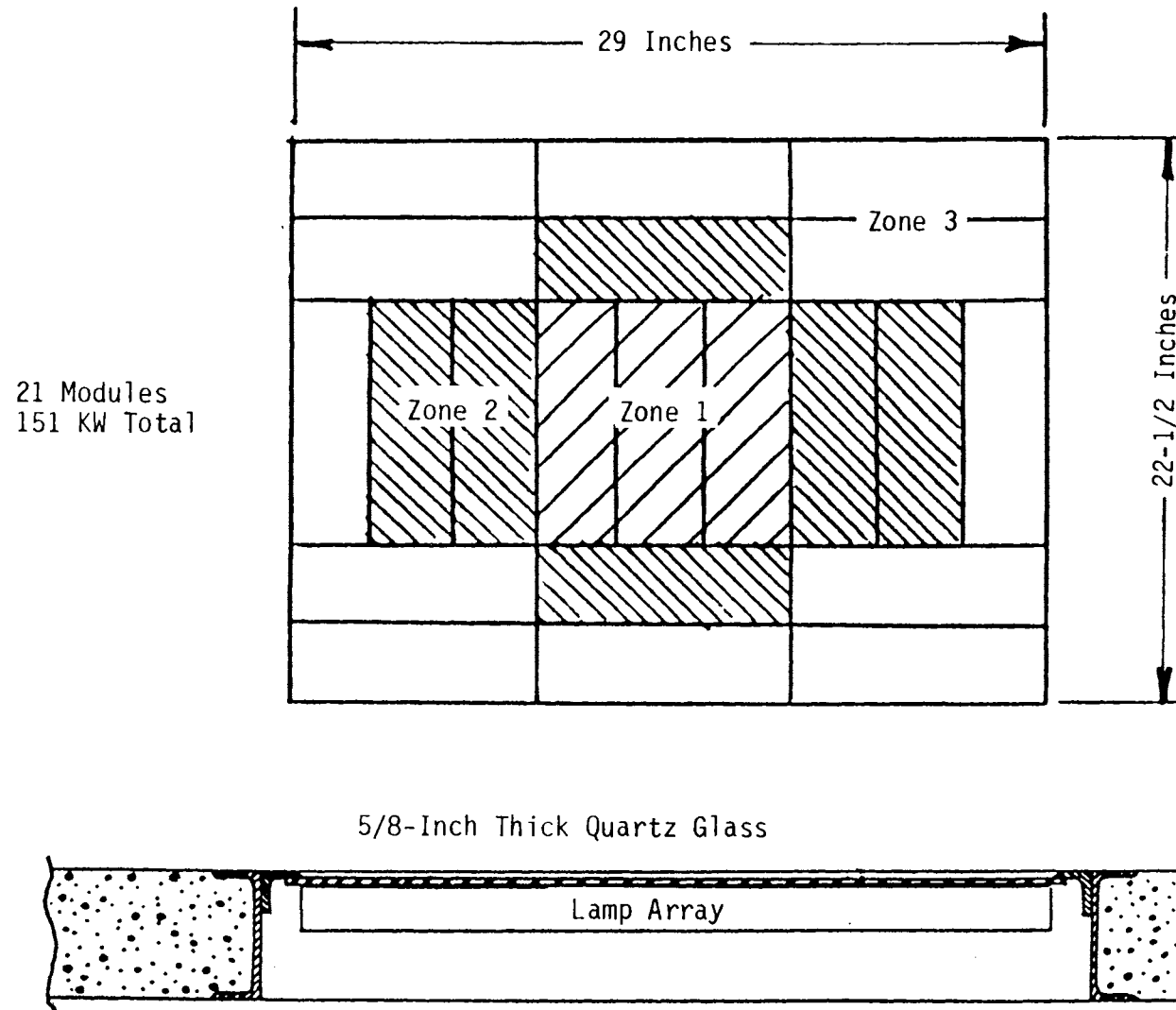


Figure 8-12. Infrared Quartz Heat Lamp Array.

8.3.4 Calibration, Data Acquisition, and Data Reduction Systems

Strain gauge calibrations are achieved by a D.C. shunt of the Wheatstone bridge network. Accelerometers are calibrated by mounting them on a shaker at a known acceleration level and frequency. A voltage insertion technique is also used. Pressure transducers (microphones) are calibrated both by applying a single frequency sound pressure level (piston-phone) and by a D.C. shunt calibration of the bridge network.

For the FFT analyzers, the known calibration sensitivity level is input manually as a voltage per engineering unit. This calibration level is then applied to the recorded data over the entire analysis bandwidth. Phase calibration between recorded channels is performed with either a sine-sweep or a white noise calibration signal across all tape channels.

Dynamic strain and acoustic pressure inputs are conditioned using Wheatstone bridge balancing techniques and then amplified to suitable recording levels using a high input impedance variable gain amplifier. Accelerometer inputs are conditioned and amplified using charge amplification techniques.

On-line data monitoring is performed during testing using both oscilloscopes and an FFT analyzer. Subsequent off-line data reduction is performed on either a B&K 2032 dual channel signal analyzer or a Spectral Dynamics SD 9000 sixteen channel signal analyzer.

The B&K 2032 is a dual channel signal processing FFT analyzer with 801 line resolution and built-in zoom capability. The functions which can be measured are:

- Instantaneous Time Function, ch. A or ch. B
- Instantaneous Time Function, ch. A vs. ch. B
- Enhanced Time Function, ch. A or ch. B
- Enhanced Time Function, ch. A vs ch. B
- Probability Density, ch. A or ch. B
- Probability Distribution, ch. A or ch. B

Instantaneous Spectrum, ch. A or ch. B

Autospectrum, ch. A or ch. B.

Cross-Spectrum

Frequency Response, H_1 , H_2

1/Frequency Response, H_1 , H_2

Coherence

Signal-to-Noise Ratio

Coherent Output Power

Autocorrelation, ch. A or ch. B

Cross-Correlation

Impulse Response

Sound Intensity

Cepstrum, ch. A or ch. B

Filtered Spectrum, ch. A or ch. B

In addition, Rohr has a data reduction program written for the B&K 2032 which includes Integrated Frequency Spectrum and Peak Amplitude Probability Density (Rayleigh Distribution)

The Spectral Dynamics SD 9000 extends the capability of traditional 1, 2, or 4 channel hardwired frequency analyzers to 16 channels and beyond. Both Time History and Frequency data are displayed on-line with interactive mouse control and Waterfall plots readily available.

Both Time History and Fourier data can be stored for subsequent detailed analysis or transferred to a multiple or other SA analysis packages. The SD 9000 allows transfer function calculations between any channel combination with up to 4096 spectral lines as standard.

Displays are completely user defined for custom plot generation and automatic plot generation.

Analyzed Function displays include:

Power and RMS Spectra

Cross Spectra

- Third Octave Bands
- Coherent Output Power
- H1, H2, and H3 FRF types
- Time Histories
- Phase
- Cepstrum
- Tabular Listings
- Auto and Cross Time Correlation
- Real and Imaginary
- Coherence
- Incoherent Output Power
- Nyquist
- Modulus
- Integrated Spectra & FRF
- Differentiated Spectral & FRF
- User Defined Random Text
- Automatic Plotting

8.3.5 High-Temperature Instrumentation

Probably the most difficult measurements to make in this program are the determination of panel displacements and strains when the panels are exposed to high acoustic loads (on the order of 168 dB) and a high temperature environment (1000°F to 2000°F). Vibration and strain measurements of coupons undergoing shaker tests at very high temperatures pose similar problems. The following discussion reviews the most promising noncontact technique for measuring vibration data and also the most recent strain gauges available for high-temperature work. The initial vibration measurement can be displacement, velocity, or acceleration. If one of these is accurately measured, the other parameters can be obtained by differentiation or integration.

After reviewing several noncontacting measurement techniques, Rohr has focused its attention on Laser Doppler Velocimeters (LDV's). LDV's rely on the detection of the Doppler shift of coherent light when it is

scattered from a moving object. This Doppler shift is linear with vibration velocity.

Four LVD's are currently being evaluated for use on this program: Dantec, Polytec, T.S.I., and B&K. A schematic of the T.S.I. system is shown in Figure 8-13. This system was designed for measuring machine vibration with the outputs conditioned for an FFT analyzer. Its maximum velocity range is about 1 inch/second. However, by increasing the maximum Doppler frequency and the bandwidth of the system, a higher velocity range can be achieved. This increased range may be necessary, since at 500 Hz and 0.01 inch D.A. displacement, the velocity is 15 inches/second. The instrument will be studied to establish its suitability for dynamic testing of panels and shaker.

Table 8-4 gives the specifications for the four LDV types. Rohr is currently evaluating a recently improved T.S.I. LDV system having a maximum velocity measuring capability of 1 meter/second. Table 8-5 lists the major factors being considered in this evaluation.

Rohr is also continuing its evaluation of recently developed high-temperature strain gauges. The best results achieved to date have been with Micro-Engineering H2102 series strain gauges with their Type H cement. On a carbon-carbon specimen, the gauge installation performed for 3 minutes at a temperature of 1800°F and a rms strain level of 1,200 microstrain. This evaluation is continuing in order to demonstrate consistency and repeatability.

8.4 SHAKER TESTS

Random fatigue shaker tests will be performed on the specimens identified in Section 8-2, Table 8-1.

The shaker test specimens utilize the same materials and fabrication techniques as the panels, so the shaker tests will establish a data base of S-N and subelement fatigue data that will be verified in the panel tests.

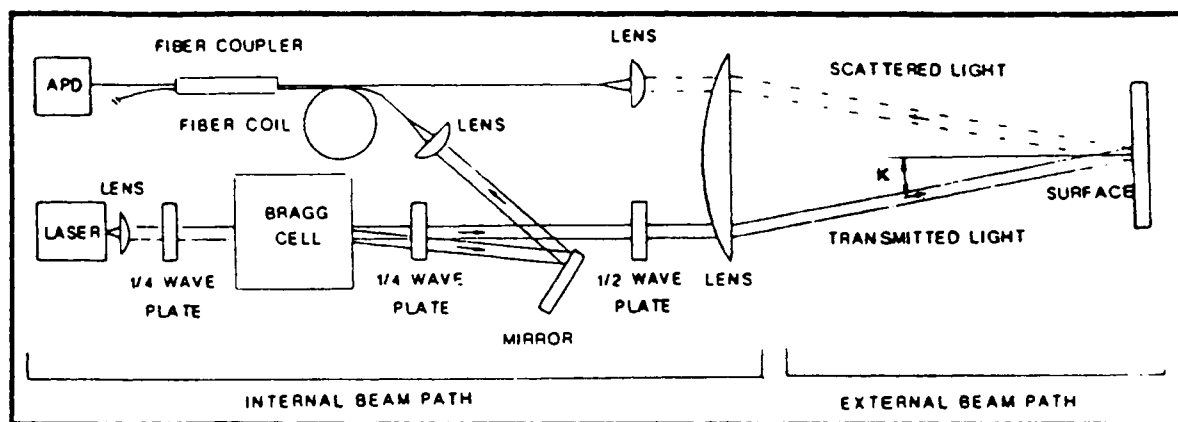


Figure 8-13. T.S.I. LDV Schematic.

Table 8-4. Comparative LDV Specifications.

	Dantec	Polytec	T.S.I.	B&K
Laser	HeNe 633nm 10 mW	HeNe 633 nm 3 mW	Laser Diode 700 nm 10 mW	HeNe 633 nm 1 mW
Dynamic Range	>160 dB	>160 dB	75 dB	60 dB
Frequency Range	DC to 740 KC	DC to 1 MHz	1 Hz to 100 KHz	DC to 20 KC
Velocity Range	10^{-6} to 3 M/sec	10^{-6} to 10 M/sec	10^{-4} to 1 M/sec	20 μ M/sec to 1 M/sec
Displacement Range	10^{-8} to 1 M	10^{-7} to 0.1 M	10^{-10} to 2×10^{-2} M	10^{-9} to 7×10^{-3} M
Acceleration Range	10^{-12} to 3000 g	0 to 300 g	10^{-2} to 10^{-5} g	10^{-5} to 10,000 g
Standoff Distance	1.7 to 20 M	0.1 to 3 M	0.5 to 1.5 M	0.2 to 0.8 M

838PROP/3-T8-4.BB
11-11-89

Table 8-5. Factors in the Choice of an LDV.

- Physical Arrangement of the Laser, Optics and Signal Conditioning.
Use of Fiber Optics by Polytec.
- Ability to Withstand the Environment and Ease of Traversing if
Equipment Requires Shielding - Water Cooling.
- Choice of Laser Power, 1 mW to 30 mW.
- Characteristic of Reflecting Surface. Use of Paint.
- Standoff Distance for Optical Head.
- Solid State Laser Versus Gas Laser.
- Use of Filters When Measuring Surface Is Glowing -- IR and Visible
Radiation.
- Range of Velocity Measurement.
- Cost.

838PROP/3-T8-5.BB
11-11-89

Shaker testing diffusion bonded joints between titanium and TMC materials is particularly important. It is possible that some material combinations may develop better structural joints than others, sufficient to be a criterion in material selection for designs that follow this program.

Another potentially important consequence of the shaker tests will be the determination of the fatigue life characteristics and damage mechanisms in terms of temperature ranges that the different materials and material joints can effectively sustain. This may revise or more accurately define the appropriate temperature ranges for materials competing for the same application area. Comparisons will also be possible between superplastically formed corrugations and hat stiffeners. Comparing the strain-life temperature relationships of integrally stiffened carbon-carbon and LID-TMC joints is of major interest. The shaker test results at various temperatures will be used to define critical test temperatures for the PWT panels.

Figure 8-8 shows the shaker to be used with a furnace for the high-temperature tests. Rohr has tested carbon-carbon coupons up to 1800°F in this facility.

Rohr's experience in the field of high-temperature shaker tests has illustrated the importance of the selection of fixing hardware used to attach the test articles to the fixtures. For example, shaker tests on carbon-carbon coupons at 1800°F require that special bolts manufactured from niobium rod be used to secure the specimens. Niobium is used because of its low oxidation and thermal expansion rates.

The shaker heating/fixturing arrangement has been modified from that shown in Figure 8-8 to that shown in Figure 8-14. This modified arrangement has the specimen tip accelerometer outside the heating chamber. The fixturing is also partially shielded from the specimen temperature.

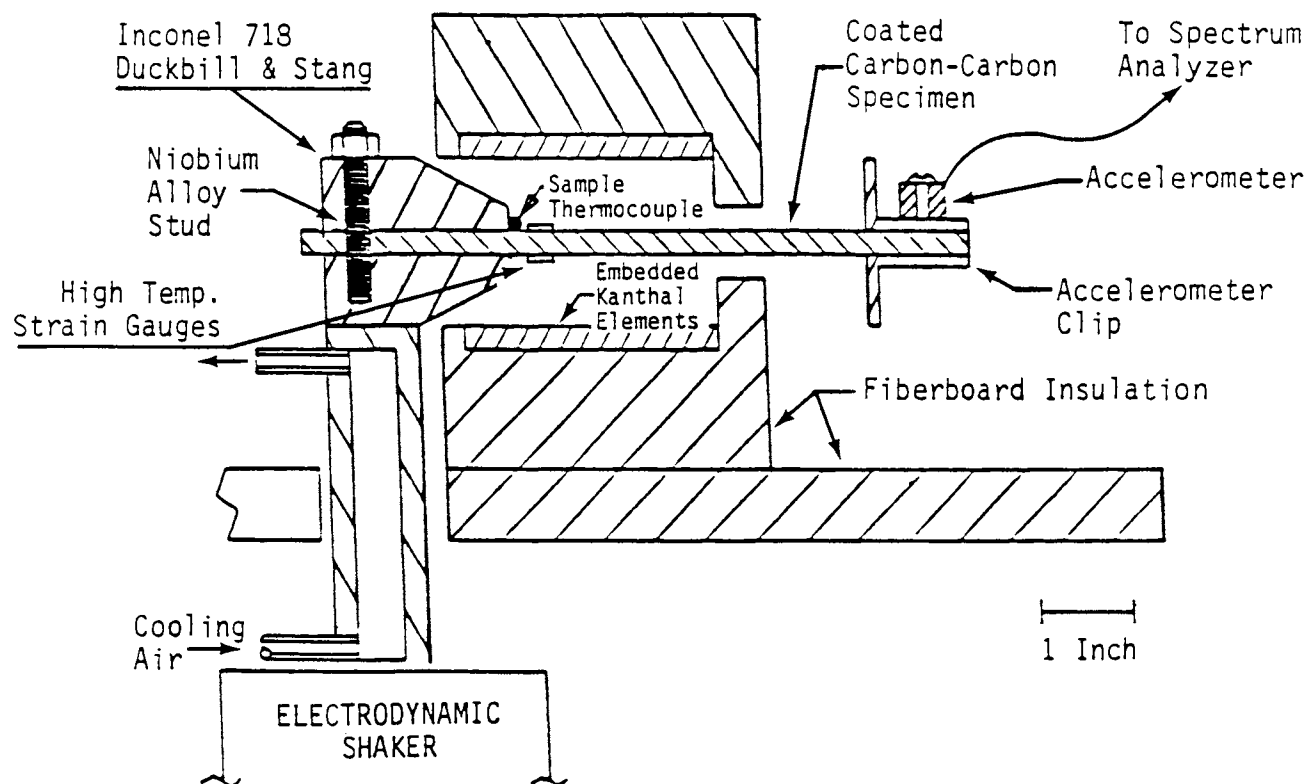


Figure 8-14. Schematic of High-Temperature, High-Cycle Fatigue Apparatus.

The exact sequence of specimen testing will be determined as specimens become available. However, the testing will be in the following general sequence:

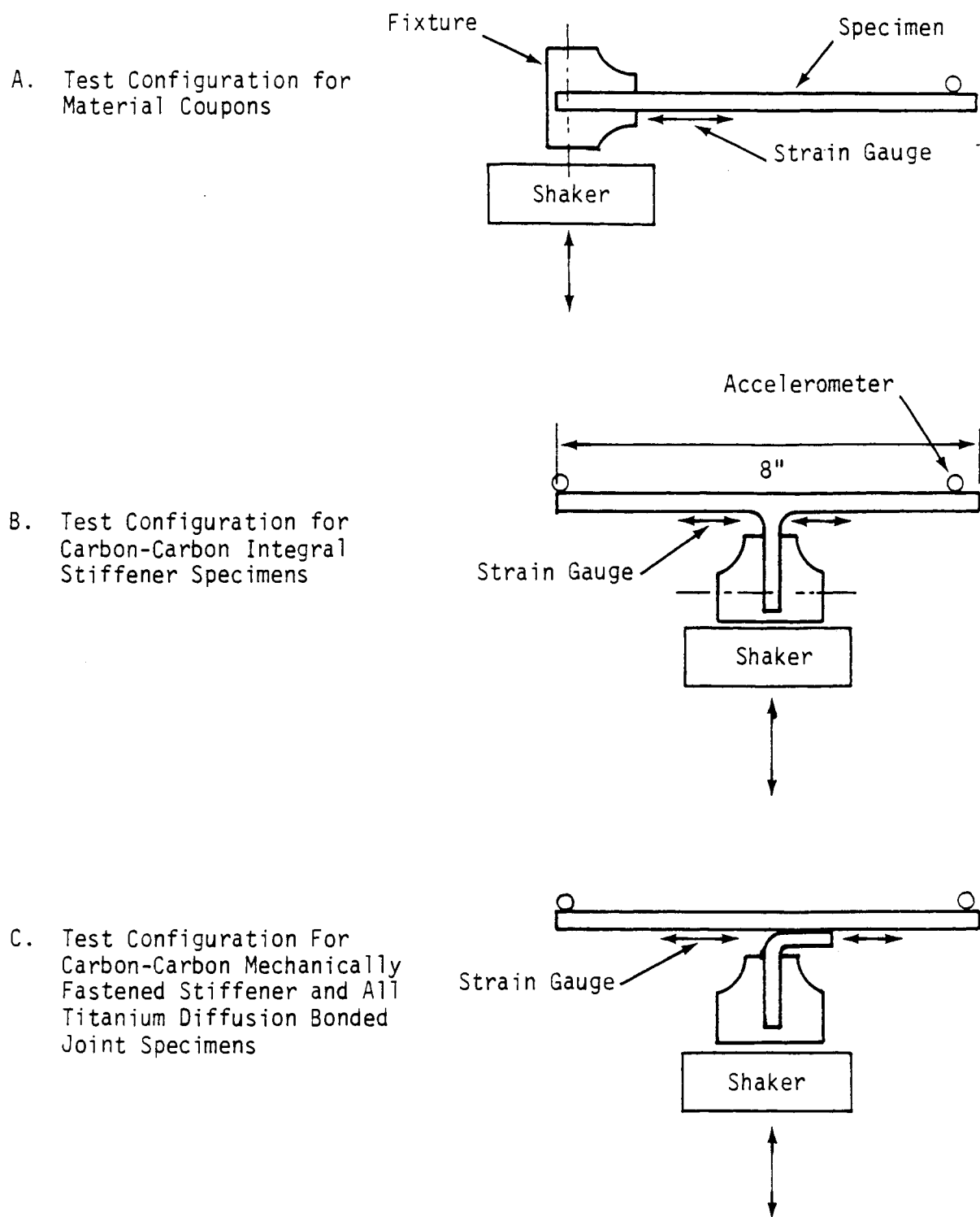
- Material coupons, room temperature.
- Material coupons, elevated temperatures in ascending order.
- Skin-stiffener subelements, room temperature.
- Skin-stiffener subelements, elevated temperatures in ascending order.

All shaker specimens for a given material will be tested prior to the corresponding panel testing. It is anticipated that the shaker test results may affect PWT test conditions. These results will be discussed with the Air Force as they become relevant.

Test setups and strain gauge locations for each specimen type are shown in Figure 8-15. Specimen test temperatures are shown in Table 8-6. Each coupon specimen will have one strain gauge and each joint specimen will have two strain gauges, as shown in Figure 8-15. An additional back-to-back strain gauge will be added to the first room-temperature specimen of each type.

Test strain levels for the majority of specimens will be determined on the basis of the results from the first specimen of each type. The first specimen of each type will be loaded to produce a failure in the 10^6 cycle region. Subsequent specimens will be targeted for the 10^6 to 10^7 cycle range. First specimen rms strain levels are as follows:

- Carbon-Carbon - 600 microstrain.
- All titanium specimens - 2000 $\mu\epsilon$.



- Notes:
1. All Specimens 2" Wide.
 2. Strain Gauges at Center of 2" Dimension.
 3. Thermocouples to be located adjacent to strain gauges.

Figure 8-15. Shaker Specimens - Test Setup and Instrumentation.

Table 8-6. Shaker Specimen Test Temperatures.

Specimen Type	Number of Specimens and Test Temperatures					
	Room Temp.	600°F	800°F	1200°F	1500°F	1800°F
Carbon-Carbon						
- Material Coupon	4	3	-	3	-	4
- Integral Joint	4	-	-	-	-	4
- Fastened Joint	4	-	-	-	-	4
Titanium Metal Matrix Composite						
- Material Coupon	4	-	-	3	3	-
- Diffusion Bonded Joint	3				3	
RSR Titanium						
- Material Coupon	4		3	3		
- Diffusion Bonded Joint	3		3			
Titanium Aluminide						
- Material Coupon	4		3	3		
- Diffusion Bonded Joint	3		3			
6-2-4-2 Titanium						
- Material Coupon	4	3	3			
- Diffusion Bonded Joint	3		3			
6-4 Titanium						
- Material Coupon	4	3	3			
- Diffusion Bonded Joint	3		3			
6-4 Titanium						
- Truss Core Coupons	3		3			

838PROP/3-T8-6.BB
11-11-89

If failures occur in less than 10^6 cycles, subsequent test loads will be decreased. If failures have not occurred by 10^7 cycles, subsequent loads will be increased.

The shaker test procedure for each specimen will comprise a sine-sweep to identify mode shapes and natural frequencies, followed by random endurance testing with one-third octave loading centered around the fundamental bending node frequency. Specimen response will be measured using strain gauges, a tip accelerometer, and a Laser Doppler Vibrometer. All transducer outputs, including the shaker table accelerometer, will be recorded on magnetic tape for subsequent data reduction.

The data generated will include overall rms levels, frequency spectra, phase (where appropriate), integrated spectral functions, damping ratios, peak amplitude distributions, fatigue lives, and temperatures.

Specimen failure will be determined by changes in natural frequency and/or visible damage. In the event of a frequency shift without visible damage, the specimen will be subjected to x-ray or ultrasonic inspection and returned to testing if no damage is detected. Cycles-to-failure will be determined from frequencies and exposure times. Fatigue curves will utilize both rms and peak strain values.

8.5 PROGRESSIVE WAVE TUBE PANEL TESTS

The eight panels identified in Section 8-2, Table 8-2, will be subjected to random response and sonic fatigue testing in Rohr's PWT. The test panels utilize the same materials and fabrication processes as the shaker test specimens listed in Table 8-1. Rohr's PWT facility and the panel heating system are described in Section 8.3.2.

Many of the test parameters and fixturing details have yet to be determined. It is anticipated that some of the panels will be endurance tested at the maximum available acoustic level of 168 dB, particularly the carbon-carbon and actively cooled panels. Shaker test results are

likely to influence acoustic load and response level requirements for the remaining panels. Similarly, the high-temperature shaker test fatigue data will influence panel test temperatures. It does not automatically follow that the maximum vehicle application temperature is the most critical for sonic fatigue. For example, the carbon-carbon configuration 2 panel, which represents the inlet ramp, has its highest acoustic load during takeoff, whereas the highest temperatures occur at high Mach numbers. In addition, carbon-carbon shows improving structural properties with increasing temperatures. In the case of the diffusion bonded titanium and TMC panels, there is a residual joint area stress at room temperature resulting from the 1000°F bonding process temperature. Consequently, some of these specimens may have better fatigue characteristics at 1000°F than at room temperature. The skin-stiffener joint shaker data will clarify critical test temperatures.

Fixturing details are difficult to define at this time because the edge details of the MDC supplied panels have not yet been fully defined. The problems involved in mounting the test articles to subject them to the combined thermo-acoustic environment are not trivial. The fixture design must provide or incorporate:

- Isolation from facility structural vibration.
- Realistic panel edge fixity.
- Thermal isolation of the test articles from structural heat sinks.
- Control of the differential thermal expansion between the test article and its mounting fixture.
- Immunity from excessive oxidation at high temperatures.
- A fatigue life in the combined environment which is greater than that of the test articles.

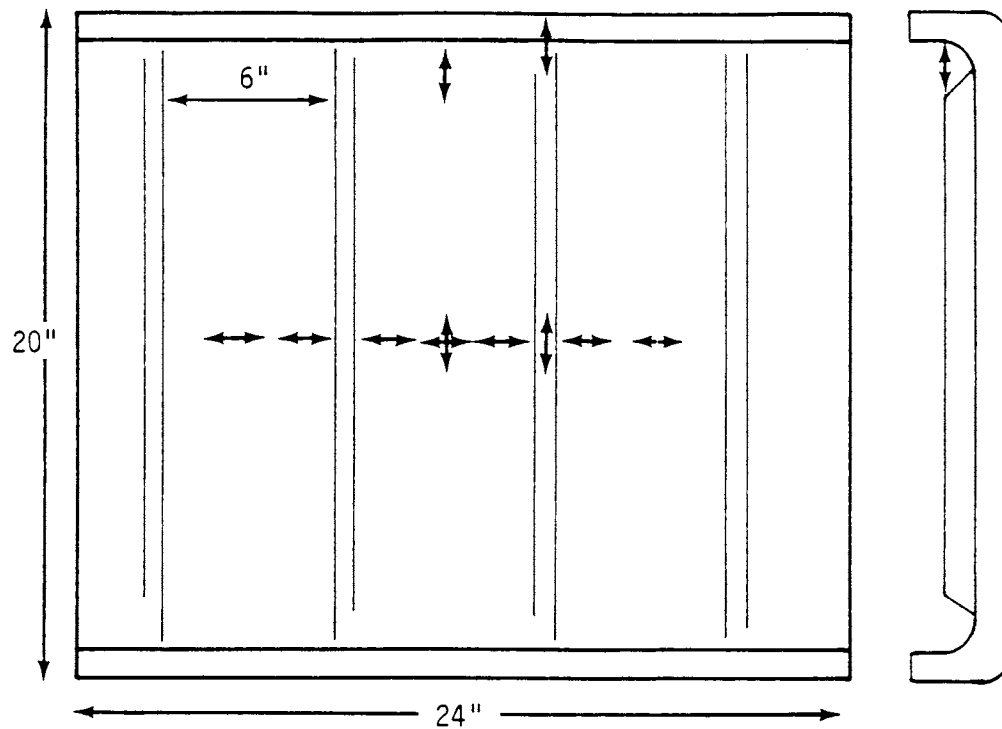
- Fixing means which will not impose unknown or variable local constraints to the test articles and will not significantly deteriorate within the test duration.

In order to achieve these objectives, the test articles will be mounted in frames suspended from the facility structure in a wire harness. The suspension of the support frames in the sonic fatigue test facility will serve a dual purpose: to provide isolation of the test articles from facility structural vibration and to provide thermal isolation between the frames and the facility structure.

Two different frame structures will be utilized: one designed to match the thermal expansion of titanium up to 1500°F and one matching the low thermal expansion of carbon-carbon at higher temperatures. These supporting frames will be maintained at temperatures approximating those of the test articles in order to reduce panel temperature nonuniformity caused by edge conduction losses. Additionally, thermal isolation will be provided between the test articles and the frames to minimize edge conduction from the panels resulting from residual temperature differentials. Fixturing details will be transmitted to the Air Force for review as they are developed.

The sequence of panel testing will be determined by the availability of the shaker test data. The only pre-determined sequence is that the TMC hat-stiffened panel will be tested prior to testing the actively cooled panel, which has TMC face sheets. Strain gauge locations for the panels are shown in Figures 8-16 through 8-19. A total of 91 strain gauges are shown. The anticipated test temperatures are given in Figures 8-1 through 8-6. Strain gauge temperature capabilities will reflect the maximum test temperatures as far as feasible. Cost constraints and the uncertain reliability associated with 1800°F strain gauges may require the use of lower-temperature strain gauges in many locations. Lower-temperature panel strain response data may then be used to identify selected critical gauge locations for 1800°F strain gauge application. It is anticipated that two LDV's will be available for panel response amplitude measurements. With one LDV at a reference location, the second

Carbon-Carbon Configurations 1 and 3: 11 Gauges Each



Carbon-Carbon Configuration 2: 11 Gauges

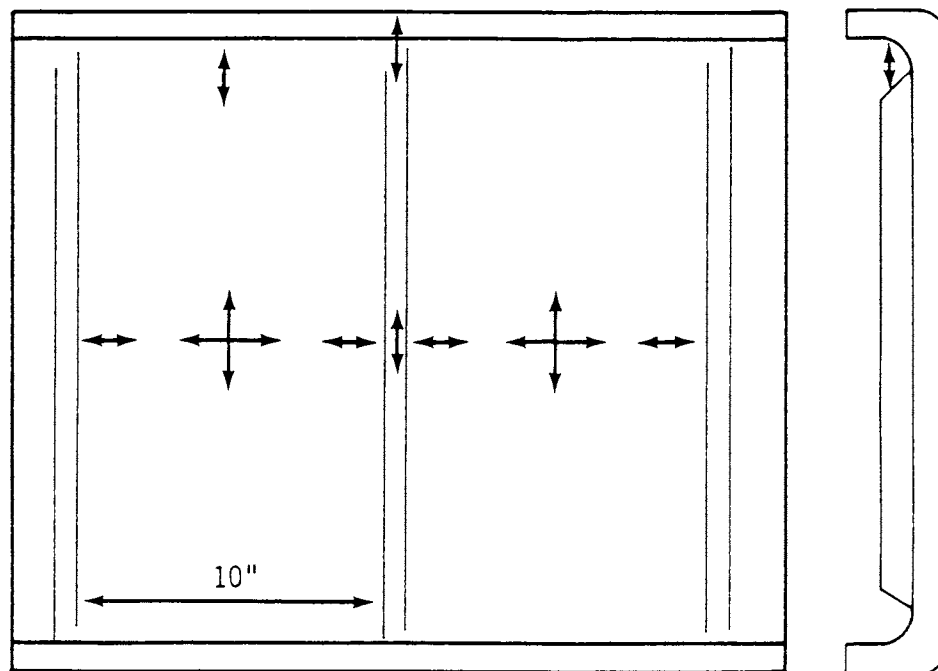


Figure 8-16. Strain Gauge Locations for Carbon-Carbon Panels.

4 Gauges Shown on Each Face Sheet = 8 Gauges
5 Additional Gauges - To be Determined

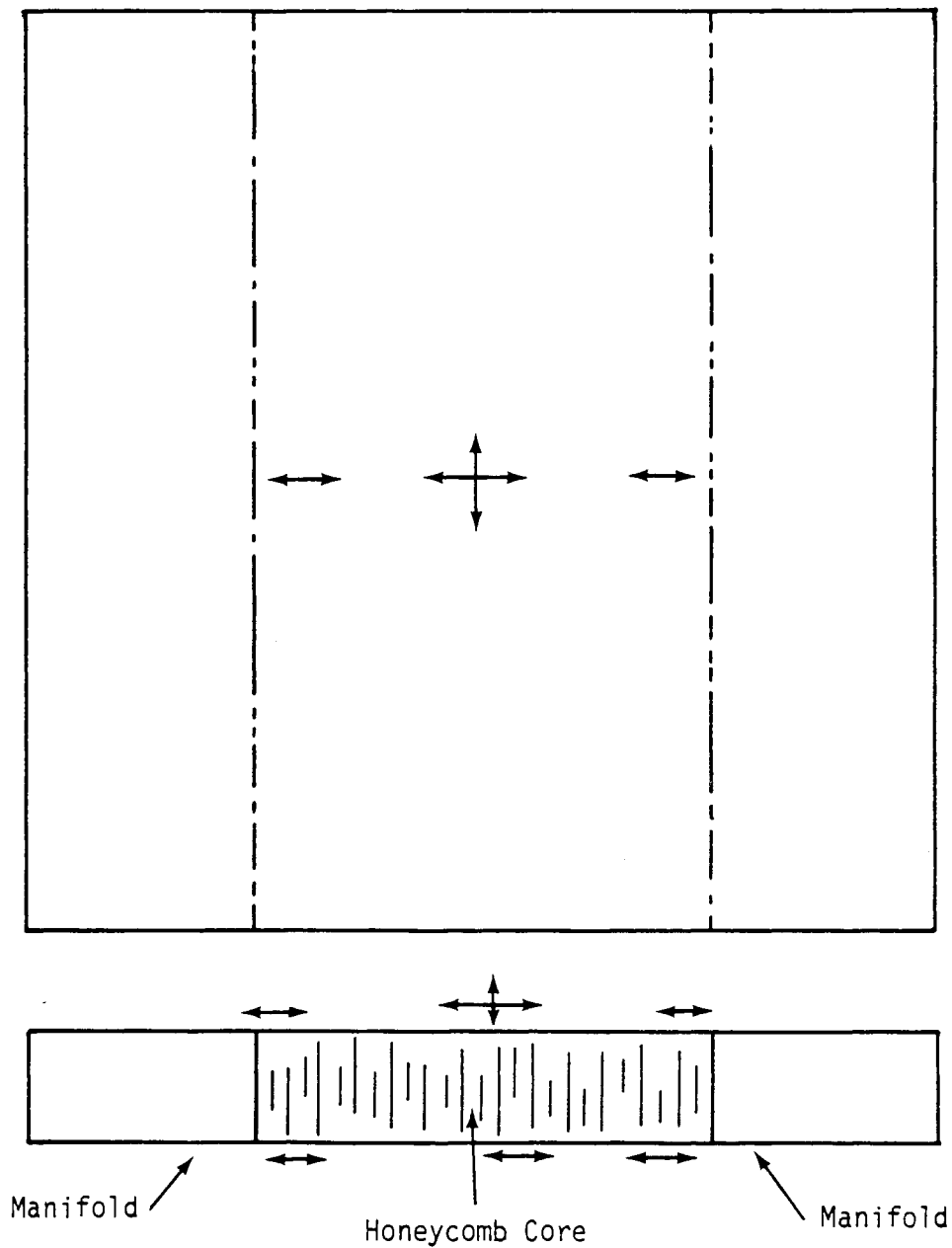
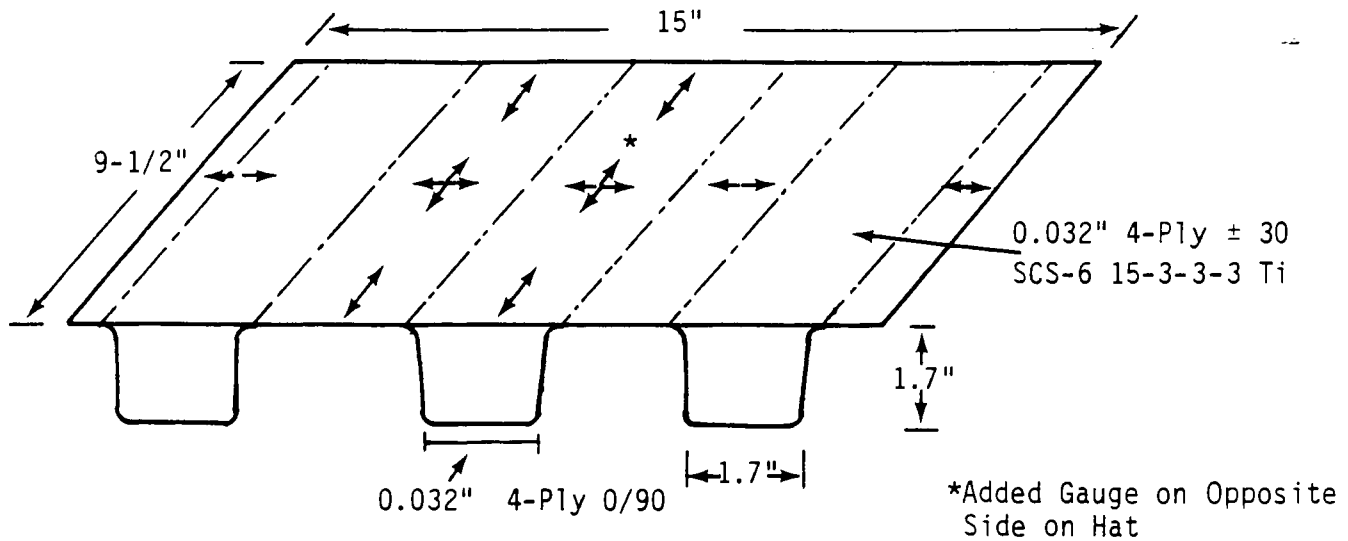


Figure 8-17. Strain Gauge Locations for Actively Cooled Panel (13 Gauges).

TMC and 6-4Ti Hat-Stiffened Panels - 12 Gauges Each



Monolithic 6-4Ti Hat-Stiffened Corrugated Panel - 11 Gauges

Material: 6Al 4V Ti

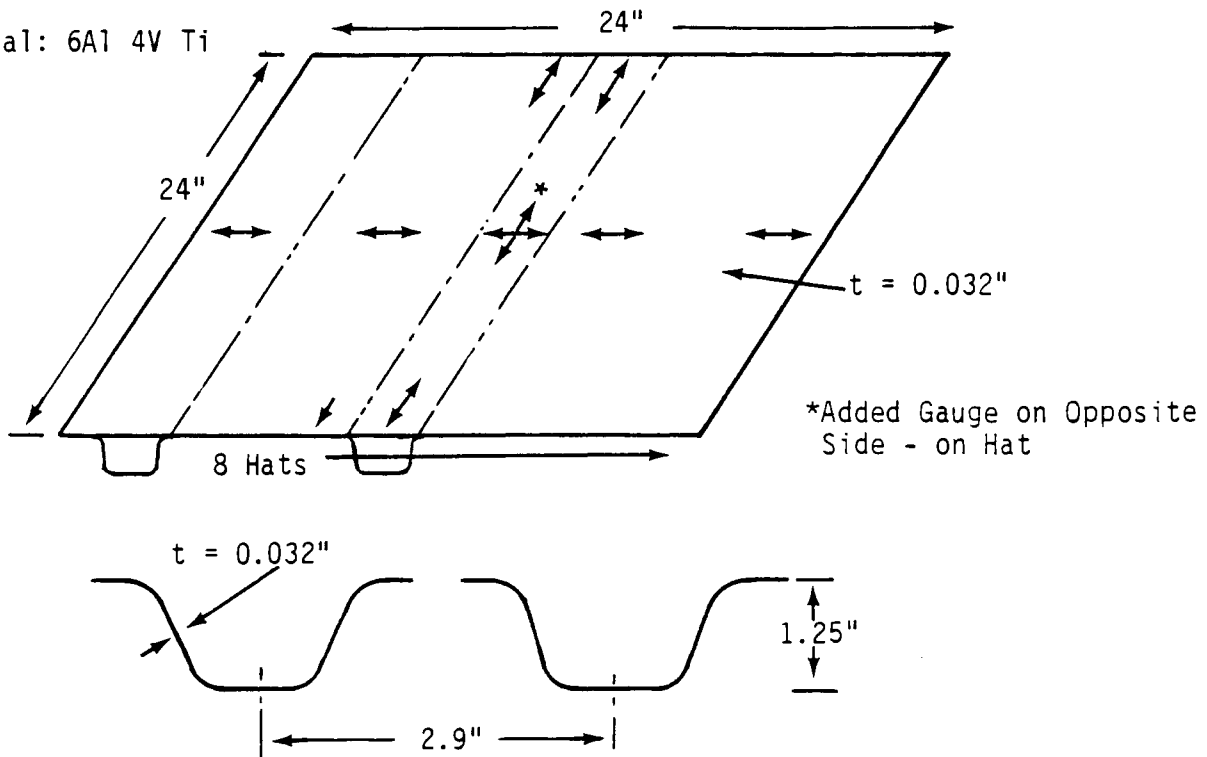


Figure 8-18. Strain Gauge Locations for Titanium Hat-Stiffened Panels.

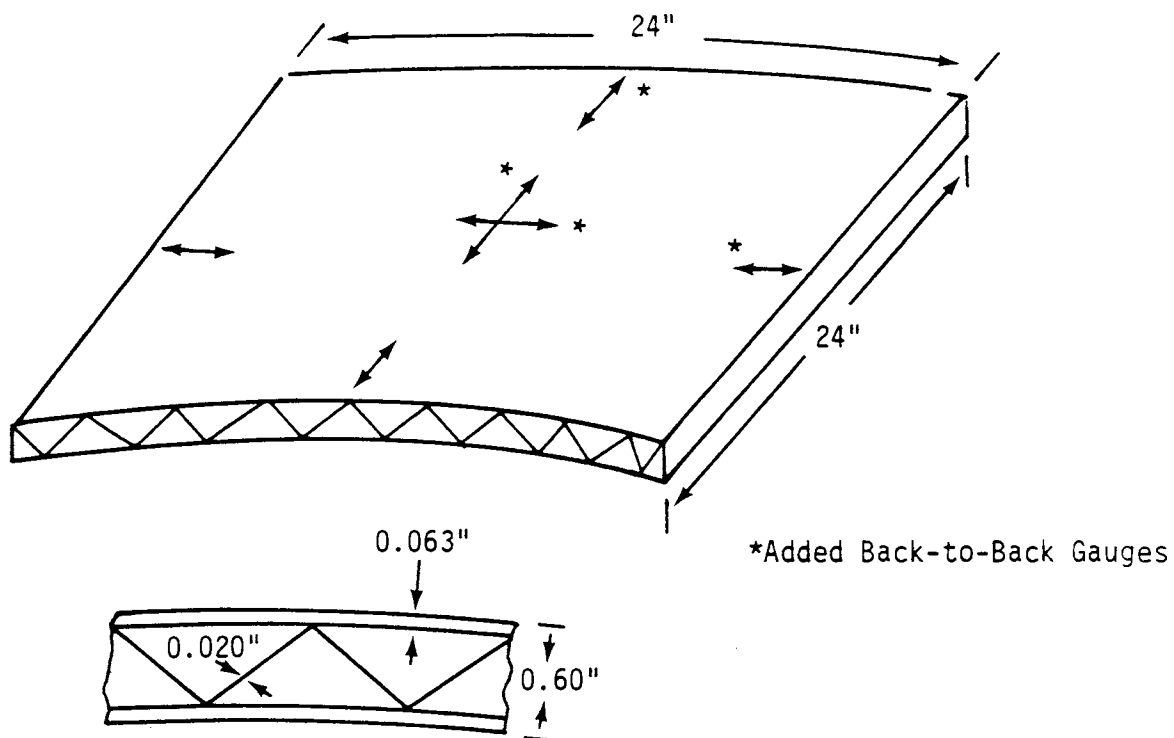


Figure 8-19. Strain Gauge Locations for Monolithic Titanium Truss Core Panel (10 Gauges).

one will be used to comprehensively map panel deflection response. Thermocouple locations have not yet been determined. However, at least four thermocouples per panel are envisaged in order to measure center panel temperatures on both the exposed and back surfaces plus at least two of the panel edges. Accelerometers will be used only to monitor fixture vibration and to check the validity and accuracy of the LDV measurements.

Rohr has a selection of B&K, Kulite, and Endevco microphones for use in this program. B&K microphones will be suspended in the PWT just outside the high-temperature area. Kulite or Endevco microphones will be flush mounted in the panel/fixture frame assembly for temperatures up to 500°F. For higher-temperature acoustic measurements, Rohr expects to procure a water cooled sleeving for a Kulite or similar type microphone.

As in the case of the shaker test specimens, panel endurance tests will be targeted to result in failures in the 10^6 to 10^7 cycle range. Consequently, test acoustic levels will be based on panel response strains in conjunction with the shaker fatigue data.

Each panel will be installed in a picture-frame type fixture and the panel-fixture assembly will be suspended on a harness system in the specimen opening of the PWT. Modal testing will then be performed using local shaker or tap hammer excitation at selected temperatures from "ambient" up to the maximum anticipated for that panel. These tests will determine resonant frequencies, mode shapes, modal stiffnesses, masses, and damping values.

Acoustic testing will commence with a sinusoidal sweep at room temperature, followed by incremental broad band random loading from 140 dB up to 168 dB, depending upon panel response levels. These initial tests will obtain basic load-response data without accumulating possible fatigue damaging strain cycles. Strain gauge, accelerometer, LDV, and microphone signals will be recorded on magnetic tape. This test procedure will be repeated at several temperatures up to 1500°F (TMC

panel) or 1800°F (carbon-carbon panels). Intermediate temperatures will include 400°F, 600°F, 800°F, 1000°F, and 1200°F.

The actively cooled panel is designed to reduce skin temperatures from 3500°F to 600°F by flowing liquid hydrogen through titanium coolant channels. The current intention is to test this panel with water as the coolant. The test temperature is to be determined. Panel temperatures will be measured using thermocouples. Strain displacement relationships will be determined during these tests from strain gauge and LDV data.

Following the ambient and intermediate temperature response testing, an endurance test temperature and acoustic load level will be selected for each panel based on a combination of the expected flight vehicle environment, shaker test fatigue data, and the preceding response data. The loads selections will be targeted for obtaining response and fatigue life data at the maximum application temperatures, with expected failures in the 10^6 to 10^7 cycle range. Panel response measured using an LDV will be converted to strains using relationships developed during the preceding response tests. Reduced bandwidth (octave, 1/3 octave) loading will be used if necessary to induce failure with increased spectrum levels.

Panel fatigue will be observed by monitoring response frequencies and displacement levels and by regular visual inspections. Reduced data will include amplitude time-histories, peak amplitude distributions, overall rms and spectrum levels, integrated spectra, phase, and coherence.

After testing on a panel has been completed, the panel will be subjected to inspection and failure detection methods. High-magnification photomicrographs will be made of damaged areas and crack surfaces.

If a panel cannot be tested to failure in the PWT, even after 10^7 cycles at the maximum 1/3 octave acoustic level available, supplementary test options will be presented to the Air Force for discussion and/or

approval. Potential options include shaker testing the entire panel or sections of it and testing beyond 10^7 cycles (subject to cost constraints).

The results from the shaker and PWT tests will be used in conjunction with the panel analysis results to develop design criteria and fatigue life prediction methods.

8.6 PROGRAM SCHEDULE

Figure 8-20 shows the program schedule. The shaker test schedule has been revised to show completion at the end of August 1990. The overall program completion date is not affected by this task schedule change.

8.7 REFERENCES

- 8-1 Thermo-Vibro-Acoustic Loads and Fatigue of Hypersonic Flight Vehicle Structure, Technical Proposal prepared for U.S. Air Force by Rohr Industries, Inc., Document No. 802-87-010, June 1987.

838PROP
3-8.BB
12-15-89

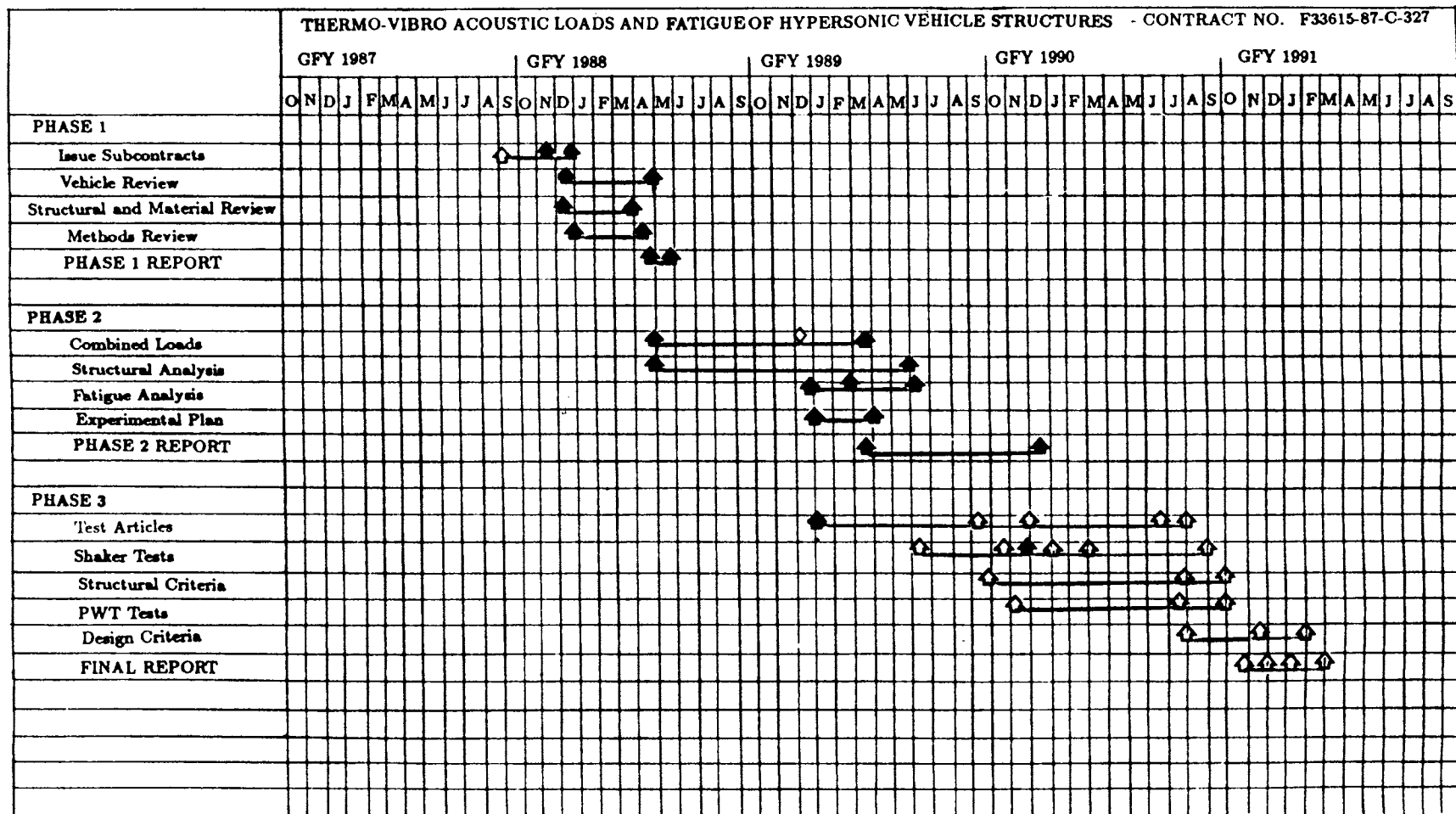


Figure 8-20. Program Schedule.

SECTION 9

DYNAMIC ANALYSIS OF CARBON-CARBON TEST PANELS

Three panel design concepts are currently proposed for testing in the progressive wave tube described in Section 8. The designs differ in the skin and rib thicknesses and the number of ribs, as shown in Table 9-1. All test panels are square (20 in. x 20 in.). Dynamic and sonic fatigue analyses were performed to help characterize their dynamic behavior in the forthcoming testing phase of the program.

The material model for carbon-carbon is idealized as orthotropic with transverse shear flexibility. The stress-strain relationship is assumed to be linear. For reasons outlined in Section 5, it was decided that the stiffness characteristics remain unchanged at elevated temperatures, a conservative assumption.

9.1 MODAL ANALYSIS

Modal analysis was carried out using SOL 3 - NASTRAN up to 600 Hz. The attach plates were incorporated in the finite element models in order to simulate the proper attachment conditions. The material model was represented by PSHELL and MAT2 NASTRAN cards and was based on Rohr data for carbon-carbon fabric.

Table 9-1. Test Panel Design Concepts.

HTC Panel Design Concept 1	(Preform) 575-0762-1 575-0763-3	4 Rib Design, 6" Spacing, 0.065" Thick Skin, 0.080" Thick Ribs	1 Specimen
HTC Panel Design Concept 2	(Preform) 575-0762-3 575-0763-1	3 Rib Design, 9" Spacing, 0.065" Thick Skin, 0.080" Thick Ribs	1 Specimen
HTC Panel Design Concept 3	(Preform) 575-0441 575-0665-503	4 Rib Design, 6" Spacing, 0.125" Thick Skin, 0.150" Thick Ribs	Use Existing HTC Program Panel

838PROP
3-T9-1.8B
11-16-89

9.1.1 Concept 1

The finite element model for design concept 1 is shown in Figure 9-1 along with all its fixities and the appropriate boundary conditions. The first mode occurs at 177 Hz and exhibits the stiffness of the attachment mechanism. The second mode occurs at 270 Hz and corresponds to an out-of-phase mode. The in-phase mode occurs at 352 Hz. These modal shapes are graphically depicted in Figure 9-2. The corresponding modal stress fields are shown in Figure 9-3. The highest modal stresses are observed at the center of the bays for the out-of-phase mode and at the center of the midbay and the top of the two middle stiffeners for the in-phase mode.

9.1.2 Concept 2

The modal analysis procedure for design concept 2 was similar to that used for design concept 1. The finite element model is shown in Figure 9-4. The first mode occurs at 176 Hz and exhibits the stiffness of the attachment mechanism. The second mode occurs at 205 Hz and corresponds to an in-phase mode. The modal shape is graphically depicted in Figure 9-5. No distinct out-of-phase mode was found up to 525 Hz. The corresponding modal stress field is shown in Figure 9-6. The highest modal stresses are observed at the center of the bays.

9.1.3 Concept 3

The finite element model for design concept 3 is shown in Figure 9-7. The first mode occurs at 259 Hz and corresponds to a rail attachment mode. The second mode occurs at 461 Hz and is an out-of-phase mode. The in-phase mode has a natural frequency of 495 Hz. These modal shapes are graphically depicted in Figure 9-8. The corresponding modal stress fields are shown in Figure 9-9. The highest modal stresses are observed at the center of the bays for the out-of-phase mode and at the center of the midbay and the top of the middle stiffeners for the in-phase mode.

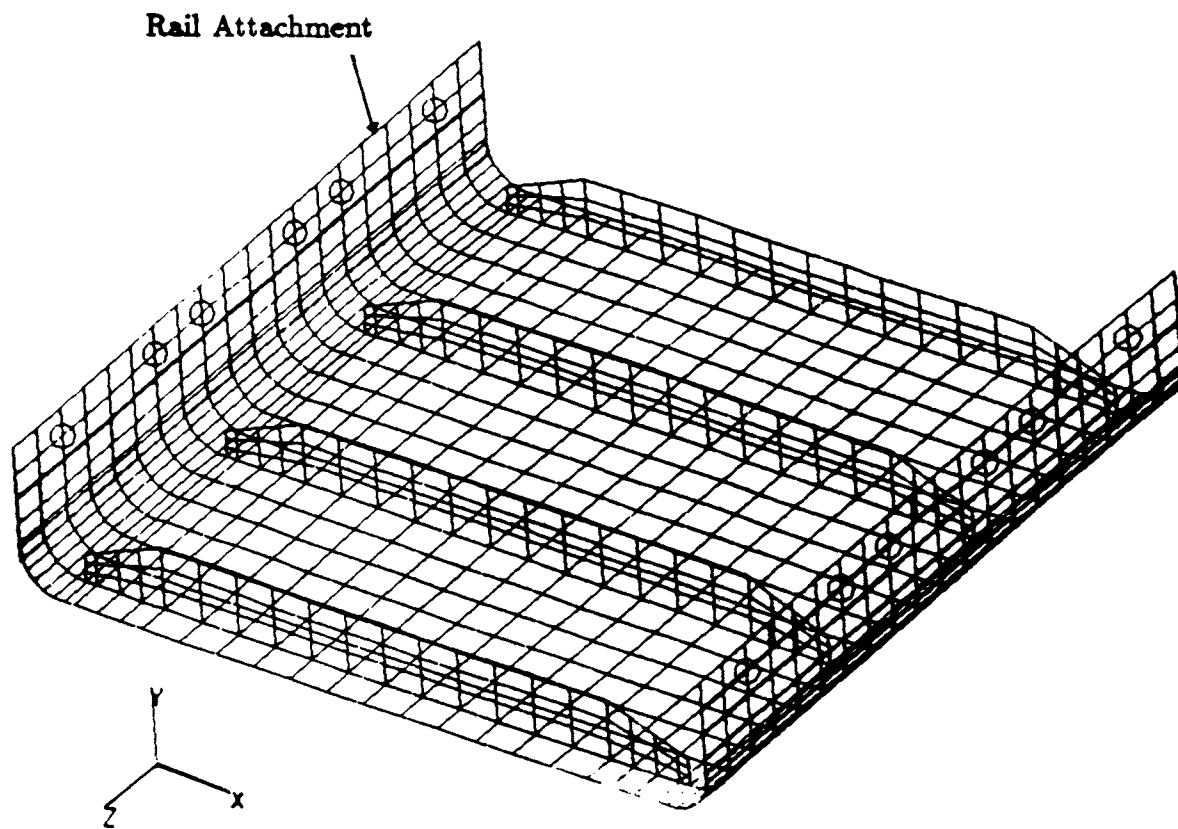
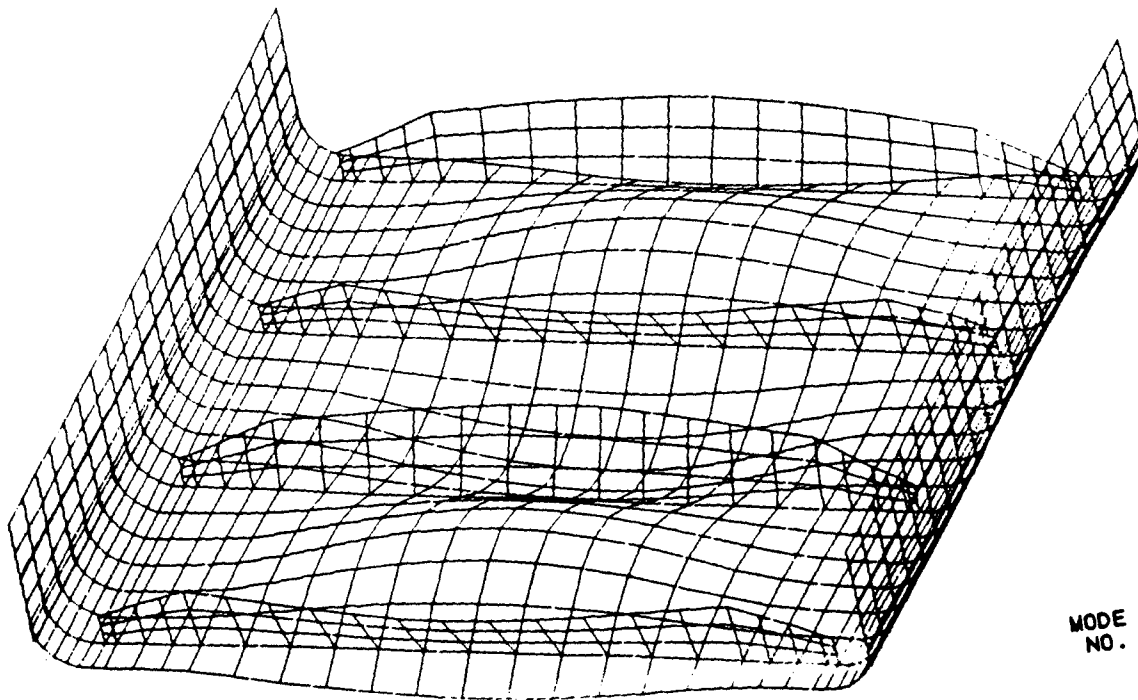
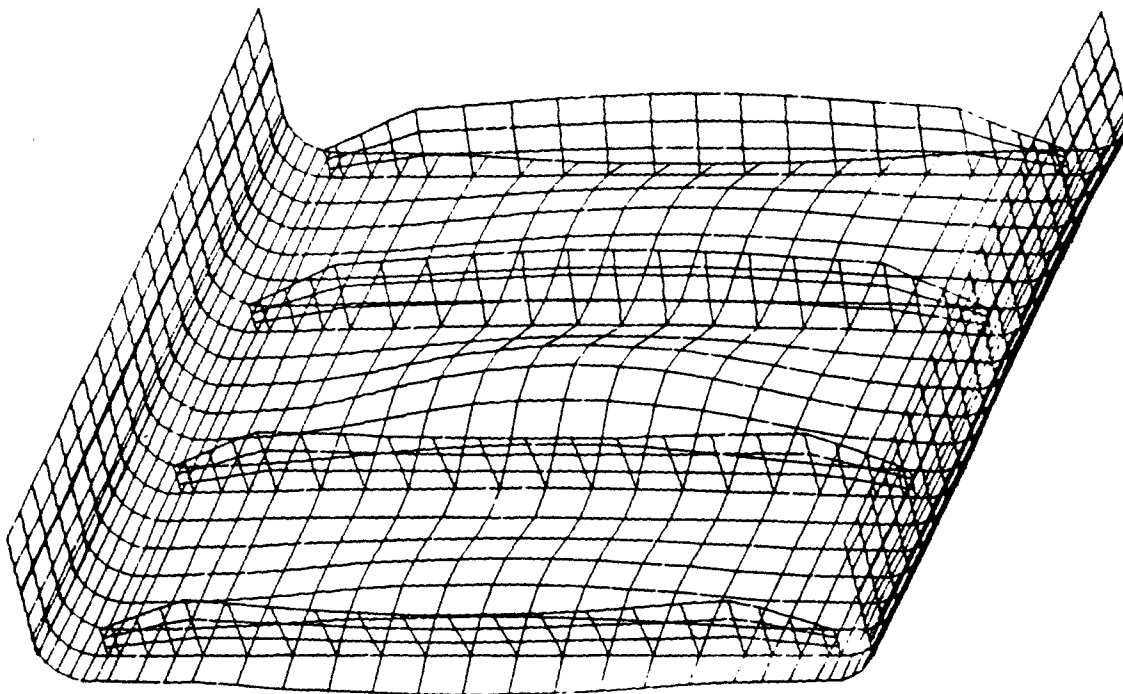


Figure 9-1. Finite Element Model for Carbon-Carbon Test Panel Design Concept 1.



CARBON/CARBON TEST PANEL - CONCEPT1
 MODAL ANALYSIS
 MODE NUMBER = 2 EIGENVALUE = 0.2874497E+07

MODE NO.	CYCLES
1	1.773718E+02
2	2.698367E+02
3	2.952990E+02
4	3.521091E+02
5	4.472852E+02
6	4.780959E+02
7	4.949029E+02
8	5.024074E+02
9	5.416628E+02
10	5.863270E+02



CARBON/CARBON TEST PANEL - CONCEPT1
 MODAL ANALYSIS
 MODE NUMBER = 4 EIGENVALUE = 0.4894568E+07

Figure 9-2. Modal Shapes for Carbon-Carbon Test Panel Design Concept 1.

CONCEPT 1
MODAL STRESS FIELD

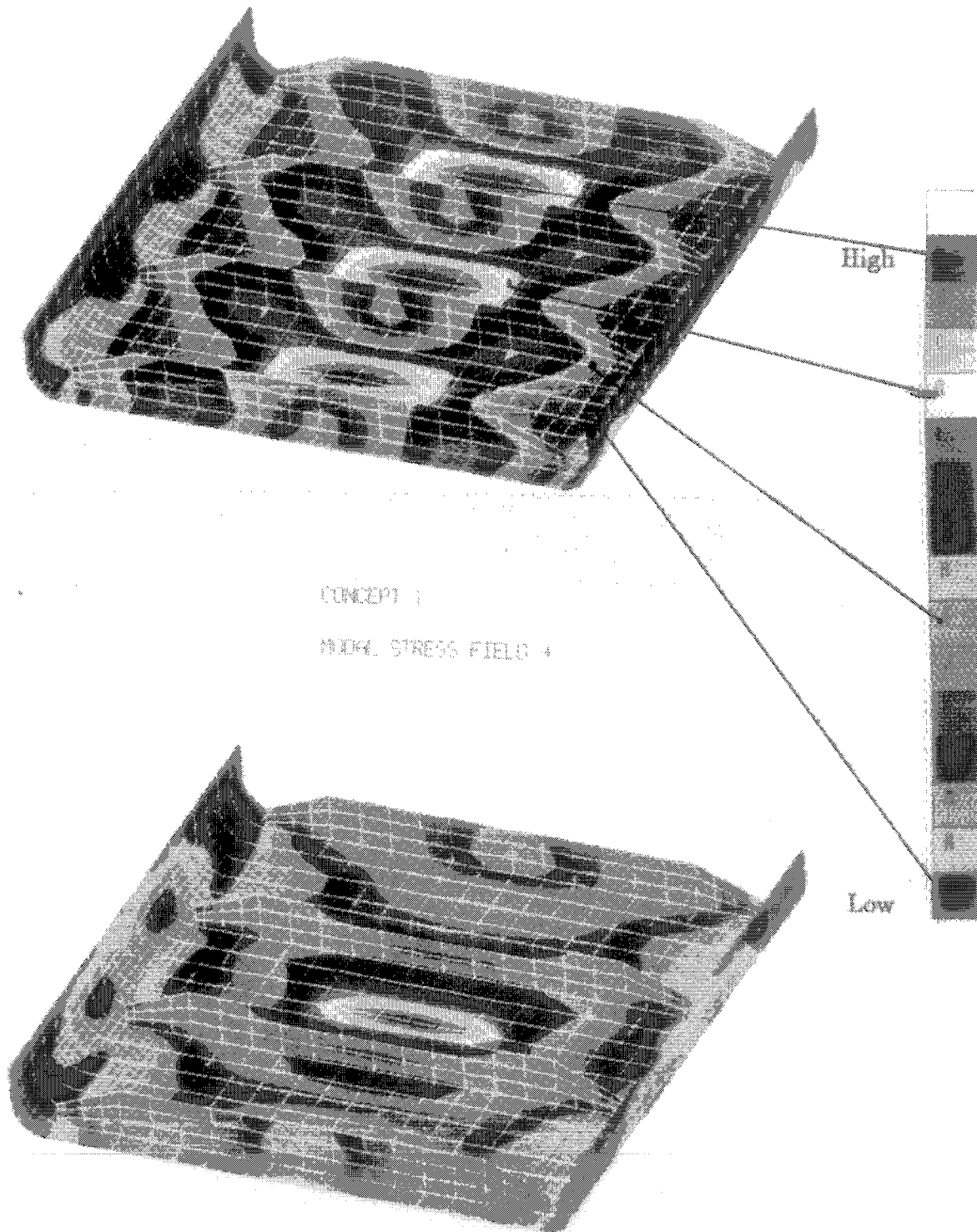


Figure 9-3. Modal Stress Fields for Carbon-Carbon Test Panel Design Concept 1.

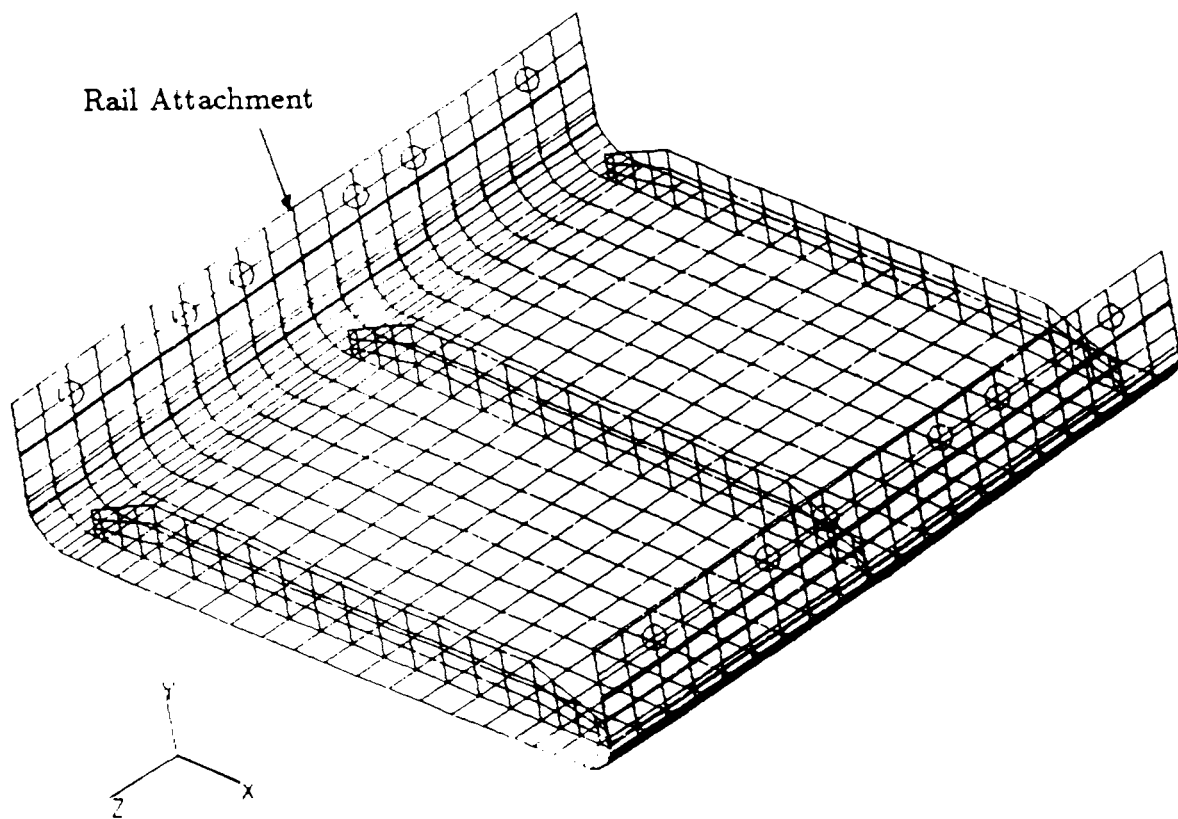
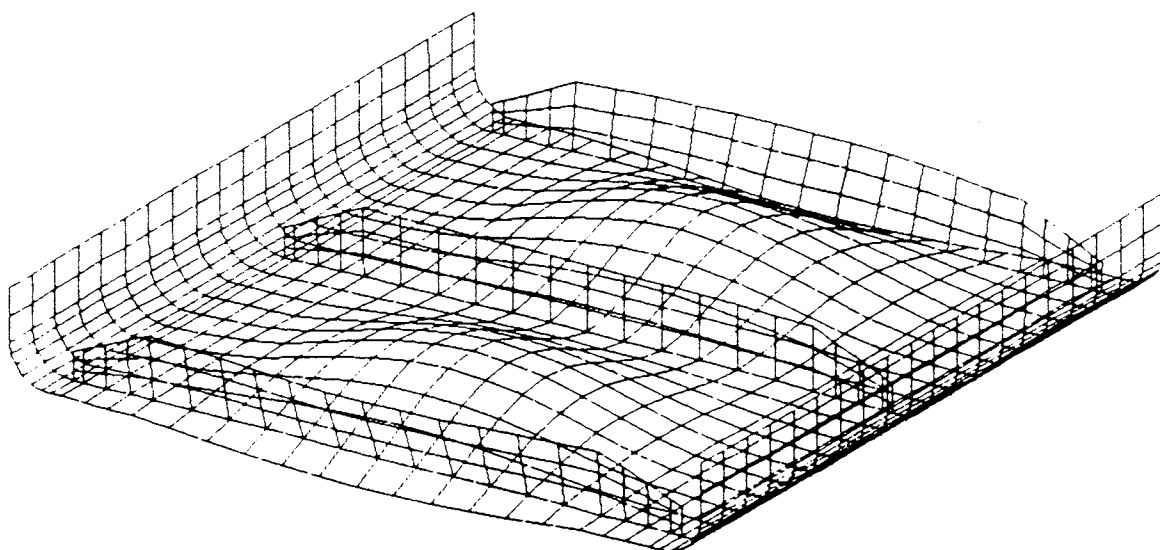


Figure 9-4. Finite Element Model for Carbon-Carbon Test Panel Design Concept 2.



CARBON/CARBON TEST PANEL - CONCEPT2
 MODAL ANALYSIS
 MODE NUMBER : 2 EIGENVALUE : 0.1650465E+07

MODE NO.	CYCLES
1	1.758671E+02
2	2.044670E+02
3	3.070595E+02
4	3.322400E+02
5	3.819938E+02
6	3.962421E+02
7	4.187639E+02
8	5.126171E+02
9	5.174569E+02
10	5.256503E+02

Figure 9-5. Modal Shape for Carbon-Carbon Test Panel Design Concept 2.

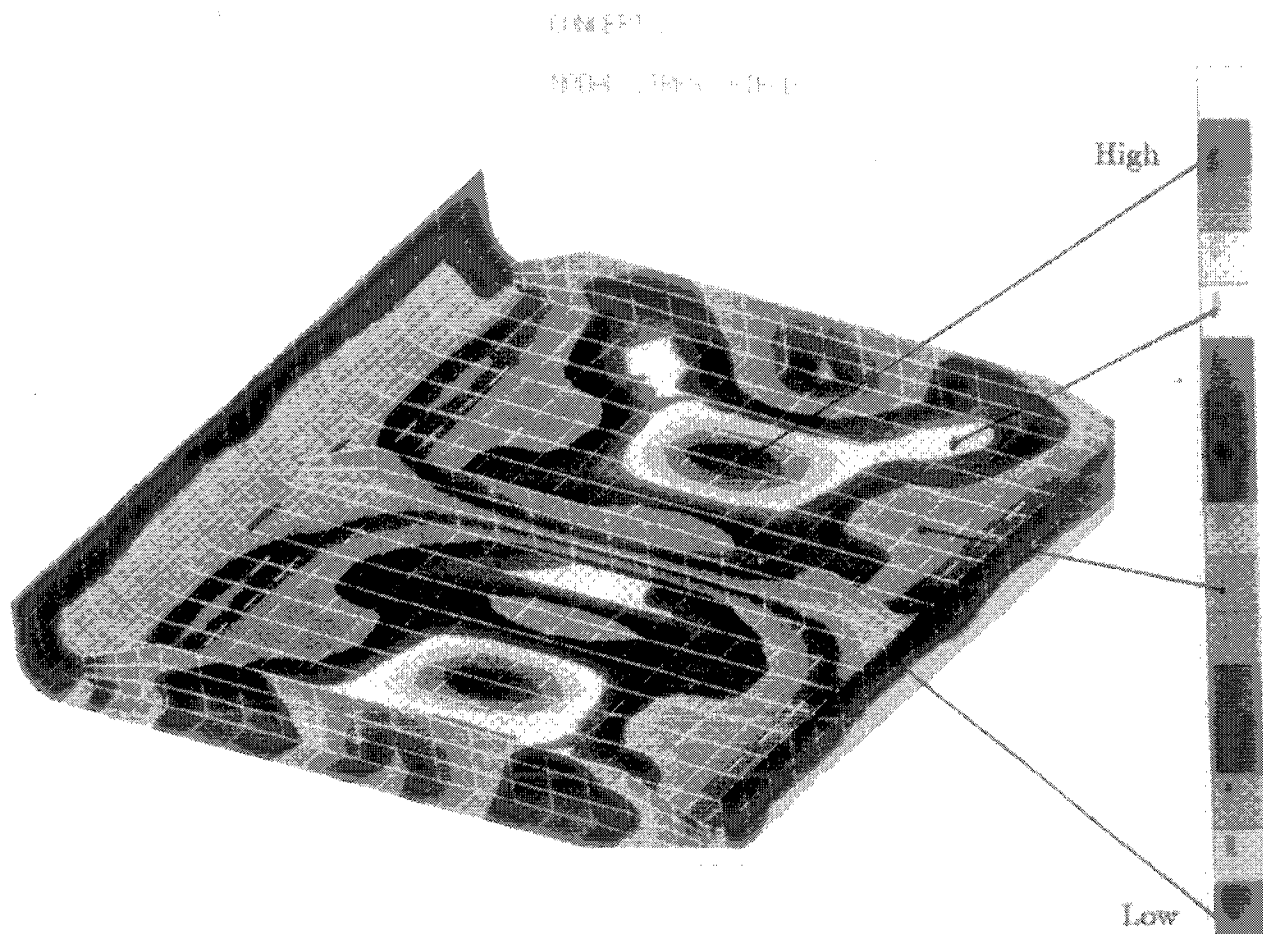


Figure 9-6. Modal Stress Field for Carbon-Carbon Test Panel Design Concept 2.

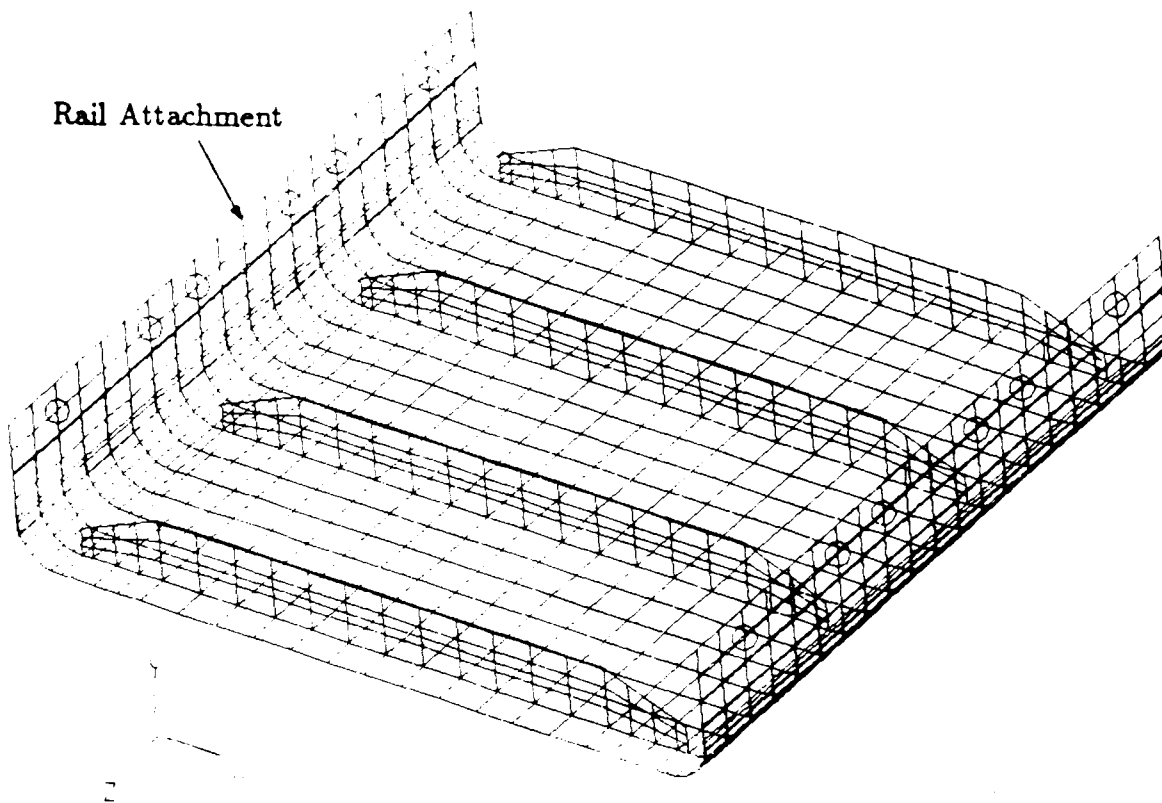
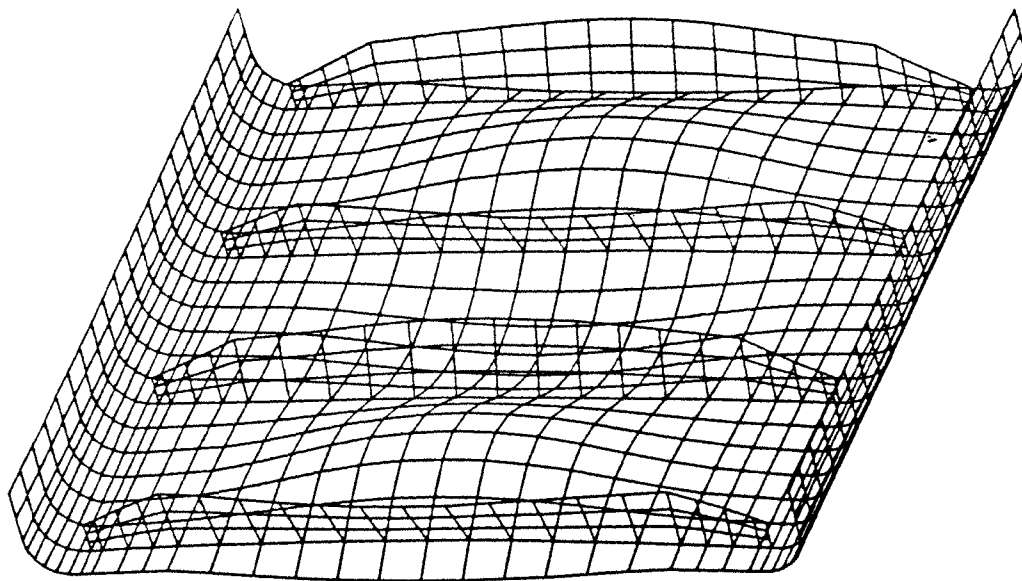


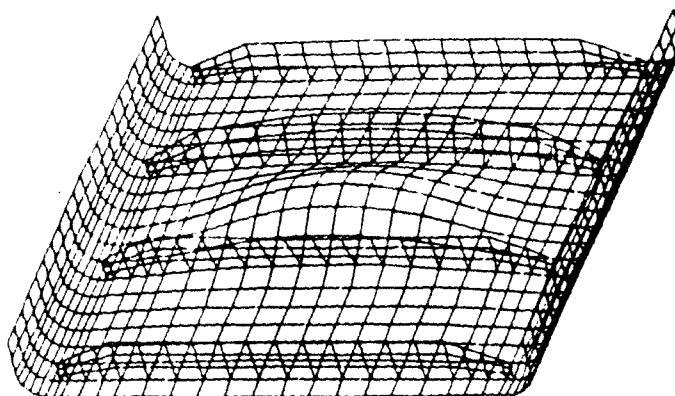
Figure 9-7. Finite Element Model for Carbon-Carbon Test Panel Design Concept 3.



CARBON/CARBON TEST PANEL - CONCEPT3
 MODAL ANALYSIS
 MODE NUMBER = 2

EIGENVALUE = $0.8398984E+07$

MODE NO.	CYCLES
1	2.591276E+02
2	4.612469E+02
3	4.657498E+02
4	4.948878E+02
5	6.323522E+02
6	6.383176E+02
7	7.623227E+02
8	8.046240E+02
9	8.178171E+02
10	8.995832E+02



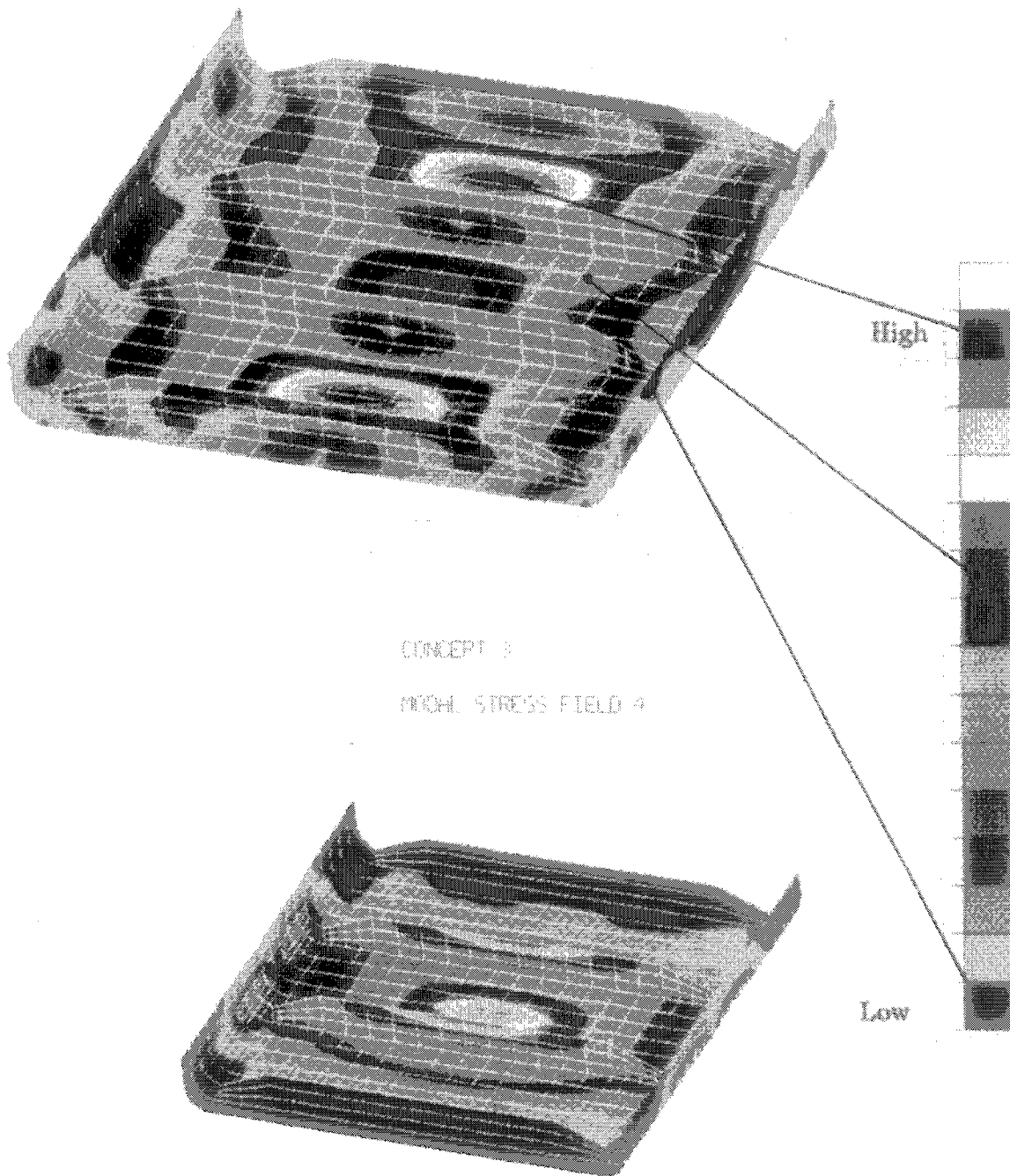
CARBON/CARBON TEST PANEL - CONCEPT3
 MODAL ANALYSIS
 MODE NUMBER = 4

EIGENVALUE = $0.9668815E+07$

Figure 9-8. Modal Shapes for Carbon-Carbon Test Panel Design Concept 3.

CONCEPT 1

MODAL STRESS FIELD 1



CONCEPT 3

MODAL STRESS FIELD 4

High

Low

CARBON-CARBON TEST PANEL - CONCEPT 3
MODAL ANALYSIS

Figure 9-9. Modal Stress Fields for Carbon-Carbon Test Panel Design Concept 3.

9.2 SONIC FATIGUE ANALYSIS

The analytical approach used in determining the response and ultimately the fatigue behavior of panels exposed to sound fields is an extension of Miles' work. The method uses the modal analysis results, i.e., normalized modal displacements and modal stresses, to obtain the load-deflection relationship. The effect of finite acoustic wavelengths on the panel response is incorporated through simultaneous consideration of spatial characteristics for both the structural modes and the acoustic field. Initially, the surface pressure distribution is approximated by the mass-weighted structural mode shape. For the fundamental mode of the panel, the estimate is similar to the assumption of uniform pressure. The advantage of this assumption is that it tends to produce a conservative estimate for each mode and the measure of spatial correlation (joint acceptance) between modal and acoustic fields is rendered unity. The accuracy of this approximation depends on the degree to which the mass-weighted mode shape reflects the actual pressure field shape. However, improvements to that joint acceptance estimate are developed which do not require detailed modeling of the acoustic field or numerical integration. This improvement is based on the relation between the structural and acoustic wavelengths. Thus, after a mode-by-mode analysis of sonic stresses is performed initially, the joint acceptance correction detects and adjusts underpredicted and/or overpredicted sonic stress estimates. Finally, the overall stresses are obtained by summing the squares of contributions of the individual modes. The analytical procedure is described in more detail in Reference [9-1]. Once the acoustically induced stresses have been determined, a direct comparison with available random fatigue data provides estimates of the number of mechanical cycles that can be sustained.

Random fatigue data for uncoated (HTC) carbon-carbon bar specimens were shown in Section 4, Figure 4-26. Data were included for specimens with various types of inhibitors, as well as uninhibited ones. All specimens were made from 3K tow T-300 carbon fabric heat treated to 2150°C (3900°F). Fiber volumes for the inhibited, filled specimens ranged from 42 percent to 48 percent. The fillers were added to the

phenolic prepregging resin in particulate form. All panels were densified using four cycles of 50-50 pitch-funaldelyde impregnation to a target porosity of less than 5 percent. To prevent reaction of the fillers with the fibers, the graphitization temperature was limited to 1650°C (3000°F). For infinite life (10^8 cycles), the lower fatigue limit is approximately 6000 psi and the upper limit is 12,000 psi.

9.2.1 Concept 1

Sonic stress levels for the design concept 1 panel were estimated for two different loading conditions: (1) narrow band resonance with a sound pressure level of 145 dB and (2) broad band resonance with a one-third octave sound pressure level of 160 dB. For broad band loading and the joint acceptance correction incorporated, the highest sonic stress is approximately 8000 psi. The dominant participating mode is the in-phase mode at 352 Hz. The maximum sonic stress for the narrow band resonance case is also obtained at 352 Hz and reaches a level of 3000 psi. The response at all other frequencies is significantly lower for both cases. Results are shown in Figure 9-10. The rms sonic stress levels for the broad band loading have a maximum value of 9089 psi and are shown in Figure 9-11.

9.2.2 Concept 2

Sonic stress levels for the design concept 2 panel were estimated for the same loading conditions. When the joint acceptance corrections are incorporated, the maximum sonic stress level with broad band loading is approximately 19,172 psi and thus higher than the concept 1 value. The dominant participating mode is at 205 Hz and corresponds to the in-phase mode. The maximum sonic stress for the narrow band resonance case is obtained at the same mode and reaches a level of 7063 psi. Results are shown in Figure 9-12. The response at all other frequencies is significantly lower. The rms sonic stress levels with broad band loading have a maximum value of 19,433 psi and are shown in Figure 9-13.

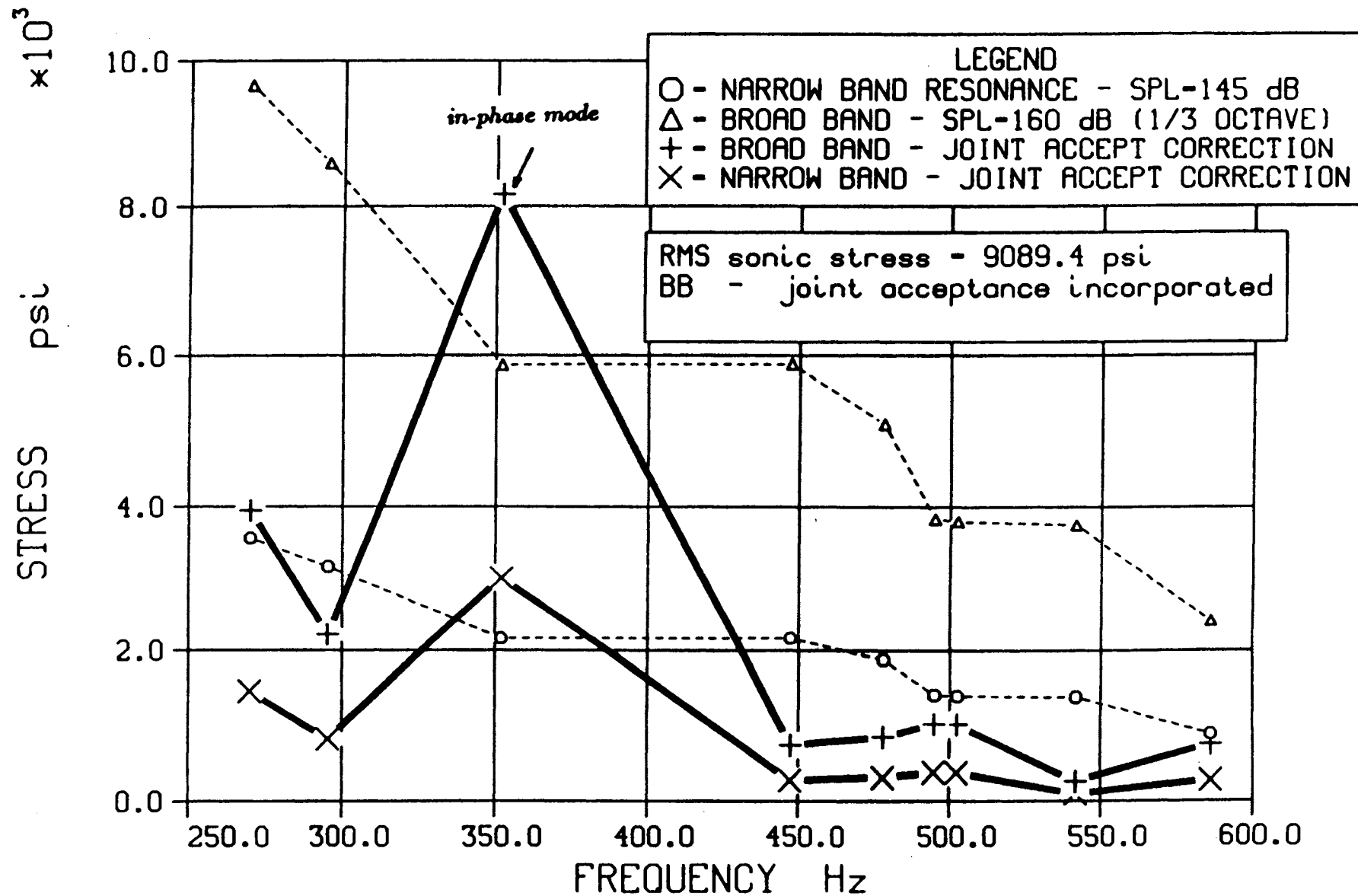


Figure 9-10. Sonic Stress Levels for Carbon-Carbon Test Panel Design Concept 1.

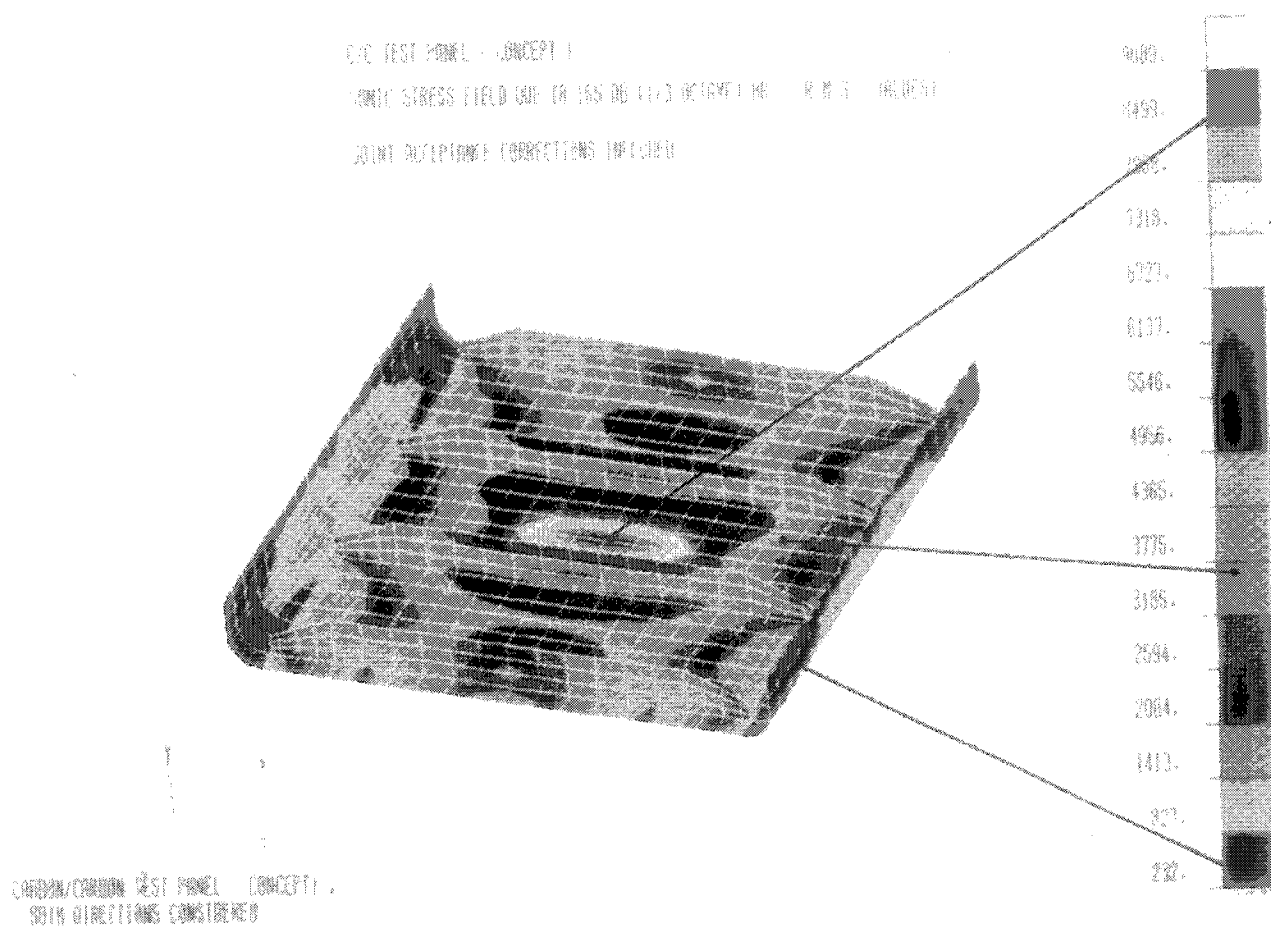


Figure 9-11. RMS Sonic Stress Levels Obtained with Broad Band Loading for Carbon-Carbon Test Panel Design Concept 1.

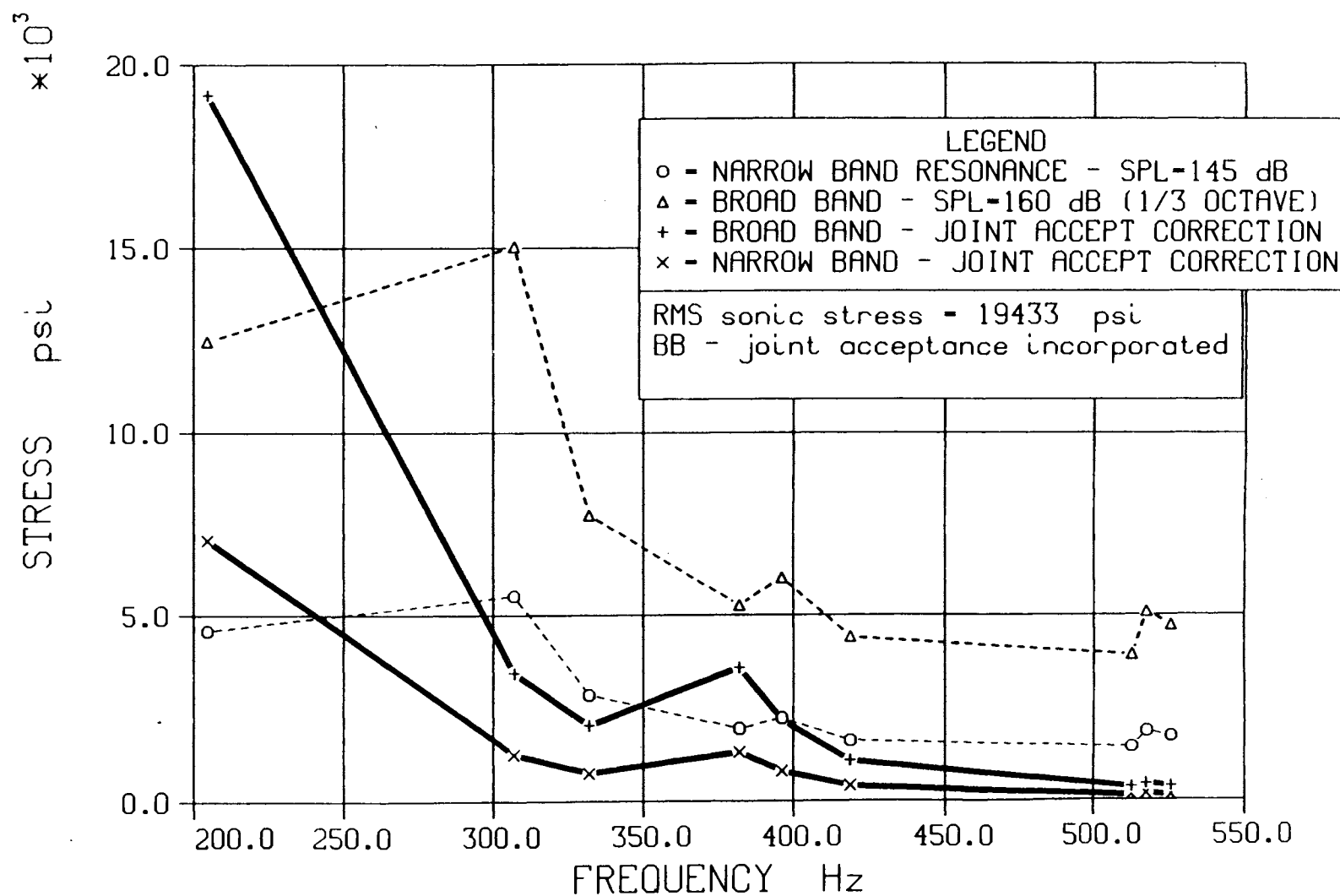


Figure 9-12. Sonic Stress Levels for Carbon-Carbon Test Panel Design Concept 2.

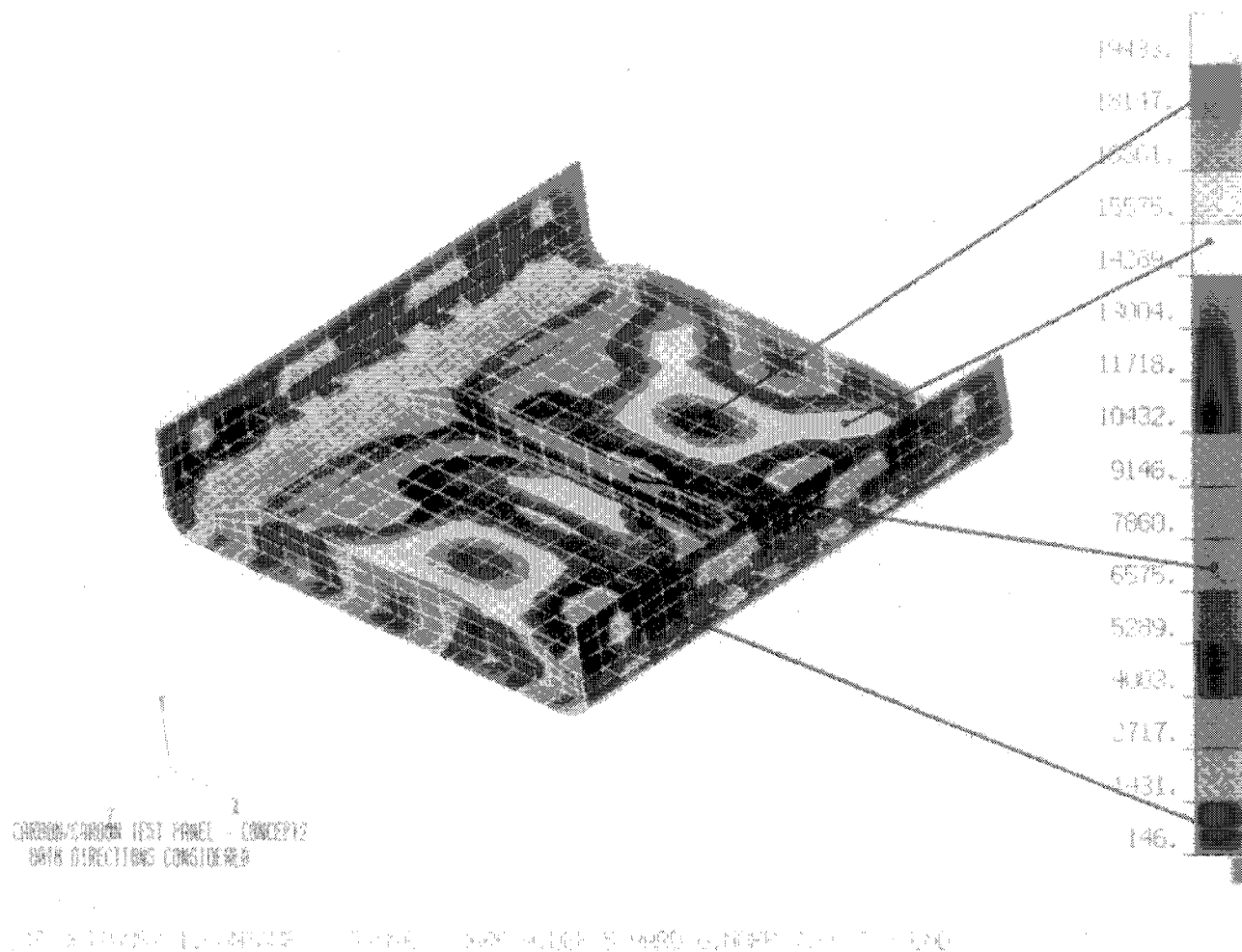


Figure 9-13. RMS Sonic Stress Levels Obtained with Broad Band Loading for Carbon-Carbon Test Panel Design Concept 2.

9.2.3 Concept 3

Sonic stress levels for the design concept 3 panel subjected to joint acceptance corrections are shown in Figure 9-14. The maximum levels are 3200 psi and 1200 psi for the broad band and narrow band resonance loading conditions, respectively. The dominant participating mode is at 495 Hz. The rms sonic stress levels with broad band loading have a maximum value of 3780 psi and are shown in Figure 9-15.

9.3 CONCLUSIONS

Based on the analytical results, it is evident that the much stiffer concept 3 panel exhibits the lowest induced sonic stress levels, as was anticipated. Based on carbon-carbon fatigue allowable data presented in Section 9.2, the concept 1 panel exhibits a fatigue life of 5×10^5 mechanical cycles (lower limit) with a stress level of 8000 psi at the dominant participating frequency of 352.1 Hz, while it has infinite life as an upper limit. The concept 2 panel exhibits a fatigue life of 3×10^5 mechanical cycles (upper limit) with a stress level of 19,433 psi at the dominant participating frequency of 204.5 Hz. Finally, the concept 3 panel exhibits infinite life. The results for the three concepts are compared in Figure 9-16 and Table 9-2.

9.4 REFERENCES

- 9-1 Blevins, R.D., "Approximate Methods for Sonic Fatigue Analysis of Plates and Shells," Journal of Sound and Vibration, Vol. 129, pages 51-71 (1989).

838PROP
3-9.BB
12-11-89

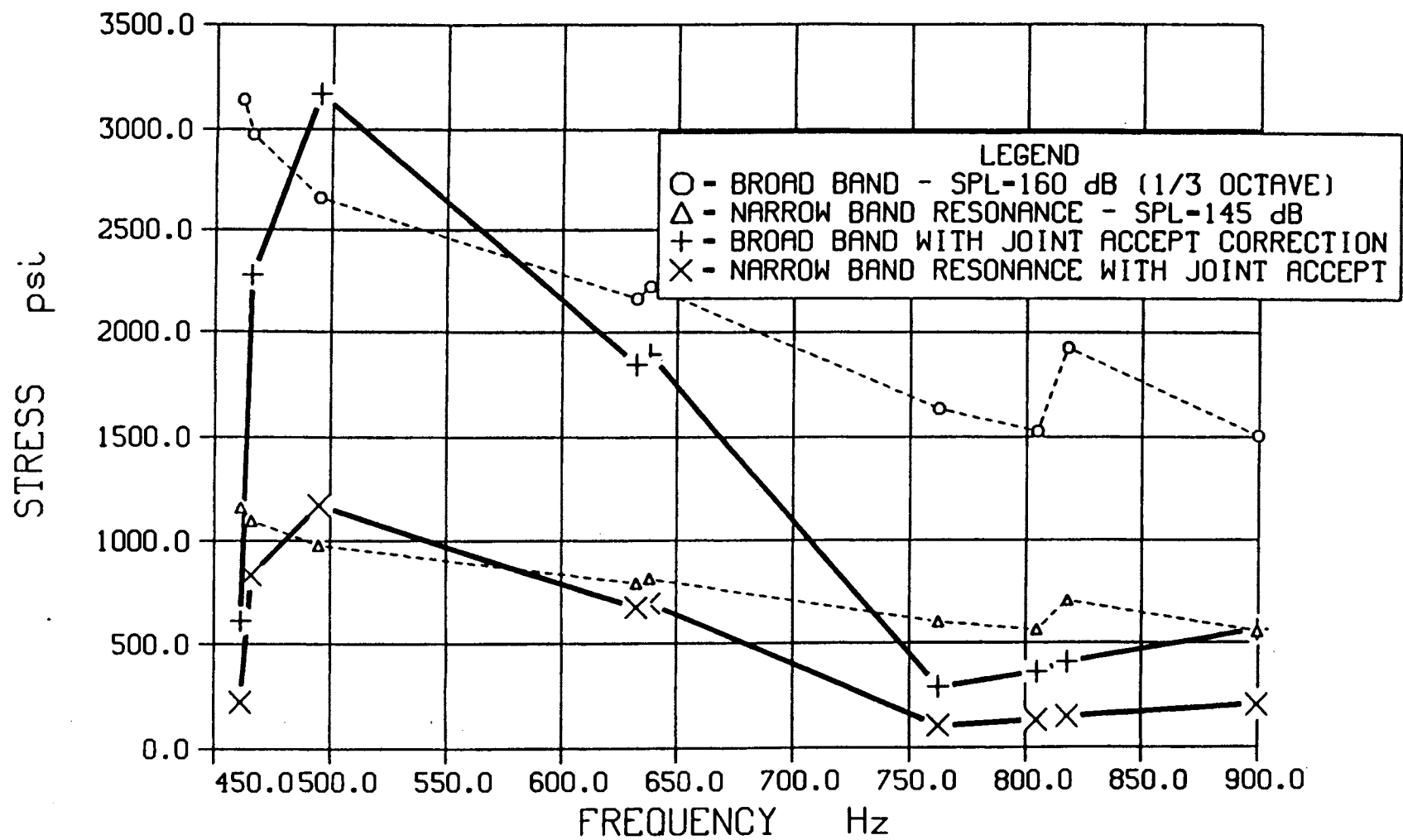


Figure 9-14. Sonic Stress Levels for Carbon-Carbon Test Panel Design Concept 3.

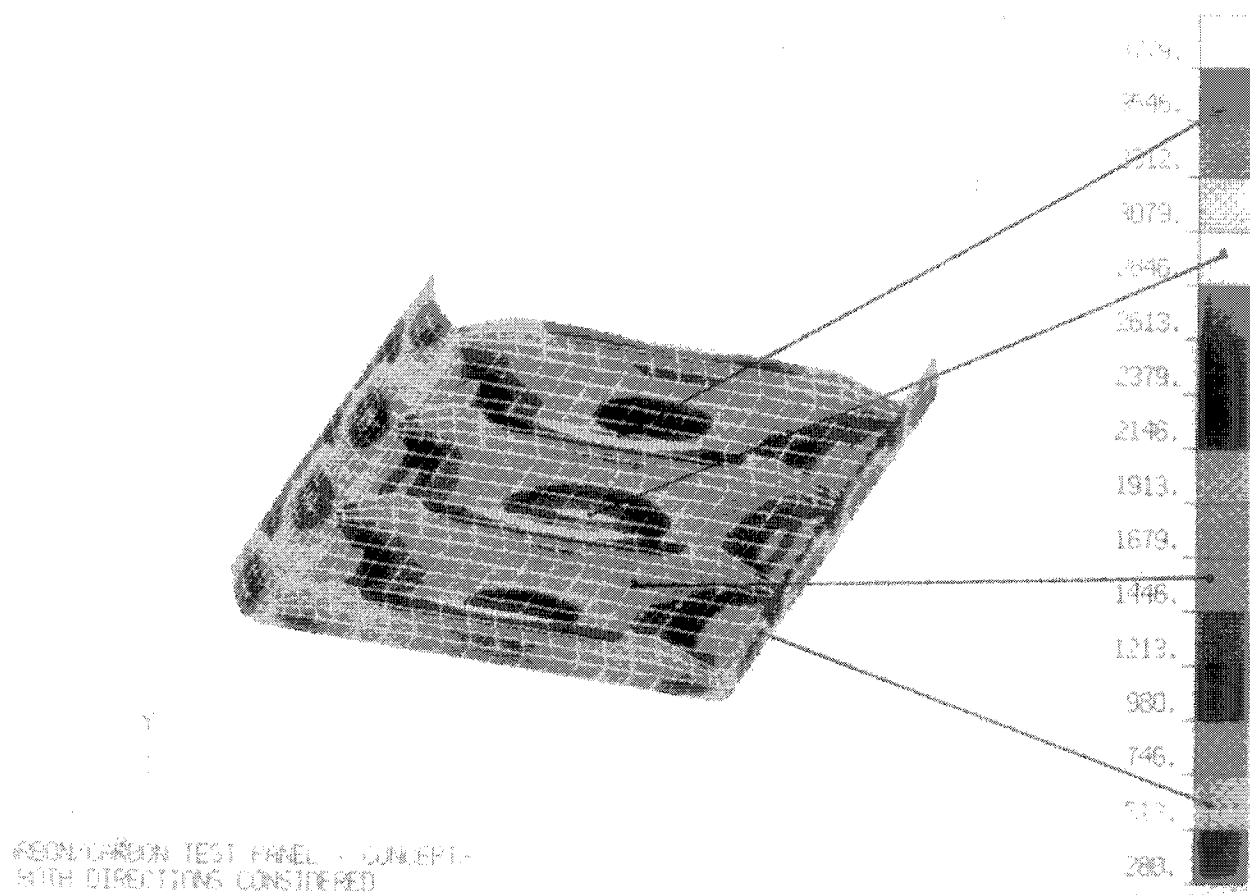


Figure 9-15. RMS Sonic Stress Levels Obtained with Broad Band Loading for Carbon-Carbon Test Panel Design Concept 3.

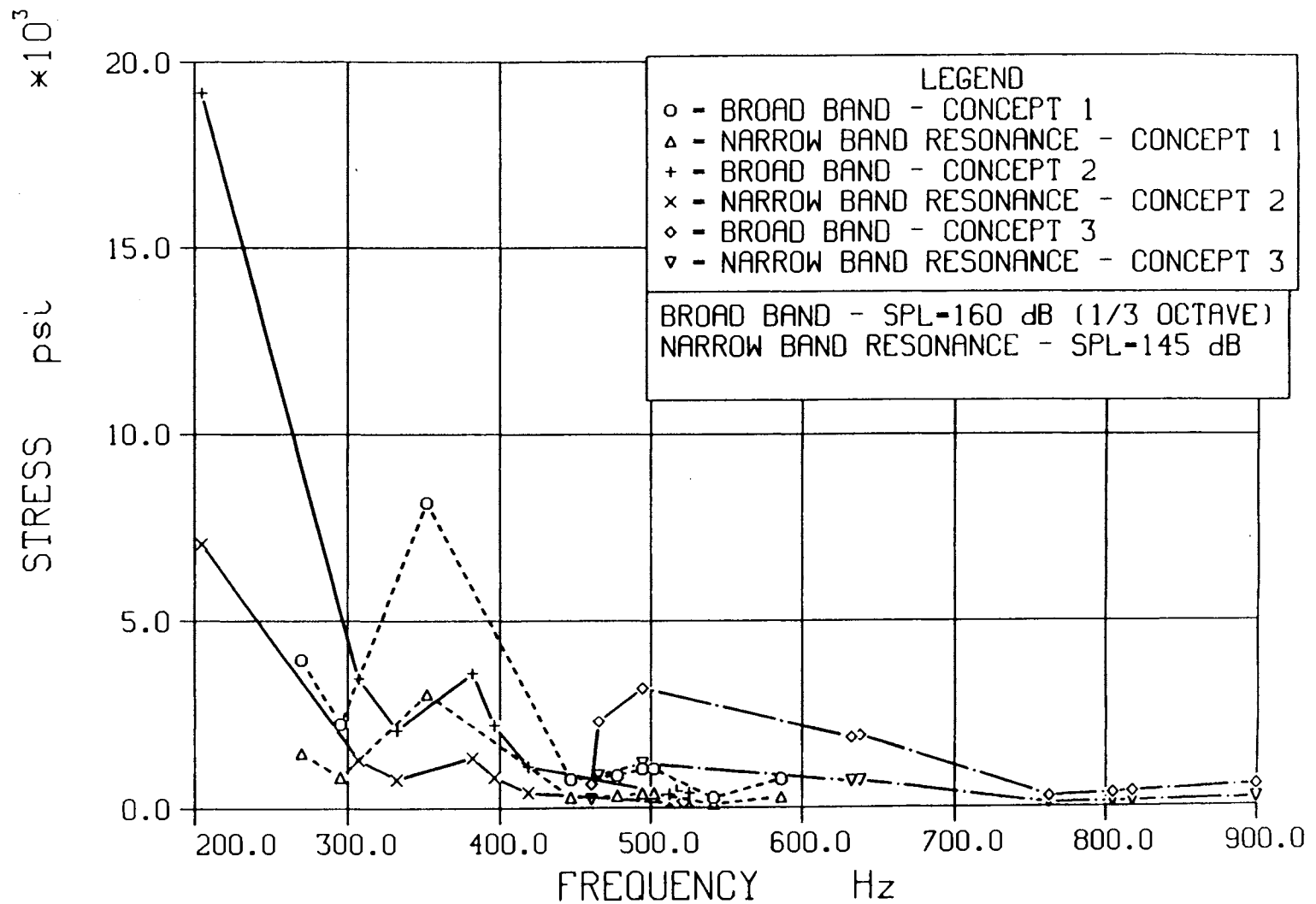


Figure 9-16. Comparison of Sonic Stress Levels for Carbon-Carbon Test Panel Design Concepts 1, 2, and 3; Joint Acceptance Correction Incorporated.

Table 9-2. Summary of Sonic Fatigue Analysis Results for Carbon-Carbon Test Panel Design Concepts 1, 2, and 3.

	FREQUENCY (Hz)	JOINT ACCEPTANCE	SONIC STRESS (psi) RESONANT SINUSOIDAL at 145 dB	SONIC STRESS (psi) BROAD BAND (1/3 oct) 160 dB
concept 1	269.8	0.408	1454	3948
	295.3	0.258	817	2218
	352.1	1.390	3008	8170
	447.3	0.128	272	739
	478.1	0.165	310	841
	494.9	0.265	374	1016
	502.4	0.268	375	1017
	541.7	0.068	94	257
	586.3	0.309	274	743
				rms=9089.4
concept 2	204.5	1.540	7063	19172
	307.1	0.229	1267	3440
	332.2	0.284	753	2045
	382.0	0.677	1315	3572
	396.2	0.361	801	2176
	418.8	0.246	399	1088
	512.6	0.089	129	351
	517.4	0.086	162	439
	525.6	0.080	140	380
				rms=19433.0
concept 3	461.2	0.195	226	613
	465.7	0.765	838	2275
	494.9	1.192	1168	3172
	632.3	0.852	678	1842
	638.3	0.853	697	1893
	762.3	0.178	107	290
	804.6	0.237	133	362
	817.8	0.212	151	409
	899.6	0.375	208	564
				rms=3780.9

SECTION 10

CONCLUSIONS

An analytical study has been made of the issues of vibroacoustic fatigue of hypersonic flight vehicles. This study completes Phase II of the present program. Phase III will be devoted to experimental shaker and progressive wave tube tests of representative structures. The Experimental Plan is given in Section 8.

In order to develop representative loads and designs for analysis, a single-stage-to-orbit mission has been postulated which is consistent with transatmospheric vehicle studies currently under way in the United States. A generic trajectory consists of a 15-minute ascent to low earth orbit of Mach 25 along the line of constant aerodynamic pressure ($Q = 1000 \text{ lb/ft}^2$ or $Q = 2600 \text{ lb/ft}^2$) and an approximately 1-hour descent. This gives rise to the design of a Blended Wing Body (BWB) transatmospheric vehicle with a skin panel using carbon-carbon where maximum temperatures are up to 3000°F and titanium metal matrix for temperatures not exceeding 1500°F . Actively cooled titanium panels with circulating liquid hydrogen as the coolant are used in areas, such as the nozzle, that are exposed to high heat flux which would produce temperatures in excess of 3000°F if active cooling were not applied.

A study was made to determine aeroacoustic loads on the vehicle. A parabolized Navier-Stokes numerical solution was used on a two-dimensional representation of the BWB to determine the external flow field and boundary layer thickness along the body for various Mach numbers representing points along the trajectory. Semiempirical

techniques were then applied to determine loads due to turbulent boundary layer and shock-boundary layer interaction. The results of that study are summarized below.

Aeroacoustic Loads

- (1) In attached flow without shock interaction, the acoustic loads and heat transfer tended to follow the pressure distribution as generated by surface geometry and trajectory. The levels were commensurate with those experienced on re-entry vehicles subject to hypersonic flow conditions.
- (2) In attached flow without shock interaction, the overall sound pressure levels on the BWB (without control surfaces) ranged from 120 to 150 dB, with the high levels being experienced in the nosetip region and along the ramp toward the cowl inlet region.
- (3) There is significant uncertainty in predicting boundary layer transition altitude and subsequent movement along the configuration. Since heat and aeroacoustic loads are an order of magnitude greater for a turbulent boundary layer than the corresponding loads with a laminar boundary layer, the location of transition can have a major impact on design of skin panels.
- (4) Interaction of the shock-boundary layer on control surfaces was shown to be a strong function of shock strength ($M \sin \theta_s$). A prediction technique, with shock generating angles $\alpha > 12^\circ$, was developed based on physical laws, flow similitude, and $M \leq 3$ experimental data.
- (5) The strongest potential interaction involved the bow shock and horizontal control surface boundary layer. For this condition, peak rms fluctuating pressure was shown to increase by factors of 30 (30 dB) to 240 (48 dB) over the approach flow level for $10 < M_\infty < 20$. Interaction of the bow shock-horizontal control

surface boundary layer for $M_\infty < 10$ did not appear likely because of the wide shock angle.

- (6) Potential interaction could exist between the horizontal and vertical control surfaces as generated by axial corner flow when the two surfaces approach a common origin. For this condition, the acoustic loads were estimated from mean flow data and heuristic techniques that showed the loads to be enhanced by the square of the inviscid pressure rise. However, with small angled shock generators ($\alpha < 4^\circ$) on the BWB, the impact was shown to be on the order of 3 times the approach flow levels (10 dB).

Engine Acoustic Loads

- (1) The relationships developed by Eldred, NASA, and Von Gierke for sound radiated by rocket engines agree to within 7 dB at a thrust of 1.8×10^6 N (40,000 lb) and to within 1 dB at a thrust of 450×10^3 N (100,000 lb).
- (2) The highest sound levels generated by the transatmospheric vehicle occur on the ground when both rocket and scramjet engines are operating.
- (3) The maximum sound engine levels on the vehicle lie between 170 and 180 dB overall. The sound levels are highest adjacent to the rocket engine exhausts and the inlet and exhaust of the scramjet engines. The lower surface of the vehicle receives higher sound levels than the upper surface owing to reflection from the runway.
- (4) The present analysis does not include aerodynamic pressure fluctuations associated with turbulence and boundary layer development (Section 2); only direct sound from engines is considered. Aerodynamic turbulence will further raise the pressures on the surface. As the speed of the hypersonic

vehicle increases beyond the subsonic range, the presence of shock waves will restrict the forward travel of sound, with the rocket and scramjet noise being felt in a corresponding smaller region.

Forebody Panel Analysis

(1) Thermal analysis results:

- (a) The maximum skin temperature at end of ascent is 2667°F for the 1000 q_{∞} ascent and 3223°F for the 2600 q_{∞} ascent. These results are based on turbulent heating. If a laminar boundary layer exists, the maximum temperature could be 1100°F lower.
- (b) The maximum temperature difference between the fastener locations on the panel edges is 1400°F for 2600 q_{∞} and 1200°F for 1000 q_{∞} . The temperature difference through the skin thickness is negligible.

(2) Static stress analysis results:

- (a) The current design proposed for the forebody panel would sustain first ply fiber failures under worst case load conditions. However, the panel ultimate strength was found to be adequate.
- (b) More detailed analysis of the forebody panel is required to evaluate interlaminar stress effects in the panel flanges.
- (c) Buckling was found not to be a concern for the forebody panel.

(3) Dynamic analysis results:

- (a) The maximum sonic stress is approximately 4000 psi and occurs at 770 Hz for a combined one-third octave sound pressure level of 155 dB when the panel is preloaded. When the sonic loading is exhaust noise only, the sonic stress reaches a value of 700 psi at 770 Hz. When the improved joint acceptance estimates are incorporated, the overall rms stress distribution has a maximum value of 2319 psi. This is within the fatigue allowable.
- (b) The highest stresses are observed on the upper side of the stiffeners and the center of the middle bay. These stress levels are below the fatigue allowable, and therefore the forebody panel will be able to sustain the loading environment for its design life.

Ramp Panel Analysis

(1) Thermal analysis results:

- (a) The maximum skin temperature at end of ascent is 2510°F for the 1000 q_{∞} ascent and 3023°F for the 2600 q_{∞} ascent. These results are based on turbulent heating. If a laminar boundary layer exists, the maximum temperature could be 700°F lower.
- (b) The maximum temperature difference between fastener locations on the panel edges is 800°F. The temperature difference through the skin thickness is negligible.

(2) Static stress analysis results:

- (a) The ramp panel design was found to be acceptable.
- (b) The results of the analysis were dependent on the boundary conditions that were assumed. The assumptions made were considered to be reasonable, but further investigation might pursue the influence of boundary conditions on panel stresses and margins of safety.
- (c) Buckling was found not to be a concern for the ramp panel.

(3) Dynamic analysis results:

- (a) The maximum stress level due to inlet noise for a one-third octave level of 165 dB is approximately 21,000 psi at 855 Hz. When the joint acceptance improvement is employed, the maximum rms stress is 16,081 psi. This is in excess of the fatigue allowable stress.
- (b) The highest stresses are observed on the upper side of the middle stiffeners and the center of the middle bay. The analytically obtained stresses exceed the fatigue allowable, and therefore the anticipated fatigue life would not satisfy design requirements.

Horizontal Stabilizer Panel Analysis

- (1) The loading on the horizontal stabilizer panel originates from four sources: (a) carry-through loads associated with thermal and mechanical loads on the horizontal stabilizer as a whole; (b) aerothermal loads associated with the turbulent boundary layer; (c) shock interaction loads due to interaction of the bow shock with the horizontal stabilizer at high Mach numbers and interaction with the shock from the vertical stabilizer; and (d) engine acoustic loads.

- (2) The overall aeroacoustic load at Mach 10 is 128 dB at $Q = 1000 \text{ lb/ft}^2$ and 135 dB at $Q = 2600 \text{ lb/ft}^2$. The inplane carry-through loads are significantly higher than for the forebody panel and much higher than for the ramp panel; hence panel buckling is a concern. Heating rates for attached boundary layer flow at 2 to 5 Btu/ft²/sec are a factor of 5 lower than for the forebody or ramp panels, which implies that temperatures will be greatly reduced, indicating that the use of metallic structure is justified.
- (3) The greatest loads imposed on the horizontal and vertical stabilizers are associated with engine acoustic loads and shock interaction loads. Engine noise can induce maximum acoustic pressures from 160 to over 170 dB for the surfaces which are in the line of sight from the engine exhaust.
- (4) It is possible for the bow shock to intersect the horizontal stabilizer at speeds in excess of Mach 10. Peak oscillating shock pressure is approximately 1.5 psi, which corresponds to 175 dB, well in excess of the turbulent boundary layer pressures. The maximum shock heating is over 100 Btu/ft²/sec, roughly a factor of 20 higher than the turbulent boundary layer heating and higher than the heating rates on the forebody and ramp panels, which result in temperatures in excess of 2500°F. The width of the shock interaction region is expected to be comparable to the boundary layer turbulences, approximately 0.1 foot. Thus, shock-boundary layer interaction on the horizontal or vertical stabilizer surfaces could lead to local hot spots with heating rates that have the capability of melting their metallic skins unless active cooling is provided.

Actively Cooled Panel Analysis

- (1) The area of the panel with the highest acoustic stresses throughout the trajectory is at the center of the inner face sheet. This was expected since the loading is normal to the panel and the bonded heat exchanger shares some of the outer face sheet load. The manifolds are not stiff enough to provide good edge fixity, so the panel responds as if simply supported.
- (2) The highest static stresses are evenly distributed through the panel face sheets since the loads are primarily membrane loads. The outer surface of the outer face sheet is most highly stressed through Mach 6, where mechanical loads are higher than thermal growth loads. At higher Mach numbers, the thermal loads dominate, causing the highest loads to be imposed on the inner face sheets.
- (3) The highest fatigue loadings result from ground taxi condition and will cause fatigue failure. Nearly all the damage will be caused by the acoustic response. The acoustic environment is high, having energy concentrated at the primary resonant frequencies of the panels. The high levels are a function of ground reflections and the use of rocket thrust augmentation.
- (4) During ascent, the contribution of acoustics dominates the thermomechanical loads through the transonic regime. However, the levels at transonic conditions are much lower than at takeoff, resulting in stresses much below the fatigue threshold.
- (5) The relative contribution of the thermomechanical stresses increases with Mach number. The loads resulting from overall vehicle thermal growth and from the through-thickness panel gradients dominate the mechanical loads. Acoustic response becomes less important with increasing Mach number. Even

though the structures become highly preloaded, the overall response is still below the panel fatigue threshold.

- (6) Descent conditions are relatively benign. The major loading results from differential growth as the vehicle heats up. The acoustic environment (and resulting panel response) is an order of magnitude lower than for ascent.

Test Panel Dynamic Analysis

Under a one-third octave broad band loading of 160 dB, the estimated endurance life will be between 5×10^5 and infinite mechanical cycles for the concept 1 panel with four 0.080-inch thick ribs spaced 6 inches apart and a skin thickness of 0.065 inch and 3×10^5 mechanical cycles for the concept 2 panel with three 0.080-inch thick ribs spaced 9 inches apart and a skin thickness of 0.065 inch. Finally, the concept 3 panel with four 0.150-inch thick ribs spaced 6 inches apart and a skin thickness of 0.125 inch exhibits infinite life under identical sonic loading conditions.

838PROP
3-10.BB
12-11-89

APPENDIX A
PNS SOLUTIONS OF HEAT TRANSFER AND SUBSEQUENT
ACOUSTIC LOAD DEFINITION ON THE BLENDED WING BODY

Figures A-1 through A-72 present the acoustic and surface heat transfer and pressure loads on the Blended Wing Body transatmospheric vehicle for the trajectory conditions shown in Figure 2-16. Table A-1 has been structured to identify the specific acoustic, heat transfer, and pressure loading relative to trajectory conditions.

838PROP
3-A.BB
11-11-89

Table A-1. Acoustic/Heat Transfer and Pressure Loads on BWB Location Table.

M_∞	q_∞ (PSF)	T_w (R)	PLANE	P/q_e	SPL(dB)	P_e/P_∞	$\frac{\text{Btu}}{\dot{q}_w \text{ ft}^2 \text{ sec}}$	P(PSF)	PSD*	$\phi(\omega)$
4	1000	540	Leeward	A1(A)	A1(B)	A2(A)	A2(B)	A3(A)	A4(A)	A4(B)
4	1000	540	Windward	A5(A)	A5(B)	A6(A)	A6(B)	A3(B)	A7(A)	A7(B)
6	1000	1600	Leeward	A8(A)	A8(B)	A9(A)	A9(B)	A10(A)	A11(A)	A11(B)
6	1000	1600	Windward	A12(A)	A12(B)	A13(A)	A13(B)	A10(B)	A14(A)	A14(B)
6	1000	2000	Leeward	A15(A)	A15(B)	A16(A)	A16(B)	A17(A)	A18(A)	A18(B)
6	1000	2000	Windward	A19(A)	A19(B)	A20(A)	A20(B)	A17(B)	A21(A)	A21(B)
10	1000	1600	Leeward	A22(A)	A22(B)	A23(A)	A23(B)	A24(A)	A25(A)	A25(B)
10	1000	1600	Windward	A26(A)	A26(B)	A27(A)	A27(B)	A24(B)	A28(A)	A28(B)
15	1000	1600	Leeward	A29(A)	A29(B)	A30(A)	A30(B)	A31(A)	A32(A)	A32(B)
15	1000	1600	Windward	A33(A)	A33(B)	A34(A)	A34(B)	A31(B)	A35(A)	A35(B)
20	1000	1600	Leeward	A36(A)	A36(B)	A37(A)	A37(B)	A38(A)	A39(A)	A39(B)
20	1000	1600	Windward	A40(A)	A40(B)	A41(A)	A41(B)	A38(B)	A42(A)	A42(B)
25	1000	1600	Leeward	A43(A)	A43(B)	A44(A)	A44(B)	A45(A)	A46(A)	A46(B)
25	1000	1600	Windward	A47(A)	A47(B)	A48(A)	A48(B)	A45(B)	A49(A)	A49(B)
6	2600	1600	Windward	A50(A)	A50(B)	A51(A)	A51(B)	A52	A53(A)	A53(B)
10	2600	1600	Leeward	A54(A)	A54(B)	A55(A)	A55(B)	A56(A)	A57(A)	A57(B)
10	2600	1600	Windward	A58(A)	A58(B)	A59(A)	A59(B)	A56(B)	A60(A)	A60(B)
15	2600	1600	Windward	A61(A)	A61(B)	A62(A)	A62(B)	A63	A64(A)	A64(B)
20	2600	1600	Windward	A65(A)	A65(B)	A66(A)	A66(B)	A67	A68(A)	A68(B)
25	2600	1600	Windward	A69(A)	A69(B)	A70(A)	A70(B)	A71	A72(A)	A72(B)

$$* \text{ PSD} = \frac{\phi(\omega) u_e}{q_e^2 \delta^*}$$

838PROP/3-TA-1.BB
11-11-89

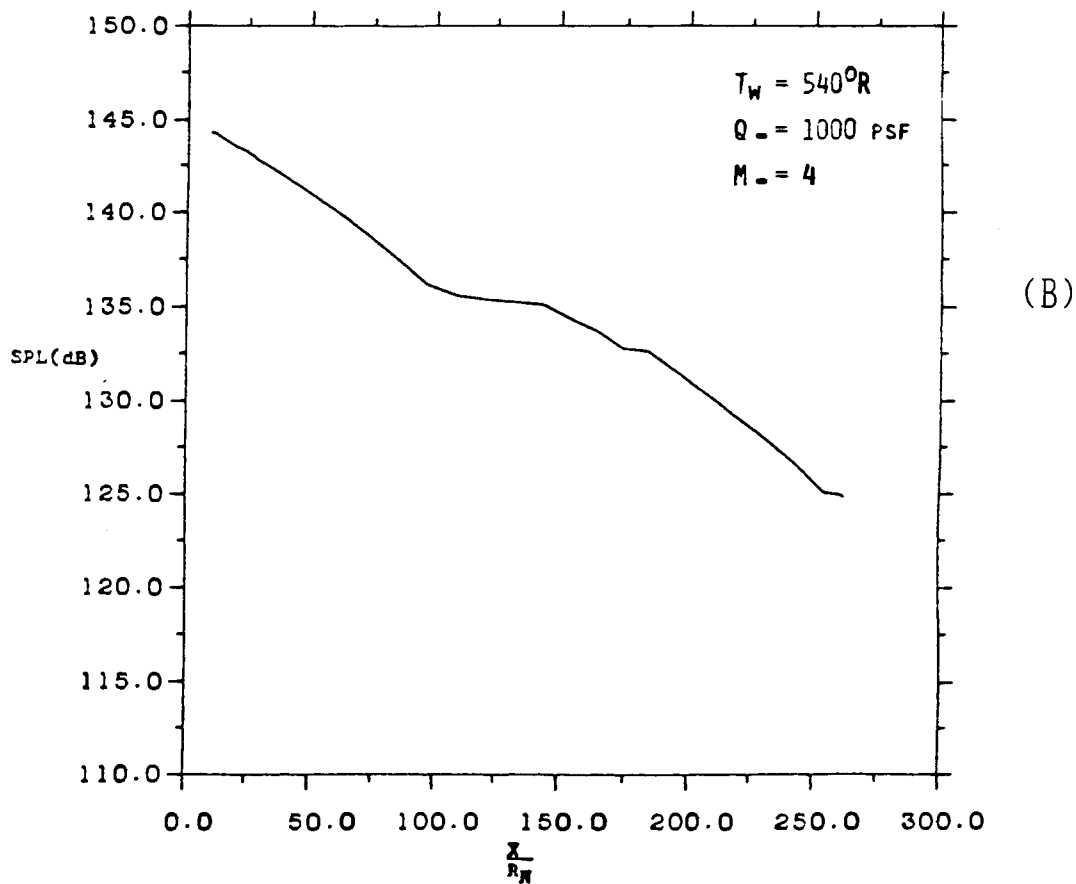
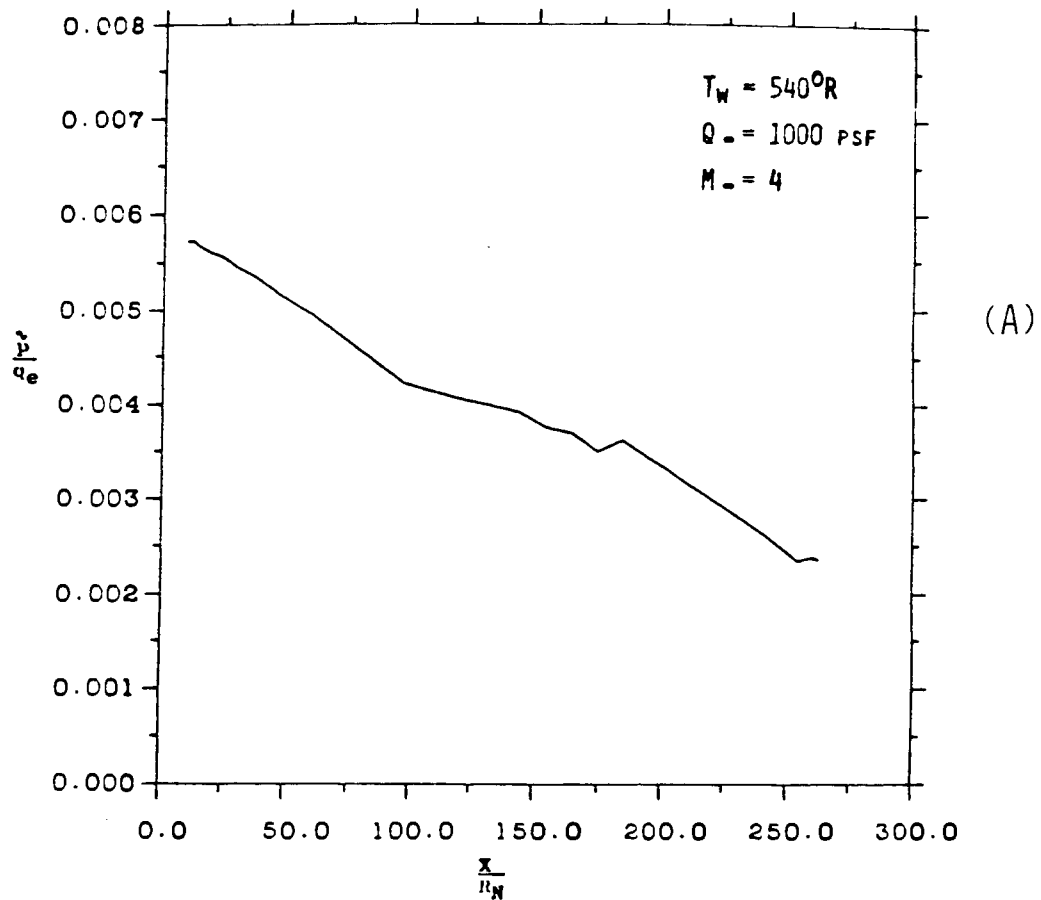
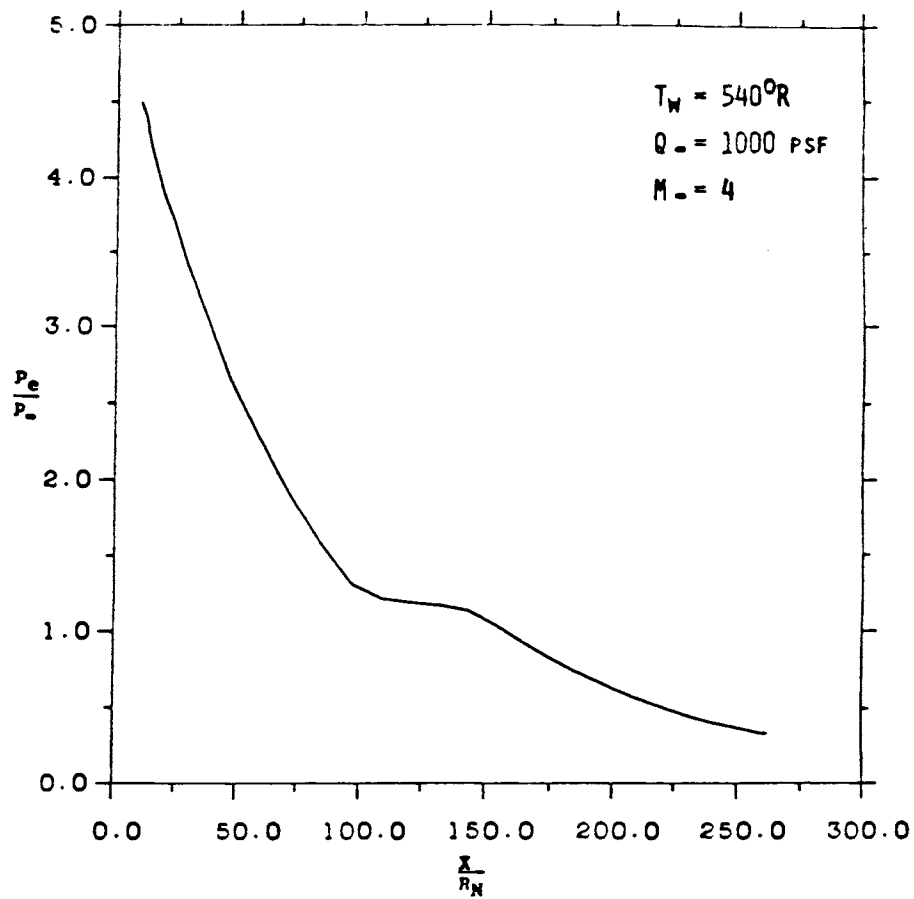
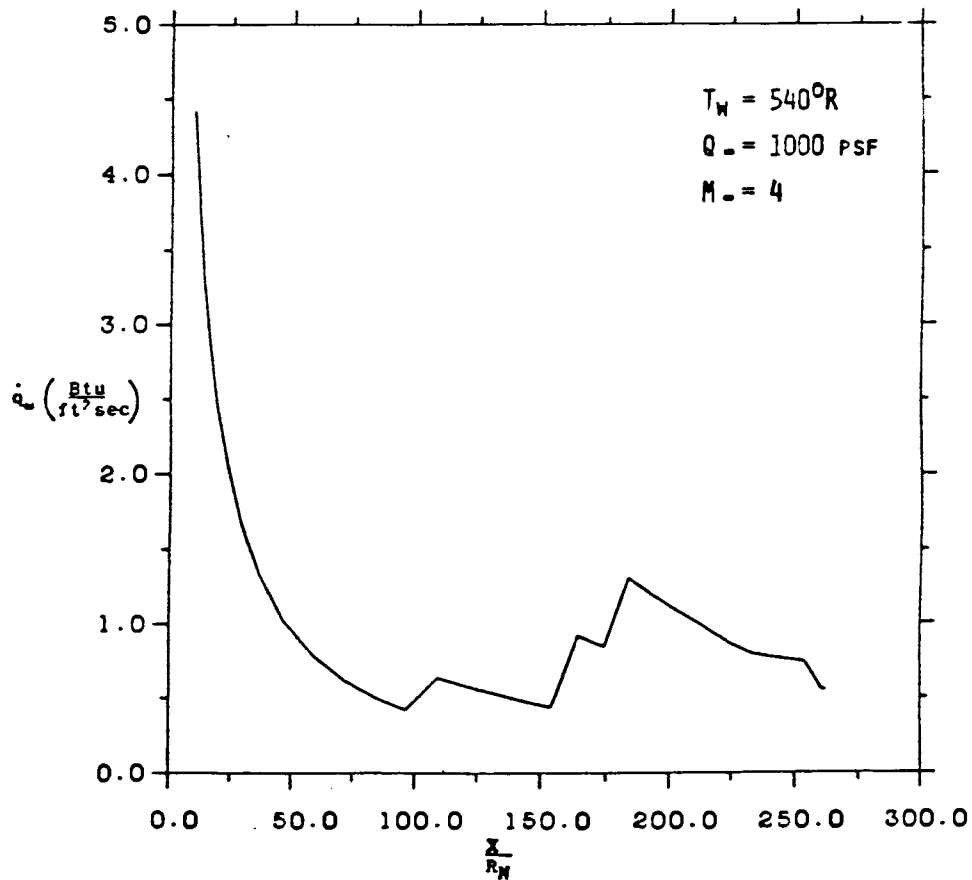


Figure A-1. RMS Pressure (A) and Sound Pressure Level (B) Distribution Along Leeward Surface of BMB.

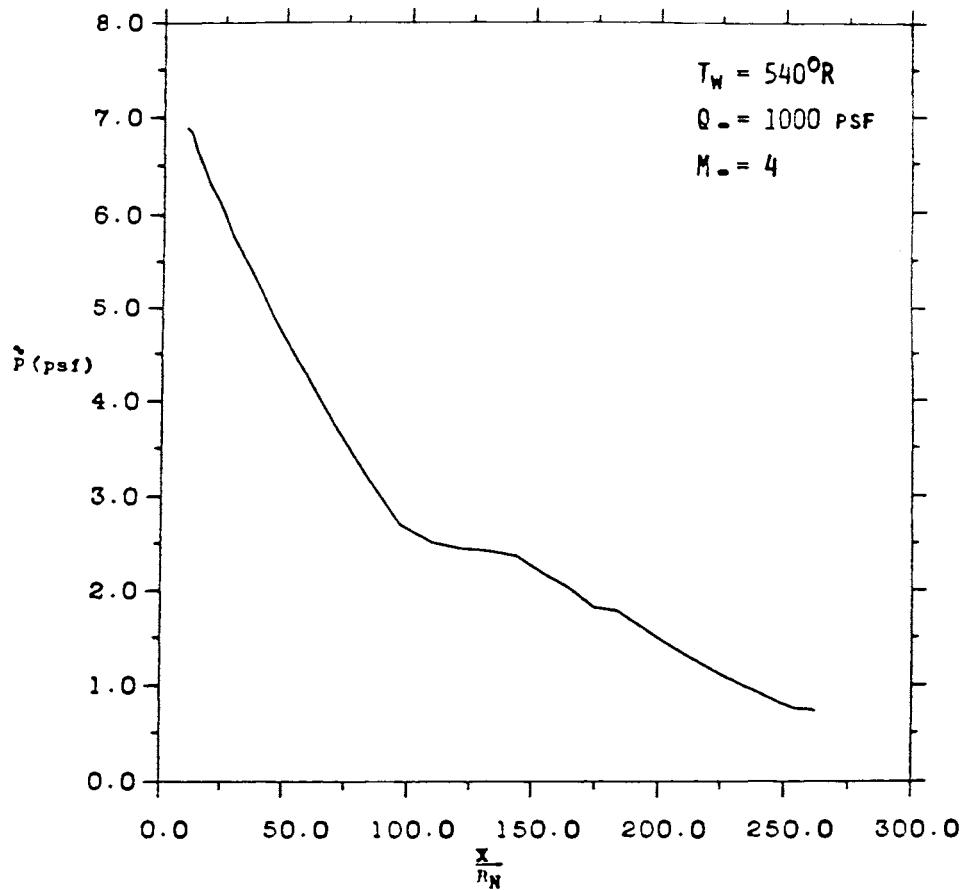


(A)

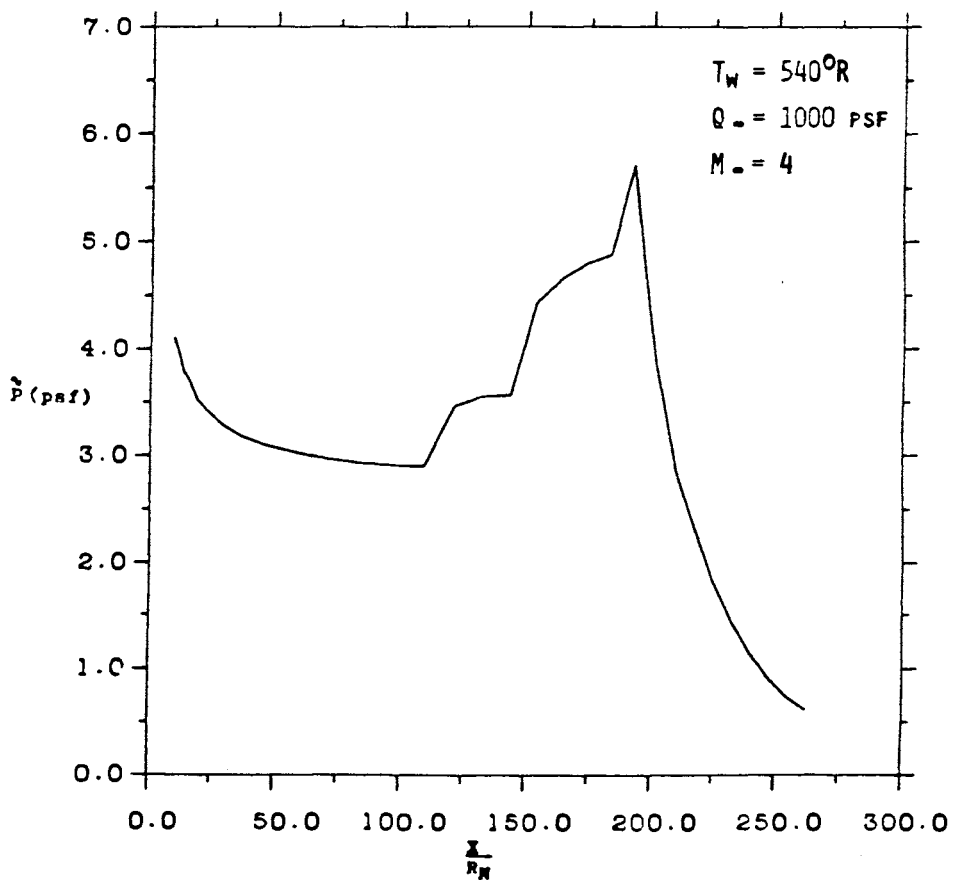


(B)

Figure A-2. Surface Pressure (A) and Heat Transfer (B) Distribution Along Leeward Surface of BWB.

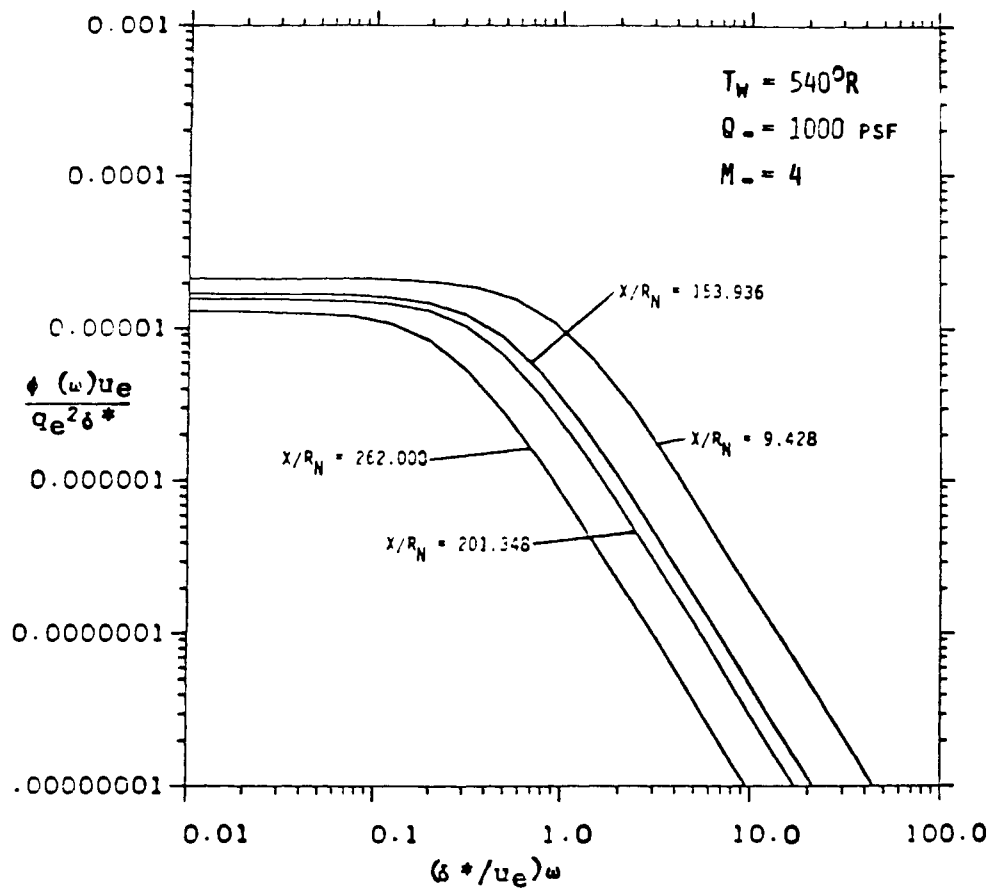


(A)

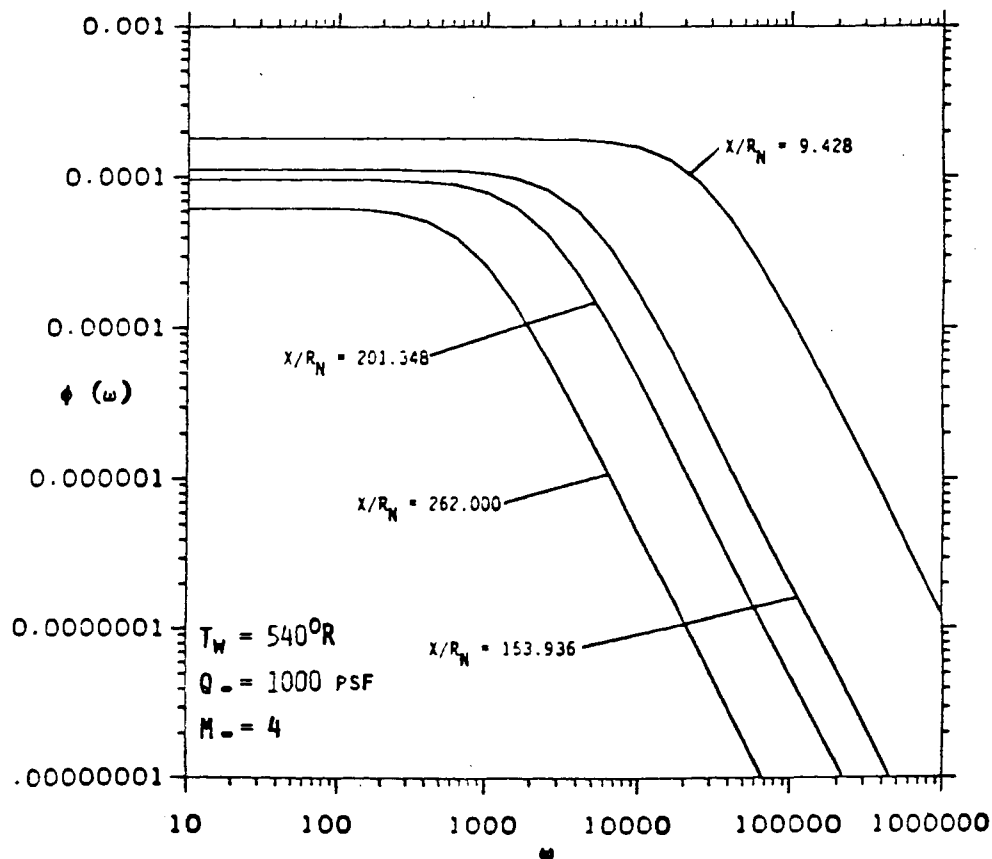


(B)

Figure A-3. RMS Fluctuating Pressure Distribution Along Leeward (A) and Windward (B) Surfaces of BWB.

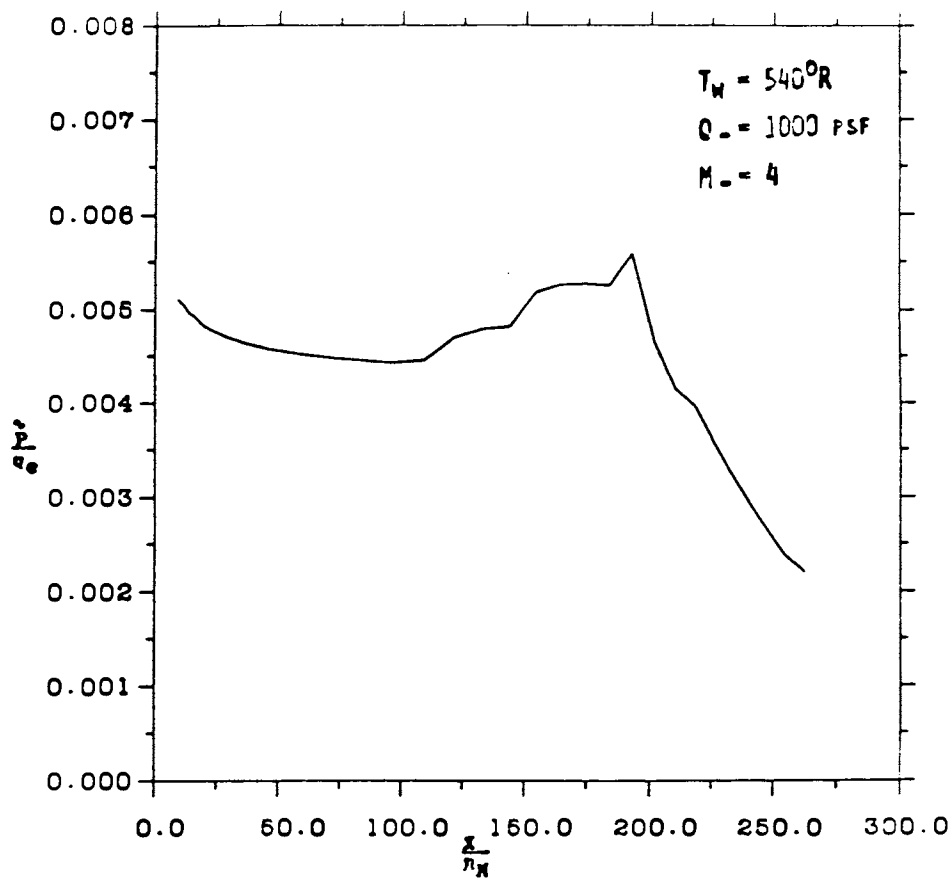


(A)

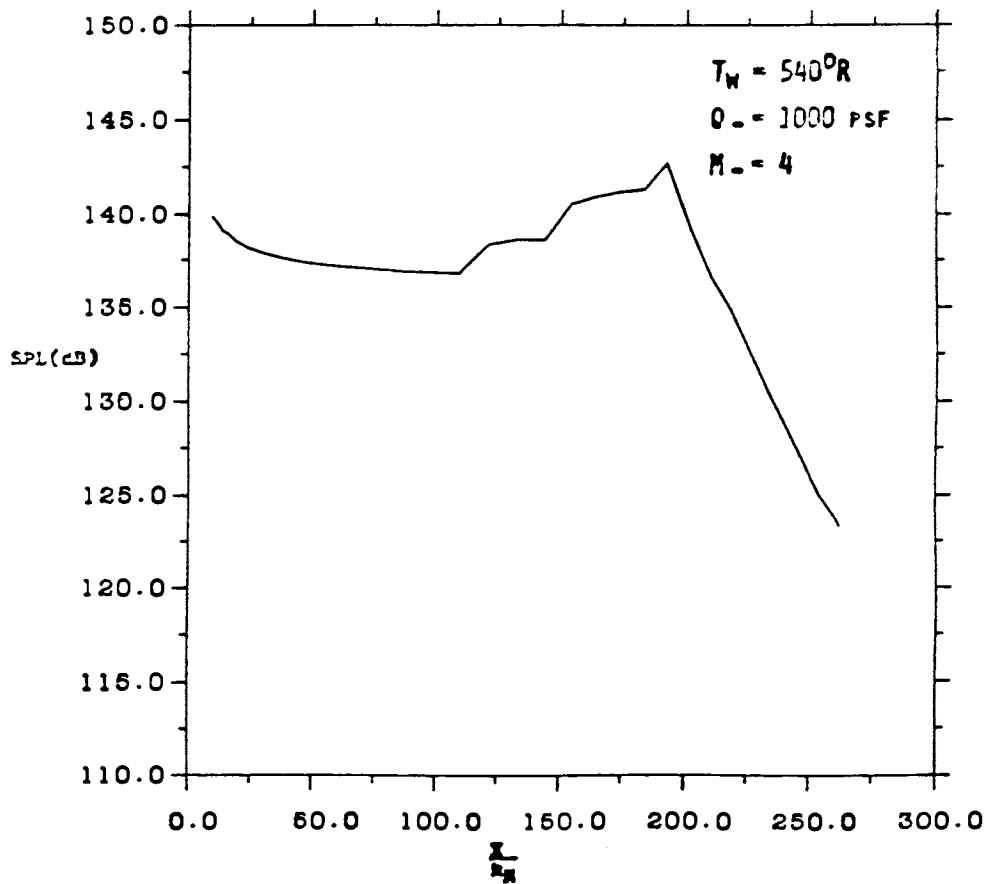


(B)

Figure A-4. Power Spectral Density Distribution Along Leeward Surface of BWB (A) Normalized and (B) Power Spectra.

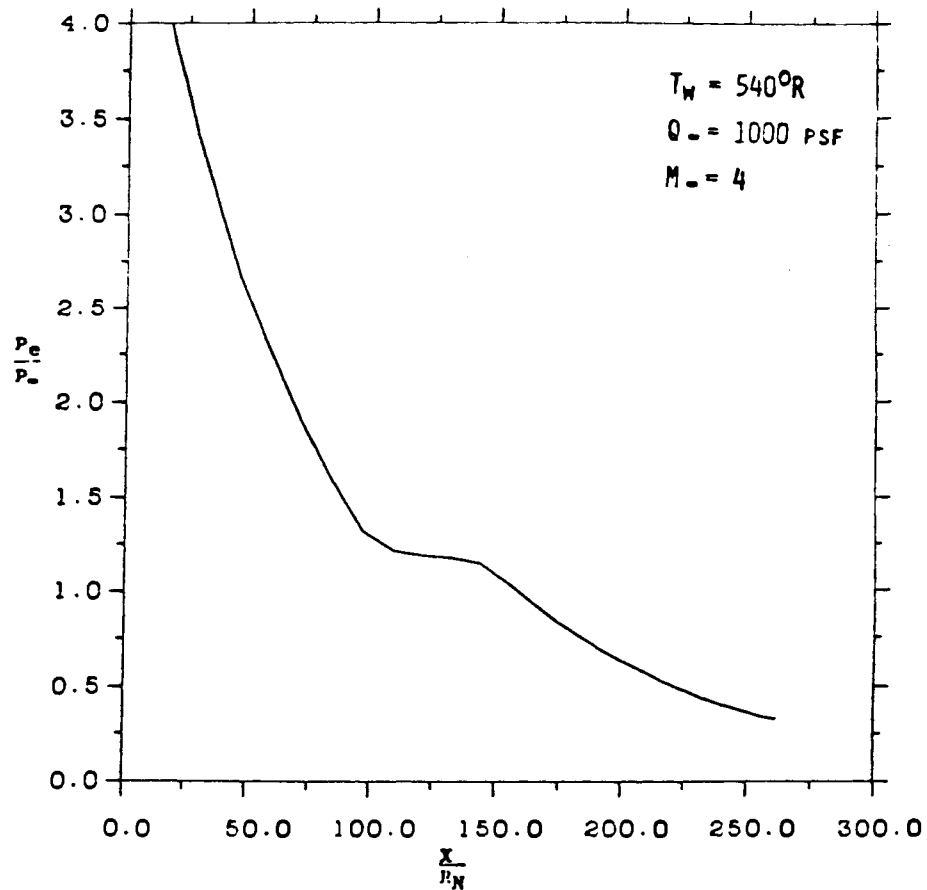


(A)

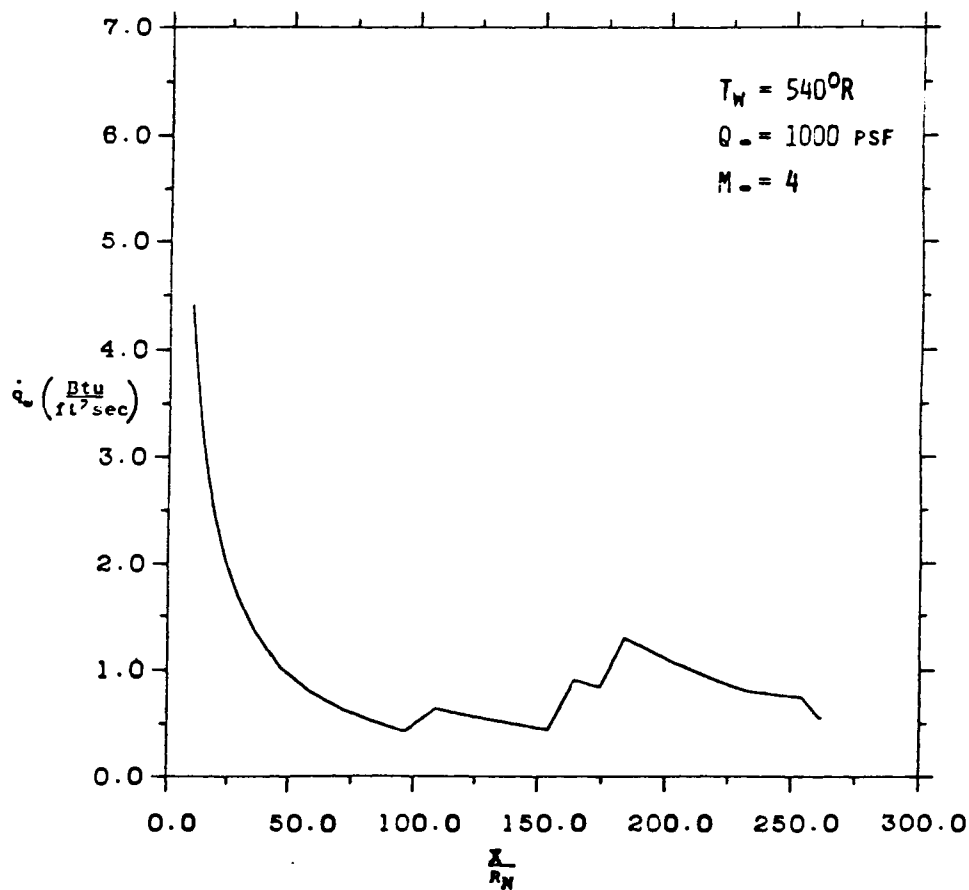


(B)

Figure A-5. RMS Pressure (A) and Sound Pressure Level (B) Distribution Along Windward Surface of BWB.

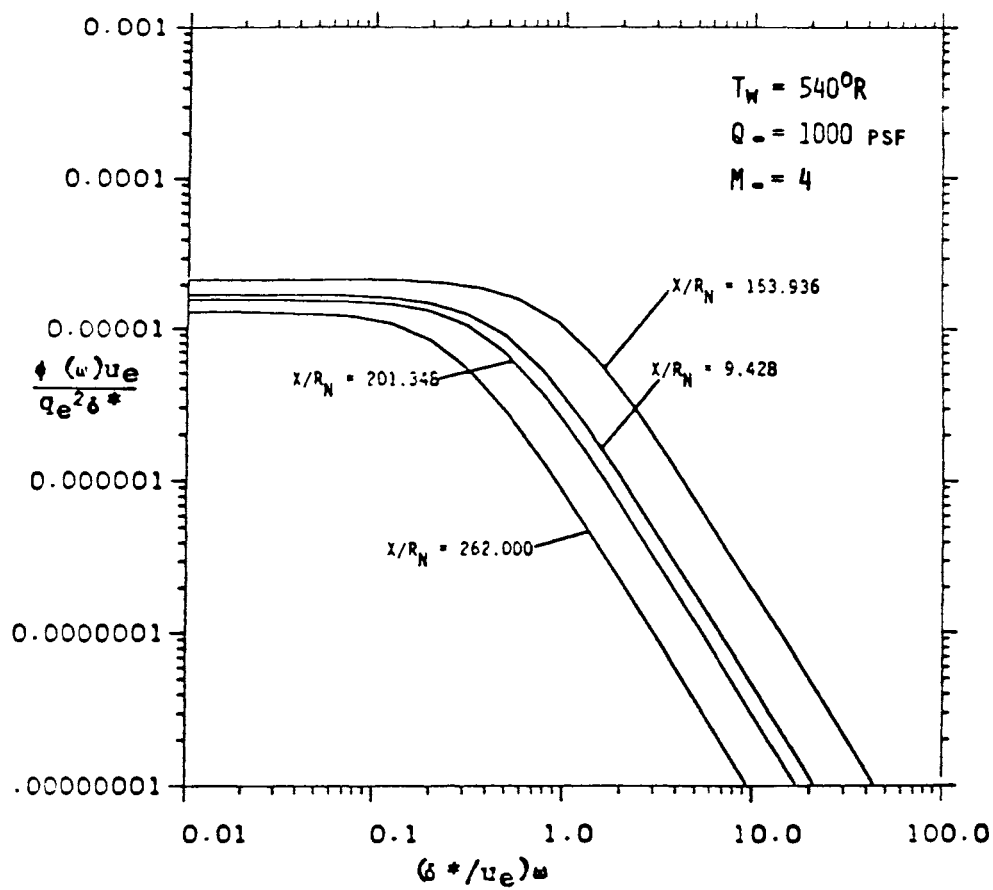


(A)

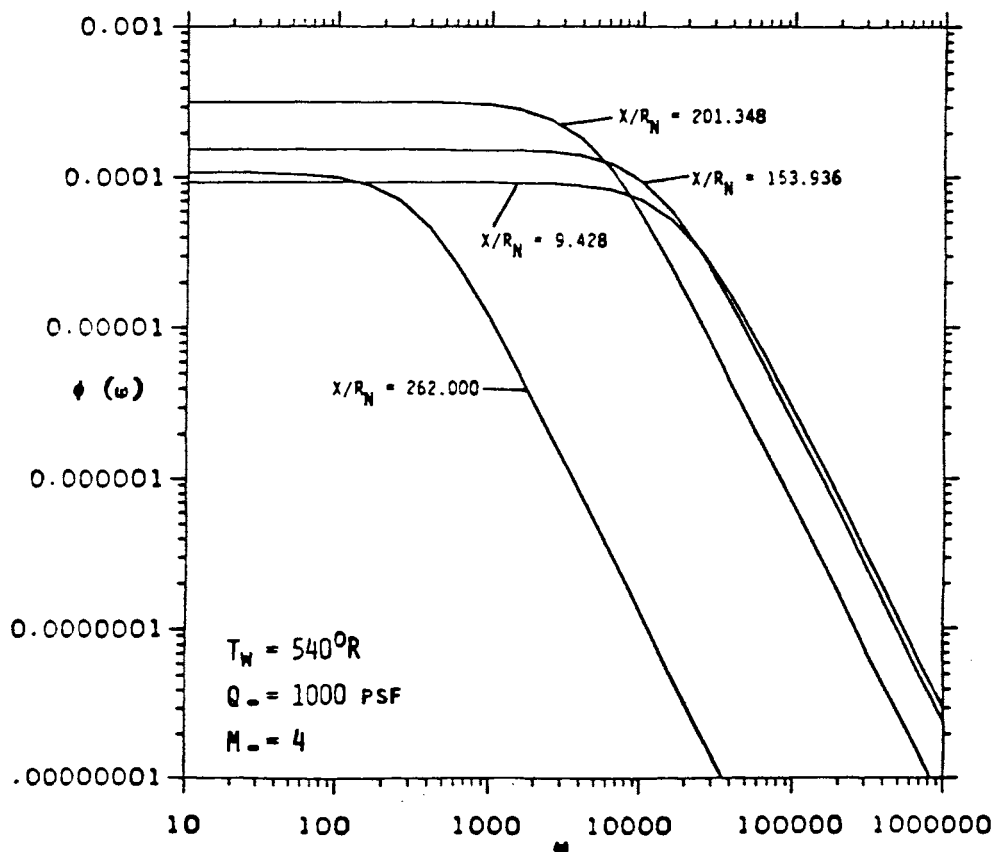


(B)

Figure A-6. Surface Pressure (A) and Heat Transfer (B) Distribution Along Windward Surface of BWB.

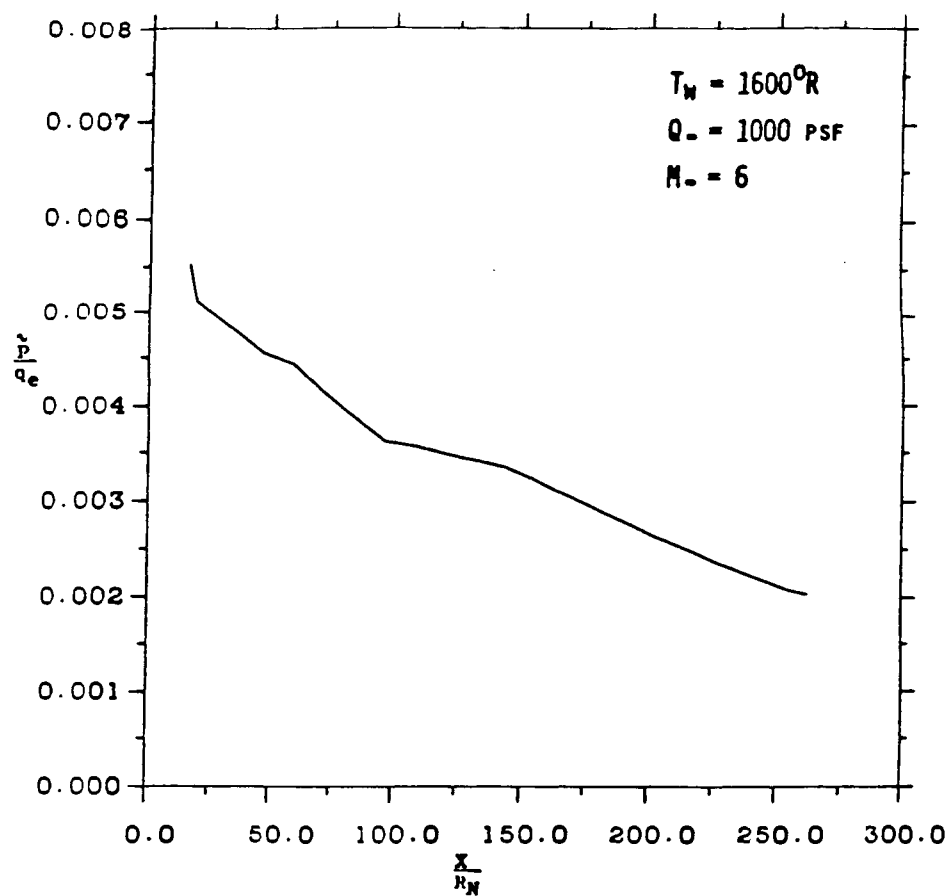


(A)

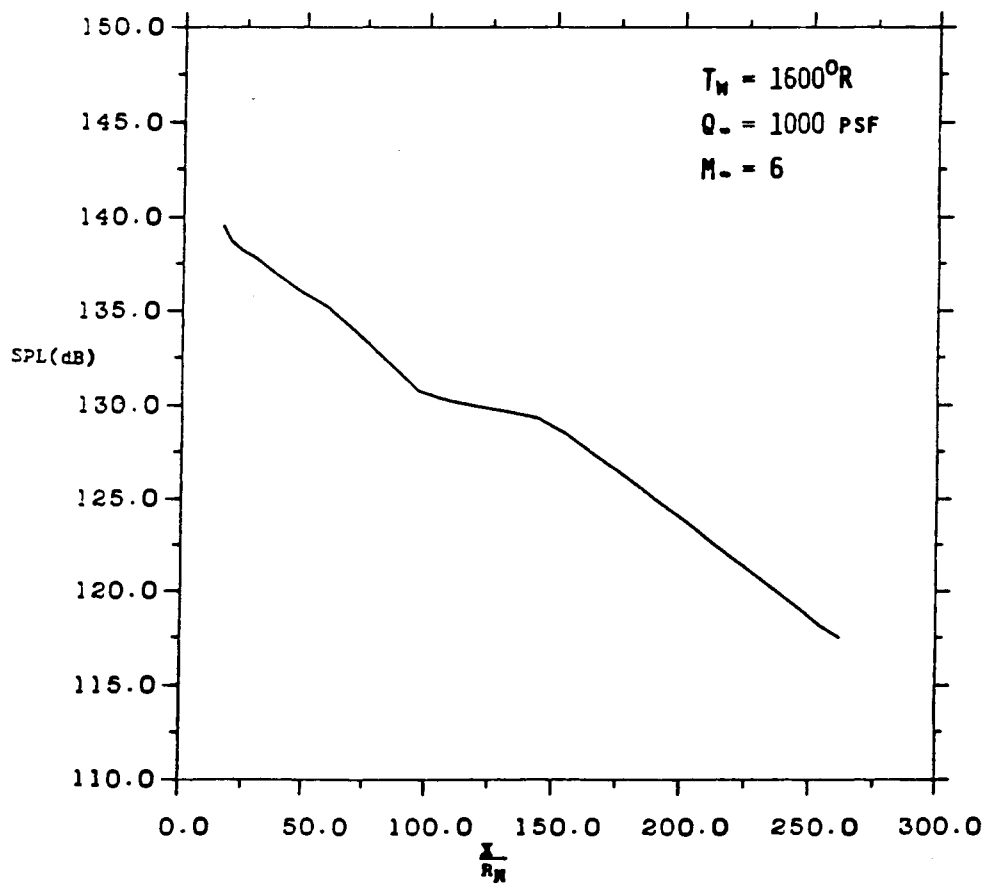


(B)

Figure A-7. Power Spectral Density Distribution Along Windward Surface of BWB (A) Normalized and (B) Power Spectra.

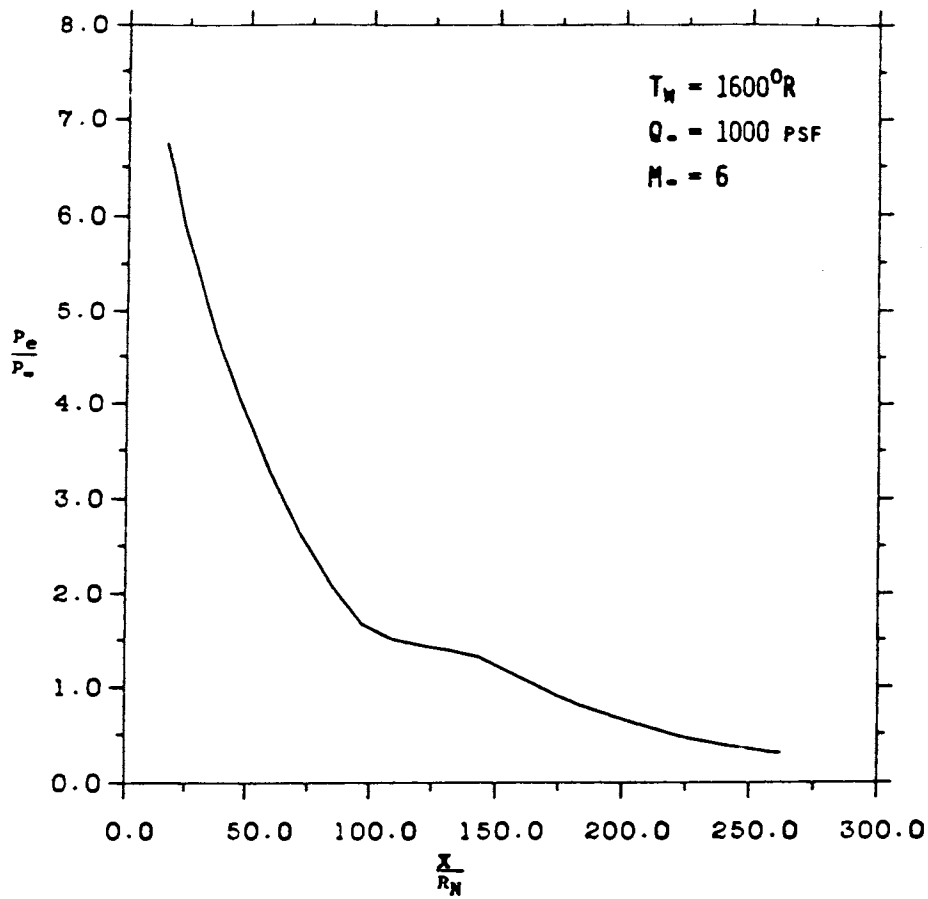


(A)

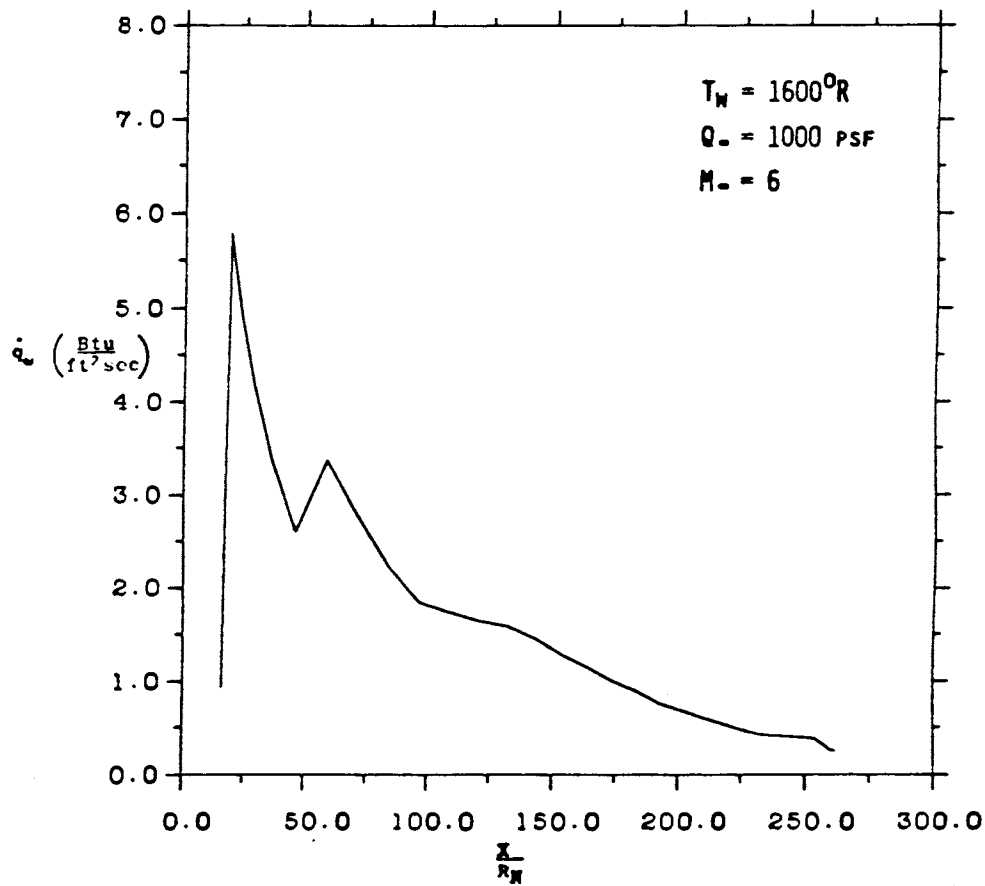


(B)

Figure A-8. RMS Pressure (A) and Sound Pressure Level (B) Distribution Along Leeward Surface of BWB.

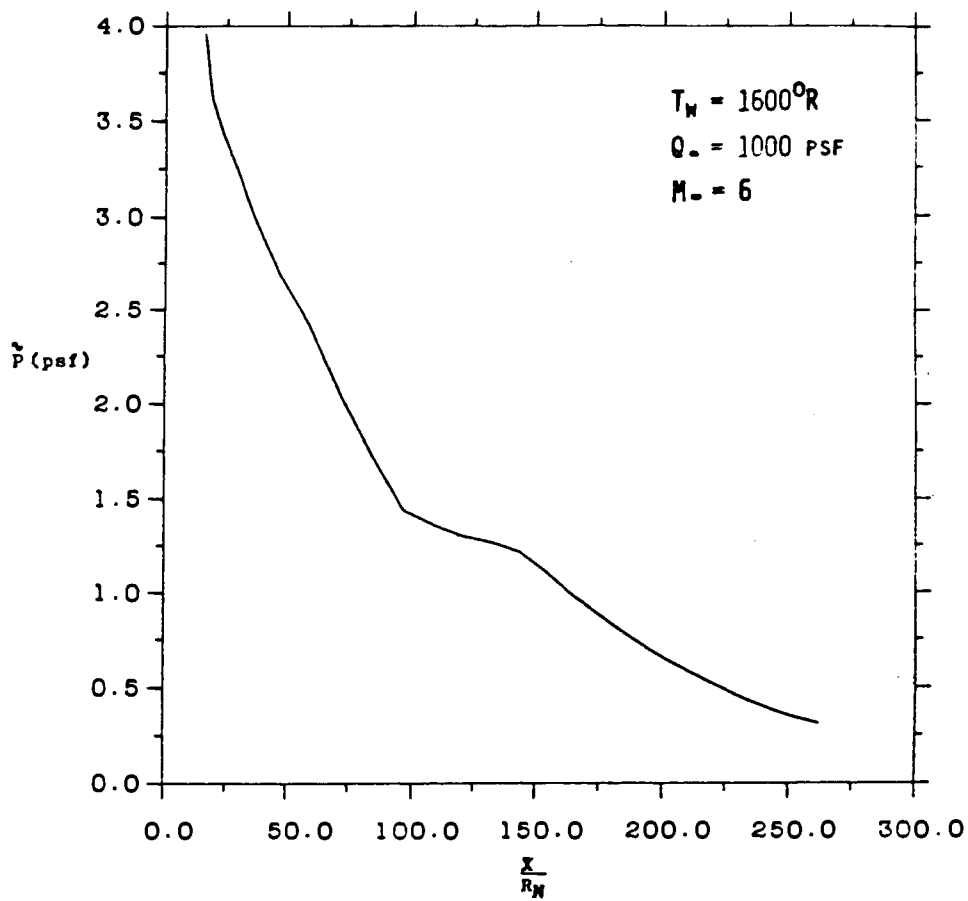


(A)

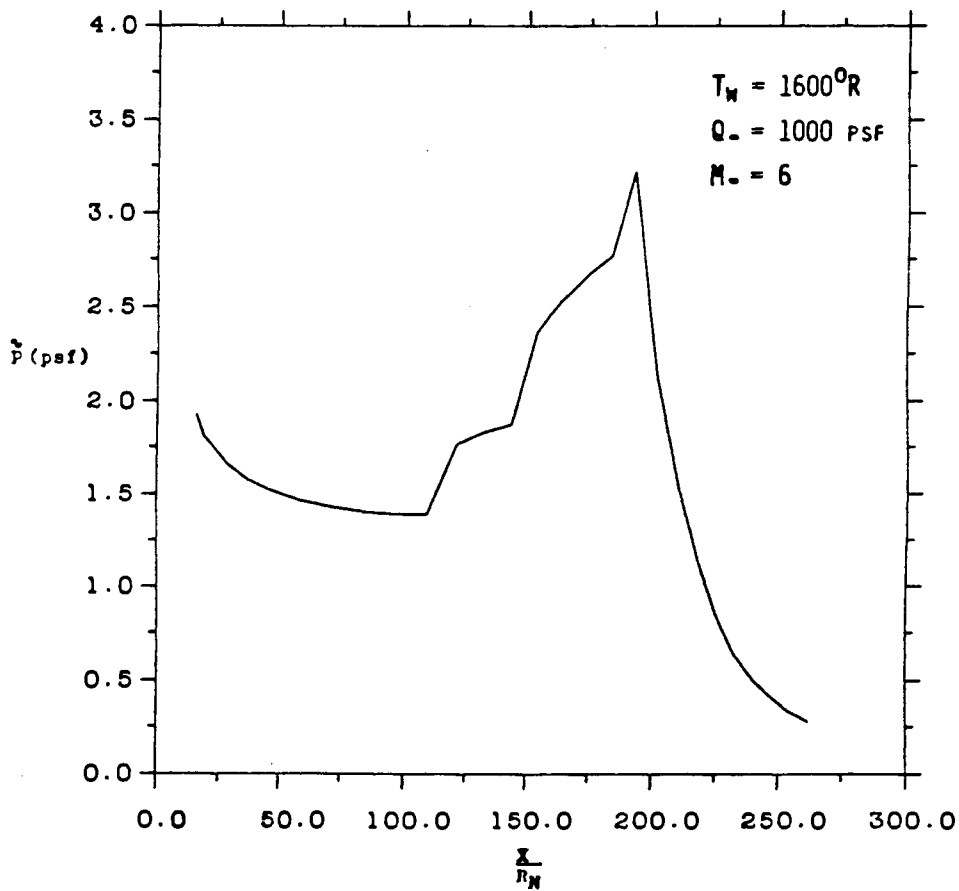


(B)

Figure A-9. Surface Pressure (A) and Heat Transfer (B) Distribution Along Leeward Surface of BWB.

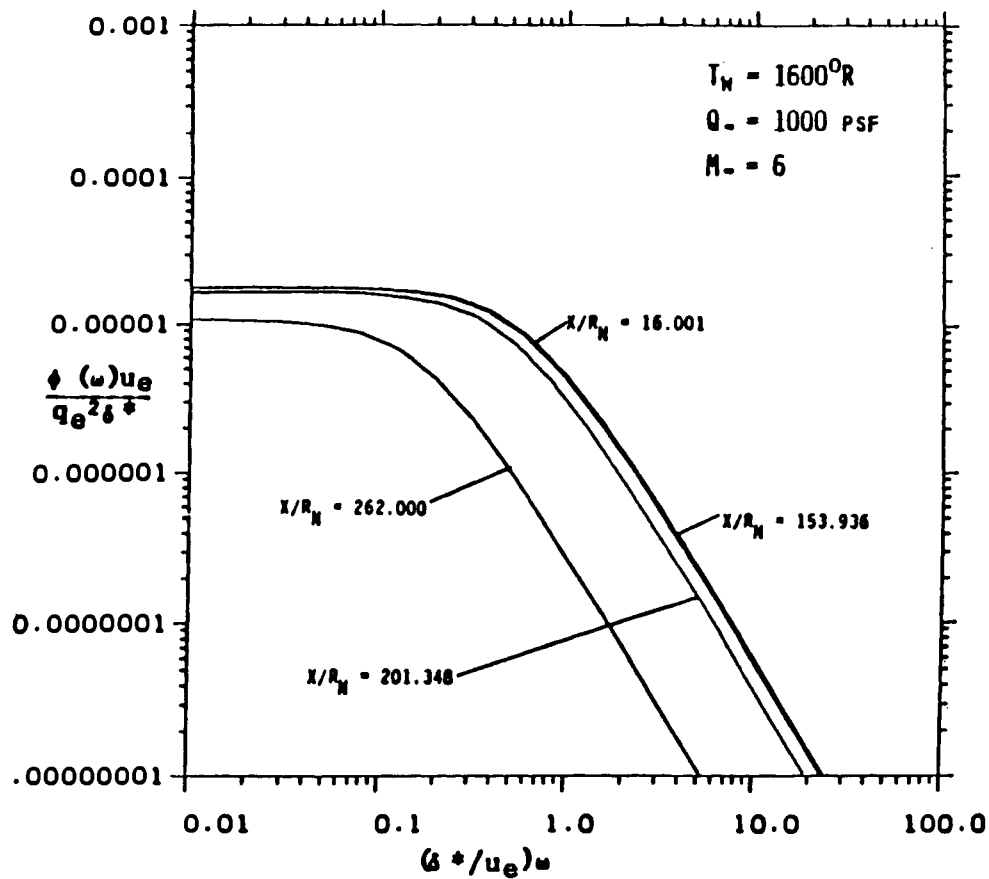


(A)

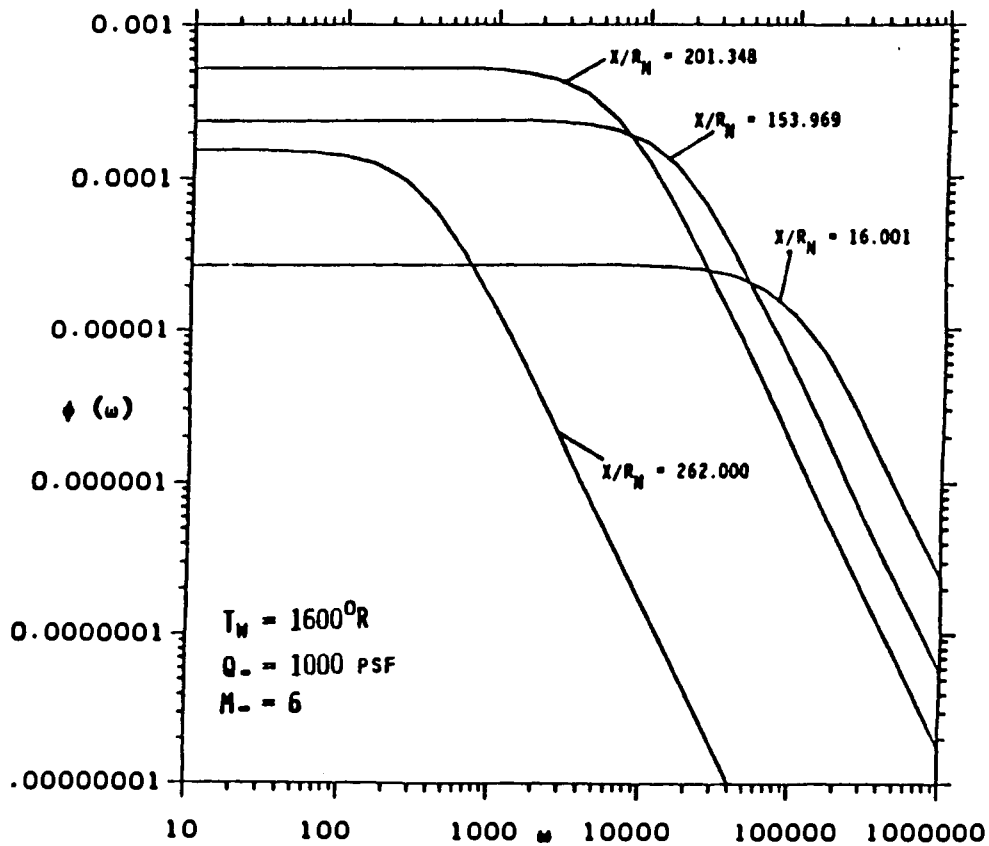


(B)

Figure A-10. RMS Fluctuating Pressure Distribution Along Leeward (A) and Windward (B) Surfaces of BWB.

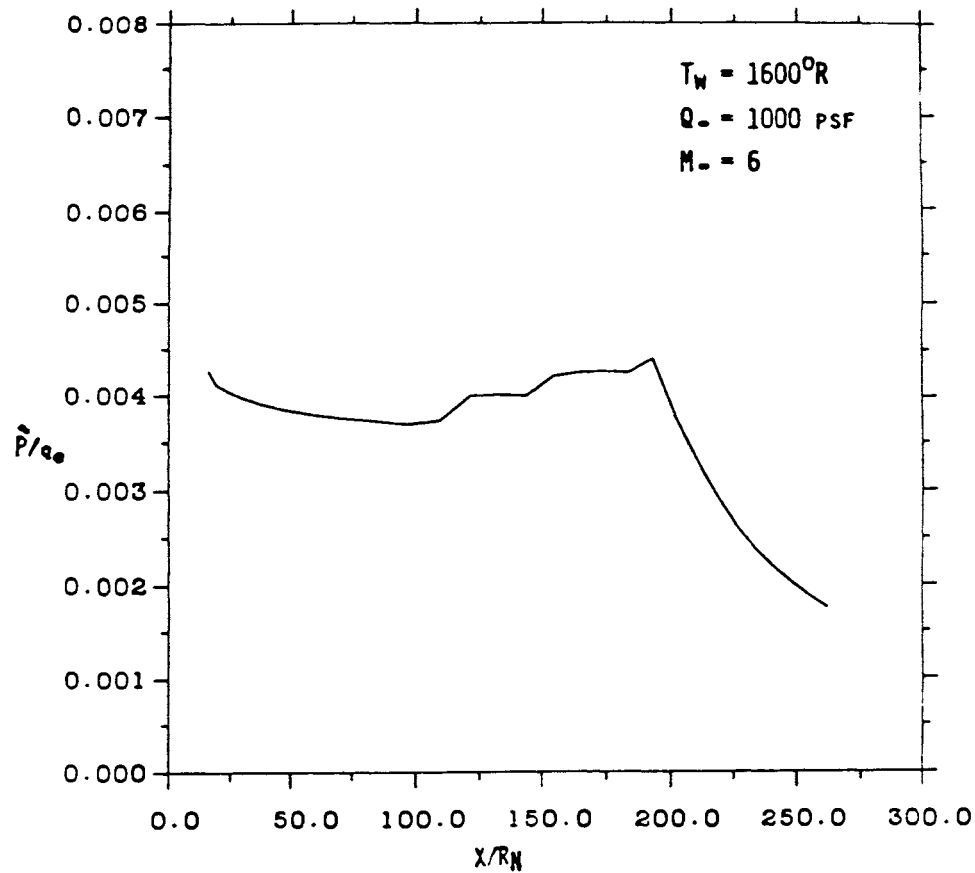


(A)

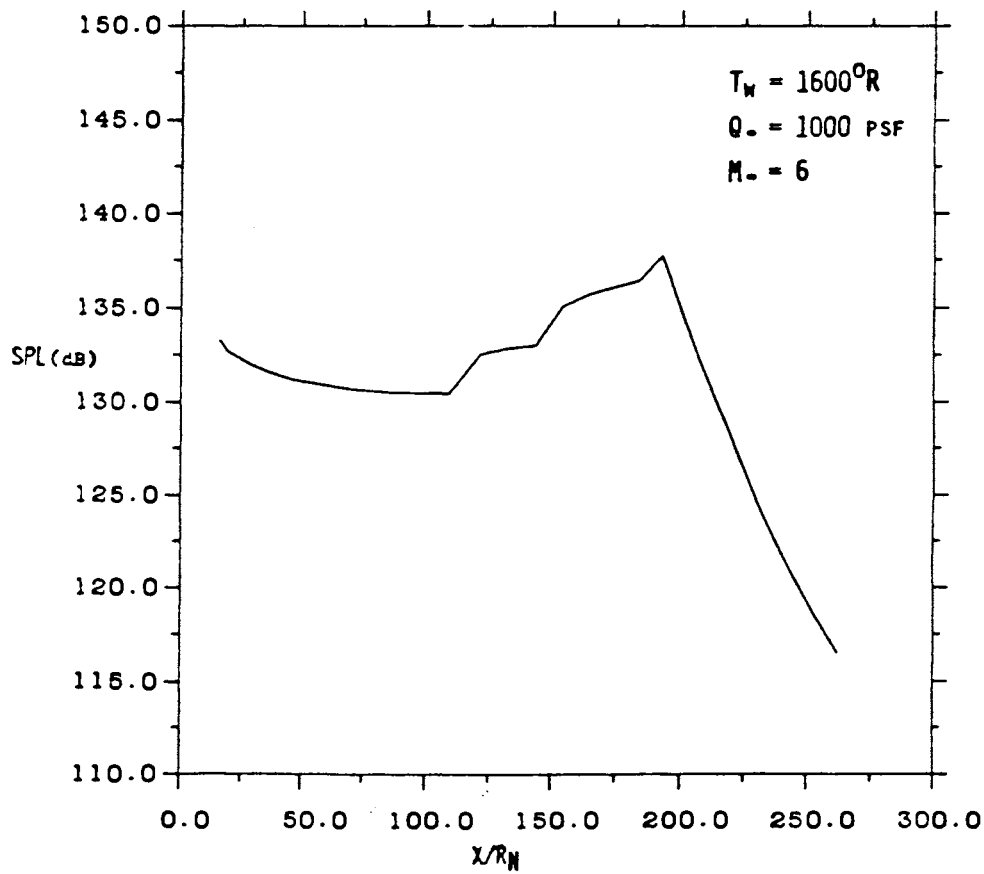


(B)

Figure A-11. Power Spectral Density Distribution Along Leeward Surface of BWB (A) Normalized and (B) Power Spectra.

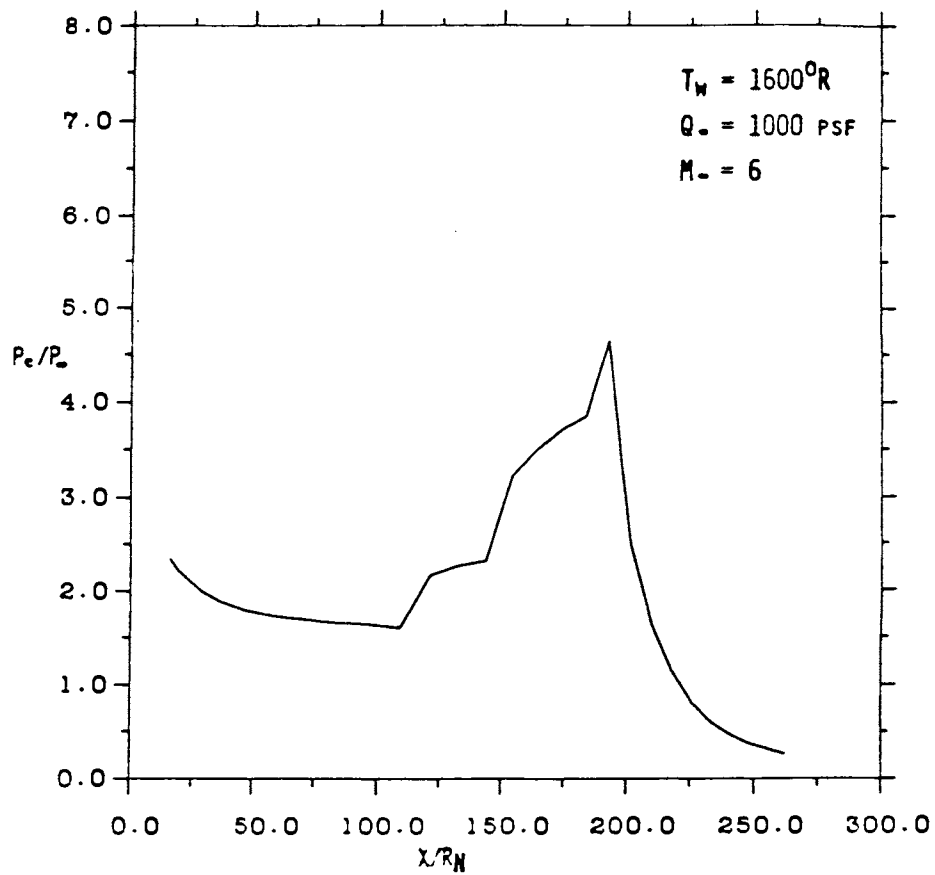


(A)

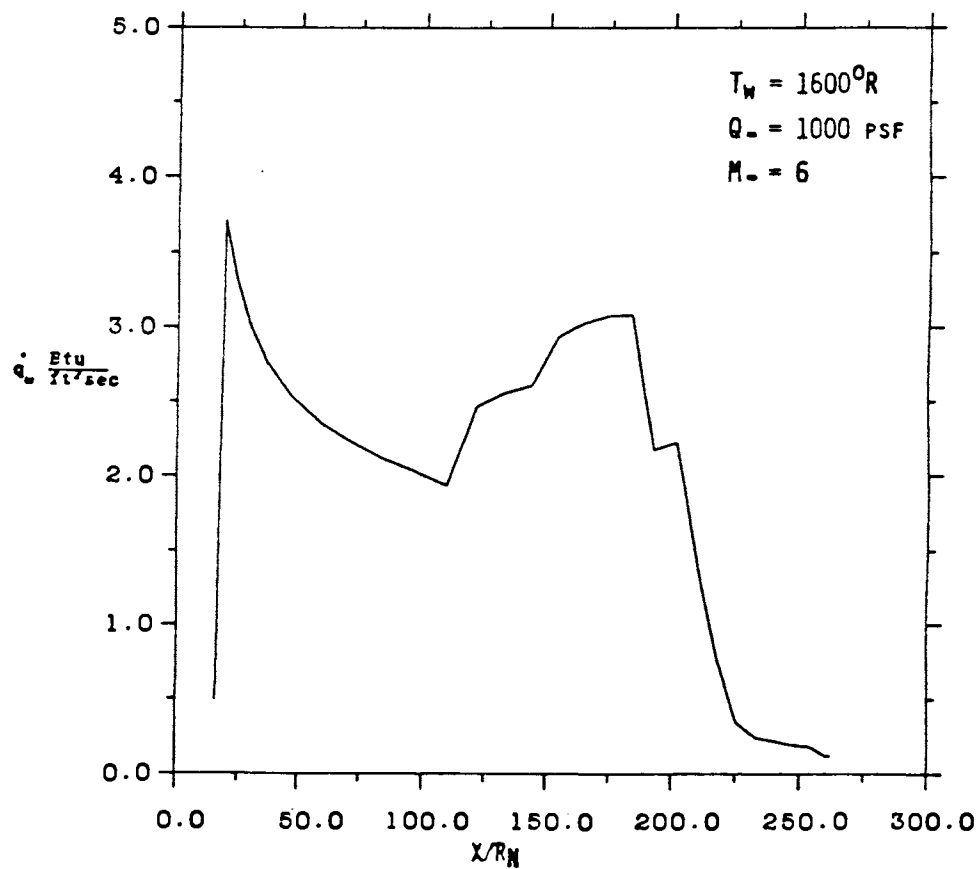


(B)

Figure A-12. RMS Pressure (A) and Sound Pressure Level (B) Distribution Along Windward Surface of BWB.



(A)



(B)

Figure A-13. Surface Pressure (A) and Heat Transfer (B) Distribution Along Windward Surface of BMB.

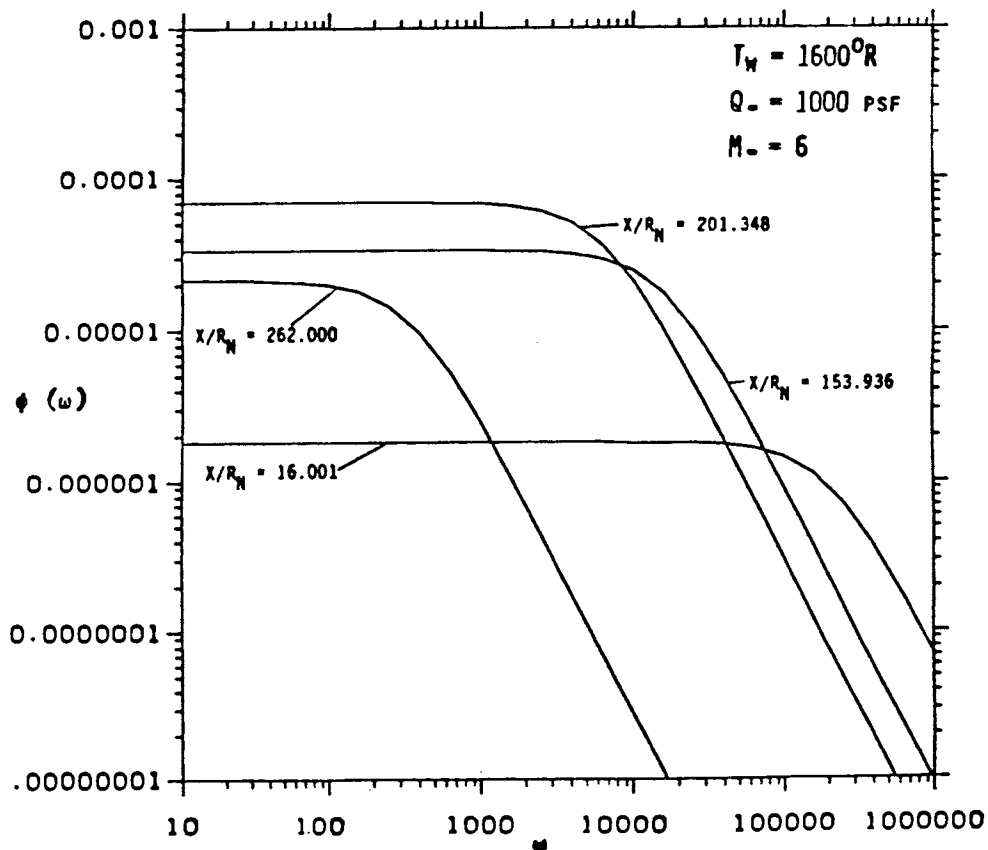
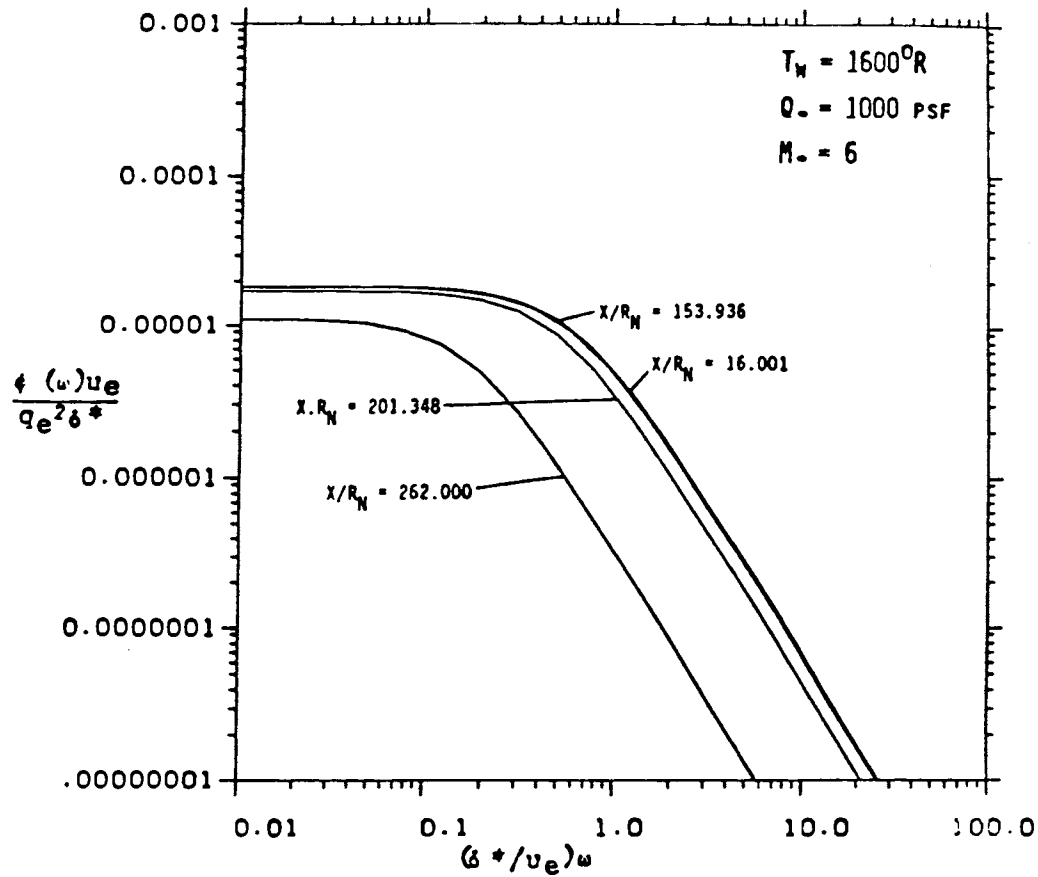
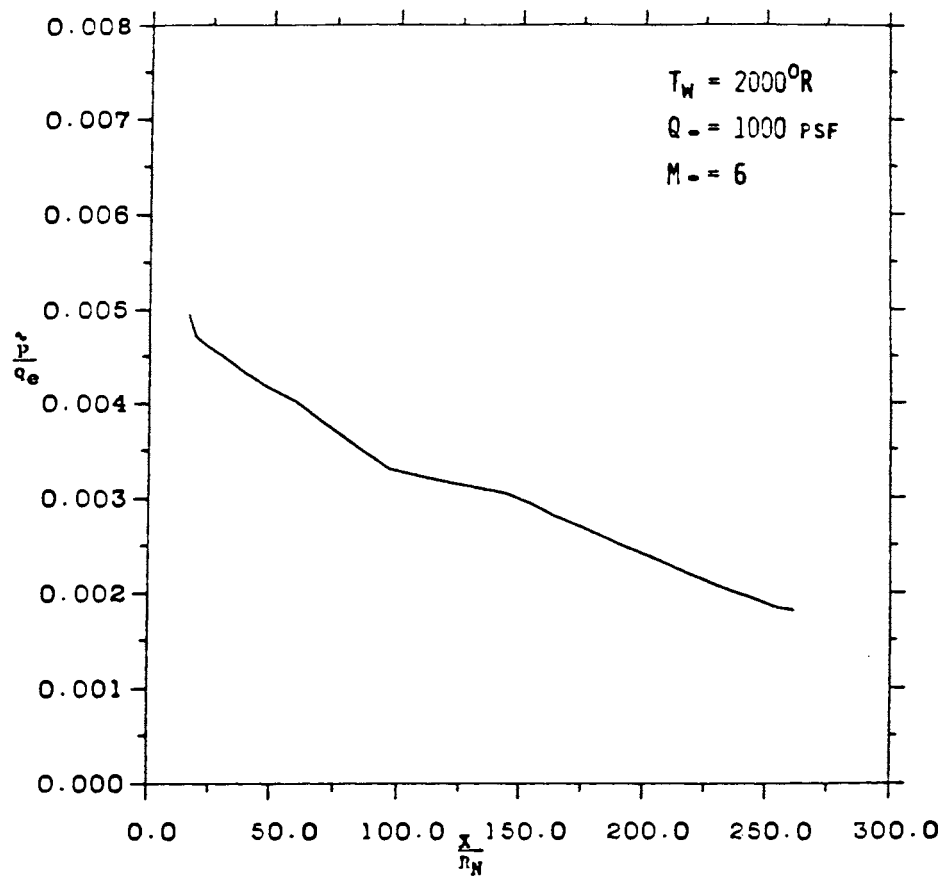
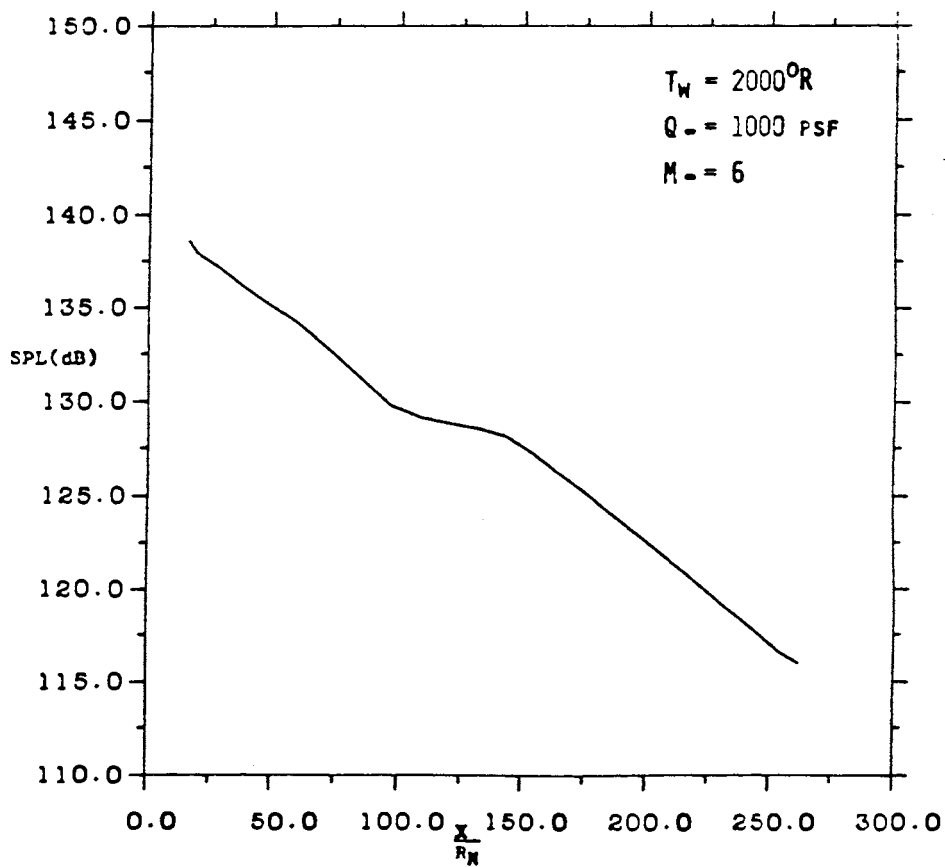


Figure A-14. Power Spectral Density Distribution Along Windward Surface of BWB (A) Normalized and (B) Power Spectra.

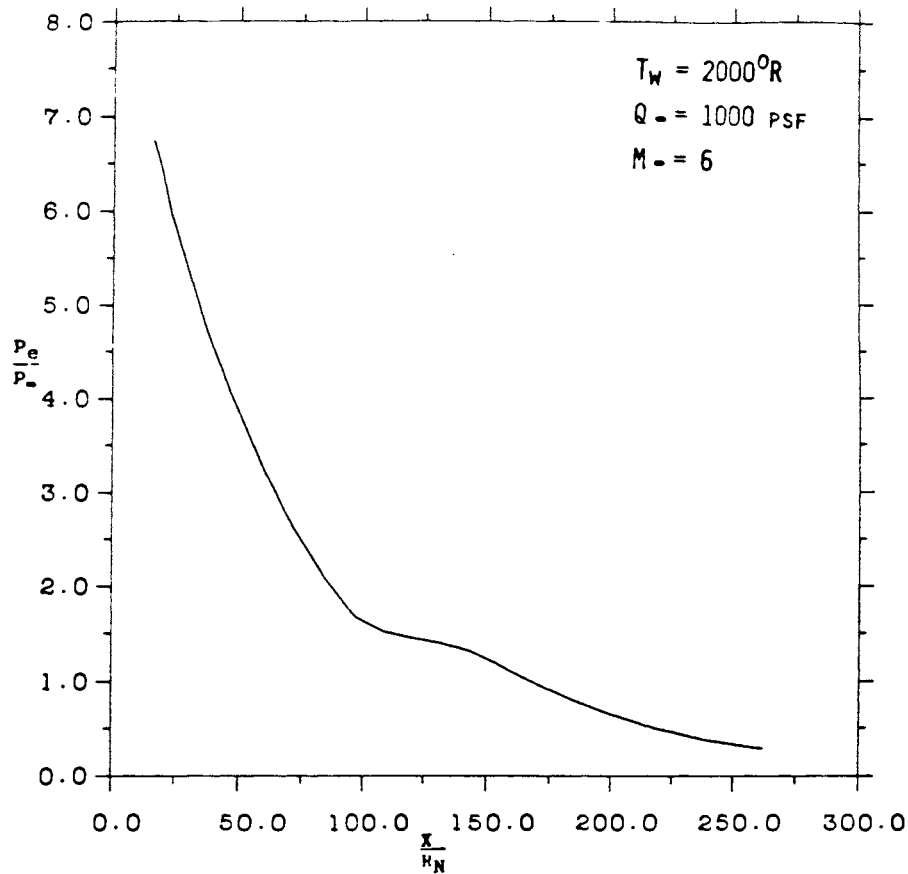


(A)

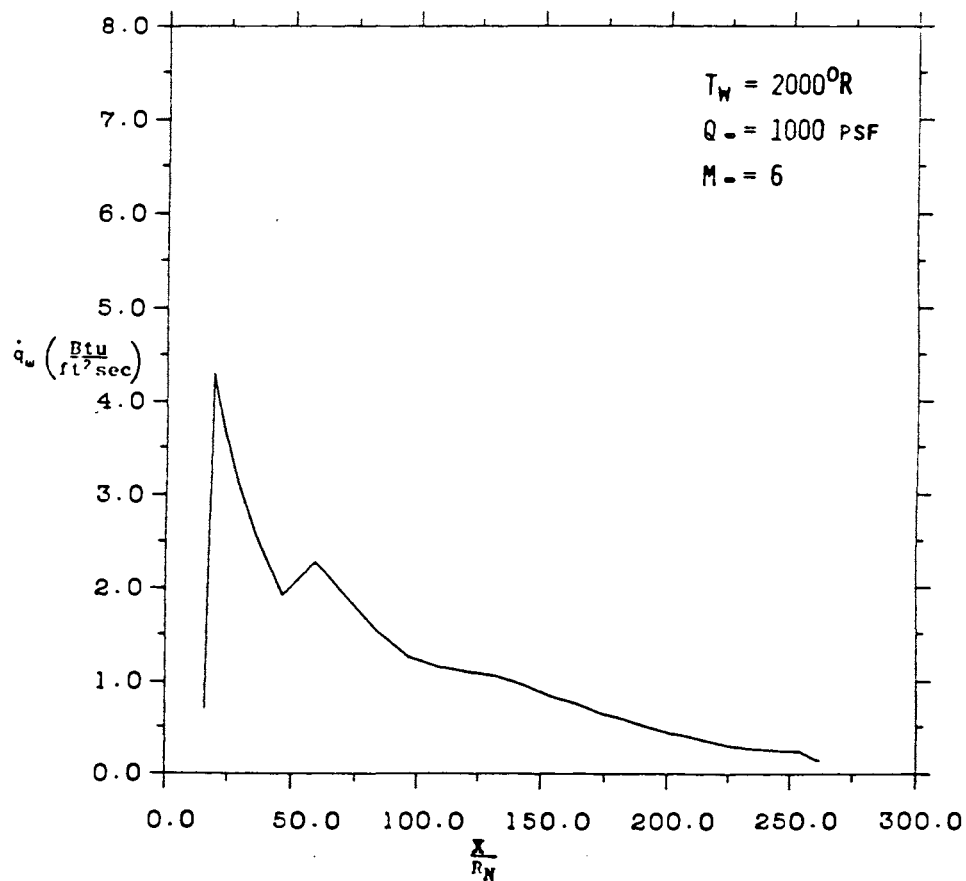


(B)

Figure A-15. RMS Pressure (A) and Sound Pressure Level (B) Distribution Along Leeward Surface of BWB.

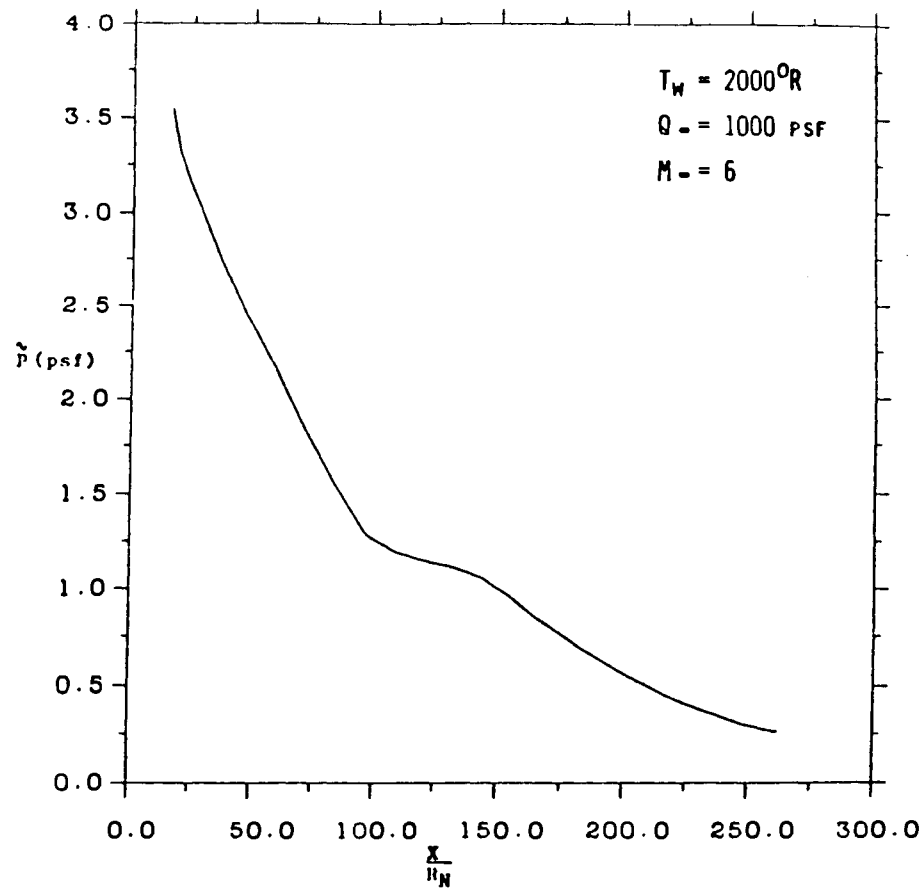


(A)

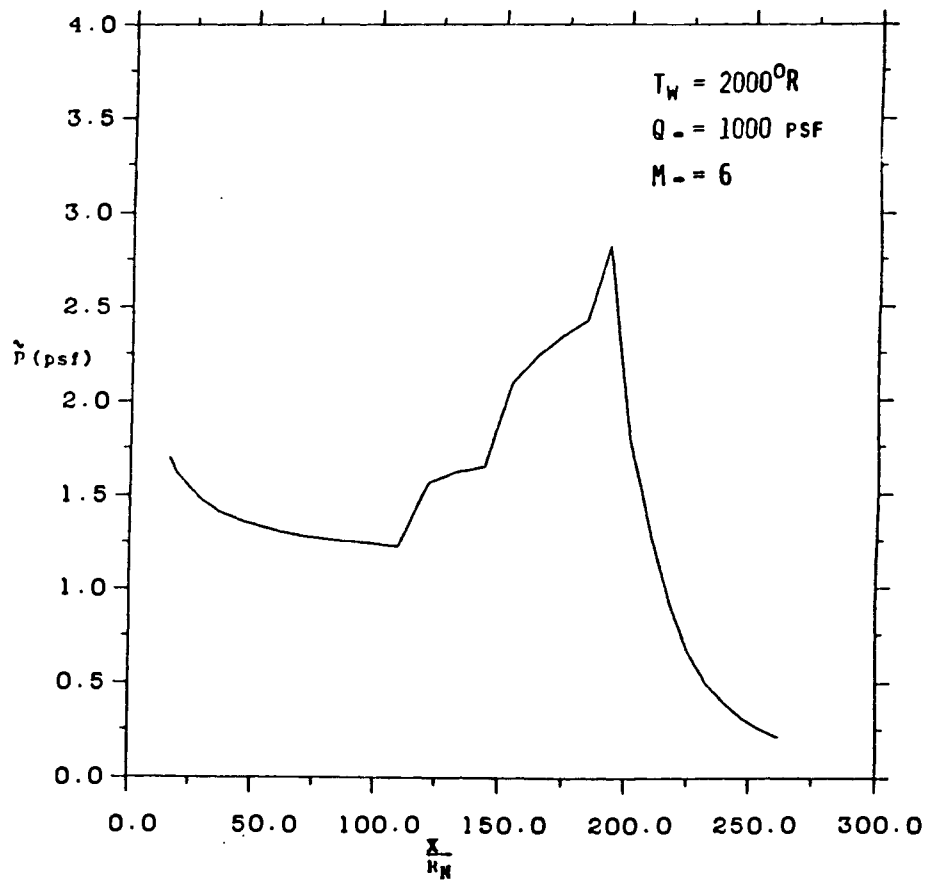


(B)

Figure A-16. Surface Pressure (A) and Heat Transfer (B) Distribution Along Leeward Surface of BWB.



(A)



(B)

Figure A-17. RMS Fluctuating Pressure Distribution Along Leeward (A) and Windward (B) Surfaces of BWB.

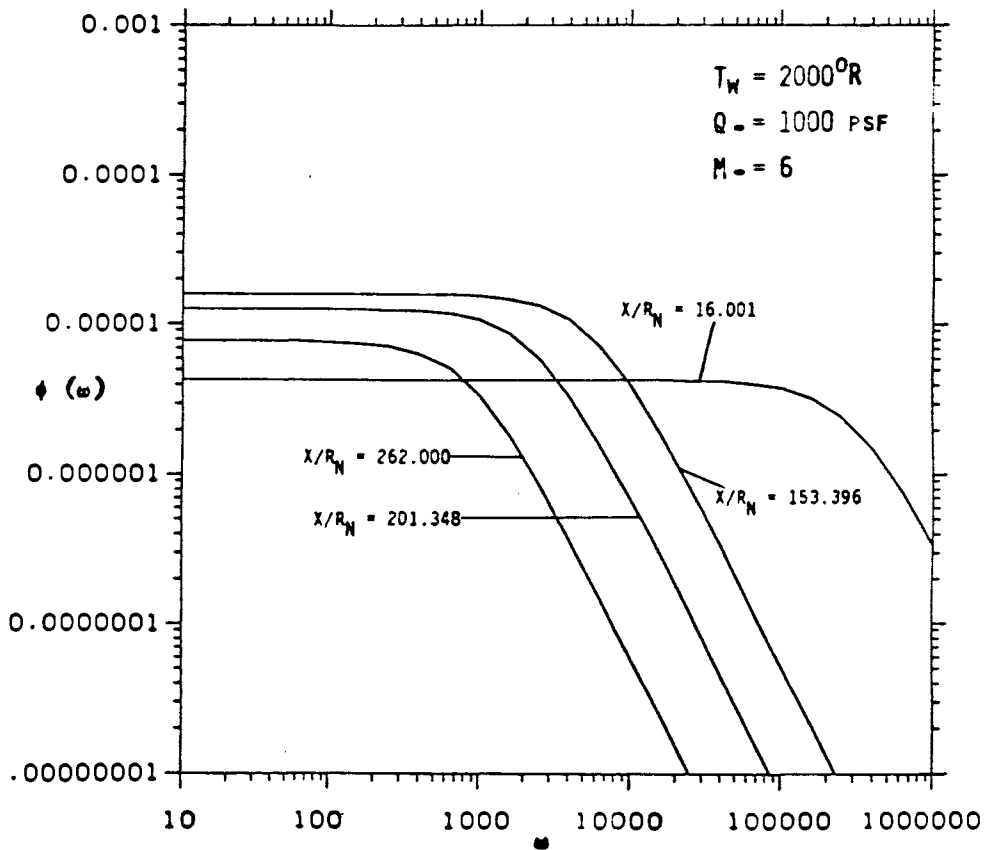
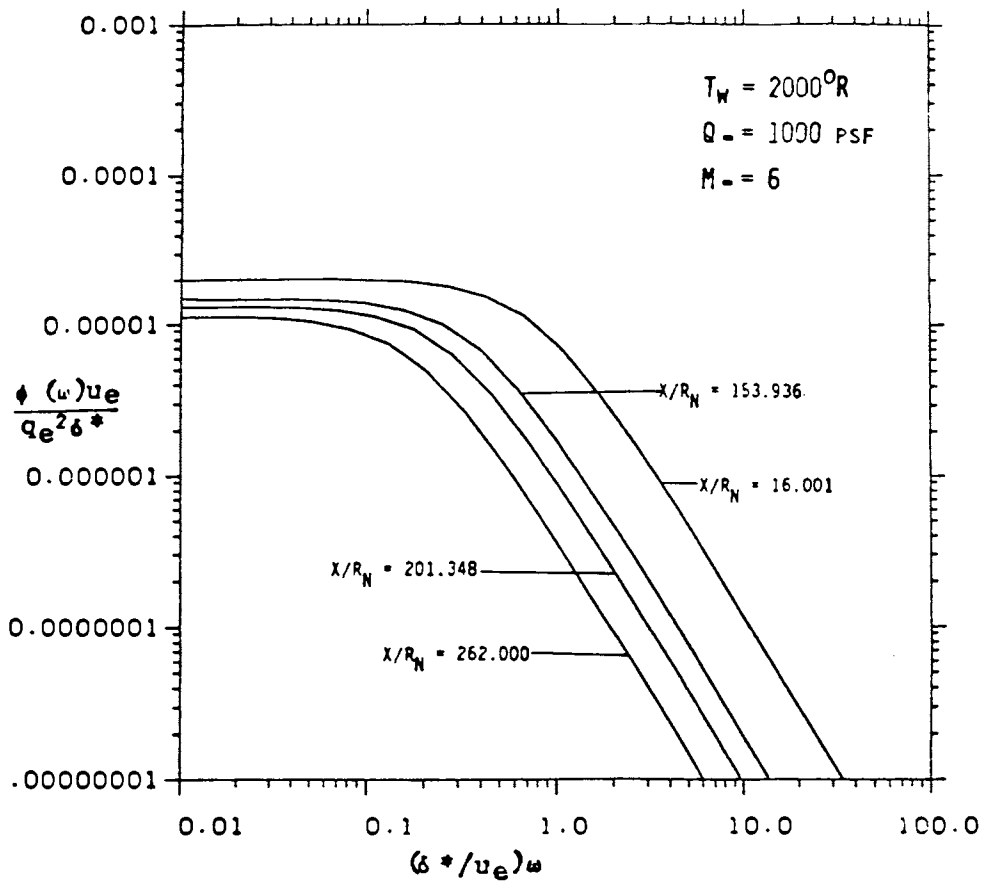
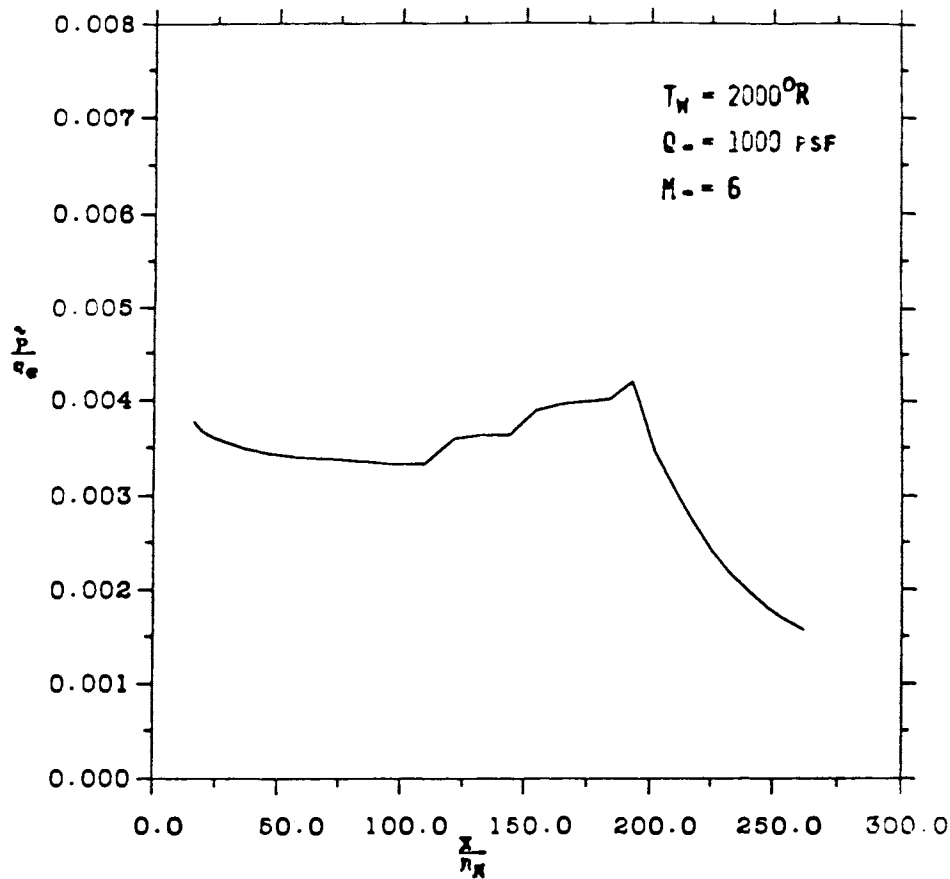
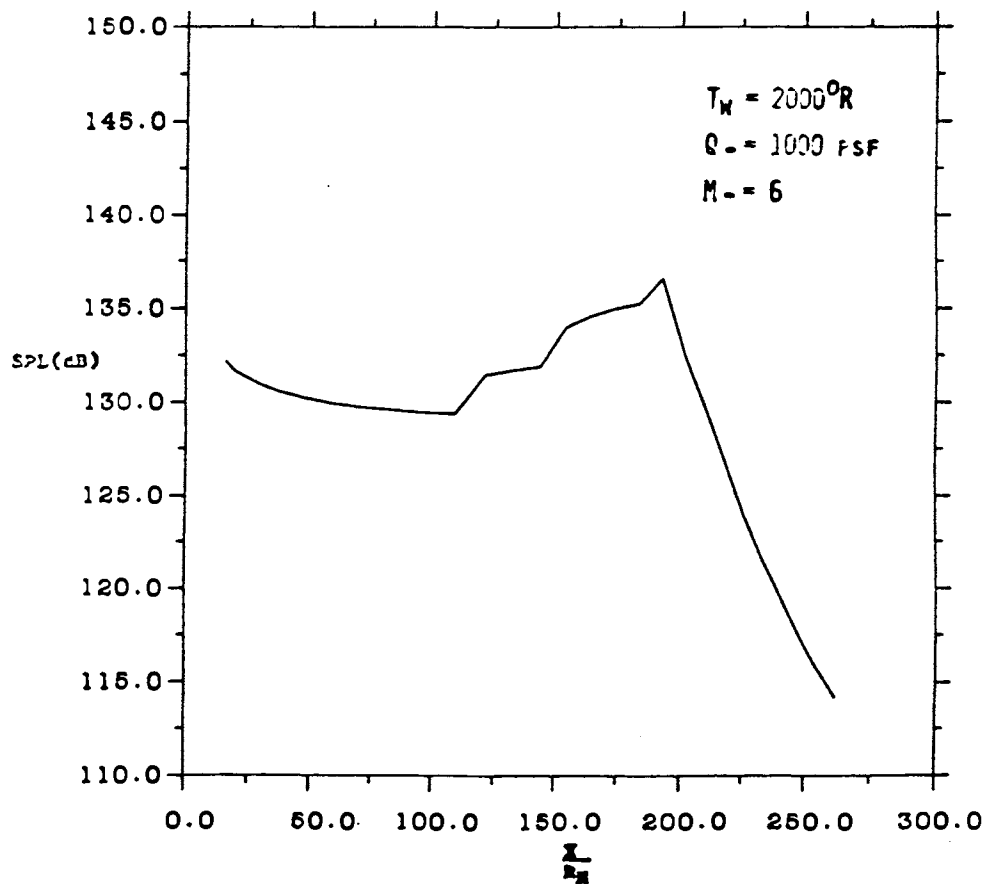


Figure A-18. Power Spectral Density Distribution Along Leeward Surface of BWB (A) Normalized and (B) Power Spectra.

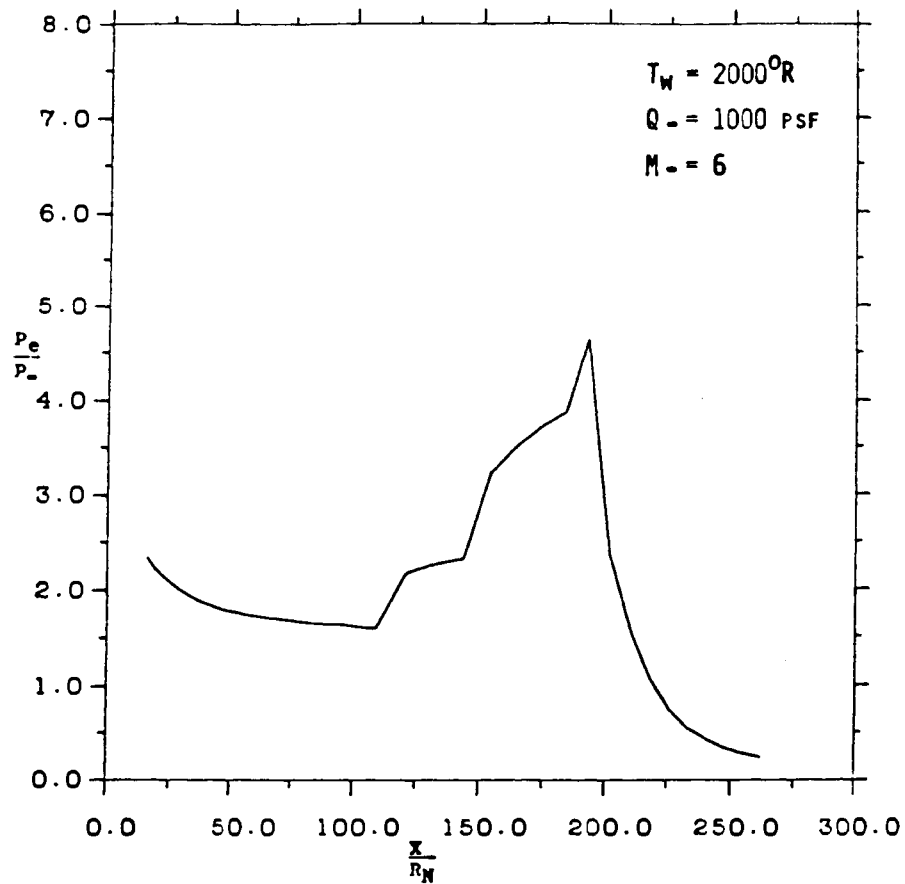


(A)

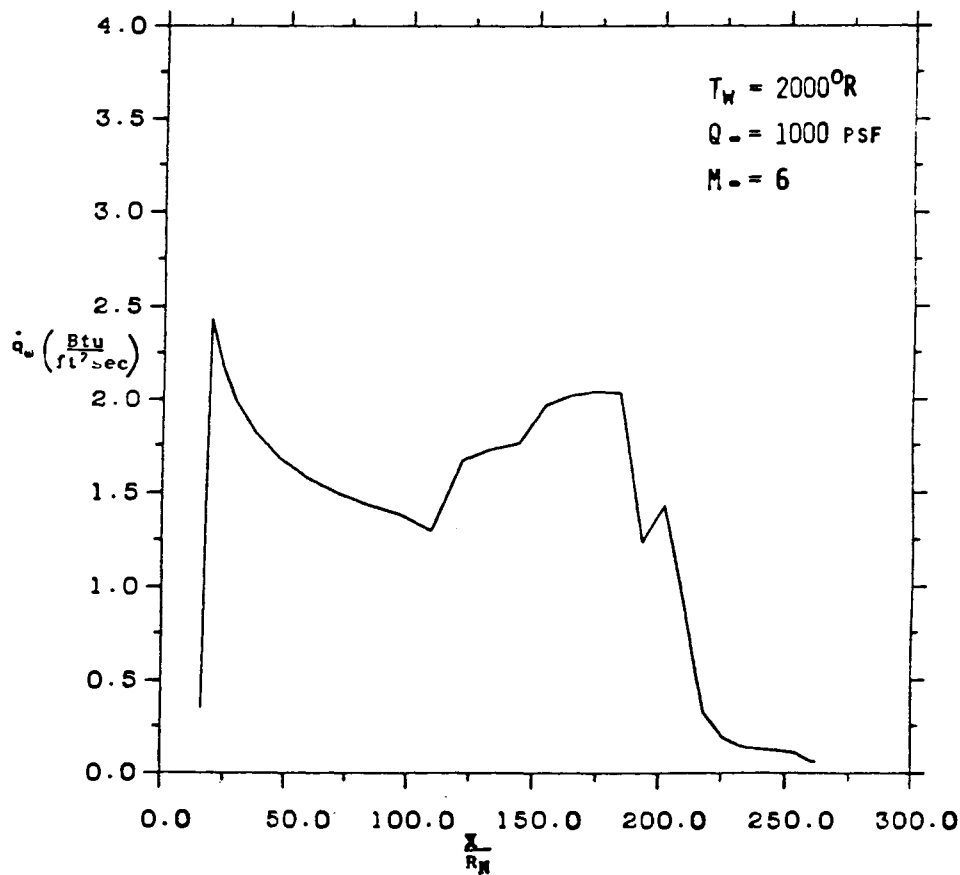


(B)

Figure A-19. RMS Pressure (A) and Sound Pressure Level (B) Distribution Along Windward Surface of BMB.

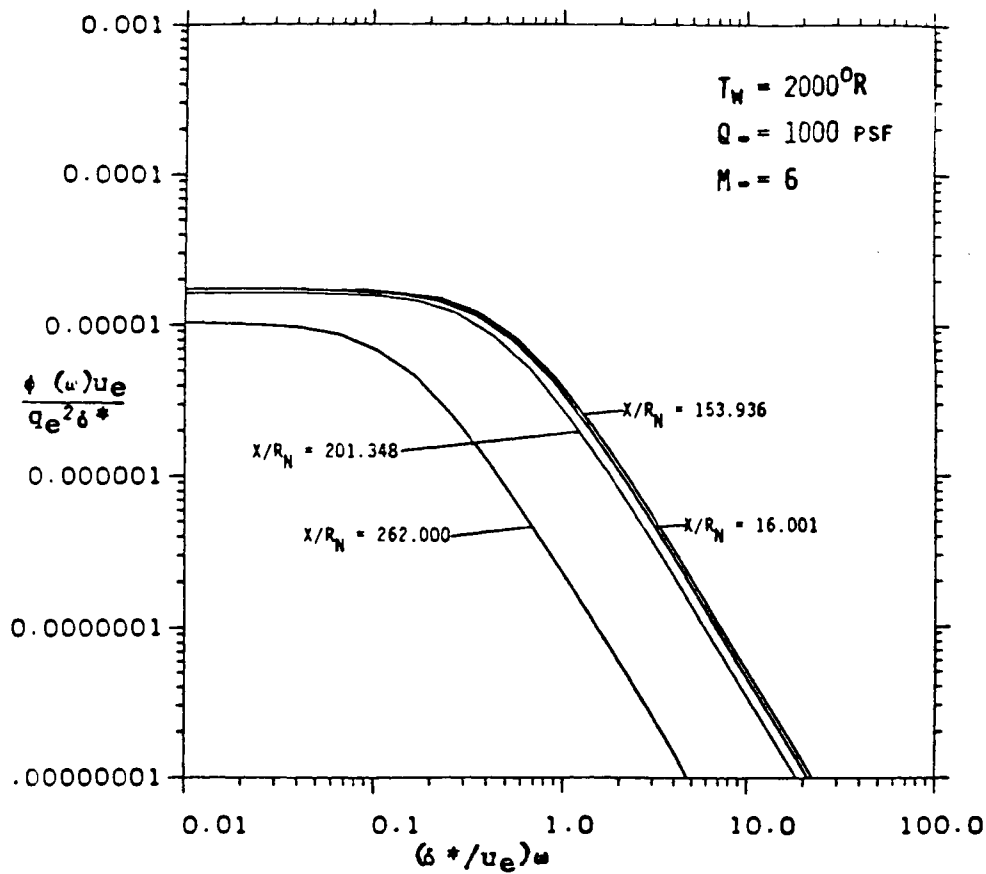


(A)

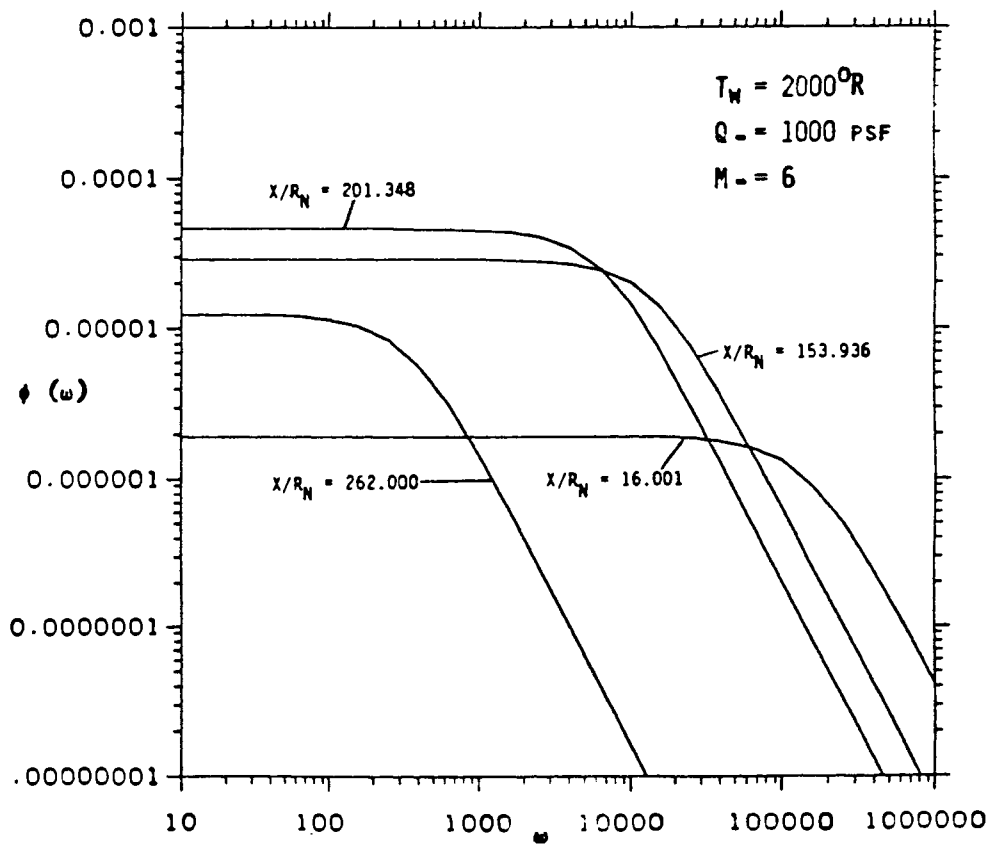


(B)

Figure A-20. Surface Pressure (A) and Heat Transfer (B) Distribution Along Windward Surface of BWB.

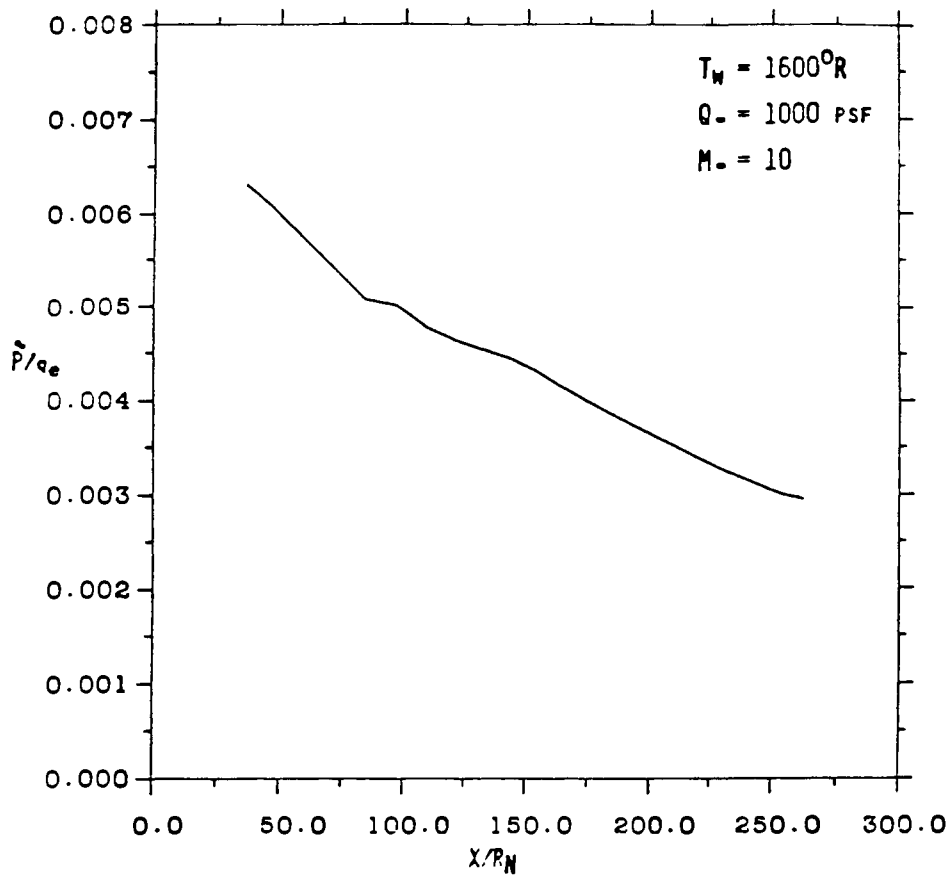


(A)

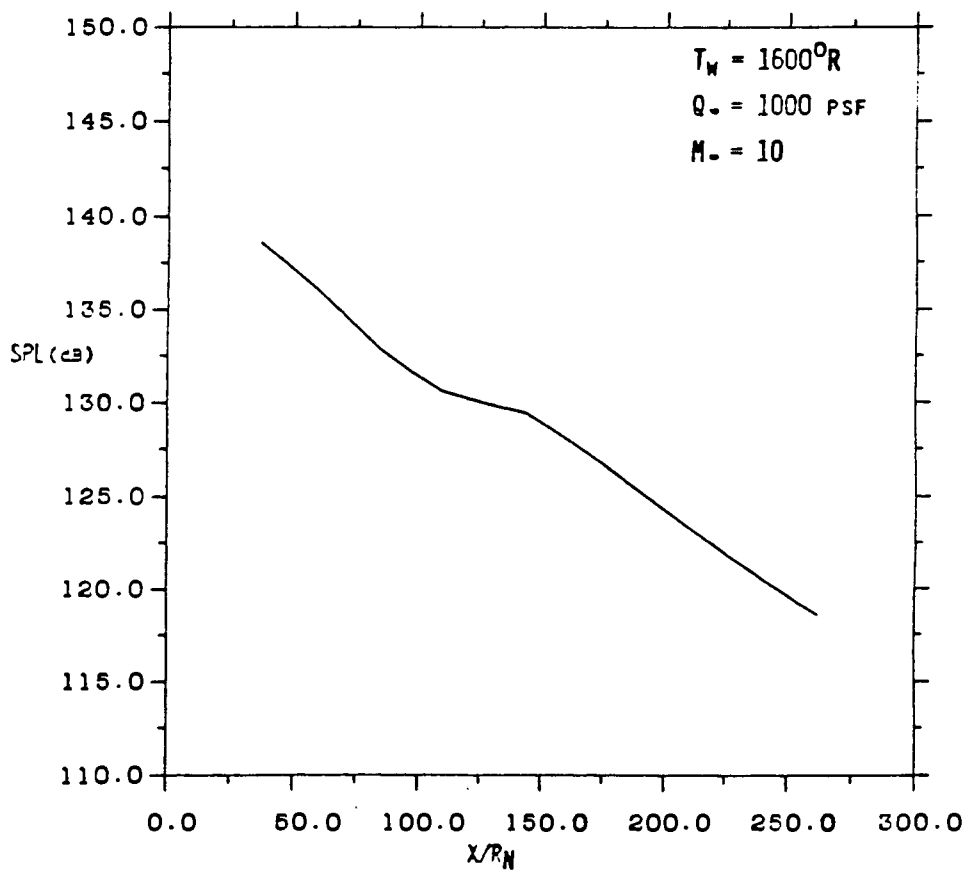


(B)

Figure A-21. Power Spectral Density Distribution Along Windward Surface of BWB (A) Normalized and (B) Power Spectra.

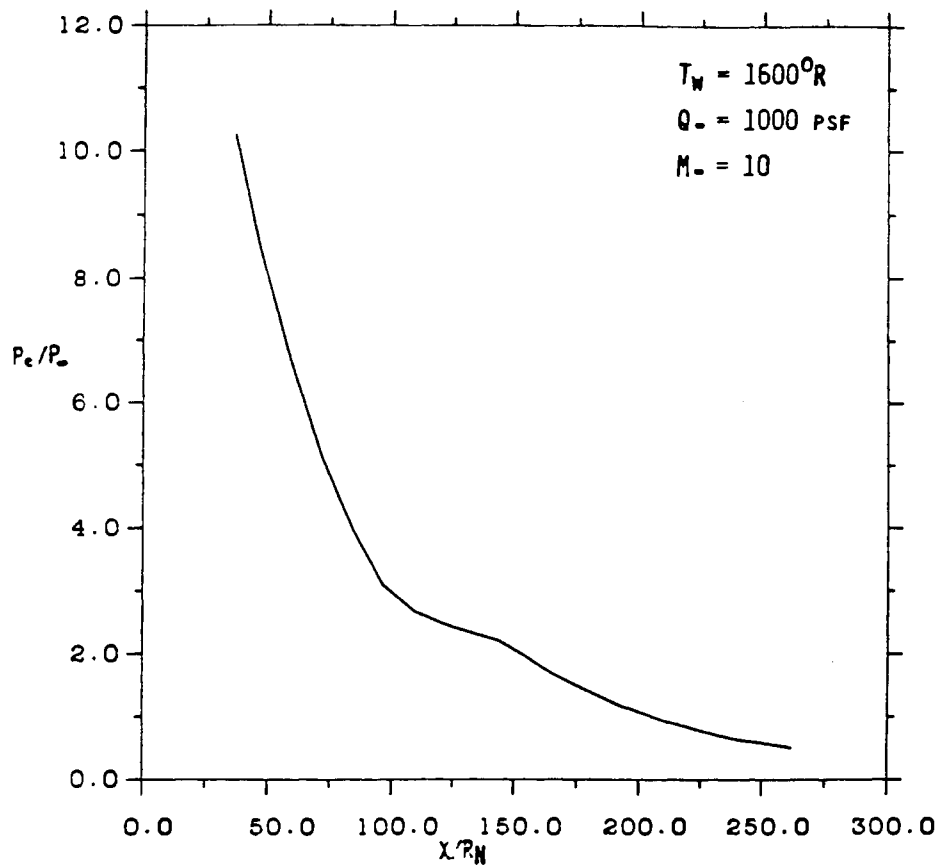


(A)

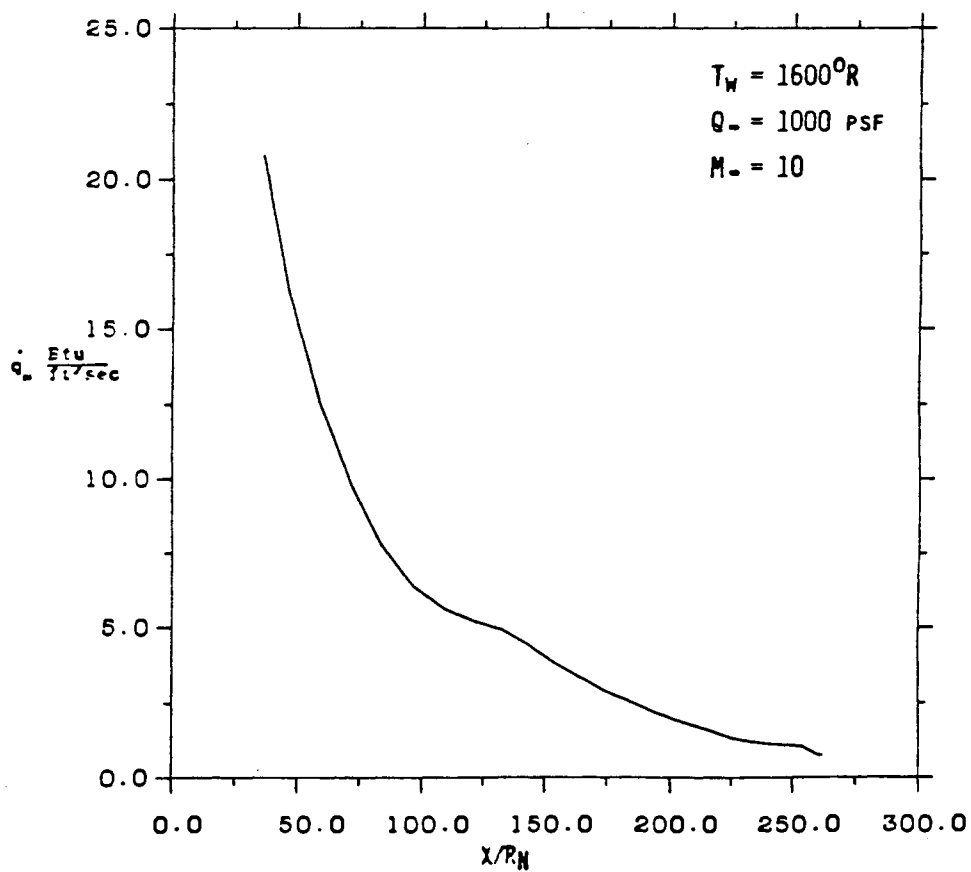


(B)

Figure A-22. RMS Pressure (A) and Sound Pressure Level (B) Distribution Along Leeward Surface of BMB.

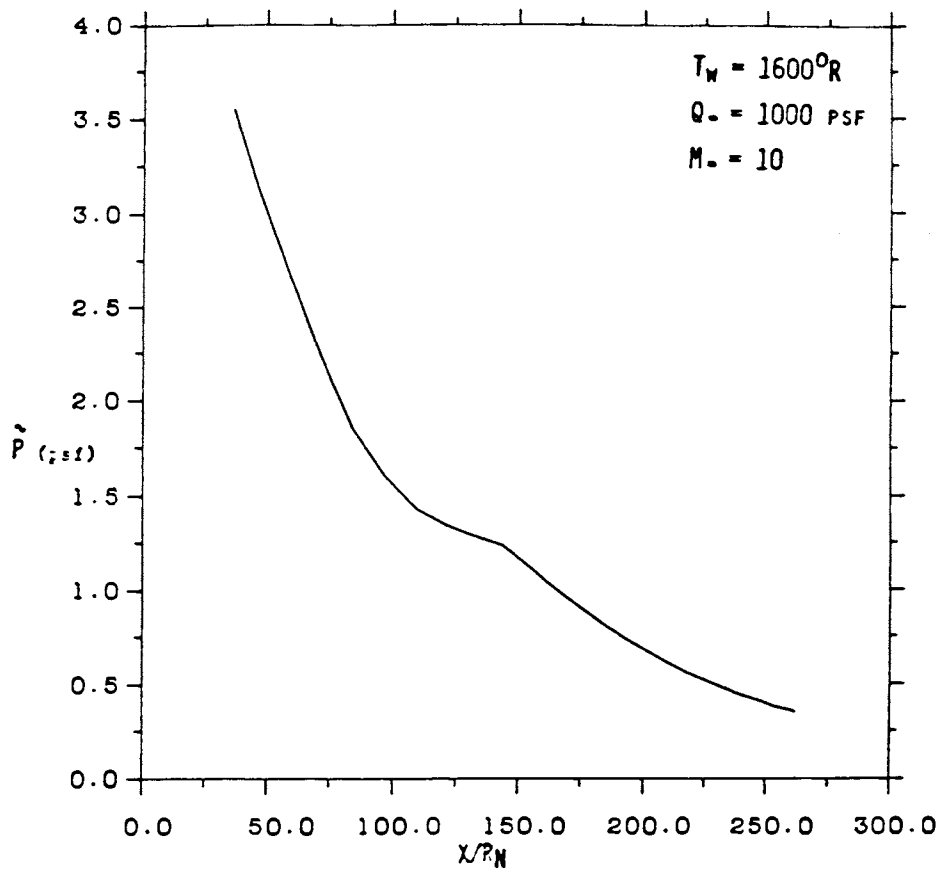


(A)

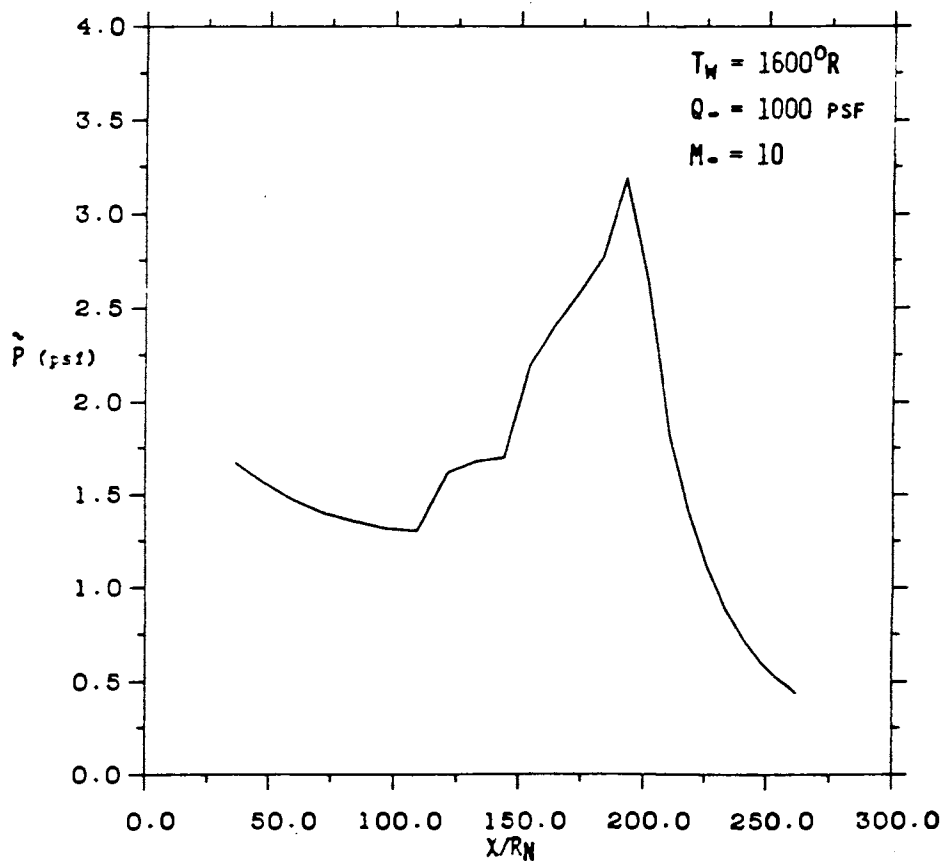


(B)

Figure A-23. Surface Pressure (A) and Heat Transfer (B) Distribution Along Leeward Surface of BWB.



(A)



(B)

Figure A-24. RMS Fluctuating Pressure Distribution Along Leeward (A) and Windward (B) Surfaces of BWB.

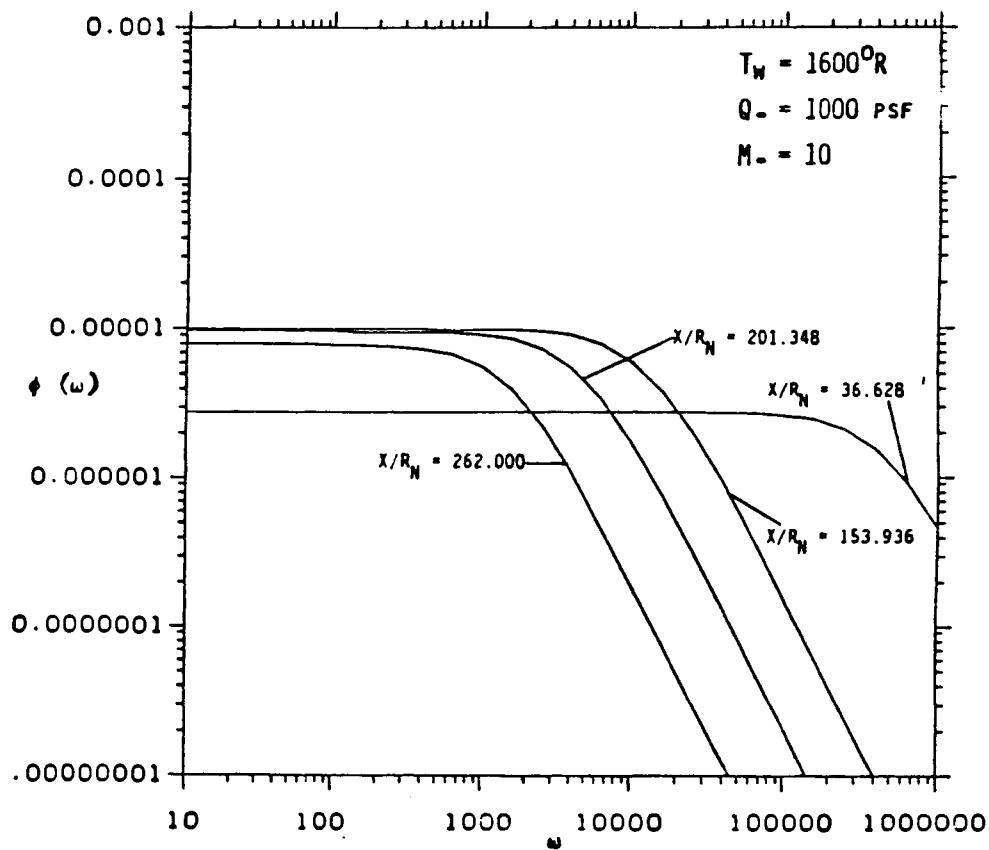
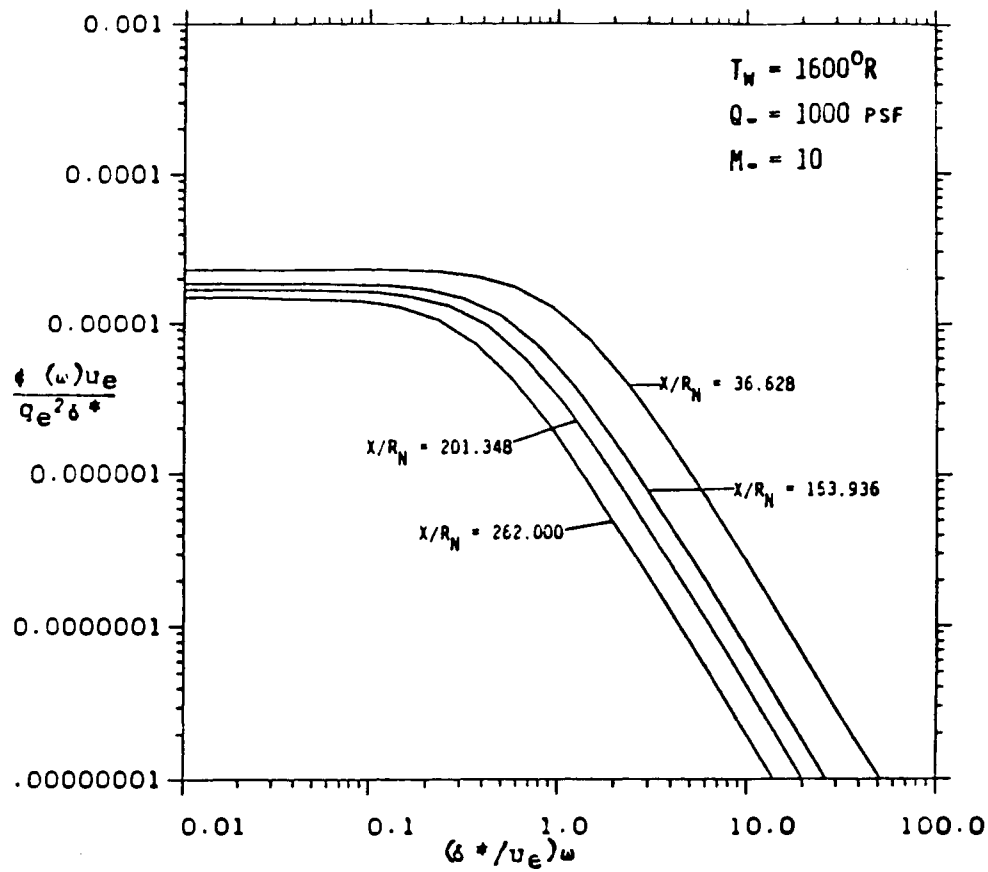


Figure A-25. Power Spectral Density Distribution Along Leeward Surface of BWB (A) Normalized and (B) Power Spectra.

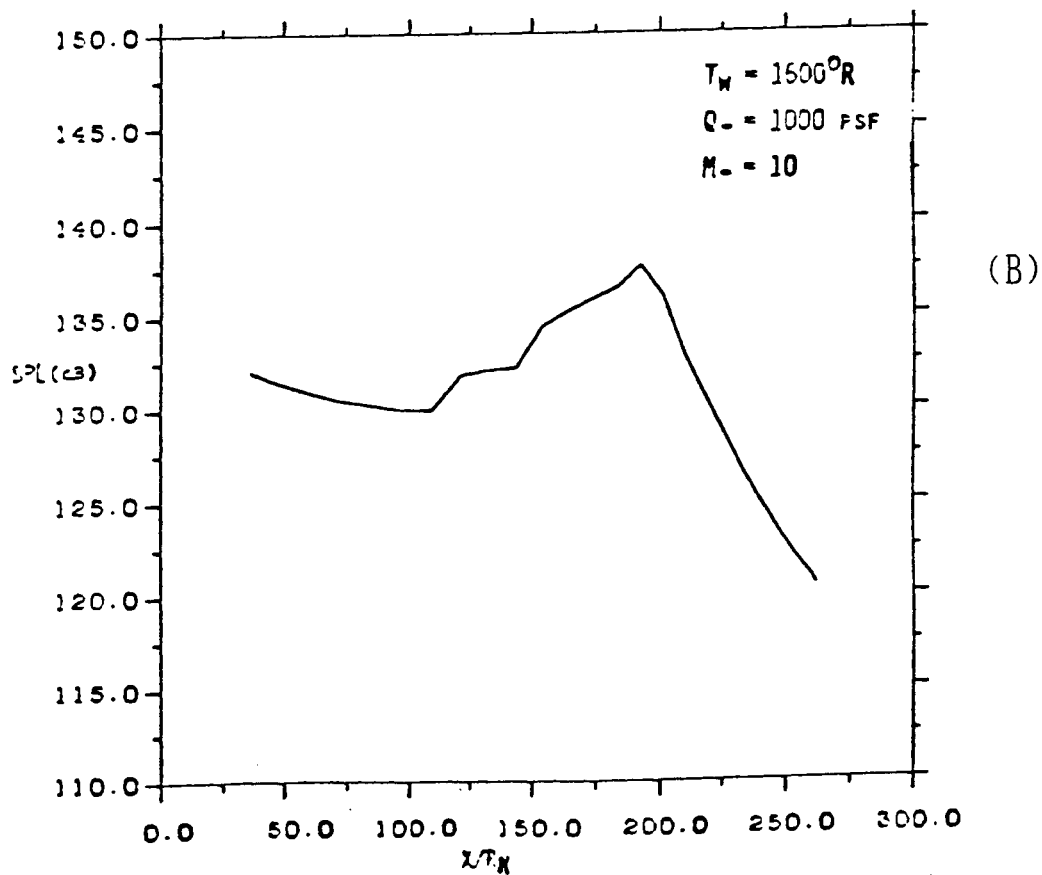
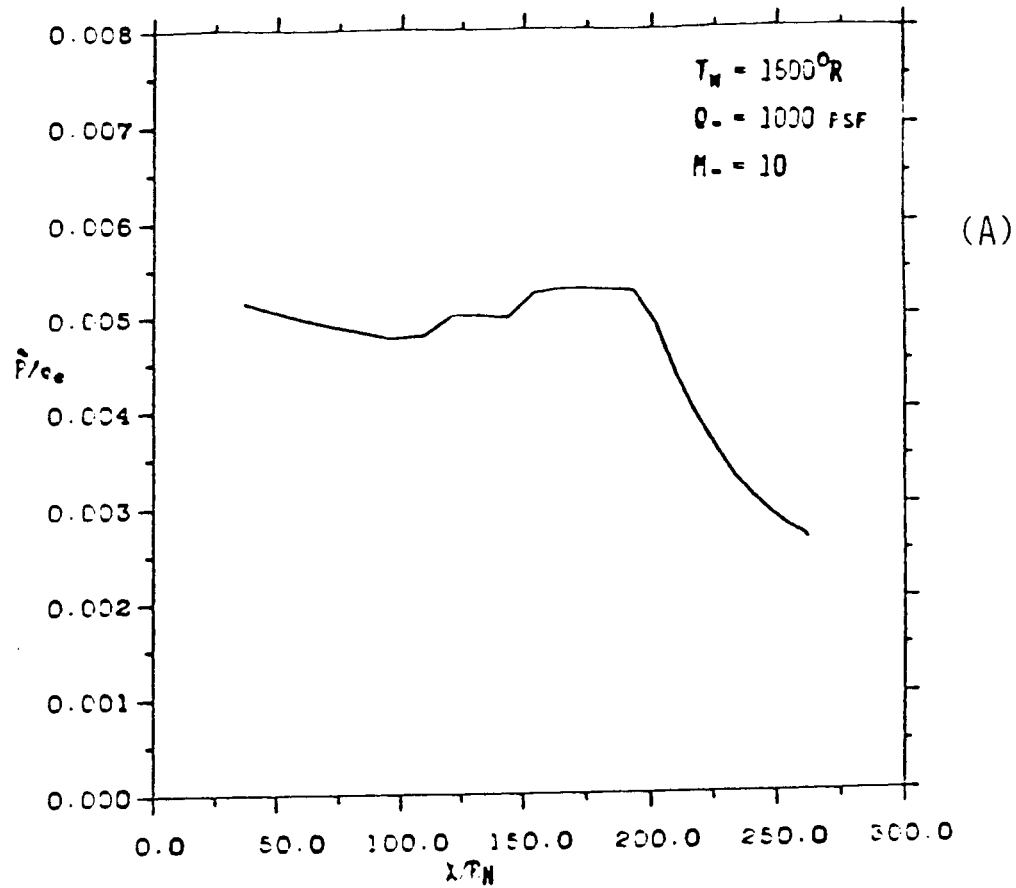
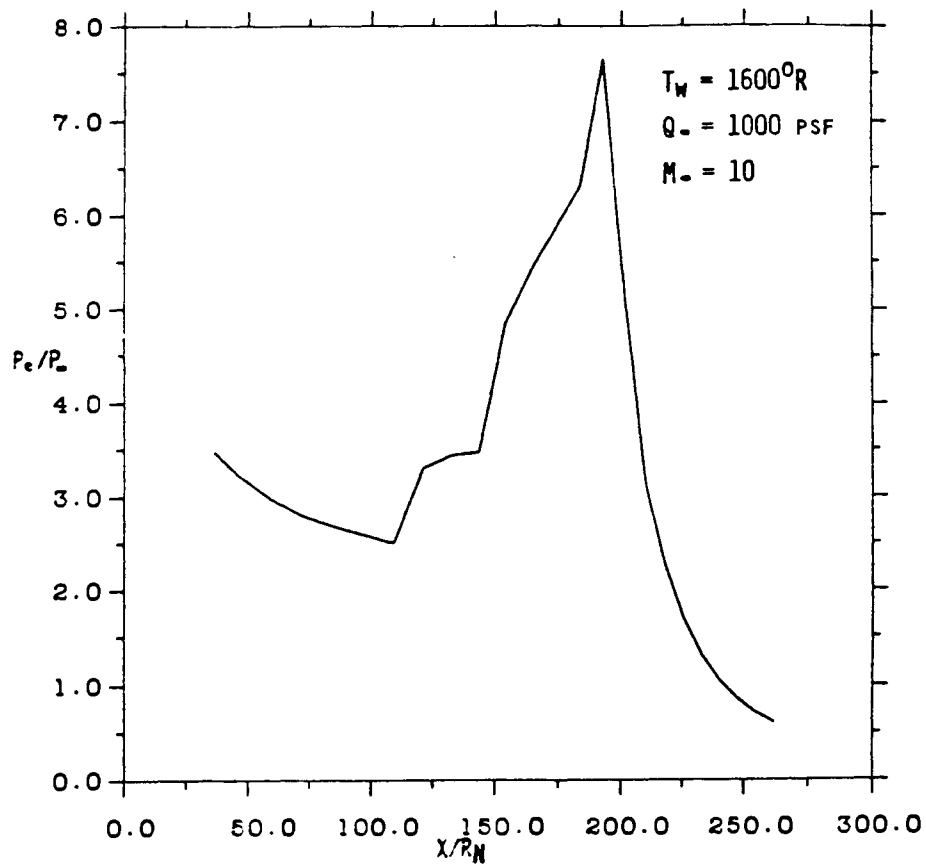
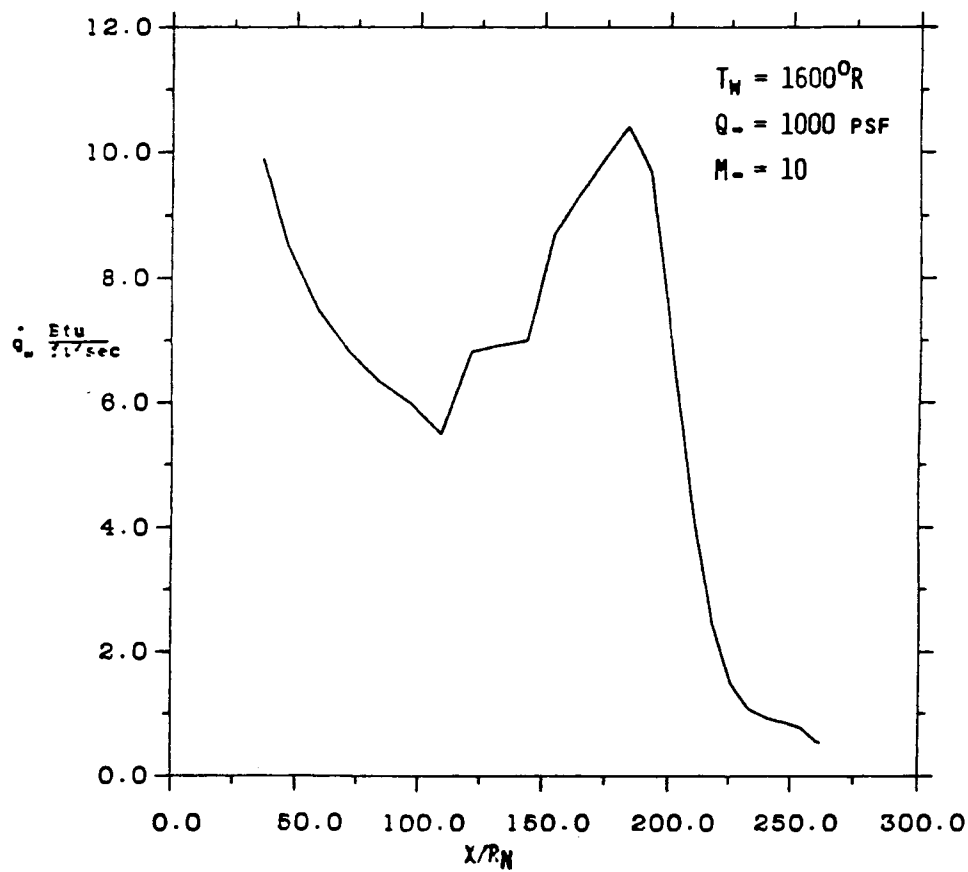


Figure A-26. RMS Pressure (A) and Sound Pressure Level (B) Distribution Along Windward Surface of BMB.

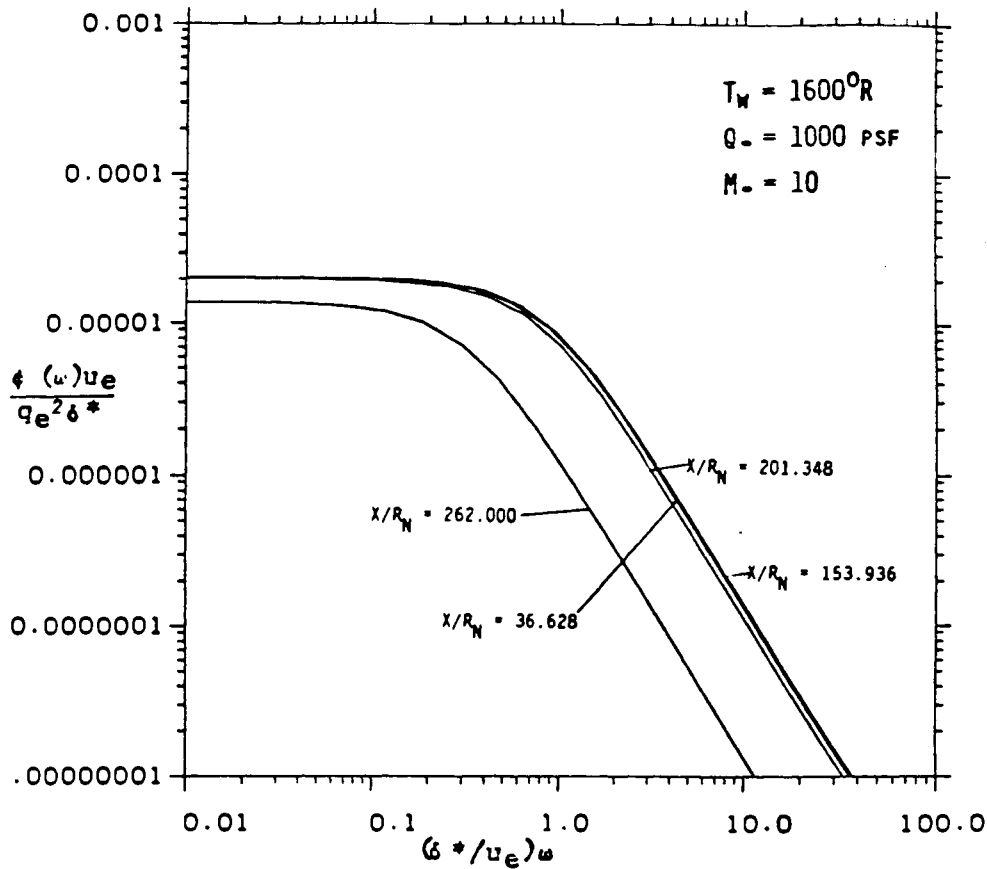


(A)

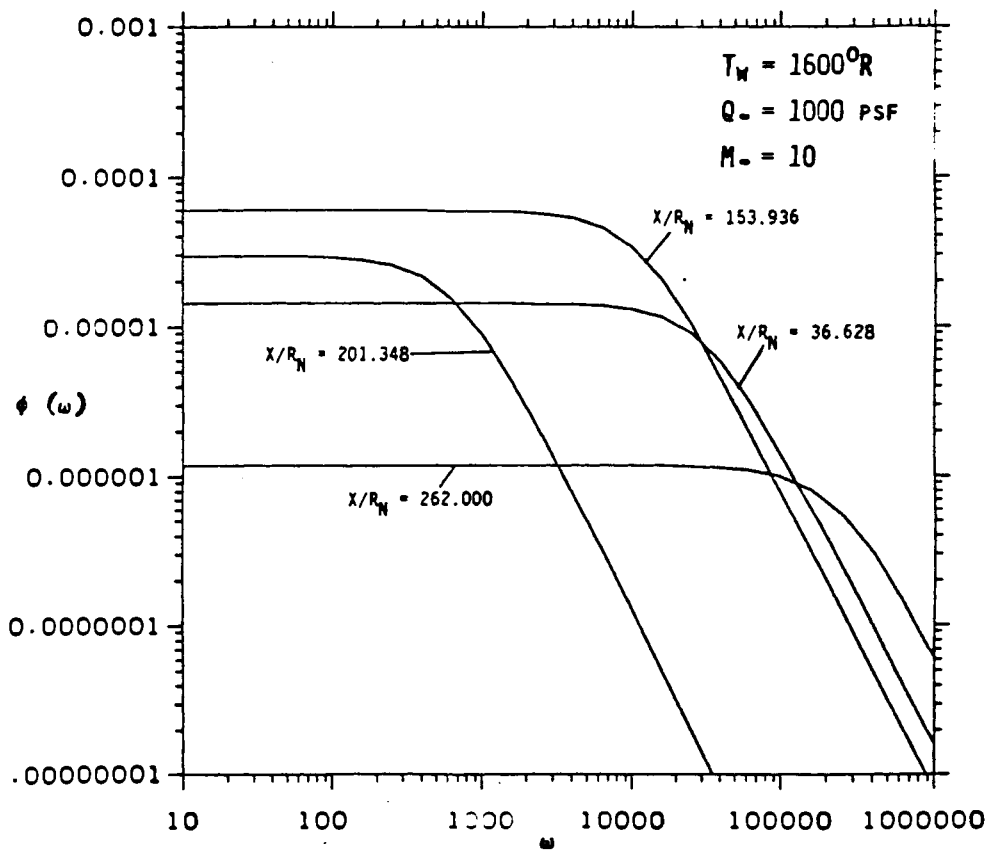


(B)

Figure A-27. Surface Pressure (A) and Heat Transfer (B) Distribution Along Windward Surface of BWB.

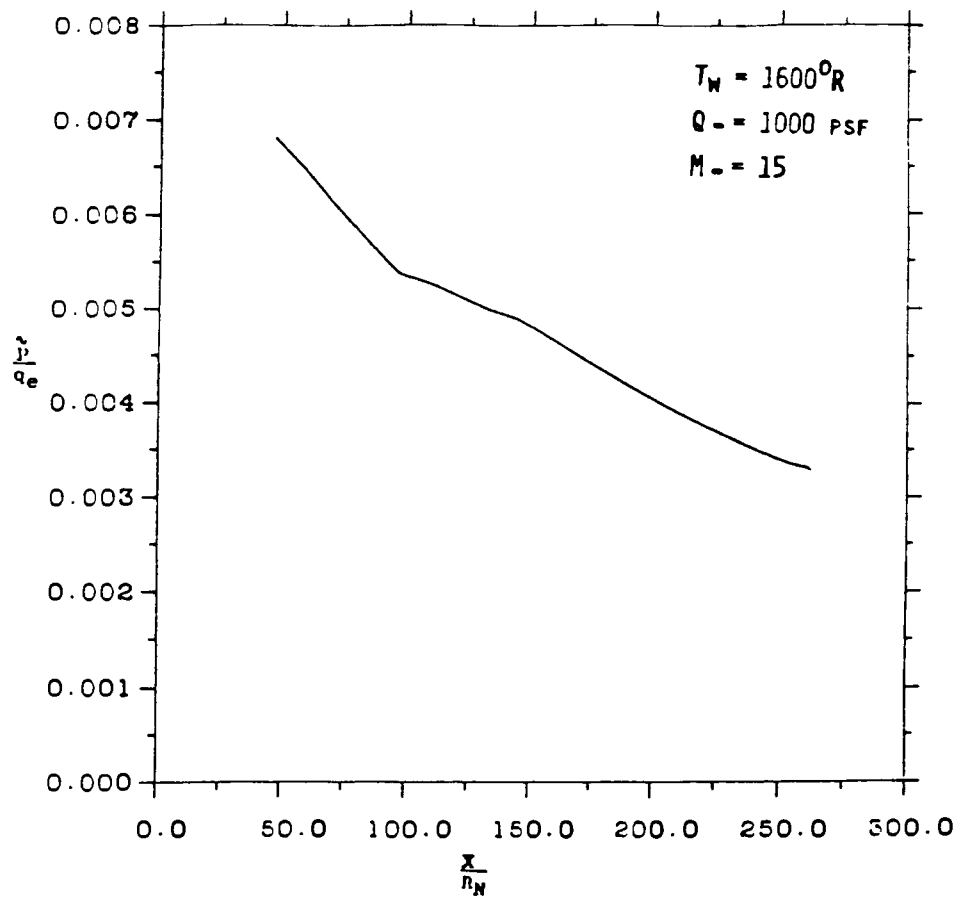


(A)

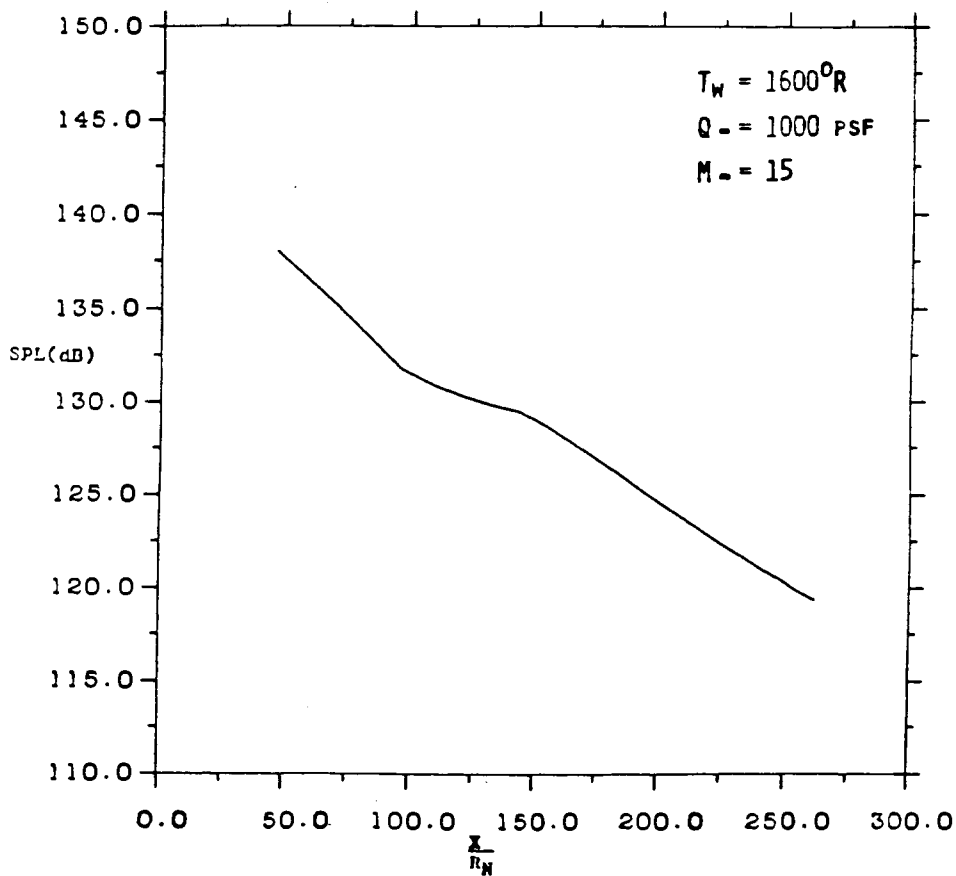


(B)

Figure A-28. Power Spectral Density Distribution Along Windward Surface of BWB (A) Normalized and (B) Power Spectra.

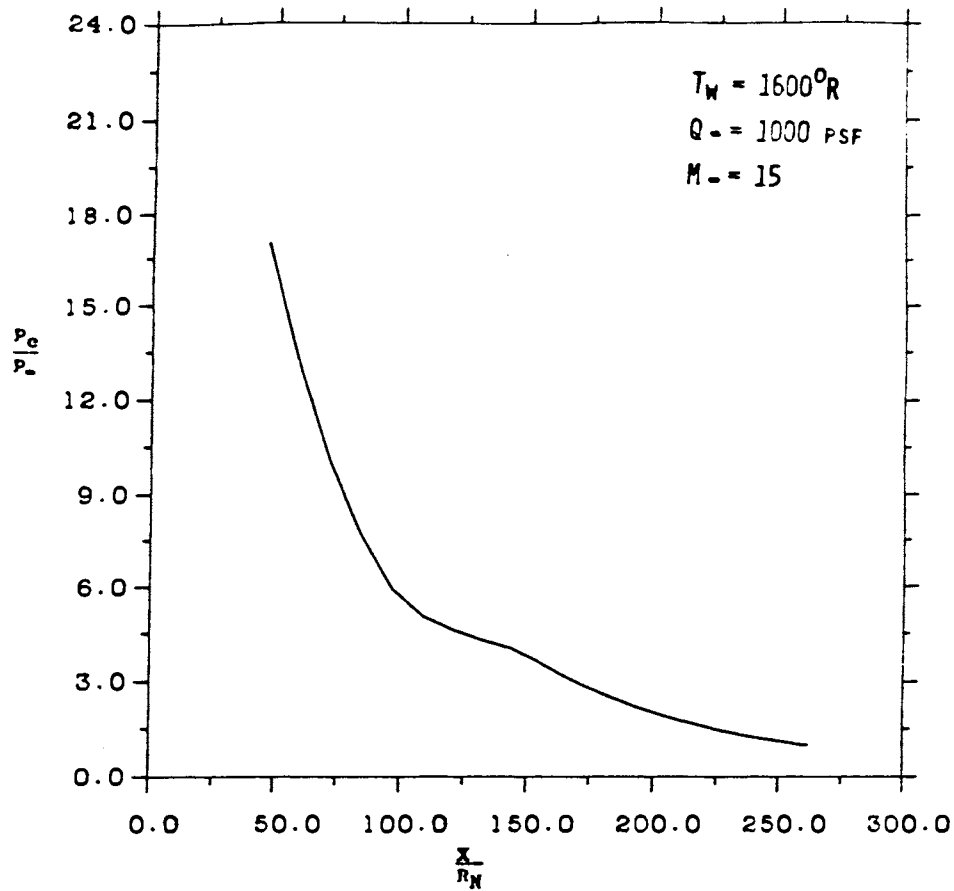


(A)

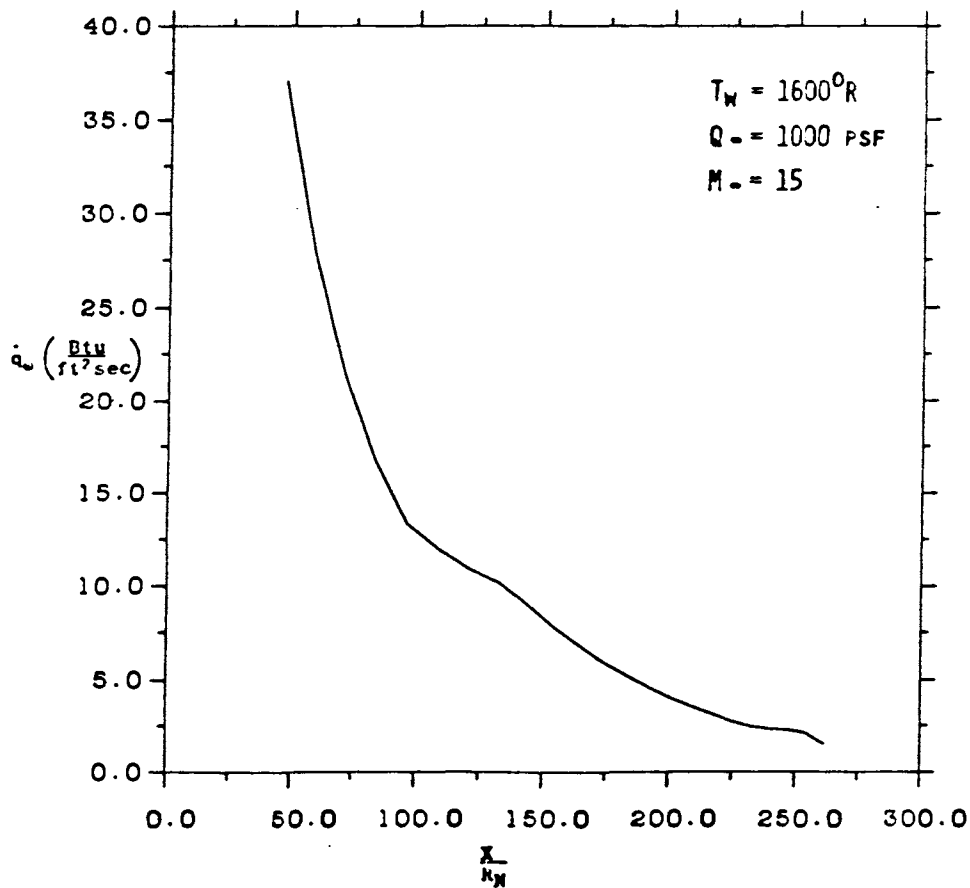


(B)

Figure A-29. RMS Pressure (A) and Sound Pressure Level (B) Distribution Along Leeward Surface of BWB.

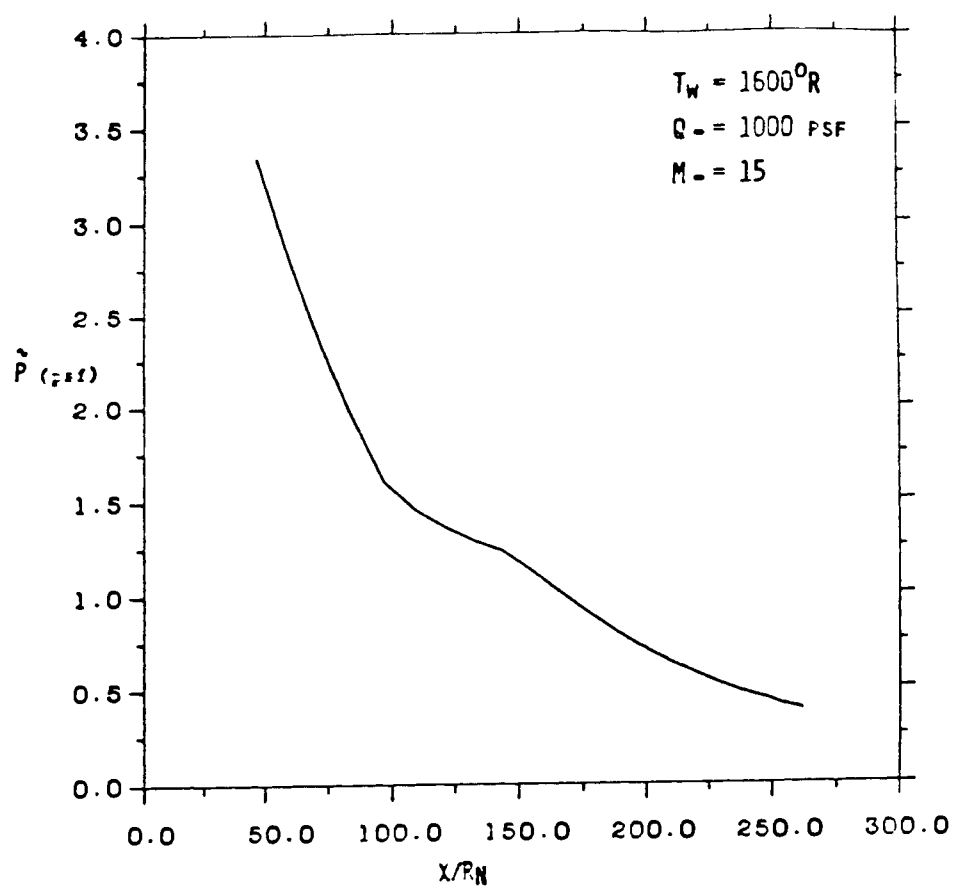


(A)

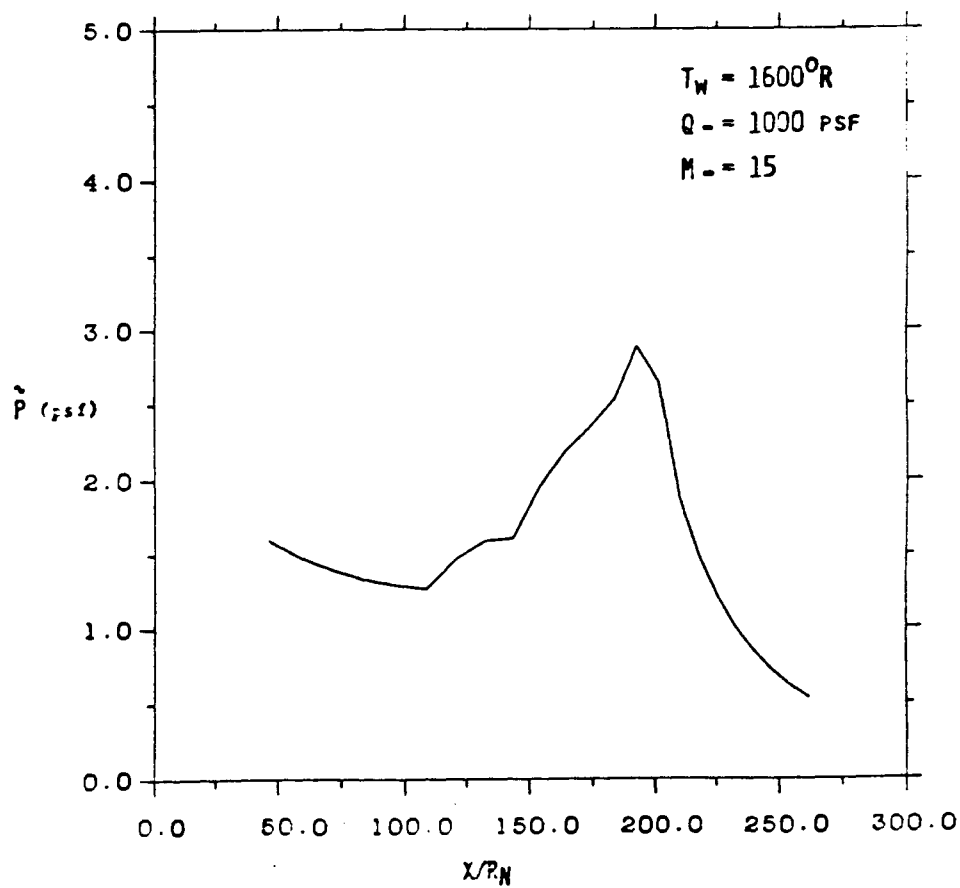


(B)

Figure A-30. Surface Pressure (A) and Heat Transfer (B) Distribution Along Leeward Surface of BWB.



(A)



(B)

Figure A-31. RMS Fluctuating Pressure Distribution Along Leeward (A) and Windward (B) Surfaces of BWB.

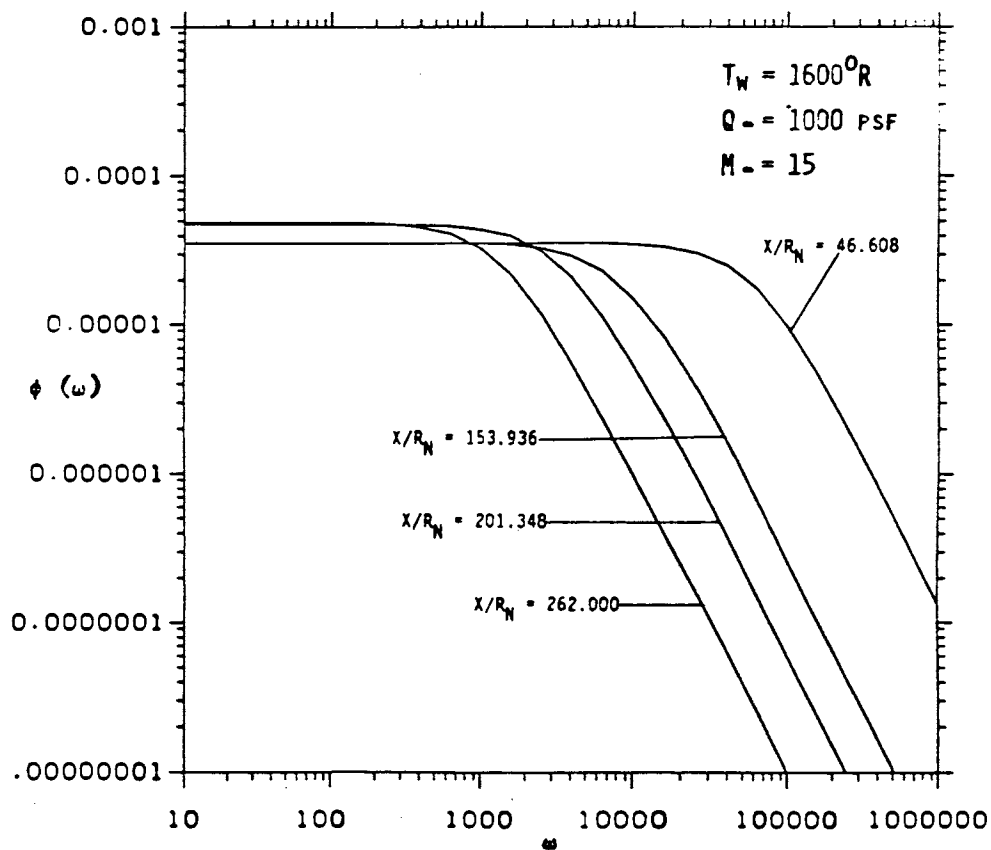
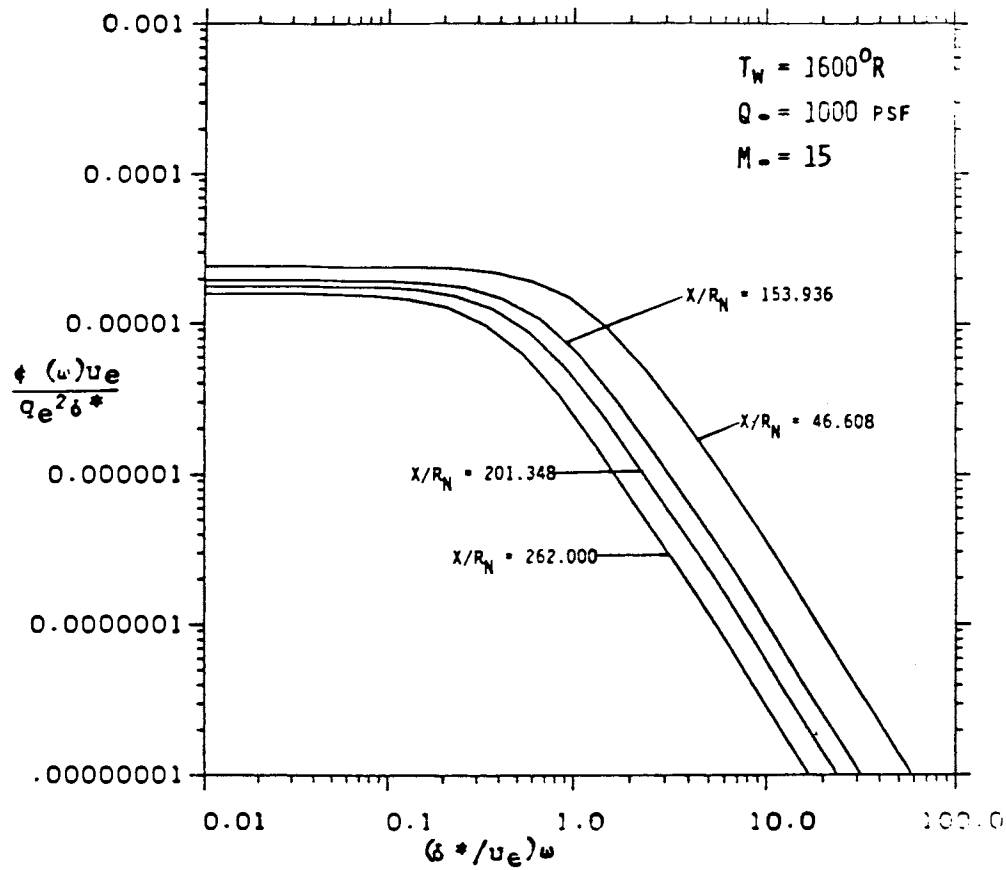
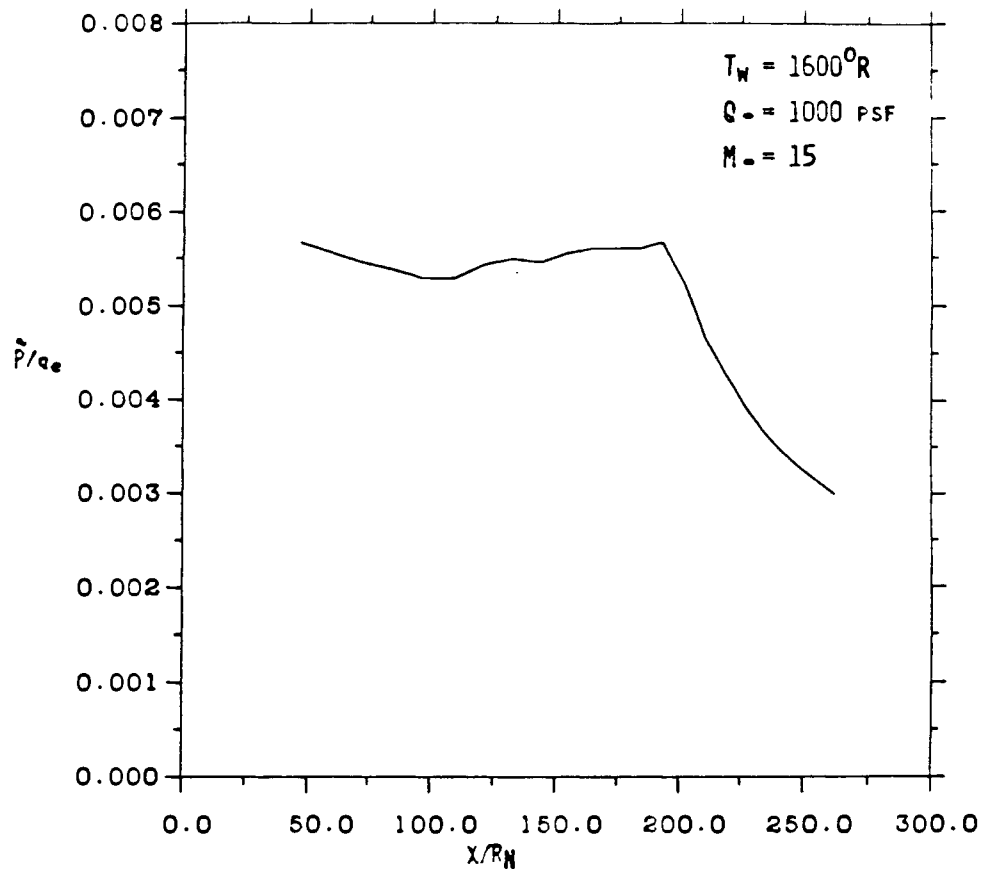
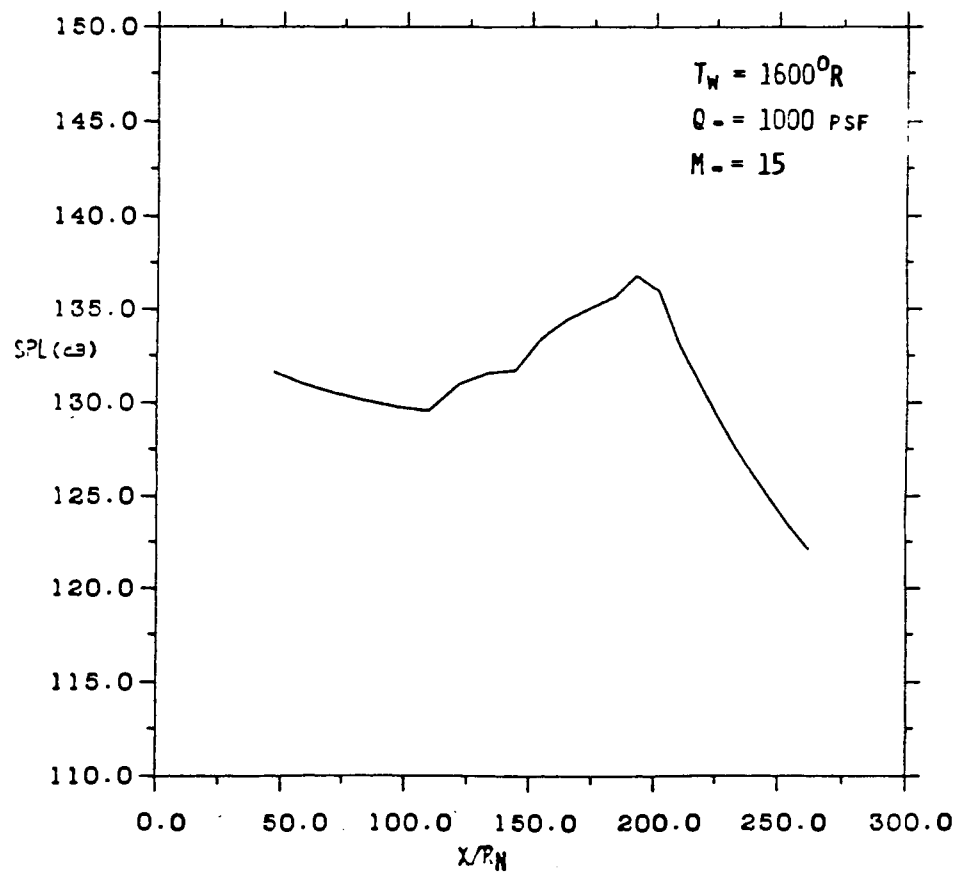


Figure A-32. Power Spectral Density Distribution Along Leeward Surface of BWB (A) Normalized and (B) Power Spectra.

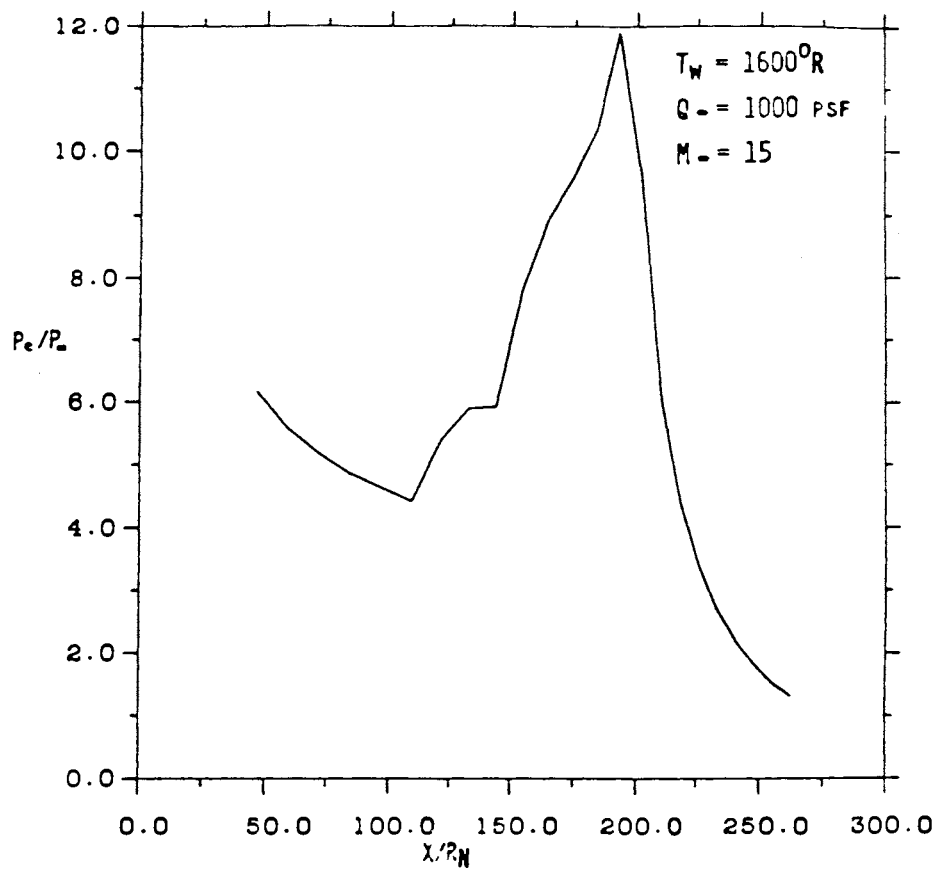


(A)

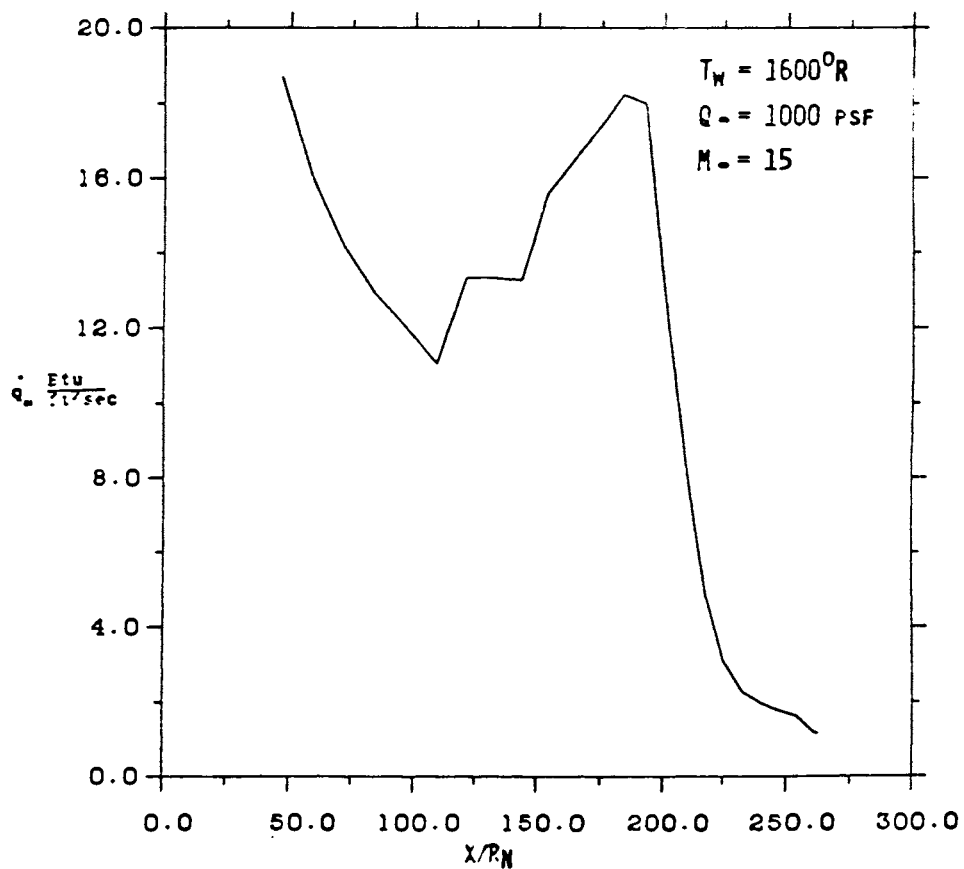


(B)

Figure A-33. RMS Pressure (A) and Sound Pressure Level (B) Distribution Along Windward Surface of BWB.



(A)



(B)

Figure A-34. Surface Pressure (A) and Heat Transfer (B) Distribution Along Windward Surface of BWB.

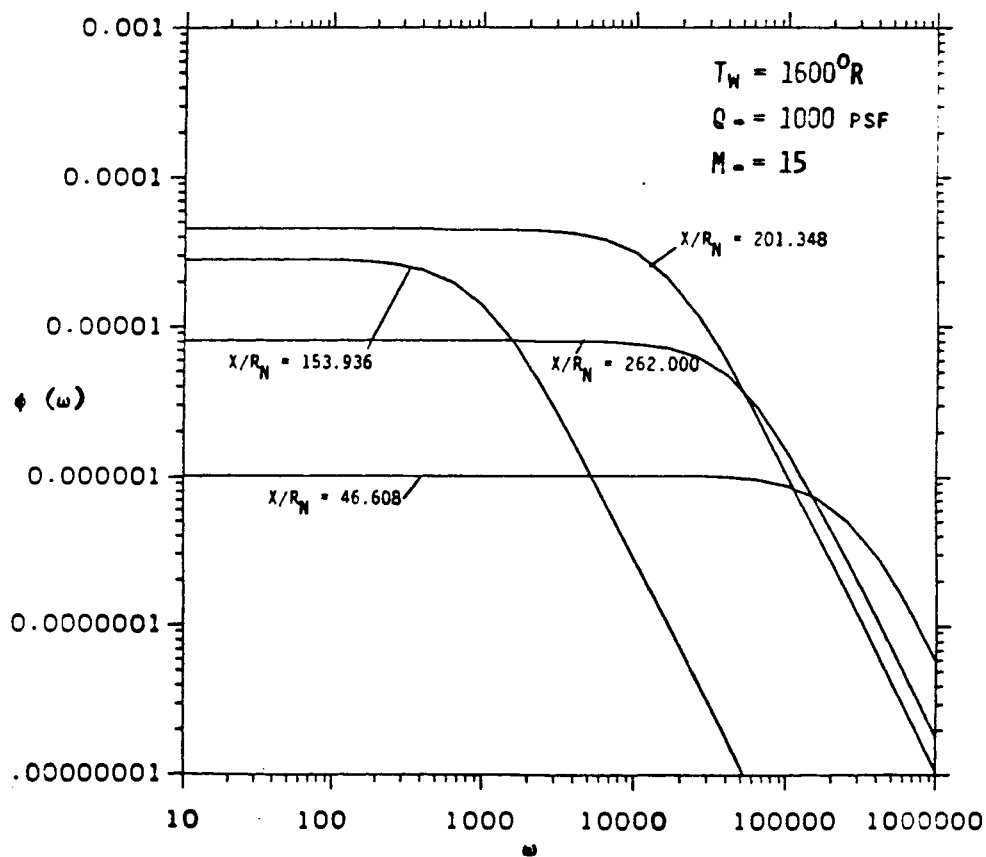
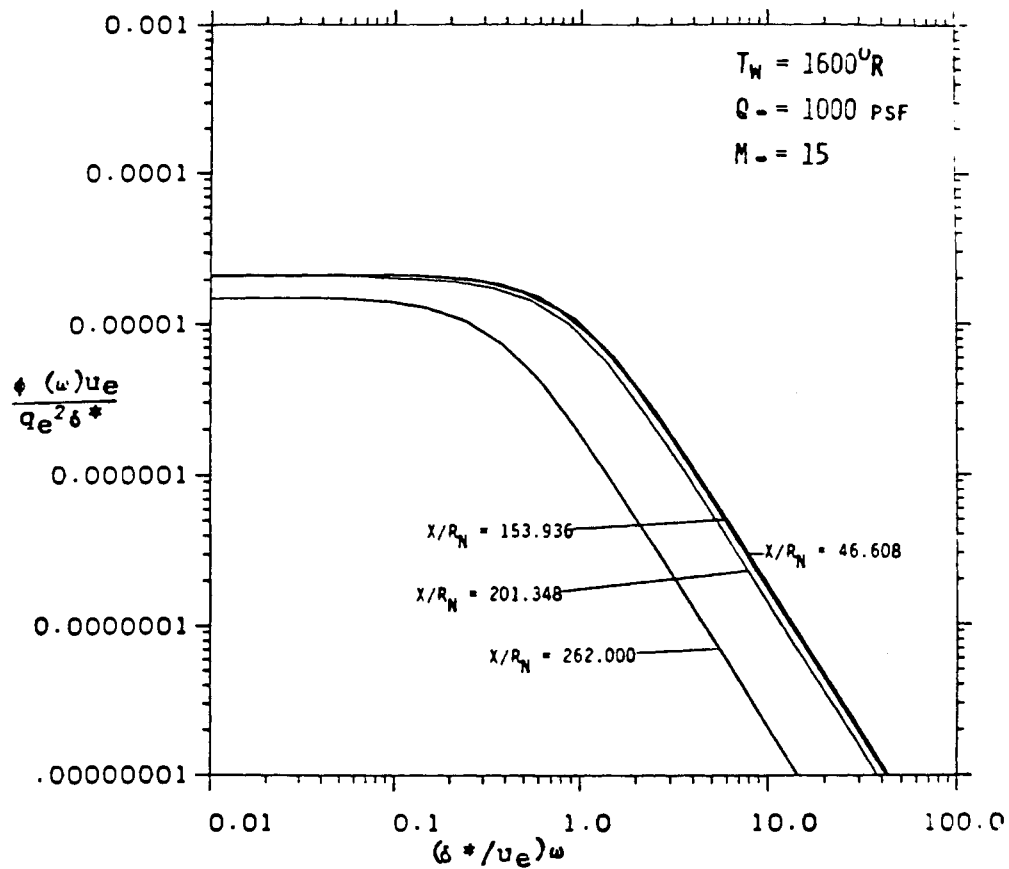
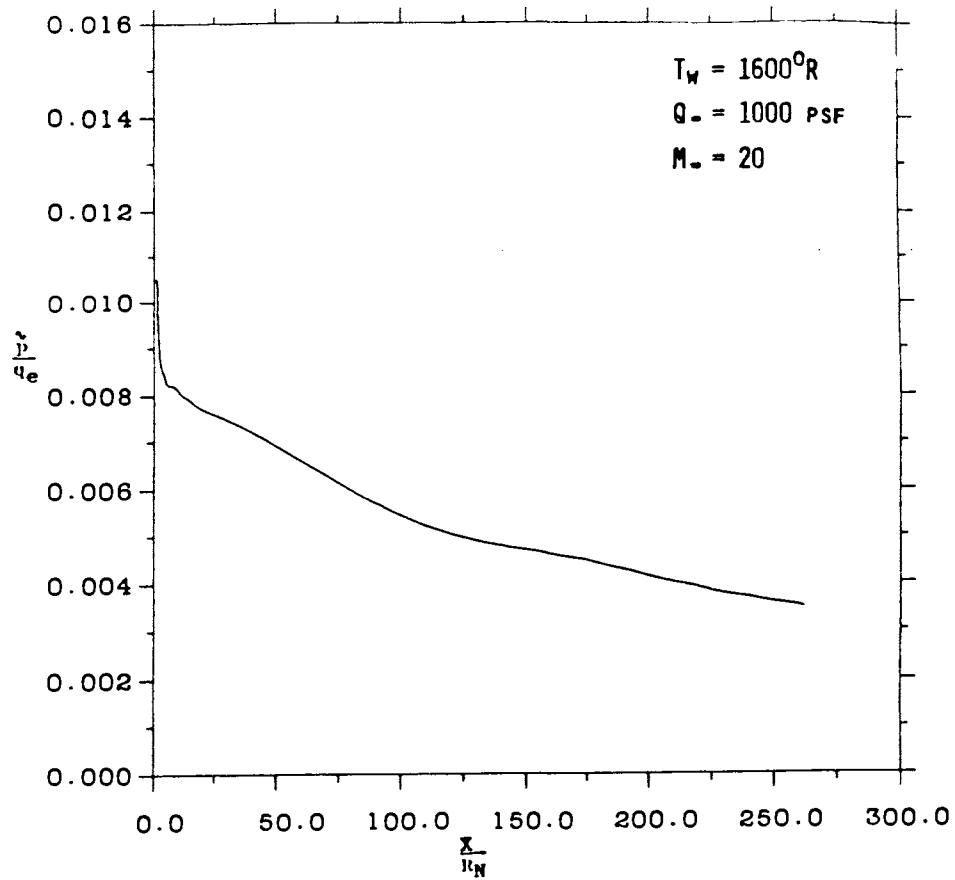
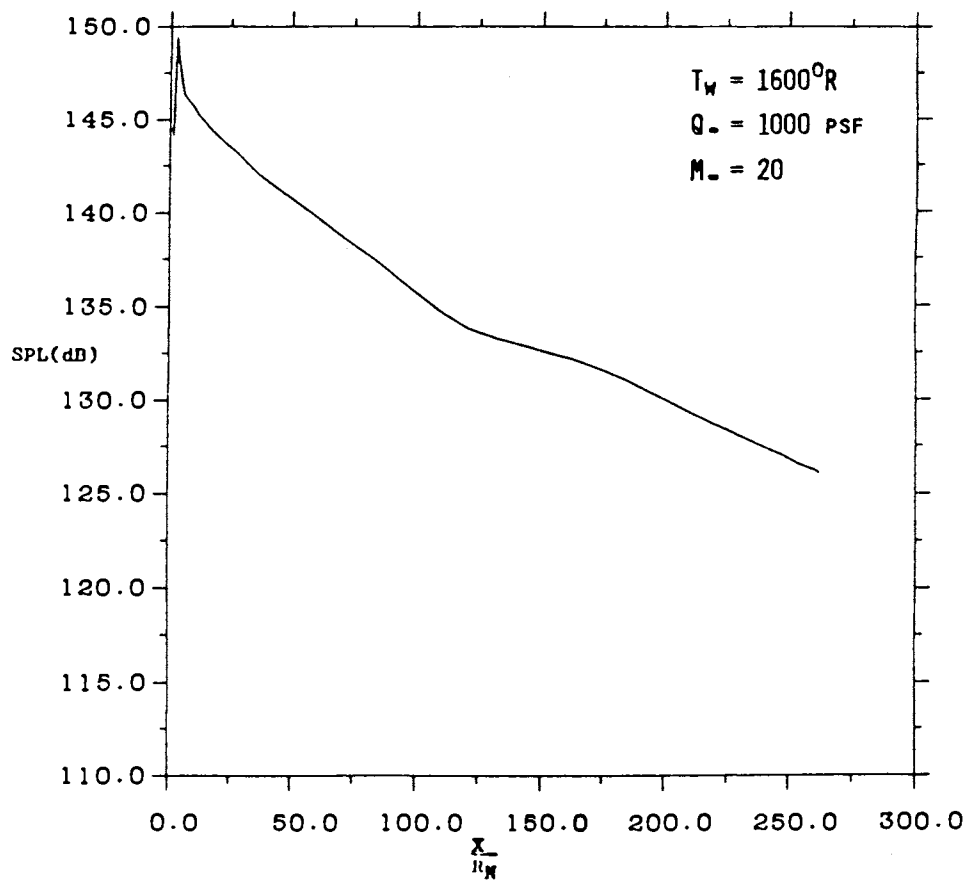


Figure A-35. Power Spectral Density Distribution Along Windward Surface of BWB (A) Normalized and (B) Power Spectra.

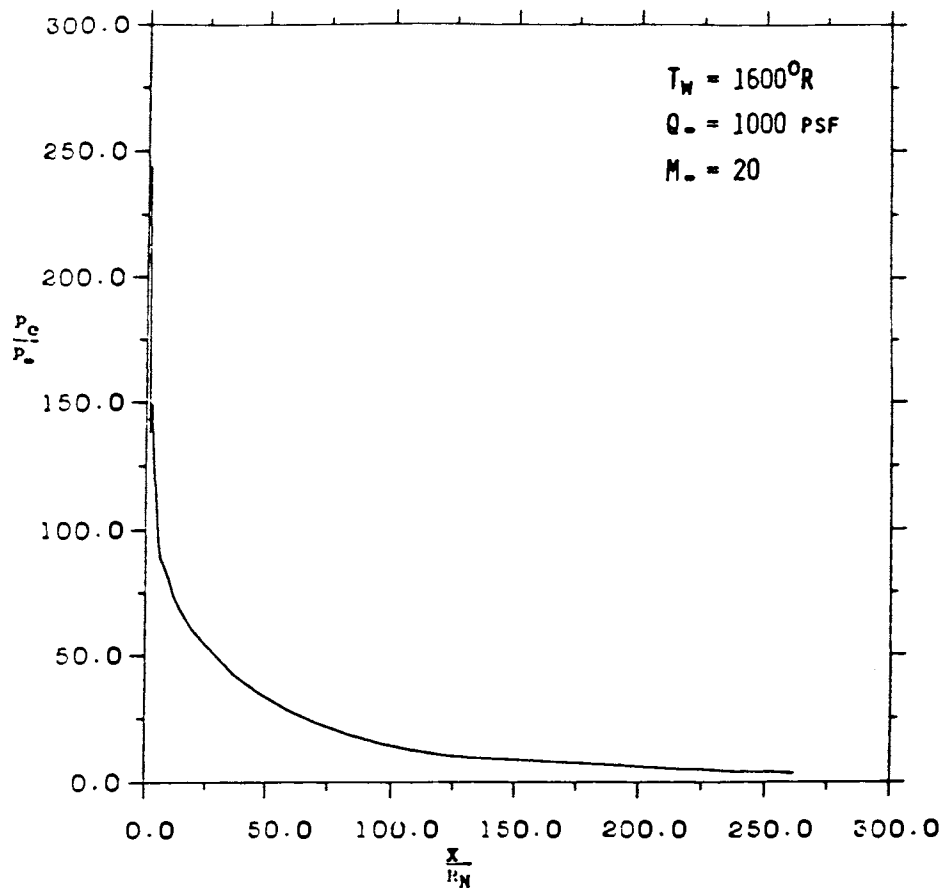


(A)

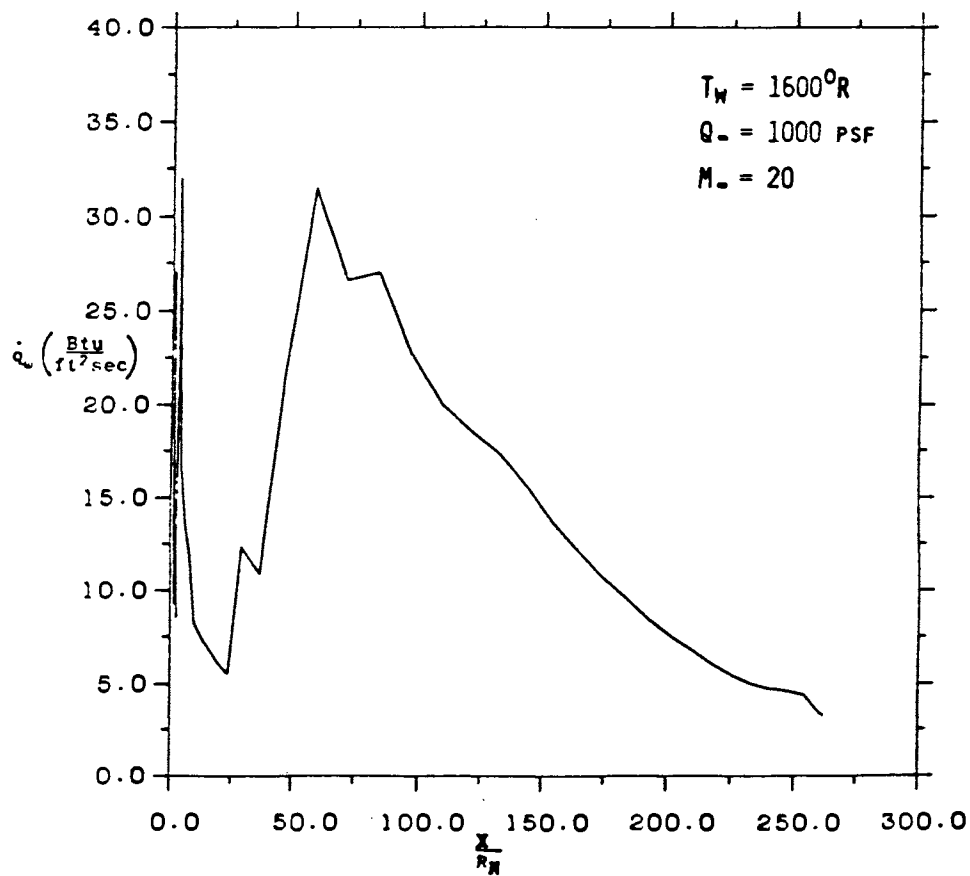


(B)

Figure A-36. RMS Pressure (A) and Sound Pressure Level (B) Distribution Along Leeward Surface of BWB.

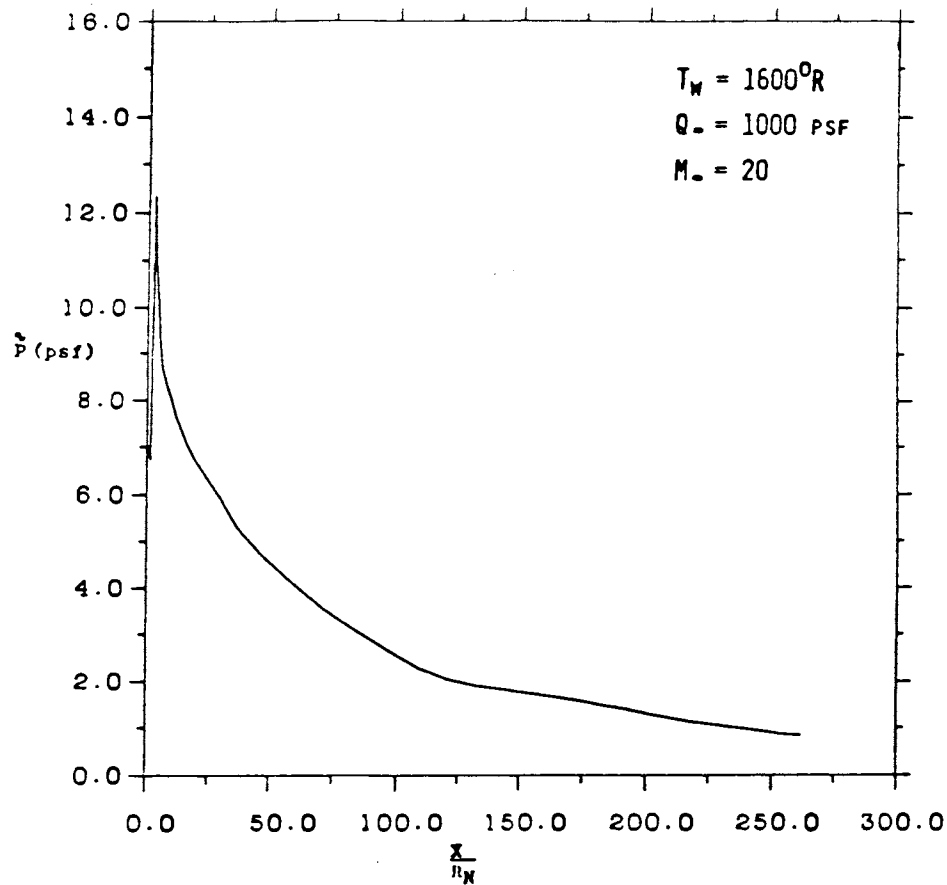


(A)

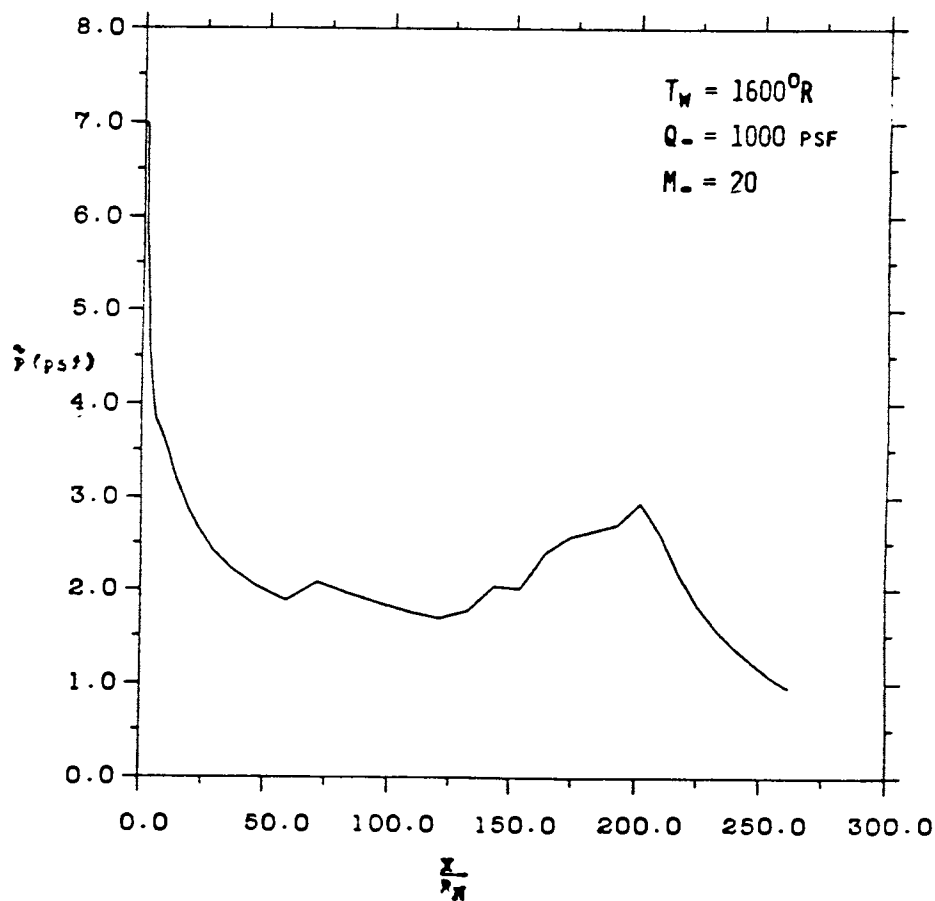


(B)

Figure A-37. Surface Pressure (A) and Heat Transfer (B) Distribution Along Leeward Surface of BWB.



(A)



(B)

Figure A-38. RMS Fluctuating Pressure Distribution Along Leeward (A) and Windward (B) Surfaces of BWB.

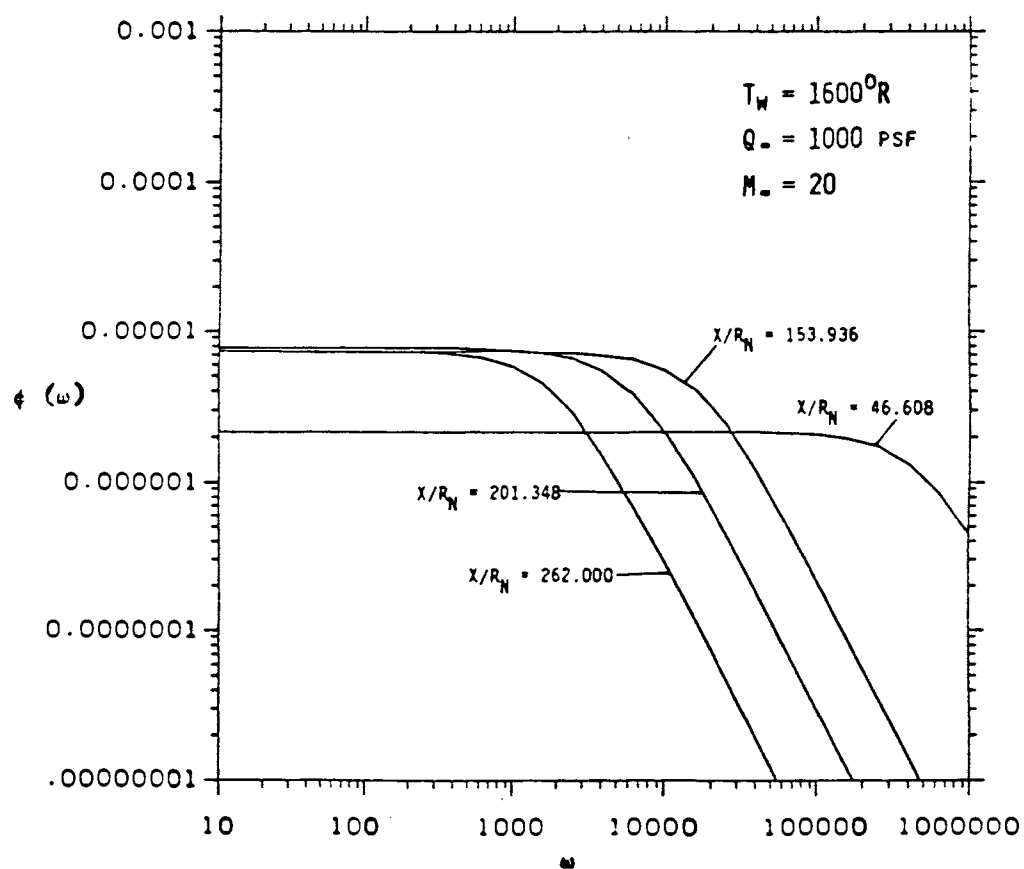
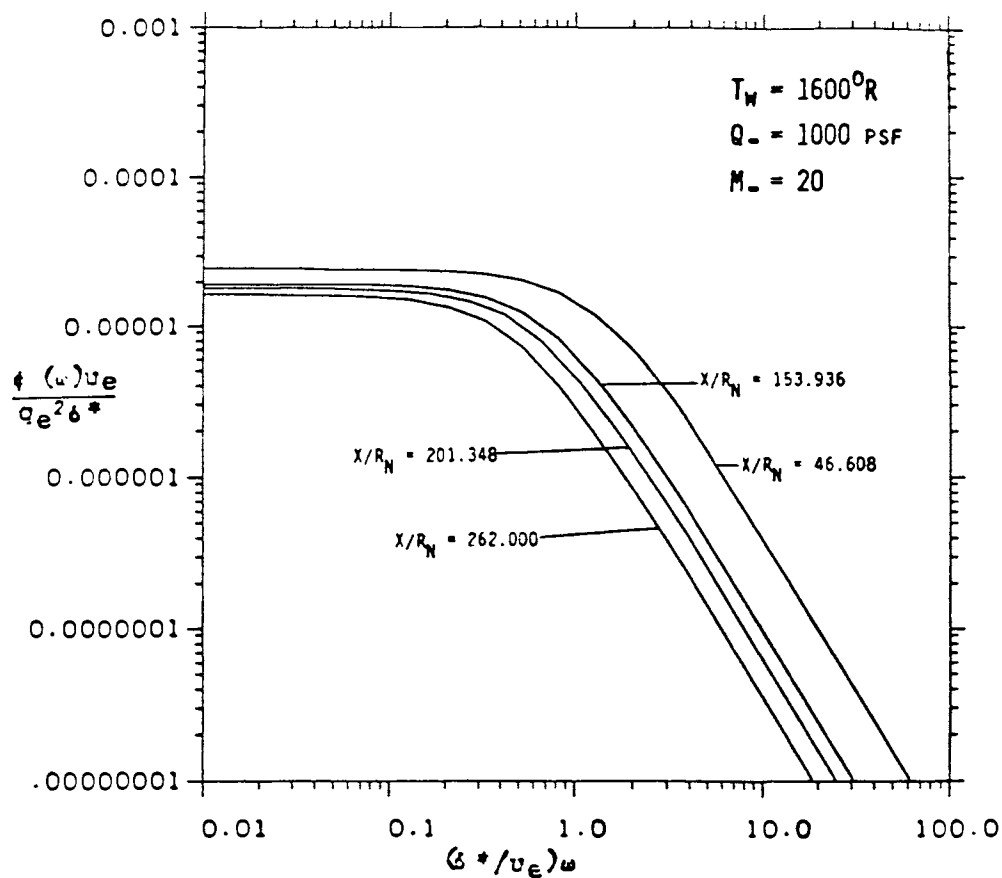
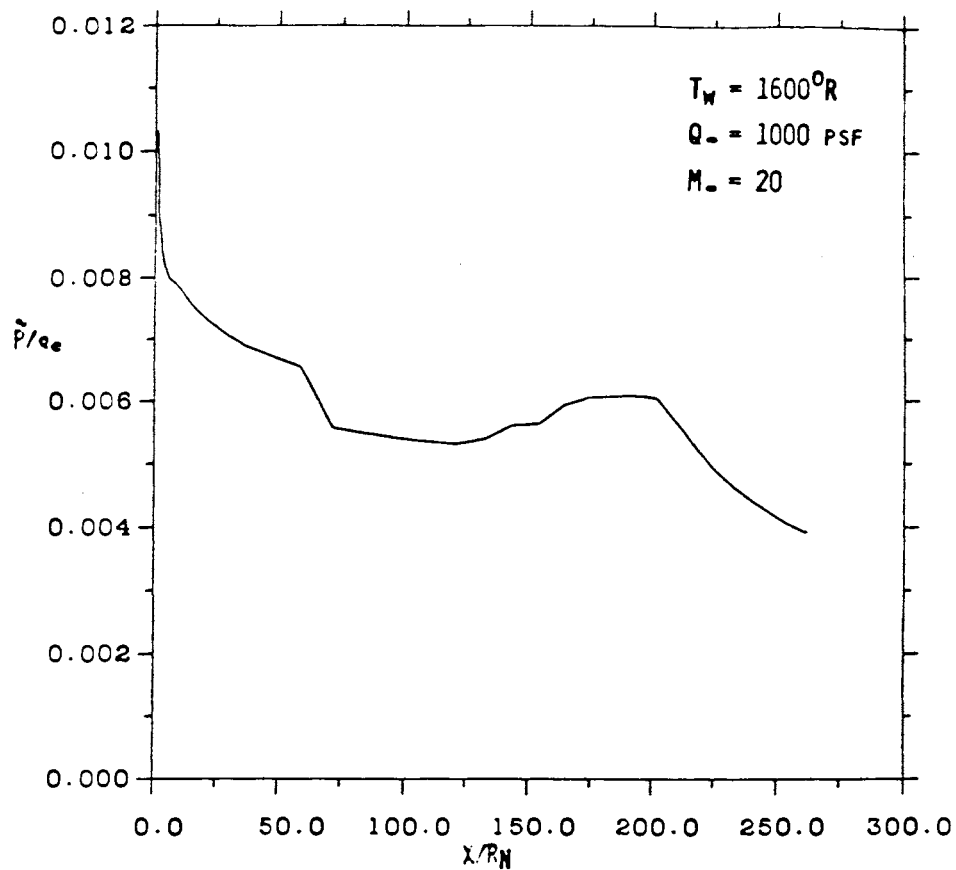
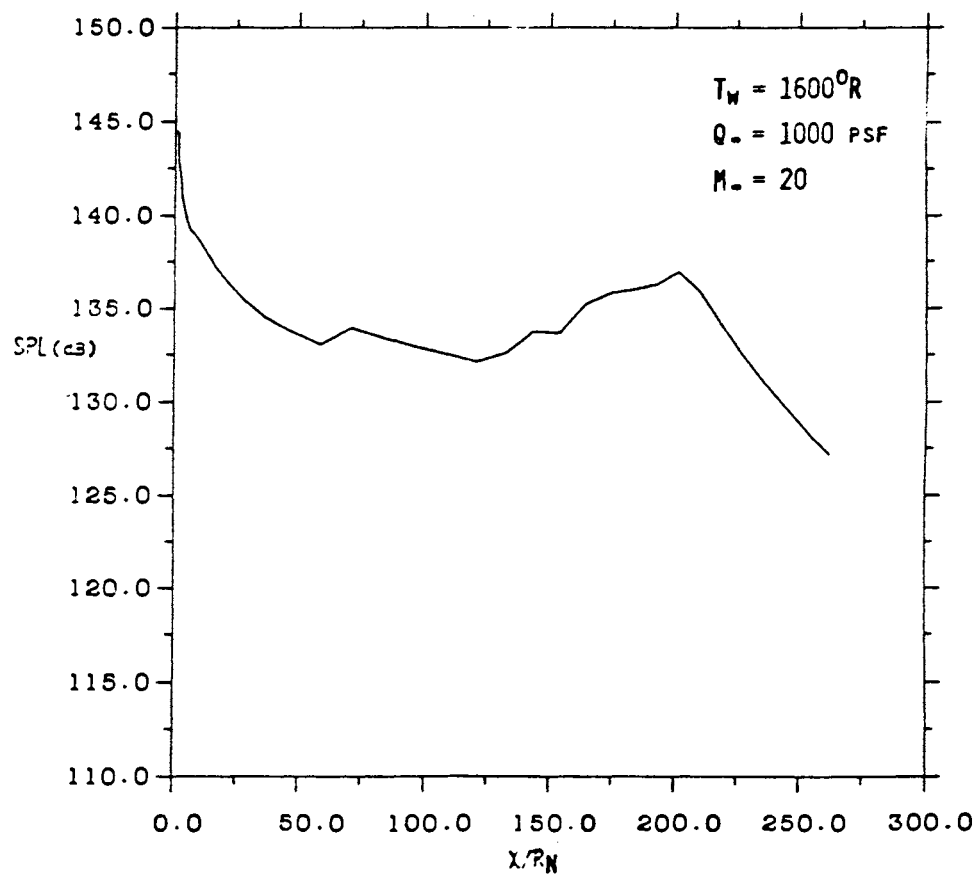


Figure A-39. Power Spectral Density Distribution Along Leeward Surface of BWB (A) Normalized and (B) Power Spectra.



(A)



(B)

Figure A-40. RMS Pressure (A) and Sound Pressure Level (B) Distribution Along Windward Surface of BWB.

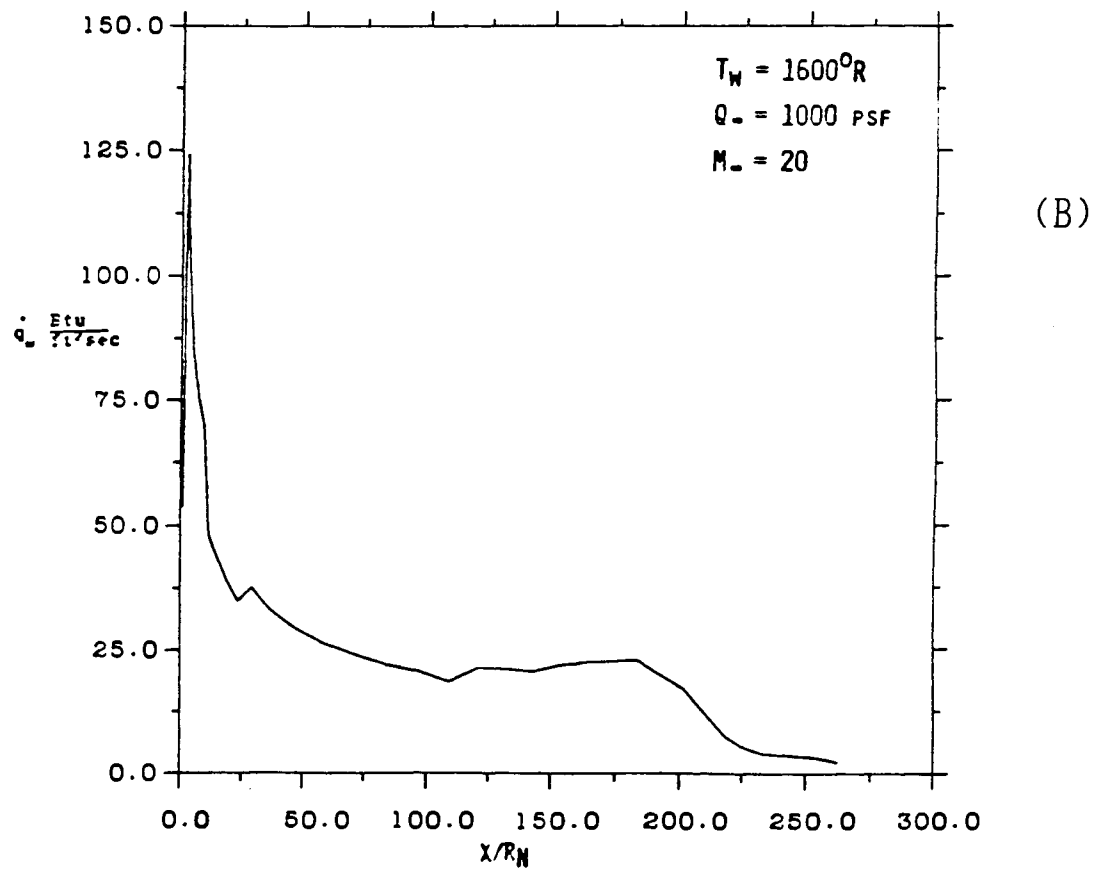
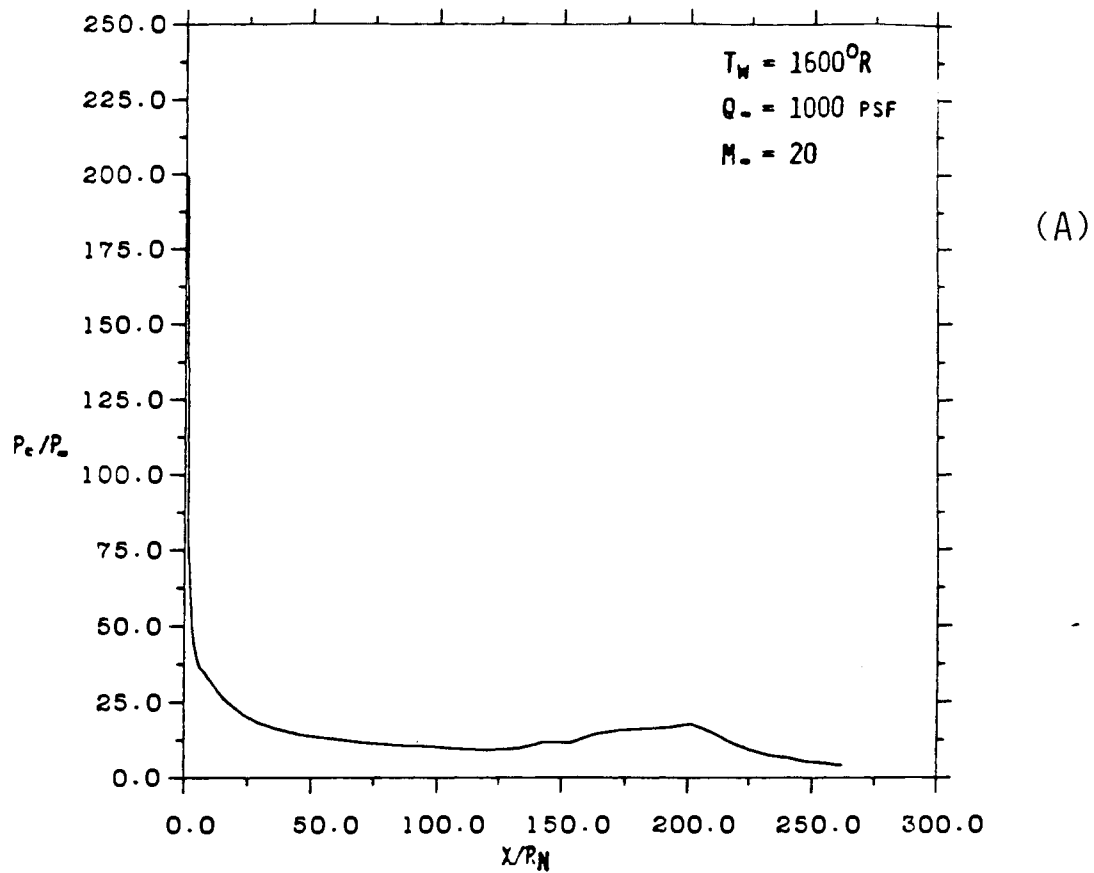
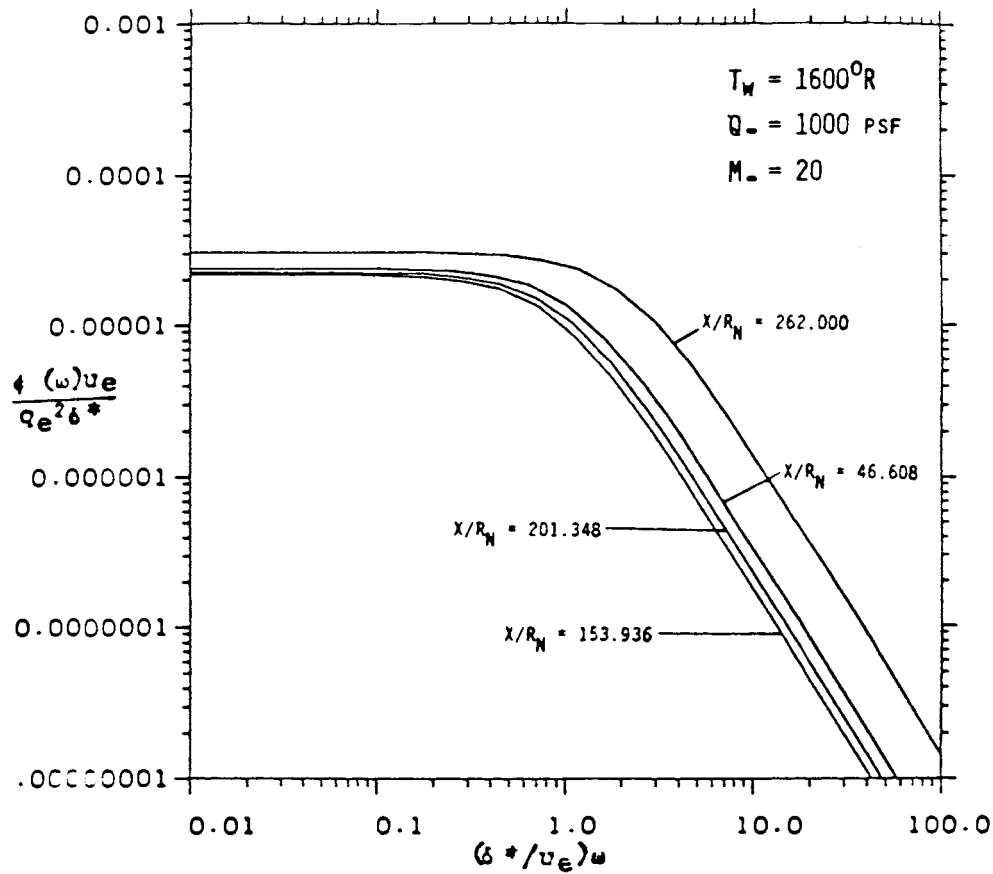
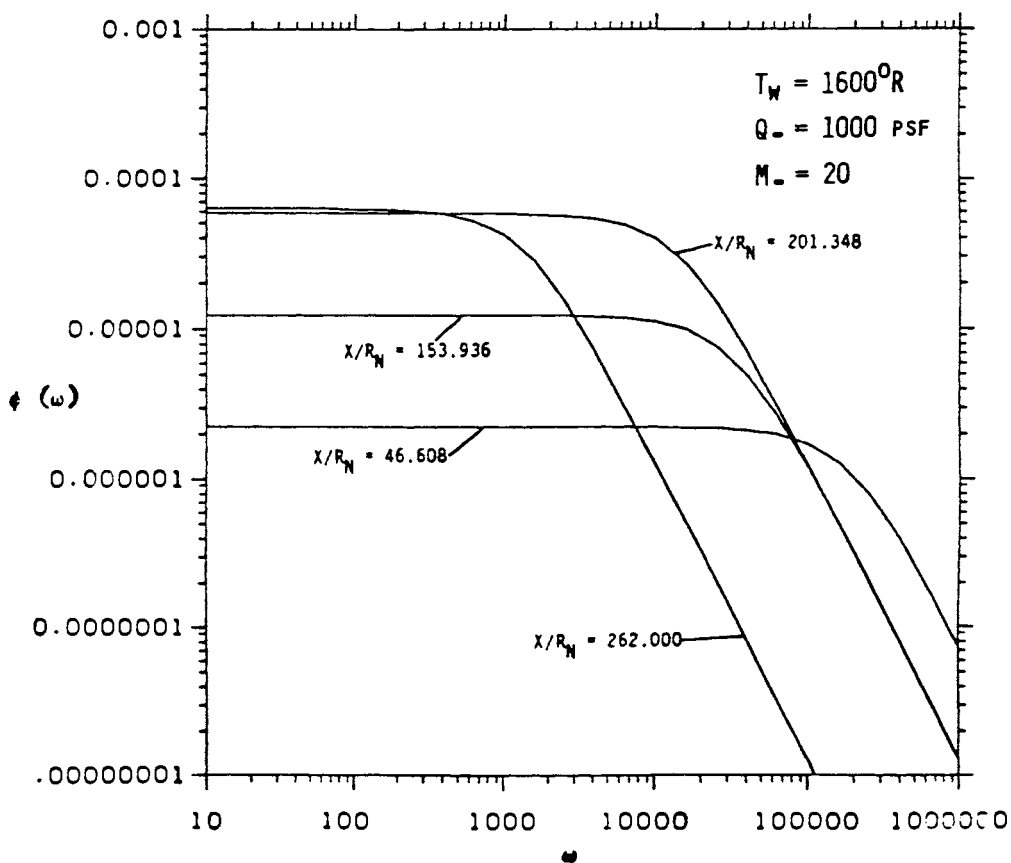


Figure A-41. Surface Pressure (A) and Heat Transfer (B) Distribution Along Windward Surface of BWB.

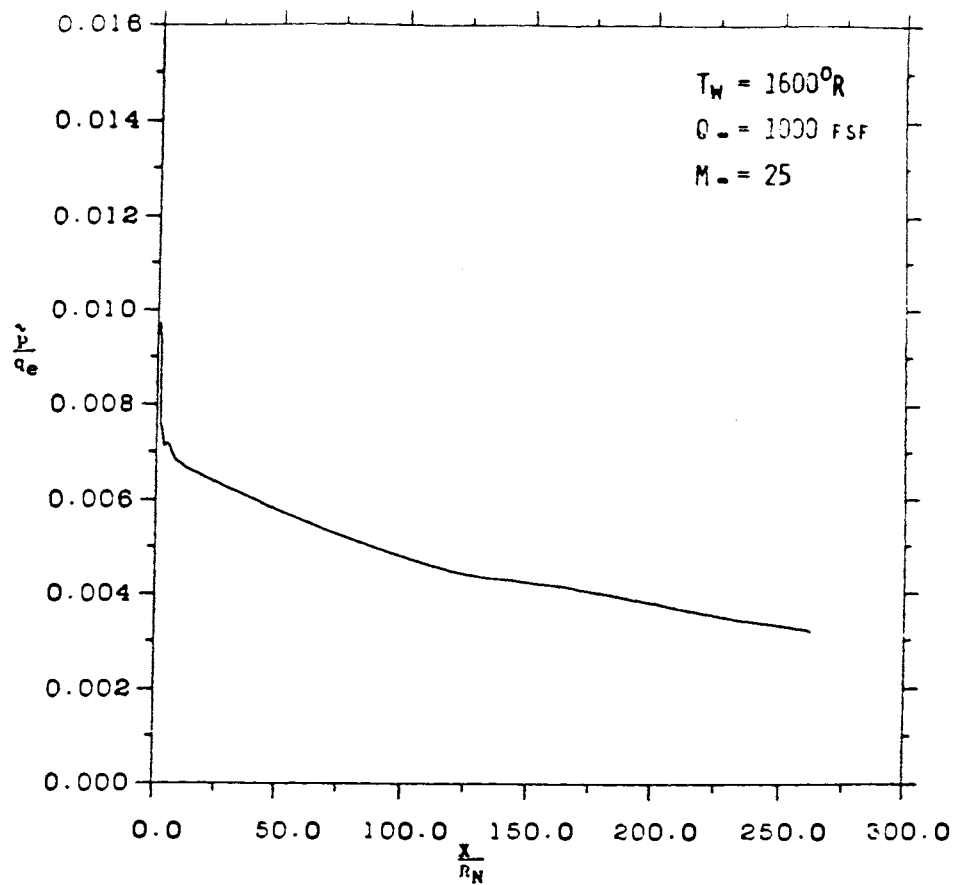


(A)

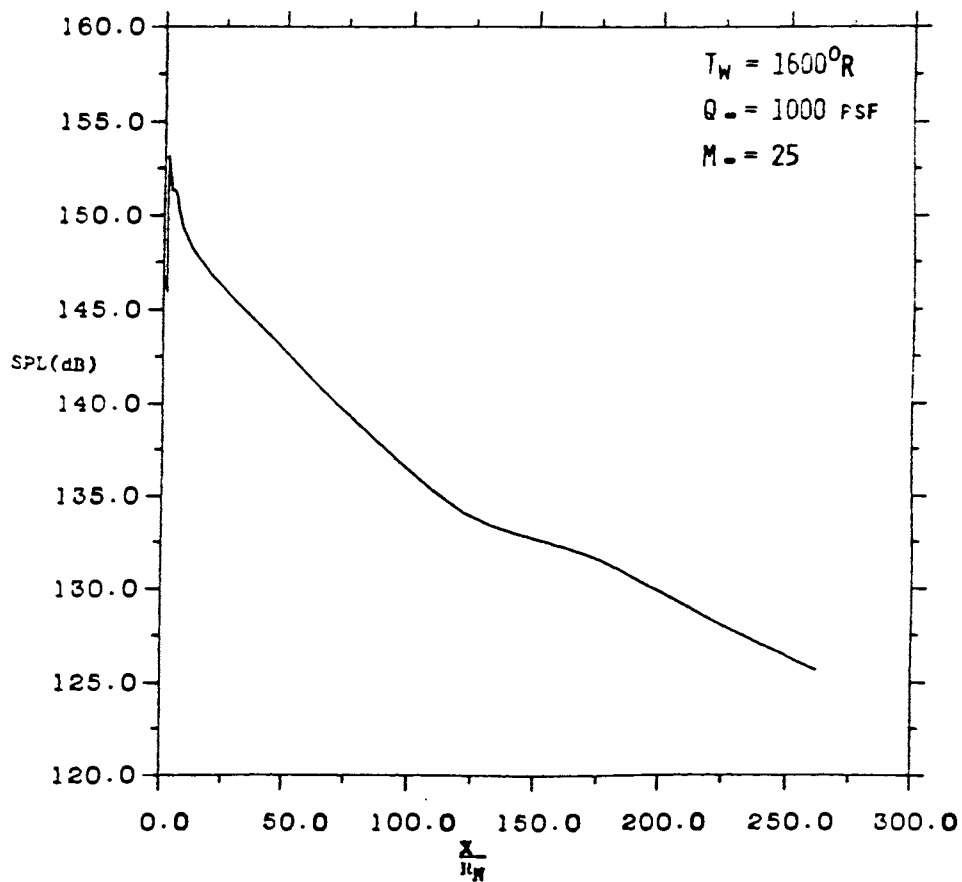


(B)

Figure A-42. Power Spectral Density Distribution Along Windward Surface of BWB (A) Normalized and (B) Power Spectra.



(A)



(B)

Figure A-43. RMS Pressure (A) and Sound Pressure Level (B) Distribution Along Leeward Surface of BWB.

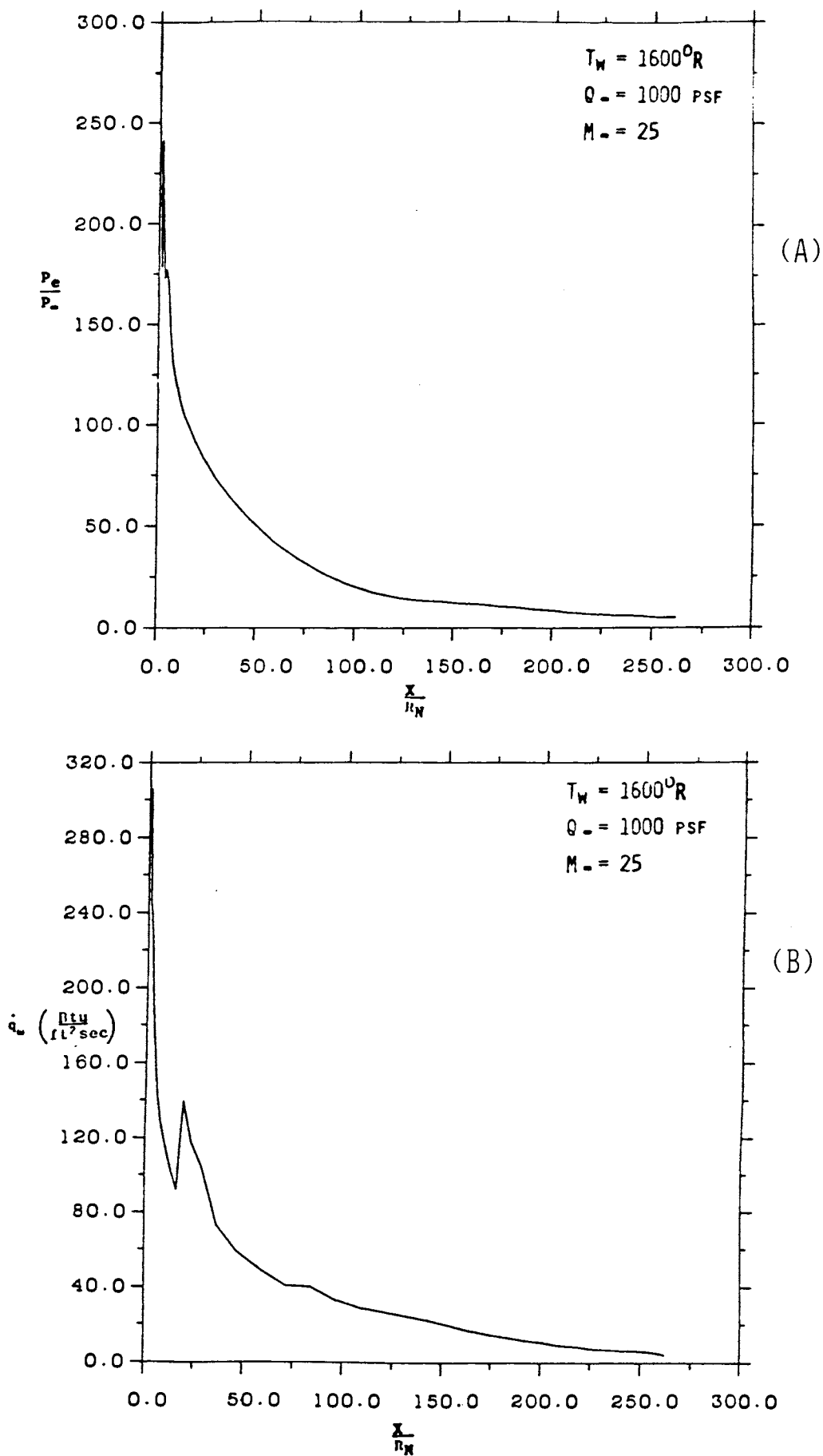
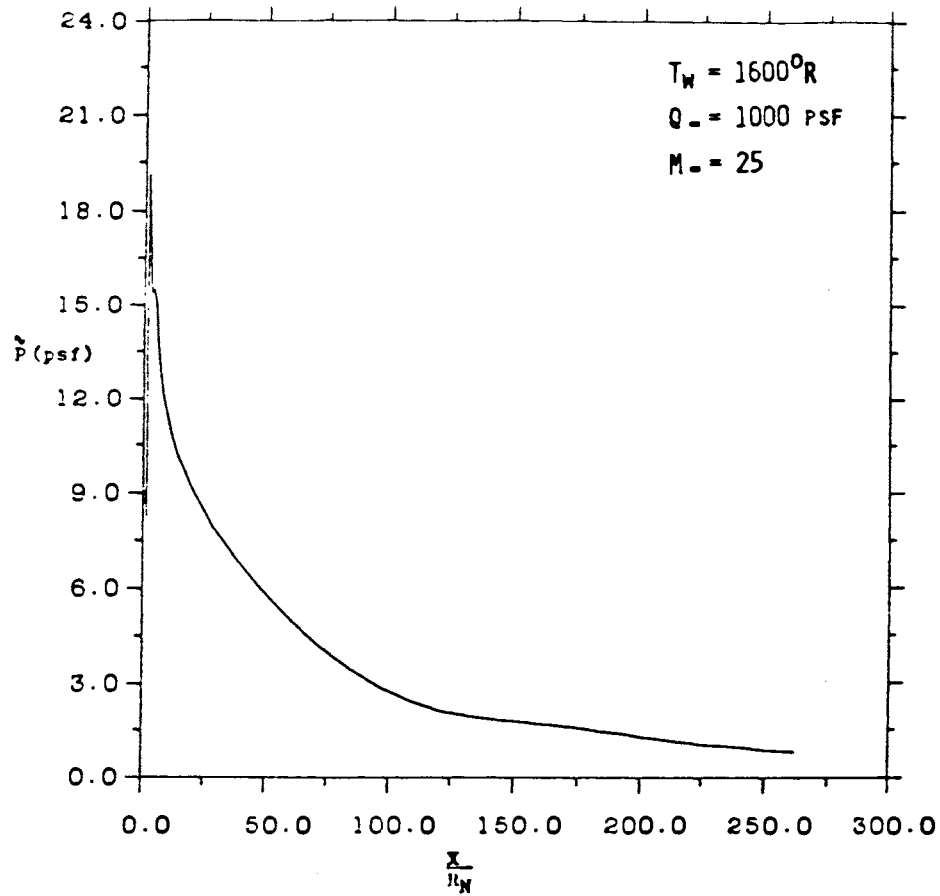
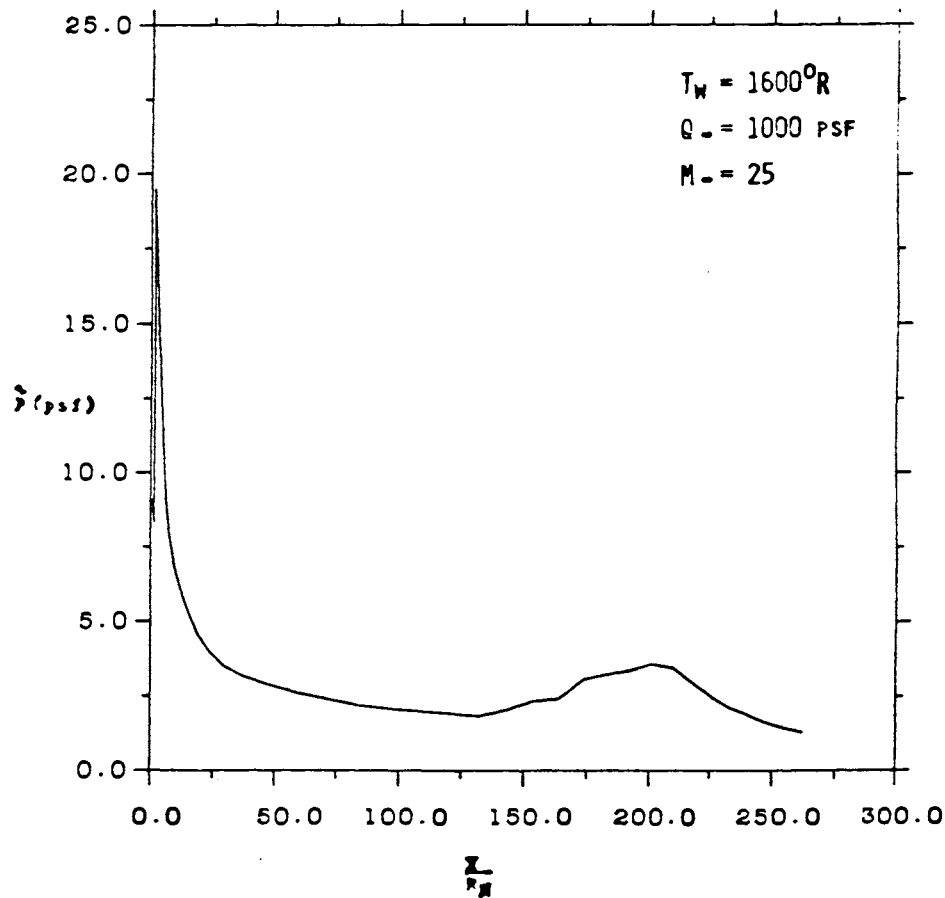


Figure A-44. Surface Pressure (A) and Heat Transfer (B) Distribution Along Leeward Surface of BWB.



(A)



(B)

Figure A-45. RMS Fluctuating Pressure Distribution Along Leeward (A) and Windward (B) Surfaces of BWB.

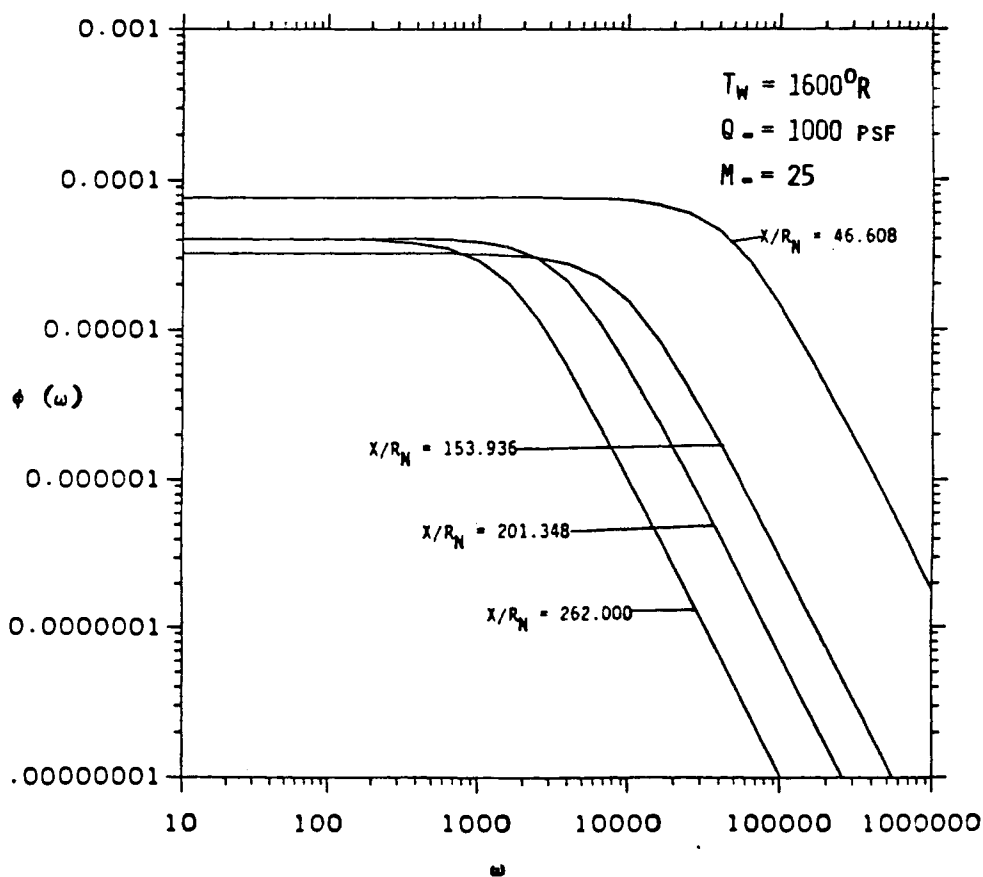
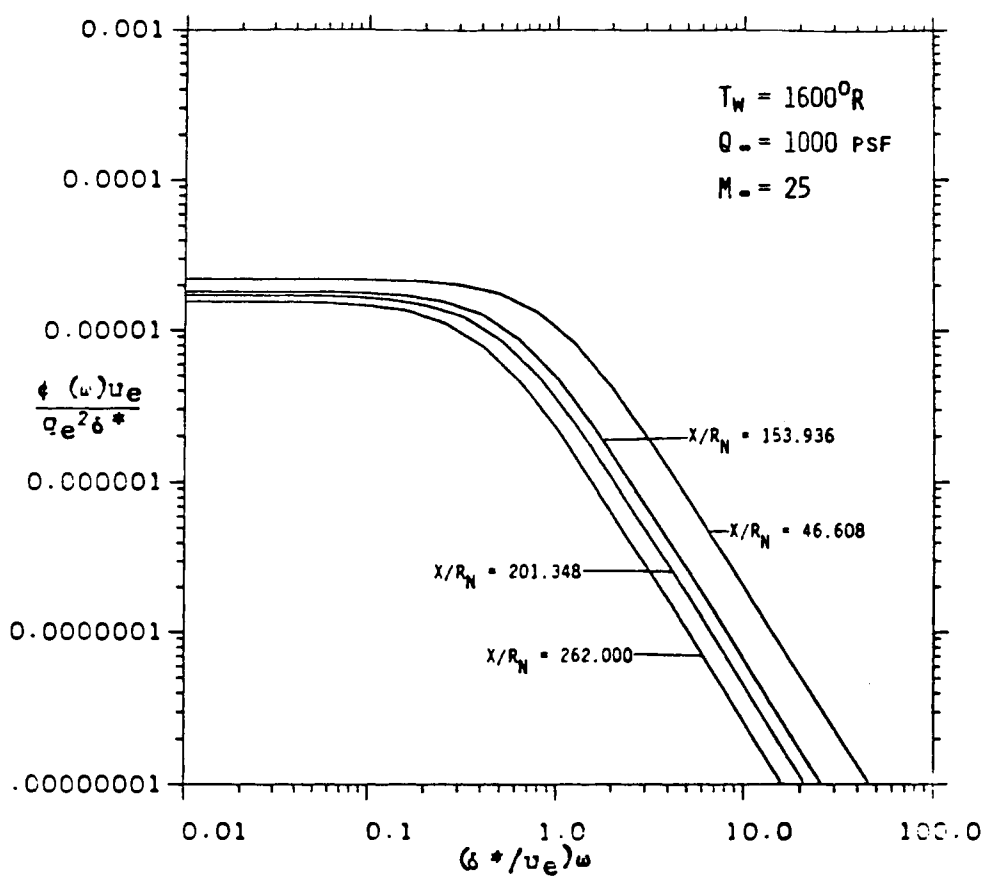


Figure A-46. Power Spectral Density Distribution Along Leeward Surface of BWB (A) Normalized and (B) Power Spectra.

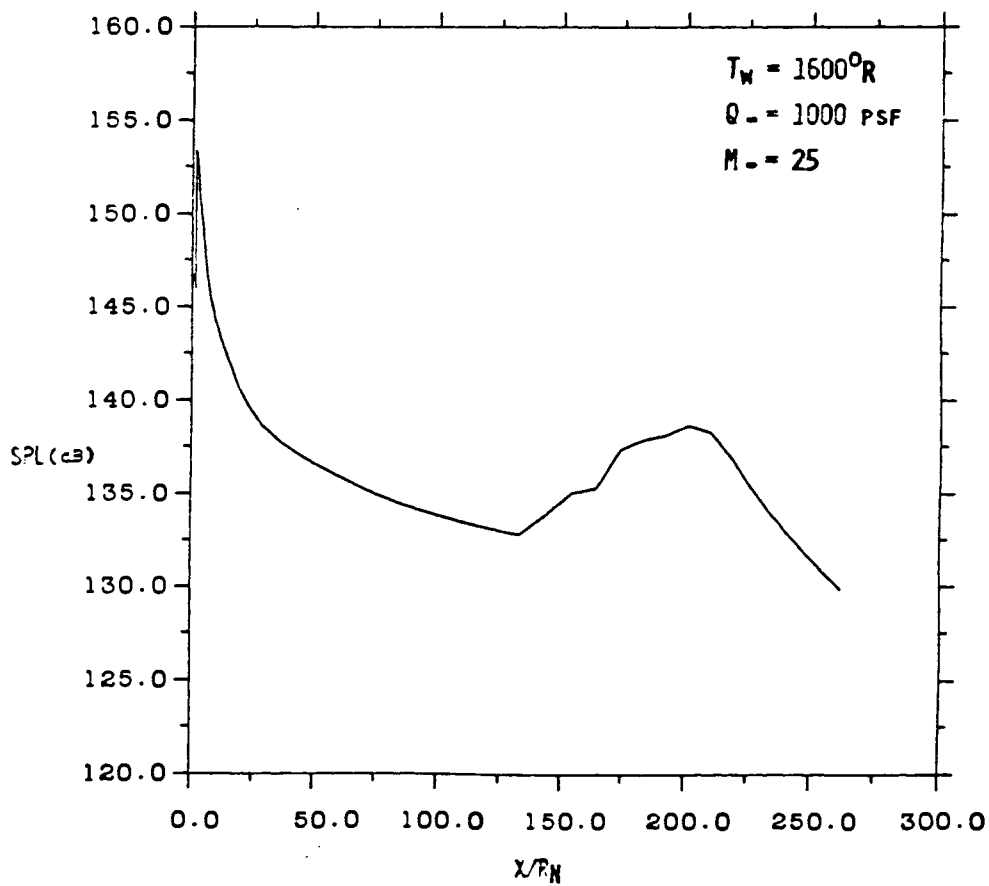
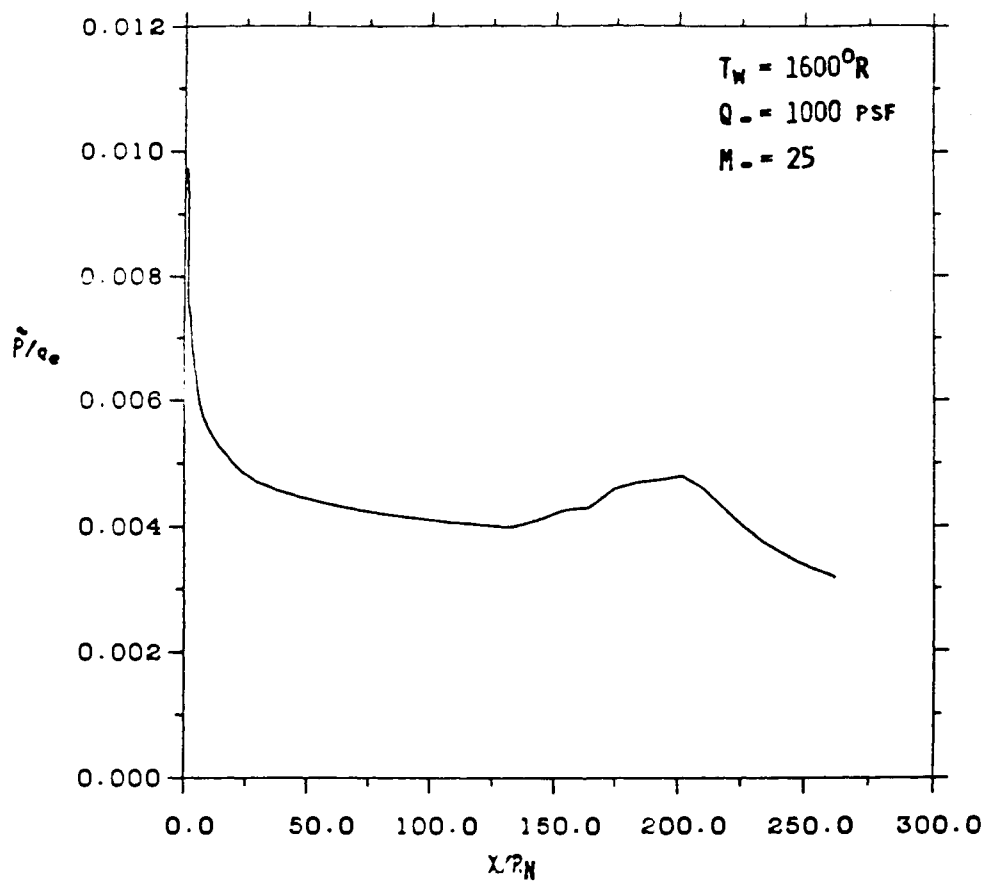
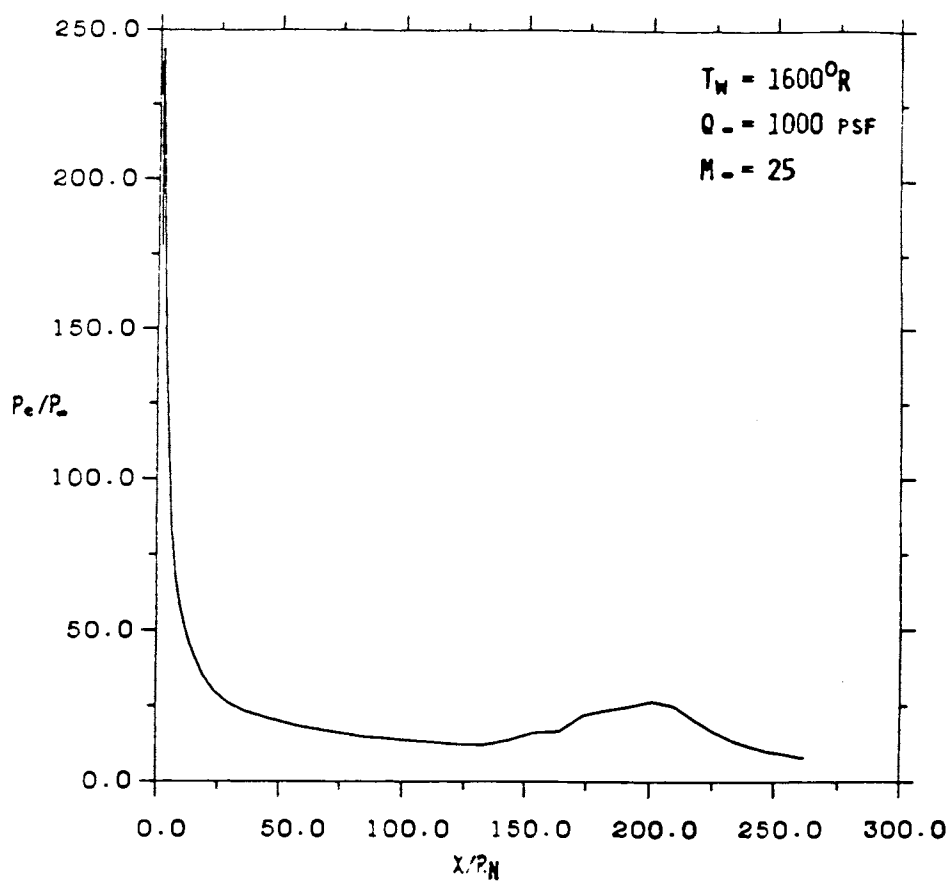
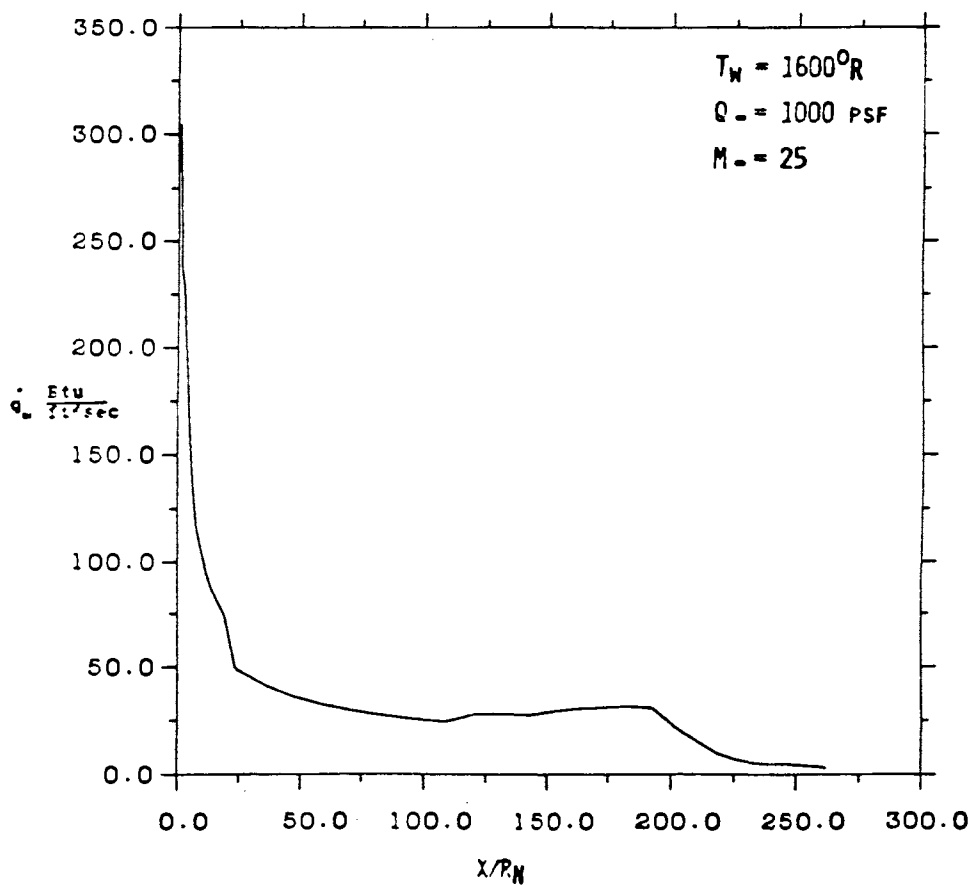


Figure A-47. RMS Pressure (A) and Sound Pressure Level (B) Distribution Along Windward Surface of BMB.

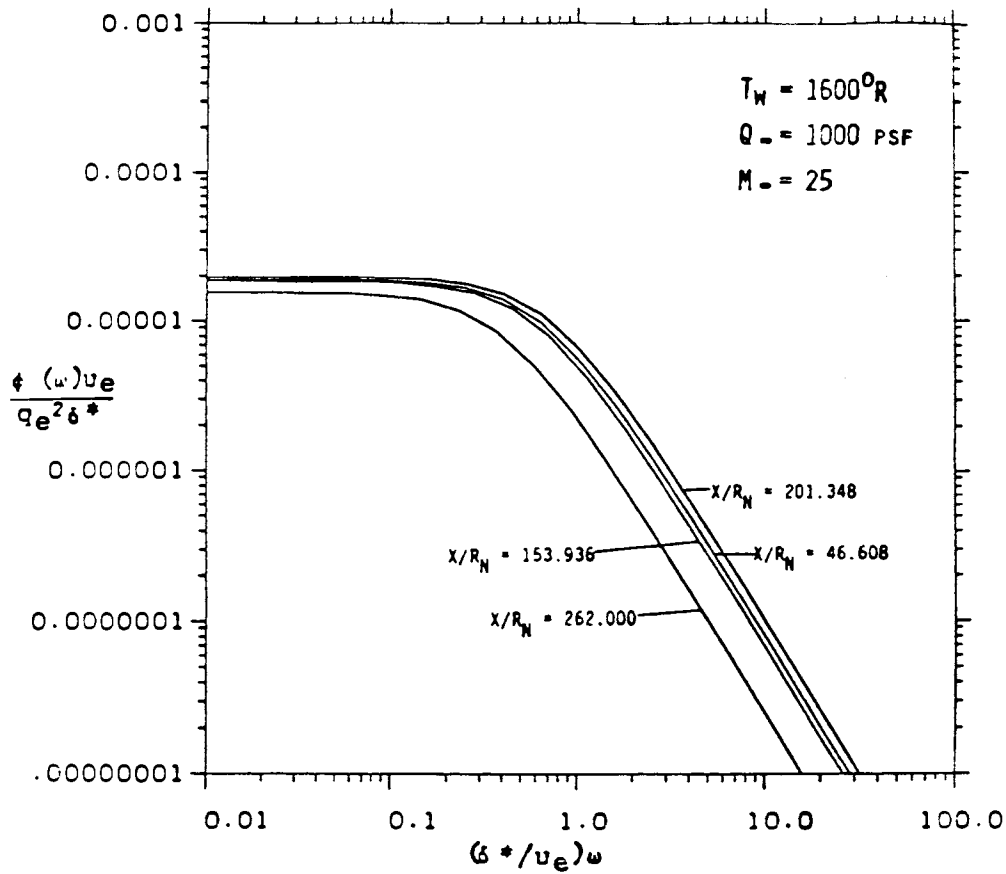


(A)

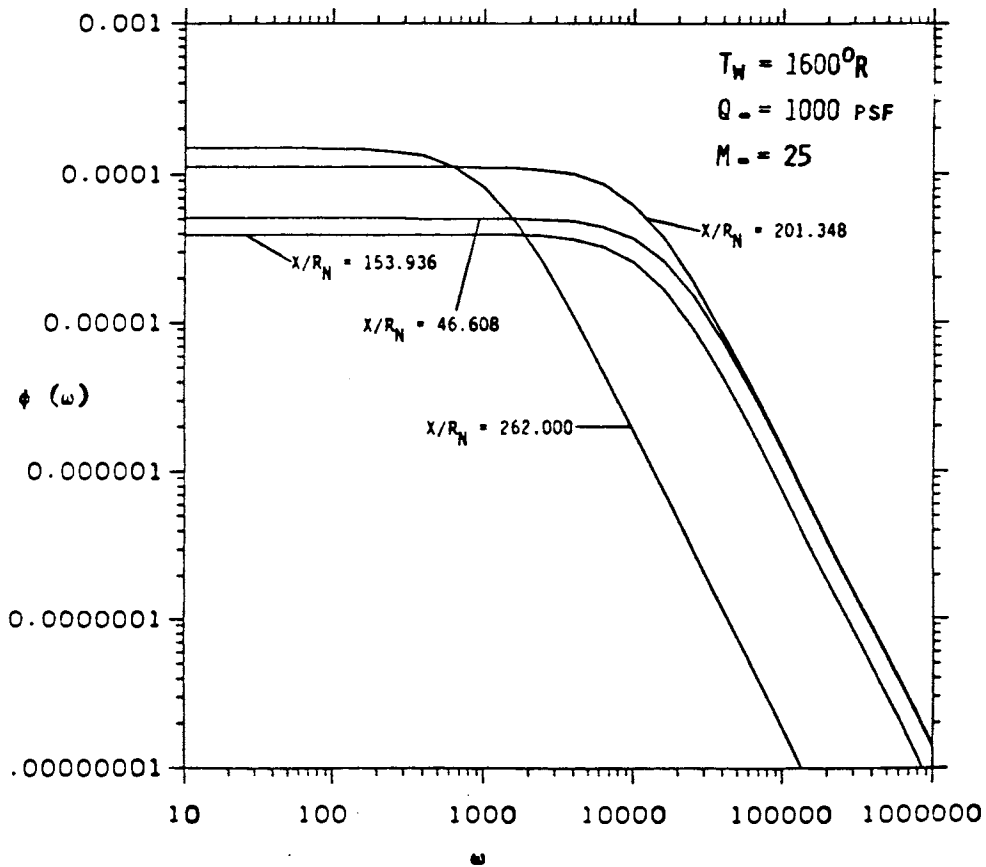


(B)

Figure A-48. Surface Pressure (A) and Heat Transfer (B) Distribution Along Windward Surface of BWB.

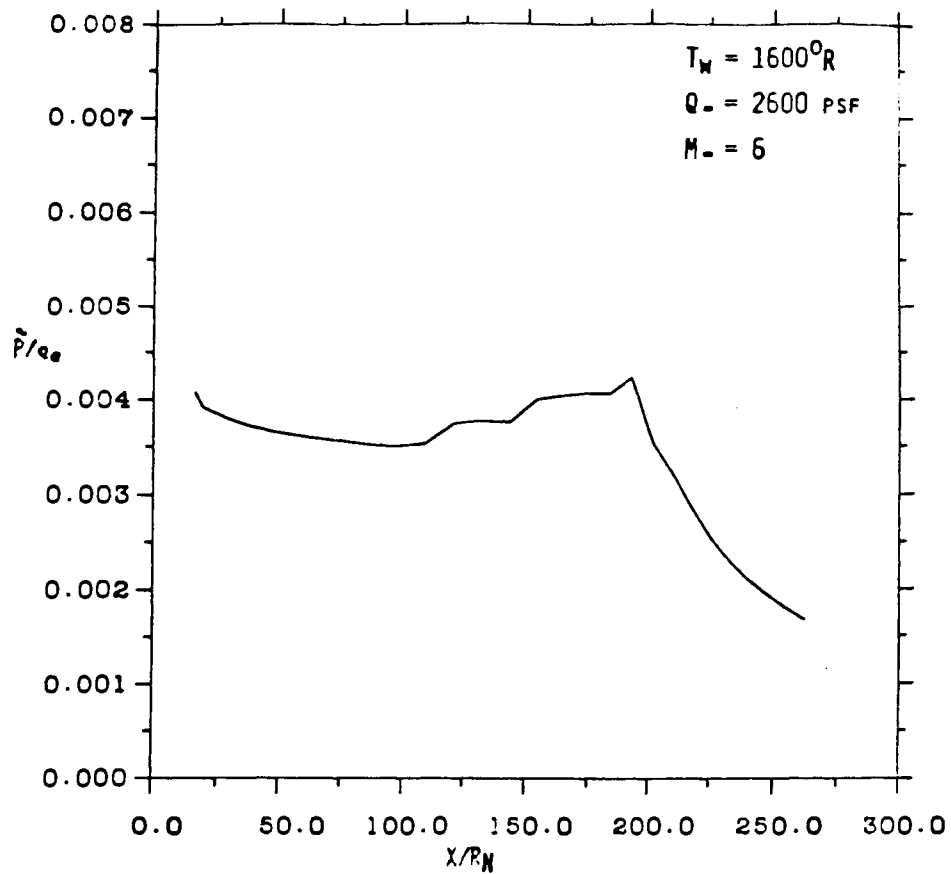


(A)

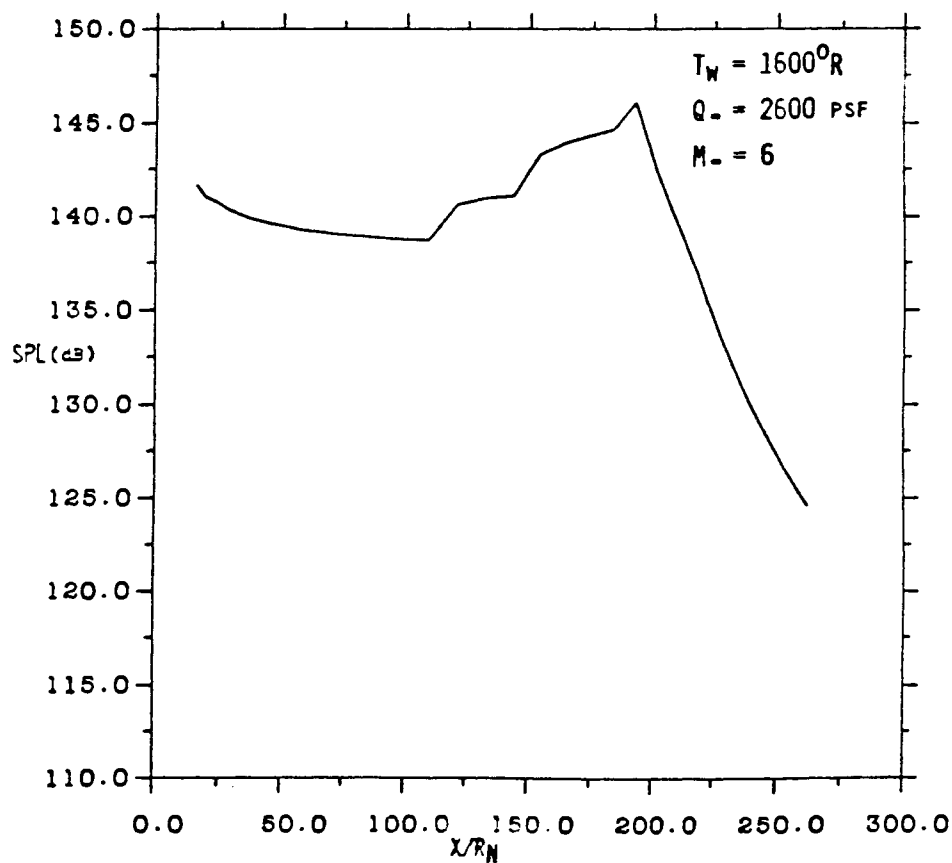


(B)

Figure A-49. Power Spectral Density Distribution Along Windward Surface of BWB (A) Normalized and (B) Power Spectra.

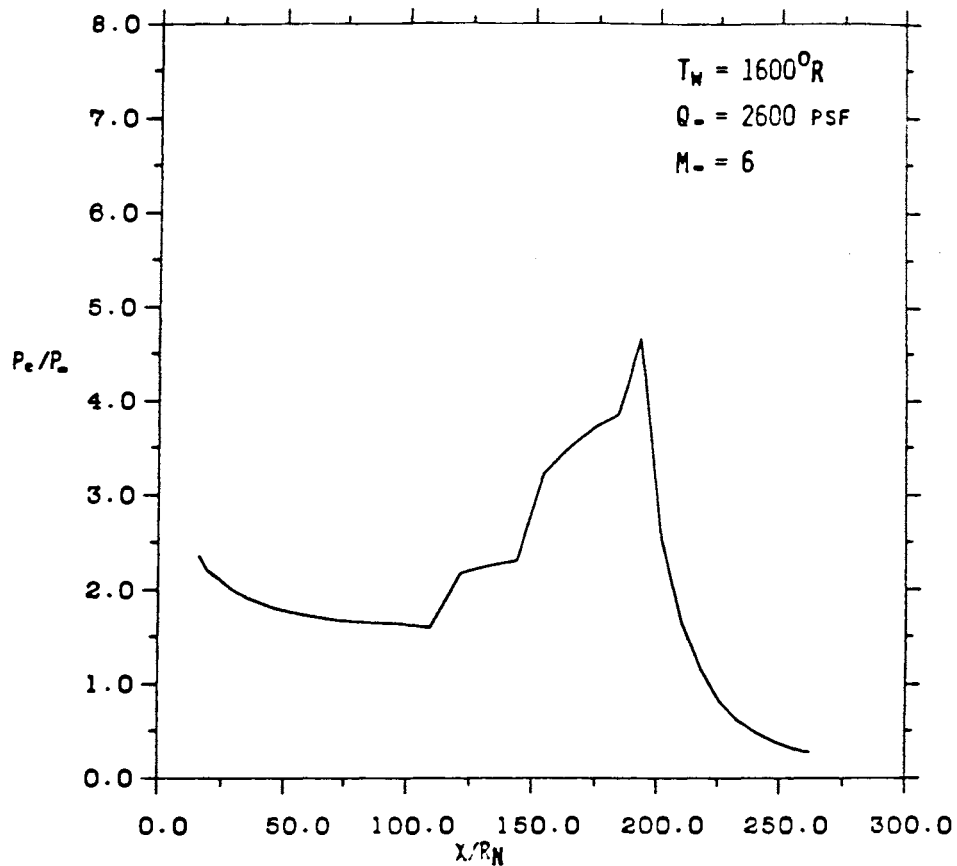


(A)

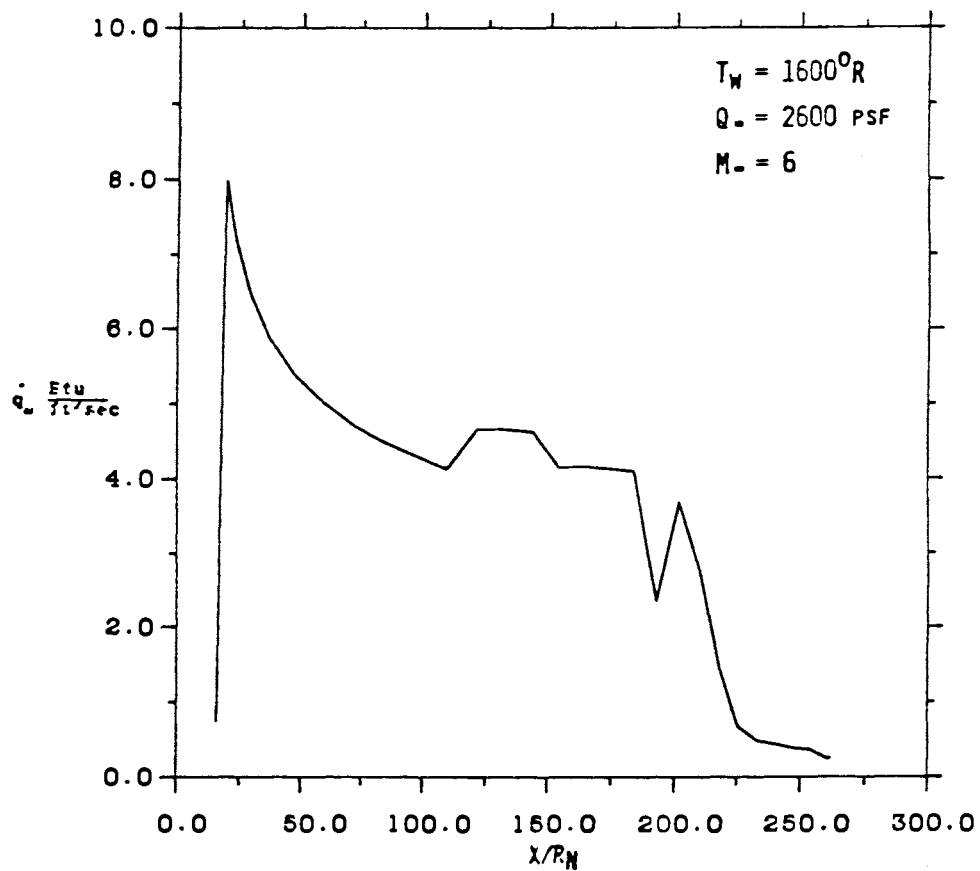


(B)

Figure A-50. RMS Pressure (A) and Sound Pressure Level (B) Distribution Along Windward Surface of BWB.



(A)



(B)

Figure A-51. Surface Pressure (A) and Heat Transfer (B) Distribution Along Windward Surface of BWB.

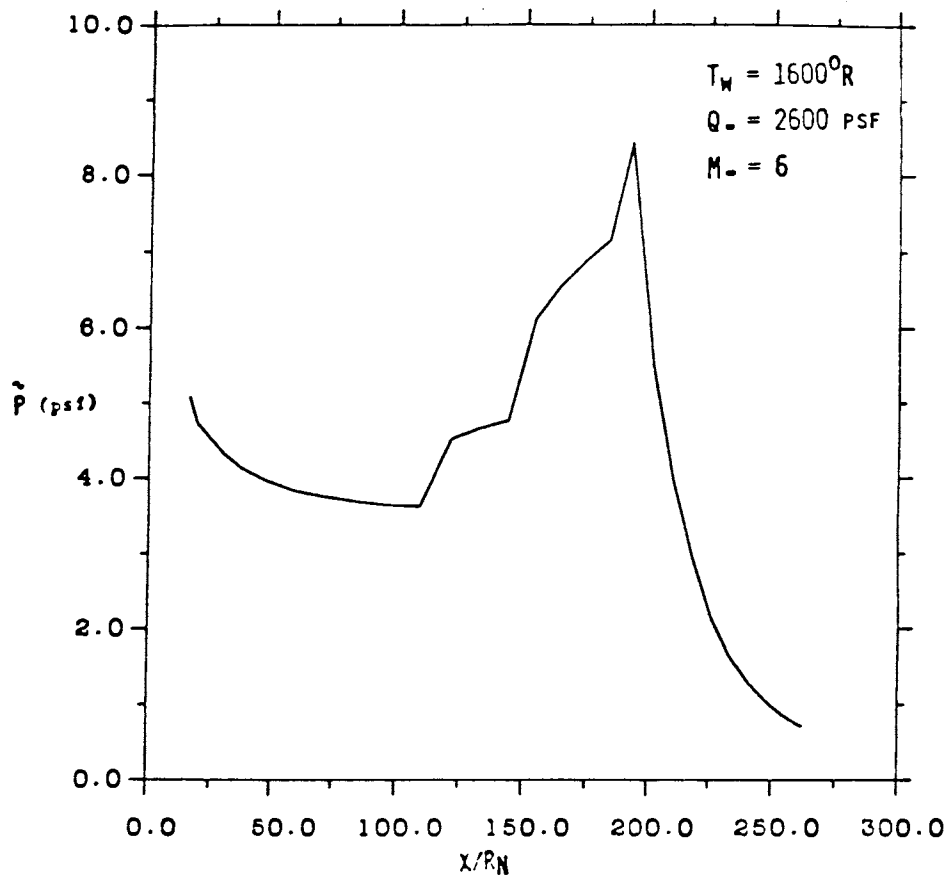
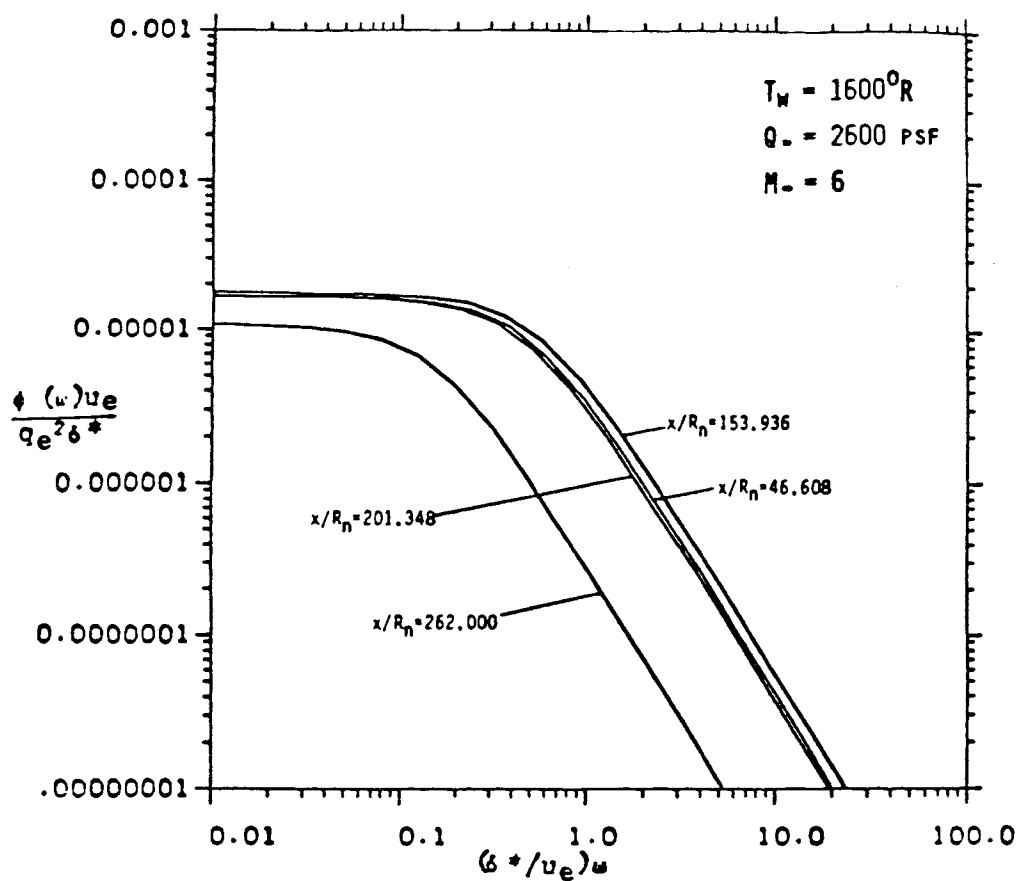
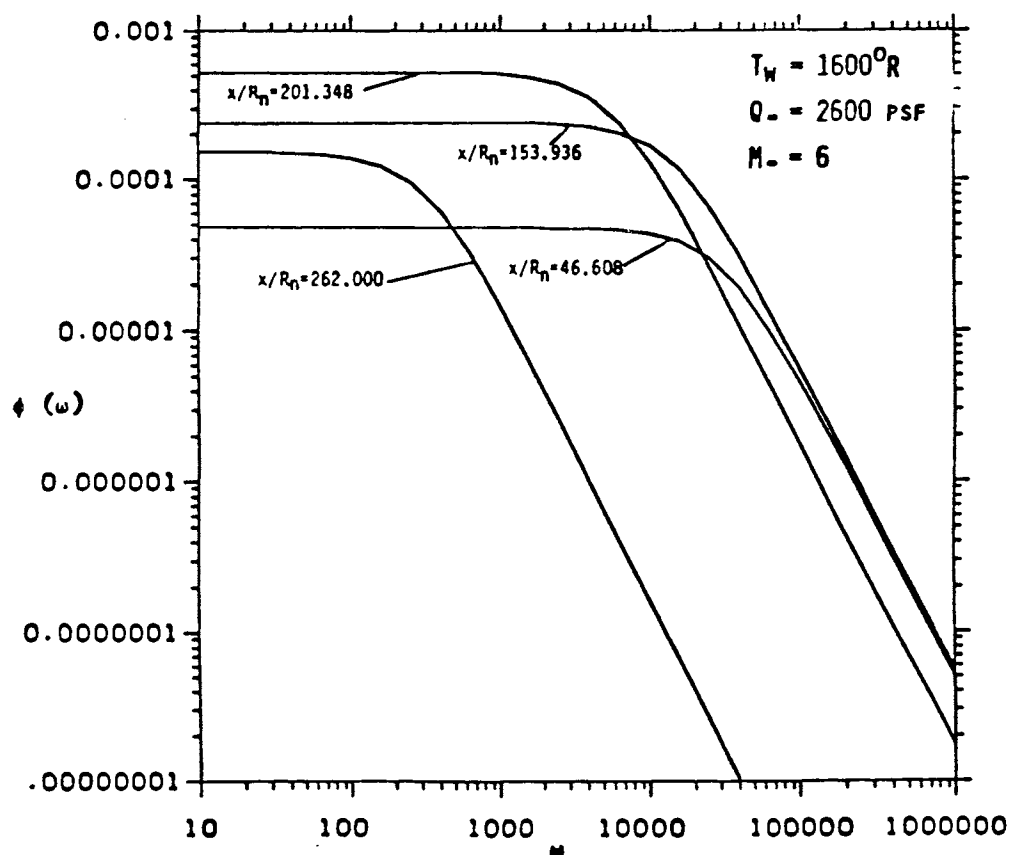


Figure A-52. RMS Fluctuating Pressure Distribution Along Windward Surface of BWB.

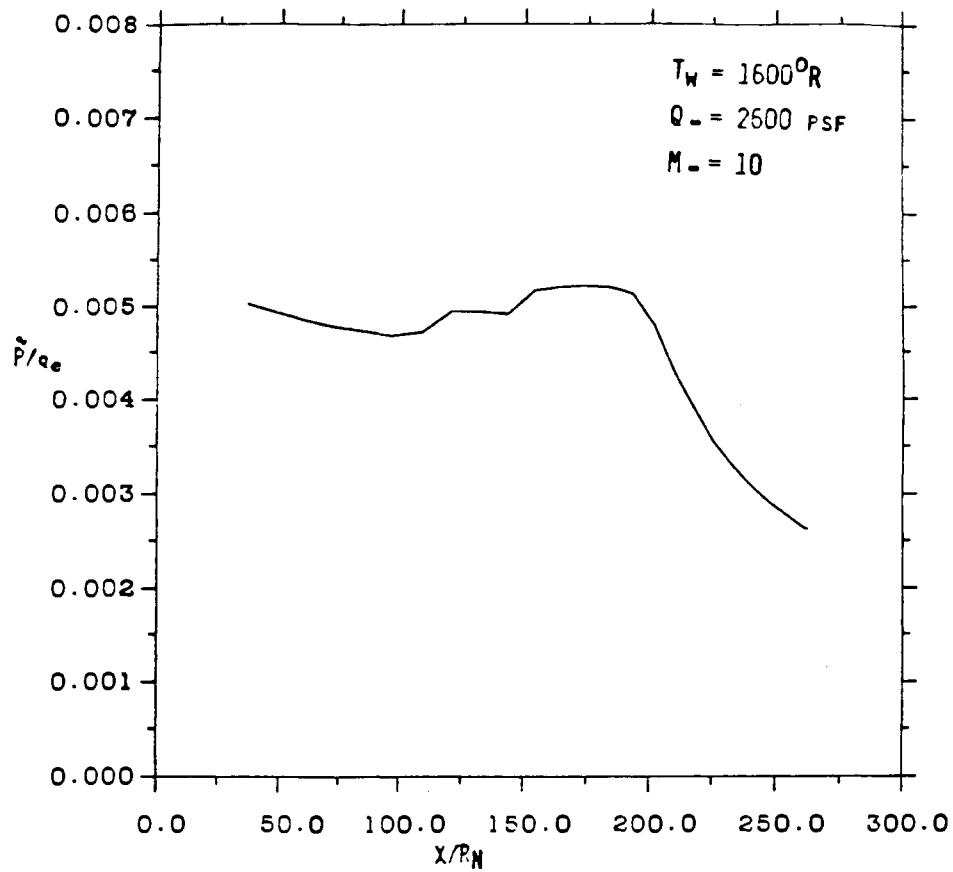


(A)

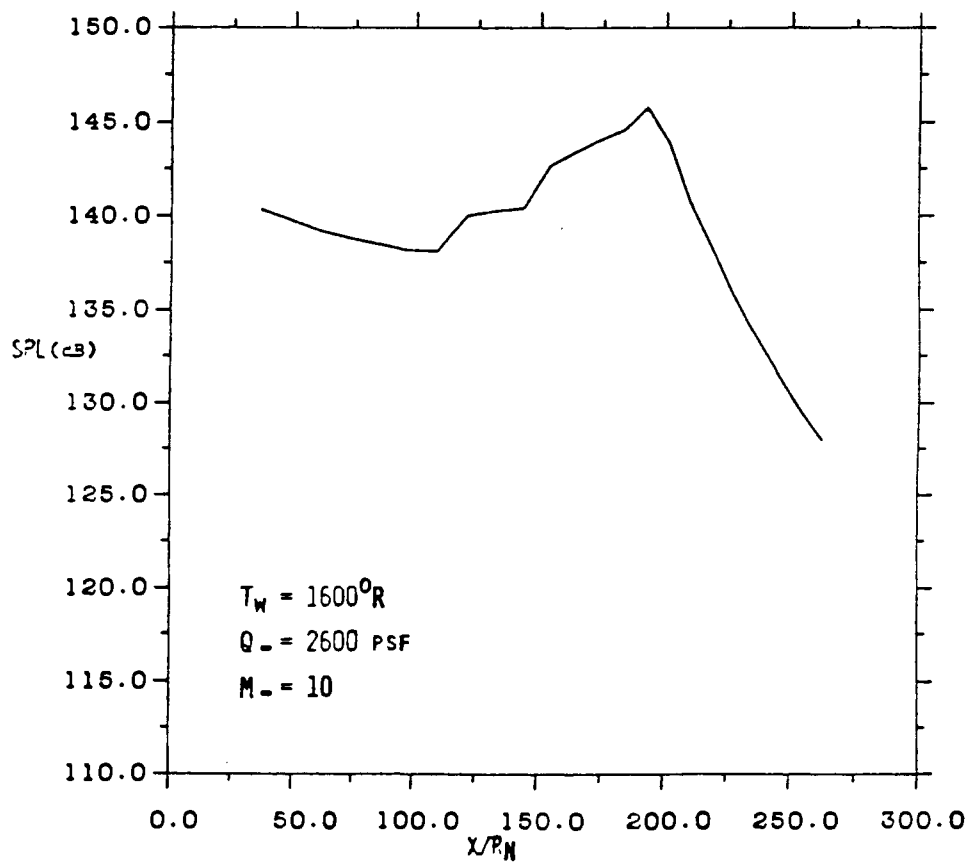


(B)

Figure A-53. Power Spectral Density Distribution Along Windward Surface of BWB (A) Normalized and (B) Power Spectra.

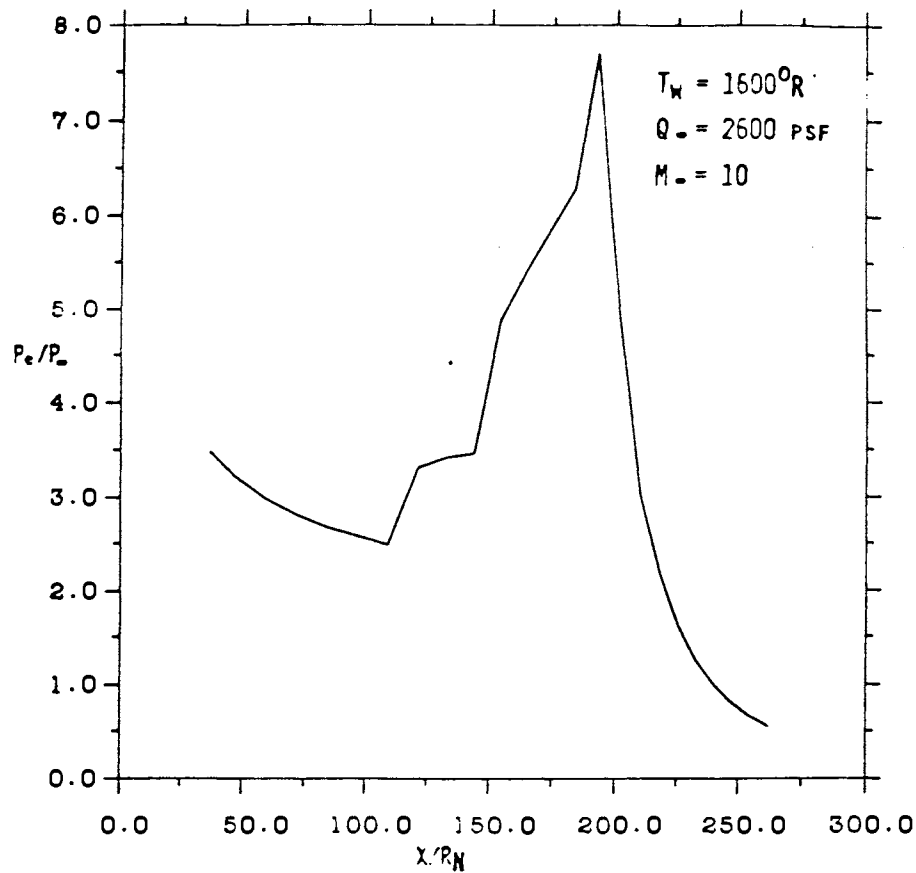


(A)

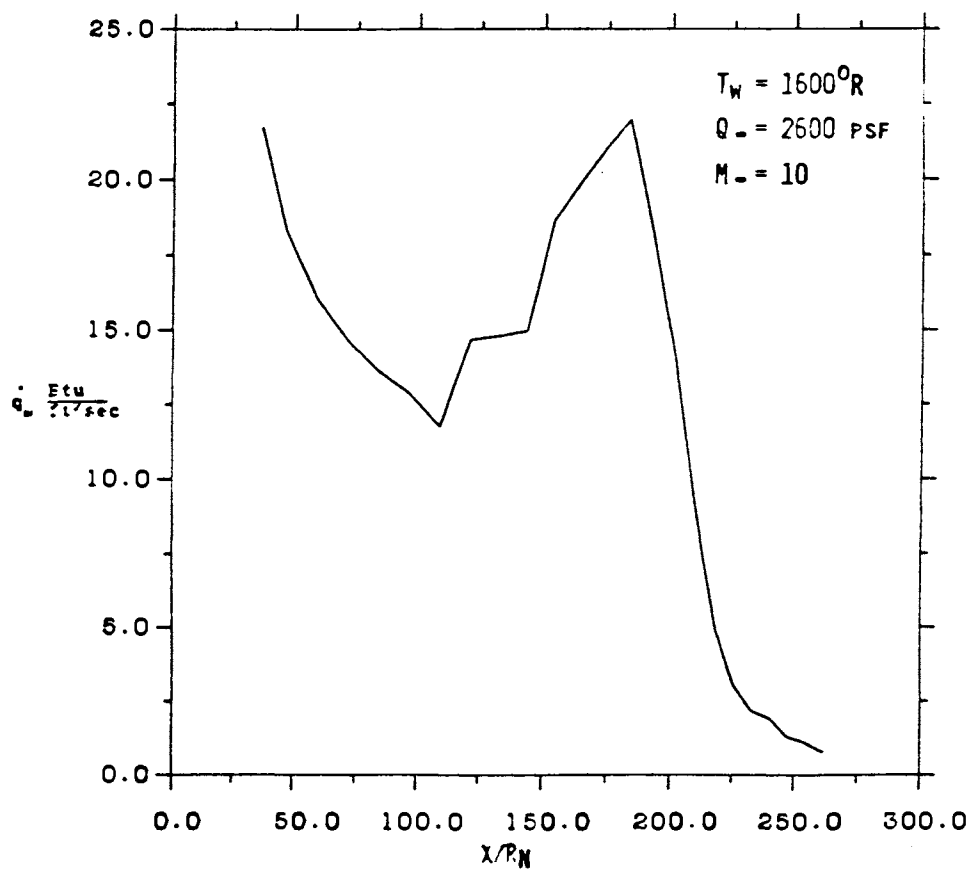


(B)

Figure A-54. RMS Pressure (A) and Sound Pressure Level (B) Distribution Along Leeward Surface of BWB.

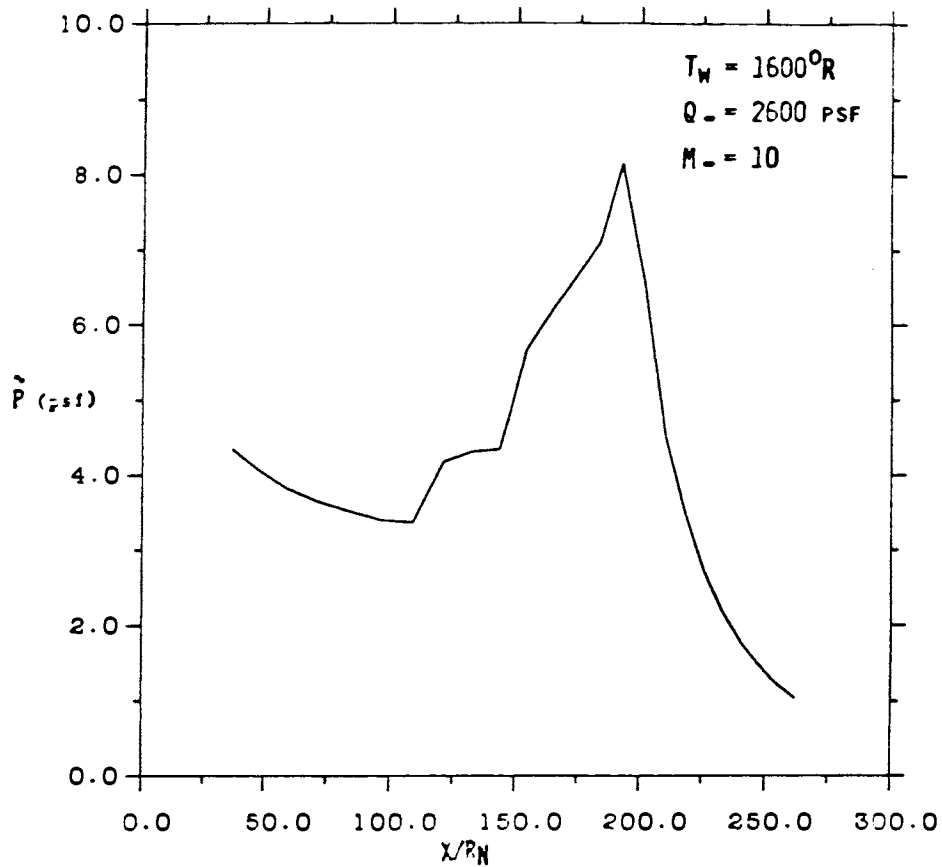


(A)

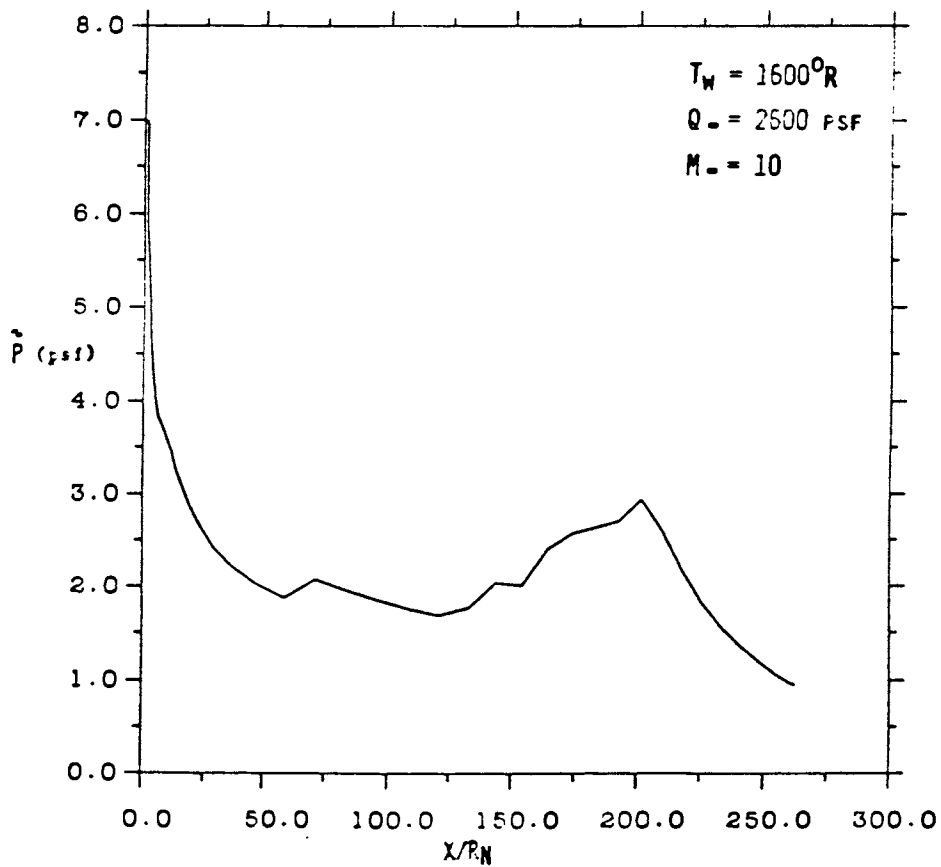


(B)

Figure A-55. Surface Pressure (A) and Heat Transfer (B) Distribution Along Leeward Surface of BWB.



(A)



(B)

Figure A-56. RMS Fluctuating Pressure Distribution Along Leeward (A) and Windward (B) Surfaces of BWB.

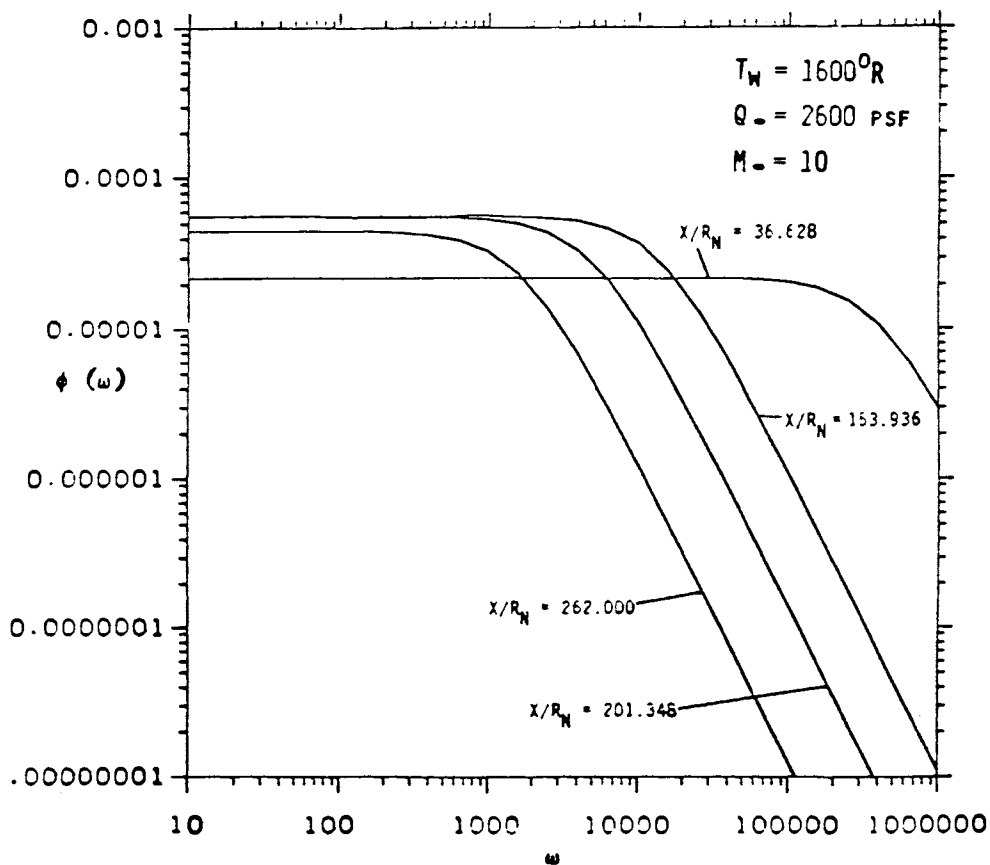
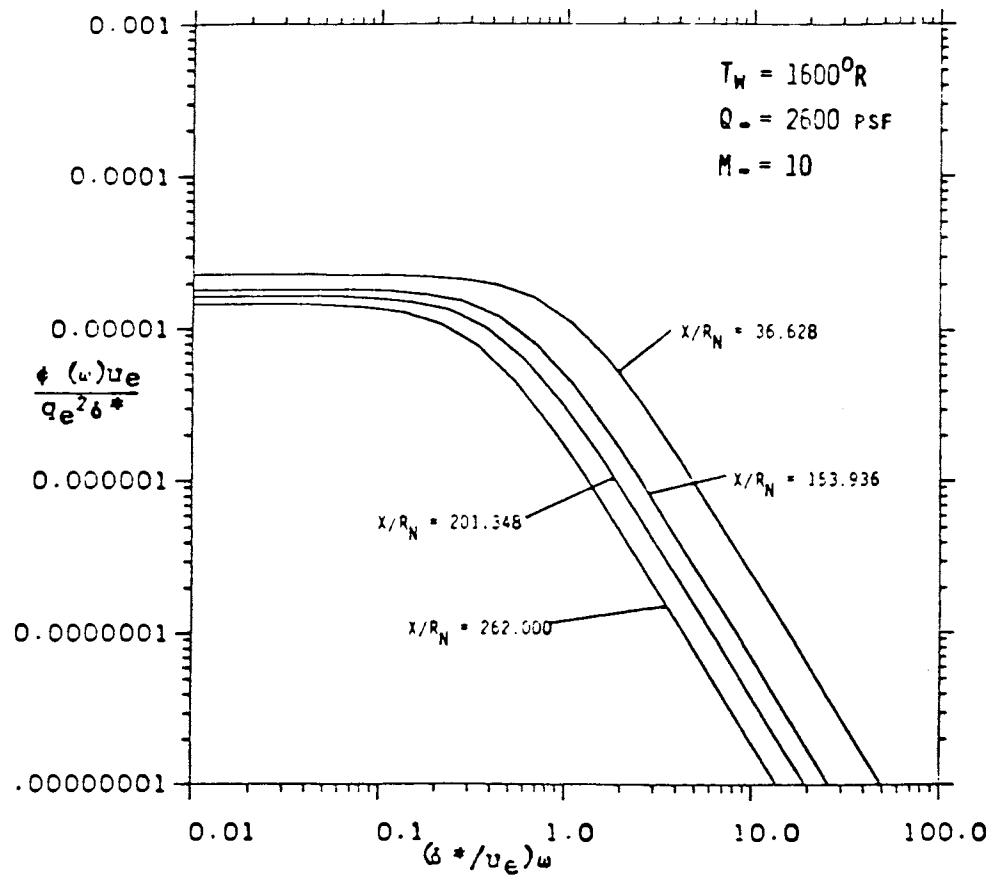
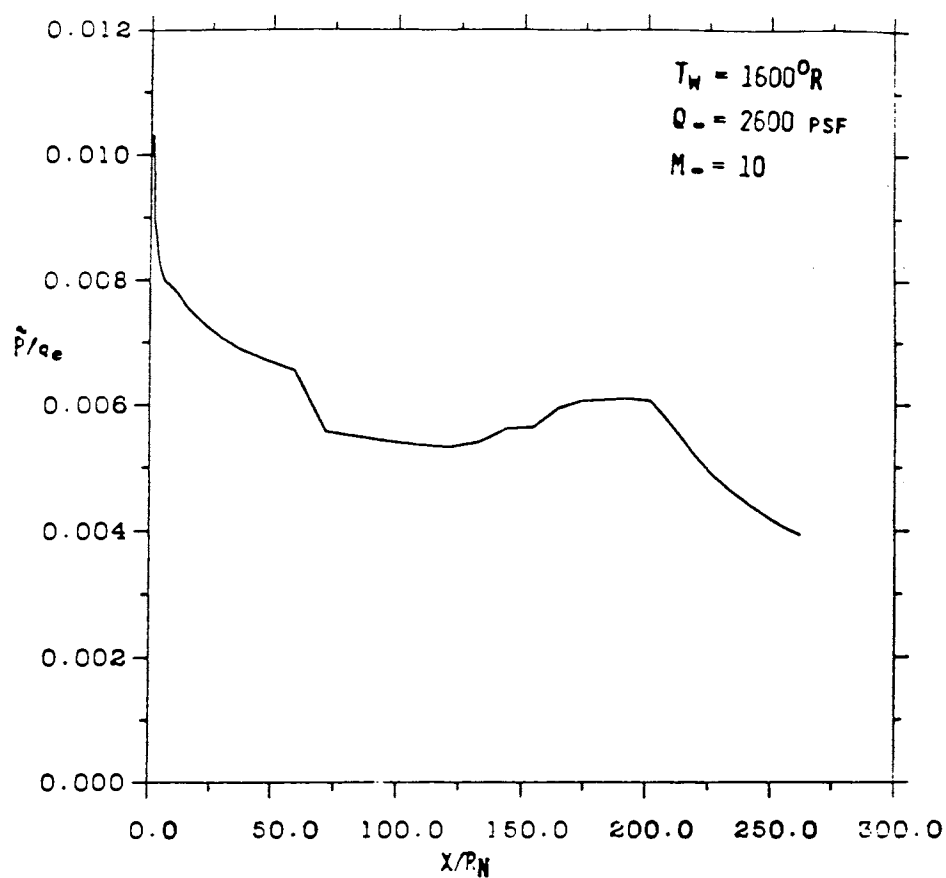
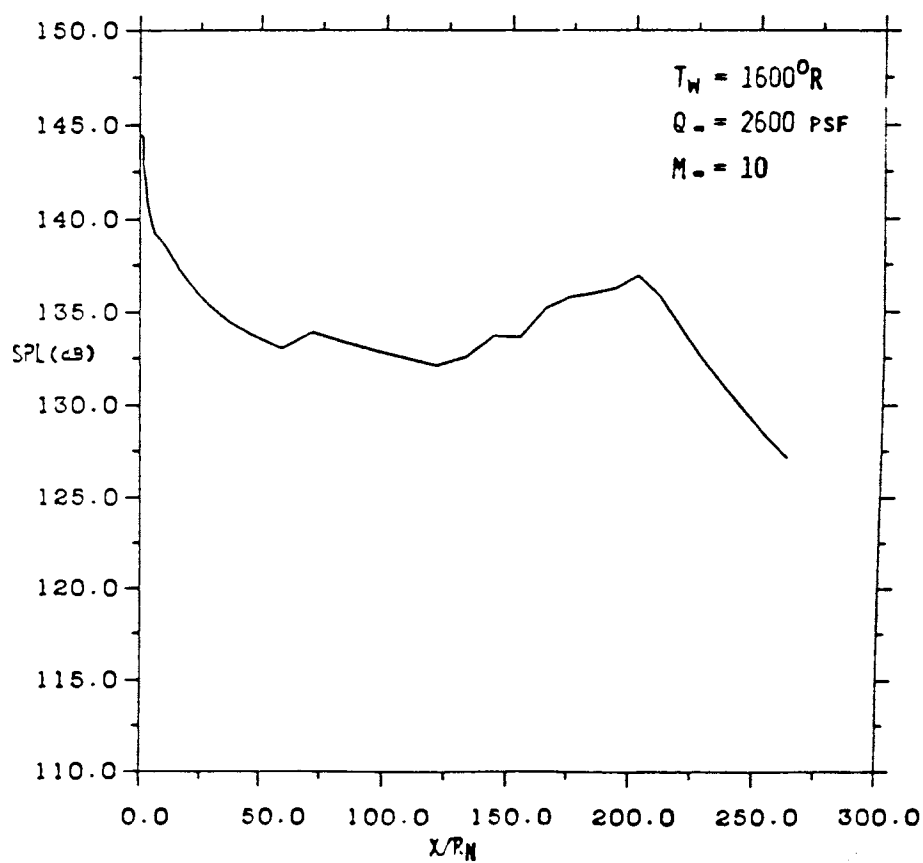


Figure A-57. Power Spectral Density Distribution Along Leeward Surface of BWB (A) Normalized and (B) Power Spectra.

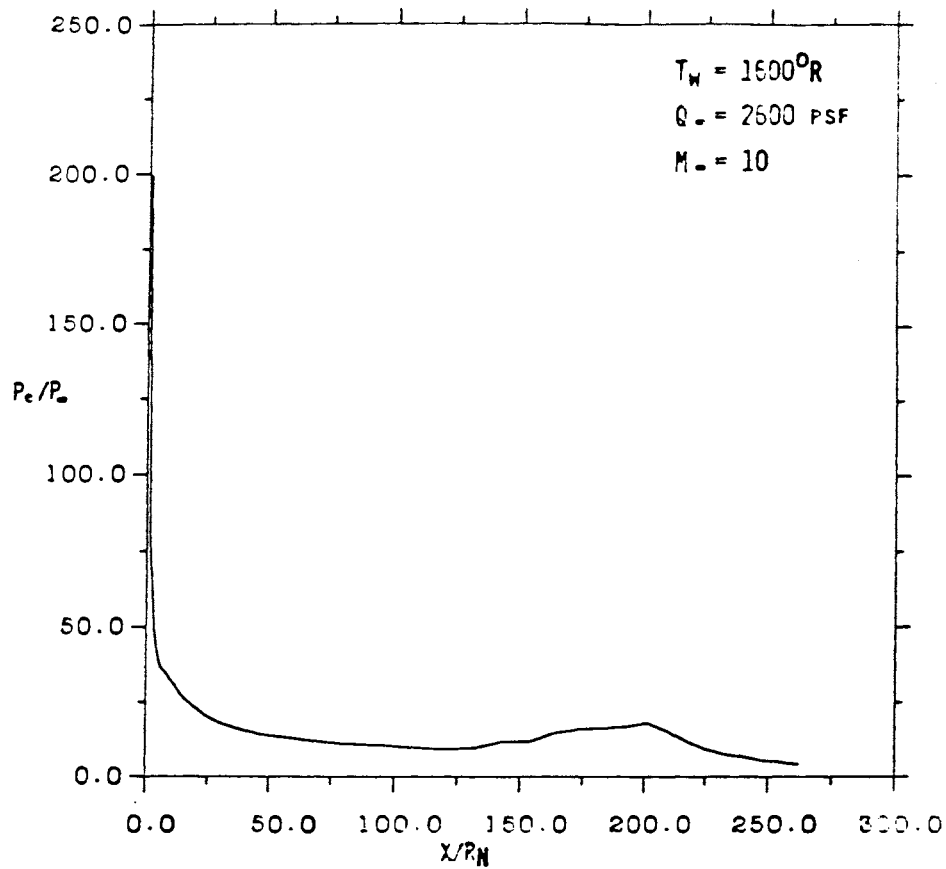


(A)

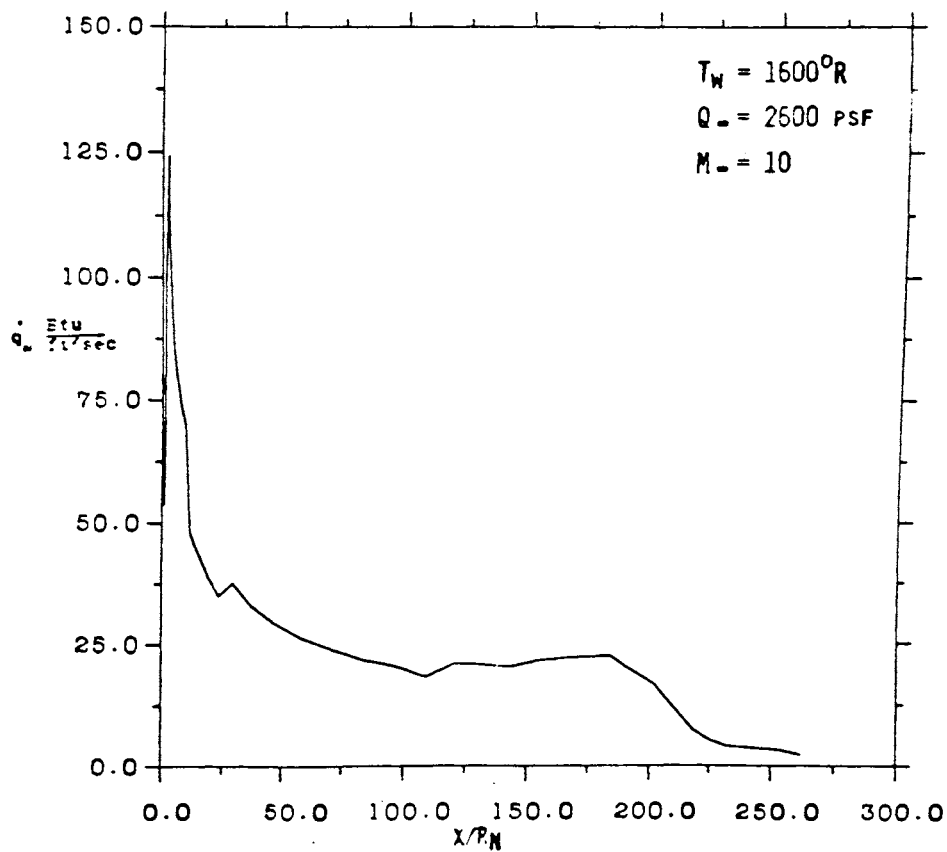


(B)

Figure A-58. RMS Pressure (A) and Sound Pressure Level (B) Distribution Along Windward Surface of BMB.



(A)



(B)

Figure A-59. Surface Pressure (A) and Heat Transfer (B) Distribution Along Windward Surface of BWB.

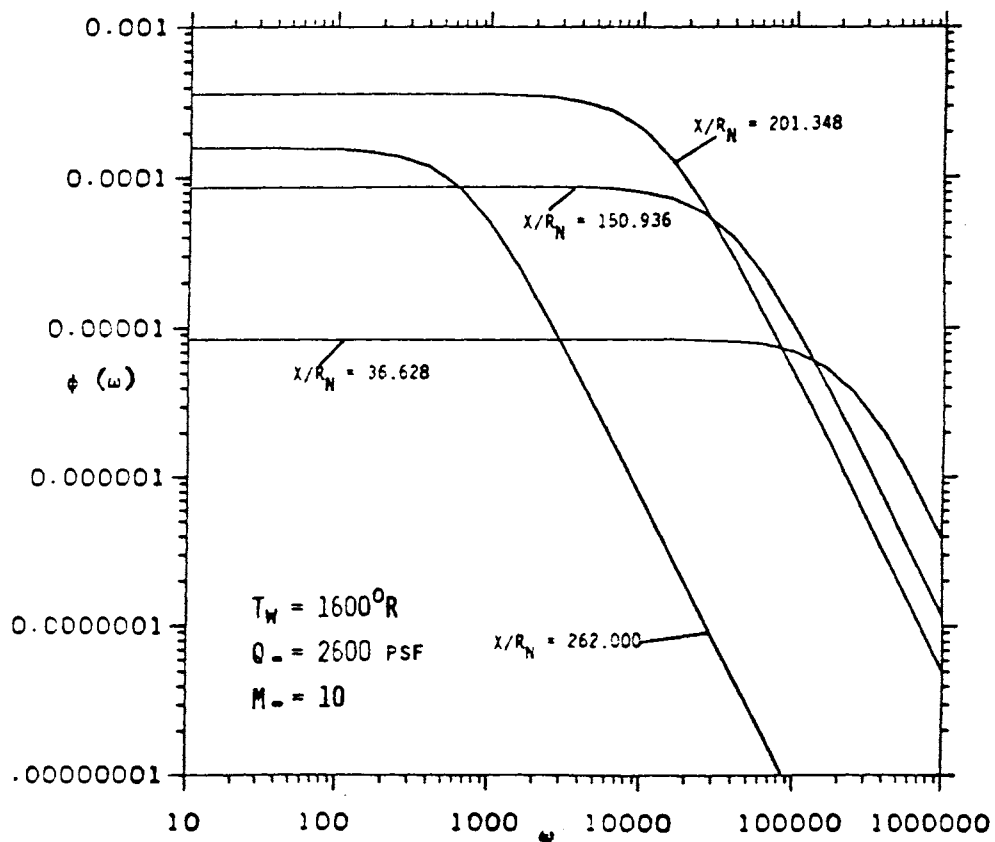
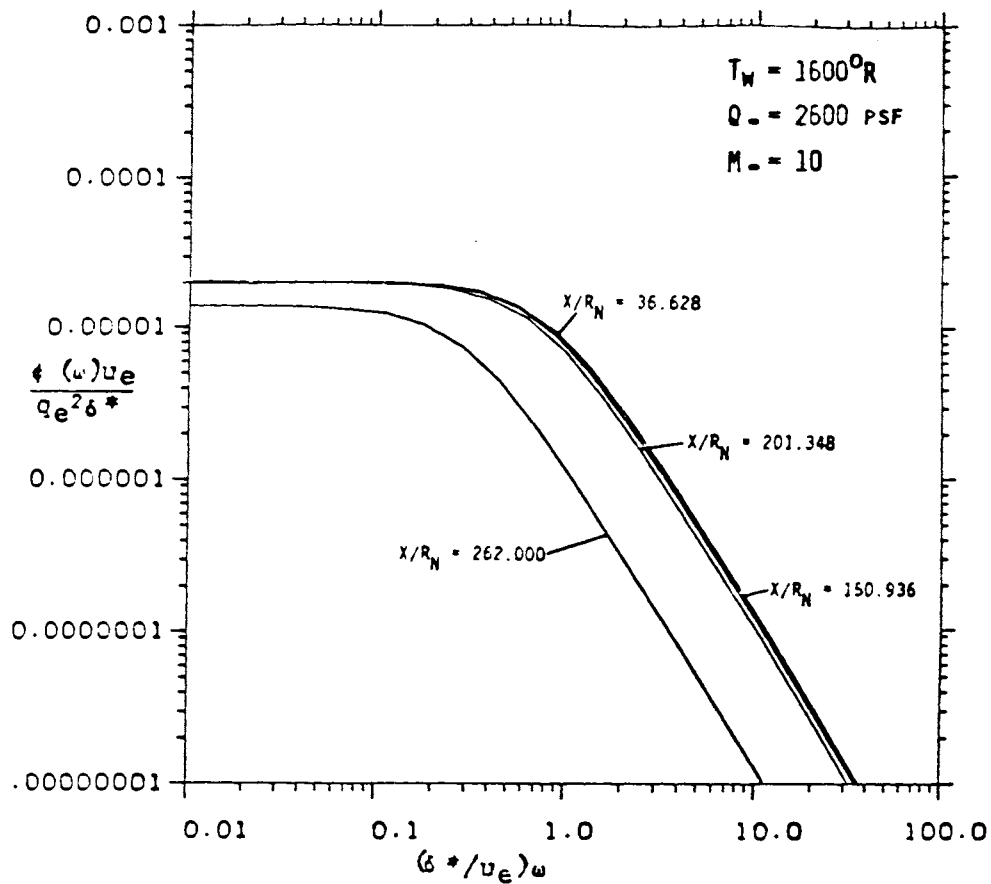


Figure A-60. Power Spectral Density Distribution Along Windward Surface of BWB (A) Normalized and (B) Power Spectra.

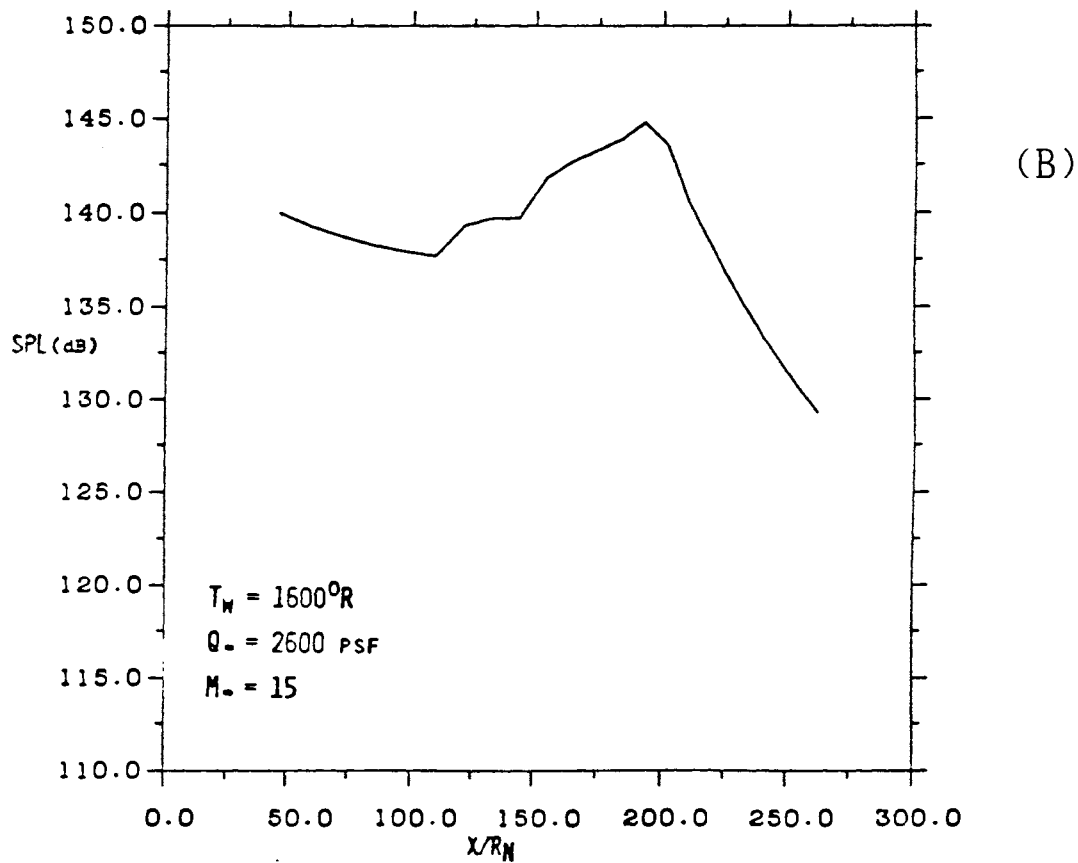
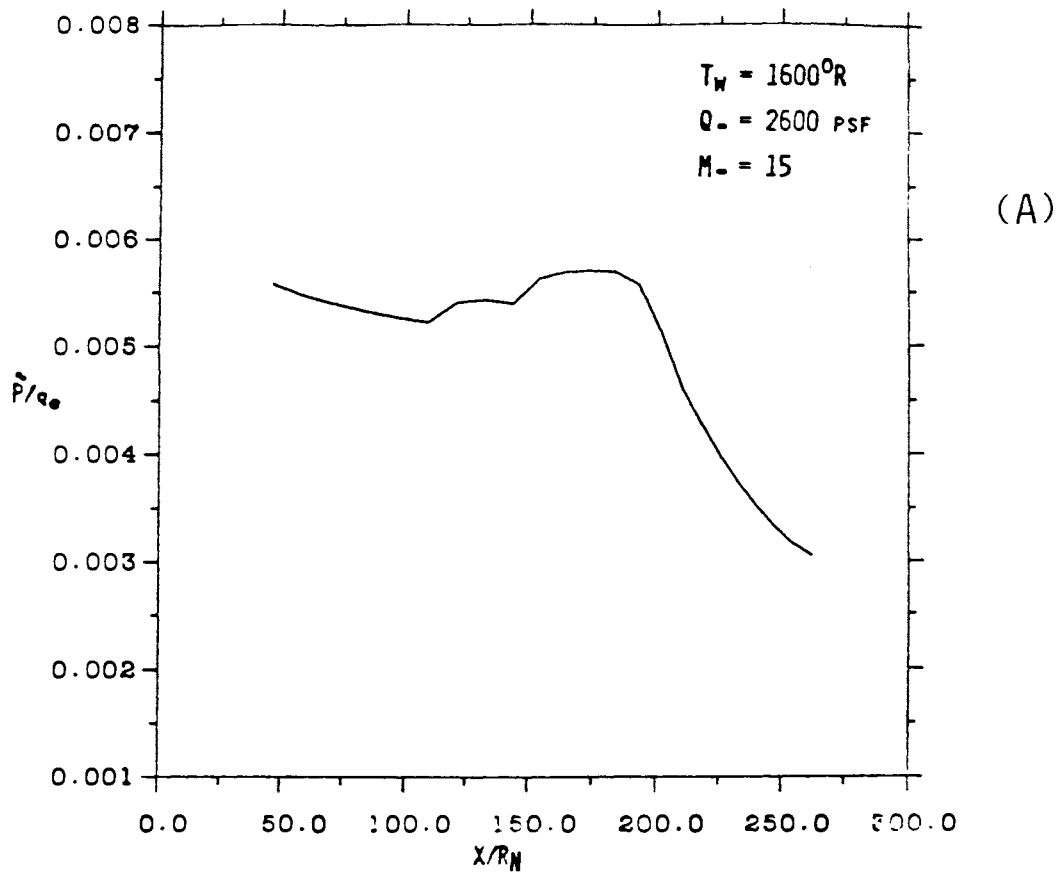
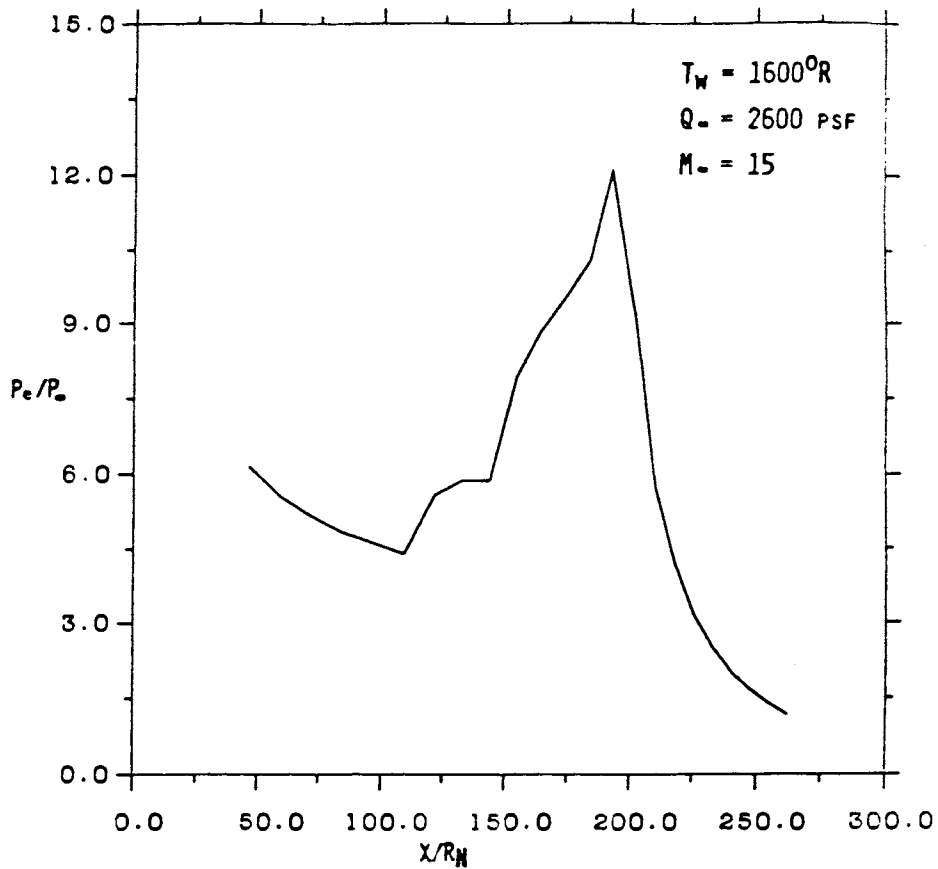
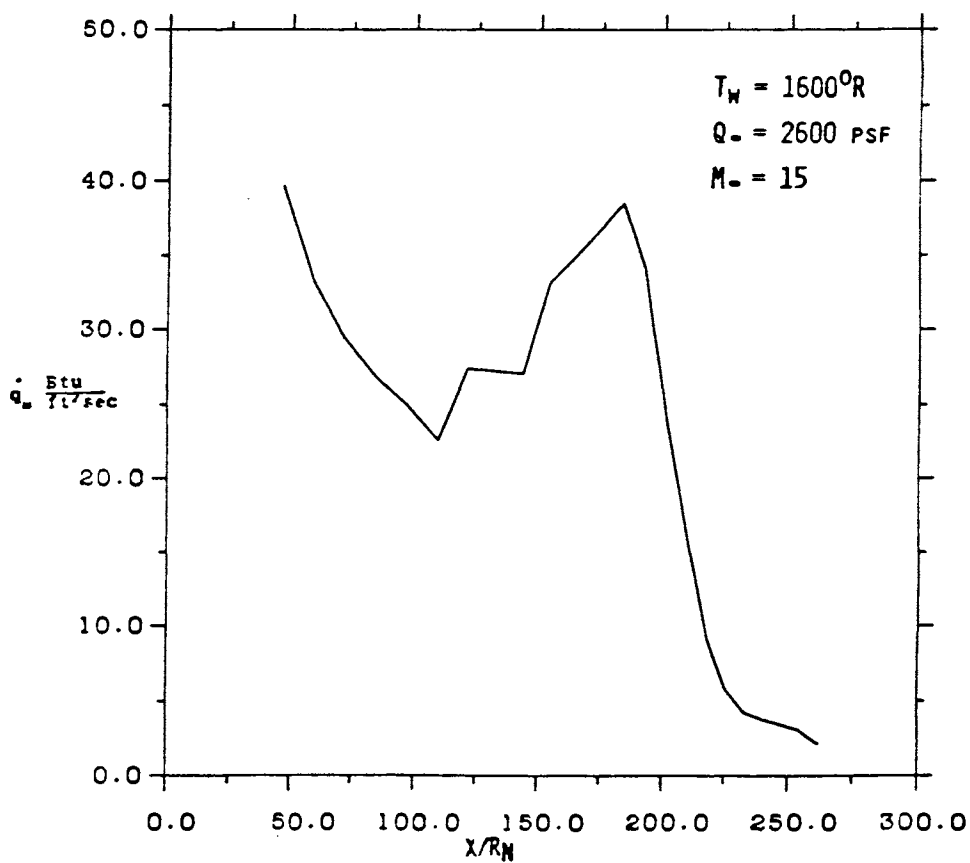


Figure A-61. RMS Pressure (A) and Sound Pressure Level (B) Distribution Along Windward Surface of BWB.



(A)



(B)

Figure A-62. Surface Pressure (A) and Heat Transfer (B) Distribution Along Windward Surface of BWB.

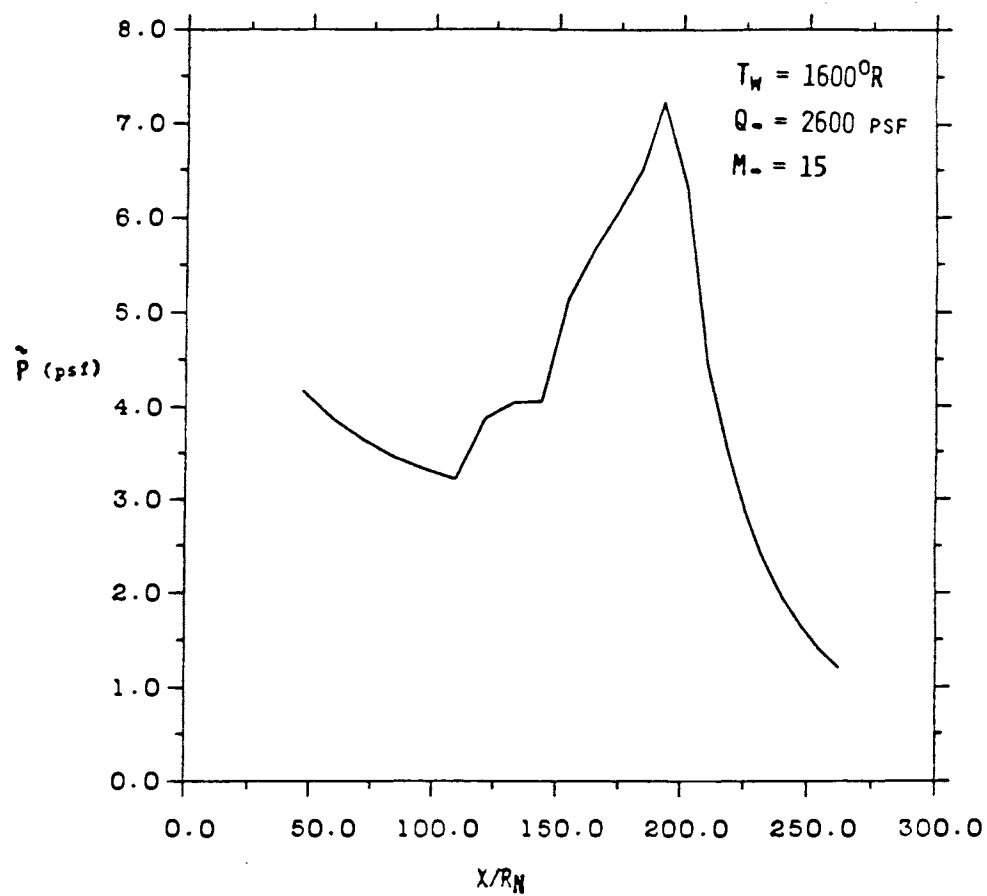


Figure A-63. RMS Fluctuating Pressure Distribution Along Windward Surface of BWB.

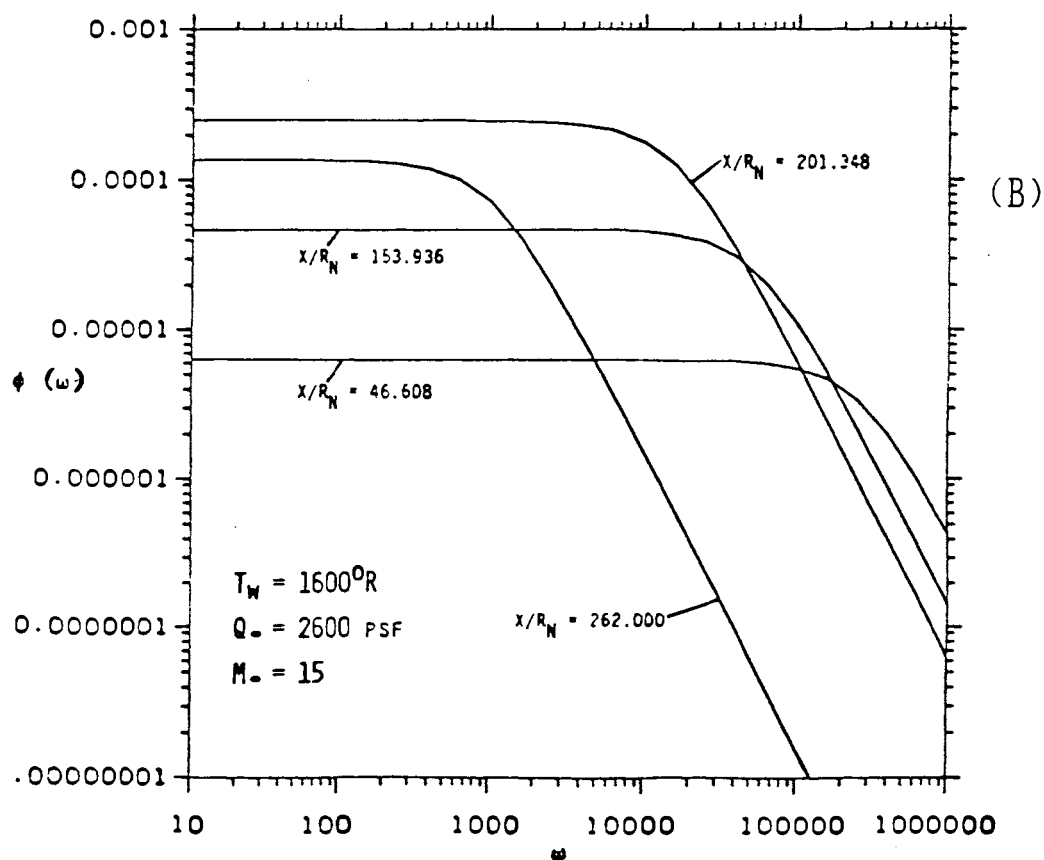
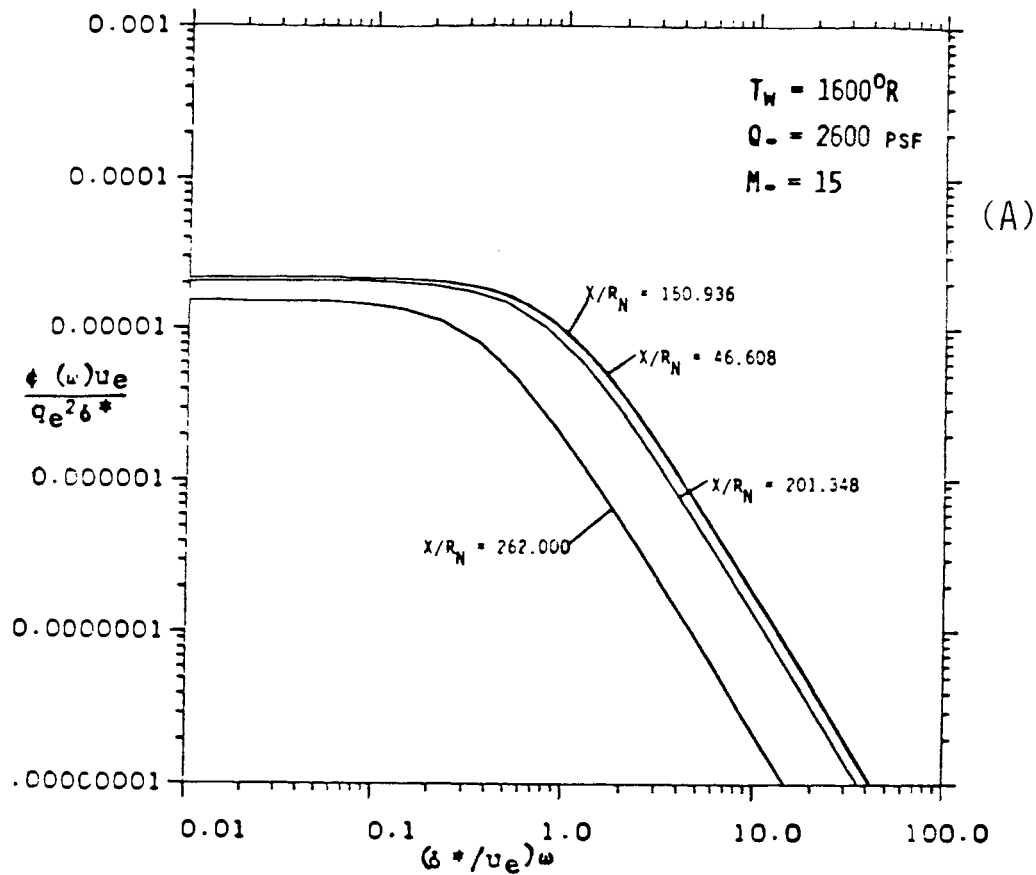


Figure A-64. Power Spectral Density Distribution Along Windward Surface of BWB (A) Normalized and (B) Power Spectra.

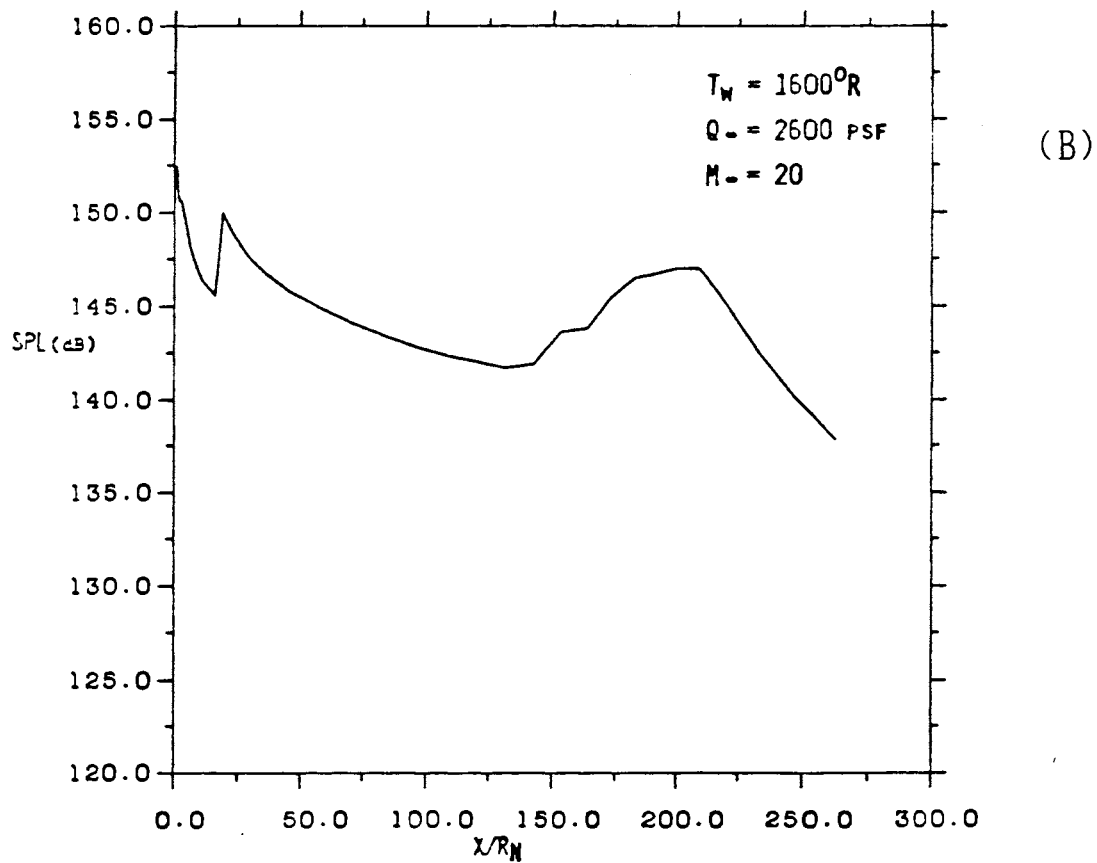
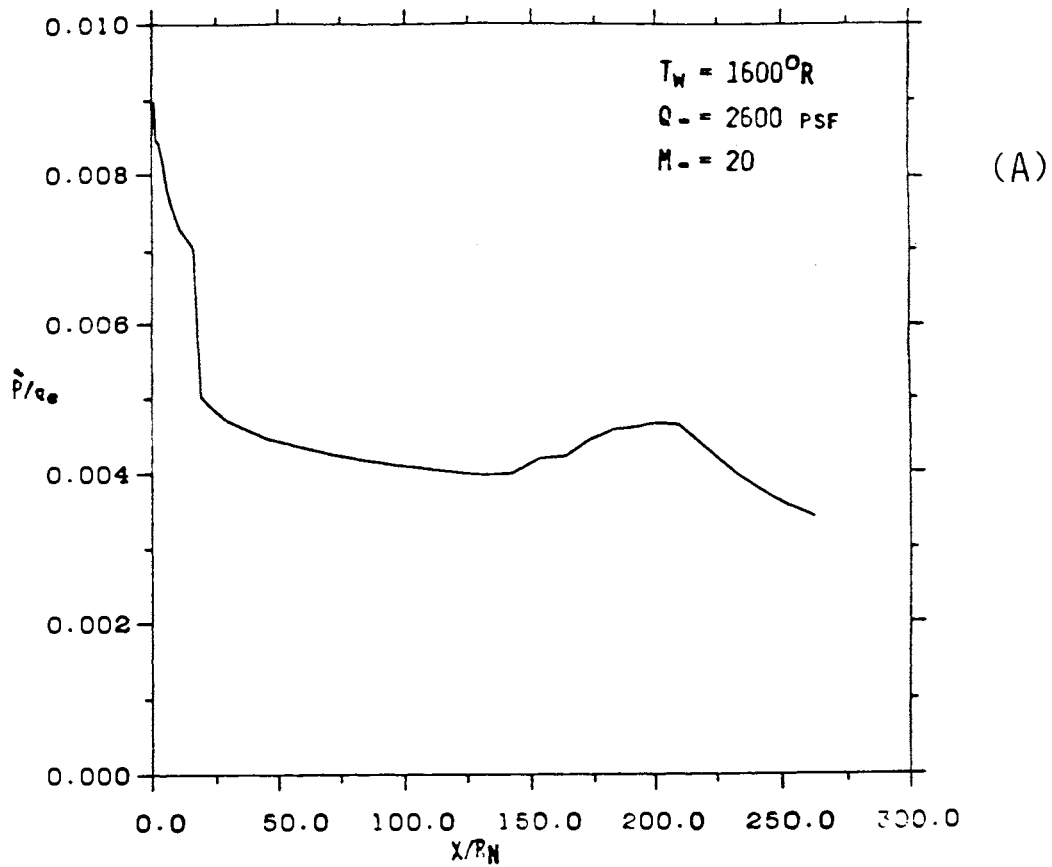


Figure A-65. RMS Pressure (A) and Sound Pressure Level (B) Distribution Along Windward Surface of BMB.

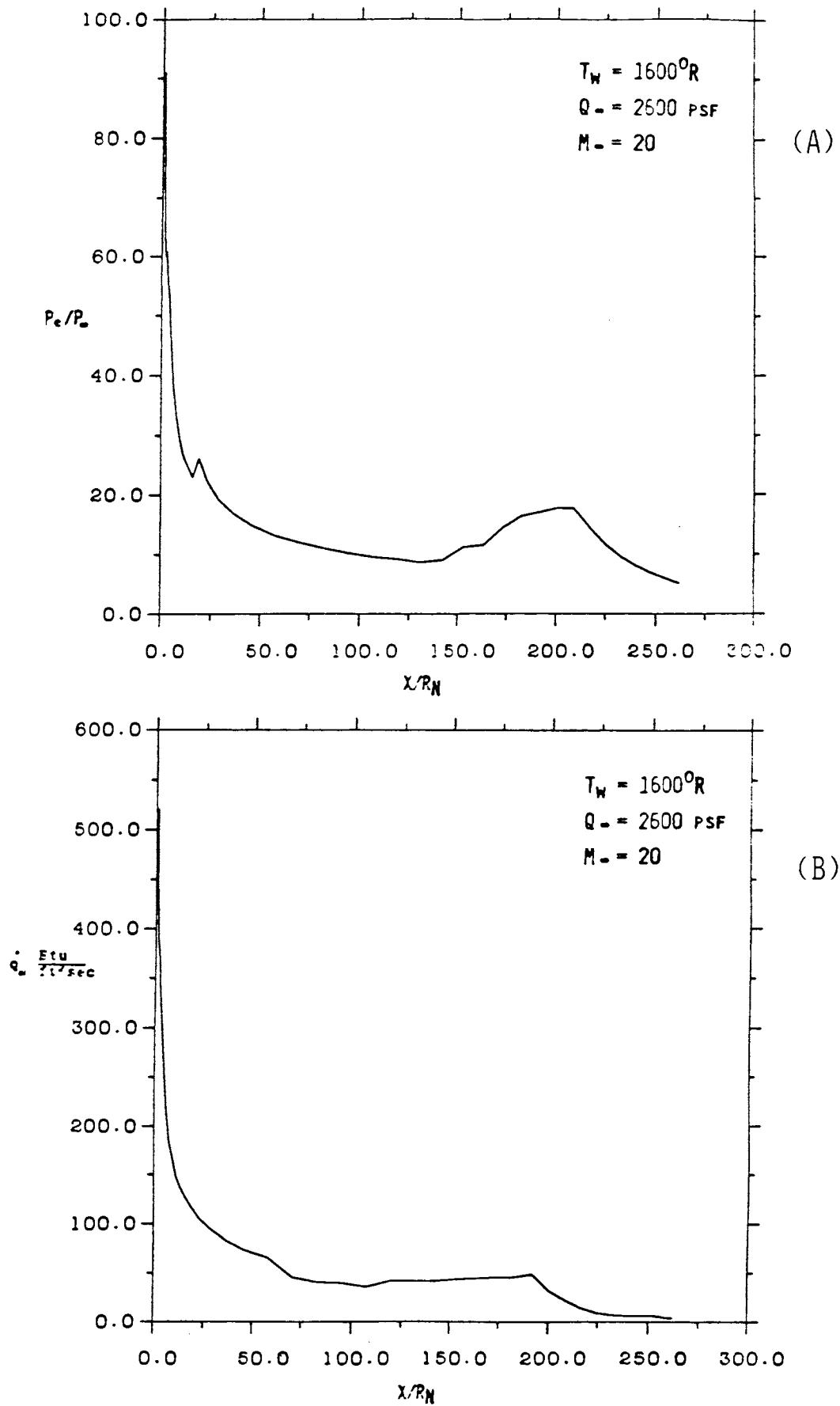


Figure A-66. Surface Pressure (A) and Heat Transfer (B) Distribution Along Windward Surface of BNW.

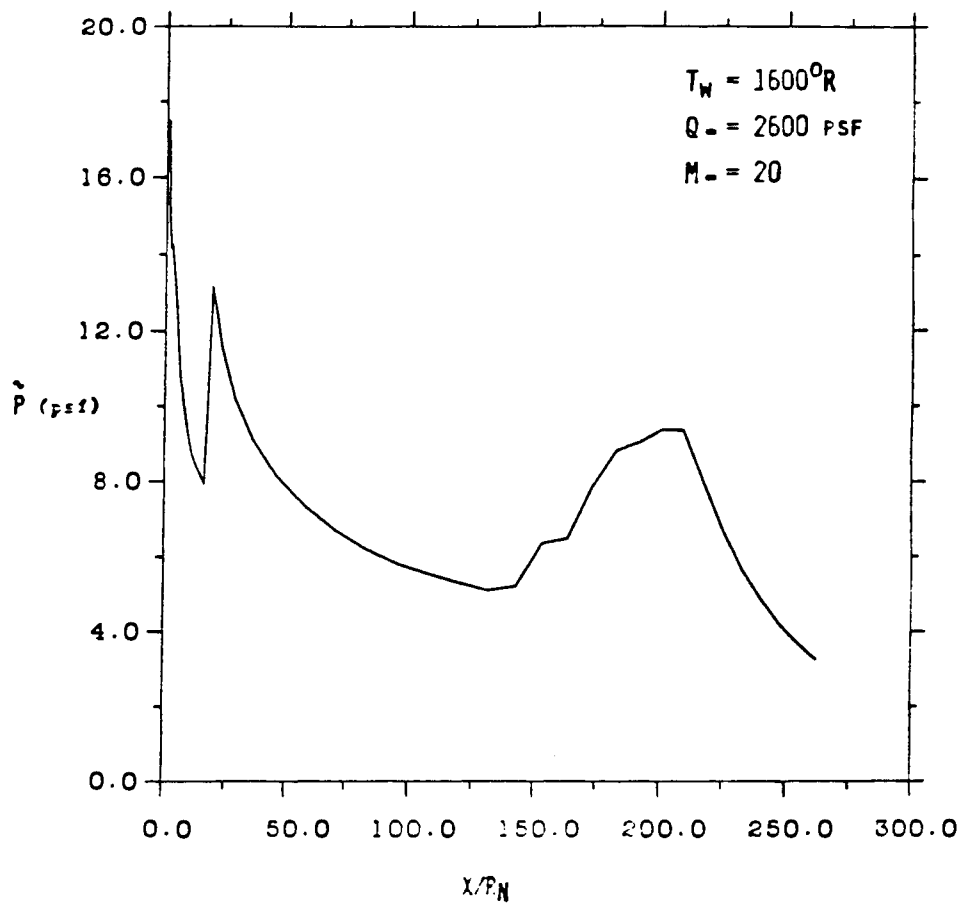


Figure A-67. RMS Fluctuating Pressure Distribution Along Windward Surface of BWB.

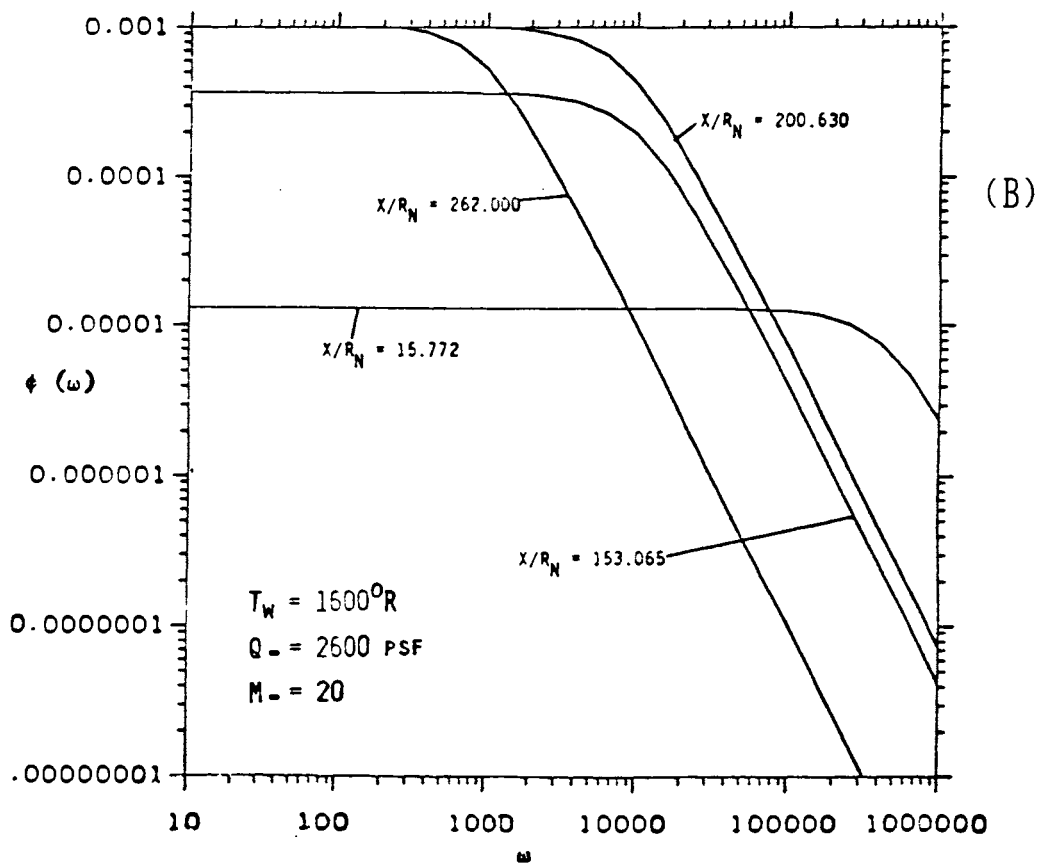
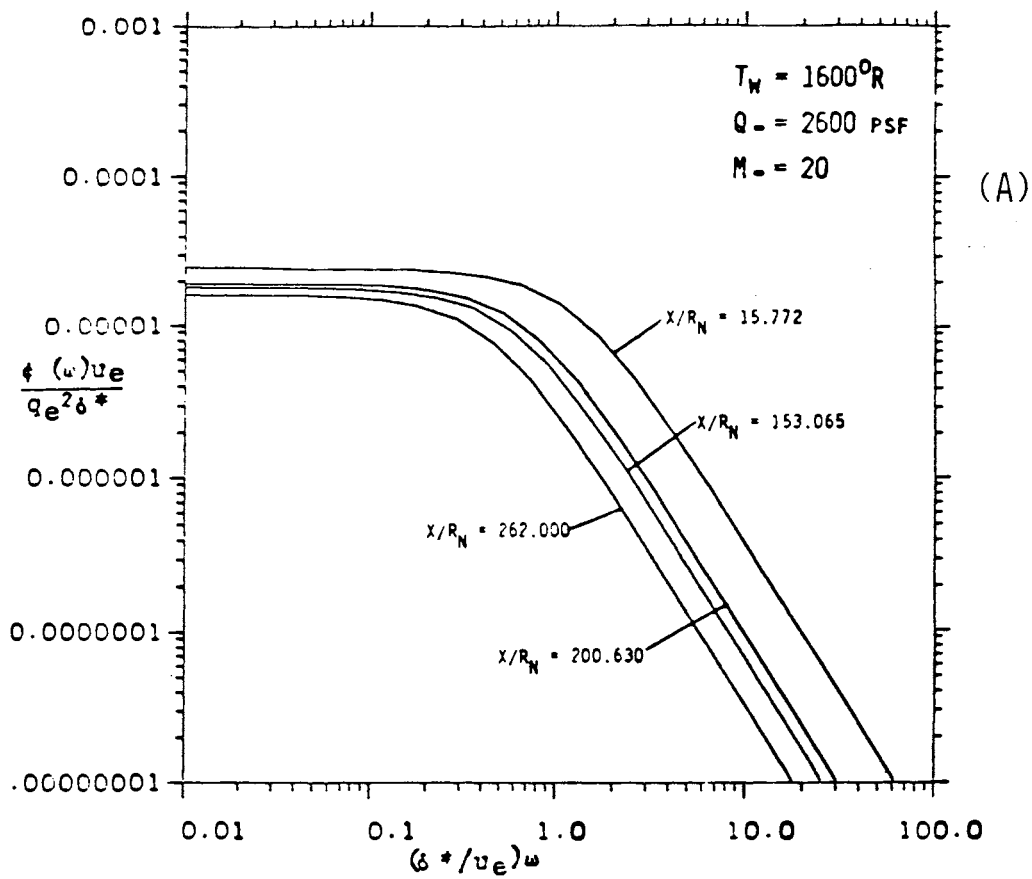
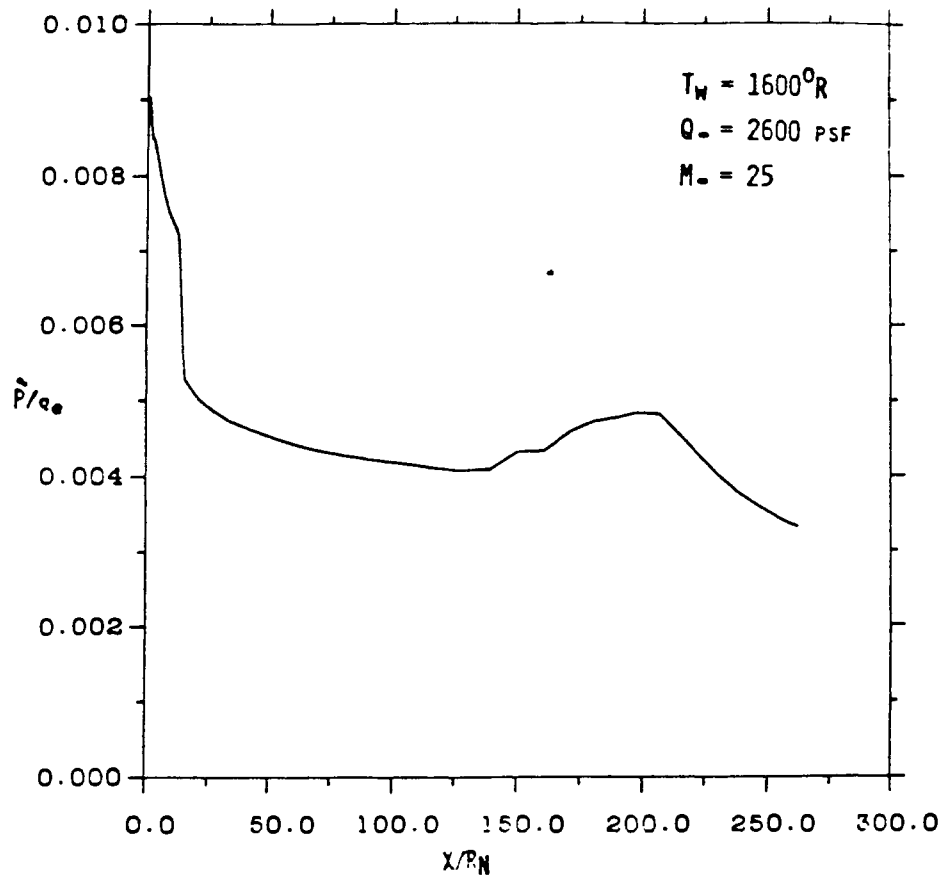
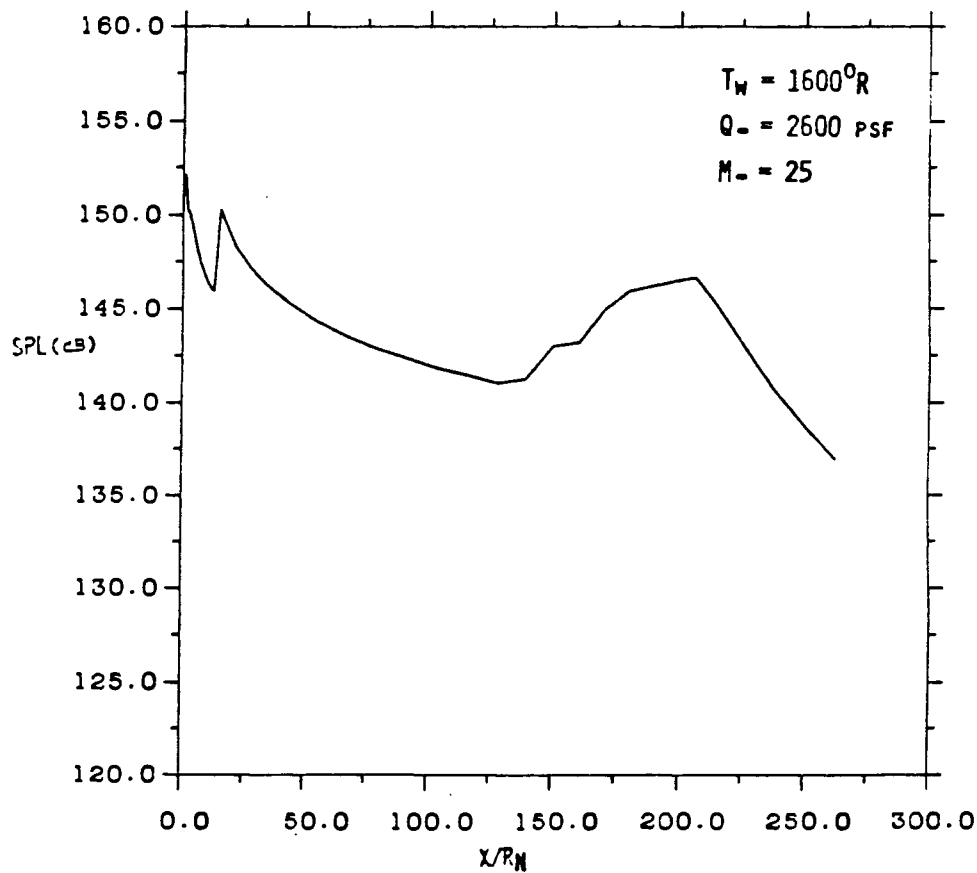


Figure A-68. Power Spectral Density Distribution Along Windward Surface of BWB (A) Normalized and (B) Power Spectra.

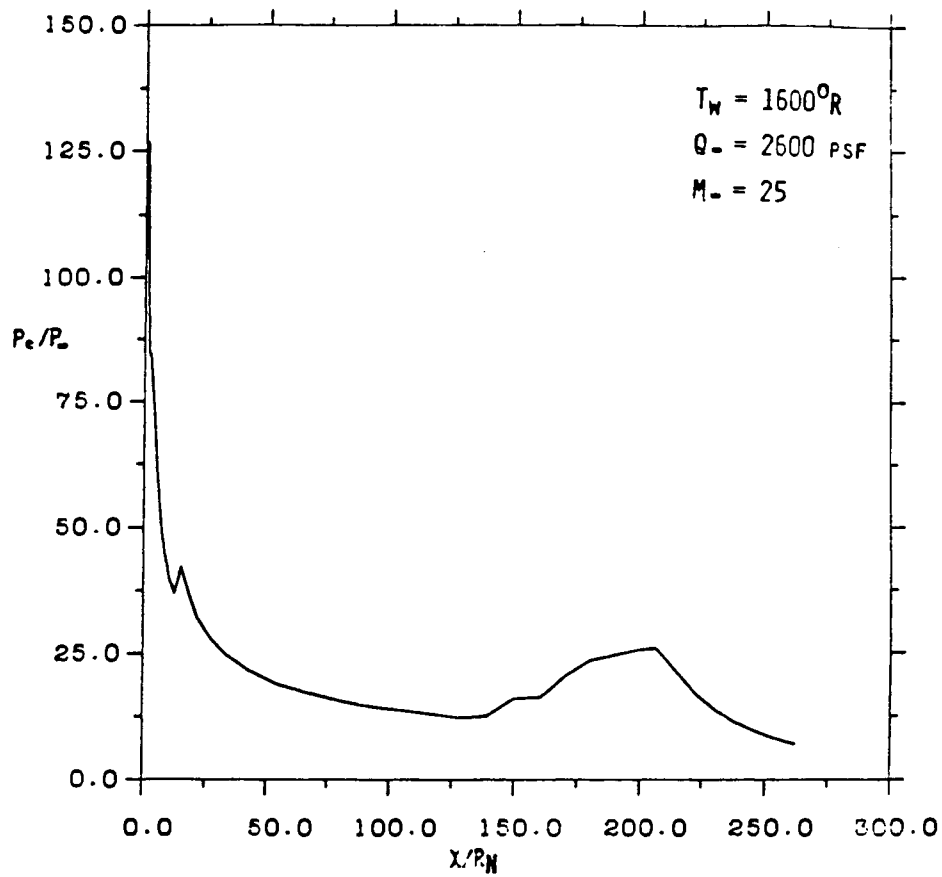


(A)

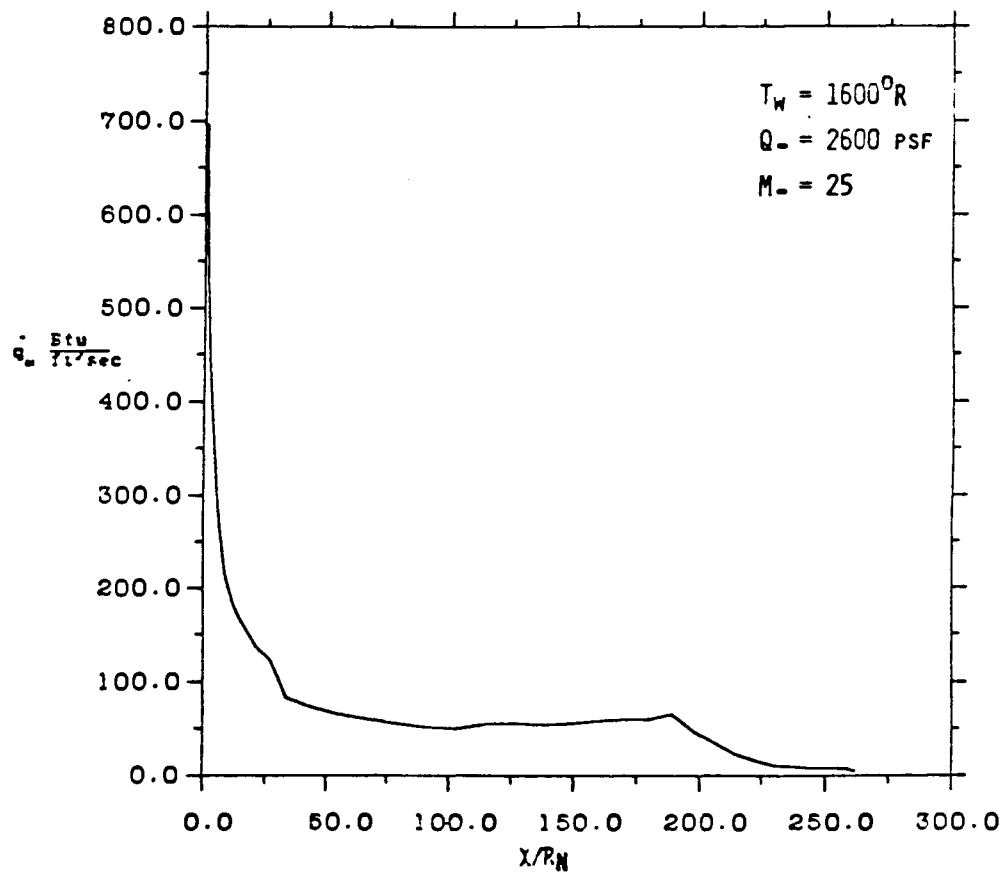


(B)

Figure A-69. RMS Pressure (A) and Sound Pressure Level (B) Distribution Along Windward Surface of BMB.



(A)



(B)

Figure A-70. Surface Pressure (A) and Heat Transfer (B) Distribution Along Windward Surface of BWB.

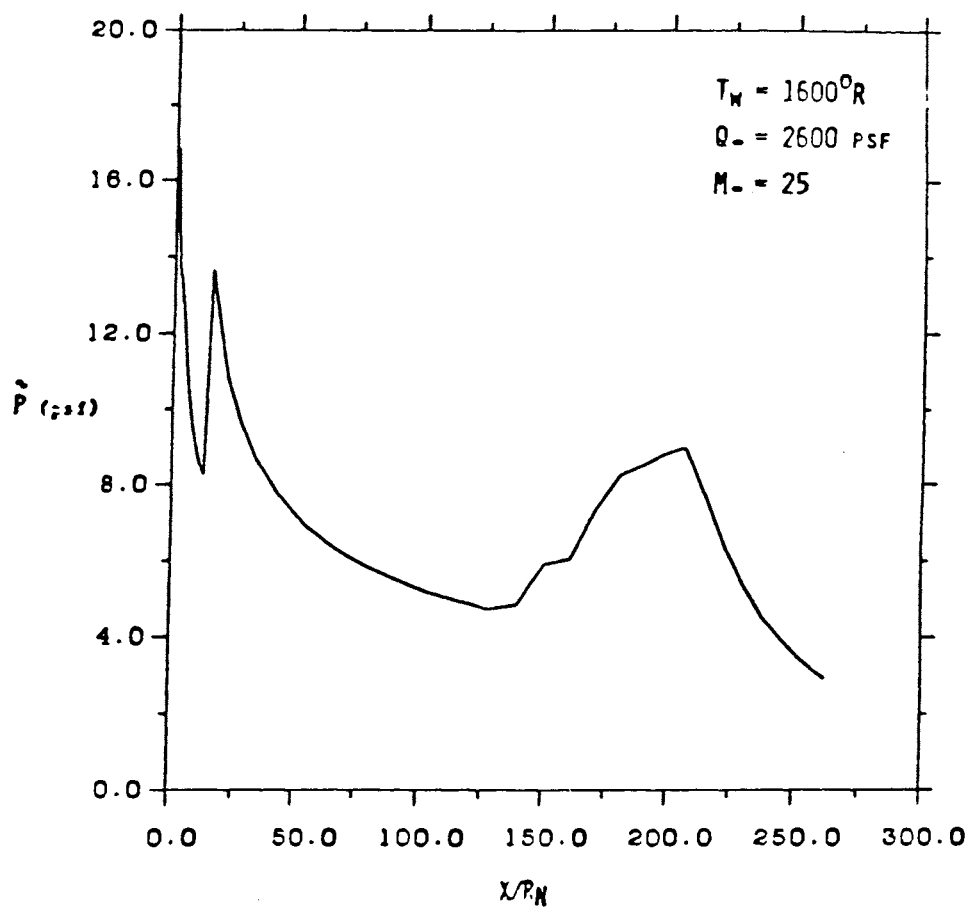
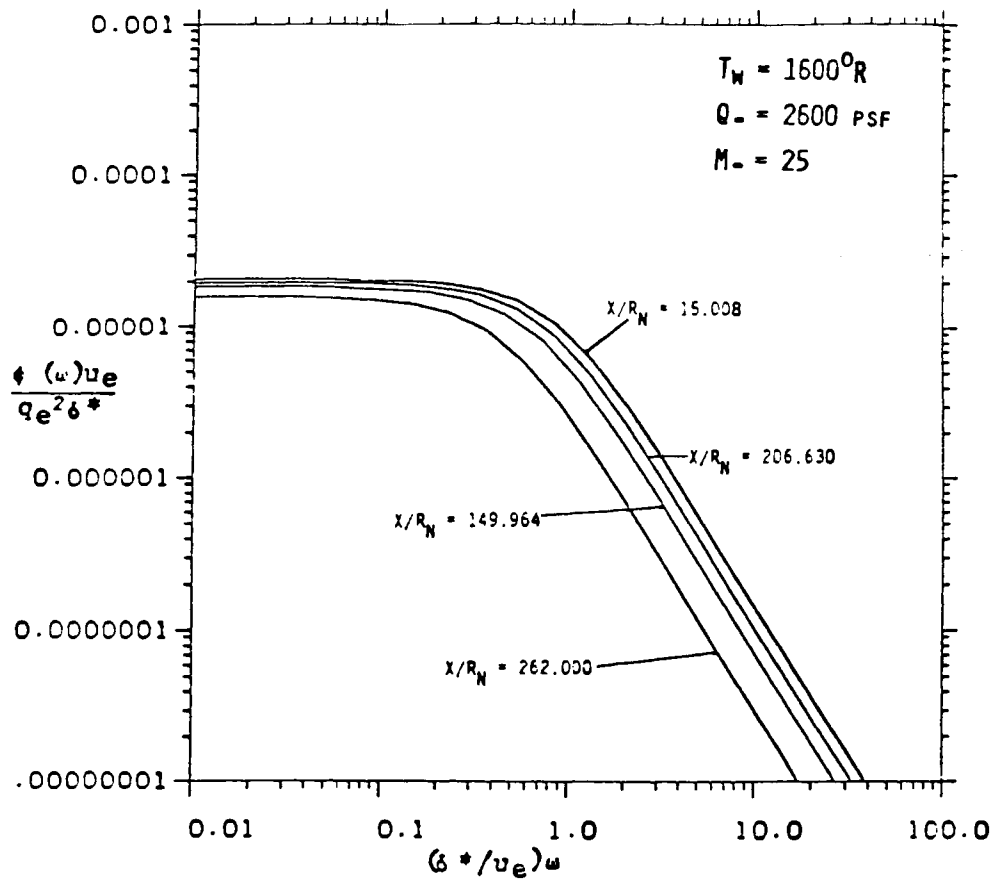
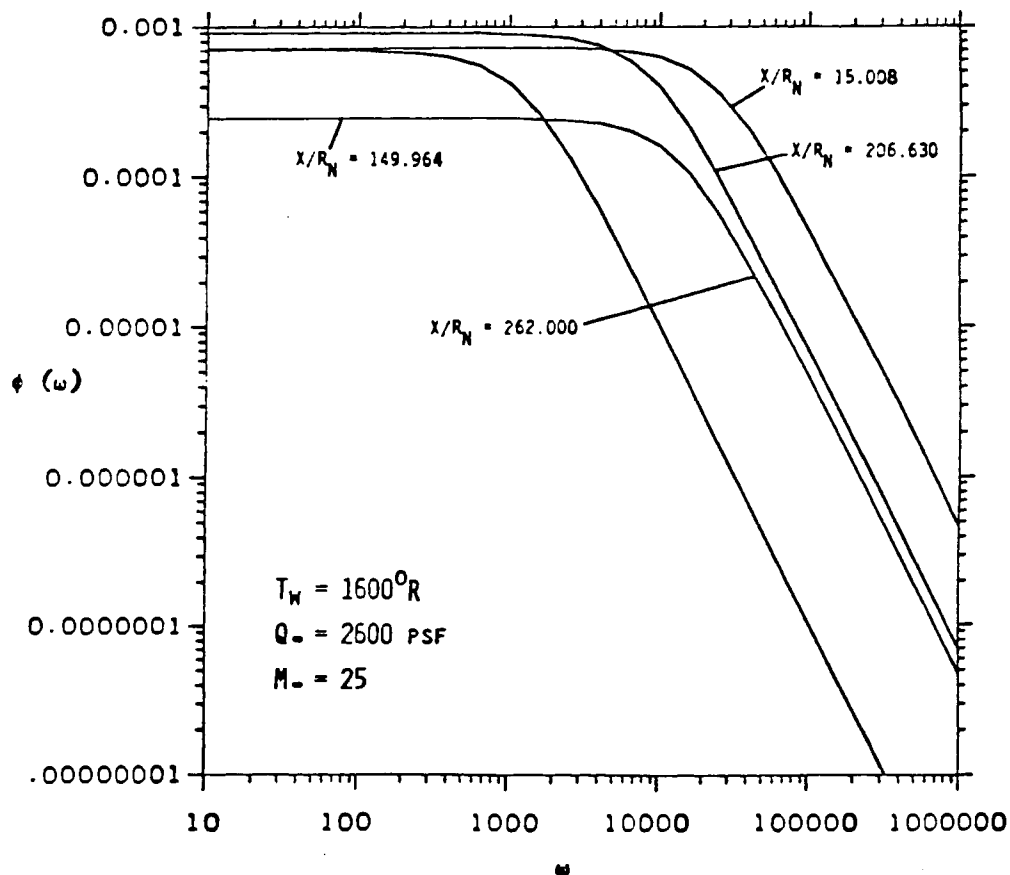


Figure A-71. RMS Fluctuating Pressure Distribution Along Windward Surface of BWB.



(A)



(B)

Figure A-72. Power Spectral Density Distribution Along Windward Surface of BWB (A) Normalized and (B) Power Spectra.

APPENDIX B

ENGINE ACOUSTIC ANALYSIS SUPPORTING DATA

B.1 EFFECT OF ACOUSTIC NONLINEARITIES ON SOUND LEVEL PREDICTION

The overall power radiated by either a rocket engine or an engine exhaust is linearly related to the local fluid density (Reference [B-1]):

$$W_{OA} \propto \rho_o \frac{V_e^8}{C_o^5} \quad (B-1)$$

where ρ_o is the ambient density and V_e and C_o are the exhaust gas velocity and the local ambient speed of sound, respectively. The acoustic power is defined as the acoustic intensity integrated over a spherical surface. The acoustic intensity I is the average rate of flow of energy through a unit area. Thus, if p is the local acoustic pressure, then

$$I = \frac{p_o^2}{\rho_o C_o} = \frac{W_{OA}}{4\pi r^2} \quad (B-2)$$

or

$$p \propto \rho_o \frac{V_e^4}{C_o^2} \quad (B-3)$$

The local acoustic pressure thus is linearly related to the ambient density. In the atmosphere, the ambient density and the speed of sound change as a function of height h (Table B-1).

It is assumed that the same exhaust gas velocity exists at different altitudes. Then if an acoustic disturbance at sea level of magnitude 1 exists, that same acoustic source will have its magnitude changed. The results are shown in Table B-2. Note that due to the reduced density at the different altitudes, the resulting acoustic pressure will also be reduced. The ratio of the acoustic pressure is seen to be reduced by an amount very close to the reduction of the ambient atmospheric pressure. Hence, the magnitude of the acoustic pressure relative to the ambient pressure is seen to be a very slowly varying function. The effect of varying altitude is thus seen to be of the order of ± 5 dB. The nonlinearities, if important, will thus be evident at all altitudes. For simplicity, sea level conditions were considered.

Table B-3 shows the fraction of the ambient pressure as a function of the sound level. Note that a sound level of 174 dB introduces an acoustic disturbance equal to 10% of the ambient pressure, while a sound level of 154 dB is required in order to have pressure perturbations of less than 1%.

The effect of acoustic nonlinearities must be considered whenever the overall acoustic pressure exceeds more than a few percent of the ambient pressure. The nonlinearities can introduce more frequencies in the system (i.e., sum and/or difference of frequencies) or may, under certain conditions, cause a structure to vibrate in a chaotic manner.

Table B-1. Properties of Standard Atmosphere.

h (ft)	ρ_o (kg/m ³)	C_o (m/sec)
0	1.24	335
50,000	1.86×10^{-1}	291
100,000	1.70×10^{-2}	291
150,000	1.54×10^{-3}	352
200,000	3.20×10^{-4}	366

Table B-2. Comparison of Acoustic Pressure and Ambient Pressure.

h (ft)	$P_{\text{acoustic}}/P_{\text{reference}}$	$P_{\text{atmospheric}}/P_{\text{sea level}}$	$P_{\text{acoustic}}/P_{\text{atmospheric}}$
0	1	1	1
50,000	1.99×10^{-1}	1.14×10^{-1}	1.75 (4.9 dB)
100,000	1.81×10^{-2}	1.06×10^{-2}	1.71 (4.7 dB)
150,000	1.12×10^{-3}	1.42×10^{-3}	0.79 (-2.0 dB)
200,000	2.16×10^{-4}	3.12×10^{-4}	0.69 (-3.2 dB)

Table B-3. Acoustic Pressure Ratio as a Function of Overall Sound Level.

Sound Level (dB)	$P_{\text{acoustic}}/P_{\text{ambient}}$
194	1
184	0.32
174	0.10
164	0.032
154	0.01

838PROP
3-TB-1.BB
11-11-89

B.2 SUPPORTING DATA

B.2.1 Sample Analysis from Reference [B-2]

- (1) Overall acoustic power W_{OA} is given by

$$W_{OA} = 0.005FU_e$$

$$F = \text{total thrust} = 9 \times 10^5 \text{ N}$$

$$U_e = \text{exit velocity} = 6100 \text{ m/sec}$$

$$W_{OA} = 2.75 \times 10^7 \text{ watts}$$

- (2) Overall sound power level is given by

$$\begin{aligned} L_W &= 10 \log_{10} W_{OA} + 120 \\ &= 194 \text{ dB (Ref } 10^{-12} \text{ watts)} \end{aligned}$$

- (3) Effective exit-nozzle diameter is

$$d_e = \sqrt{n} d_{ei} = 80 (0.05) = 0.45 \text{ m}$$

- (4) From Figure 3-1, the power spectrum in the octave frequency band with the center frequency of 125 Hz is obtained. Strouhal number is 0.009.

$$\begin{aligned} L_{W,b} &= 10 \log_{10} \left[\frac{W(f)}{W_{OA}} \frac{U_e}{d_e} \right] + L_W - 10 \log_{10} \frac{U_e}{d_e} + 10 \log_{10} 88 \\ &= 9 + 194 - 10 \log_{10} \left(\frac{6100}{0.45} \right) + 10 \log_{10} 88 \\ &= 9 + 194 - 41.3 + 19.4 = 181.1 \text{ dB} \end{aligned}$$

- (5) From Figure 3-2, at a frequency of 125 Hz, the apparent source is located at about $26 d_e$ from the nozzle.
- (6) Location 2 corresponds to an angle of about 90 degrees with respect to flow direction. From Figure 3-3, at the center frequency of 125 Hz, a directivity index of

$$DI = -5.5 \text{ dB}$$

is obtained.

- (7) The sound pressure level at location 2 is then given by

$$SPL_2 = L_{w,b} - 10 \log_{10} r^2 - 11 + D$$

where r is the distance from the apparent location of the sound source to point 2 on the vehicle,

$$r = \sqrt{[26(0.45)-2]^2 + (4.5)^2} = 10.7 \text{ m}$$

$$\begin{aligned} SPL_2 &= 181.1 - 10 \log_{10} (10.7)^2 - 11 - 5.5 \\ &= 144 \text{ dB} \end{aligned}$$

- (8) In evaluating the sound pressure level on the vehicle lower surface, complete reflection from the ground has been assumed with a corresponding longer path.

B.2.2 Conversion to One-Third Octave Band

In order to convert from the octave band levels to the one-third octave band, the following formula is used:

$$SPL_{1/3} = SPL_o - 10 \log_{10} \frac{f_o}{f_{1/3}}$$

where f_o and $f_{1/3}$ are the octave and the one-third octave bandwidths, respectively. In general,

$$\Delta f = \left(\frac{2^n - 1}{2^{n/2}} \right) f$$

where n is equal to unity for the octave band and is equal to one third for the one-third octave band. Thus,

$$SPL_{1/3} = SPL_o = 4.85$$

This final equation is valid at all frequencies.

B.3 REFERENCES

B-1 Goldstein, M.E., Aeroacoustics, McGraw-hill, 1976.

B-2 Acoustic Loads Generated by the Propulsion System, NASA SP-8072, June 1971.

838PROP
3-B.BB
11-11-89

APPENDIX C
FINITE ELEMENT ACTIVELY COOLED PANEL RESULTS

838PROP
3-C.BB
11-11-89

C-1

PANEL 1 GEOMETRIC AND MATERIAL PROPERTIES

FACE SHEET:

THICKNESS (IN) 0.016
SEPARATION (IN) 0.75
SPAN (IN) 48.0

HONEY COMB:

DENSITY (lb/ft**3) 5.8009
(lb/in**3) 0.003357

THERMAL GRADIENT (180 BTU/FT2) AND ASSOCIATED FACESHEET PROPERTIES:**

	T(F)	DENSITY (lb/in**3)	E1,E2 (psi)	ALPHA (in/in/F)	NU
Tref	70	0.145	2.444E+7	3.23E-6	0.25920
OUTER F/S - OUTER SURFACE	721	0.145	1.974E+7	3.73E-6	0.20752
OUTER F/S - INNER SURFACE	583	0.145	2.074E+7	3.62E-6	0.21848
OUTER F/S - AVERAGE TEMP	652	0.145	2.024E+7	3.68E-6	0.21300
INNER F/S - AVERAGE TEMP	224	0.145	2.333E+7	3.35E-6	0.24698

RESULTING FACE SHEET THERMAL STRESSES:

	TOTAL (psi)
OUTER F/S - OUTER SURFACE	-28449
- INNER SURFACE	-17247
INNER F/S - BOTH SURFACES	22848

Figure C-1

F.E.M. THERMOMECHANICAL RUNNING LOADS ON PANEL 1:

CASE		Nx lb/in	Ny lb/in	Nxy lb/in	Mx in-lb/in	My in-lb/in	Mxy in-lb/in	SAFETY FACTOR INCLUDED
1	MCH	-55	-69	-52	-8	-19	-1	1.5
	THM	-192	-53	13	-6	-5	1	1.0
2	MCH	1258	178	-238	141	-110	-37	1.5
	THM	-95	-41	11	0	0	1	1.0
3	MCH	-29	60	71	40	79	11	1.5
	THM	155	41	19	0	0	0	1.0
4	MCH	-212	-49	70	46	76	-13	1.5
	THM	155	41	19	0	0	0	1.0
5	MCH	-274	78	190	64	137	16	1.5
	THM	345	29	44	10	0	0	1.0
6	MCH	-456	-69	187	68	133	17	1.5
	THM	345	29	44	10	0	0	1.0
7	MCH	395	-38	-42	43	-127	-19	1.5
	THM	523	165	-4	19	-12	-2	1.0
8	MCH	273	-150	-51	46	130	-21	1.5
	THM	523	165	-4	19	-12	-2	1.0
9	MCH	813	-104	-212	45	-167	-26	1.5
	THM	299	151	-33	12	13	-2	1.0
10	MCH	791	-112	-196	48	-163	-26	1.5
	THM	299	151	-33	12	13	-2	1.0
11	MCH	424	-54	-110	24	-87	-13	1.5
	THM	169	231	-61	-7	16	-3	1.0
12	MCH	412	-59	-102	25	-85	-14	1.5
	THM	169	231	-61	-7	16	-3	1.0
13	MCH	158	-15	-17	17	-51	-8	1.5
	THM	-273	32	-25	-10	11	-1	1.0
14	MCH	109	-60	-20	19	52	-8	1.5
	THM	-273	32	-25	-10	11	-1	1.0

POSITIVE LOADS SIGN CONVENTION:

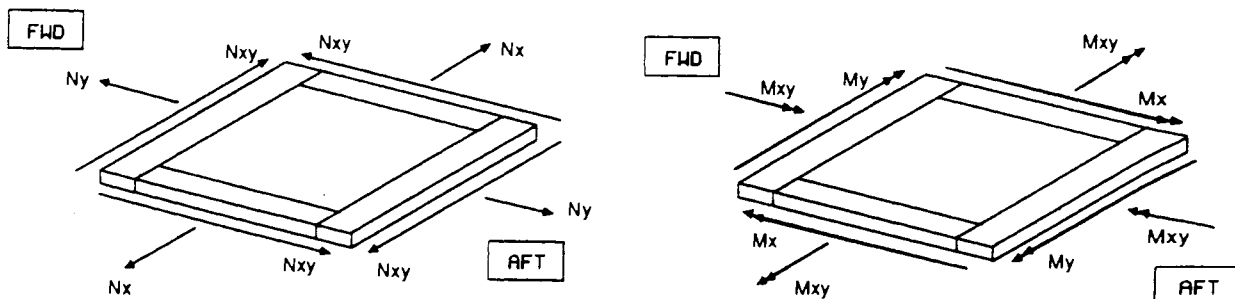


Figure C-2

PANEL 1
ACOUSTIC LEVEL - RMS STRESS

MATERIAL PROPERTIES FOR ACOUSTIC SCREENING:

FACESHEET:

E (psi) 2.178E+7
NU 0.23
RHO (lb/in**3) 0.145

HONEYCOMB:

RHO (lb/in**3) 0.003357

CRITICAL DAMPING FACTOR 0.02

APPROXIMATED PANEL FREQ FOR SCREENING (HZ)

192

STATIC STRESS DUE TO UNIFORM UNIT NORMAL PRESSURE (psi)

9849.6

CASE	PHI	STRESS
	psi sq/Hz	psi rms
1	2.867E-3	45806
2	6.417E-5	6853
3	3.804E-6	1669
4	3.804E-6	1669
5	8.878E-6	2549
6	8.878E-6	2549
7	2.748E-5	4485
8	2.748E-5	4485
9	1.329E-5	3119
10	1.329E-5	3119
11	0	0
12	0	0
13	0	0
14	0	0

Figure C-3

PANEL 2 GEOMETRIC AND MATERIAL PROPERTIES

FACE SHEET:

THICKNESS (IN) 0.016
SEPARATION (IN) 1.00
SPAN (IN) 48.0

HONEY COMB:

DENSITY (lb/ft**3) 9.6681
(lb/in**3) 0.005595

THERMAL GRADIENT (180 BTU/FT2-SEC) AND ASSOCIATED FACESHEET PROPERTIES:**

	T(F)	DENSITY (lb/in**3)	E1,E2 (psi)	ALPHA (in/in/F)	NU
Tref	70	0.145	2.444E+7	3.23E-6	0.25920
OUTER F/S - OUTER SURFACE	721	0.145	1.974E+7	3.73E-6	0.20752
OUTER F/S - INNER SURFACE	583	0.145	2.074E+7	3.62E-6	0.21848
OUTER F/S - AVERAGE TEMP	652	0.145	2.024E+7	3.68E-6	0.21300
INNER F/S - AVERAGE TEMP	224	0.145	2.333E+7	3.35E-6	0.24698

RESULTING FACE SHEET THERMAL STRESSES:

	TOTAL (psi)
OUTER F/S - OUTER SURFACE	-28449
- INNER SURFACE	-17247
INNER F/S - BOTH SURFACES	22848

Figure C-4

F.E.M. THERMOMECHANICAL RUNNING LOADS ON PANEL 2:

CASE		Nx lb/in	Ny lb/in	Nxy lb/in	Mx in-lb/in	My in-lb/in	Mxy in-lb/in	SAFETY FACTOR INCLUDED
1	MCH	197	280	-115	843	-841	7	1.5
	THM	-220	-153	-17	-9	-8	0	1.0
2	MCH	1888	873	114	973	-925	-53	1.5
	THM	-85	-90	-6	0	0	0	1.0
3	MCH	1148	144	-194	-1039	907	-17	1.5
	THM	35	-56	19	0	0	0	1.0
4	MCH	-238	-464	-78	-962	851	-35	1.5
	THM	35	-56	19	0	0	0	1.0
5	MCH	1222	326	-241	-931	899	-26	1.5
	THM	149	-70	38	9	8	0	1.0
6	MCH	101	-351	-109	-946	-845	-19	1.5
	THM	149	-70	38	9	8	0	1.0
7	MCH	953	245	-139	904	962	-12	1.5
	THM	469	200	51	14	18	7	1.0
8	MCH	84	-103	83	980	932	-9	1.5
	THM	469	200	51	14	18	7	1.0
9	MCH	575	369	185	1018	974	-23	1.5
	THM	355	112	-35	16	12	0	1.0
10	MCH	327	105	121	1023	968	-19	1.5
	THM	355	112	-35	16	12	0	1.0
11	MCH	300	192	96	100	77	-12	1.5
	THM	262	92	-42	-34	8	0	1.0
12	MCH	170	55	63	103	74	-10	1.5
	THM	262	92	-42	-34	8	0	1.0
13	MCH	382	98	-56	31	54	0	1.5
	THM	-198	-719	-108	10	19	0	1.0
14	MCH	34	-41	33	62	42	0	1.5
	THM	-198	-719	-108	10	19	0	1.0

POSITIVE LOADS SIGN CONVENTION:

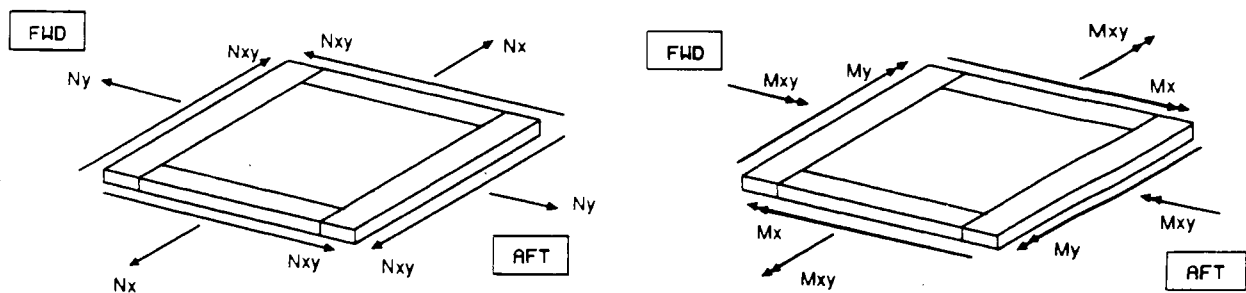


Figure C-5

PANEL 2
ACOUSTIC LEVEL - RMS STRESS

MATERIAL PROPERTIES FOR ACOUSTIC SCREENING:

FACESHEET:		HONEYCOMB:	
E (psi)	2.178E+7	RHO (lb/in**3)	0.005595
NU	0.23		
RHO (lb/in**3)	0.145		

CRITICAL DAMPING FACTOR 0.02

APPROXIMATED PANEL FREQ FOR SCREENING (HZ)	214
STATIC STRESS DUE TO UNIFORM UNIT NORMAL PRESSURE (psi)	7387.2

CASE	PHI	STRESS
	psi sq/Hz	psi rms
1	2.867E-3	36276
2	6.417E-5	5427
3	3.804E-6	1321
4	3.804E-6	1321
5	8.878E-6	2019
6	8.878E-6	2019
7	2.748E-5	3552
8	2.748E-5	3552
9	1.329E-5	2470
10	1.329E-5	2470
11	0	0
12	0	0
13	0	0
14	0	0

Figure C-6

PANEL 1 STRESSES:

CASE	LOADING	OUTER FACESHEET						INNER FACESHEET		
		UPPER SURFACE			INNER SURFACE			INNER & OUTER SURFACE		
		Sx (psi)	Sy (psi)	Txy (psi)	Sx (psi)	Sy (psi)	Txy (psi)	Sx (psi)	Sy (psi)	Txy (psi)
	F/S THERMAL	-28449.1	-28449	0	-17247	-17247	0	22848	22848	0
1	MCH	-701	-382	-1028	-701	-382	-1028	-1590	-2493	-1139
	THM	-5500	-1240	323	-5500	-1240	323	-6500	-2073	490
	ACOUSTIC	45806	45806	0	45806	45806	0	45806	45806	0
2	MCH	18375	9819	-2903	18375	9819	-2903	34042	-2403	-7014
	THM	-2969	-1281	260	-2969	-1281	260	-2969	-1281	427
	ACOUSTIC	6853	6853	0	6853	6853	0	6853	6853	0
3	MCH	-2826	-3139	868	-2826	-3139	868	1618	5639	2090
	THM	4844	1281	594	4844	1281	594	4844	1281	594
	ACOUSTIC	1669	1669	0	1669	1669	0	1669	1669	0
4	MCH	-6972	-5243	2181	-6972	-5243	2181	-1861	3201	736
	THM	4844	1281	594	4844	1281	594	4844	1281	594
	ACOUSTIC	1669	1669	0	1669	1669	0	1669	1669	0
5	MCH	-9264	-5986	3069	-9264	-5986	3069	-2153	9236	4847
	THM	9948	906	1375	9948	906	1375	11615	906	1375
	ACOUSTIC	2549	2549	0	2549	2549	0	2549	2549	0
6	MCH	-13278	-8826	2951	-13278	-8826	2951	-5722	5951	4840
	THM	9948	906	1375	9948	906	1375	11615	906	1375
	ACOUSTIC	2549	2549	0	2549	2549	0	2549	2549	0
7	MCH	5840	6264	181	5840	6264	181	10618	-7847	-1931
	THM	14760	6156	42	14760	6156	42	17927	4156	-292
	ACOUSTIC	4485	4485	0	4485	4485	0	4485	4485	0
8	MCH	3132	-10347	104	3132	-10347	104	8243	4097	-2229
	THM	14760	6156	42	14760	6156	42	17927	4156	-292
	ACOUSTIC	4485	4485	0	4485	4485	0	4485	4485	0
9	MCH	14438	7111	-2972	14438	7111	-2972	19438	-11444	-5861
	THM	8344	3635	-865	8344	3635	-865	10344	5802	-1198
	ACOUSTIC	3119	3119	0	3119	3119	0	3119	3119	0
10	MCH	13813	6722	-2639	13813	6722	-2639	19146	-11389	-5528
	THM	8344	3635	-865	8344	3635	-865	10344	5802	-1198
	ACOUSTIC	3119	3119	0	3119	3119	0	3119	3119	0
11	MCH	7500	3708	-1569	7500	3708	-1569	10167	-5958	-3014
	THM	5865	5885	-1656	5865	5885	-1656	4698	8552	-2156
	ACOUSTIC	0	0	0	0	0	0	0	0	0
12	MCH	7194	3493	-1347	7194	3493	-1347	9972	-5951	-2903
	THM	5865	5885	-1656	5865	5885	-1656	4698	8552	-2156
	ACOUSTIC	0	0	0	0	0	0	0	0	0
13	MCH	2347	2521	90	2347	2521	90	4236	-3146	-799
	THM	-7698	83	-698	-7698	83	-698	-9365	1917	-865
	ACOUSTIC	0	0	0	0	0	0	0	0	0
14	MCH	1215	-4139	28	1215	-4139	28	3326	1639	-861
	THM	-7698	83	-698	-7698	83	-698	-9365	1917	-865
	ACOUSTIC	0	0	0	0	0	0	0	0	0

Figure C-7

PANEL 2 STRESSES:

CASE	LOADING	OUTER FACESHEET						INNER FACESHEET		
		UPPER SURFACE			INNER SURFACE			INNER & OUTER SURFACE		
		Sx (psi)	Sy (psi)	Txy (psi)	Sx (psi)	Sy (psi)	Txy (psi)	Sx (psi)	Sy (psi)	Txy (psi)
	F/S THERMAL	-28449	-28449	0	-17247	-17247	0	22848	22848	0
1	MCH	-31021	40875	-2688	-31021	40875	-2688	39229	-29208	-2104
	THM	-6313	-4281	-531	-6313	-4281	-531	-7438	-5281	-531
	ACOUSTIC	36276	36276	0	36276	36276	0	36276	36276	0
2	MCH	-1208	56729	4583	-1208	56729	4583	79875	-20354	167
	THM	-2656	-2813	-188	-2656	-2813	-188	-2656	-2813	-188
	ACOUSTIC	5427	5427	0	5427	5427	0	5427	5427	0
3	MCH	67208	-34792	-3333	67208	-34792	-3333	-19375	40792	-4750
	THM	1094	-1750	594	1094	-1750	594	1094	-1750	594
	ACOUSTIC	1321	1321	0	1321	1321	0	1321	1321	0
4	MCH	35125	-45125	-167	35125	-45125	-167	-45042	25792	-3083
	THM	1094	-1750	594	1094	-1750	594	1094	-1750	594
	ACOUSTIC	1321	1321	0	1321	1321	0	1321	1321	0
5	MCH	64250	-30667	-3938	64250	-30667	-3938	-13333	44250	-6104
	THM	4094	-2688	1188	4094	-2688	1188	5219	-1688	1188
	ACOUSTIC	2019	2019	0	2019	2019	0	2019	2019	0
6	MCH	41521	27896	-1479	41521	27896	-1479	-37313	-42521	-3063
	THM	4094	-2688	1188	4094	-2688	1188	5219	-1688	1188
	ACOUSTIC	2019	2019	0	2019	2019	0	2019	2019	0
7	MCH	-17813	-34979	-2396	-17813	-34979	-2396	57521	45188	-3396
	THM	13781	5125	1156	13781	5125	1156	15531	7375	2031
	ACOUSTIC	3552	3552	0	3552	3552	0	3552	3552	0
8	MCH	-39083	-40979	2104	-39083	-40979	2104	42583	36688	1354
	THM	13781	5125	1156	13781	5125	1156	15531	7375	2031
	ACOUSTIC	3552	3552	0	3552	3552	0	3552	3552	0
9	MCH	-30438	-32896	4813	-30438	-32896	4813	54396	48271	2896
	THM	10094	2750	-1094	10094	2750	-1094	12094	4250	-1094
	ACOUSTIC	2470	2470	0	2470	2470	0	2470	2470	0
10	MCH	-35813	-38146	3313	-35813	-38146	3313	49438	42521	1729
	THM	10094	2750	-1094	10094	2750	-1094	12094	4250	-1094
	ACOUSTIC	2470	2470	0	2470	2470	0	2470	2470	0
11	MCH	2083	792	2500	2083	792	2500	10417	7208	1500
	THM	10313	2375	-1313	10313	2375	-1313	6063	3375	-1313
	ACOUSTIC	0	0	0	0	0	0	0	0	0
12	MCH	-750	-1938	1729	-750	-1938	1729	7833	4229	896
	THM	10313	2375	-1313	10313	2375	-1313	6063	3375	-1313
	ACOUSTIC	0	0	0	0	0	0	0	0	0
13	MCH	6667	-208	-1167	6667	-208	-1167	9250	4292	-1167
	THM	-6813	-23656	-3375	-6813	-23656	-3375	-5563	-21281	-3375
	ACOUSTIC	0	0	0	0	0	0	0	0	0
14	MCH	-1875	-2604	688	-1875	-2604	688	3292	896	688
	THM	-6813	-23656	-3375	-6813	-23656	-3375	-5563	-21281	-3375
	ACOUSTIC	0	0	0	0	0	0	0	0	0

Figure C-8

PANEL 1 FATIGUE CRITICAL SCREENING:

$S_a/(CN^{**b}) + S_m/C = 1$
 S_a = ACOUSTIC RMS STRESS (psi)
 S_m = MEAN OR STATIC STRESS (psi)
 CN^{**b} = S from S/UTS vs cycles to failure (psi)
 C = ultimate tensile strength (UTS or FTu) (psi)

S/UTS 0.11

	OUTER FACESHEET			INNER FACESHEET		
	UPPER SURFACE		INNER SURFACE	INNER & OUTER SURFACE		
	Sx (psi)	Sy (psi)	Txy (psi)	Sx (psi)	Sy (psi)	Txy (psi)
FTu	122256	122256		125508	125508	
CN ^{**b}	13448	13448		13806	13806	

THE FOLLOWING IS $ABS(S_a/(CN^{**b})) + ABS(S_m/C)$:

CASE						
1	3.69	3.65	3.50	3.47	3.22	3.24
2	0.62	0.67	0.51	0.57	0.87	0.61
3	0.34	0.37	0.24	0.27	0.33	0.34
4	0.37	0.39	0.28	0.29	0.31	0.32
5	0.42	0.46	0.32	0.36	0.41	0.42
6	0.45	0.49	0.35	0.39	0.39	0.39
7	0.40	0.46	0.35	0.36	0.69	0.45
8	0.42	0.60	0.33	0.50	0.67	0.54
9	0.28	0.38	0.27	0.28	0.60	0.34
10	0.28	0.38	0.27	0.28	0.60	0.34
11	0.12	0.15	0.03	0.06	0.28	0.19
12	0.13	0.16	0.03	0.06	0.28	0.19
13	0.28	0.21	0.18	0.12	0.13	0.16
14	0.29	0.27	0.19	0.17	0.13	0.20

Figure C-9

PANEL 2 FATIGUE CRITICAL SCREENING:

$S_a/(CN^{**b}) + S_m/C = 1$ S_a = ACOUSTIC RMS STRESS (psi)
 S_m = MEAN OR STATIC STRESS (psi)
 CN^{**b} = S from S/UTS vs cycles to failure (psi)
 C = ultimate tensile strength (UTS or FTu) (psi)

S/UTS 0.11

	OUTER FACESHEET						INNER FACESHEET		
	UPPER SURFACE			INNER SURFACE			INNER & OUTER SURFACE		
	Sx (psi)	Sy (psi)	Txy (psi)	Sx (psi)	Sy (psi)	Txy (psi)	Sx (psi)	Sy (psi)	Txy (psi)
FTu	122256	122256		125508	125508		133969	133969	
CN**b	13448	13448		13806	13806		14737	14737	

THE FOLLOWING IS ABS($S_a/(CN^{**b})$) + ABS(S_m/C):

CASE							
1	3.24	2.76	3.06	2.78	2.87	2.55	
2	0.67	0.61	0.56	0.69	1.12	0.37	
3	0.42	0.63	0.50	0.52	0.12	0.55	
4	0.16	0.71	0.25	0.61	0.25	0.44	
5	0.48	0.66	0.55	0.55	0.25	0.63	
6	0.29	0.18	0.37	0.21	0.21	0.30	
7	0.53	0.74	0.43	0.63	0.96	0.80	
8	0.70	0.79	0.60	0.68	0.85	0.74	
9	0.58	0.66	0.48	0.56	0.83	0.73	
10	0.63	0.71	0.52	0.60	0.80	0.69	
11	0.13	0.21	0.04	0.11	0.29	0.25	
12	0.15	0.23	0.06	0.13	0.27	0.23	
13	0.23	0.43	0.14	0.33	0.20	0.04	
14	0.30	0.45	0.21	0.35	0.15	0.02	

Figure C-10

PANEL 1 FINITE ELEMENT ANALYSIS STRESS RESULTS

STATIC STRESS RESULTS

SECTION	<----- INNER FACESHEET ----->								
	1			2			3		
	Sx (psi)	Sy (psi)	Sz (psi)	Sx (psi)	Sy (psi)	Sz (psi)	Sx (psi)	Sy (psi)	Sz (psi)
THERMOMECH. ONLY (1200 DEG PROP)									
CASE #1	-3416	-6708	0	-4035	-3899	-125	-3617	-3623	-110
CASE #2	4068	16320	0	-3325	5799	-44	-2121	7181	-13
CASE #6	4712	6368	0	6915	5068	204	5289	3618	143
COOL FROM 1200 TO 70 DEG	-16904	-6990	-4	-6653	-17870	1569	-8498	-17647	1503
CASE #1 THM-MCH LOAD INCLUDED	-20082	-13716	-4	-10832	-22284	1358	-12309	-21734	1314
CASE #2 THM-MCH LOAD INCLUDED	-14297	9715	-6	-9964	-11861	1485	-10274	-10005	1483
CASE #6 THM-MCH LOAD INCLUDED	-12340	-676	-5	480	-12109	1910	-3039	-13504	1746
CONSTANT THERMAL GRADIENT (33 BTU)	-12083	-3233	-3	-4617	-11643	1903	-5863	-12792	1839
CASE #1 THM-MCH LOAD INCLUDED	-15153	-10171	-3	-8768	-16150	1698	-9641	-16949	1656
CASE #2 THM-MCH LOAD INCLUDED	-9921	14200	-5	-8027	-5320	1826	-7765	-4875	1823
CASE #6 THM-MCH LOAD INCLUDED	-7481	3147	-4	2513	-5817	2234	-409	-8618	2074
ACTUAL VARYING THERMAL GRAD. (33 BTU)	-16229	-13850	1	-6089	-5098	933	-6946	-5772	882
CASE #1 THM-MCH LOAD INCLUDED	-19187	-20355	2	-10239	-9694	709	-10750	-1023	681
CASE #2 THM-MCH LOAD INCLUDED	-14459	2447	0	-9525	1226	843	-800	2185	861
CASE #6 THM-MCH LOAD INCLUDED	-11765	-7840	0	1011	843	1293	-1510	-1459	1139

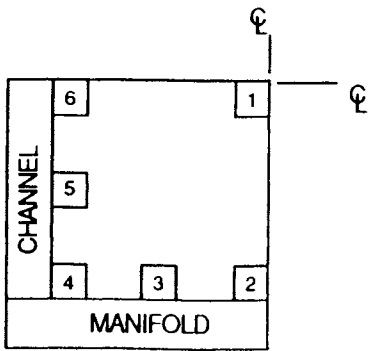


Figure C-11

PANEL 1 FINITE ELEMENT ANALYSIS STRESS RESULTS

STATIC STRESS RESULTS

SECTION	<===== INNER FACESHEET =====>											
	4			5			6					
	Sx (psi)	Sy (psi)	Sz (psi)	Sx (psi)	Sy (psi)	Sz (psi)	Sx (psi)	Sy (psi)	Sz (psi)			
THERMOMECH. ONLY (1200 DEG PROP)												
CASE #1	-2916	-4733	-215	-2676	-7261	-204	-3060	-7659	-215			
CASE #2	3781	15313	542	4192	26323	717	2758	26160	671			
CASE #6	2946	3831	174	2936	5336	134	4989	6854	200			
COOL FROM 1200 TO 70 DEG	-14819	-11410	1923	-21995	-4021	1096	-22375	-3152	1113			
CASE #1 THM-MCH LOAD INCLUDED	-17913	-16251	1570	-25368	-11470	740	-26179	-10951	741			
CASE #2 THM-MCH LOAD INCLUDED	-10492	3899	2805	-15557	22787	2355	-17451	23347	2294			
CASE #6 THM-MCH LOAD INCLUDED	-11687	-7390	2214	-18559	1451	1329	-16702	3847	1448			
CONSTANT THERMAL GRADIENT (33 BTU)	-12224	-13228	1988	-13899	-2540	1230	-12893	-1925	1243			
CASE #1 THM-MCH LOAD INCLUDED	-15292	-18092	1646	-17237	-10038	885	-16677	-9767	883			
CASE #2 THM-MCH LOAD INCLUDED	-8001	2203	2842	-7663	-7663	24453	-8142	24703	2383			
CASE #6 THM-MCH LOAD INCLUDED	-9093	-9205	2269	-10451	2921	1453	-7195	5088	1568			
ACTUAL VARYING THERMAL GRAD. (33 BTU)	-7626	-3723	1273	-14287	-3007	1004	-13864	-4941	1166			
CASE #1 THM-MCH LOAD INCLUDED	-10767	-8633	895	-17780	-10501	635	-17720	-12675	817			
CASE #2 THM-MCH LOAD INCLUDED	-3207	11770	2217	-7561	23973	2307	-8916	21289	2301			
CASE #6 THM-MCH LOAD INCLUDED	-44448	408	1588	-10778	2496	1244	-8121	1938	1489			

Figure C-11 (Continued)

PANEL 1 FINITE ELEMENT ANALYSIS STRESS RESULTS

STATIC STRESS RESULTS

SECTION	<----- OUTER FACESHEET ----->								
	1			2			3		
	Sx (psi)	Sy (psi)	Sz (psi)	Sx (psi)	Sy (psi)	Sz (psi)	Sx (psi)	Sy (psi)	Sz (psi)
THERMOMECH. ONLY (1200 DEG PROP)									
CASE #1	-394	-3676	0	-632	-2802	-12	-578	-2370	-8
CASE #2	-3374	13299	0	1634	6656	67	1996	7137	88
CASE #6	-929	15	0	-1888	2363	-23	-2401	804	-32
COOL FROM 1200 TO 70 DEG	-39870	-32386	2	-41708	-31328	478	-41062	-32374	444
CASE #1 THM-MCH LOAD INCLUDED	-40597	-36638	3	-42634	-34471	455	-41879	-35050	429
CASE #2 THM-MCH LOAD INCLUDED	-42945	-17483	3	-39492	-23583	596	-38547	-24144	589
CASE #6 THM-MCH LOAD INCLUDED	-40859	-32280	3	-43842	-29130	429	-43863	-31858	382
CONSTANT THERMAL GRADIENT (33 BTU)	-33564	-26788	-3	-32538	-31269	840	-32559	-32783	707
CASE #1 THM-MCH LOAD INCLUDED	-34237	-31066	-3	-33396	-34341	819	-33318	-35409	694
CASE #2 THM-MCH LOAD INCLUDED	-36495	-11617	-3	-30446	-23669	948	-30180	-24701	838
CASE #6 THM-MCH LOAD INCLUDED	-34547	-26702	-3	-34605	-29083	796	-35243	-32213	652
ACTUAL VARYING THERMAL GRAD. (33 BTU)	-35526	-38592	49	-45824	-31291	371	-45272	-32815	311
CASE #1 THM-MCH LOAD INCLUDED	-36119	-42649	50	-46756	-34364	347	-46103	-35437	297
CASE #2 THM-MCH LOAD INCLUDED	-38672	-24337	49	-43582	-23590	494	-42749	-24711	459
CASE #6 THM-MCH LOAD INCLUDED	-36522	-38439	49	-47973	-29270	317	-48042	-32372	245

Figure C-11 (Continued)

PANEL 1 FINITE ELEMENT ANALYSIS STRESS RESULTS

STATIC STRESS RESULTS

SECTION	<===== OUTER FACESHEET =====>								
	4			5			6		
	Sx (psi)	Sy (psi)	Sz (psi)	Sx (psi)	Sy (psi)	Sz (psi)	Sx (psi)	Sy (psi)	Sz (psi)
THERMOMECH. ONLY (1200 DEG PROP)									
CASE #1	-660	-1881	-29	-1429	-3095	-49	-1881	-3101	-50
CASE #2	1277	6549	217	99	9196	221	-1510	8349	206
CASE #6	-1654	-1193	-16	830	-1095	44	3019	-620	54
COOL FROM 1200 TO 70 DEG	-36319	-36677	-11	-33953	-34493	-342	-33392	-34939	-410
CASE #1 THM-MCH LOAD INCLUDED	-37260	-38951	-79	-35862	-38151	-444	-35791	-38667	-516
CASE #2 THM-MCH LOAD INCLUDED	-34446	-28942	413	-32804	-23871	80	-34041	-25365	-22
CASE #6 THM-MCH LOAD INCLUDED	-38208	-38097	-46	-33253	-35815	-276	-30320	-35537	-319
CONSTANT THERMAL GRADIENT (33 BTU)	-33585	-34698	146	-32241	-26799	-382	-31062	-26825	-432
CASE #1 THM-MCH LOAD INCLUDED	-34487	-36984	83	-34079	-30543	-479	-33373	-30634	-532
CASE #2 THM-MCH LOAD INCLUDED	-31737	-26908	536	-31064	-15833	13	-31546	-16852	-69
CASE #6 THM-MCH LOAD INCLUDED	-35411	-36098	113	-31567	-28189	-324	-28145	-27547	-349
ACTUAL VARYING THERMAL GRAD. (33 BTU)	-38822	-37546	-86	-38256	-37053	-457	-30435	-30411	-418
CASE #1 THM-MCH LOAD INCLUDED	-39788	-39802	-156	-40168	-40668	-556	-32796	-34169	-518
CASE #2 THM-MCH LOAD INCLUDED	-36820	-29896	346	-36896	-26548	-51	-30764	-20592	-55
CASE #6 THM-MCH LOAD INCLUDED	-40685	-38968	-125	-37571	-38376	-394	-27501	-31072	-34

Figure C-11 (Continued)

PANEL 1 FINITE ELEMENT ANALYSIS STRESS RESULTS

ACOUSTIC RMS STRESS RESULTS

SECTION	<===== INNER FACESHEET =====>								
	1			2			3		
	Sx (psi)	Sy (psi)	Sz (psi)	Sx (psi)	Sy (psi)	Sz (psi)	Sx (psi)	Sy (psi)	Sz (psi)
THERMOMECH. ONLY (1200 DEG PROP)									
CASE #1	76362	73717	40	8947	9803	90	6253	6612	56
CASE #2	9802	9466	6	1214	1263	13	846	855	8
CASE #6	2857	2760	2	395	371	5	269	251	3

NO ACOUSTIC ANALYSIS PERFORMED FOR THERMAL LOAD

COOL FROM 1200 TO 70 DEG

CASE #1 THM-MCH LOAD INCLUDED

CASE #2 THM-MCH LOAD INCLUDED

CASE #6 THM-MCH LOAD INCLUDED

CONSTANT THERMAL GRADIENT (33 BTU)

CASE #1 THM-MCH LOAD INCLUDED

CASE #2 THM-MCH LOAD INCLUDED

CASE #6 THM-MCH LOAD INCLUDED

ACTUAL VARYING THERMAL GRAD. (33 BTU)

CASE #1 THM-MCH LOAD INCLUDED

CASE #2 THM-MCH LOAD INCLUDED

CASE #6 THM-MCH LOAD INCLUDED

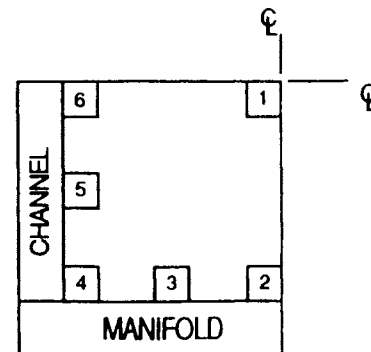


Figure C-12

PANEL 1 FINITE ELEMENT ANALYSIS STRESS RESULTS

ACOUSTIC RMS STRESS RESULTS

SECTION	<===== INNER FACESHEET =====>											
	4			5			6					
	Sx (psi)	Sy (psi)	Sz (psi)	Sx (psi)	Sy (psi)	Sz (psi)	Sx (psi)	Sy (psi)	Sz (psi)			
THERMOMECH. ONLY (1200 DEG PROP)												
CASE #1	9646	8326	58	5537	5594	54	8101	7809	78			
CASE #2	1242	1071	74	716	746	8	1041	1040	11			
CASE #6	359	310	21	211	231	3	305	327	4			

NO ACOUSTIC ANALYSIS PERFORMED FOR THERMAL LOAD

COOL FROM 1200 TO 70 DEG
CASE #1 THM-MCH LOAD INCLUDED
CASE #2 THM-MCH LOAD INCLUDED
CASE #6 THM-MCH LOAD INCLUDED

CONSTANT THERMAL GRADIENT (33 BTU)
CASE #1 THM-MCH LOAD INCLUDED
CASE #2 THM-MCH LOAD INCLUDED
CASE #6 THM-MCH LOAD INCLUDED

ACTUAL VARYING THERMAL GRAD. (33 BTU)
CASE #1 THM-MCH LOAD INCLUDED
CASE #2 THM-MCH LOAD INCLUDED
CASE #6 THM-MCH LOAD INCLUDED

Figure C-12 (Continued)

PANEL 1 FINITE ELEMENT ANALYSIS STRESS RESULTS

ACOUSTIC RMS STRESS RESULTS

SECTION	<===== OUTER FACESHEET =====>								
	1			2			3		
	Sx (psi)	Sy (psi)	Sz (psi)	Sx (psi)	Sy (psi)	Sz (psi)	Sx (psi)	Sy (psi)	Sz (psi)
THERMOMECH. ONLY (1200 DEG PROP)									
CASE #1	30045	36890	19	2729	8864	69	2006	5811	62
CASE #2	3857	4740	3	378	1138	9	273	749	8
CASE #6	1125	1382	1	127	333	3	89	219	2

NO ACOUSTIC ANALYSIS PERFORMED FOR THERMAL LOAD

COOL FROM 1200 TO 70 DEG

CASE #1 THM-MCH LOAD INCLUDED

CASE #2 THM-MCH LOAD INCLUDED

CASE #6 THM-MCH LOAD INCLUDED

CONSTANT THERMAL GRADIENT (33 BTU)

CASE #1 THM-MCH LOAD INCLUDED

CASE #2 THM-MCH LOAD INCLUDED

CASE #6 THM-MCH LOAD INCLUDED

ACTUAL VARYING THERMAL GRAD. (33 BTU)

CASE #1 THM-MCH LOAD INCLUDED

CASE #2 THM-MCH LOAD INCLUDED

CASE #6 THM-MCH LOAD INCLUDED

Figure C-12 (Continued)

PANEL 1 FINITE ELEMENT ANALYSIS STRESS RESULTS

ACOUSTIC RMS STRESS RESULTS

SECTION	<===== OUTER FACESHEET =====>								
	4			5			6		
	Sx (psi)	Sy (psi)	Sz (psi)	Sx (psi)	Sy (psi)	Sz (psi)	Sx (psi)	Sy (psi)	Sz (psi)
THERMOMECH. ONLY (1200 DEG PROP)									
CASE #1	1664	3692	98	3390	2303	43	5248	3085	55
CASE #2	215	477	13	438	311	5	674	421	7
CASE #6	63	137	4	128	98	2	197	134	2

NO ACOUSTIC ANALYSIS PERFORMED FOR THERMAL LOAD

COOL FROM 1200 TO 70 DEG

CASE #1 THM-MCH LOAD INCLUDED

CASE #2 THM-MCH LOAD INCLUDED

CASE #6 THM-MCH LOAD INCLUDED

CONSTANT THERMAL GRADIENT (33 BTU)

CASE #1 THM-MCH LOAD INCLUDED

CASE #2 THM-MCH LOAD INCLUDED

CASE #6 THM-MCH LOAD INCLUDED

ACTUAL VARYING THERMAL GRAD. (33 BTU)

CASE #1 THM-MCH LOAD INCLUDED

CASE #2 THM-MCH LOAD INCLUDED

CASE #6 THM-MCH LOAD INCLUDED

Figure C-12 (Continued)

PANEL 1 FINITE ELEMENT ANALYSIS STRESS RESULTS

ULTIMATE TENSILE STRENGTH (Ftu) 122256
CN**b 13448

(STATIC STRESS)/Ftu + (ACOUSTIC RMS STRESS)/CN**b

SECTION	<===== INNER FACESHEET =====>								
	SX	1 SY	SZ	SX	2 SY	SZ	SX	3 SY	SZ
THERMOMECH. ONLY (1200 DEG PROP)									
CASE #1	5.706	5.536	0.003	0.698	0.761	0.008	0.495	0.521	0.005
CASE #2	0.762	0.837	0.000	0.117	0.141	0.001	0.080	0.122	0.001
CASE #6	0.251	0.257	0.000	0.086	0.069	0.002	0.063	0.048	0.001

ACOUSTIC STRESS NOT INCLUDED FOR THE FOLLOWING

COOL FROM 1200 TO 70 DEG	0.138	0.057	0.000	0.054	0.146	0.013	0.070	0.144	0.012
CASE #1 THM-MCH LOAD INCLUDED	0.164	0.112	0.000	0.089	0.182	0.011	0.101	0.178	0.011
CASE #2 THM-MCH LOAD INCLUDED	0.117	0.079	0.000	0.082	0.097	0.012	0.084	0.082	0.012
CASE #6 THM-MCH LOAD INCLUDED	0.101	0.006	0.000	0.004	0.099	0.016	0.025	0.110	0.014
CONSTANT THERMAL GRADIENT (33 BTU)	0.099	0.026	0.000	0.038	0.095	0.016	0.048	0.105	0.015
CASE #1 THM-MCH LOAD INCLUDED	0.124	0.083	0.000	0.072	0.132	0.014	0.079	0.139	0.014
CASE #2 THM-MCH LOAD INCLUDED	0.081	0.116	0.000	0.066	0.044	0.015	0.064	0.040	0.015
CASE #6 THM-MCH LOAD INCLUDED	0.061	0.026	0.000	0.021	0.048	0.018	0.003	0.070	0.017
ACTUAL VARYING THERMAL GRAD. (33 BTU)	0.133	0.113	0.000	0.050	0.042	0.008	0.057	0.047	0.007
CASE #1 THM-MCH LOAD INCLUDED	0.157	0.166	0.000	0.084	0.079	0.006	0.088	0.008	0.006
CASE #2 THM-MCH LOAD INCLUDED	0.118	0.020	0.000	0.078	0.010	0.007	0.007	0.018	0.007
CASE #6 THM-MCH LOAD INCLUDED	0.096	0.064	0.000	0.008	0.007	0.011	0.012	0.012	0.009

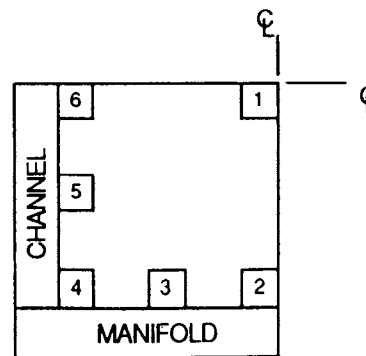


Figure C-13

PANEL 1 FINITE ELEMENT ANALYSIS STRESS RESULTS

ULTIMATE TENSILE STRENGTH (Ftu)
CN**b

(STATIC STRESS)/Ftu + (ACOUSTIC RMS STRESS)/CN**b

SECTION	<----- INNER FACESHEET ----->								
	SX	4 SY	SZ	SX	5 SY	SZ	SX	6 SY	SZ
THERMOMECH. ONLY (1200 DEG PROP)									
CASE #1	0.741	0.658	0.006	0.434	0.475	0.006	0.627	0.643	0.008
CASE #2	0.123	0.205	0.010	0.088	0.271	0.006	0.100	0.291	0.006
CASE #6	0.051	0.054	0.003	0.040	0.061	0.001	0.063	0.080	0.002
ACOUSTIC STRESS NOT INCLUDED FOR THE FOLLOWING									
COOL FROM 1200 TO 70 DEG	0.121	0.093	0.016	0.180	0.033	0.009	0.183	0.026	0.009
CASE #1 THM-MCH LOAD INCLUDED	0.147	0.133	0.013	0.207	0.094	0.006	0.214	0.090	0.006
CASE #2 THM-MCH LOAD INCLUDED	0.086	0.032	0.023	0.127	0.186	0.019	0.143	0.191	0.019
CASE #6 THM-MCH LOAD INCLUDED	0.096	0.060	0.018	0.152	0.012	0.011	0.137	0.031	0.012
CONSTANT THERMAL GRADIENT (33 BTU)	0.100	0.108	0.016	0.114	0.021	0.010	0.105	0.016	0.010
CASE #1 THM-MCH LOAD INCLUDED	0.125	0.148	0.013	0.141	0.082	0.007	0.136	0.080	0.007
CASE #2 THM-MCH LOAD INCLUDED	0.065	0.018	0.023	0.063	0.063	0.200	0.067	0.202	0.019
CASE #6 THM-MCH LOAD INCLUDED	0.074	0.075	0.019	0.085	0.024	0.012	0.059	0.042	0.013
ACTUAL VARYING THERMAL GRAD. (33 BTU)	0.062	0.030	0.010	0.117	0.025	0.008	0.113	0.040	0.010
CASE #1 THM-MCH LOAD INCLUDED	0.088	0.071	0.007	0.145	0.086	0.005	0.145	0.104	0.007
CASE #2 THM-MCH LOAD INCLUDED	0.026	0.096	0.018	0.062	0.196	0.019	0.073	0.174	0.019
CASE #6 THM-MCH LOAD INCLUDED	0.364	0.003	0.013	0.088	0.020	0.010	0.066	0.016	0.012

Figure C-13 (Continued)

PANEL 1 FINITE ELEMENT ANALYSIS STRESS RESULTS

ULTIMATE TENSILE STRENGTH (Ftu)
CN**b

(STATIC STRESS)/Ftu + (ACOUSTIC RMS STRESS)/CN**b

SECTION	<===== OUTER FACESHEET =====>								
	SX	1 SY	SZ	SX	2 SY	SZ	SX	3 SY	SZ
THERMOMECH. ONLY (1200 DEG PROP)									
CASE #1	2.237	2.773	0.001	0.208	0.682	0.005	0.154	0.451	0.005
CASE #2	0.314	0.461	0.000	0.041	0.139	0.001	0.037	0.114	0.001
CASE #6	0.091	0.103	0.000	0.025	0.044	0.000	0.026	0.023	0.000
ACOUSTIC STRESS NOT INCLUDED FOR THE FOLLOWING									
COOL FROM 1200 TO 70 DEG	0.326	0.265	0.000	0.341	0.256	0.004	0.336	0.265	0.004
CASE #1 THM-MCH LOAD INCLUDED	0.332	0.300	0.000	0.349	0.282	0.004	0.343	0.287	0.004
CASE #2 THM-MCH LOAD INCLUDED	0.351	0.143	0.000	0.323	0.193	0.005	0.315	0.197	0.005
CASE #6 THM-MCH LOAD INCLUDED	0.334	0.264	0.000	0.359	0.238	0.004	0.359	0.261	0.003
CONSTANT THERMAL GRADIENT (33 BTU)	0.275	0.219	0.000	0.266	0.256	0.007	0.266	0.268	0.006
CASE #1 THM-MCH LOAD INCLUDED	0.280	0.254	0.000	0.273	0.281	0.007	0.273	0.290	0.006
CASE #2 THM-MCH LOAD INCLUDED	0.299	0.095	0.000	0.249	0.194	0.008	0.247	0.202	0.007
CASE #6 THM-MCH LOAD INCLUDED	0.283	0.218	0.000	0.283	0.238	0.007	0.288	0.263	0.005
ACTUAL VARYING THERMAL GRAD. (33 BTU)	0.291	0.316	0.000	0.375	0.256	0.003	0.370	0.268	0.003
CASE #1 THM-MCH LOAD INCLUDED	0.295	0.349	0.000	0.382	0.281	0.003	0.377	0.290	0.002
CASE #2 THM-MCH LOAD INCLUDED	0.316	0.199	0.000	0.356	0.193	0.004	0.350	0.202	0.004
CASE #6 THM-MCH LOAD INCLUDED	0.299	0.314	0.000	0.392	0.239	0.003	0.393	0.265	0.002

Figure C-13 (Continued)

PANEL 1 FINITE ELEMENT ANALYSIS STRESS RESULTS

ULTIMATE TENSILE STRENGTH (Ftu)
CN**b

(STATIC STRESS)/Ftu + (ACOUSTIC RMS STRESS)/CN**b

SECTION	<===== OUTER FACESHEET =====>								
	SX	4 SY	SZ	SX	5 SY	SZ	SX	6 SY	SZ
THERMOMECH. ONLY (1200 DEG PROP)									
CASE #1	0.129	0.290	0.008	0.264	0.197	0.004	0.406	0.255	0.004
CASE #2	0.026	0.089	0.003	0.033	0.098	0.002	0.062	0.100	0.002
CASE #6	0.018	0.020	0.000	0.016	0.016	0.001	0.039	0.015	0.001
ACOUSTIC STRESS NOT INCLUDED FOR THE FOLLOWING									
COOL FROM 1200 TO 70 DEG	0.297	0.300	0.000	0.278	0.282	0.003	0.273	0.286	0.003
CASE #1 THM-MCH LOAD INCLUDED	0.305	0.319	0.001	0.293	0.312	0.004	0.293	0.316	0.004
CASE #2 THM-MCH LOAD INCLUDED	0.282	0.237	0.003	0.268	0.195	0.001	0.278	0.207	0.000
CASE #6 THM-MCH LOAD INCLUDED	0.313	0.312	0.000	0.272	0.293	0.002	0.248	0.291	0.003
CONSTANT THERMAL GRADIENT (33 BTU)	0.275	0.284	0.001	0.264	0.219	0.003	0.254	0.219	0.004
CASE #1 THM-MCH LOAD INCLUDED	0.282	0.303	0.001	0.279	0.250	0.004	0.273	0.251	0.004
CASE #2 THM-MCH LOAD INCLUDED	0.260	0.220	0.004	0.254	0.130	0.000	0.258	0.138	0.001
CASE #6 THM-MCH LOAD INCLUDED	0.290	0.295	0.001	0.258	0.231	0.003	0.230	0.225	0.003
ACTUAL VARYING THERMAL GRAD. (33 BTU)	0.318	0.307	0.001	0.313	0.303	0.004	0.249	0.249	0.003
CASE #1 THM-MCH LOAD INCLUDED	0.325	0.326	0.001	0.329	0.333	0.005	0.268	0.279	0.004
CASE #2 THM-MCH LOAD INCLUDED	0.301	0.245	0.003	0.302	0.217	0.000	0.252	0.168	0.000
CASE #6 THM-MCH LOAD INCLUDED	0.333	0.319	0.001	0.307	0.314	0.003	0.225	0.254	0.000

Figure C-13 (Continued)

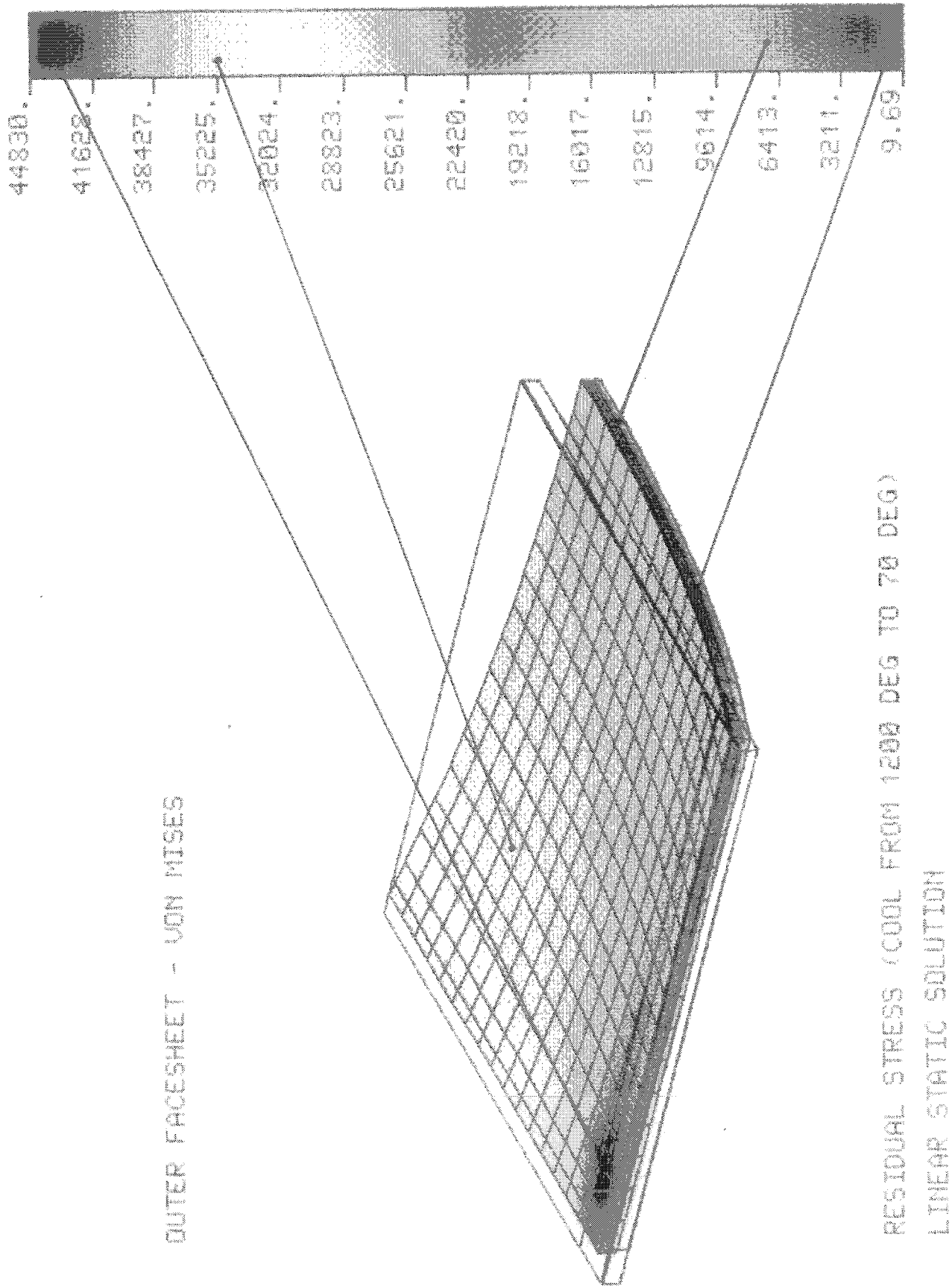
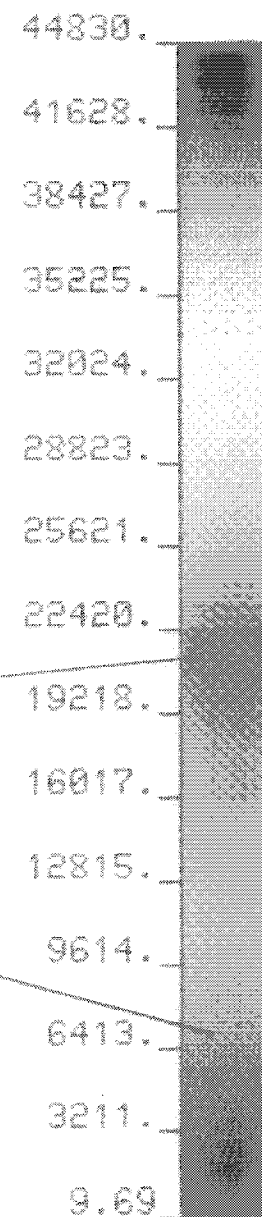
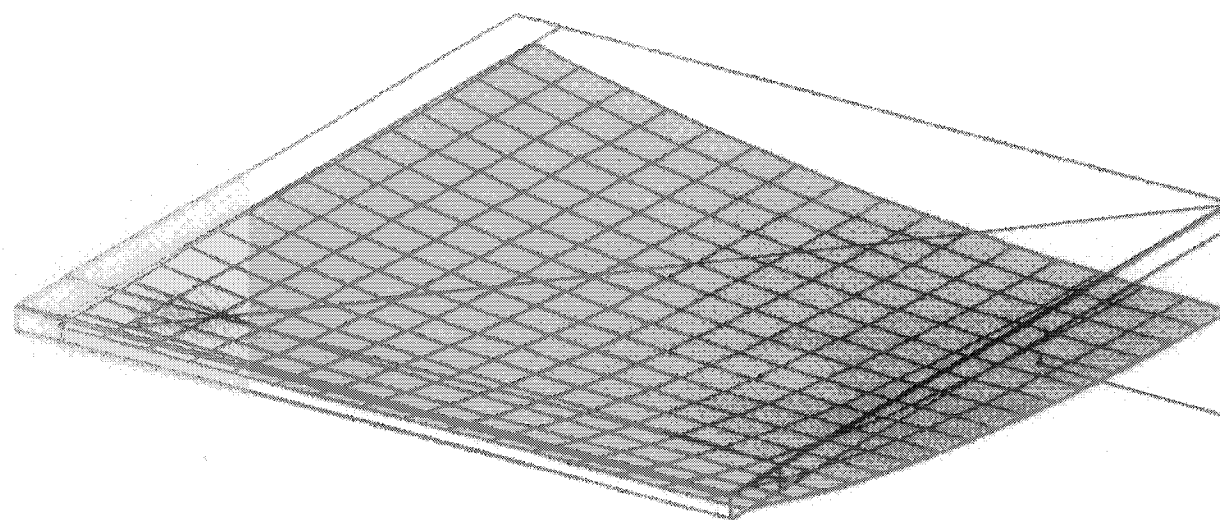


Figure C-14

INNER FACESHEET - VON MISES



RESIDUAL STRESS (COOL FROM 1200 DEG TO 70 DEG)
LINEAR STATIC SOLUTION

Figure C-15

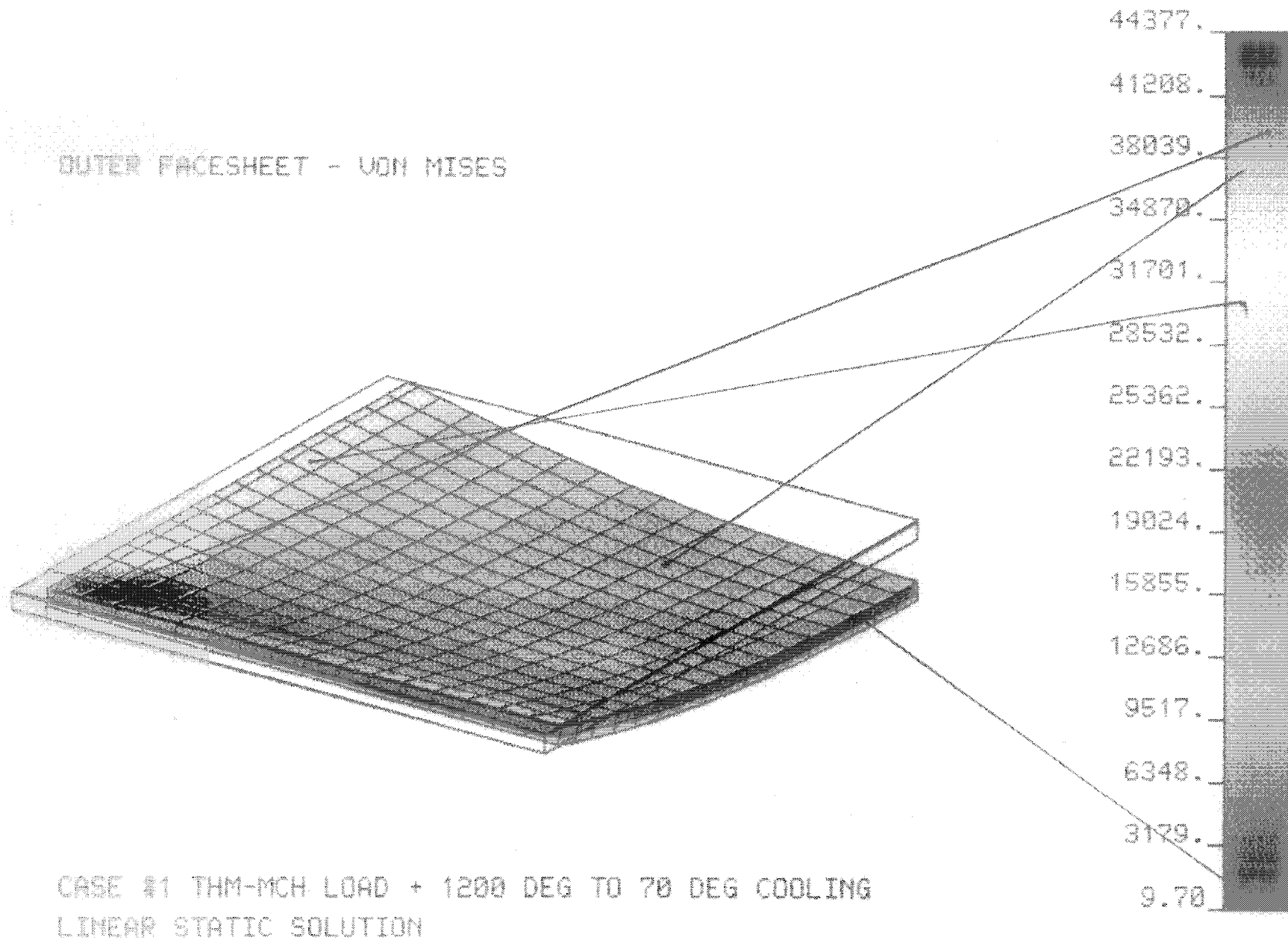


Figure C-16

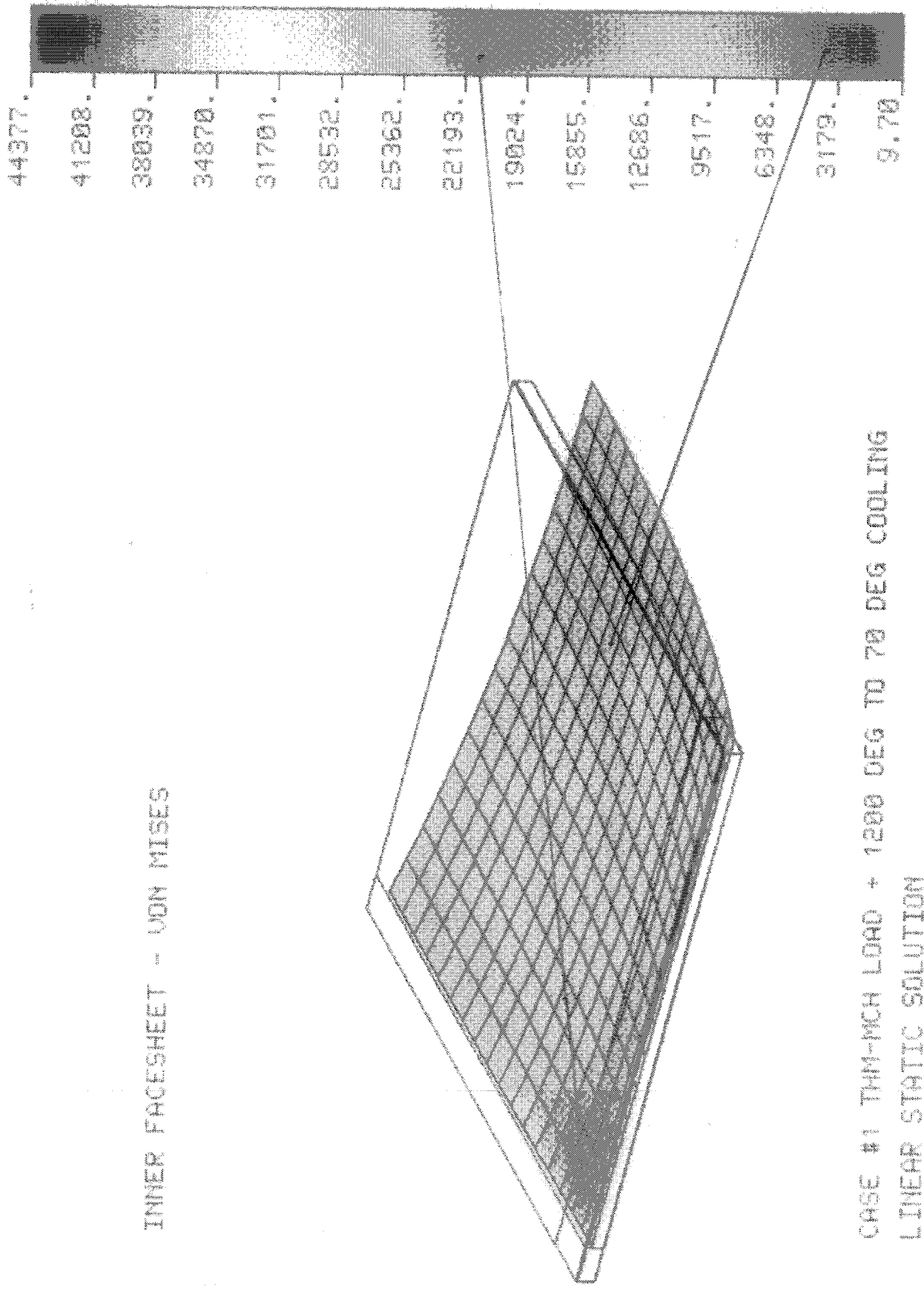


Figure C-17

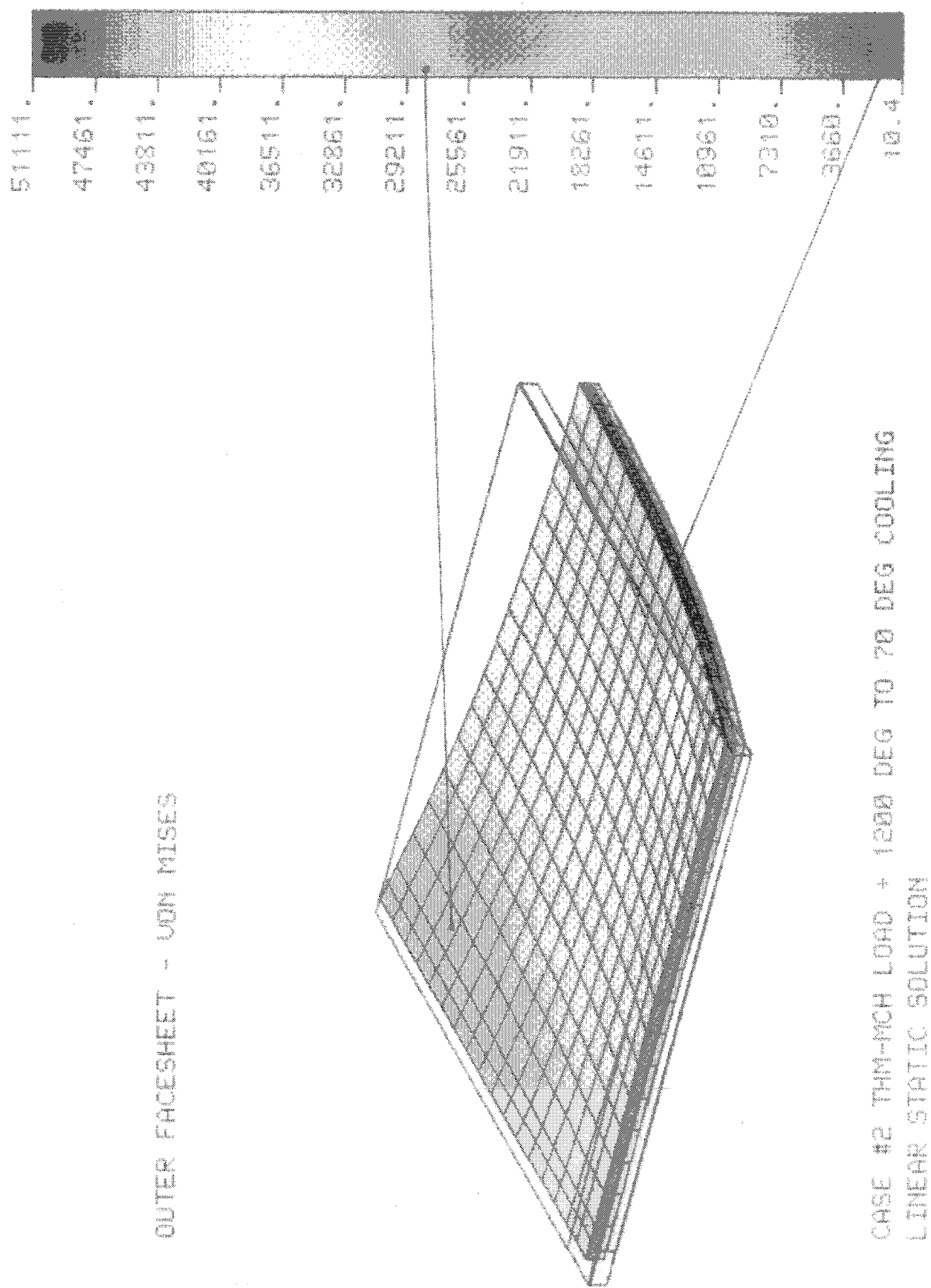


Figure C-18

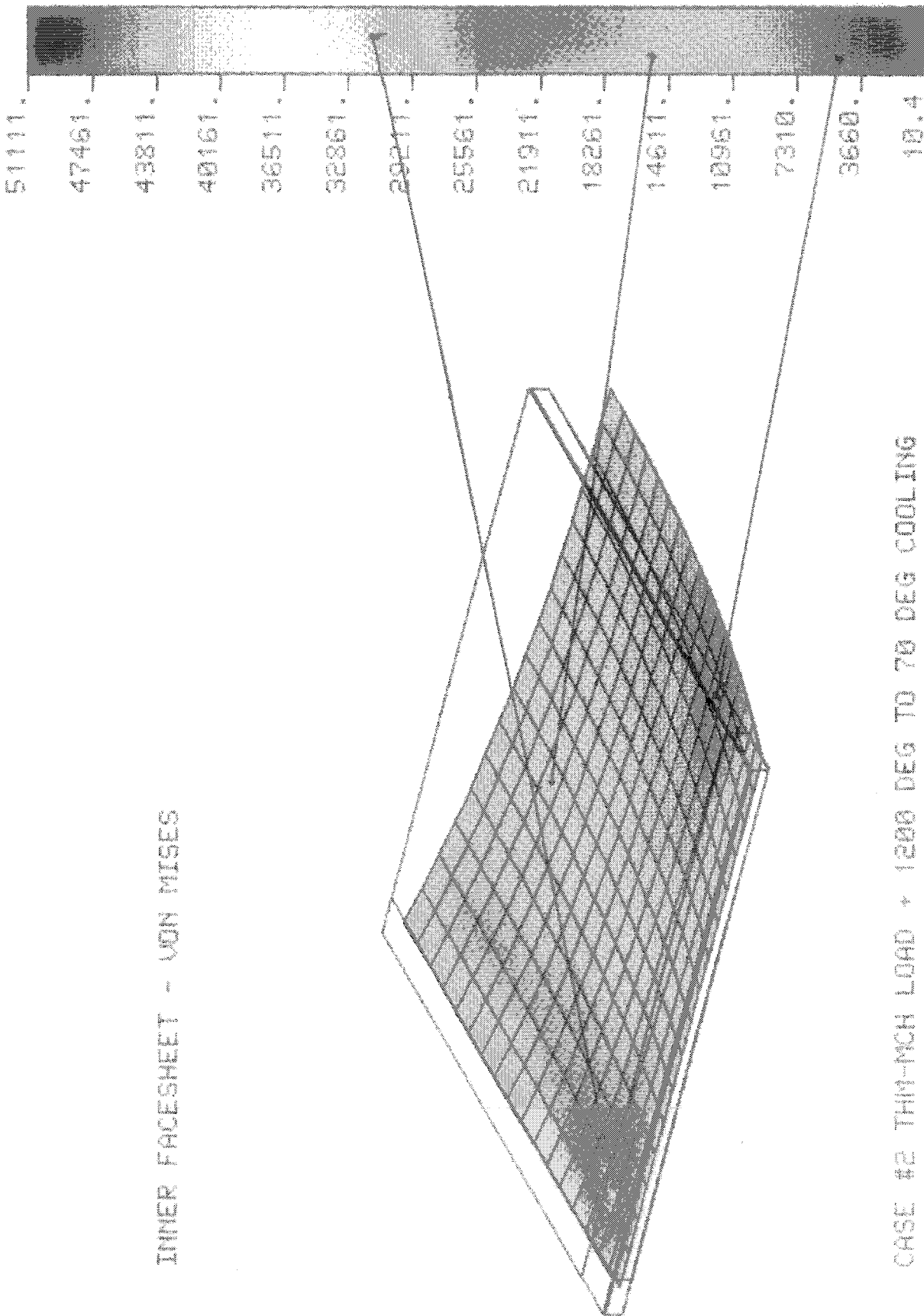


Figure C-19

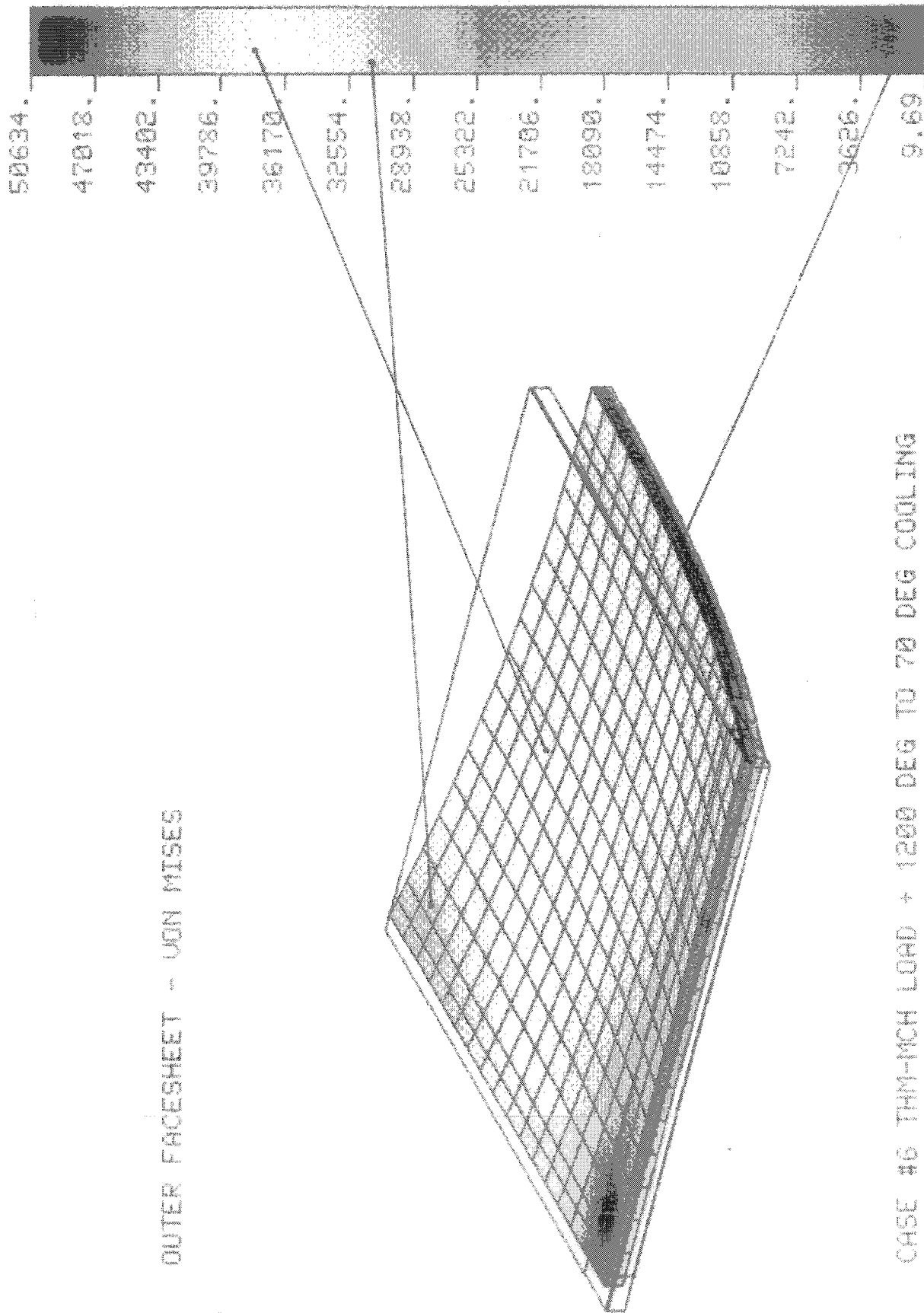


Figure C-20

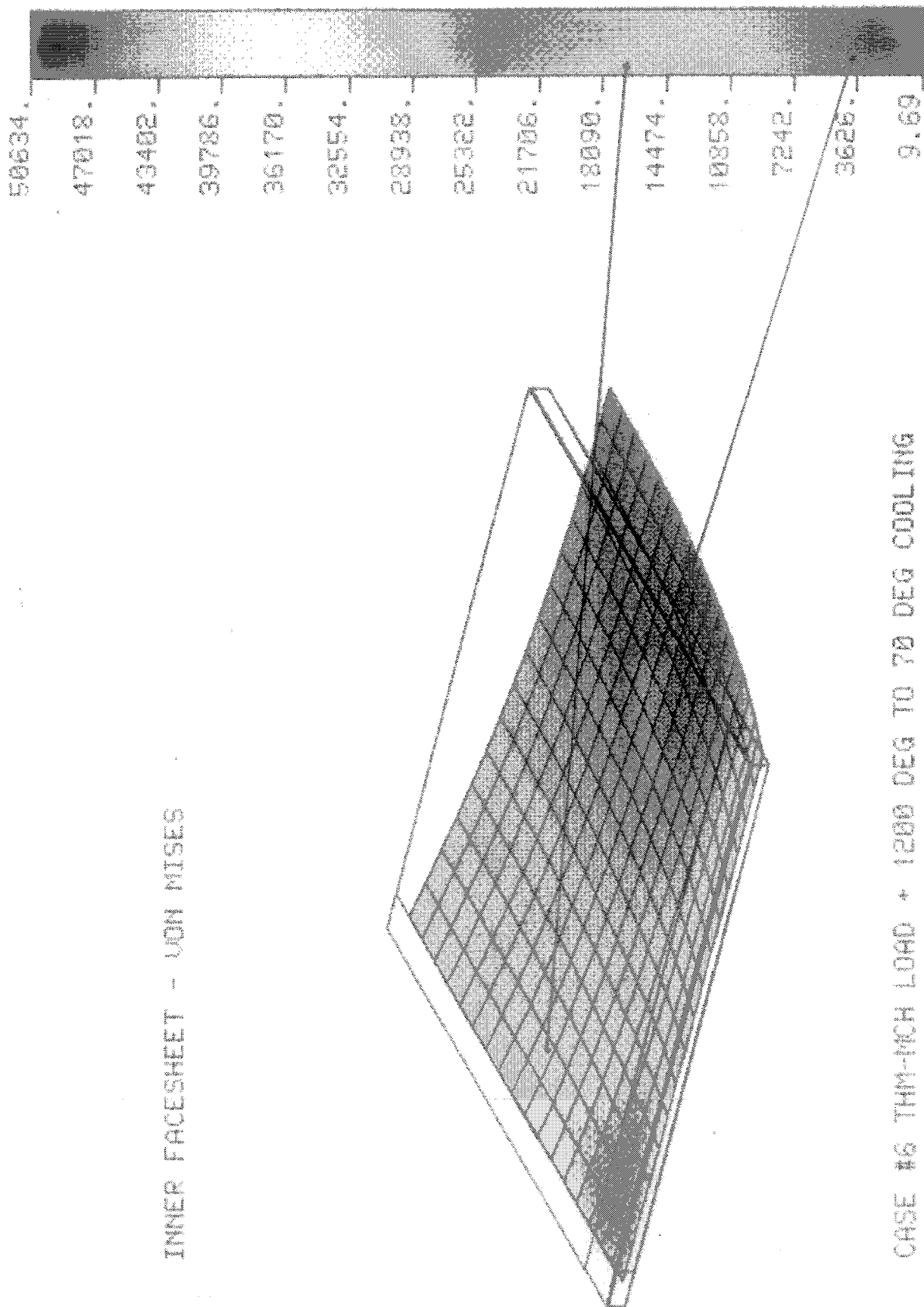


Figure C-21

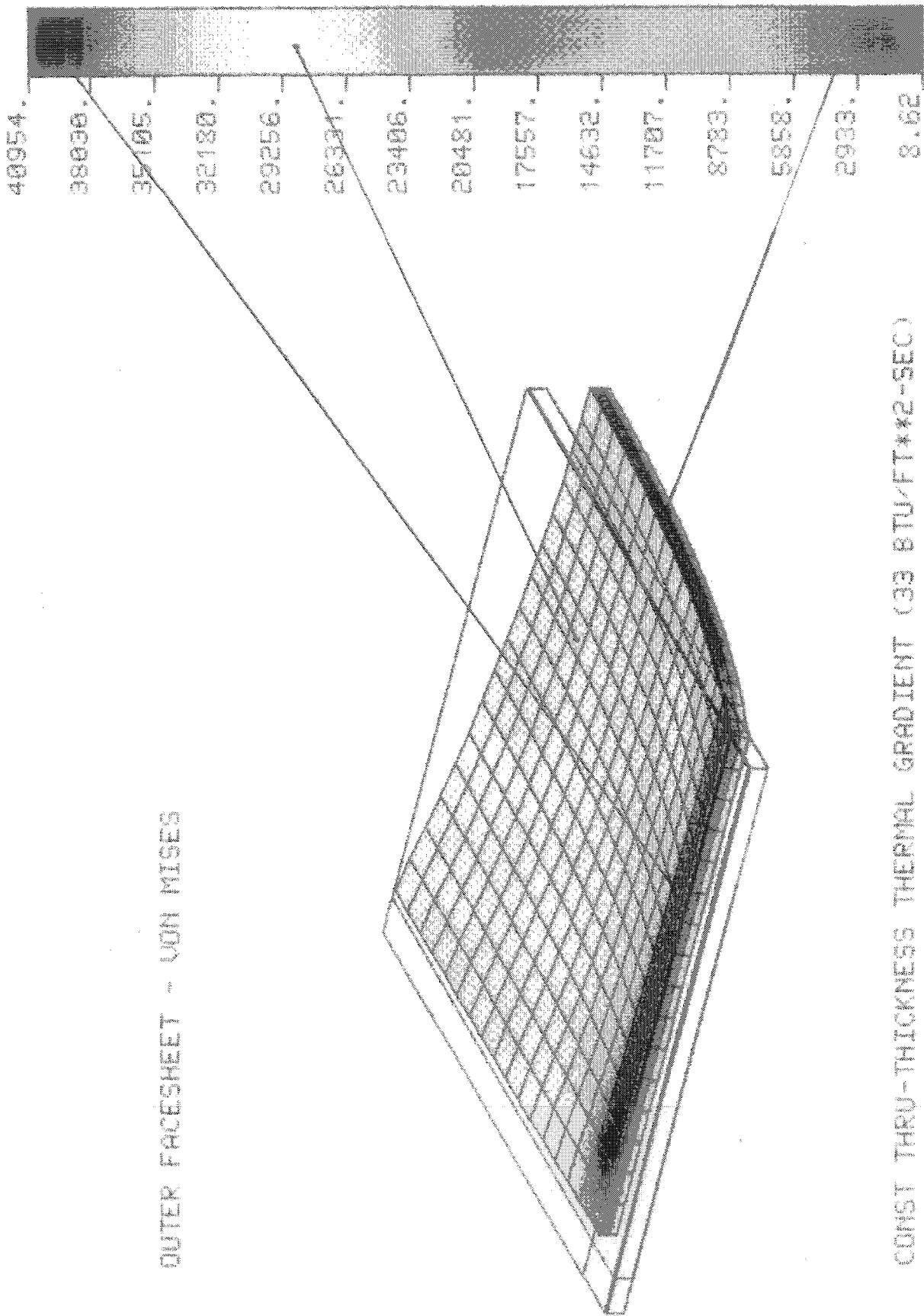


Figure C-22

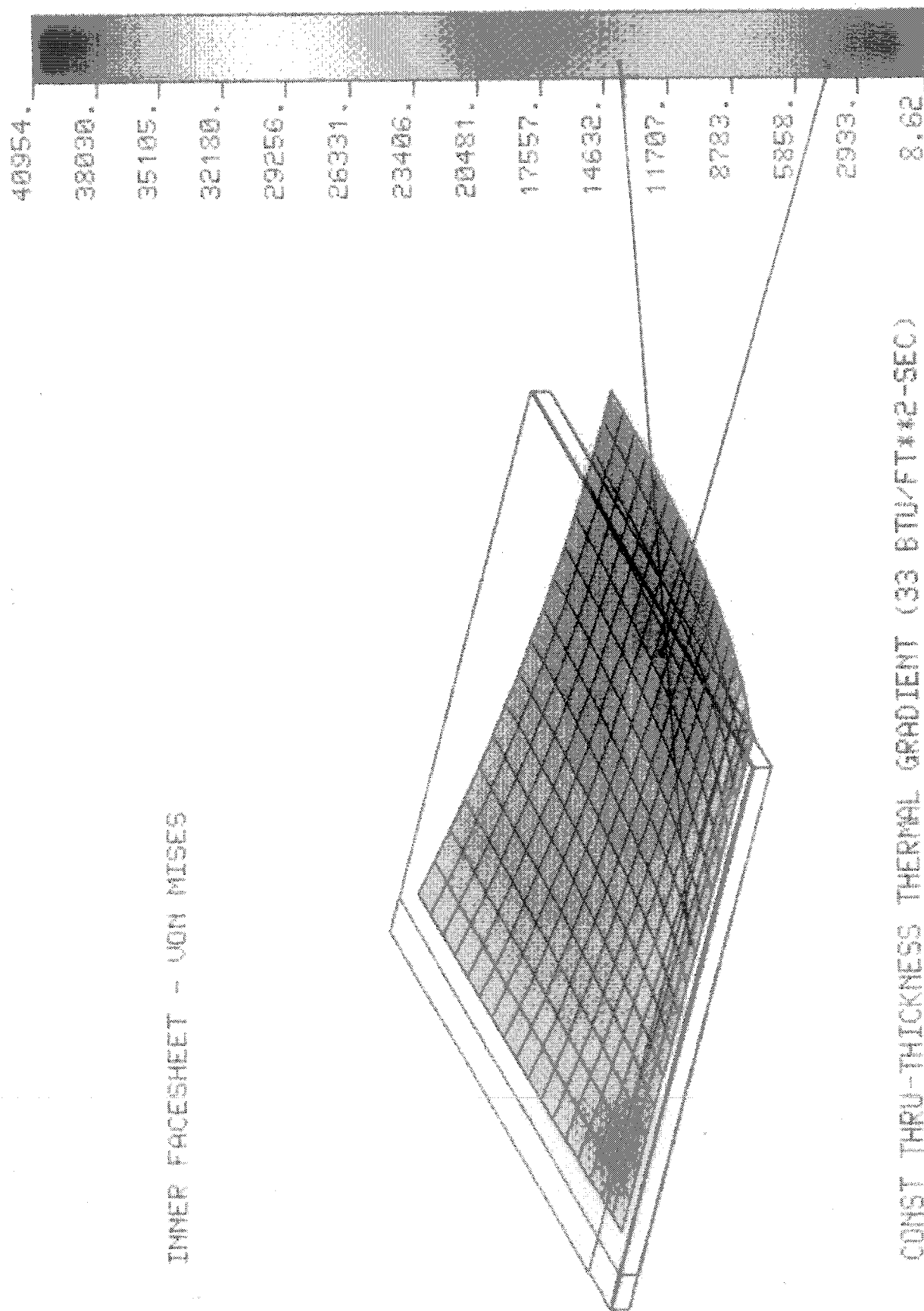


Figure C-23

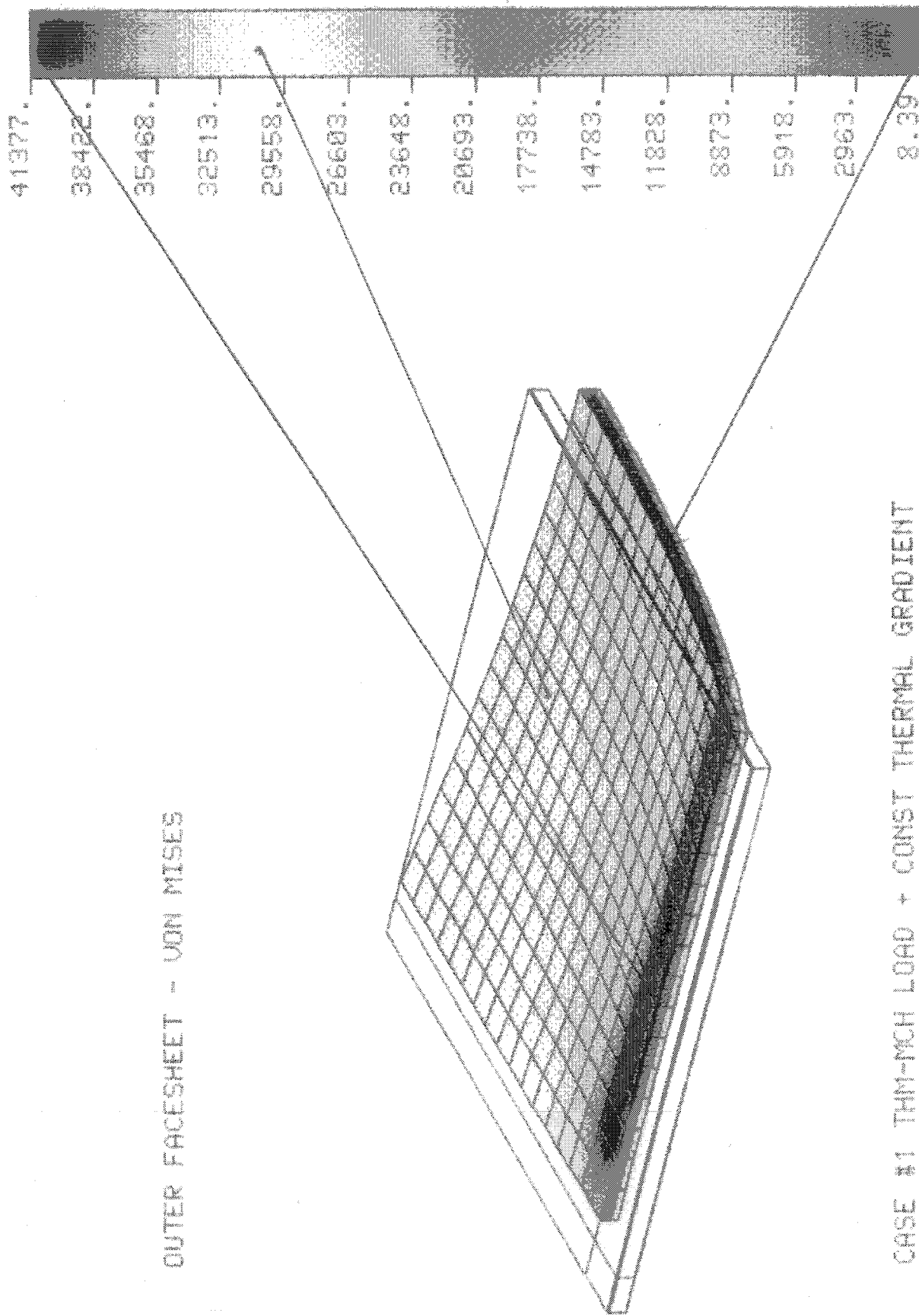
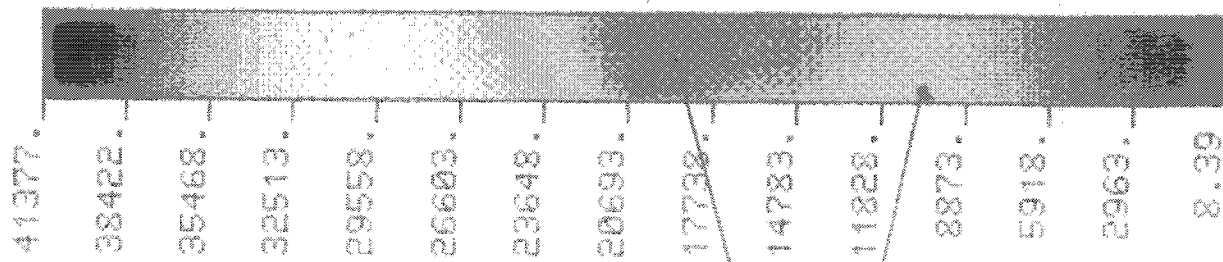
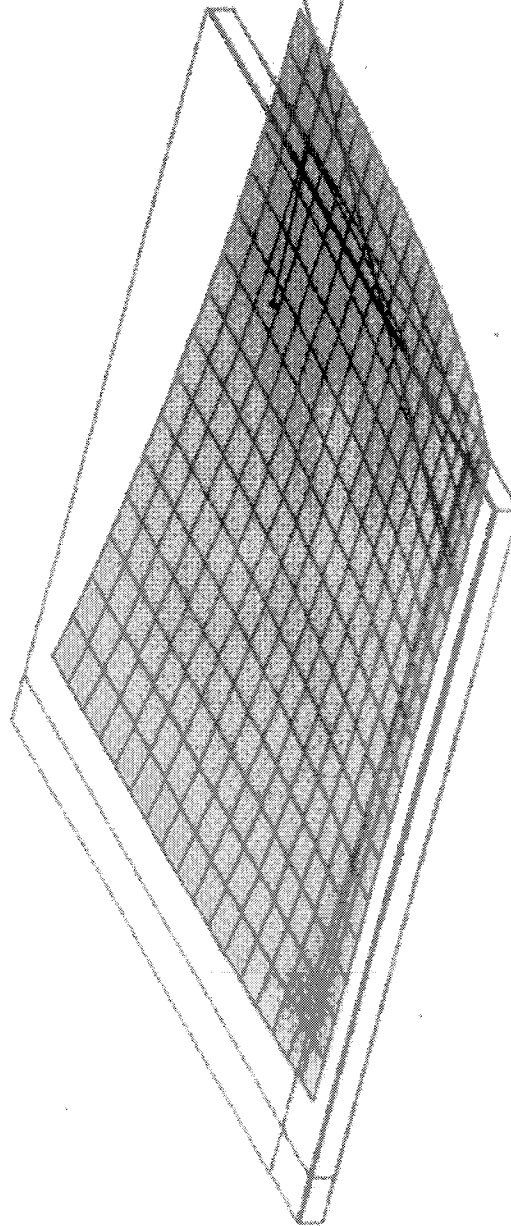


Figure C-24



INNER FACESHEET - VON MISES



CASE #1 THIN-MCH LOAD + CONST THERMAL GRADIENT
LINEAR STATIC SOLUTION

Figure C-25

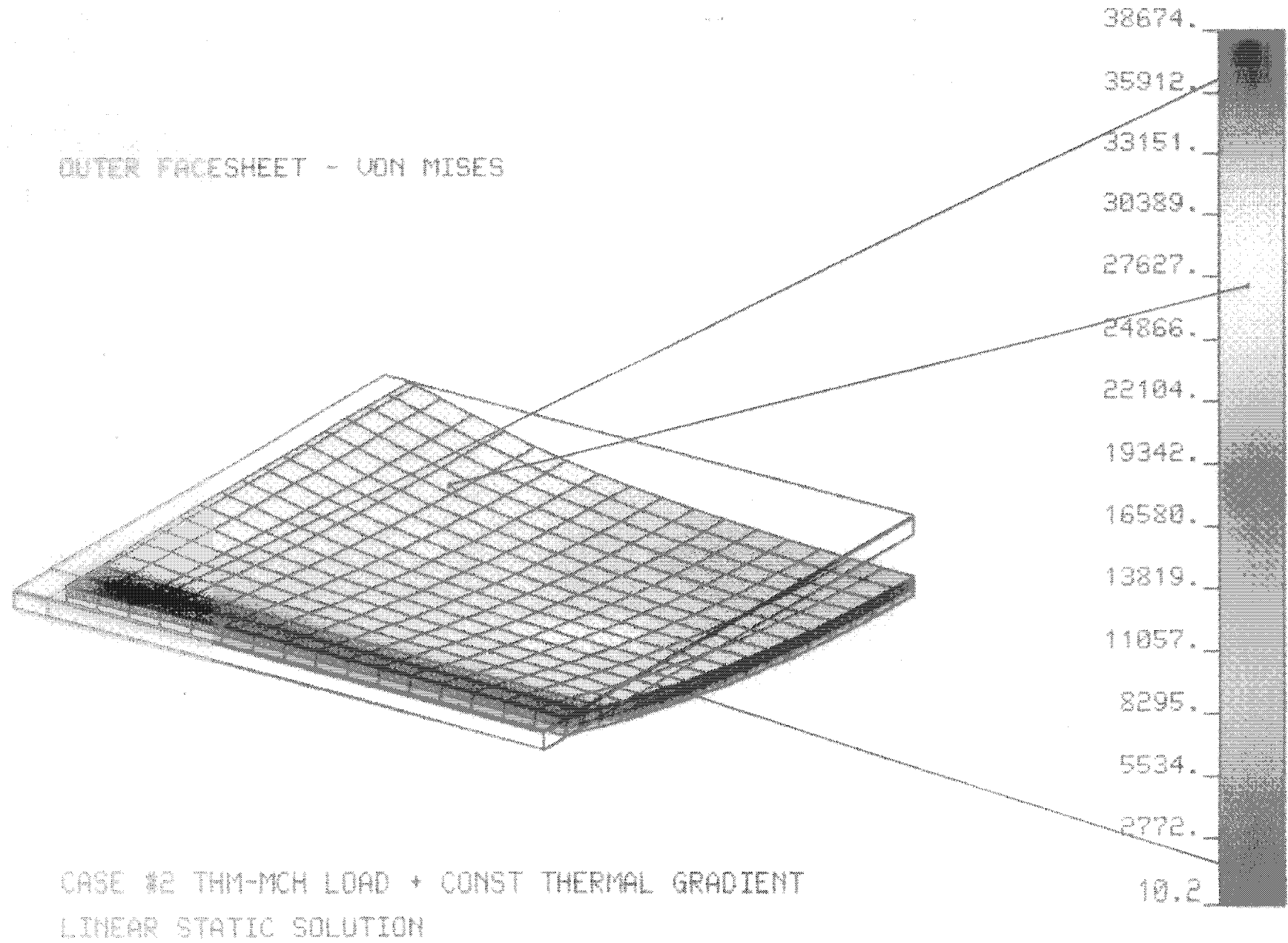
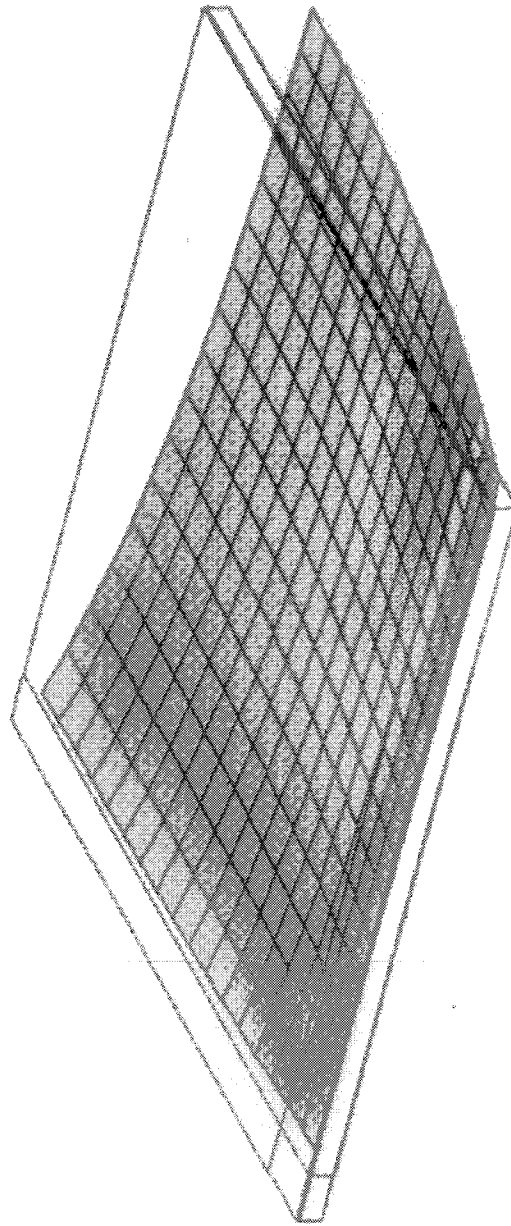


Figure C-26

INNER FACESHEET - VON MISES



CASE #2 THIN-MCH LOAD + CONST THERMAL GRADIENT
LINEAR STATIC SOLUTION

38674.
35912.
33151.
30389.
27627.
24866.
22104.
19342.
16580.
13819.
11057.
8295.
5534.
2772.
10.2

Figure C-27

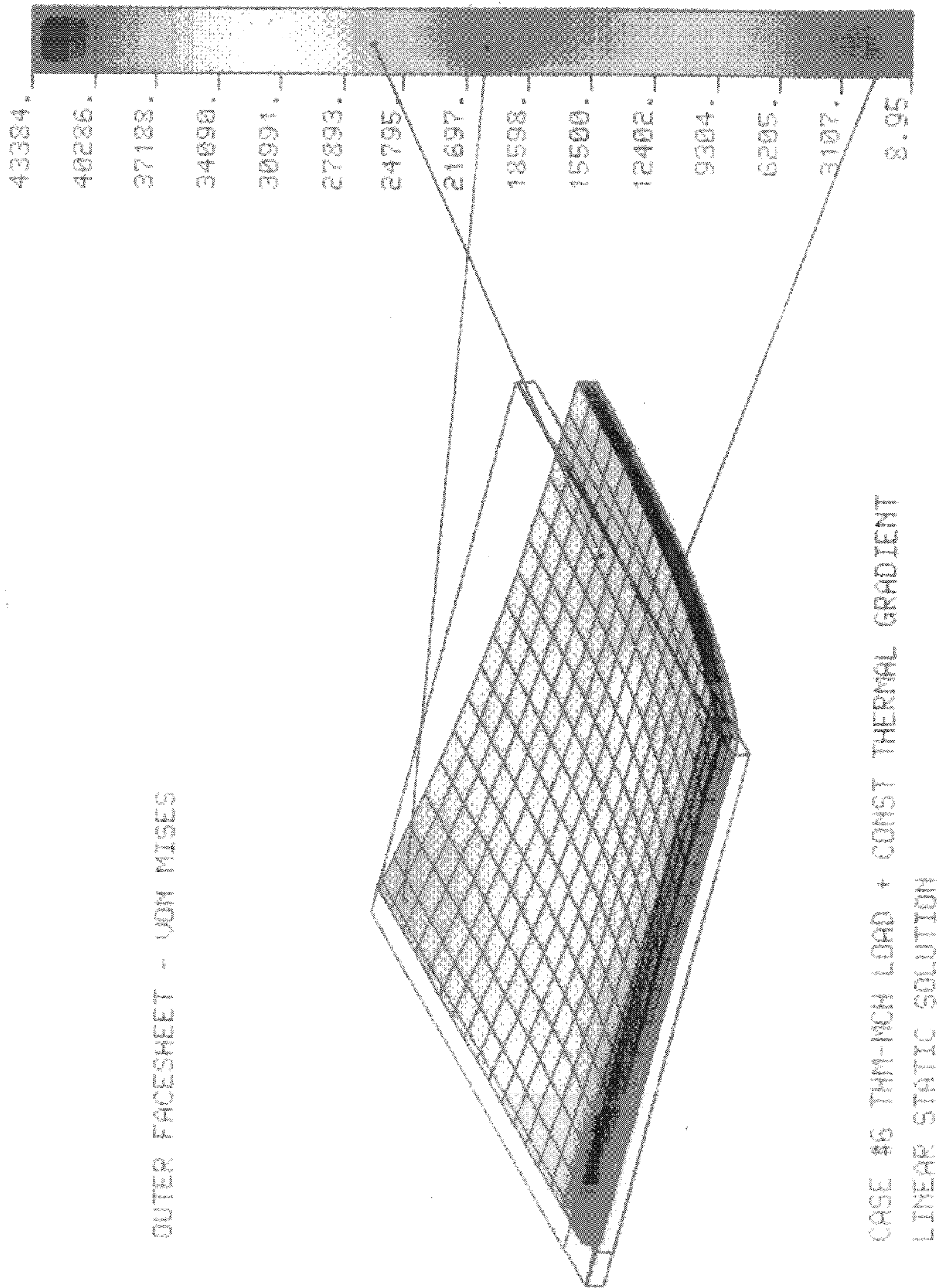


Figure C-28

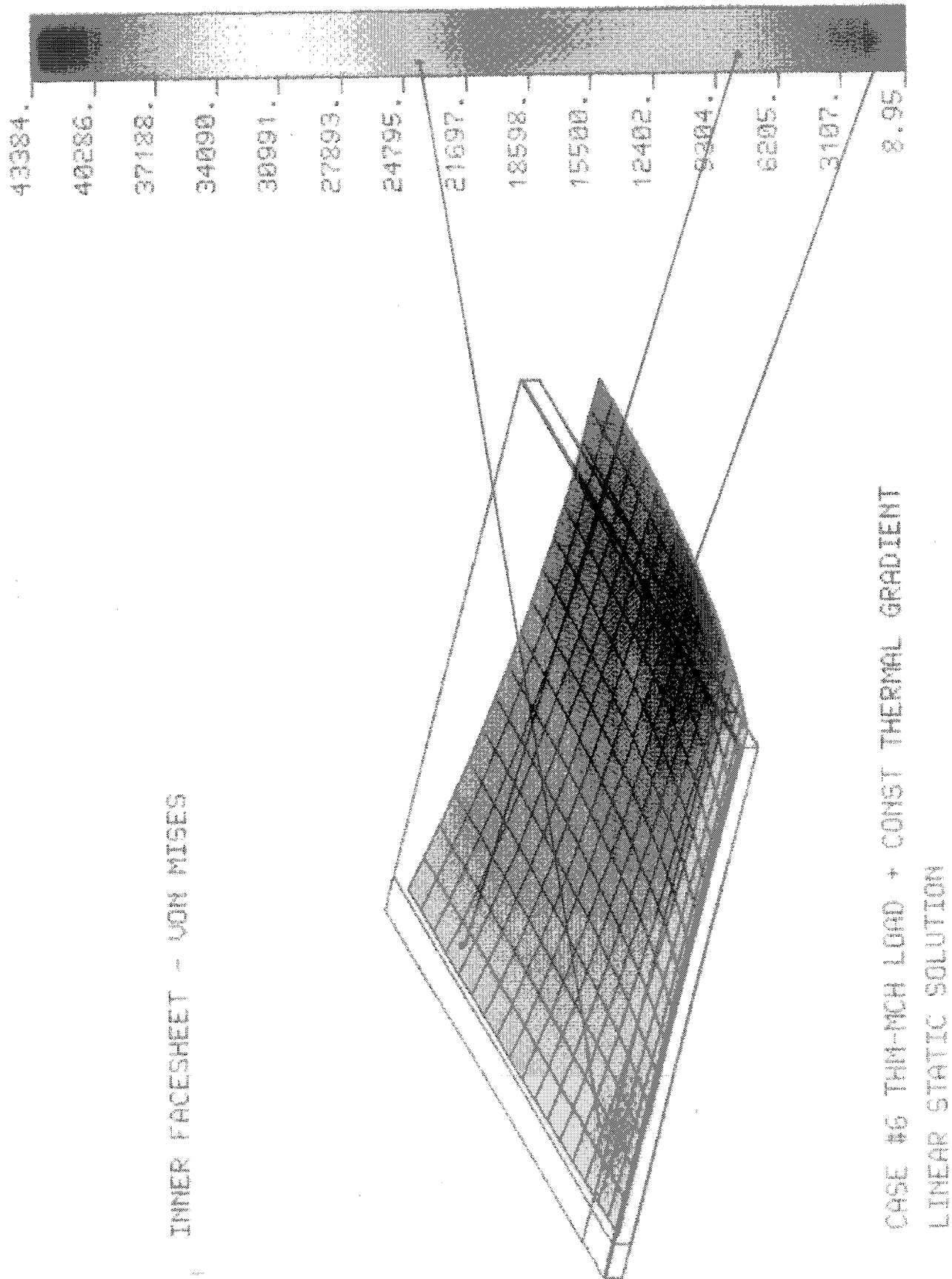


Figure C-29

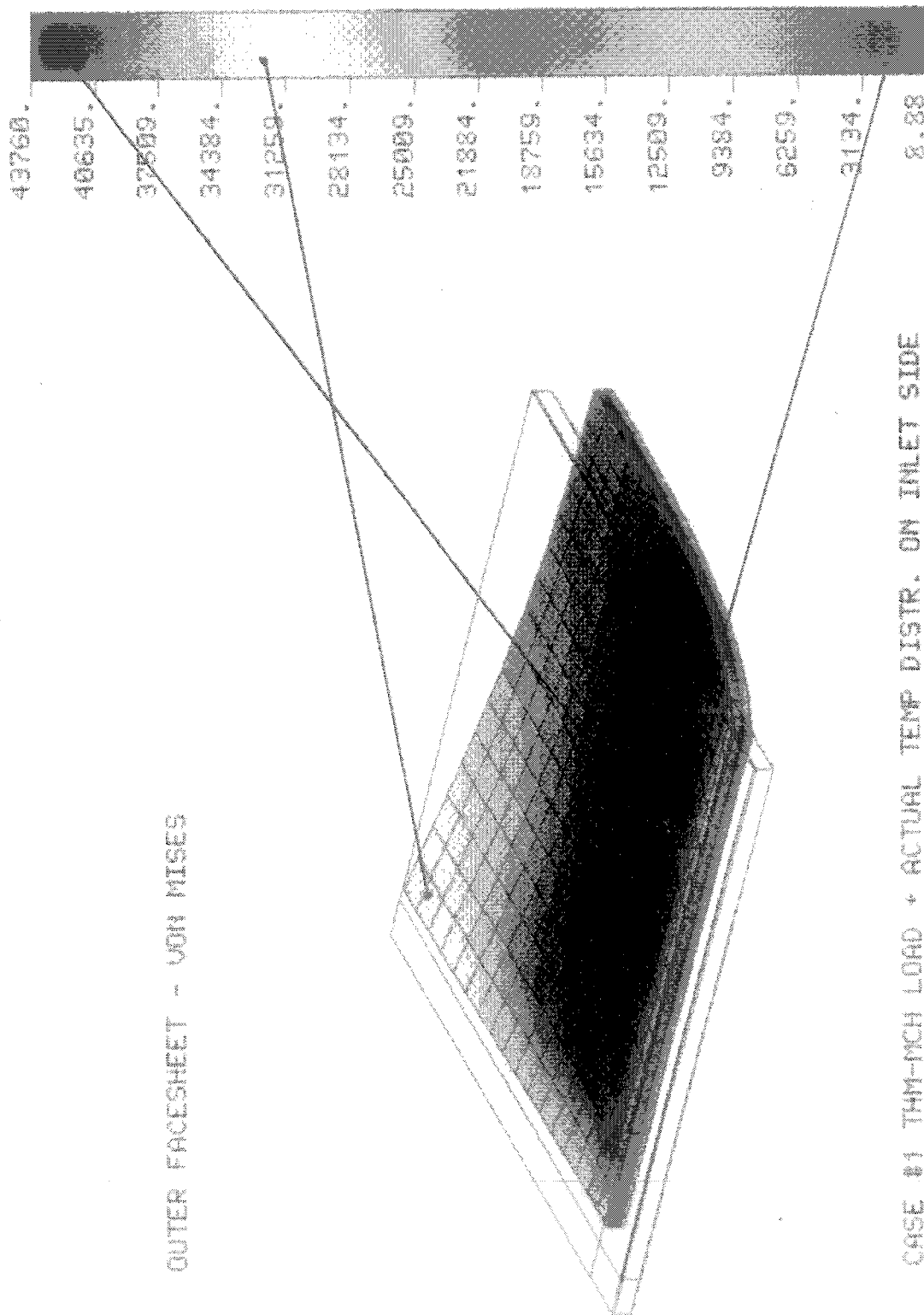
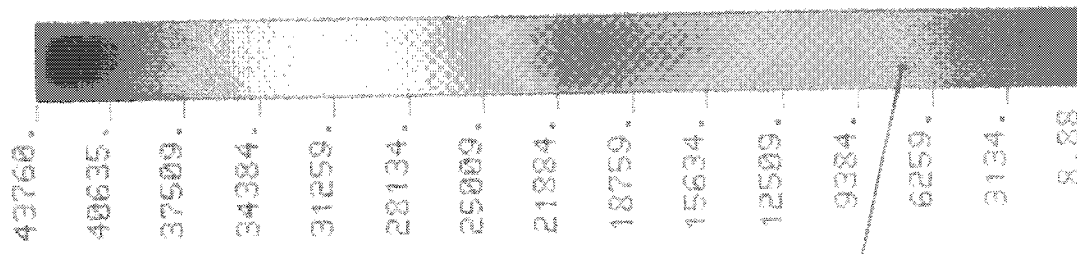
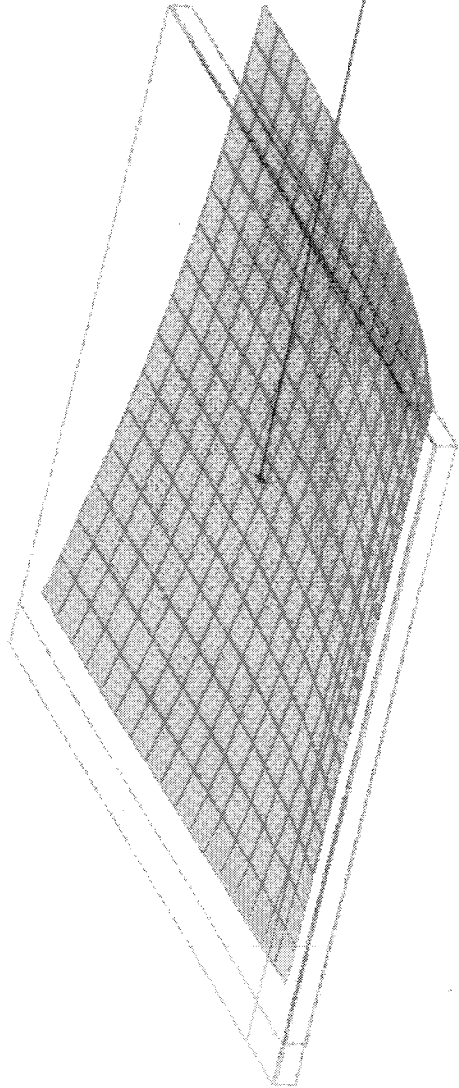


Figure C-30



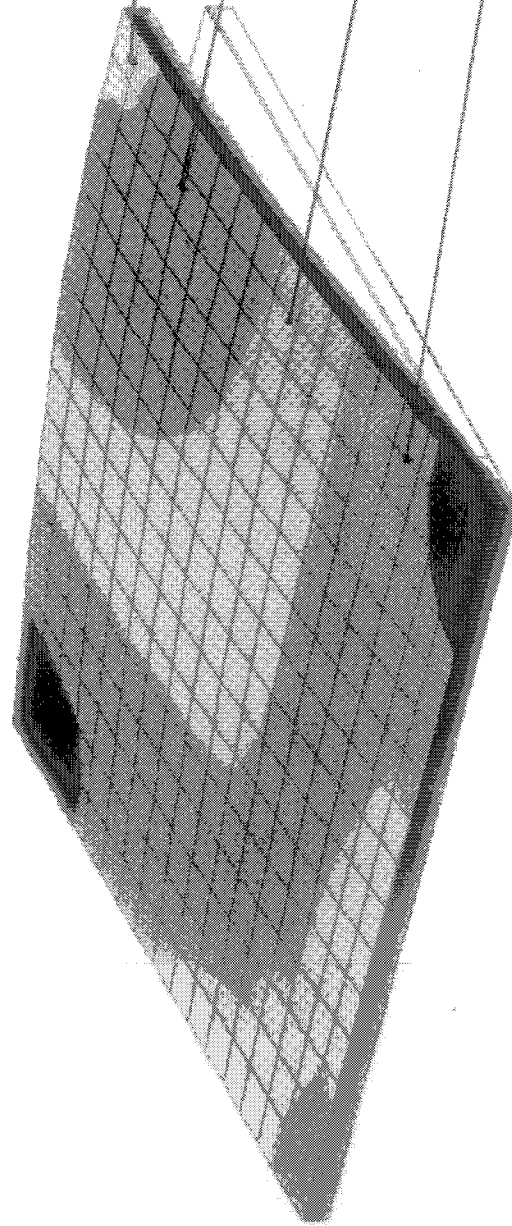
INNER FACESHEET - VON MISES



CASE #1 THIN-WALL LOAD + ACTUAL TEMP DISTR. ON INLET SIDE
 LINEAR STATIC SOLUTION

Figure C-31

OUTER FACESHEET - VON MISES

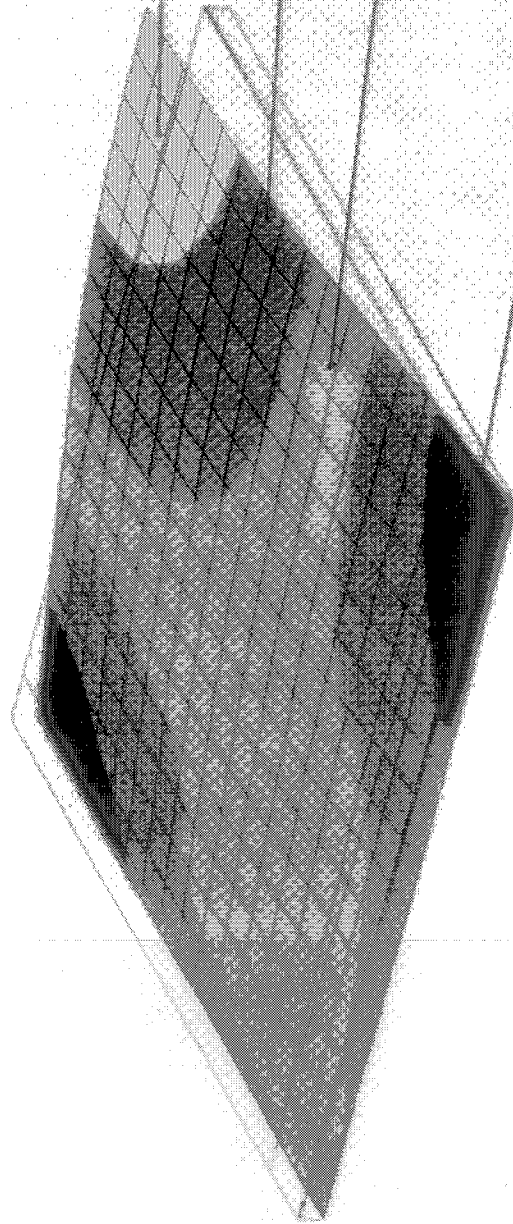


537260.
478107.
418155.
358602.
298850.
239097.
179345.
119592.
59939.
86.9

CASE #1 THIN-WALL LOAD. FIRST BENDING MODE, 60.9 HZ
MODAL SOLUTION - PRELOADED STIFFNESS MATRIX

Figure C-32

INNER FACESHEET - VON MISES



CASE #1 TWA-MCH LOAD. FIRST BENDING MODE, 60.9 HZ
MODAL SOLUTION - PRELOADED STIFFNESS MATRIX

537860

478107

418355

358602

298850

239097

179345

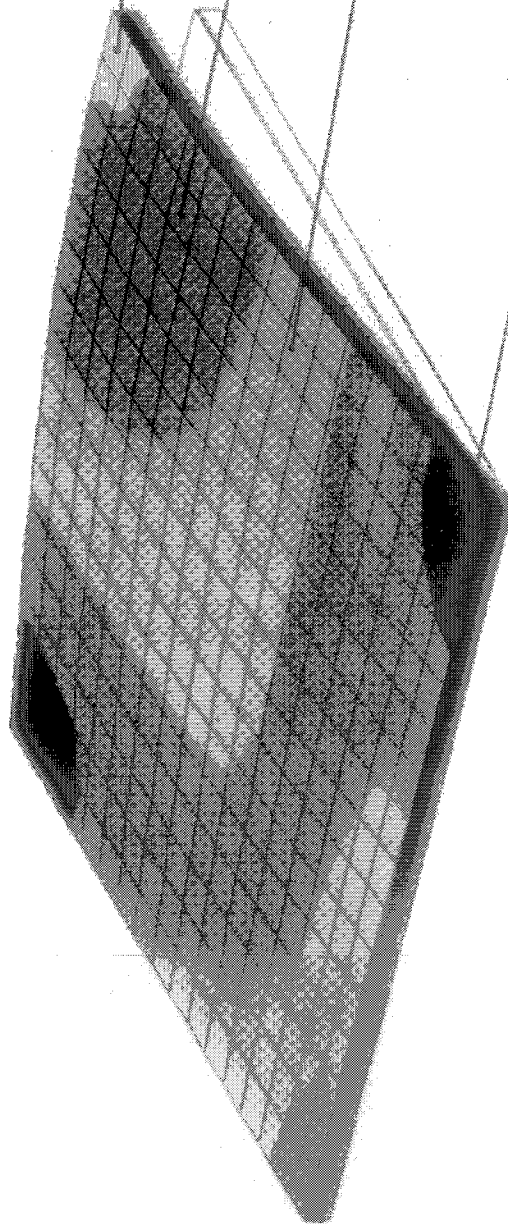
119592

59839

86.9

Figure C-33

OUTER FACESHEET - VON MISES



CASE P2 THIN-WALL LOAD. FIRST BENDING MODE, 62.0 HZ
MODAL SOLUTION - PRELOADED STIFFNESS MATRIX

537554.

477836.

418117.

358399.

298680.

238962.

179243.

119525.

59806.

87.6

Figure C-34

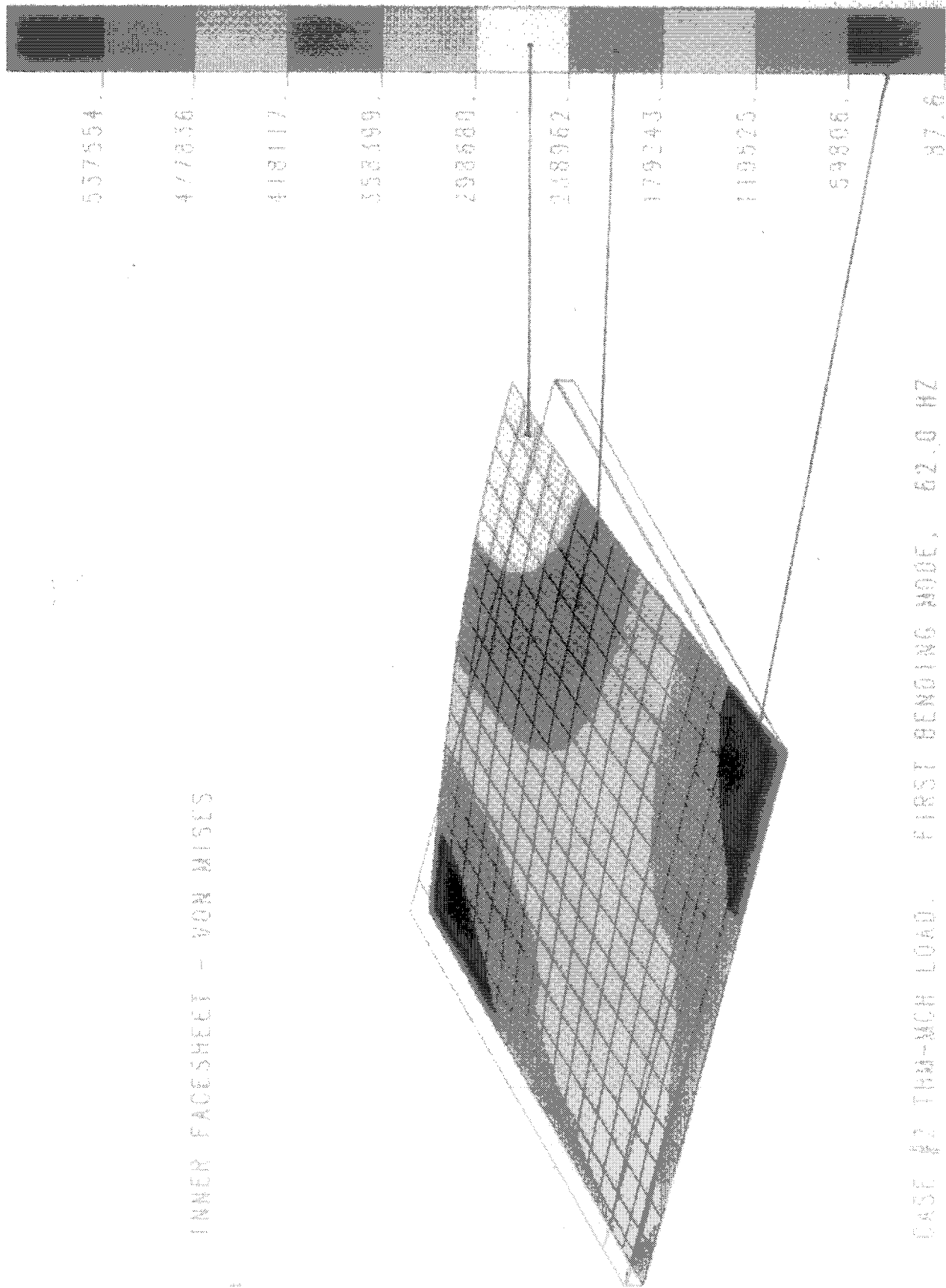


Figure C-35

APPENDIX D
DAMAGE ACCUMULATION FOR HIGH CYCLE FATIGUE

There is no theory available to predict the effect of temperature on the high cycle fatigue of materials. Reviews of the literature (References [D-1, D-2, D-3], for example) indicate that experiments are required. Existing high cycle fatigue correlations imply that the fatigue allowable falls in proportion to the rupture strength. However, the effects of creep or oxidation on rupture strength are undoubtedly different from their effects on high cycle fatigue. Thus, it is not possible to extrapolate the results of room temperature fatigue tests to high temperature without additional testing at temperature.

Although the Miner-Palmgren linear damage rule,

$$\sum_i \frac{n_i}{N_i} = 1 \quad (D-1)$$

where n_i is the number of cycles at a loading at which the allowable number of cycles is N_i , is widely used in analyzing cumulative fatigue damage, is it not confirmed by experiments, which show that the order of loading significantly affects the contribution of cycles to the damage (Reference D-4). In particular, it has been observed that if low stress cycles are applied first, followed by high stress cycles, the life is greater than if this order is reversed. The explanation for this seems to be as follows (Reference [D-5]). In high cycle fatigue testing, it is virtually always observed that the specimen vibrates for a long period of time with no detectable damage; then near the end of the specimen's life, a crack propagates through it in a relatively few cycles. In low cycle fatigue, the situation is reversed; cracks appear after a relatively few

cycles, but they propagate slowly over many cycles to eventually produce failure. Thus, if high stress cycles are applied first to a specimen, they can induce a significant flaw or crack which will be rapidly propagated by subsequent low stress vibration cycles, and the life is short. However, if the low stress vibration cycles are applied first, then no detectable flaw is created, subsequent high stress cycles are essentially starting from scratch, and the life is greater.

Various theories for damage accumulation are reviewed by Collins (Reference [D-6]). Here a brief example is made using the Manson and Halford double linear damage rule. Consider a block of loading that consists of n_1 cycles at a level for which, if there were no other cycles, the allowable number of cycles would be N_1 , followed by n_2 cycles at a different level. According to Manson and Halford (Reference [D-7]), the allowable number of cycles at the second level is

$$\frac{n_2}{N_2} = 1 - \left(\frac{n_1}{N_1} \right) (N_1/N_2)^{0.4} \quad (D-2)$$

where N_2 is the allowable number of cycles at the second level if there are no other cycles. Assume that the first cycles are low cycle fatigue $N_1 = 1000$ and the second cycles are high cycle fatigue $N_2 = 10^7$, and apply $n_1 = 500$, i.e., half the life, of the low cycle fatigue cycles. According to the Miner-Palmgren rule, half the high cycle fatigue cycles should be left before failure; but the Manson-Halford theory predicts

$$\frac{n_2}{N_2} = 1 - \left(\frac{500}{1000} \right) (1000/10000000)^{0.4} = 1 - 0.9827 = 0.01726$$

Thus, only 1.7 percent or 1.7×10^5 of the high cycle fatigue cycles would be left before failure. If this loading is reversed and half the high cycle fatigue cycles are used up first, then the theory predicts that 999.9 of the low cycle fatigue cycles can occur before failure.

The consequence of the effect of loading order on hypersonic aircraft design is as follows. If flight cycle loadings due to thermal

and mechanical loads are high so that they limit the aircraft to a relatively few operational cycles, the life fraction available for high cycle fatigue due to acoustic loading or buffeting will be seriously limited beyond what simple theory would predict. The order of loading and the magnitude of both high cycle and low cycle effects must be considered simultaneously.

REFERENCES

- D-1 Bartel, H.W., and Schneider, C.W., High Cycle Random Fatigue Testing, Technical Report AFFDL-TR-76-50, Air Force Flight Dynamics Laboratory, Wright-Patterson Air Force Base, Ohio, July 1975.
- D-2 Schneider, C.W., Acoustic Fatigue of Aircraft Structures at Elevated Temperatures, Technical Report AFFDL-TR-73-155, Air Force Flight Dynamics Laboratory, Wright-Patterson Air Force Base, Ohio, March 1974.
- D-3 Skelton, R.P. (Ed.), Fatigue at High Temperature, Applied Science Publishers, London, 1983.
- D-4 Manson, S.S., and Halford, G.R., "Practical Implementation of the Double Linear Damage Rule and Damage Curve Approach for Treating Cumulative Fatigue Damage." International Journal of Fracture, Vol. 17, pp. 169-191, 1981.
- D-5 Halford, G.R., Personal Communication, April 1988.
- D-6 Collins, J.A., Failure of Materials in Mechanical Design, John Wiley, New York, 1981.
- D-7 Manson, S.S., and Halford, G.R., "Re-Examination of Cumulative Fatigue Damage Analysis - An Engineering Perspective." Engineering Fracture Mechanics, Vol. 25, pp. 539-571, 1986.

838PROP/3-D.BB
12-15-89

APPENDIX E

VEHICLE CARRY-THROUGH LOADS

In addition to surface pressure loads, the skin panels are subject to inplane loads associated with deformation of the vehicle as a whole. Vehicle loads were predicted for 14 conditions representing critical points in the flight trajectory, including taxi, ascent, cruise, and descent. The thermomechanical loads were supplied by MDC and are based on a linear NASTRAN finite element model of a blended wing vehicle configuration. The model includes effects of flight maneuvers, aerodynamic surface pressures, and thermal growth due to unequal vehicle heating. For both panels the local thermomechanical forces, acoustic pressure, and through-thickness temperature gradient for each condition were determined using simplified models for the skin panels and models for the aeroacoustic loads.

The vehicle loads are given in Tables E-1 through E-4. The sign convention is shown in Figure E-1. The panels are designed so that vehicle loads are transferred as membrane loads. Bending moments in the panel are induced only by the aerodynamic pressures on the external panel skins. The relative magnitude of the membrane forces will be much greater than the bending moments since local aerodynamic forces are small. Thus, the panels are designed as membrane elements which transfer forces biaxially. Case 9 tends to be the critical case. The ramp panel is a thermal shield and bears no vehicle carry-through loads.

838PROP/3-E.BB
12-11-89

Table E-1. Thermomechanical Running Loads on Forebody Panel.

Condition No.	N _x (lb/in.)	N _y (lb/in.)	N _{xy} (lb/in.)	M _x (in.-lb/in.)	M _y (in.-lb/in.)	M _{xy} (in.-lb/in.)	OML Temp (°F)	Δ T (°F)	Pressure (psi)
1 Mechanical	-16	69	-7	0	0	0	70	0	0.00
Thermal	1	-3	1	0	0	0			
2 Mechanical	1158	-241	94	33	37	1	200	0	-0.83
Thermal	63	34	-9	0	0	0			
3 Mechanical	135	-88	34	37	-44	1	504	0	-0.74
Thermal	191	112	-23	0	0	0			
4 Mechanical	-376	48	27	11	-14	0	504	0	-0.18
Thermal	191	112	-23	0	0	0			
5 Mechanical	291	-176	61	46	-54	1	1350	0	-0.95
Thermal	540	241	-90	-7	-15	0			
6 Mechanical	-167	-77	15	20	-24	0	1350	0	-0.38
Thermal	540	241	-90	-7	-15	0			
7 Mechanical	162	-130	41	38	-45	1	1292	0	-0.77
Thermal	1153	666	-198	17	-24	0			
8 Mechanical	-217	-57	15	19	-22	0	1292	0	-0.34
Thermal	1153	666	-198	17	-24	0			
9 Mechanical	130	-55	23	16	-19	0	1826	0	-0.32
Thermal	1784	821	-225	-22	-31	0			
10 Mechanical	-7	-38	9	6	-7	0	1826	0	-0.13
Thermal	1784	821	-225	-22	-31	0			
11 Mechanical	68	-29	12	8	-10	0	1422	0	0.00
Thermal	1493	623	-164	-18	-22	0			
12 Mechanical	-4	-20	5	0	0	0	1422	0	0.00
Thermal	1493	623	-164	-18	-22	0			
13 Mechanical	65	-52	17	15	-18	0	864	0	0.00
Thermal	905	414	-116	-11	-16	0			
14 Mechanical	-87	-23	6	7	-9	0	864	0	0.00
Thermal	905	414	-116	-11	-16	0			

838PROP/3-T2-3.BB
12-11-89

Table E-2. Thermomechanical Running Loads on Horizontal Stabilizer Panel.

Condition No.	N _x (lb/in.)	N _y (lb/in.)	N _{xy} (lb/in.)	M _x (in.-lb/in.)	M _y (in.-lb/in.)	M _{xy} (in.-lb/in.)	OML Temp (°F)	Δ T (°F)	Pressure (psi)
1 Mechanical	-85	-7	20	16	0	0	-120	0	0
Thermal	0	0	0	0	0	0			
2 Mechanical	2687	217	-688	-455	0	14	200	20	0
Thermal	0	0	0	0	0	0			
3 Mechanical	-498	-38	114	115	0	7	491	188	0.29
Thermal	18	0	0	-6	0	0			
4 Mechanical	-1653	-111	384	322	0	17	491	188	0.68
Thermal	18	0	0	-6	0	0			
5 Mechanical	-1438	-96	299	246	0	17	1408	369	0.39
Thermal	387	-63	100	-533	0	-41			
6 Mechanical	-2802	-182	597	515	0	28	1408	369	0.50
Thermal	387	-63	100	-533	0	-41			
7 Mechanical	-442	-27	78	89	0	0	904	143	0.15
Thermal	-134	67	-61	91	0	5			
8 Mechanical	-1304	-74	239	248	0	12	904	143	0.22
Thermal	-134	67	-61	91	0	5			
9 Mechanical	222	14	-36	-56	0	0	1112	79	-0.19
Thermal	380	87	59	-219	0	-19			
10 Mechanical	0	0	0	0	0	0	1112	79	0.01
Thermal	380	87	59	-219	0	-19			
11 Mechanical	116	7	-19	-29	0	0	650	100	0
Thermal	311	133	-89	100	0	0			
12 Mechanical	0	0	0	0	0	0	650	100	0
Thermal	311	133	-89	100	0	0			
13 Mechanical	-177	-11	31	36	0	0	639	50	0
Thermal	130	56	-48	44	0	0			
14 Mechanical	-523	-30	96	99	0	0	639	50	0
Thermal	130	56	-48	44	0	0			

838PROP/3-T2-4.BB
12-11-89

Table E-3. Thermomechanical Running Loads on Aftbody Panel.

Condition No.	N _x (lb/in.)	N _y (lb/in.)	N _{xy} (lb/in.)	M _x (in.-lb/in.)	M _y (in.-lb/in.)	M _{xy} (in.-lb/in.)	OML Temp (°F)	Δ T (°F)	Pressure (psi)
1 Mechanical	772	93	35	-59	0	0	70	4	0
Thermal	11	22	6	-26	0	0			
2 Mechanical	-2273	140	-123	151	0	-1	200	20	0.44
Thermal	-100	122	44	-81	0	1			
3 Mechanical	-17	26	16	-29	0	0	488	144	-0.01
Thermal	-288	337	-129	-193	0	2			
4 Mechanical	797	28	38	68	0	0	488	144	-0.58
Thermal	-288	337	-129	-193	0	2			
5 Mechanical	-692	-15	46	29	0	0	1258	368	0.03
Thermal	-773	870	-268	-445	0	5			
6 Mechanical	192	-18	18	-57	0	0	1258	368	-0.33
Thermal	-773	870	-268	-445	0	5			
7 Mechanical	-291	-7	20	-10	0	0	1604	72	-0.04
Thermal	-1195	956	-340	-527	0	5			
8 Mechanical	434	26	22	37	0	0	1604	72	-0.32
Thermal	-1195	956	-340	-527	0	5			
9 Mechanical	-84	-27	-12	17	0	0	902	137	0
Thermal	-667	260	-186	149	0	-2			
10 Mechanical	-71	24	-4	-9	0	0	902	137	-0.04
Thermal	-667	260	-186	149	0	-2			
11 Mechanical	-44	-14	-6	9	0	0	619	163	0
Thermal	-119	196	-42	62	0	-1			
12 Mechanical	-37	12	-2	0	0	0	619	163	0
Thermal	-119	196	-42	62	0	-1			
13 Mechanical	-117	-3	8	9	0	0	582	167	0
Thermal	-349	176	-155	-98	0	-1			
14 Mechanical	174	11	9	15	0	0	582	167	0
Thermal	-349	176	-155	-98	0	-1			

838PROP/3-T2-5.BB
12-11-89

E-4

Table E-4. Thermomechanical Running Loads on Actively Cooled Panel.

Condition No.	N_x (lb/in.)	N_y (lb/in.)	N_{xy} (lb/in.)	M_x (in.-lb/in.)	M_y (in.-lb/in.)	M_{xy} (in.-lb/in.)	Safety Factor Included
1 Mechanical	-55	-69	-52	-8	-19	-1	1.5
Thermal	-192	-53	13	-6	-5	1	1.0
2 Mechanical	1258	178	-238	141	-110	-37	1.5
Thermal	-95	-41	11	0	0	1	1.0
3 Mechanical	-29	60	71	40	79	11	1.5
Thermal	155	41	19	0	0	0	1.0
4 Mechanical	-212	-49	70	46	76	-13	1.5
Thermal	155	41	19	0	0	0	1.0
5 Mechanical	-274	78	190	64	137	16	1.5
Thermal	345	29	44	10	0	0	1.0
6 Mechanical	-456	-69	187	68	133	17	1.5
Thermal	345	29	44	10	0	0	1.0
7 Mechanical	395	-38	-42	43	-127	-19	1.5
Thermal	523	165	-4	19	-12	-2	1.0
8 Mechanical	273	-150	-51	46	130	-21	1.5
Thermal	523	165	-4	19	-12	-2	1.0
9 Mechanical	813	-104	-212	45	-167	-26	1.5
Thermal	299	151	-33	12	13	-2	1.0
10 Mechanical	791	-112	-196	48	-163	-26	1.5
Thermal	299	151	-33	12	13	-2	1.0
11 Mechanical	424	-54	-110	24	-87	-13	1.5
Thermal	169	231	-61	-7	16	-3	1.0
12 Mechanical	412	-59	-102	25	-85	-14	1.5
Thermal	169	231	-61	-7	16	-3	1.0
13 Mechanical	158	-15	-17	17	-51	-8	1.5
Thermal	-273	32	-25	-10	11	-1	1.0
14 Mechanical	109	-60	-20	19	52	-8	1.5
Thermal	-273	32	-25	-10	11	-1	1.0

838PROP/3-T2-6.BB
12-11-89

POSITIVE LOADS SIGN CONVENTION:

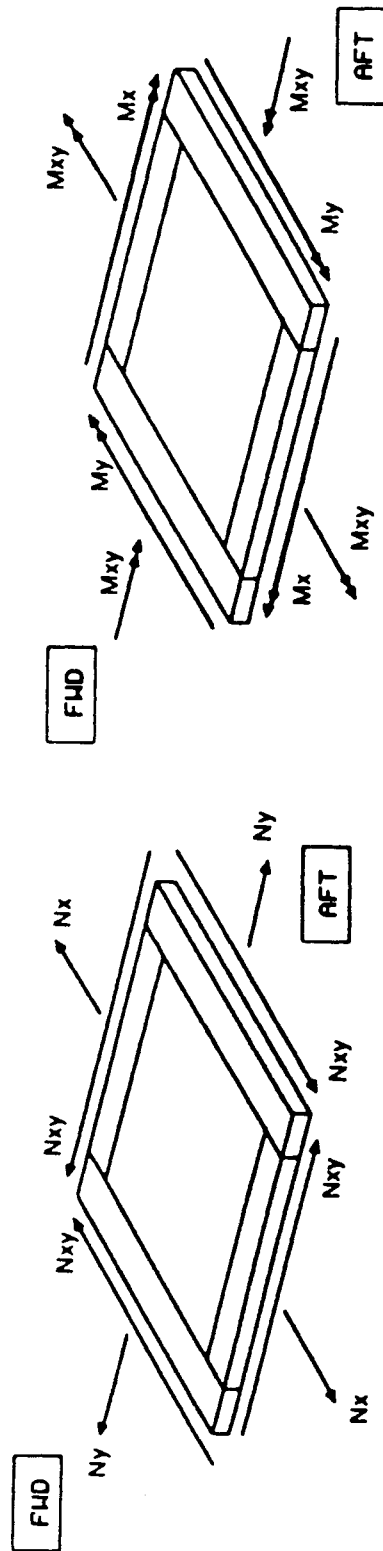


Figure E-1. Positive Load Sign Convention.